Undefined myasthenias: clinical and molecular characterisation and optimised therapy



Pedro M Rodríguez Cruz
Green Templeton College
University of Oxford

A thesis submitted for the degree of
Doctor of Philosophy
[Michaelmas Term 2017]

Approximate word count 48,000

In loving memory of my grandmother Teresa

and my dearest friends Pablo Osante and Janos Nagy

Authorship Statement

The DPhil thesis I am submitting is entirely my own work except where otherwise indicated.

Abstract

Congenital myasthenic syndromes (CMS) are a group of heterogeneous disorders caused by mutations in genes encoding for proteins that are essential for neuromuscular transmission. All CMS share the clinical feature of fatigable muscle weakness. The differential diagnosis of CMS is wide, with a range of diseases going from autoimmune myasthenia gravis to muscle disorders. In this thesis, it was shown that measuring antibodies to clustered acetylcholine receptors (AChRs) by cell-based assay is helpful in the differential diagnosis of CMS.

The findings of the current investigations showed that mutations in *COL13A1,* encoding the Collagen Type XIII α1 chain, were responsible for the symptoms of several patients with previously undefined myasthenias. In addition, this work described the clinical and complementary features of a novel CMS subtype due to mutations in the glycosylation-pathway gene *GMPPB*. Investigations on a novel *MUSK* missense mutation (p.Ala617Val) uncovered previously unrecognised mechanisms of how levels of MuSK phosphorylation are critical to maintain synaptic structure, and guided suitable treatment for the patient.

The study on the clinical and molecular basis of stridor, a novel clinical feature recently identified in patients with DOK7-CMS, prompted the identification of a novel DOK7 isoform, which warrants further investigation to elucidate its role in AChR clustering.

Finally, the therapy of patients with severe AChR-deficiency was optimised thanks to a case series study that showed a robust improvement following the addition of ß2-adrenergic agonists to their long-term treatment regime that included pyridostigmine.

Acknowledgements

I am deeply grateful to my supervisors, Dr Jacqueline Palace and Prof David Beeson for giving me the life-changing opportunity to undertake DPhil studies in Clinical Neurosciences at the University of Oxford. I would like to acknowledge their guidance, constant availability, and continuous support along this journey, which has been crucial for the completion of this thesis.

I would like to thank all the members of the CMS service at the John Radcliffe Hospital in Oxford including Dr Sandeep Jayawant, Dr Stephanie Robb, and Dr Sithara Ramdas for sharing their knowledge on the care of patients with myasthenia. Special thanks go to the CMS coordinator, Birute Saul, for her outstanding work and dedication to this service, and for taking good care of me.

I am deeply indebted to all members of the Neuroscience group at the Weatherall Institute of Molecular Medicine for the training I received in molecular biology. I am greatly indebted to Dr Jonathan Cheung for sharing his technical knowledge and teaching me the basics of laboratory work that helped me to become independent. I would also like to acknowledge his continuous support and patience in answering an endless number of questions. Special thanks to Dr Judy Cossins who has been an additional supervisor of all my work. I am also grateful to Dr Wei Wei Luo and Susan Maxwell for their teaching and help in sorting out all kind of laboratory issues.

Mr Stuart Winter (ENT Department) and Drs Stephen Amato and Ketan Shah (Pathology

Department) were of great help in providing me with the human laryngeal samples.

Furthermore, I would like to thank Prof Angela Vincent for her useful comments, discussions and advice, and for sharing precious samples of patients with SNMG for the antibody work of this thesis. Dr Isabel Leite was of great help in the work done on antibodies to clustered-AChRs and I am very grateful for this.

To the members of my thesis committee Dr David Hilton-Jones and Dr Steve Twigg. I would like to thank them for the time they took to review my work and for their useful comments. Many thanks to my college advisor Prof Keith Frayn for his continuous support during this period.

I am also grateful to Prof Frank Mastaglia (Western Australia Neuromuscular Research Institute) for supporting my application as a DPhil student. I cannot obviate to mention Dr Macarena Cabrera (Seville, Spain) and Dr José Luis Muñoz Blanco (Madrid, Spain) from whom I heard the words DOK7 and MuSK for the first time and somehow connected me with Oxford. I would also like to thank my tutor during my medical training in Madrid, Dr David Ezpeleta, for training me in the development of medical communication skills. Furthermore, I would like to thank my colleagues in Madrid Dr Juan Cuello and Dr Javier Pérez Sánchez for sharing their motivation and enthusiasm in Clinical Neurology and encouraging me to take this further.

The Clinical Fellows at the West Wing of the John Radcliffe hospital Drs George Tackley, Ruth Geraldes, and Maciej Jurynczyk have been of enormous importance in this period.

They have been close friends and more than a family to me. I would like to thank them for being of great help to overcome everyday difficulties. I am indebted to Adriana Roca and Dr Silvia Messina for their support and to Dr Manon Lee and Dr Romina Mariano for proof-reading this thesis. I am also thankful to have known Dr Joana Domingos who I will always remember for her enthusiasm and motivation for research.

I am grateful to my lifelong friends Alvaro Briales, Antonio Ramos, Carlos Fernandez, Javier Teigell, and Miguel López for their friendship, which is one of the most precious things I have. In addition, Carlos helped me to produce some of the graphic illustrations presented in this work, and I would like to thank him for that.

To my parents, Carmen and Pedro, for giving me an education. I am very grateful to my family for their care and support throughout life and for providing me with the skills necessary to undertake this opportunity. Special thanks to my mother for teaching me the "art of being curious" without which I would have never pursued this challenge. Special thanks to my father for teaching me how to persevere and be resilient in the face of everyday challenges. I would like to thank my aunt Encarna, my late grandmother Teresa, and my grandfather Francisco for all the love they have given me.

Finally, I am most grateful to my partner Sophie Janet for her outstanding patience, support and love during these years, which have given me, without a doubt, the strength, happiness and motivation necessary to complete this journey. Furthermore, I would like to thank Sophie for bringing our daughter Zoe to this world, which is the most outstanding proof of our love and commitment to build a life together.

Table of Contents

Authorship Statement 1

Abstract 2

Acknowledgements 3

Table of Contents 6

List of Figures 12

List of Tables 17

Abbreviations 18

Publications 20

Chapter 1: The Neuromuscular Junction and the Wide Heterogeneity of Congenital Myasthenic Syndromes 22

1.1 Introduction 22
1.2 Clinical diagnosis 22
1.3 Genetic diagnosis 25
1.4 Epidemiology and genetics 29
1.5 CMS and the margin of safety of neuromuscular transmission 30
1.6 Presynaptic syndromes 30
1.6.1 Axonal transport 32
1.6.2 Synthesis and recycling of acetylcholine 32
1.6.3 Synaptic vesicles exocytosis 35
1.7 Synaptic or basal-lamina associated syndromes 38
1.8 Postsynaptic syndromes 42
1.8.1 Primary AChR deficiency 42
1.8.2 Kinetic abnormalities of the AChR (with or without AChR deficiency) 43
1.8.3 Defects within the AChR-clustering pathway 45
1.8.4 Rapsyn deficiency 50
1.9 CMS due to mutations in genes encoding proteins without specific NMJ function 52
1.10 Treatment 58
1.11 Objectives 60

Chapter 2: Patients, Materials and Methods 63

2.1 Patients 63
2.1.1 CMS patients 63
2.1.2 Muscle biopsy samples 63
2.1.3 Laryngeal muscle samples 63
2.1.4 Serum samples 64
2.2 DNA methods 64
2.2.1 DNA extraction from bacterial cultures 64
2.2.2 DNA extraction from mammalian cells 65
2.2.3 Resolution of DNA in agarose gels 65
2.2.4 DNA extraction from agarose gels 65
2.2.5 DNA Sequencing 65
2.2.6 Polymerase chain reaction (PCR) 66

2.2.7 Mutagenesis 68
2.2.8 Molecular cloning 70
2.2.9 Plasmids 73
2.3 CRISPR/Cas9 Genome engineering system 75
2.3.1 Introduction to CRISPR/Cas9 75
2.3.2 Generation of the CRISPR-Cas9 construct 77
2.3.3 Generation of Musk KO C2C12 muscle cell lines using the CRISPR-Cas9n system 79
2.4 RNA methods 80
2.4.1 RNA extraction from mammalian cells 80
2.4.2 RNA extraction from muscle tissue 81
2.4.3 Removal of DNA from RNA preparations 82
2.4.4 Reverse-transcription PCR 83
2.4.5 Real time PCR (qPCR) 83
2.5 Protein methods 87
2.5.1 Protein extraction from cell cultures 87
2.5.2 Protein extraction form muscle tissue 87
2.5.3 Determination of protein concentration 88
2.5.4 Sodium dodecyl sulphate polyacrylamide gel electrophoresis 88
2.5.5 Blue native polyacrylamide gel electrophoresis 90
2.5.6 Protein gel staining methods 92
2.5.7 Immunoprecipitation and coimmunoprecipitation assays 94
2.5.8 Phosphorylation assays 96
2.5.9 Cyclohexamide chase assay 97
2.5.10 Fluorescence-activated cell sorting 97
2.5.11 AChR-clustering assay 98
2.5.12 Immunofluorescence staining of muscle sections 99
2.5.13 Fibre typing of muscle sections 101
2.5.14 Immunofluorescence labelling of teased muscle fibres 102
2.5.15 Immunocytofluorescence 103
2.6 Mass spectrometry methods 104
2.6.1 LC-MS/MS analysis 104
2.6.2 Data processing and database analysis 105
2.7 Bacterial cell culture 105
2.7.1 Type of cells used 105
2.7.2 Transformations 106
2.7.3 Growth conditions 106
2.8 Mammalian cell culture 107
2.8.1 Growth conditions 107
2.8.2 Differentiation conditions 107
2.8.3 Selection conditions 108
2.8.4 Polyethylenamine transfection 108
2.8.5 Electroporation transfection 109
2.8.6 Retroviral production and infection 110
2.8.7 Production of recombinant agrin and soluble COL13A1 110
2.9 Cell based assay for the detection of autoantibodies to COL13A1 111
2.9.1 Developing a cell-based assay 111
2.9.2 Cell-based assay scoring 112
2.9.3 Methodology for the testing and interpretation of CBA results 113
2.10 Standard Buffers 113
2.11 In vivo methods 114
2.11.1 Mouse In-vivo electroporation 114

2.11.2 Quantitative Myasthenia Gravis (QMG) test 115
2.12 Microscopy methods 117
2.12.1 Fluorescence microscopy 117
2.12.2 Confocal microscopy 117
2.12.3 Quantification of mean fluorescence intensity 117
2.12.4 Quantification of AChR clusters 118
2.13 Bioinformatics 119
2.14 Statistical analysis 120

Chapter 3: The Differential Diagnosis of CMS and SNMG: Usefulness of the Clustered-AChR Cell-based Assay 121

3.1 Introduction 121
3.1.1 Seronegative myasthenia gravis 122
3.1.2 Congenital myopathies with abnormalities in the neuromuscular transmission 125
3.2 Aims 126
3.3 Clinical material 126
3.4 Subjects included in the study 128
3.5 Antibody results on RIA and CBA in total cohort 129
3.6 Clinical characterisation of MG patients with positive CBA and negative results on RIA 130
3.7 Comparison with MG subjects without clustered–AChR antibodies 133
3.8 Discussion 135

Chapter 4: Clinical and Molecular Characterisation of Congenital Myasthenic Syndrome due to Mutations in *COL13A1* 139

4.1 Introduction 139
4.2 Aims 143
4.3 Clinical features of individuals with mutations in *COL13A1* 143
4.3 Genetic results 151
4.3.1 Identification of mutations in COL13A1 151
4.3.2 Segregation analysis of COL13A1 mutations 153
4.4 Study of COL13A1 predicted cleavage site 153
4.5 COL13A1 expression in human muscle tissue 157
4.5.1 Validation of antibodies against the N- and C-terminus domains of COL13A1 157
4.5.2 Immunofluorescence of human muscle sections in control and affected individuals 162
4.5.3 COL13A1 expression studies in human muscle by western blot 168
4.5.4 Study of COL13A1 transcripts in human muscle 169
4.6 COL13A1 interacting partners 171
4.6.1 Study of COL13A1 – Collagen Q interaction 171
4.6.2 Study of COL13A1 – MUSK / LRP4 /Agrin interaction 173
4.7 Effect of *COL13A1* c.1171delG mutation on acetylcholinesterase expression 176
4.8 Effect of *COL13A1* mutations on protein expression 178
4.9 Study of functional effects of COL13A1 on AChR clustering 179
4.9.1 Incubation of C2C12 myotubes with the soluble fraction of COL13A1 179
4.9.2 Effect of the COL13A1 c.1171delG mutation on AChR clustering 182
4.10 Screening of autoantibodies to COL13A1 in patients with MG 183
4.10.1 Cohort of patients with MG 183
4.10.2 Disease control cohort 183
4.10.3 Developing a CBA for the detection of antibodies to COL13A1 186
4.10.4 Results of the COL13A1 cell-based assay in the MG cohort 189

4.10.5 Colocalisation of human IgG and guinea pig anti-COL13A1 antibody 192
4.10.6 Results of COL13A1 cell-based assay in the disease control cohort 193
4.11 Discussion 195

Chapter 5: Clinical Characterisation of the Myasthenic Syndrome Arising from Mutations in *GMPPB* 201

5.1 Introduction 201
5.2 Aims 204
5.3 Patients included in the study 204
5.4 Mutations identified in GMPPB 204
5.5 Clinical features 206
5.5.1 Clinical presentation 206
5.5.2 Pattern of weakness at assessment 207
5.5.3 Additional clinical features 207
5.5.4 Course of disease 208
5.5.5 Response to treatment 209
5.6 Investigations 209
5.6.1 Neurophysiological studies 209
5.6.2 Cardiac studies 212
5.6.3 Muscle biopsy 212
5.6.4 Muscle MRI 212
5.6.5 Serum creatine kinase values 216
5.7 Discussion 217

Chapter 6: Unravelling Impaired Mechanisms of Neuromuscular Transmission in CMS due to *MUSK* mutations 223

6.1 Introduction 223
6.1.1 MuSK kinase activity and the Agrin-LRP4-MuSK-DOK7 pathway 224
6.1.2 Regulation of MuSK kinase activity 224
6.1.3 Mutations in MUSK 227
6.2 Aims 227
6.3 Clinical features of the patient with congenital myasthenic syndrome 228
6.4 Identification of *MUSK* mutations 228
6.5 Molecular modelling of *MUSK* mutations 230
6.6 Generation of *Musk* KO C2C12 muscle cells using the CRISPR-Cas9n system 232
6.7 Functional effects of MuSK variants on agrin-induced AChR clustering 233
6.7.1 Retroviral infection of MuSK KO cell line 233
6.7.2 Effect of MuSK variants on AChR clusters formation 233
6.7.3 Effect of MuSK variants on AChR clusters formation in the presence of non-saturating concentrations of agrin 238
6.7.4 Effect of MuSK variants on the stability of AChR clusters 239
6.8 Effect of MuSK variants on protein expression, localisation and stability 244
6.8.1 Study of MuSK protein expression and localisation 244
6.8.2 Study of MuSK protein stability 244
6.9 Effect of MuSK A617V on MuSK interaction with LRP4 and DOK7 246
6.10 Effect of MuSK A617V on MuSK phosphorylation 248
6.10.1 Study of MuSK phosphorylation in HEK-293T cells 248
6.10.2 Study of MuSK phosphorylation in C2C12 muscle cells 250
6.11 Study of potential molecular mechanisms leading to abnormal MuSK phosphorylation 254
6.11.1 Dysregulation of MuSK kinase activity 254

6.11.2 Abnormal dimerisation of MuSK 256
6.12 Effect of MuSK variants in vivo 262
6.14 Response to treatment with ß2-adrenergic agonists 264
6.15 Discussion 265

Chapter 7: Clinical and Molecular Basis of Stridor in Patients with CMS and *DOK7* mutations 270

7.1 Introduction 270
7.1.1 Stridor in DOK7-CMS 271
7.1.2 Stridor in other myasthenic disorders 272
7.1.3 The mechanisms underlying stridor in DOK7-CMS 272
7.2 Aims 273
7.3 Presence of stridor in the different CMS-subtypes 275
7.4 Clinical features of stridor in patients with DOK7-CMS and other CMS-subtypes 276
7.4.1 Clinical presentation 276
7.4.2 Outcome and course of stridor 277
7.4.3 Additional clinical features related to abnormalities in the vocal cords 278
7.5 Complementary findings in patients with stridor 278
7.6 Phenotype-genotype correlation of patients with *DOK7* mutations and stridor 280
7.7 Study of MuSK and DOK7 expression by indirect immunofluorescence 286
7.7.1 Optimisation of MuSK and DOK7 fluorescence staining in muscle sections 286
7.7.2 Quantification of MuSK and DOK7 fluorescence intensity at endplates from human laryngeal muscles 288
7.8 Study of MuSK and DOK7 expression in fast and slow muscle fibres by indirect immunofluorescence 290
7.8.1 Fibre typing of human PCA muscle 290
7.8.2 Quantification of MuSK and DOK7 expression in PCA fast and slow muscle fibres 291
7.9 Study of MuSK and DOK7 expression in human laryngeal muscles by western blotting 294
7.9.1 DOK7 protein expression 294
7.9.2 MuSK protein expression 294
7.10 Study of DOK7 muscle isoforms in human laryngeal muscles 297
7.10.1 Study of DOK7 isoforms by RT_PCR 298
7.10.2 Study of DOK7 isoforms by Mass Spectrometry 299
7.10.3 Study of DOK7 isoforms by site-directed mutagenesis of DOK7 Met residues 306
7.11 Study of NMJ gene expression levels in human laryngeal muscles by QPCR 307
7.11.1 mRNA expression levels normalised to GAPDH 307
7.11.2 mRNA expression levels normalised to CHRNE & GAPDH
7.12 Discussion 311

Chapter 8: Optimisation of Pharmacological Therapy in Severe Cases of AChR-deficiency due to *CHRNE* Mutations 317

8.1 Introduction 317
8.2 Aims 318
8.3 Study design 318
8.3.1 Inclusion criteria 318
8.3.2 Medication dosages 319
8.3.3 Clinical outcomes 319
8.4 Patients included in the study 319
8.4.1 Case 1 (Patient 2) 321
8.4.2 Case 2 (Patient 4) 323

8.5 Medication dosage and adverse effects **323**
8.6 Quantitative myasthenia gravis (severity) score **324**
8.7 Quantitative myasthenia gravis score components **324**
8.8 Mobility scores **326**
8.9 Long term follow-up analysis **326**
8.10 Discussion **327**

Chapter 9: Conclusions and Future Perspectives **332**
9.1 Conclusions **332**
9.2 Future perspectives **335**

Bibliography **339**

Appendix **366**
10.1 Generation of C2C12 *Col13a1* 1171delG cell line **366**
10.2 Generation of C2C12 *MuSK* KO cell lines **367**
10.2.1 Use of CRISPR-Cas9 genome engineering system 367
10.2.2 MuSK protein expression in C2C12 Musk KO clonal cell lines 373
10.3 Details of patients with *DOK7* mutations included in this thesis **374**
10.4 Review on congenial myopathies with secondary neuromuscular transmission abnormalities **378**

List of Figures

Figure 1-1. Schematic representation of the neuromuscular junction and the principle molecules involved in congenital myasthenia 23
Figure 1-2. Proposed algorithm for targeted genetic screening of suspected CMS cases. 28
Figure 1-3. Relative frequency of genetically confirmed CMS subtypes in the UK 29
Figure 1-4. Schematic representation of the nerve terminal and the main molecules involved in presynaptic CMS 31
Figure 1-5. Schematic of synaptic vesicles at the active zones of presynaptic terminals 36
Figure 1-6. Schematic representation of the synaptic basal lamina and its main components 38
Figure 1-7. Schematic representation of AChE and its collagenic-like tail 40
Figure 1-8. Schematic representation of the adult AChR and the genetics of AChR-deficiency 42
Figure 1-9. Genetics of CMS due to kinetic abnormalities of the AChR 43
Figure 1-10. Schematic representation of the Agrin-induced AChR clustering andACh-CdK5 dispersal pathways. 46
Figure 1-11. Schematic representation of agrin drawn to linear scale and location of variants reported in the literature. 47
Figure 1-12. Schematic representation of DOK7 drawn to linear scale and localisation of mutations identified in CMS patients referred to Oxford. 50
Figure 1-13. Schematic representation of RAPSN drawn to linear scale and localisation of mutations identified in CMS patients referred to Oxford. 52
Figure 1-14. Schematic representation of the N-glycosylation pathway of proteins and the main molecules involved in CMS. 53
Figure 1-15. Schematic representation of DPAGT1 drawn to linear scale and localisation of mutations identified in patients with CMS and CDG type Ij. 57
Figure 1-16. Treatment strategy at the Oxford CMS Service for most common CMS subtypes 59
Figure 2-1. Outline of COL13A1 cloning into pcDNA3.1/Hygro(+) 67
Figure 2-2. Schematic representation of the CRISPR/Cas9 genome engineering system 71
Figure 2-3. Schematic representation of px335-Musk-Guide A / B cloning process 79
Figure 2-4. Assessment of qPCR primers efficiency and specificity. 84
Figure 2-5. Schematic representation of the AChR clustering assay. 112
Figure 2-6. Visual score used to measure the intensity of the red fluorescent staining after indirect immunofluorescence 112
Figure 2-7. Representative images of muscle endplates for image analysis 110
Figure 2-8. ImageJ macro commands for the analysis of AChR clusters in C2C12 myotubes 111
Figure 2-9. Representative images of ImageJ macro analysis of AChR clusters in C2C12 myotubes and C2C12 *Musk*-KO cells 119
Figure 3-1. Schematic representation of the NMJ and the tests used for the detection of AChR antibodies 124
Figure 3-2. Flowchart showing patients included in the study 128

Figure 3-3. Maximum MGFA and age at onset in patients with antibodies to clustered-AChRs on CBA (negative on RIA) or no detectable AChR antibodies (SNMG)..... 131
Figure 3-4. MGFA post intervention status and age at onset in patients with antibodies to clustered-AChRs on CBA (negative on RIA) or no detectable AChR antibodies (SNMG)..... 133
Figure 4-1. Schematic representation of the COL13A1 main transcript..... 140
Figure 4-2. mRNA expression in normal tissues for *COL13A1* gene 142
Figure 4-3. Clinical features of individuals with *COL13A1* mutations..... 146
Figure 4-4. Muscle biopsy of Individual I at 6 months of age..... 147
Figure 4-5. Muscle biopsy of Individual I at 6 months of age..... 148
Figure 4-6. Neurophysiological studies of individual 1 at 6 months of age 150
Figure 4-7. Sequence analysis of *COL13A1* mutations and schematic representations of the COL13A1 protein together with the localisation of COL13A1 variants..... 152
Figure 4-8. Segregation analysis of COL13A1 c.523-1del splice-site mutation in family 2 153
Figure 4-9. Analysis of the COL13A1 cleavage site by immunocytofluorescence..... 155
Figure 4-10. Analysis of the COL13A1 cleavage site by western blotting..... 156
Figure 4-11. COL13A1 peptide sequence and immunogenic targets from the different COL13A1 antibodies used in this chapter..... 157
Figure 4-12. Validation of the guinea pig antibody against the COL13A1 C-terminal region 159
Figure 4-13. Validation of the antibody against the N-terminal region of COL13A1 160
Figure 4-14. Specificity of the antibody against the N-terminal region of COL13A1 161
Figure 4-15. Representative images of human muscle endplates stained with an antibody against the C-terminal region of COL13A1 163
Figure 4-16. Representative images of control muscle endplates stained with an antibody against the N-terminal region of COL13A1..... 165
Figure 4-17. Representative images of muscle endplates from individual 1 using antibodies against the N-terminal region of COL13A1 and S100β 167
Figure 4-18. Representative images of muscle endplates from individual 1 using different NMJ markers 168
Figure 4-19. Study of COL13A1 transcripts in human muscle. 170
Figure 4-20. Study of COL13A1-COLQ interaction by immunocytofluorescence..... 172
Figure 4-21. Study of COL13A1-COLQ interaction by coimmunoprecipitation..... 173
Figure 4-22. Study of COL13A1-Agrin / MuSK/ LRP4 interaction by immunocytofluorescence 174
Figure 4-23. Study of COL13A1-MuSK and COL13A1-LRP4 interaction by Co-IP 175
Figure 4-24. Representative images of acetylcholinesterase expression in muscle biopsy from individual 1 carrying the c.1171delG mutation..... 177
Figure 4-25. Western blotting analysis of COL13A1 WT and variants..... 178
Figure 4-26. Quantification of AChR clusters in C2C12 myotubes incubated with the soluble fraction of COL13A1 180
Figure 4-27. Quantification of AChR clusters in C2C12 myotubes incubated with the soluble fraction of COL13A1 181
Figure 4-28. Quantification of AChR clusters in *COL13A1* c.1171delG C2C12 myotubes182
Figure 4-29. Cohort of patients with MG included in the study..... 184
Figure 4-30. Disease control cohort of patients included in the study..... 186

Figure 4-31. Quantification of transfection efficiency in HEK-293T cells expressing WT and membrane bound COL13A1 constructs 187
Figure 4-32. Procedure for the screening of serum samples and interpretation of results for the COL13A1 CBA 188
Figure 4-33. Summary of the screening for COL13A1 antibodies in the MG cohort 189
Figure 4-34. Representative images of the screening for COL13A1 antibodies in the MG cohort 190
Figure 4-35. Representative images of colocalisation experiment 192
Figure 4-36. Summary of the screening for COL13A1 antibodies in the disease control cohort 193
Figure 4-37. Representative images of the screening for COL13A1 antibodies in the disease control cohort. 194
Figure 5-1. Schematic representation of the N-glycosylation pathway 203
Figure 5-2. Schematic representation of GMPPB and location of mutations 210
Figure 5-3. Neurophysiological studies in patients with GMPPB-CMS 210
Figure 5-4 Representative images of muscle biopsy 213
Figure 5-5 Representative images of muscle MRI study from case 2 214
Figure 5-6 Representative images of muscle MRI study from case 4 215
Figure 5-7 CMS subtype-specific serum creatine kinase levels 216
Figure 6-1. Schematic representation of the NMJ and the Agrin-LRP4-MuSK-DOK7 pathway 225
Figure 6-2. Inactive and active states of the LRP4-MuSK complex 225
Figure 6-3. Ribbon diagram of MuSK kinase domain and its regulatory elements 226
Figure 6-4. MUSK domains structure and conservation 230
Figure 6-5. Molecular modelling of MuSK variants 231
Figure 6-6. Effect of MuSK variants on AChR clustering 234
Figure 6-7. Representative images of AChR clusters in C2C12 *Musk* KO cells overexpressing human MuSK WT 228
Figure 6-8. Representative images of AChR clusters in C2C12 *Musk* KO cells overexpressing human MuSK A617V 228
Figure 6-9. Representative images of AChR clusters in C2C12 *Musk* KO cells overexpressing human MuSK C317R 237
Figure 6-10. Quantification of AChR clusters following agrin titration 238
Figure 6-11. Quantification of carbachol-induced AChR-cluster loss (0.4 mM) in C2C12 *Musk* KO myotubes expressing human WT and A617V MuSK 2
Figure 6-11. Quantification of carbachol-induced AChR-cluster loss (2 mM) in C2C12 *Musk* KO myotubes expressing human WT and A617V MuSK 241
Figure 6-13. Representative images of AChR-clusters loss in C2C12 *Musk* KO myotubes expressing human WT and A617V MuSK 243
Figure 6-14. Effect of MuSK variants on protein expression, stability and localisation . 245
Figure 6-15. Coimmunoprecipitation assays of MuSK WT and variants with LRP4 and DOK7 247
Figure 6-16. Effect of MuSK A617V on MuSK tyrosine phosphorylation in HEK-293T cells 249
Figure 6-17. Effect of MuSK variants on MuSK tyrosine phosphorylation in HEK-293T cells 250
Figure 6-18. Effect of MuSK A617V on baseline MuSK kinase activity in muscle cell 251

Figure 6-19. Effect of variants on the temporal activation profile of MuSK in muscle cells 253
Figure 6-20. Effect of MuSK variants on MuSK S751 phosphorylation in muscle cells .. 255
Figure 6-21. Molecular modelling of MuSK KD dimerisation based on the IGF1R KD dimer structure..... 258
Figure 6-22. Molecular modelling of MuSK KD dimerisation based on the EGFR KD dimer structure..... 259
Figure 6-23. Effect of MuSK A617 mutagenesis on MuSK Tyr-P in HEK-293T cells..... 261
Figure 6-24. Representative images of mouse muscles electroporated with MuSK constructs..... 263
Figure 6-25. Clinical response to treatment with ß2-adrenergic agonists..... 264
Figure 7-1. Schematic representation of human laryngeal muscles 274
Figure 7-2. Presence of stridor in the different CMS subtypes 276
Figure 7-3. Laryngoscopy findings in patients with *DOK7* mutations..... 279
Figure 7-4. Circular representation of DOK7 mutations grouped by domains 281
Figure 7-5. Circular presentation of *DOK7* mutations in the non-stridor group 283
Figure 7-6. Circular presentation of *DOK7* mutations in the stridor group 284
Figure 7-7. Frequency and distribution of DOK7 mutations 285
Figure 7-8. Representative images of human laryngeal muscle endplates stained with antibodies to DOK7 and MuSK..... 287
Figure 7-9. Representative images of human laryngeal muscle endplates stained with antibodies to DOK7 and MuSK..... 289
Figure 7-10. Photomicrographs of immunohistochemical staining for slow and fast myosin in PCA muscle sections 291
Figure 7-11. Representative images and quantification of DOK7 expression in endplates from fast and slow muscle fibres 292
Figure 7-12. Representative images and quantification of MuSK expression in endplates from fast and slow muscle fibres 293
Figure 7-13. Western blot analysis of DOK7 expression in human PCA and IA muscles 295
Figure 7-14. Western blot analysis of MuSK expression in human PCA and IA muscles 296
Figure 7-15. Resolution of PCR products encompassing DOK7 amplification in human laryngeal muscles..... 298
Figure 7-16. DOK7 immunoprecipitation from HEK-293T cells..... 299
Figure 7-17. Silver stain in-gel protein detection following DOK7-IP 300
Figure 7-18. Analysis of DOK7 peptides sequence data (higher protein band) 303
Figure 7-19. Analysis of peptides sequence data (lower protein band) 304
Figure 7-20. Alignment of DOK7 protein isoforms 1/2/3/4 and peptides sequences obtained by tandem mass spectrometry analysis of the lower protein band 305
Figure 7-21. DOK7 expression following site-directed mutagenesis of methionine residues..... 306
Figure 7-22. mRNA expression levels in PCA and IA muscle normalised to GAPDH 301
Figure 7-23. mRNA expression levels in PCA and IA muscle normalised to CHRNE & GAPDH 310
Figure 8-1. Representative images showing the response to salbutamol in Patient 2 .. 322
Figure 8-2. Change in performance for the QMG score 324
Figure 8-3. Change in performance for subcomponents of the QMG score..... 325
Figure 8-4. Long-term follow-up in performance for the QMG score. 327

Figure 9-1. Representative images of AChR clusters in C2C12 myotubes engineered with CRISPR-Cas9n after incubation with agrin 368
Figure 9-2. Genotype analysis of CRISPR-generated *Musk* KO clonal line KO-1 370
Figure 9-3. Genotype analysis of CRISPR-generated *Musk* KO clonal line KO-7 371
Figure 9-4. Alignment of amino acid sequences from mutant MuSK alleles in KO-1 and KO-2 clonal cell lines to WT sequence (NP_001032204.2) 373
Figure 9-5. MuSK expression in C2C12 WT and *Musk* KO cell lines 374

List of Tables

Table 1-1. Congenital myopathies with secondary neuromuscular transmission defects 24
Table 1-2. CMS subtypes and associated genes 26
Table 2-1. Oligonucleotides used for Sanger sequencing 66
Table 2-2. Thermocycler conditions used for standard PCR 67
Table 2-3. Thermocycler conditions for high-fidelity PCR 67
Table 2-4. Primers used for the amplification of full-length human DOK7 68
Table 2-5. Sequences of the oligonucleotides used in Site-Directed Mutagenesis 68
Table 2-6. Components of reaction mix for the use of pGEM®-T Easy Vector System 71
Table 2-7. Primers used for the amplification of COL13A1 image clone 73
Table 2-8. Primers to determine the correct orientation of COL13A1 into pcDNA3.1 Hygro(+) 73
Table 2-9. List of plasmids used in this thesis 74
Table 2-10. Musk guides oligonucleotide sequences 77
Table 2-11. Components of annealing and ligation reactions 78
Table 2-12. Sequences of oligonucleotides used for the amplification of *Musk* exon 3 .. 80
Table 2-13. Thermocycler conditions for Reverse transcription PCR (RT-PCR) 83
Table 2-14 Sequences of oligonucleotides used in qPCR reactions 85
Table 2-15. Summary of antibodies used in western blotting 89
Table 2-16. Antibodies used in pull-down assays 95
Table 2-17. Antibodies used for immunofluorescence staining of muscle sections 100
Table 2-18. Conditions for transformation of competent cells 106
Table 2-19. Antibiotics used for selection of bacterial cultures 107
Table 2-20. Growth conditions for mammalian cells 107
Table 2-21. Antibiotics used for selection of mammalian cultures 108
Table 2-22. Conditions used for PEI transfection 109
Table 2-23. Conditions used for electroporation 110
Table 2-24. Quantitate myasthenia gravis score 116
Table 3-1. Patients with other diagnosis included in the study 129
Table 3-2. Clinical features of with antibodies to clustered AChRs (negative on RIA) ... 132
Table 3-3. Clinical features of seronegative MG patients compared to patients with antibodies only to clustered AChRs 134
Table 4-1. Summary of clinical features of individuals with mutations in *COL13A1* 145
Table 4-2. Details of patients with MG included in the study 185
Table 4-3. Clinical data of MG patients with positive results on the COL13A1-CBA. 191
Table 5-1 Clinical features of patients with GMPPB-CMS 205
Table 5-2. Clinical investigations of patients with GMPPB-CMS 211
Table 5-3. CMS subtype-specific serum creatine kinase levels within the Oxford CMS Cohort 217
Table 7-1. Optimisation of MuSK and DOK7 antibodies in muscle tissue 286
Table 7-2. DOK7 transcript variants and DOK7 protein isoforms in *Homo sapiens* 297
Table 8-1. Patients with severe AChR deficiency included in the study 320
Table 8-2. Mean values at baseline and at 6- to 8-month follow-up and percentage increment in relation to baseline measures 326

Abbreviations

α-butx	Alpha-bungarotoxin
AChE	Acetylcholinesterase
AChR	Acetylcholine receptor
BSA	Bovine serum albumin
ADM	*abductor digiti minimi*
ADRB2	Adrenoreceptor β2
APB	*abductor pollicis brevis*
BuTx	Bungarotoxin
CASPR2	Contactin Associated Protein 2
CBA	Cell-based assay
CMAP	Compound muscle action potentials
CMD	Congenital muscular dystrophy
CMS	Congenital myasthenic symptoms
COLQ	Collagen Like Tail Subunit Of Asymmetric Acetylcholinesterase
CRISPR	Clustered regulatory interspaced short palindromic repeats
DMEM	Dulbecco's Modified Eagle's medium
DNA	Deoxyribonucleic acid
DOK7	Docking Protein 7
ECG	*Electrocardiogram*
EDC	*extensor digitorum communis*
EDL	*Extensor digitorum longus*
EGFP	*Enhanced Green Fluorescent Protein*
EMG	Electromyography
FCU	*flexor carpi ulnaris*
FCS	foetal calf serum
FVC	Forced vital capacity
HEK-293T	Human embryonic kidney cells 293T
HPLC	High performance liquid chromatography
HRP	Horseradish peroxidase
IA	Interarytenoid muscle
IP	Immunoprecipitation
IgG	Immunoglobulin G
JMG	Juvenile Myasthenia Gravis
KDa	Kilo Dalton
KO	Knock out
LB	Lysogeny Broth
LCA	Lateral cricoarytenoid muscle
LEMS	Lambert-Eaton myasthenic syndrome
LGMD	Limb-girdle muscular dystrophy
LRP4	LDL Receptor Related Protein 4
MDDGA1	muscular-dystrophy-dystroglycanopathy type A1
MG	Myasthenia gravis

MGFA	Myasthenia gravis foundation of America
MGFA-PIS	Myasthenia gravis foundation of America Post-intervention status
MHC	Myosin heavy chain
MRI	Magnetic resonance imaging
MuSK	Muscle specific kinase
NGS	Next generation sequencing
NMT	Neuromuscular transmission
NRS	*Normal rabbit serum*
OO	Orbicularis oculi
PCR	polymerase chain reaction
PBS	Phosphate Buffer Saline
PBST	Phosphate buffer Saline – 0.1% Tween® 20
PCA	Posterior cricoarytenoid muscle
PEI	Polyethylenamine
PFA	Paraformaldehyde
PSA	Penicillin, Streptomycin and Amphotericin B
PTB	Phosphotyrosine binding domain
QMG	Quantitative Myasthenia Gravis
RIA	Radioimmunoprecipitation assay
RNA	Ribonucleic acid
RNS	Repetitive nerve stimulation
RTKs	Receptor tyrosine kinases
SD	Standard deviation
SEM	Standard error of the mean
SFEMG	Single fibre electromyography
SNAP25B	Synaptosomal-associated protein 25B
SNMG	Seronegative myasthenia gravis
TA	Thyroarytenoid
WB	Western Blot
WCL	Whole cell lysates
WT	Wild type

Publications

List of publications generated within the scope of this thesis in chronological order

1. *The neuromuscular junction and wide heterogeneity of congenital myasthenic syndromes.* Rodriguez Cruz PM, Palace J, Beeson D. Int J Mol Sci. 2018 Jun 5;19(6)

2. *Molecular characterization of congenital myasthenic syndromes in Spain.* Natera-de Benito D, Töpf A, Vilchez JJ, González-Quereda L, Domínguez-Carral J, Díaz-Manera J, Ortez C, Bestué M, Gallano P, Dusl M, Abicht A, Müller JS, Senderek J, García-Ribes A, Muelas N, Evangelista T, Azuma Y, McMacken G, Paipa Merchan A, **Rodríguez Cruz PM**, Camacho A, Jiménez E, Miranda-Herrero MC, Santana-Artiles A, García-Campos O, Dominguez-Rubio R, Olivé M, Colomer J, Beeson D, Lochmüller H, Nascimento A. Neuromuscul Disord. 2017 Dec;27(12):1087-1098.

3. *Clinical features of the myasthenic syndrome arising from mutations in GMPPB.* **Rodríguez Cruz PM**, Belaya K, Basiri K, Sedghi M, Farrugia ME, Holton JL, Liu WW, Maxwell S, Petty R, Walls TJ, Kennett R, Pitt M, Sarkozy A, Parton M, Lochmüller H, Muntoni F, Palace J, Beeson D. J Neurol Neurosurg Psychiatry. 2016 Aug;87(8):802-9.

4. *Muscle MRI in congenital myasthenic syndromes.* Finlayson S, Morrow JM, **Rodriguez Cruz PM**, Sinclair CD, Fischmann A, Thornton JS, Knight S, Norbury R, White M, Al-Hajjar M, Carboni N, Jayawant S, Robb SA, Yousry TA, Beeson D, Palace J. Muscle Nerve 2016 Aug;54(2):211-9

5. *Congenital Myasthenic Syndrome Type 19 Is Caused by Mutations in COL13A1, Encoding the Atypical Non-fibrillar Collagen Type XIII α1 Chain.* Logan CV*, Cossins J*, **Rodríguez Cruz PM***, Parry DA, Maxwell S, Martínez-Martínez P, Riepsaame J, Abdelhamed ZA, Lake AV, Moran M, Robb S, Chow G, Sewry C, Hopkins PM, Sheridan

E, Jayawant S, Palace J, Johnson CA, Beeson D. *Equal contributions. Am J Hum Genet. 2015 Dec 3;97(6):878-85.

6. *Salbutamol and ephedrine in the treatment of severe AChR deficiency syndromes*. **Rodríguez Cruz PM**, Palace J, Ramjattan H, Jayawant S, Robb SA, Beeson D. Neurology. 2015 Sep 22;85(12):1043-7.

7. *Mutations in GMPPB cause congenital myasthenic syndrome and bridge myasthenic disorders with dystroglycanopathies.* Belaya K, **Rodríguez Cruz PM**, Liu WW, Maxwell S, McGowan S, Farrugia ME, Petty R, Walls TJ, Sedghi M, Basiri K, Yue WW, Sarkozy A, Bertoli M, Pitt M, Kennett R, Schaefer A, Bushby K, Parton M, Lochmüller H, Palace J, Muntoni F, Beeson D. Brain. 2015 Sep;138(Pt 9):2493-504

8. *Use of cell-based assays in myasthenia gravis and other antibody-mediated diseases.* **Rodriguez Cruz PM**, Huda S, López-Ruiz P, Vincent A. Exp Neurol. 2015 Aug;270:66-71.

9. *Clinical Features and Diagnostic Usefulness of Antibodies to Clustered Acetylcholine Receptors in the Diagnosis of Seronegative Myasthenia Gravis*. **Rodríguez Cruz PM**, Al-Hajjar M, Huda S, Jacobson L, Woodhall M, Jayawant S, Buckley C, Hilton-Jones D, Beeson D, Vincent A, Leite MI, Palace J. JAMA Neurol. 2015 Jun 1;72(6):642-9.

10. *Congenital myopathies with secondary neuromuscular transmission defects; a case report and review of the literature*. **Rodríguez Cruz PM**, Sewry C, Beeson D, Jayawant S, Squier W, McWilliam R, Palace J. Neuromuscul Disord. 2014 Dec;24(12):1103-10

11. *Inherited disorders of the neuromuscular junction: an update.* **Rodríguez Cruz PM**, Palace J, Beeson D. J Neurol. 2014 Nov;261(11):2234-43.

12. *Congenital myasthenic syndrome and the neuromuscular junction*. **Rodriguez Cruz PM**, Palace J, Beeson D. Curr Opin Neurol. 2014 Oct;27(5):566-75

Chapter 1

The Neuromuscular Junction and the Wide Heterogeneity of Congenital Myasthenic Syndromes

1.1 Introduction

Congenital myasthenic syndromes (CMS) are a group of heterogeneous inherited disorders caused by mutations in genes encoding for proteins that are essential for the integrity of neuromuscular transmission (Palace and Beeson, 2008). At present, mutations in more than 25 different genes are known to cause CMS **(Figure 1-1)**. All subtypes of CMS share the clinical feature of fatigable muscle weakness, but age at onset, presenting symptoms, distribution of weakness, and response to treatment vary, depending on the molecular mechanism that results from the underlying genetic defect.

1.2 Clinical diagnosis

The clinical diagnosis of CMS is based on the presence of fatigable muscle weakness in conjunction with abnormal findings on the neurophysiological studies, in particular decremental response greater than 10% on 3Hz repetitive nerve stimulation (RNS) or abnormal jitter and/or blocking on single-fibre electromyography (SFEMG), and positive response to pharmacological treatment. It is important to understand that although most patients have symptoms from birth or early childhood, some do present later in life during teenage years or adulthood. The classic myasthenic phenotype exhibits weakness of the ocular and facial muscles but certain subtypes can present with apnoeic episodes or isolated limb-girdle weakness, thus increasing the diagnostic challenge.

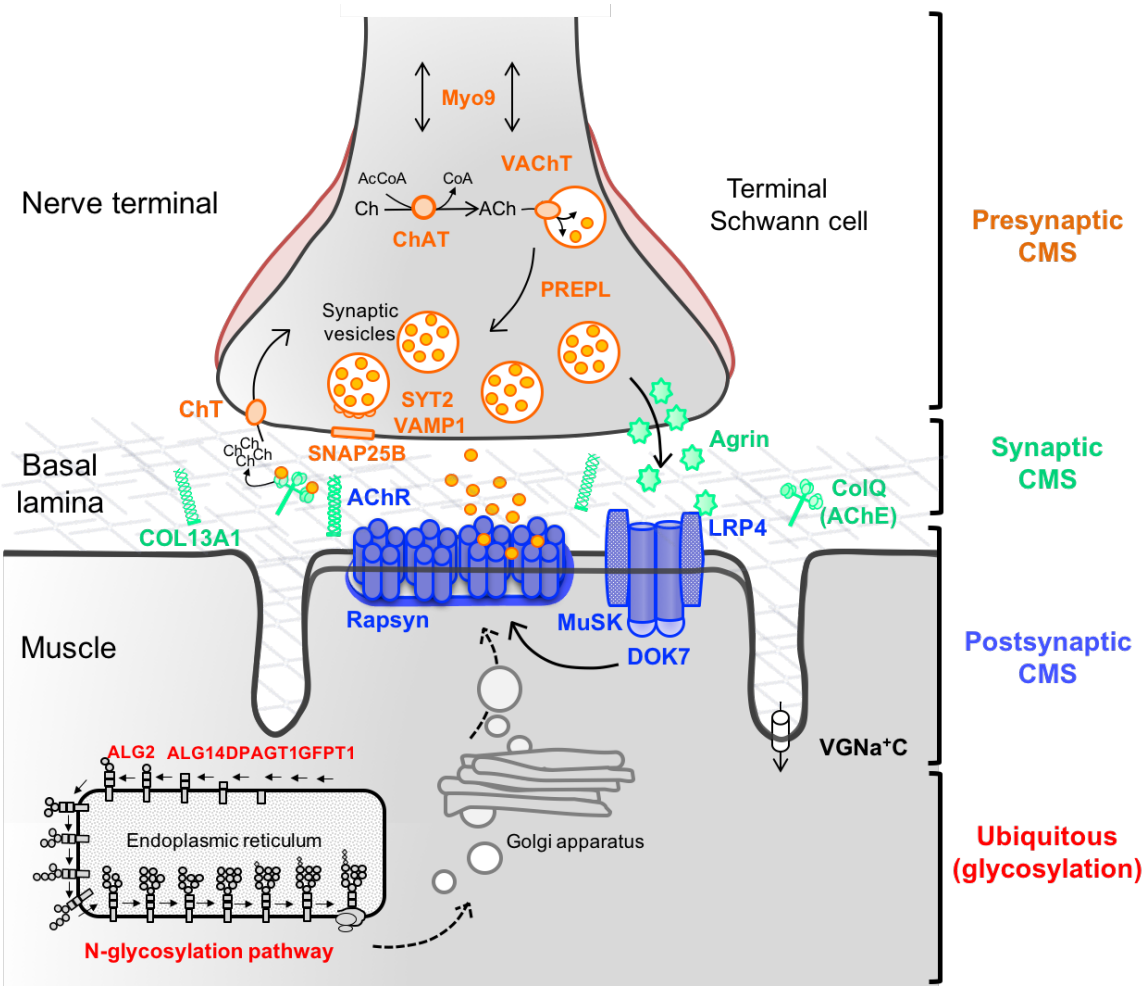


Figure 1-1. Schematic representation of the neuromuscular junction and the principle molecules involved in congenital myasthenia

The heterogeneous spectrum of mutated proteins and molecular mechanisms involved in CMS are illustrated. CMS results from presynaptic (ChAT, ChT, MUNC13-1, MYO9, PREPL, SYT2, VAChT, VAMP1), synaptic basal lamina abnormalities (COLQ, COL13A1) and postsynaptic defects (AChR subunits: α, β, δ and ε, AGRN, DOK7, MUSK, LRP4 and RAPSN). Additionally, the new genes encoding for molecules not confined to the NMJ (GFPT1, DPAGT1, ALG2, ALG14 and GMPPB) are represented in the endoplasmic reticulum (ER), in a simplified view of the N-glycosylation pathway, together with the post-translational modifications of the saccharide structure of the AChR and other NMJ proteins inside the ER and Golgi apparatus, before reaching the muscle cell surface as mature proteins. ACh, acetylcholine; AChE, acetylcholinesterase; AcCoA, acetyl coenzyme A; Ch, choline; VGNa+C, voltage-gated sodium channel.

Testing for antibodies against the acetylcholine receptor (AChR) and the muscle-specific kinase (MuSK) is useful to rule out autoimmune myasthenia gravis (MG). However, negative results do not always exclude the presence of antibodies to the neuromuscular junction (NMJ) since novel targets have been recently identified (Pevzner *et al.*, 2012; Zhang *et al.*, 2014) and antibody testing is not always readily available. An additional challenge are patients whose AChR antibody titre is negative on the classic radioimmunoprecipitation assay (RIA) but are positive for antibodies to clustered AChRs using a cell-based assay (CBA) (Leite *et al.*, 2008). A detailed explanation on the use of the CBA is given in chapter 3, where the use of this test is further explored.

Further complexity is encountered where congenital myopathies associate with secondary neuromuscular transmission abnormalities **(Table 1-1)**. A detailed review on this group of disorders is provided in the appendix.

Table 1-1. Congenital myopathies with secondary neuromuscular transmission defects

Congenital myopathy type	Genes	References
Centronuclear myopathy	*BIN1, DNM2 **	(Claeys *et al.*, 2010) (Gibbs *et al.*, 2013)
X-linked myotubular myopathy	*MTM1*	(Robb *et al.*, 2011)
Congenital fibre type disproportion	*TPM3, RYR1*	(Munot *et al.*, 2010) (Illingworth *et al.*, 2014)
Cap myopathy	*TPM2*	⌈Rodríguez Cruz *et al.*, 2014)

BIN1, Bridging Integrator 1; *DNM2*, Dynamin 2; *MTM1*, Myotubularin 1; *TPM3*, Tropomyosin 3; *RYR1*, Ryanodine Receptor 1; *TPM2*, Tropomyosin 2 (ß). * Additional cases of centronuclear myopathy without genetic diagnosis.

In order to manage patients correctly, it is of crucial importance to make an early and accurate diagnosis. Providing the appropriate symptomatic treatment requires the

genetic subtype to be identified because treatments useful in some CMS subtypes can make other CMS subtypes weaker. Furthermore, identifying a genetic cause for myasthenic weakness can avoid unnecessary immunosuppression and thymectomy. Also, a diagnosis allows the appropriate support and genetic counselling to be delivered.

1.3 Genetic diagnosis

The genetic diagnosis of CMS is complex due to the existence of more than 30 CMS causative genes identified to date **(Table 1-2)**. This number is likely to increase in the future due to the wider availability of Next Generation Sequencing (NGS). Currently, the most utilised approach for the genetic diagnosis of CMS is the targeted screening guided by the clinical phenotype. Features of the phenotype that help to tailor screening include age at onset, distribution of weakness, electromyographic findings and response to treatment **(Figure 1-2)**. The discovery of novel variants within known genes often requires further investigation using functional studies to demonstrate their pathogenicity. Special techniques such as MLPA (Multiplex ligation-dependent probe amplification) are useful to detect medium-sized and big deletions that would otherwise be undetectable by Sanger sequencing.

If genetic screening for candidate genes is negative but the clinical diagnosis of CMS is firm, NGS can be useful to identify novel CMS genes (Taylor *et al.*, 2015). Despite the drop in the cost of NGS technology, the identification of novel genes usually involves an arduous laboratory work to study whether the specific changes in the DNA are responsible for the patient's disease (Sboner *et al.*, 2011). Whole exome sequencing has a number of limitations including reduced coverage (~10% of exons may not be covered at sufficient

levels to reliably determine heterozygous variants), inability to identify large deletions or duplications, mutations in GC-rich regions, and pathogenic variants in non-coding regions. Whole genome sequencing is able to characterise genetic variation in all parts of the genome but cost is higher and interpretation of the results can be challenging due to genetic variation within the general population (Taylor *et al.*, 2015). In all cases, DNA analysis from parents and other family members is useful to interpret the results.

Current technology already allows the use of targeted gene panels for diagnostic testing. In the near feature, it is likely that the continuing decrease in the cost of NGS will allow the use of this technology as first-tier genetic test. In addition, the efforts to characterise the distribution of genetic variation in the population will make easier the interpretation of genetic data (*The 1000 Genomes Project*, 2015; Lek *et al.*, 2016).

Table 1-2. CMS subtypes and associated genes

CMS subtype	Gene
Proteins with defined NMJ function	
Presynaptic	
Choline O-Acetyltransferase	*CHAT*
* Unconventional myosin 9	*MYO9*
* PREPL	*PREPL*
* Vesicular ACh transporter (VAChT)	*SLC18A3*
* High-affinity choline transporter 1 (ChT)	*SLC5A7*
* Synaptosome Associated Protein 25	*SNAP25B*
* Synaptotagmin 2	*SYT2*
* Munc13-1	*UNC13-1*
* Synaptobrevin 1	*VAMP1*
Synaptic	
* Collagen Type XIII Alpha 1 Chain	*COL13A1*
Endplate AChE deficiency	*COLQ*

* Laminin α5 deficiency	*LAMA5*
* Laminin ß2 deficiency	*LAMB2*
Postsynaptic	
Agrin (neuronal)	*AGRN*
Primary AChR deficiency	*CHRNA, CHRNB, CHRND, CHRNE*
Slow channel syndrome	*CHRNA, CHRNB, CHRND, CHRNE*
Fast channel syndrome	*CHRNA, CHRNB, CHRND, CHRNE*
* Low conductance syndrome	*CHRNE*
Escobar syndrome	*CHRNG*
DOK7	*DOK7*
* LRP4	*LRP4*
* MuSK	*MUSK*
* Plectin deficiency	*PLEC1*
Rapsyn	*RAPSN*
* Na channel myasthenia	*SCN4A*
Ubiquitously expressed proteins	
Protein Glycosylation	
* ALG2	*ALG2*
* ALG14	*ALG14*
DPAGT1	*DPAGT1*
GFPT1	*GFPT1*
GMPPB	*GMPPB*
SLC25A1	*SCL25A1*

ALG2, Alpha-1,3/1,6-Mannosyltransferase; ALG14, UDP-N Acetylglucosaminyltransferase Subunit; DOK7, Docking protein 7; DPAGT1, Dolichyl-Phosphate N-Acetylglucosaminephosphotransferase 1; GFPT1, Glutamine-Fructose-6-Phosphate Transaminase 1; GMPPB, GDP-Mannose Pyrophosphorylase B; LRP4, LDL Receptor Related Protein 4; MuSK, Muscle specific kinase; PREPL, Prolyl Endopeptidase-Like gene; SLC25A1, Solute Carrier Family 25 Member 1.

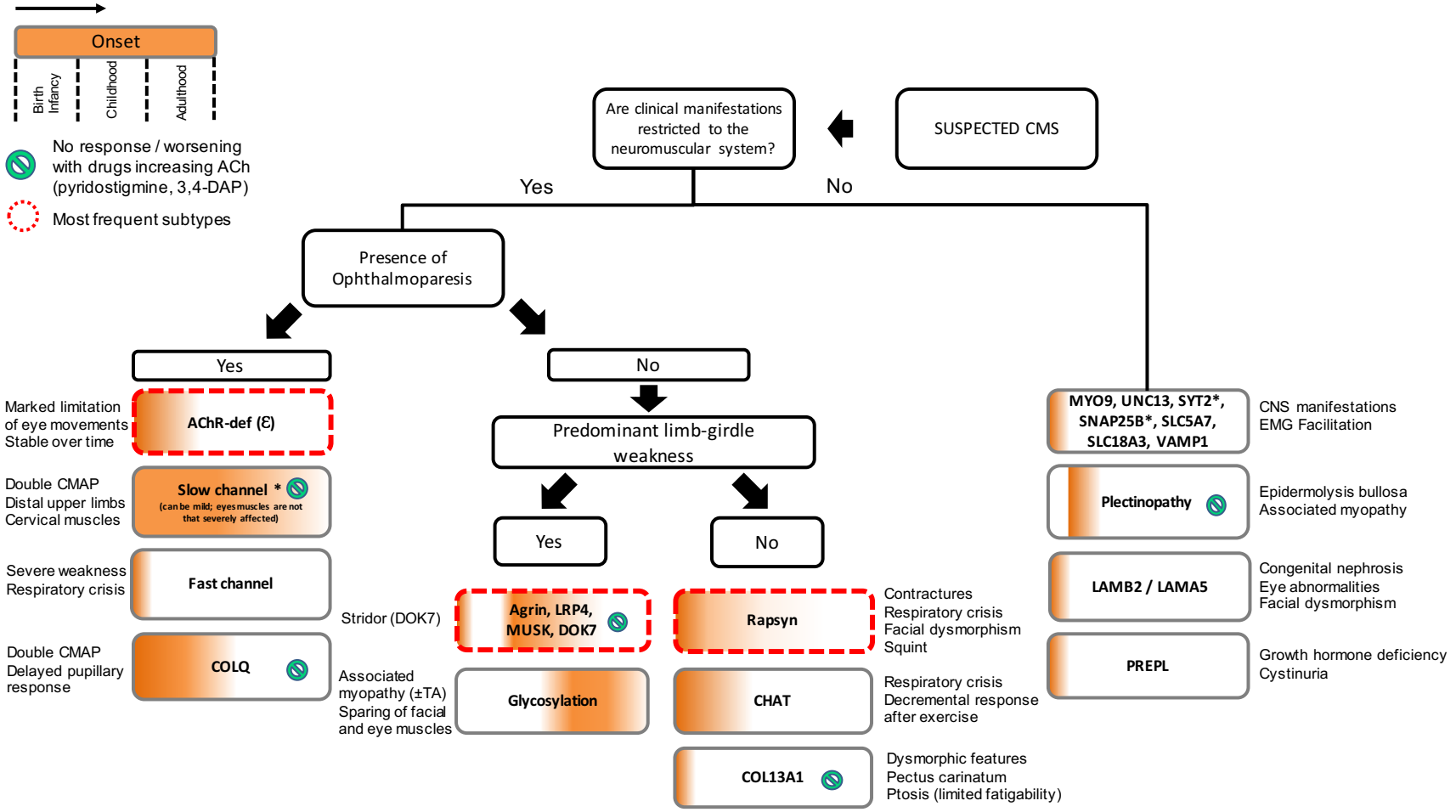


Figure 1-2. Proposed algorithm for targeted genetic screening of suspected CMS cases. Clinical evaluation should explore age at onset and presence of manifestations outside the neuromuscular system. Ophthalmoplegia and limb girdle weakness are clinically useful to guide genetic screening. Key diagnostic features are provided outside the boxes. (*) Slow channel syndrome, SYT2-CMS and SNAP25B-CMS are dominantly inherited.

1.4 Epidemiology and genetics

CMS are rare disorders in the general population. A recent study showed that the UK detected prevalence of genetically confirmed CMS was approximately 9.2 cases per million children under 18 years of age (Parr *et al.*, 2014). There was a variation across regions of the UK (between 2.8 and 15.5 per million children) with Northern Ireland and East England having the highest prevalence. This could be related to medical ascertainment being low in some areas although other factors such as presence of certain ethnic groups and consanguinity could play a role. The identified prevalence of CMS is likely to increase in future years, since a number of clinically diagnosed cases do not yet have a genetic diagnosis (Abicht *et al.*, 2012). However, it is likely that the discovery of CMS due to glycosylation defects (Guergueltcheva *et al.*, 2012; K Belaya *et al.*, 2012; Cossins *et al.*, 2013) has brought the proportion of CMS patients without genetic diagnosis down to approximately 10% of total. The relative frequency of the various CMS subtypes was calculated with DOK7, Rapsyn and AChR-deficiency found to be the most common syndromes accounting for nearly 70% of all cases **(Figure 1-3).**

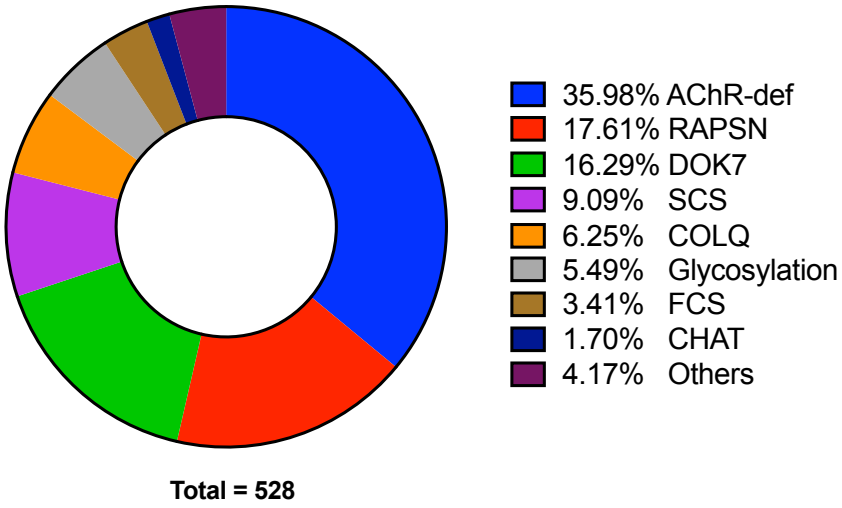


Figure 1-3. Relative frequency of genetically confirmed CMS subtypes in the UK

The increase in the relative proportion of AChR-deficiency syndromes compared to

previous (Finlayson, 2013) could be related to recent Eastern European migration to the United Kingdom. Updated September 2017.

1.5 CMS and the margin of safety of neuromuscular transmission

The margin of safety of neuromuscular transmission reflects that depolarisation caused by an endplate potential (EPP), following the release of ACh, is greater than the threshold needed to activate the $Na_v1.4$ voltage-gated sodium channels to trigger an action potential (Engel *et al.*, 2015). Under different conditions and stresses this margin can be affected (Wood and Slater, 2001). In CMS these include factors affecting the number of ACh molecules per synaptic vesicle, abnormal ACh release (quantal content) and reduced efficiency of released quanta in generating postsynaptic depolarisation (Engel, 2012a). The latter dictated by the structure of the endplates, AChE expression, and by the number, distribution and kinetics of AChRs.

1.6 Presynaptic syndromes

The number of CMS subtypes caused by mutations in genes encoding presynaptic proteins has expanded in recent years **(Table 1-2; Figure 1-4)**. Depending on the pathogenic mechanism, this group of CMS can be subdivided into disorders affecting axonal transport, the synthesis and recycling of ACh, and the exocytosis of synaptic vesicles. A considerable proportion of patients in this group present with episodic apnoeas and central deficits derived from the additional expression of the encoded proteins within the central nervous system.

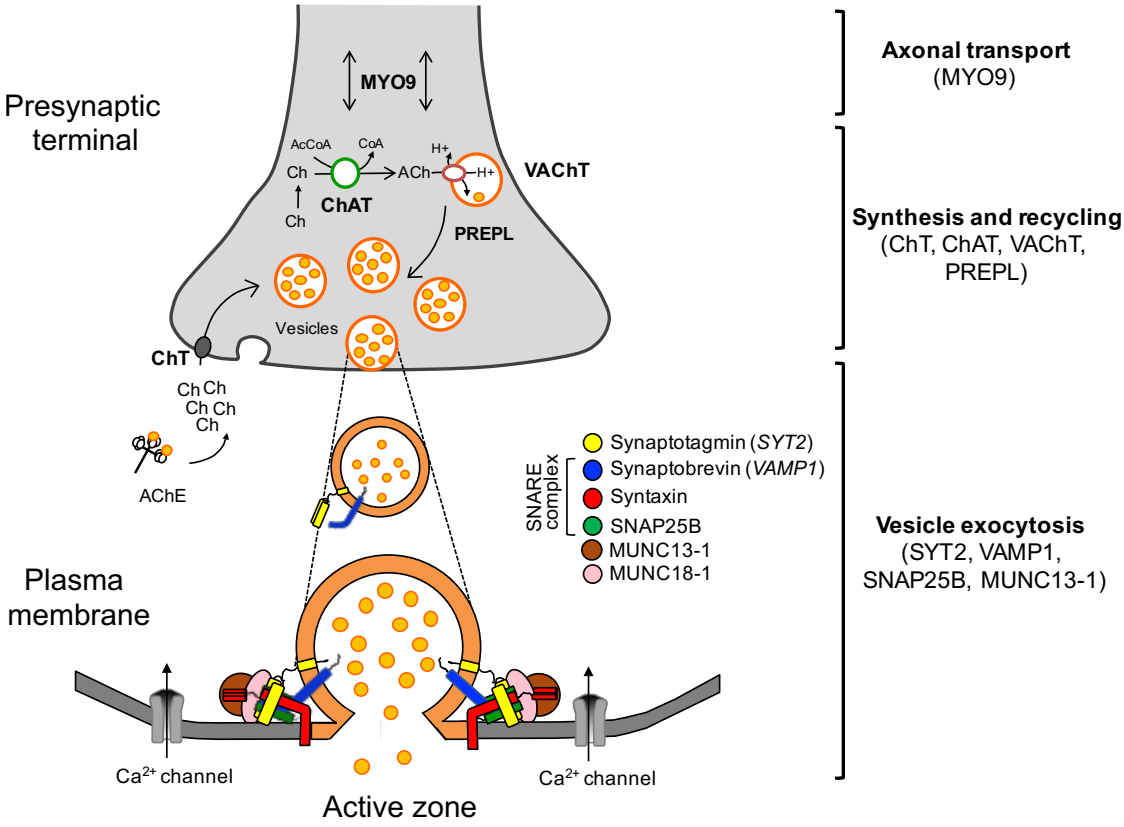


Figure 1-4. Schematic representation of the nerve terminal and the main molecules involved in presynaptic CMS

In the synaptic cleft, acetylcholinesterase (AChE) breaks down acetylcholine (ACh) into acetate and choline (Ch), which is uptaken by the sodium-dependent high-affinity choline transporter 1 (ChT) to the presynaptic terminal. The enzyme choline acetyltransferase (ChAT) catalyses the synthesis of ACh from acetyl coenzyme A (AcCoA) and choline, and the vesicular acetylcholine transporter (VAChT) loads ACh into synaptic vesicles. PREPL encodes a protein that acts as an effector of the clathrin-associated adaptor protein 1 in the trafficking of VAChT (Jaeken *et al.*, 2006). The synaptic vesicles accumulate adjacent to the nerve terminal ready for exocytosis. Upon the arrival of an action potential, voltage-dependent Ca^{2+} channels open and the influx of Ca^{2+} cause the fusion of vesicles to the plasma membrane through the Soluble N-ethylmaleimide-sensitive factor Attachment Receptor (SNARE) complex (synaptobrevin, syntaxin and SNAP25B) and the Ca2+ sensor Synaptotagmin. Additionally, Munc 13-1 and Munc 18-1 (syntaxin-binding protein 1) take part in the assembly and disassembly of the complex through mechanisms not fully understood (Lai *et al.*, 2017). Adapted from Ma *et al.*, Science 2013; 339: 421-426.

1.6.1 Axonal transport

MYO9

MYO9 encodes the protein Myosin-IXA belonging to the superfamily of unconventional myosins (Hartman *et al.*, 2011). There is increasing evidence that atypical myosins are expressed in peripheral neurons, and might play a role in axonal transport (Bridgman, 2009). A recent study has reported three patients from two kinships with missense heteroallelic mutations in *MYO9* (O'Connor *et al.*, 2016). All patients had severe neonatal onset with ptosis, hypotonia, respiratory and bulbar involvement. Additional features included developmental delay, nystagmus and oculomotor apraxia. There was a positive response to pyridostigmine and 3,4-Diaminopyridine. Knockdown of *MYO9A* in zebrafish produced defects in neuronal branching and axon guidance suggesting a role in the integrity of the presynaptic terminal.

1.6.2 Synthesis and recycling of acetylcholine

CHAT

The enzyme choline acetyltransferase (ChAT) catalyses the synthesis of acetylcholine from acetyl coenzyme A and choline in cholinergic neurons. Until recent years, mutations in *CHAT* were the only cause of presynaptic CMS. The pathogenic mechanisms of *CHAT* mutations include low expression of ChAT, abnormal catalytic efficiency and compromise in thermal stability (Shen *et al.*, 2011). There are no apparent abnormalities in the NMJ structure (Maselli *et al.*, 2003). The safety margin of neuromuscular transmission is compromised by a use-dependent reduction of the quantal size due to a reduction in the number of ACh molecules per synaptic vesicle (Arredondo *et al.*, 2016). In keeping with

this, 3Hz RNS can be normal at rest if the tested muscles are not previously fatigued using exercise or 10Hz stimulation.

The classic phenotype is neonatal onset CMS with life-threatening apnoeic crisis (Ohno *et al.*, 2001). Some of the patients can develop cerebral atrophy, most likely related to hypoxic episodes, although the effect of ChAT deficiency in the CNS, where it is widely expressed, cannot be ruled out. More recently, patients with onset of apnoeic episodes during infancy or early childhood and a milder course between crisis have been reported (Schara *et al.*, 2010). Pyridostigmine therapy might help to prevent respiratory crisis.

PREPL deficiency

The prolyl-endopeptidase-like gene (*PREPL*) encodes a protein that belongs to the prolyl-oligopeptidase subfamily of serine peptidases (Lone *et al.*, 2010). PREPL is ubiquitously expressed, with highest levels in the brain, kidney and muscle (Martens *et al.*, 2006). A known function of PREPL at the NMJ is to act as an effector of the clathrin-associated adaptor protein 1 in the trafficking of the vesicular ACh transporter (Kim and Hersh, 2004). A single case of CMS due to an isolated PREPL deficiency has been reported (Régal *et al.*, 2014). The subject had severe hypotonia and feeding difficulties at birth, but positive response to AChE inhibitors and improvement with age. Additional features included growth hormone deficiency. The endplate study revealed reduced postsynaptic response with normal AChR density and kinetics and normal endplate geometry. (Régal *et al.*, 2014). The hypotonia-cystinuria syndrome (HCS), associated with combined mutations in *PREPL* and *SLC3A1* (contiguous gene to *PREPL* on chromosome 2p21) comprises type A cystinuria, growth hormone deficiency and muscle weakness (Jaeken *et al.*, 2006).

SLC5A7

SLC5A7 encodes the presynaptic sodium-dependent high-affinity choline transporter 1 (ChT), which uptakes choline to the presynaptic terminal after the breakdown of ACh by AChE in the synaptic cleft (Okuda *et al.*, 2000). There is a single report to date of *SLC5A7* loss-of-function mutations in seven individuals from six unrelated families (Bauché *et al.*, 2016). Four subjects had a neonatal onset CMS with episodic apnoeas and positive response to AChE inhibitors while two had a more severe disease with arthrogryposis, malformations and early death. Three patients suffered from cognitive delay. Ultrastructural analysis showed the presence of small nerve terminals and empty synaptic gutters.

SLC18A3

SLC18A3 encodes the vesicular acetylcholine transporter (VAChT), which loads ACh into synaptic vesicles in neurons (Arvidsson *et al.*, 1997). Mutations in *SLC18A3* were first reported in two patients with episodic apnoeas, bilateral ptosis and ophthalmoplegia. (O'Grady *et al.*, 2016). Additional features included learning difficulties and left ventricular dysfunction. The individual compound heterozygous for p.Gly186Ala and a genomic deletion in *SLC18A3* was able to walk independently at age 14 years and had positive response to pyridostigmine. The individual homozygous for p.Asp298His lost independent ambulation at the age of 5 years. A second study reported two siblings carrying a homozygous p.Gly360Arg substitution characterised by extreme hypotonia, breathing difficulties, microcephaly, and developmental delay (Aran *et al.*, 2017). One sibling died from respiratory failure soon after birth, and the other needed constant mechanical ventilation.

1.6.3 Synaptic vesicles exocytosis

This is a novel group of CMS caused by mutations in genes encoding proteins involved in synaptic vesicles exocytosis. Most comprise the Soluble N-ethylmaleimide-sensitive factor Attachment protein REceptor (SNARE) complex and related proteins (Chen *et al.*, 2001), which are involved in the docking and Ca^{2+} triggered fusion of synaptic vesicles with the presynaptic membrane at both central and neuromuscular synapses **(Figure 1-5)**. Therefore, is not surprising that patients exhibit evident central manifestations. Clinical neurophysiology can show post-exercise amplitude facilitation as seen in LEMS (Eaton and Lambert, 1957).

UNC13A1

UNC13A1 encodes Munc13-1 (mammalian uncoordinated-13) protein, which plays a role in the priming of synaptic vesicles into a fusion competent state (Brose *et al.*, 1995). The only patient with *UNC13A1* mutations reported to date was homozygous for p.Gln102*, which eliminates the syntaxin 1B binding site of Munc13-1 (Engel *et al.*, 2016). The patient had a very severe phenotype with profound hypotonia and permanent need of ventilator support, and died at age 50 months from respiratory failure. There was no apparent clinical response to treatment with pyridostigmine or 3,4-Diaminopyridine. Additional features included the presence of an abnormally thin *corpus callosum* in brain magnetic resonance imaging (MRI). *In vitro* neurophysiology showed dramatic reduction of miniature endplate potentials (MEPP) frequencies and quantal content of endplate potentials (EPP) compared to control.

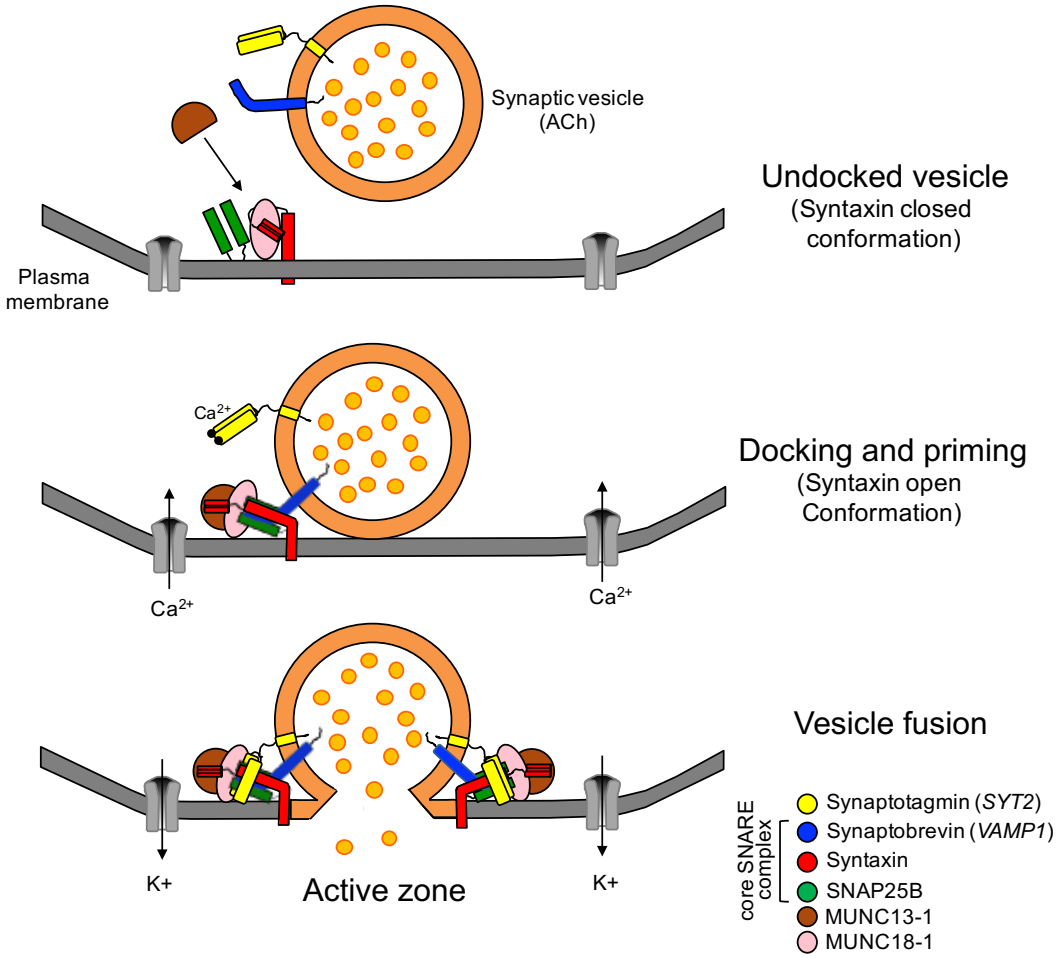


Figure 1-5. Schematic of synaptic vesicles at the active zones of presynaptic terminals

Once the synaptic vesicles are loaded with ACh, they need to dock and be primed near release sites. Upon the arrival of an action potential, the influx of Ca2+ causes synaptic vesicles to fuse to the plasma membrane through SNARE proteins releasing ACh at the synaptic cleft. The calcium current persists until the membrane potential is returned to normal by outward fluxes of potassium. Munc18-1 is a chaperone that binds to a self-inhibited "closed" conformation of syntaxin-1B and to SNARE complexes. Munc13, is believed to be involved in synaptic vesicle priming prior to vesicle fusion by catalysing the transition of syntaxin 1B from a closed configuration with Munc18-1 into an open state ready to form SNARE complexes and fuse rapidly. The core SNARE complex, a 4-α helix structure formed by the synaptic vesicle-associated synaptobrevin (v-SNARE) and the presynaptic SNAP25B and syntaxin 1B (t-SNARES) proteins, brings the vesicle and plasma membranes together. Finally, calcium-bound Synaptotagmin (a vesicle Ca2+ sensor) triggers vesicle fusion and exocytosis. Adapted from Ma *et al.*, Science 2013.

SNAP25

SNAP25 codifies the synaptosomal-associated protein of 25 Kd, a core element of the SNARE-complex (Oyler *et al.*, 1989; Chapman *et al.*, 1994). A single case of SNAP25 deficiency causing CMS has been reported to date (Shen *et al.*, 2014). The patient harboured the p.Ile67Asn de novo dominant mutation that was shown to inhibit synaptic vesicle exocytosis *in vitro*. The patient had contractures and breathing difficulties at birth, achieving limited walking from age 7 years. Additional features included developmental delay, cortical hyperexcitability and ataxic gait. Treatment with 3,4-DAP was beneficial.

SYT2

SYT2 encodes the synaptic vesicle membrane protein Synaptotagmin 2, which serves as a Ca^{2+} sensor for the exocytosis of synaptic vesicles (Pang *et al.*, 2006). Dominant mutations in *SYT2* (p.Asp307Ala and p.Pro308Leu) were first reported in two kinships featuring a non-progressive motor neuropathy and a presynaptic syndrome resembling LEMS (Herrmann *et al.*, 2014). The individuals suffered from foot deformities from childhood and a variable degree of proximal and distal weakness. No treatment was reported.

VAMP1

VAMP1 encodes the vesicle associated membrane protein 1 (Synaptobrevin 1), which is part of the SNARE complex, and has an essential role in Ca^{2+}-triggered ACh release at the NMJ (Liu *et al.*, 2011). Synaptobrevin 1 is also expressed in the brain, but in a less abundant manner that the highly homologous isoform Synaptobrevin 2 (Elferink and Trimbles, 1989). Only four patients with CMS due to *VAMP1* mutations have been reported to date from 2 different kinships (Salpietro *et al.*, 2017). All patients suffered

from a severe condition with hypotonia, muscle weakness and feeding difficulties at birth.

1.7 Synaptic or basal-lamina associated syndromes

The basal lamina of the NMJ is a structured form of extracellular matrix located at the synaptic cleft that is essential for the alignment, organisation and maintenance of pre- and postsynaptic structures (Sanes, 2003). The main components of the basal lamina are laminins, collagens, heparan sulfate proteoglycans (muscle agrin and perlecan) and nidogens (Shi *et al.*, 2012) **(Figure 1-6)**. Mutations in *COLQ* cause the most frequent CMS subtype in this category. Other basal-lamina associated CMS are very rare.

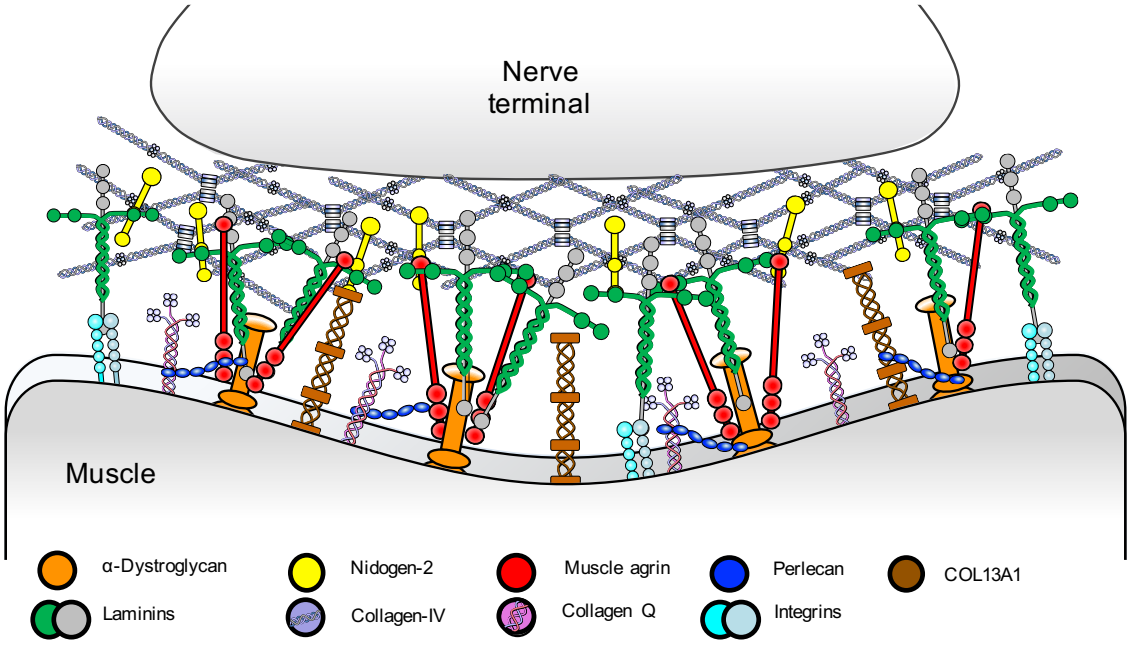


Figure 1-6. Schematic representation of the synaptic basal lamina

Laminins are heterotrimeric proteins of high molecular weight formed by the incorporation of α, β and γ chains into a cruciform structure. Laminins self-assemble, but also interact with integrins and α-dystroglycan (Mouw *et al.*, 2014). Collagen IV, which is the most abundant protein at the basal lamina, self-assembles into dimers and hexamers thanks to its globular domains (Mouw *et al.*, 2014). Nidogen-2 are non-collagenous glycoproteins responsible for linking collagen IV and laminin networks (Fox *et al.*, 2008;

Mokkapati *et al.*, 2008). Additional collagens include COL13A1 (Latvanlehto *et al.*, 2010) and COLQ, a collagen-like tail responsible for anchoring AChE to the synaptic cleft. Muscle agrin binds to the basal lamina via laminin (Denzer *et al.*, 1997) and α-dystroglycan (Sugiyama *et al.*, 1994), and this is important for maintenance of the NMJ (Samuel *et al.*, 2012). This differs from the role of neuronal agrin as a key organiser of the postsynaptic apparatus via the AChR clustering pathway (Ferns *et al.*, 1996). Perlecan, another synaptic heparan sulphate proteoglycan, is linked to both ColQ (Arikawa-hirasawa *et al.*, 2002) and α-dystroglycan (Peng *et al.*, 1998).

COLQ

COLQ encodes the collagen-like tail subunit of asymmetric acetylcholinesterase (AChE), which anchors AChE to the basal lamina **(Figure 1-7)**. Mutations in *COLQ* cause synaptic basal-lamina CMS with endplate AChE deficiency (Ohno *et al.*, 1998). The prolonged time of ACh at the synaptic cleft produces desensitization of AChRs and secondary endplate myopathy with loss of AChRs due to sarcoplasmic Ca^{2+} overload (Ohno *et al.*, 1998). *COLQ* mutations have been reported in all domains of the protein with no phenotype-genotype correlation (Mihaylova *et al.*, 2008). It is assumed that AChE loss of function mutations are incompatible with life.

The clinical features of patients with COLQ mutations are very variable. The classic phenotype is that of neonatal or early onset severe disease with ptosis, ophthalmoparesis, generalised weakness, respiratory difficulties and progressive course (Ohno *et al.*, 1998). Additional phenotypes include early onset disease but with a mild course without significant progression of weakness, and cases reminiscent of DOK7-CMS (Section 1.8.3) (Mihaylova *et al.*, 2008). Late onset mild disease at 6-7 years of age has

also been described (Donger *et al.*, 1998; Shapira *et al.*, 2002). Repetitive CMAP in response to a single nerve stimulation can be seen due to prolonged endplate currents outlasting the refractory period of the muscle fibre (Hutchinson *et al.*, 1993). Pyridostigmine and 3,4-DAP are contraindicated but some patients do respond to treatment with ß2-adrenergic agonists (Bestue-Cardiel *et al.*, 2005).

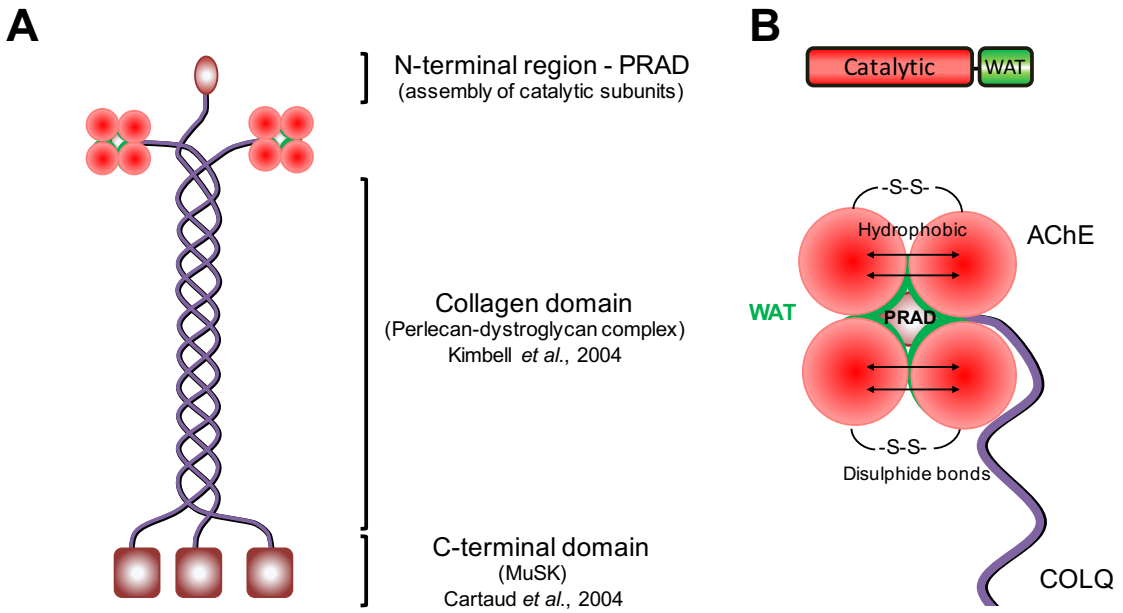


Figure 1-7. Schematic representation of AChE and its collagenic-like tail

(A) ColQ is composed of a N-terminal domain with a Proline Rich Attachment Domain (PRAD) that binds to the catalytic subunits of AChE, a triple-helix collagenic domain, and a C-terminal domain. Interactions with key NMJ proteins are shown in brackets. Mutations in PRAD hinder the assembly of ColQ with AChE, while variants in the collagen domain prevent the formation of the triple helix (Ohno *et al.*, 2000). Mutations in the C-terminal domain, mostly missense variants, compromise ColQ-MuSK interaction (Nakata *et al.*, 2013). **(B)** AChE is composed of a catalytic domain followed by a WAT (tryptophan (W) amphiphilic tetramerisation) domain at the C-terminal region. The association between catalytic subunits is primarily driven by the interaction between WAT domains (green colour) and PRAD (Luk *et al.*, 2011). Additional forces include hydrophobic interactions and disulphide bonds.

COL13A1

COL13A1 encodes the alpha chain of a non-fibrillar collagen, which has shown *in vitro* binding with other extracellular matrix proteins such as integrin α1ß1 (Nykvist *et al.*, 2000), nidogen and perlecan (Tu *et al.*, 2002). Studies in animal models lacking Col13a1 identified abnormal maturation of the neuromuscular junction (Latvanlehto *et al.*, 2010). A detailed clinical and molecular characterisation of the first cases of *COL13A1* loss of function mutations in humans is given in Chapter 4.

Laminin ß2 and laminin α5 deficiencies

A single CMS case of laminin ß2 deficiency due to heteroallelic frameshift mutations in *LAMB2* has been reported to date (Maselli *et al.*, 2009). The patient suffered from a severe neonatal-onset CMS, in addition to congenital nephrosis and distinct eye abnormalities with microcoria (Pierson syndrome) (Zenker *et al.*, 2004). Laminin ß2 is an important component of the glomerular basement membrane and intraocular muscles. The neuromuscular phenotype included neonatal onset with breathing difficulties, ptosis, ophthalmoplegia and profound proximal weakness. Cholinesterase inhibitors were deleterious in this single case.

Homozygous missense mutations in *LAMA5*, encoding laminin α5, have been reported in a neonatal onset CMS combining myopia, facial tics and abnormal neuromuscular transmission (Maselli *et al.*, 2017). The endplates study found normal postsynaptic membrane but small nerve terminals, and neurophysiological abnormalities in keeping with a LEMS-like presynaptic defect. There was a positive response to treatment with pyridostigmine and 3,4-diaminopyridine.

1.8 Postsynaptic syndromes

1.8.1 Primary AChR deficiency

The adult nicotinic AChR is a pentameric complex composed of four different transmembrane subunits (2 α, ß, δ and ε) encoded by *CHRNA1*, *CHRNB1*, *CHRND* and *CHRNE, respectively* **(Figure 1-8)**. Primary AChR deficiency is characterised by reduced AChR numbers (10 to 30% of normal) with mild effect on the integrity of postsynaptic folding (Vincent *et al.*, 1993). This CMS subtype accounts for 36% of all CMS in the UK and is mainly caused by *CHRNE* mutations. These are found along the length of the gene including the promoter region (Ealing *et al.*, 2002) and result in protein truncation or loss of essential residues (glycosylation sites, Cys-loop) for AChR assembly or function (Abicht *et al.*, 2016). It is believed that incorporation of the foetal AChR γ-subunit into the AChR pentamer enables subjects with null ε-subunits alleles to survive (Cossins *et al.*, 2004).

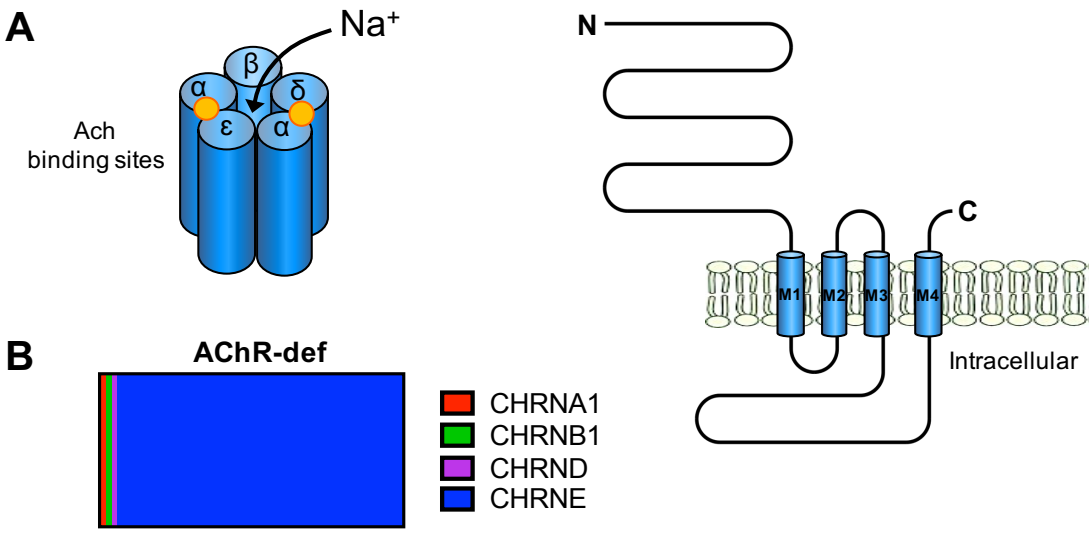


Figure 1-8. Schematic representation of the adult AChR and genetics of AChR-deficiency
(A) The AChR is made up of five subunits arranged around a central pore. Each subunit is composed of an extracellular domain, four transmembrane domains (M1-M4) and a large cytoplasmic loop that links M3 and M4.
(B) AChR-deficiency is mainly caused by mutations in *CHRNE.*

The phenotypic spectrum of patients with primary AChR-deficiency is wide from mild to severe disease (Burke *et al.*, 2004). Most patients have a marked limitation of ocular movements. Treatment with cholinesterase inhibitors and 3,4-DAP is beneficial, although the long-term response in severe cases is often incomplete (Engel, 2007).

Mutations in the foetal subunit (γ) of the AChR, encoded by *CHRNG*, cause Escobar syndrome (a form of arthrogryposis multiplex congenita) and foetal akinesia deformation sequence (Hoffmann *et al.*, 2006).

1.8.2 Kinetic abnormalities of the AChR (with or without AChR deficiency)

Mutations in any of the four AChR adult subunits can also alter ion channel function leading to prolonged openings (slow channel syndrome - SCS), abbreviated openings (fast channel syndrome - FCS) or reduced conductance. However, mutations in *CHRNA1* and *CHRNE* are the most frequent **(Figure 1-9)**. This group represents approximately 15% of total CMS cases.

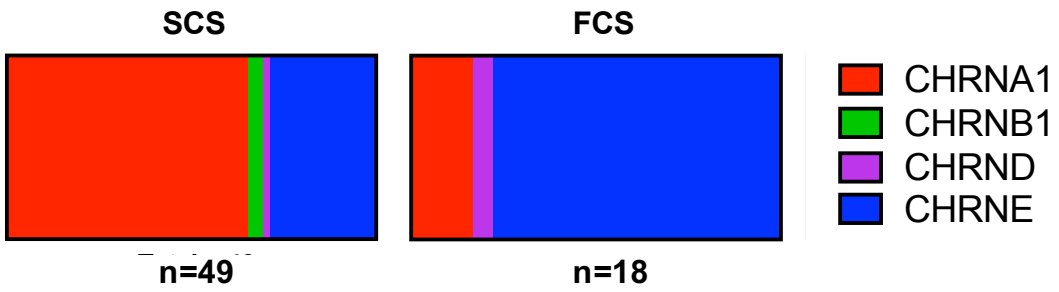


Figure 1-9. Genetics of CMS due to kinetic abnormalities of the AChR
SCS is often caused by mutations in *CHRNA1* encoding the AChR α-subunit, while FCS is most commonly due to mutations in *CHRNE* encoding the ε-subunit of the AChR.

SCS was the only CMS with autosomal dominant inheritance until the recent descriptions of presynaptic CMS due to *SNAP25* and *SYT2* mutations. The underlying pathogenic mechanism is prolonged AChR opening, which causes desensitisation of AChRs and secondary endplate myopathy due to cationic overload (Ohno *et al.*, 1995) and focal activation of caspases (Zhu *et al.*, 2014). The age of symptom onset in SCS is very variable, from birth to the fifth decade, but patients are in general not as severely affected as other CMS subtypes. There is often selective involvement of cervical and distal upper limb muscles, especially finger extensors and thumb abductors. Ptosis and ophthalmoparesis can be present but to a lesser degree than in primary AChR deficiency. Repetitive CMAPS can be seen in 50% of patients (Finlayson, 2013). The treatment of SCS is with AChR open channel blockers such as fluoxetine or quinidine (Chaouch *et al.*, 2012). Salbutamol has shown improvement in isolated cases (Sarah Finlayson *et al.*, 2013). Drugs increasing ACh levels (pyridostigmine and 3,4-DAP) are deleterious in SCS.

FCS result in brief channel openings with secondary reduced postsynaptic depolarisation and failure to trigger muscle action potentials (Ohno *et al.*, 1996). FCS is rare because in order to define the clinical phenotype, the FCS mutation needs to be in compound heterozygosis with a null or low expressor mutation. The εP121L variant, which is critical for binding of acetylcholine (Sine *et al.*, 2003), is the most common FCS mutation in the UK (Palace *et al.*, 2012). FCS is characterised by severe weakness from birth, ptosis, ophthalmoplegia and life-threatening respiratory crises in infancy and childhood that may be fatal (Palace *et al.*, 2012). Pyridostigmine and 3,4-DAP are beneficial although the effect may decrease with time.

Finally, the spectrum of kinetic abnormalities was extended by the report of a single case with a p.εΔF266 deletion in the M2 transmembrane domain of the ε-subunit causing decreased AChR ion-channel conductance (Webster *et al.*, 2012). This variant reduced the amplitude of channel openings without affecting burst duration. Clinical features were similar to FCS.

1.8.3 Defects within the AChR-clustering pathway

The AChR clustering signaling pathway is essential for the formation and maintenance of the NMJ (Wu *et al.*, 2010) **(Figure 1-10)**. Upon release of agrin by the nerve terminal, agrin binds to LRP4 at the postsynaptic membrane resulting in MuSK dimerisation and activation (Kim *et al.*, 2008). This leads to the recruitment of DOK7, a muscle-specific cytoplasmic adaptor of MuSK, which further stimulates MuSK kinase activity propagating the signal downstream through mechanisms still not elucidated. This results in the phosphorylation of the AChR ß-subunit, which facilitates binding of the cytoplasmic anchoring protein Rapsyn and final stabilisation of innervated AChR clusters (Burden *et al.*, 2013). Additional players (although their role is still poorly understood) include CrK/CrKL (Hallock *et al.*, 2010) and the mammalian homolog of Drosophila Tumorous Imaginal Discs, Tid1, (Linnoila *et al.*, 2008), which mediate agrin signaling, and Dishevelled (Luo *et al.*, 2002), a scaffold protein involved in Wnt signaling pathways (Henriquez *et al.*, 2008).

By contrast to the AChR clustering pathway, a negative signal disperse aneural AChR clusters not stabilised by agrin signaling **(Figure 1-10)**. This pathway is believed to be driven by ACh trough a cyclin-dependent kinase 5 (Cdk5) mechanism (Lin *et al.*, 2005)

linked to the interaction of rapsyn and the calcium-dependent protease calpain (Chen *et al.*, 2007). Calpain activity promotes the cleavage of p35 to p25, a potent activator of Cdk5 (Patrick *et al.*, 1999). Rapsyn is believed to stabilise AChR clusters by suppressing calpain activity (Chen *et al.*, 2007).

CMS patients harboring mutations within the AChR clustering pathway present common clinical features such as relative sparing of eye muscles, predominant limb girdle weakness, worsening of symptoms with drugs increasing ACh levels and improvement on long-term therapy with ß2-adrenergic agonists.

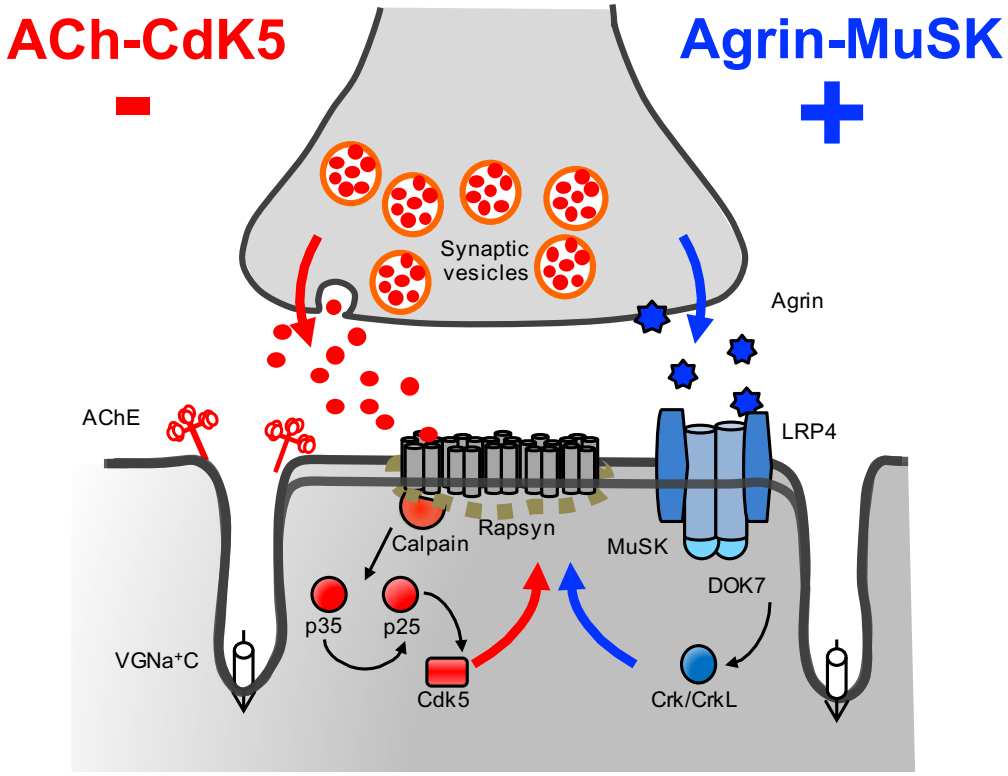


Figure 1-10. Schematic representation of the Agrin-induced AChR clustering and ACh-CdK5 dispersal pathways

Main molecules with a role in synapse formation and maintenance are represented although additional, still unknown, positive and negative factors are very likely to be involved. The AChR clustering pathway is shown blue and the dispersal pathway in red.

AGRN

A neuronal isoform of agrin, generated by alternative splicing, is secreted from the nerve terminal into the basal lamina as the first step of the AChR clustering pathway. *AGRN* mutations account for a rare CMS subtype with only four reports published to date **(Figure 1-11)**. The phenotypic spectrum is variable from very severe disease with respiratory failure (Ricardo A Maselli *et al.*, 2012) to a mild CMS with running difficulties (Richard *et al.*, 2009) or dropped head presentation (Karakaya *et al.*, 2017). Overall, there is no clear phenotype-genotype correlation, including a recent report of five patients from three different kinships with a similar phenotype comprising CMS with distal muscle weakness and atrophy (Nicole *et al.*, 2014). Of note, extraocular muscles were usually spared or modestly affected in keeping with other CMS impairing the AChR clustering pathway. Most patients were unresponsive to pyridostigmine and 3,4-DAP, but some had a clear benefit on ß2-adrenergic agonists (Nicole *et al.*, 2014).

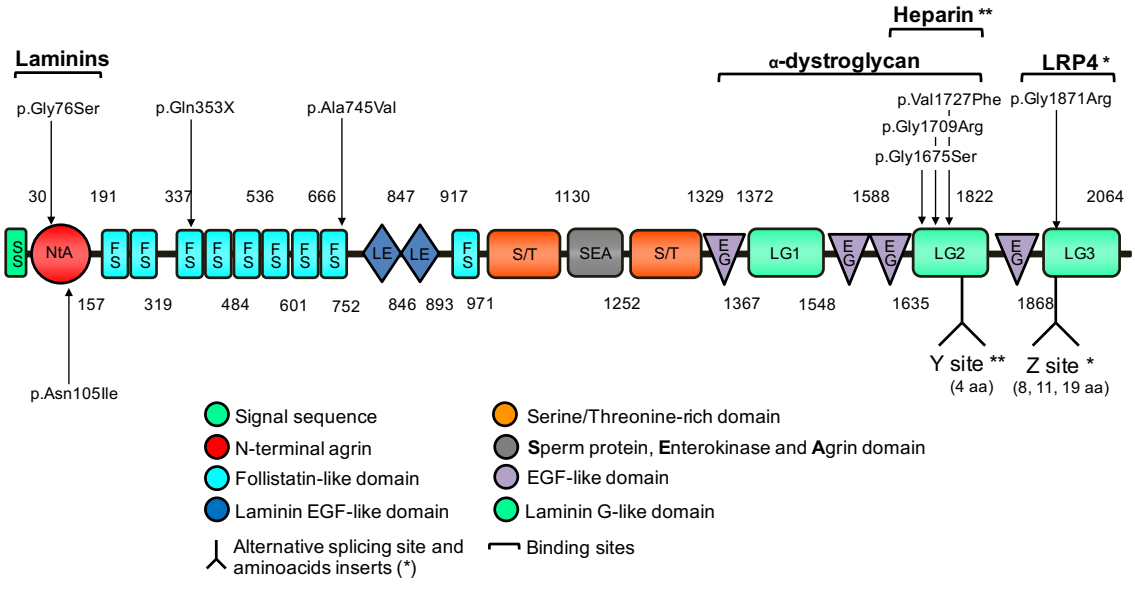


Figure 1-11. Schematic representation of agrin drawn to linear scale and location of variants reported in the literature

Agrin (RefSeq NP_001292204.1) is a large proteoglycan (>200 KDa) with multiple domains that binds to laminins through the N-terminal domain, and to LRP4 and α-dystroglycan via C-terminus. Two of the three laminin G-like domains are required for binding to α-dystroglycan. Agrin mRNA undergoes cell-specific alternative splicing at different sites (Ferns *et al.*, 1993). When agrin is produced by motor neurons, the Z site contain amino acid inserts specifically required for MuSK activation. The *AGRN* mutations reported to date are located within the carboxy-terminal part of agrin, the N-terminal domain, and the follistatin-like sequences. Adapted from Ruegg and Bixby, Trends Neurosci 1998;21(1):22-7.

LRP4

The nerve terminal releases agrin that binds to the low-density lipoprotein receptor-related protein 4 (LRP4) forming a ternary complex with MuSK that triggers MuSK phosphorylation (Kim *et al.*, 2008; Zhang *et al.*, 2011). CMS due to *LRP4* mutations is extremely rare with only three patients from two different kinships reported to date (Ohkawara *et al.*, 2013; Selcen *et al.*, 2015). All harboured missense mutations located at the third propeller domain of LRP4 that prevent MuSK activation. The clinical features of the few patients reported were variable with one case of early onset severe myasthenia and two milder cases with onset in childhood after normal or slightly delayed motor milestones. In a similar fashion to DOK7-CMS, patients improved dramatically on salbutamol while pyridostigmine worsened muscle weakness.

MuSK

MUSK encodes the muscle specific kinase (MuSK), a key element of the agrin signalling pathway (DeChiara *et al.*, 1996). *MUSK* mutations represent a very rare cause of CMS with only few cases reported (Chevessier *et al.*, 2004; Maselli *et al.*, 2010; Ammar *et al.*, 2013).

However, given the role of MuSK and DOK7 in the same pathway, it is noteworthy that the clinical features and treatment response are similar in both conditions, with predominant limb girdle weakness, spearing of eye muscles, and worsening with cholinesterase inhibitors. In chapter 6, the molecular mechanisms of impaired synaptic transmission in a severe case of CMS harbouring two missense variants in *MUSK* will be discussed.

DOK7

DOK7 is a muscle-specific cytoplasmic adaptor protein of MuSK, which is essential for postsynaptic specialization of the NMJ (Okada *et al.*, 2006). Mutations in *DOK7* underlie a NMJ synaptopathy (Beeson *et al.*, 2006), which accounts for approximately 16% of total CMS cases in the UK. The spectrum of *DOK7* mutations is wide although most patients have at least one mutation within the C-terminus, with c.1124_1127dupTGCC present in approximately 65% of the cases (Cossins *et al.*, 2012). Patients homozygous or compound heterozygous for mutations localised 5' to this domain are relatively infrequent **(Figure 1-12**). There is no clear genotype-phenotype correlation (Palace *et al.*, 2007).

The classic phenotype is characterised by onset of symptoms in childhood after normal motor milestones, with progressive limb-girdle weakness and walking difficulties (Beeson *et al.*, 2006). Patients have ptosis but eye movements are typically normal. The clinical spectrum varies from mild limb-girdle weakness to generalised and severe weakness. Patients can improve dramatically on ß2-adrenergic agonists in the course of months (Lashley *et al.*, 2010).

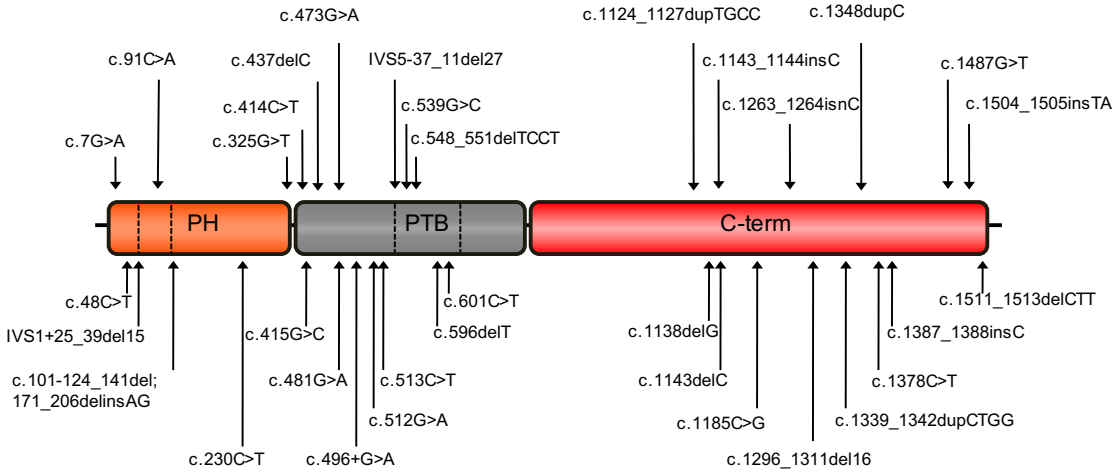


Figure 1-12. Schematic representation of DOK7 drawn to linear scale and localisation of mutations identified in CMS patients referred to Oxford

DOK7 (RefSeq NM_173660.4) is composed of a N-terminal pleckstrin homology (PH) domain, a phosphotyrosine-binding (PTB) domain and a C-terminal domain. Dashes are used to mark the different exons. Adapted from Cossins et al., Hum. Mol. Genet. 2012; 21: 3765–75.

Another group of patients harbouring *DOK7* mutations present at birth with stridor in the context of bilateral vocal cord palsy. This can cause respiratory failure, often without significant weakness elsewhere (Klein *et al.*, 2013). While this might be useful as a diagnostic clue, the underlying reasons for the selective affection of laryngeal muscles are unknown. In chapter 7, the clinical and molecular characterisation of stridor in patients with DOK7-CMS will be discussed.

1.8.4 Rapsyn deficiency

RAPSN encodes the 43 kDa receptor-associated scaffold protein of the synapse (Sobel *et al.*, 1977), which is essential for stabilisation of AChR clusters at the NMJ (Gautam *et al.*, 1995; Moransard *et al.*, 2003). Rapsyn is enriched at postsynaptic membranes and acts as

a linker between the AChRs and the cytoskeleton via the dystrophin-associated glycoprotein complex (Apel *et al.*, 1995). However, the detailed organisation of the AChRs-rapsyn network is not fully understood since the crystallographic structure has not been solved (Zuber and Unwin, 2013).

Rapsyn-CMS is characterised by deficiency of AChRs at the postsynaptic membrane and poor development of postjunctional folds (Ohno *et al.*, 2002). *RAPSN* mutations have been reported across the entire length of the gene **(Figure 1-13)**, although most patients are either homozygous for p.N88K mutation or heteroallelic for p.N88K and a second mutation (Cossins *et al.*, 2006). Several mechanisms have been shown to disrupt rapsyn function, including reduced protein expression, abnormal clustering of rapsyn, diminished co-clustering of AChRs with rapsyn, and abnormal agrin-induced formation and stabilisation of AChR clusters (Ohno *et al.*, 2002; Cossins *et al.*, 2006; Muller *et al.*, 2006). The major effect of p.N88K is to reduce the stability of AChR clusters (Cossins *et al.*, 2006).

Most patients with *RAPSN* mutations present at birth or early in life with generalised hypotonia, respiratory weakness and feeding difficulties (Burke *et al.*, 2003; Milone *et al.*, 2009). Mild arthrogryposis, facial dysmorphism, ptosis and strabismus are usually present but ophthalmoplegia is rare. Life-threatening respiratory crisis are frequent during infancy and early childhood. Additional phenotypes include lethal foetal akinesia (Vogt *et al.*, 2008) and a milder disease with onset in adulthood mimicking seronegative MG (Burke *et al.*, 2003). There is not a clear phenotype-genotype correlation although it is believed that in patients heteroallelic for p.N88K, the dysfunction of the second allele influences disease severity (Cossins *et al.*, 2006). Treatment with pyridostigmine and 3,4-DAP is

beneficial. Most patients improve with age and have a good long-term prognosis (Natera-de Benito *et al.*, 2016).

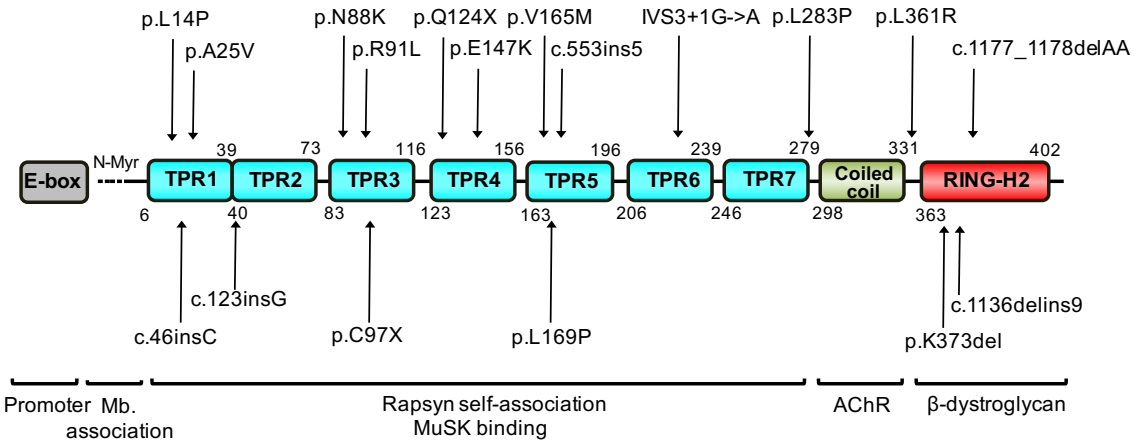


Figure 1-13. Schematic representation of RAPSN drawn to linear scale and localisation of mutations identified in CMS patients referred to Oxford

Rapsyn (RefSeq NP_005046.2) is composed of a N-terminal myristoylation moiety (N-Myr) necessary for submembrane localization; seven tetratricopeptide (TRP) domains responsible for rapsyn self-association and MuSK binding (Ramarao *et al.*, 2001; Lee *et al.*, 2008); a coiled-coil domain that binds to the cytoplasmic loops of AChRs (Lee *et al.*, 2008), and a RING-H2 domain that interacts with the dystroglycan complex and links rapsyn to the cytoskeleton (Apel *et al.*, 1995). Adapted from Cossins et al., Brain (2006), 129, 2773–2783.

1.9 CMS due to mutations in genes encoding proteins without specific NMJ function

The N-linked glycosylation pathway is a ubiquitous process in eukaryote cells defined by the sequential attachment of sugar moieties to an amino acid residue in a protein **(Figure 1-14)**. Membrane-bound and exported proteins are modified in the endoplasmic reticulum (ER) by the addition and processing of glycans that can be crucial for protein folding and thus function and intracellular transport. Mutations in components within this

pathway produce a spectrum of severe multisystemic disorders known as congenital disorders of glycosylation (Jaeken and Matthijs, 2001; Thiel *et al.*, 2003; Wu *et al.*, 2003).

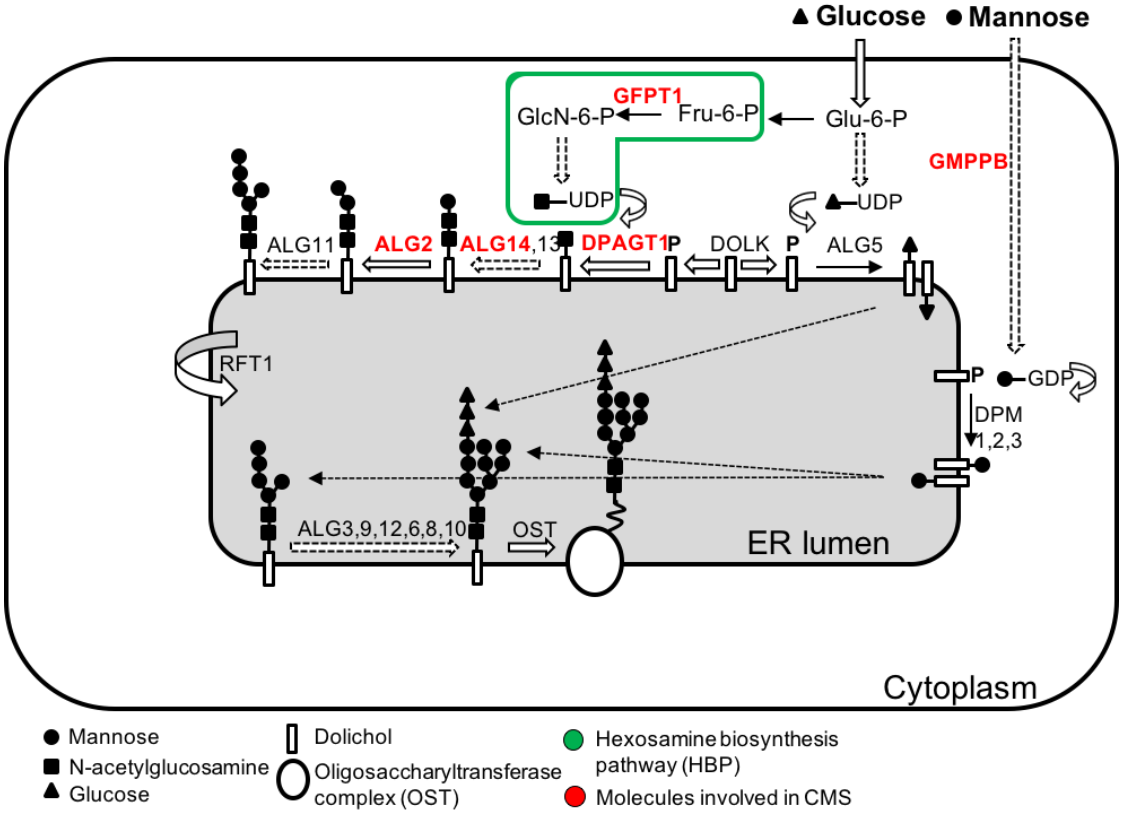


Figure 1-14. Schematic representation of the N-glycosylation pathway of proteins and the main molecules involved in CMS

The N-linked protein glycosylation takes place in the endoplasmic reticulum (ER). It starts with the assembly of the core glycan (*N*-acetylglucosamine, glucose and mannose) on the lipid dolichol. On the cytoplasmic face of the ER, a series of cytosolic glycosyltransferases proceed to dolichol glycosylation: GFPT1 synthesises UDP-GlcNAc (Uridine diphosphate *N*-acetylglucosamine); DPAGT1 and the ALG13/14 complex are involved respectively in adding the first and second sugar *N*-acetylglucosamine to dolichol. ALG2 and other enzymes add additional sugar residues until the resulting product is flipped into the ER lumen by RFT1. Subsequent sugar moieties are incorporated inside the ER lumen until the core glycan is then transferred to asparagine residues of nascent proteins by the multimeric oligosaccharyl transferase complex (OST) that subsequently will be modified inside the ER and Golgi. DOLK, dolichol kinase; DPM, dolichol-phosphate mannose

synthase; Fru-6-P, fructose-6-phosphate; GlcN-6-P, glucosamine- 6-phosphate; Glu-6-P, glucose-6-phosphate; GMPPB, GDP-mannose pyrophosphrylase B.

NGS has aided the discovery of an unexpected relationship between glycosylation defects in the early stages of the N-glycosylation pathway and CMS (Senderek *et al.*, 2011; Katsiaryna Belaya *et al.*, 2012; Cossins *et al.*, 2013). Since glycosylation of AChR subunits is required for the correct assembly of AChR pentamers and for efficient export to the cell surface (Gehle *et al.*, 1997), abnormal glycosylation results in reduced AChRs at the muscle endplates (Zoltowska *et al.*, 2013). In addition, it is possible that impaired glycosylation of other NMJ proteins could also have a role in the pathogenesis.

These patients constitute a distinctive clinical group where muscle weakness is often confined to the limb girdles, and classic myasthenic manifestations such as ptosis, ophthalmoplegia or facial weakness are not present. In addition, concomitant myopathy is often present, which makes it a progressive condition. Intellectual disability is also seen in some cases. The myasthenic component can be treated with a combination of pyridostigmine, 3,4-DAP and salbutamol. This group of disorders account for approximately 6% of total CMS cases in the UK. CMS should be part of the differential diagnosis of limb girdle muscle weakness.

GFPT1

GFPT1 encodes glutamine-fructose-6-phosphate transaminase-1 (GFAT1), which catalyses the first step in the biosynthesis of UDP-N-acetylglucosamine, an essential

substrate for *N*- and *O*- glycosylation of proteins (Haltiwanger and Lowe, 2004). The knock-down of GFPT1 orthologue in zebrafish embryos confirmed that GFPT1 is required for normal NMJ formation (Senderek *et al.*, 2011). Multiple synaptic proteins at the neuromuscular junction are glycosylated (Martin, 2003) and understanding the full pathogenic mechanisms leading to myasthenia is complex. However, inhibiting the enzymatic activity of GFPT1 or siRNA 'knock down' of its expression result in decreased of cell-surface AChR expression indicating that endplate AChR deficiency is likely to be one key contributing factors (Zoltowska *et al.*, 2013)

Mutations in *GFPT1* have been identified in more than 50 patients to date causing an autosomal recessive limb-girdle CMS, commonly with tubular aggregates (TA) on muscle biopsy (Senderek *et al.*, 2011; Huh *et al.*, 2012; Selcen *et al.*, 2013; Bauché *et al.*, 2017). The clinical presentation is usually with proximal weakness in girdles and sparing of ocular and facial muscles, with variable onset of symptoms from early childhood to the second and third decades. Modestly elevated serum creatine kinase (CK) levels and additional myopathic changes on needle EMG can be seen suggesting a concomitant myopathy with normal expression of alpha-dystroglycan (Bauché *et al.*, 2017). The endplates of patients with GFPT1-CMS are composed of small single or 'grape-like' units with simplified postsynaptic membranes and abnormal nerve endings (Selcen *et al.*, 2013). To date a precise genotype-phenotype correlation for *GFPT1* mutations has not been determined. Treatment with AChE inhibitors and 3,4-DAP is beneficial (Guergueltcheva *et al.*, 2012).

DPAGT1

DPAGT1 encodes the enzyme dolichyl-phosphate-N-acetylglucosamine-phophotranferase-1, a transmembrane ER protein essential for N-linked glycosylation that catalyses the first step in the dolichol oligosaccharide pathway for glycoprotein biosynthesis (Bretthauer, 2009). The specific inhibition of DPAGT1 by tunicamycin (Merlie *et al.*, 1982) reduces the cell surface expression of AChRs in transfected HEK-293T cells (Katsiaryna Belaya *et al.*, 2012), which suggests that AChR-deficiency is the main pathogenic mechanism causing myasthenia.

CMS due to *DPAGT1* mutations has been reported in 12 patients (K Belaya *et al.*, 2012; Basiri *et al.*, 2013; Selcen *et al.*, 2014) **(Figure 1-15)**. Presentation is during infancy or childhood with prominent limb-girdle weakness and minimal craniobulbar manifestations (S Finlayson *et al.*, 2013). The spectrum of severity is variable: some patients walk independently while others are wheelchair bound from an early age. Life-threatening respiratory crisis are rare (Basiri *et al.*, 2013). A concomitant myopathy is present with or without tubular aggregates. Cognitive manifestations can vary from none to mild learning difficulties or major intellectual disability (Selcen *et al.*, 2014). Endplate studies have shown pre- and postsynaptic abnormalities with reduction of postsynaptic folding, small nerve terminals, and reduce α-bungarotoxin labelling. Treatment with pyridostigmine and 3,4-DAP is usually beneficial. Of note, ß2-adrenergic agonists had a clear benefit in two patients (S Finlayson *et al.*, 2013; Selcen *et al.*, 2014).

DPAGT1 mutations also cause congenital disorder of glycosylation type Ij characterised by severe hypotonia, intractable seizures, mental retardation and microcephaly (Wu *et al.*,

2003). The variability of the manifestations derived from the genetic changes is not well understood.

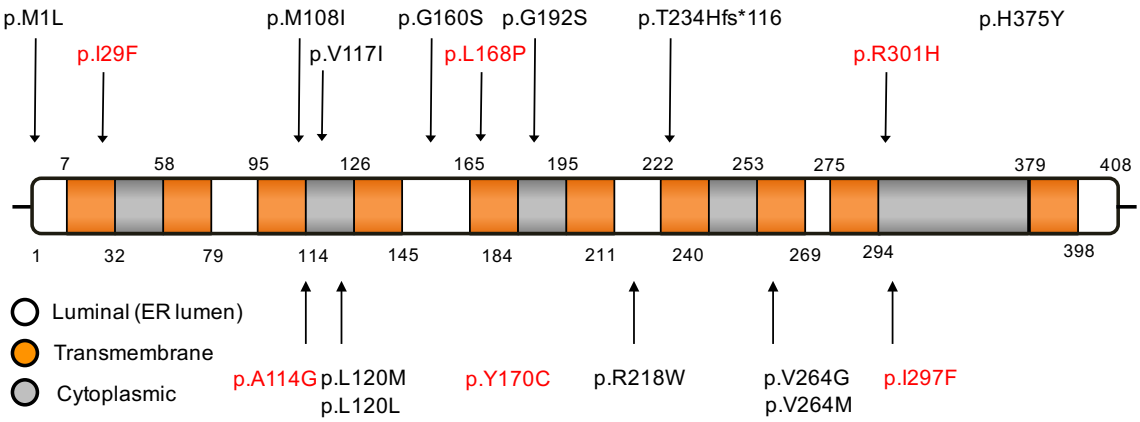


Figure 1-15. Schematic representation of DPAGT1 drawn to linear scale and localisation of mutations identified in patients with CMS and CDG type Ij

DPAGT1 (RefSeq NP_001373.2) is a multipass integral membrane protein of the endoplasmic reticulum. CMS mutations are represented in black while CDG mutations are presented in red colour.

ALG2 and ALG14

ALG14 encodes a protein that together with ALG13 is thought to form a functional multienzyme complex involved in the initial steps of endoplasmic reticulum N-linked glycosylation (Lu *et al.*, 2012). *ALG2* encodes alpha-1,3-mannosyltransferase that catalyses the second and third mannosylation steps for the elongation of the carbohydrate chain linked to dolichol (Jackson *et al.*, 1993). Both ALG2 and ALG14 are concentrated at motor endplates and RNA silencing of ALG14 results in reduced cell-surface expression of AChRs in heterologous cells (Cossins *et al.*, 2013). CMS due to mutations in *ALG2* and *ALG14* is very rare with only 9 patients from 3 different kinships reported to date (Cossins *et al.*, 2013; Monies *et al.*, 2014).

In a similar fashion to GFPT1 and DPAGT1-CMS, patients with *ALG2* and *ALG14* mutations present predominant proximal and truncal weakness with relative sparing of facial and oculobulbar muscles (Cossins *et al.*, 2013). The age at onset is variable from infancy and early childhood to 7 years of age. The condition is progressive with some patients losing ambulation in late childhood and teenage years. Needle EMG can show myopathic motor unit potentials, and serum CK levels are within the normal range. Only one case had presence of tubular aggregates on muscle biopsy. The myasthenic component can be treated with cholinesterase inhibitors.

GMPPB

GMPPB encodes GDP-mannose pyrophosphorylase B that catalyses the conversion of mannose-1-phosphate and GTP to GDP-mannose. *GMPPB* contributes to both the N-glycosylation and the *O*-mannosylation pathways. Mutations within the O-mannosylation pathway were originally identified in patients with a form of muscular dystrophy within the spectrum of dystroglycanopathies (Muntoni *et al.*, 2011). These disorders are characterised by reduced α-dystroglycan glycosylation. More recently, our group showed that autosomal recessive mutations in *GMPPB* can also cause CMS and bridge myasthenic disorders with dystroglycanopathies (Belaya, 2015). In Chapter 5, the clinical characterisation of this novel disorder will be addressed.

1.10 Treatment

The CMS treatment strategy used in the Oxford CMS Service is provided for the most common CMS subtypes **(Figure 1-16)**. As shown in the figure, the response to pharmacological treatment depends on the CMS subtype, and thus the importance of

genetic diagnosis. Classic treatments include acetylcholinesterase inhibitors (pyridostigmine – Mestinon®) to inhibit acetylcholinesterase from breaking down acetylcholine (Schwab and Timberlake, 1954); 3,4-DIaminopyridine (3,4-DAP) that works by blocking presynaptic potassium channels and thus increases the action potential duration and acetylcholine release (Palace *et al.*, 1991); Fluoxetine and quinide that work as open channel blockers to restore synaptic channel function (Harper *et al.*, 2003).

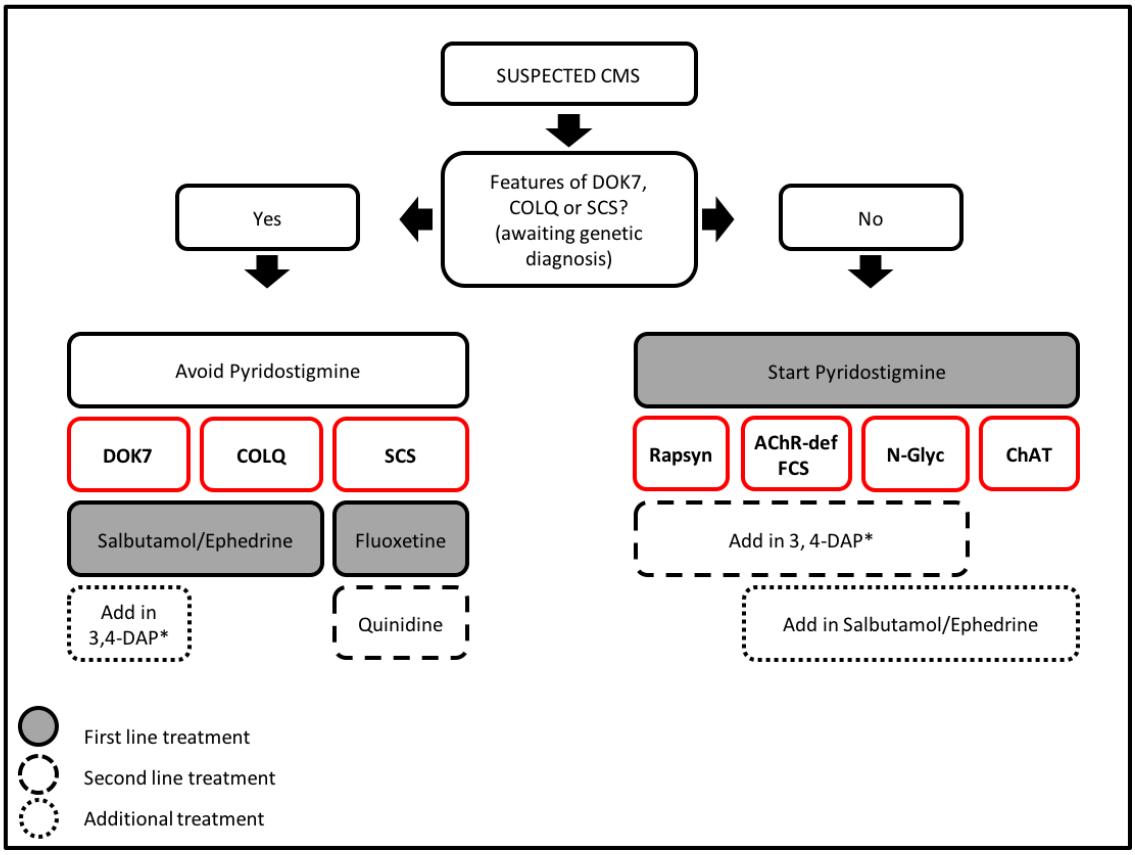


Figure 1-16. Treatment strategy at the Oxford CMS Service for most common subtypes
First-line treatment with pyridostigmine should be avoided if features of DOK7 and other members of the AGRN–MUSK pathway, COLQ or SCS are present. Combined therapy with salbutamol or ephedrine may be tried on AChR deficiency, CMS due to glycosylation defects and FCS. 3,4-DAP can be added in with caution (asterisk) in patients with DOK7, Rapsyn, CMS due to glycosylation defects, AChR-deficiency and FCS. In cases of slow channel syndrome, quinidine may be used as an alternative to fluoxetine. FCS, Fast channel syndrome; N-glyc, N-glycosylation pathway; SCS, slow channel syndrome.

Recently, a number of studies have reported great benefit of therapy with β2-adrenergic agonists such as salbutamol and ephedrine in DOK7-CMS (Lashley *et al.*, 2010; Burke *et al.*, 2013; Lorenzoni *et al.*, 2013). The molecular mechanism for salbutamol and ephedrine at the NMJ is unknown, although for patients with mutations in the AGRN-MUSK-DOK7 pathway, there is a slow but progressive response starting within weeks and increasing in effect before stabilising out at between 6-24 months. The use of these drugs is increasing in other CMS subtypes such as acetylcholinesterase deficiency (Mihaylova *et al.*, 2008; Liewluck *et al.*, 2011) and CMS due to abnormal glycosylation (S Finlayson *et al.*, 2013; Selcen *et al.*, 2014). In chapter 8, the effects of β2-adrenergic agonists in severe AChR deficiency despite optimal therapy with anticholinesterase and 3,4-DAP are described.

1.11 Objectives

The main goal of the presented thesis is to deliver better care to patients with CMS by improving our understanding of the clinical and molecular basis of this condition, and by providing more accurate diagnosis and better treatment strategies. Different aspects of CMS will be explored and the work is divided in 5 parts.

1) Improve the differential diagnosis of CMS

The differential diagnosis of CMS is complex with MG patients lacking detectable AChR and MuSK antibodies by RIA (seronegative MG) being the most challenging group. For the improved detection of AChR antibodies, a cell-based assay was developed using AChRs clustered by the anchoring protein Rapsyn (Leite *et al.*, 2008). This study aimed to explore the diagnostic usefulness of the clustered-AChR CBA in the diagnosis of seronegative myasthenia gravis (SNMG) and in the differential diagnosis of CMS. The overall

importance of getting the right diagnosis lies on the possibility of providing adequate treatment, avoiding unnecessary immunosuppression, and to give the appropriate advice and genetic counselling for the patients.

2) Characterise previously undefined myasthenic syndromes

Approximately 10% of individuals with clinically diagnosed CMS in the UK have no identified mutations in the known CMS-associated genes (Finlayson, 2013). The use of NGS in clinical diagnosis is allowing the identification of new disease genes (Taylor *et al.*, 2015), which help to increase our knowledge on the molecular architecture of the NMJ. The objective of this study is to define the clinical and molecular characteristics of two novel myasthenic syndromes caused by mutations in *COL13A1* (collagen type XIII alpha 1 chain) and *GMPPB* (GDP-mannose pyrophosphorylase B).

3) Study of novel clinical features

The discovery of *DOK7* mutations resulted in the identification of a group of patients with limb-girdle myasthenic syndrome (Beeson *et al.*, 2006). Patients harbouring *DOK7* mutations typically present with walking difficulties after normal motor milestones, proximal muscles weakness greater than distal, and spared eye movements (Palace *et al.*, 2007). A more recent feature described is the presence of stridor (Klein *et al.*, 2013). This study aimed at exploring the clinical and molecular basis of stridor in patients with DOK7-CMS with the purpose of gaining further insight into why certain muscles are specifically targeted in this condition.

4) Unravel novel mechanisms of impaired synaptic transmission

A patient harbouring two missense variants in *MUSK* (p.C317R, p.A617V) had clinical features suggestive of severe CMS from birth. However, initial studies were unsuccessful to prove the pathogenicity of the p.A617V variant. Hence a study was performed using novel techniques to gain insight into the underlying molecular mechanisms of impaired synaptic transmission. The ultimate goal is to direct the appropriate treatment strategy for the patient based on the molecular findings.

5) Improve the treatment strategy for CMS

Optimal treatment with cholinesterase inhibitors and 3,4-DAP does not provide a sustained clinical benefit in patients with CMS due to severe AChR-deficiency. A number of studies have reported great benefit of therapy with β2-adrenergic agonist in DOK7-CMS (Lashley *et al.*, 2010) and congenital endplate AChE deficiency (Mihaylova *et al.*, 2008), thus it has been hypothesised that these agents would be beneficial for patients with severe AChR deficiency who are already treated with pyridostigmine. Hence a cohort study was designed to evaluate the response to the addition of β2-adrenergic agonists to their regular medication over the course of 6- to 8- months.

Chapter 2

Patients, Materials and Methods

2.1 Patients

2.1.1 CMS patients

The majority of patients reported in this work attended the Oxford – Referral Centre for Congenital Myasthenic Syndromes, based at the John Radcliffe Hospital, which is funded through the UK National Specialist Commissioning (NSC) Department of Health. Ethical approval for the use of clinical data and molecular genetics research studies was obtained from the Oxfordshire Research Ethics Committees OXREC B (04/OXB/017) and OXREC C (09/H0606/74). Informed consent was obtained from all participant individuals or families presented in this thesis.

2.1.2 Muscle biopsy samples

A muscle biopsy was taken from an individual of White British origin diagnosed with CMS harbouring the homozygous mutation c.1171delG in *COL13A1*. Patient informed consent was obtained from the family with ethical approval.

2.1.3 Laryngeal muscle samples

Human laryngeal muscle samples from individuals undergoing partial or total laryngectomy were collected from the Churchill Hospital in Oxford in order to study their molecular properties. Prior to the surgery, patients were asked by the Ear, Nose and Throat (ENT) team to sign the Oxford University Hospital (OUH) Surgical Consent Form 1

– Section Donation of tissue – that allows the use of discarded tissue for research. Exclusion criteria included previous radiotherapy, known neuromuscular disease or Surgical Consent Form 1 not signed. All surgical procedures were performed by Mr. Stuart Winter (OUH ENT Consultant) at the Churchill Hospital in Oxford. Upon removal of the larynx, the specimen was reviewed by the OUH Histopathology Consultants (Dr. Keith Shah and Dr. Stephen Damato) who performed the dissection of the laryngeal muscles whenever diagnostic procedures were not compromised. The muscles typically dissected were the posterior cricoarytenoid (PCA) and the interarytenoid (IA) muscles. The PCA muscle is typically affected in DOK7-CMS. The IA muscle is not affected and more easily dissectible than other intrinsic muscles of the larynx and, therefore, it was used as control.

2.1.4 Serum samples

Two cohorts of serum samples from patients with Myasthenia Gravis (MG) selected by Prof. Angela Vincent and Dr. Angelina Maniaol were used for the detection of antibodies against COL13A1. Testing was supported by ethics approval OXREC B (04/OXB/017) and OXREC C (09/H0606/74). Disease control samples were provided by the Oxford Neuromyelitis Optica Research Tissue Bank with ethical approval OXREC 10/H0606/56.

2.2 DNA methods

2.2.1 DNA extraction from bacterial cultures

DNA from bacterial cultures was extracted with the QIAprep Spin Miniprep Kit (Quiagen - Cat. No. 27106) following the manufacturer´s protocol. The PureLink® HiPure Plasmid Filter Maxiprep Kit (Invitrogen – Cat. No. K2100-17) was used for DNA extraction on a large scale following the manufacturer´s instructions.

2.2.2 DNA extraction from mammalian cells

The DNA from mammalian cells was extracted using QuickExtract ™ DNA Extraction Solution (Epibio, Cat. No. QE09050) according to the manufacturer´s protocol.

2.2.3 Resolution of DNA in agarose gels

Agarose gels were prepared by dissolving UltraPure™ agarose (Invitrogen – Cat. No. 16500-50) in 1XTBE buffer (90 mM Trizma Base, 90 mM boric acid, 2 mM EDTA) supplemented with ethidium bromide solution at 10 mg/ml (Invitrogen – Cat. No. 15585-011) to enable visualisation of DNA with an ultraviolet transiluminator. The concentration of agarose (1-5%) was chosen depending on the size of the expected DNA product. 5X DNA loading buffer blue (Bioline – Cat. No. Bio-37045) was added to the samples to allow visualization during the running of the gel in 1XTBE buffer at 60-80 V. GelDoc-It®2 Imaging System and VisionWorks® Acquisition and Analysis software was used to visualised DNA.

2.2.4 DNA extraction from agarose gels

DNA bands were excised using a clean scalpel under a UV transiluminator, and the DNA was purified using a QIAquick Gel Extraction Kit (Qiagen – Cat. No. 28706). DNA concentration was measured using a NanoDrop™ 2000 Spectrophotometer (Thermo Fisher Scientific).

2.2.5 DNA Sequencing

Sanger sequencing was carried out by the Weatherall Institute of Molecular Medicine (WIMM) DNA Sequencing Facility following their recommendations. Sequence of oligonucleotides used for this purpose is provided in **Table 2-1**.

Table 2-1. Oligonucleotides used for Sanger sequencing

Target	Primer name	Primer Sequence 5'-3'
COL13A1	COL13A1 F2	TTGGGCTGGACGGCAAACCGGGCCA
COL13A1	COL13A1 F3	AGGGATCCCAGGAACCAAGGGTGAG
COL13A1	COL13A1 F4	TTCCAGGCCAGAAGGGGGAGATTGG
COL13A1	COL13A1 F5	GGTACTCCAGGACCAATTGGAGTTC
COL13A1	HuCOL13A1R	TCACTTGTTCCAGCAGCCTTGGACT
DOK7	D7R1	CAAGACGAGGACATCATTGC
DOK7	D7R2	CTGTAGGGTTTCCAGGGCTT
DOK7	D7F8	AGGCCAGTCACTTGGACGTCA
MUSK	MUSK F1	AATCCCAAACCATCAGTGTC
MUSK	MUSK F2	GGGAGGTGTGTAATGCAGTC
MUSK	MUSK F3	TCACCTACATACTCCATGAC
MUSK	MUSK F4	TGCAGCCTCAGTCACAGTGA
MUSK	MUSK R1	AATGCCTGTTGCTGTACAGT

2.2.6 Polymerase chain reaction (PCR)

2.2.6.1 Standard PCR

Standard PCR was performed with MegaMix-Blue (Microzone™). This PCR master mix contains recombinant *Taq* polymerase in 1.1x reaction buffer (2.75 mM MgCl2) with 220 µM deoxyribonucleotide triphosphates (dNTPs), blue agarose loading dye and stabiliser. Reactions were performed with 47 µl or less of MegaMix-Blue, DNA template (1 to 2 µl) and primers (0.5 to 1 µl of each from ~10 µM stock). Oligonucleotides used in PCR reactions were synthesised by Life Technologies. Thermocycler conditions are specified in **Table 2-2.**

Table 2-2. Thermocycler conditions used for standard PCR

Step	Temperature	Duration
Initial denaturation	95°C	3 mins
Amplification (30-40 cycles)	95°C	30 secs
	Optimal annealing temp. of primers (T_M-5°C)	30 – 60 secs
	72°C (Extension)	60 secs / 1Kb of target DNA
Final extension	72°C	10 mins
Cooling	4°C	∞

2.2.6.2 High-fidelity PCR

High-fidelity PCR was performed using *PfuUltra* II Fusion HS DNA Polymerase (Agilent Technologies – Cat. No. 600670) with proof-reading activity. Reactions mixture (50 µl) included 40.5µl nuclease free water, 5µl *PfuUltra* II reaction buffer, 0.5 µl dNTP mix (25mM each DNTP), 1µl DNA template (100 ng/µl), 1µl of each primer (10µM) and 1µl of *PfuUltra* II Fusion HS DNA Polymerase. Thermocycler parameters are provided in **Table 2-3.** Oligonucleotides used in PCR reactions, synthesised by Life Technologies, are detailed in **Table 2-4**.

Table 2-3. Thermocycler conditions for high-fidelity PCR

	Number of cycles	Temperature	Duration (vector or genomic DNA)	Duration (cDNA)
1	x1	95°C	2 minutes	1 minutes
2	x30 (genomic DNA or vector) x40 (cDNA)	95°C	20 secs	20 secs
		Primer Tm – 5°C	20 secs	20 secs
		72°C	15 secs for targets ≤1 kb. 15 secs per kb for targets >1 kb	30 secs for targets ≤1 kb. 30 secs per kb for targets >1 kb
3	1	72°C	3 minutes	3 minutes

Table 2-4. Primers used for the amplification of full-length human DOK7 and mouse MuSK

Target	Primer name	Primer sequence 5'-3'
DOK7	DOK7_F_amp	ATGACCGAGGCGGCGCTGGTGGA
DOK7	DOK7_R_amp	TCAAGGAGGGGGGTTTACCTTGAGT
Musk	Ms_MusK_F	CTTCAGCGGGACTGAGAAAC
Musk	Ms_Musk_R	CCGGTAGGAGGTGTTGAAGA

2.2.7 Mutagenesis

The QuickChange® Multi Site-Directed Mutagenesis Kit (Agilent Technologies – Cat. No. 200514) was used for site-directed mutagenesis of double-stranded plasmid DNA. This was used to produce site-specific mutations in pcDNA3.1-hygro(+)COL13A1, pcDNA3.1-hygro(+)MuSK, pBabe-MuSK-EGFP-PURO, and pEGFP-N1-DOK7 constructs. For the generation of each mutation, a specific mutagenic primer with centrally located mutation was designed using the QuickChange® Primer Design Tool (http://genomics.agilent.com/primerDesignProgram.jsp). The mutagenic primers used for this purpose are listed in **Table 2-5**.

Table 2-5. Sequences of the oligonucleotides used in Site-Directed Mutagenesis

Mutation	Primer name	Primer Sequence 5'-3'
COL13A1 c.1171delG	c.1171delG_F	CTGGCCCTCCAGGCTCCCTGGGCCC
COL13A1 c.523delG	c.523delG_F	CTGGATTTCCGGTCCCATTGGGCTG
COL13A1 p.R108-111Adel	COL13A1_cleavagesite	GTCTTTGGGGCCTCCGCGGCCGCCGCTG AGTGGAGCTTCCATTTCTCGTCCAGCA
MuSK p.C317R	MuSK C317R_F	AGATAACAAAGGCTACCGCGCCCAGTACAGAGG

MuSK p.A617V	MuSK A617V_F	CTTTCAGAGGGAGGTAGCCCTCATGGCAG
DOK7 p.M1A	DOK7_Met1	GAACCATGACAGAAGGCGACCGAGGCGGCGCT
DOK7 p.M38A	DOK7_Met2	GGCAGACTGCCTGCTGGCGCTGGTCTACAAGGAC
DOK7 p.M88A	DOK7_Met3	CTGTCCCAGGCCATCGCGCTGGGCTTTGACAG
DOK7 p.M97A	DOK7_Met4	ACAGCCACGAGGCCGCGTGTGCGTGGGATG
DOK7 p.M311A	DOK7_Met5	CGCCGGGGAAGCCGCGGTGGGTGCCTCA

During the PCR reaction, the mutagenic primers anneal to the denatured templated DNA, and the PfuTurboDNA polymerase extents the mutagenic primers generating a dsDNA with one strand bearing the desired mutation. Afterwards, the *Dpn*I endonuclease, which is specific for methylated and hemimethylated DNA, is used to digest the parental DNA template. This is because the DNA isolated from most *Escherichia Coli* is DAM (Deoxyadenosine methylase) methylated and, therefore, prone to digestion. The products were transformed into *TOP10* competent cells (Thermo Fisher Scientific – Cat. No. C404006) where the mutant single stranded DNA was transformed in vivo into double stranded. Finally, the product was plated on Lysogeny Broth (LB)-Agar plates supplemented with the corresponding antibiotics. Several colonies were screened for the presence of the plasmids with the desired mutations by Sanger sequencing after DNA extraction with QIAprep® Spin Miniprep Kit (Qiagen – Cat. No. 27104).

2.2.8 Molecular cloning

2.2.8.1 DNA digestion

DNA digestion was performed with restriction enzymes from New England Biolabs and Thermo Fisher Scientific according to the manufacturer´s instructions.

2.2.8.2 DNA dephosphorylation

After digestion of plasmids with a single restriction enzyme, the linearised plasmid was dephosphorylated to prevent re-annealing with the heat-labile Antartic Phosphatase (New England Biolabs, Cat. No. M0289). Reaction mix included 1-5 μg of DNA, 1 μl of Antartic Phosphatase, 2 μl of 10X Antartic Phosphatase Reaction Buffer, and nuclease-free water up to 20 μl. The mix was incubated at 37°C for 1 hour, and then the enzyme was heat-inactivated by heating at 80°C for 2 minutes.

2.2.8.3 DNA ligation

DNA ligations were performed using a T4 DNA ligase (Roche – Cat. No. 10481220001). Reaction mix included 2 μl of 10X T4 DNA ligase buffer, 50 of μg vector DNA, x insert DNA, 2 μl T4 DNA ligase, and nuclease free water to 20 μl. Reactions were carried out using a 1:3 molar ratio of vector and insert DNA for sticky ends and 1:5 for blunt end ligation.

2.2.8.4 Oligonucleotides annealing

Annealing of oligonucleotides was performed by using equal volumes of both complementary nucleotides at equimolar concentrations re-suspended in annealing buffer. The mix was incubated at 95°C for 5 minutes and then temperature was decreased by 5°C per minute to room temperature.

2.2.8.5 PGEM®-T Easy cloning

The pGEM®-T Easy Vector System (Promega – Cat. No. A1380) is a linearised vector with a single 3' terminal thymidine overhang at both ends for the cloning of PCR products. For the ligation of PCR products into the vector, the blunt ends of the PCR products need to undergo prior deoxyadenosine (A)-tailing with *Taq* polymerase as specified in **Table 2-6**. The ligation product (2 μl) was transformed into JM109 competent cells. The cells were plated onto LB-Agar plates containing ampicillin, isopropyl ß-D-1-thiogalactopyranoside (IPTG) and 5-bromo-4-choro-3-indolyl-ß-D-galactopyranoside (X-Gal), and incubated overnight at 37°C. Screening of recombinant clones was performed using the blue/white screening system, which allows the recognition of successful cloning via insertional inactivation of the alpha-peptide region of the ß-galactasidose enzyme in the vector.

Table 2-6. Components of reaction mix for the use of pGEM®-T Easy Vector System

Poly-(A) tailing of PCR products		
PCR product	7 μl	70°C – 30 minutes
Taq Buffer	1 μl	
dATP (2nM)	1 μl	
MgCl2 (50nm)	0.33 μl	
Taq polymerase	1 μl	
Ligation into pGEM®-T Easy		
pGEM®-T Easy vector (50ng)	1 μl	16°C – overnight
PCR product	x μl (5:1 molar ratio)	
2x Rapid Ligation Buffer	10 μl	
T4 DNA ligase	1 μl	
Nuclease free water	Up to 20 μl	

2.2.8.6 Outline of COL13A1 cloning

An IMAGE clone containing cDNA from transcript variant 1 of *COL13A1* (RefSeq NM_001130103.1) was purchased from Source BioScience Ltd., Nottingham, UK (clone number 9020372). The coding sequence of COL13A1 image clone **(Figure 2-1)** was amplified using *PFuUltra* II Fusion HS DNA polymerase and a pair of specific primers **(Table 2-7)**. A-tailing of the PCR product was performed prior to being ligated into pGEM®-T Easy

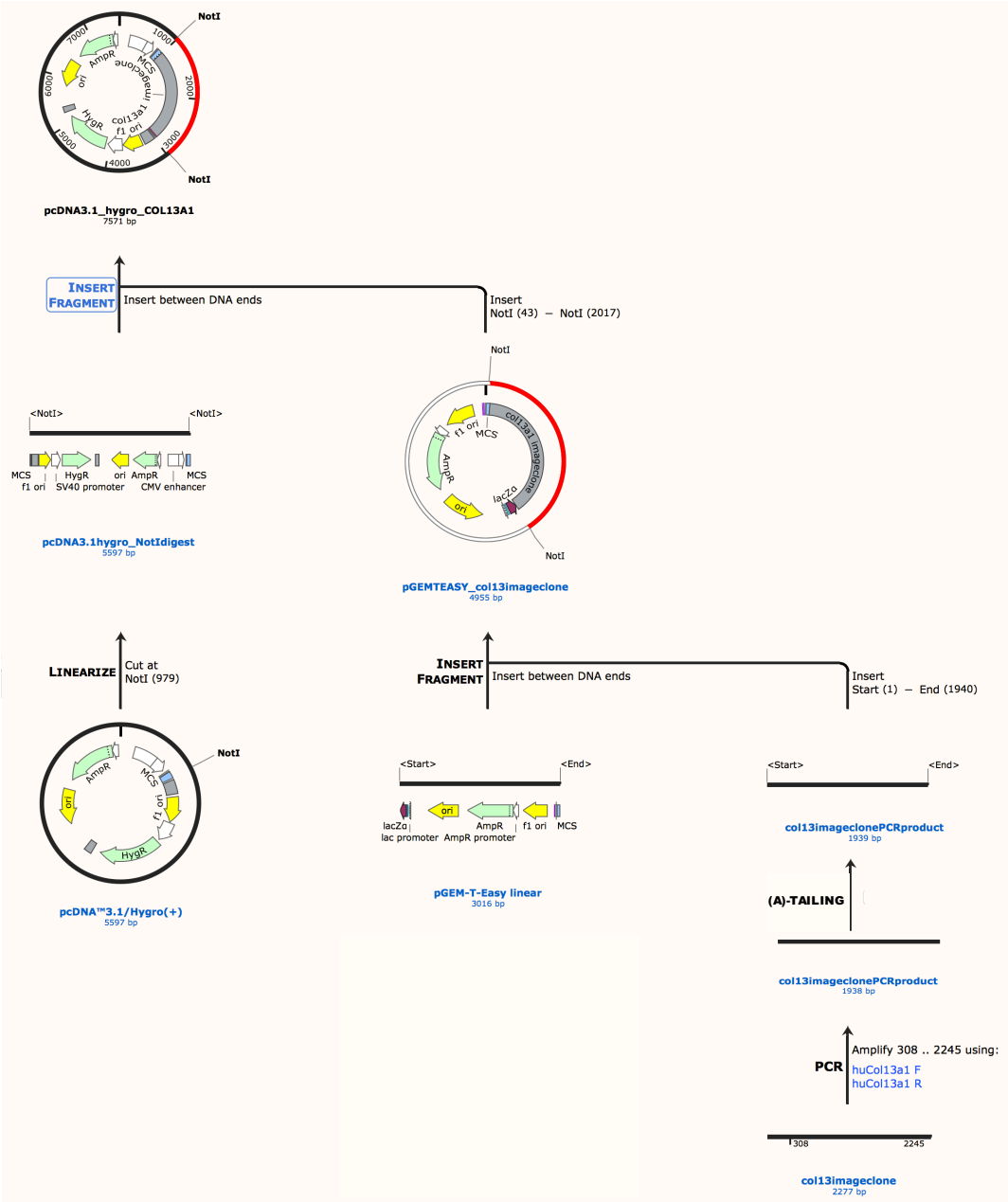


Figure 2-1. Outline of COL13A1 cloning into pcDNA3.1/Hygro(+)

Table 2-7. Primers used for the amplification of COL13A1 image clone

Target	Primer name	Primer sequence 5'-3'
COL13A1	huCol13a1_F	ATGGTAGCGGAGCGCACCCACAAAG
COL13A1	huCol13a1_R	TCACTTGTTCCAGCAGCCTTGGACT

The ligation product and the pcDNA3.1Hygro(+) plasmid were digested using a *NotI* restriction endonuclease according to the manufacturer´s instructions, and resolved by gel electrophoresis. The bands corresponding to COL13A1 (1.93 Kb) and pcDNA3.1Hygro(+) (5.59 Kb) were extracted and gel purified for subsequent ligation (section 2.1.8.3). The products were transformed using *TOP10* competent cells, plated into LB-agar plates supplemented with ampicillin, and purified with QIAprep Spin Miniprep Kit (Quiagen - Cat. No. 27106). The correct orientation of the insert was determined by PCR amplification using primers from **Table 2-8**. The PCR products were resolved by gel electrophoresis producing a band of approximately 733 base pairs (bp). The correct sequence of pcDNA3.1/Hygro(+)-COL13A1 was confirmed by Sanger sequencing using primers from **Table 2-1**.

Table 2-8. Primers used to determine the correct orientation of COL13A1 into pcDNA3.1/ Hygro(+)

Target	Primer name	Primer sequence 5'-3'
COL13A1	COL13A1 orientation check F	GGAAAAGGGACCTCGCGGTAAACCA
COL13A1	COL13A1 orientation check R	GCACGGGGGAGGGGCAAACAACAGA

2.2.9 Plasmids

The plasmids used in this thesis are summarised in **Table 2-9.**

Table 2-9. List of plasmids used in this thesis

Plasmid	Description
nls-p*EGFP*	Expression plasmid encoding EGFP with a nuclear localisation signal (NLS) (Addgene #67652)
pBABE-puro-IRES-*EGFP*	Retroviral vector for the expression of EGFP (empty)
pBABE-puro-*MUSK*-IRES-*EGFP*	Retroviral vector for the expression of human MUSK with an internal ribosome entry site (IRES)for EGFP expression
pcDNA3.1-*ADRB2*	Expression plasmid encoding the β2-Adrenoreceptor
pcDNA3.1-*AGRN*	Expression plasmid encoding full-length human agrin
pcDNA3.1-*CHRNA1*	Expression plasmid encoding the human AChR-α subunit
pcDNA3.1-*CHRNB1*	Expression plasmid encoding the human AChR-β subunit
pcDNA3.1-*CHRND*	Expression plasmid encoding the human AChR-δ subunit
pcDNA3.1-*CHRNE*	Expression plasmid encoding the human AChR-ε subunit
pcDNA3.1-*CHRNG*	Expression plasmid encoding the human AChR-γ subunit
pcDNA3.1-*COL13A1*	Expression plasmid encoding human COL13A1
pcDNA3.1-*MUSK*	Expression plasmid encoding human MuSK
pcDNA3.1-*MUSK-mCherry*	Expression plasmid encoding human MuSK tagged with the fluorescent marker mCherry
pcDNA- *AGRN-CASPR2TM*	Expression plasmid encoding full-length human agrin with a C-terminal CASPR2 transmembrane domain
pcDNA-*Myc-COLQ-CASPR2TM*	Expression plasmid encoding human COLQ with a transmembrane domain from CASPR2 fused to its C-terminus and a myc-tag introduced downstream the N-terminal signal peptide
pEGFP-N1	Expression plasmid encoding human MuSK tagged with the fluorescent marker mCherry
pEGFP-N1-*DOK7*	Expression plasmid encoding human DOK7 tagged with the fluorescent marker EGFP
pEGFP-N1-*LRP4*	Expression plasmid encoding human MuSK tagged with the fluorescent marker EGFP
pEGFP-N1-*MUSK*	Expression plasmid encoding human MuSK tagged with the fluorescent marker EGFP
pEGFP-N1-*RAPSN*	Expression plasmid encoding human RAPSYN tagged with the fluorescent marker EGFP
Px335-U6-Chimeric_BB Cbh-hSPCas9n(D10A)	Plasmid expressing the Cas9-D10A nickase

2.3 CRISPR/Cas9 Genome engineering system

The CRISPR/Cas9 system was used to generate a *Musk* KO C2C12 mouse muscle cell line via non-homologous end joining. A double-nicking strategy was selected in order to minimise off-target cleavage (Fa Ann Ran *et al.*, 2013) with minor modifications.

2.3.1 Introduction to CRISPR/Cas9

CRISPR/Cas (*Clustered Regularly Interspaced Short Palindromic Repeats*) is a prokaryotic immune system that confers resistance to foreign genetic elements (Mojica *et al.*, 2000). Small clusters of *Cas* (CRISPR-associated system) genes are located next to the CRISPR sequences.

A modified version of the CRISPR/Cas system, CRISPR/Cas9, has been generated for genome-editing purposes (Cong *et al.*, 2013; Mali *et al.*, 2013). The CRISPR/Cas9 system is made of two main components: two small RNA molecules named CRISPR RNA (crRNA) and trans-activating crRNA (tracrRNA), which are fused into a single guide RNA (sgRNA) (Jinek *et al.*, 2012), and a RNA-guided DNA endonuclease (*Cas9)* derived from *Streptococcus pyogenes*. The latter can be programmed to target any DNA sequence by a complementary 20-nucleotide sequence hybridised 5' of the sgRNA **(Figure 2-2)**. A 5'-NGG protospacer adjacent motif (PAM) is required downstream of the target sequence for Cas9 DNA cleavage (Jinek et al., 2012).

Following DNA cleavage of the genomic target sequence, the DNA undergoes damage repair by either non-homologous end joining (NHEJ) or homology-directed repair (HDR) (Fa Ann Ran *et al.*, 2013). In the NHEJ mechanism, the DNA break ends are directly ligated

without the need for a homologous template. This is often used to generate indels in the coding sequence, which results in frameshift mutations and premature stop codons. On the other hand, HDR requires a homologous sequence containing the desired DNA modification (repair template). This is used to introduce specific DNA modifications.

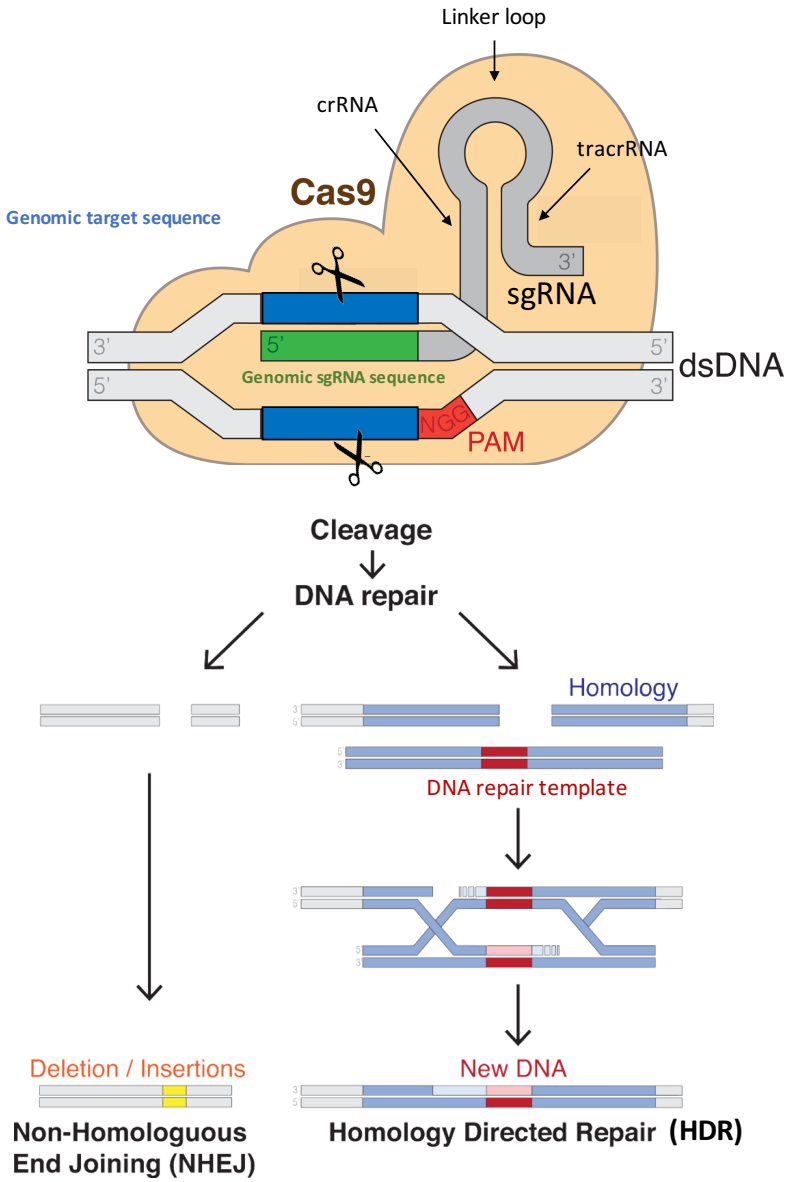


Figure 2-2. Schematic representation of the CRISPR/Cas9 genome engineering system

The Cas9 nuclease uses a sgRNA to target the specific genomic sequence through Watson-crick base pairing. Following the double-stranded DNA break, the DNA can be repaired via non-homologous end joining (NHEJ) or Homology directed repair (HDR) depending on the presence of homologous DNA repair template. Modified from original source under *Creative Commons Attribution-ShareAlike 4.0 International Public License*.

A mutant (D10A) nickase version of Cas9, Cas9n, induces single-stranded DNA breaks, and can be directed by a pair of sgRNA to opposite strands of the target DNA to mediate a DSB. (F. Ann Ran *et al.*, 2013) The double nicking offers higher target specificity (Ran et al., 2013a).

2.3.2 Generation of the CRISPR-Cas9 construct

Musk oligonucleotides Guide A and B **(Table 2-10)** (Integrated DNA Technologies Inc., Coralville, IO, USA) were designed and independently cloned into a modified version of plasmid pX335-U6-Chimeric_BB-CBh-hSpCas9n(D10A) purchased from Addgene (plasmid # 42335) using a *BBs1* restriction site **(Figure 2-3)**. The oligonucleotide guide sequences (Musk guide A and B), complementary to the exon 3 of mouse *Musk*, were designed using the online CRISPR Design Tool (http://crispr.mit.edu/). Both pairs of oligonucleotides rated high in quality and scored 0 in off-target effects. Additional overhangs (underlined) were added to the sequences to allow the ligation into the *BBsI* digested pX335_Cas9 constructs.

Table 2-10. Musk guides oligonucleotide sequences

Oligonucleotide name		Oligonucleotide sequence 5'-3'
Musk Guide A	Forward	CACCGCATTCTCCCGGATGCTGTAG
	Reverse	AAACCTACAGCATCCGGGAGAATGC
Musk Guide B	Forward	CACCGCTCCTCACCATTCTGAGCG
	Reverse	AAACCGCTCAGAATGGTGAGGAGC

The single strand oligonucleotides guides were annealed by assembling the reaction described in **Table 2-11** in a sterile microcentrifuge tube. The px335 plasmid was digested

for 3 hours at 37°C using a *Bbs*I restriction enzyme and the following components : 2μg plasmid, 1μl *Bbs*I enzyme (NEB – Cat. No. R0539S), 2μ Buffer 2.1 (NEB – Cat. No. B7202S) and nuclease free water up to 20 μl. The product was resolved in a 1% agarose gel and purified using a QIAquick® gel extraction kit (Qiagen – Cat. No. 28706). The annealed oligonucleotides were ligated into the px335 plasmid at 4°C overnight as shown in **Table 2-11**.

Table 2-11. Components of annealing and ligation reactions

Annealing of oligonucleotides reaction		
Component	Amount	Thermocycler parameters
Guide forward (100 μM)	1 μl	85°C – 10 minutes Decrease 5°C / min until 20°C
Guide reverse (100 μM)	1 μl	
T4 ligation buffer 10X	1 μl	
Nuclease free water	7 μl	
Ligation of annealed oligonucleotides into px335 plasmid		
Annealed oligonucleotides	2 μl	4°C overnight
Px335 digested plasmid (100 ng)	2 μl	
T4 DNA ligase (Promega)	1 μl	
T4 DNA ligase buffer	10 μl	
Nuclease free water	5 μl	

The ligation products were transformed into JM109 competent cells and plated onto LB agar plates enriched with ampicillin. DNA from the bacterial colonies was extracted using a QIAprep® Spin Miniprep Kit (Qiagen – Cat. No. 27104). The products were resolved by gel electrophoresis upon amplification with a U6 Forward primer: 5'-GAGGGCCTATTT

CCCATGATTCC-3’ to check the orientation of the insert. Finally, the DNA of the colonies with the correct orientation was confirmed by DNA sequencing using a px335_EGFP_F primer: 5’- GAGGGCCTATTTCCCATGATTCCTTCATAT-3’.

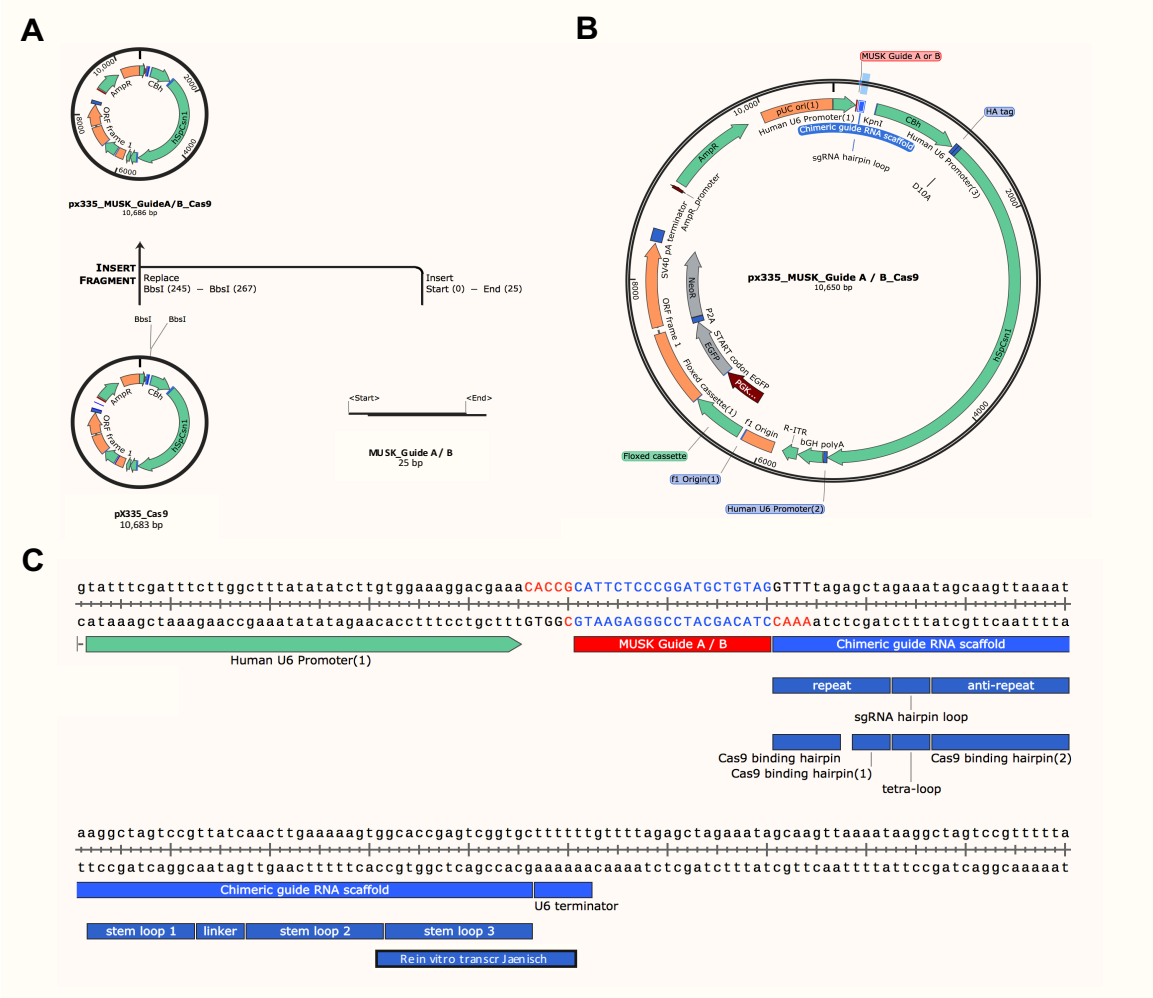


Figure 2-3. Schematic representation of px335-Musk-Guide A / B cloning process

(A) The Musk guides A and B were independently inserted into the px335_Cas9 plasmid using a *BsbI* restriction site. **(B, C)** The Musk guide A/B is followed by a chimeric sgRNA (single-guide RNA) scaffold that directs the Cas9 nuclease to the target via Watson-Crick base paring.

2.3.3 Generation of Musk KO C2C12 muscle cell lines using the CRISPR-Cas9n system

C2C12 myoblast were electroporated with 10µg of each pX335_Cas9n plasmid using a Neon® Transfection System (Life Technologies), and selected with Geneticin® Selective

Antibiotic (Life Technologies, Cat. No. 10131027) after 24 hours for 3 days. Subsequently, the cells were re-suspended and cloned in 96-well flat-bottomed culture plates using Fluorescence-activated cell sorting (FACS) to isolate the cells expressing the enhanced green fluorescent protein (EGFP) from the expression vector. The different clones were expanded for approximately 2 weeks and passaged in 6-well plates. At the same time, the clones were plated in 24 wells, differentiated into myotubes using standard methods (Section 2.8.2) and incubated with full-length agrin overnight for the induction of AChR clusters (Section 2.5.11). Since MuSK is essential for the clustering of AChRs, clones unable to produce AChR clusters were suggestive of *Musk* KO. The DNA from each of these clones was extracted using 60 μl QuickExtrac solution (Epibio, Cat. No. QE09050) according to the manufacturer´s protocol. The DNA was amplified using 1μl DNA, 20 μl MegaMix-Blue (Microzone™) and 0.5 μl of primer mix covering the genomic boundaries of MUSK exon 3 **(Table 2-12)**. The expected product size for MUSK WT amplification was 810 bp. The products were resolved by gel electrophoresis, purified, and analysed by Sanger sequencing.

Table 2-12. Sequences of oligonucleotides used for the amplification of *Musk* exon 3

Oligonucleotide name		Oligonucleotide sequence 5'-3'
Musk Exon 3	Forward	TGGTGCTTTGGTTATGGAGCC
	Reverse	GAGGAGGGGTCTAAGGCTTG

2.4 RNA methods

2.4.1 RNA extraction from mammalian cells

Total RNA was extracted from mammalian cells using RNA Bee isolation reagent (Amsbio – Cat no. CS-104B). Cells grown in a 6-well plate were lysed in the culture dish by the

addition of 1 ml RNA-Bee, and transferred to a microcentrifuge tube. Then, 0.2 ml of chloroform per 1 ml of RNA-Bee were added and the tube was shaken vigorously for 15-30 seconds. The sample was placed in ice for 5 minutes, and centrifuged at 12,000 g for 15 minutes at 4°C. The supernatant located in the upper colourless aqueous phase was removed and transferred to a clean tube. For precipitation of RNA, 0.5 ml isopropanol were added per sample and incubated for 5-10 minutes at room temperature. The samples were further centrifuged at 12,000 g for 1 minutes at 4°C. The supernatant was removed and the RNA pellet was washed in 1 ml of 75% ethanol. The samples were quickly vortexed to dislodge the pellet form the side of the tube, and centrifuged at 7,500 g for 5 minutes at 4°C. Ethanol was removed and the RNA pellet was air-dried for 5-10 minutes at room temperature. Finally, the RNA pellet was solubilised in 20-50 µl of nuclease free water (Ambion – Cat. No. AM9937) and incubated at 55°C for 10 minutes. RNA quality was measured in NanoDrop 2000 Spectrophotometer (Life Technologies) by using the 260/280 absorbance ratio.

2.4.2 RNA extraction from muscle tissue

Total RNA was isolated from muscle tissue using a RNeasy Fibrous Tissue Mini Kit (Quiagen – Cat. No. 74704). A maximum of 10 mg of human muscle tissue were homogenised in 500 µl of Buffer RLT using Precellys® 24 system from Bertin instruments (VWR – Cat no. 432-3750) at 6000 rpm – 2 x 30-5 seconds. Afterwards, 590 µl of RNase-free water and 10 µl of proteinase K were added to the sample, mixed and incubated at 55°C for 10 minutes. The samples were centrifuged at 10,000 g for 3 minutes. The supernatant was transferred into a new 1.5 ml microcentrifuge tube and mixed well by pipetting with 0.5 volumes of 96-100% ethanol. After this, 700 µl of sample were transferred to a RNeasy Mini column

(in a 2 ml collection tube) and centrifuged for 30 seconds at 13,000 rpm. The flow-through was discarded and the procedure was repeated until the complete sample was used. The RNeasy column was washed with 700 μl of Buffer RW1, centrifuged and washed twice with 500 μl Buffer RPE. The RNeasy column was placed in a new 2ml collection tube and further centrifuged for 2 minutes at 13.000 rpm to ensure appropriate washing. Finally, RNA elution was carried out by adding 30-50 μl RNase-free water to the column membrane and centrifugation at 13,000 rpm for 1 minute.

2.4.3 Removal of DNA from RNA preparations

Digestion of contaminating DNA in RNA solutions was performed in solution with RNase-Free DNase Set Kit (Qiagen, Cat No. 79254). The RNA solution was mixed with 10 μl Buffer RDD, 2.5 μl DNase I stock solution and RNase-free water up to a volume of 100 μl, and incubated at room temperature for 10 minutes. Subsequently, 350 μl of Buffer RLT were added and mixed thoroughly. Then 250 μl of ethanol 96-100% were added and mixed well by pipetting. The sample was transferred to a RNeasy Mini spin column placed into a 2 ml collection tube, centrifuged for 30 seconds at 13.000 rpm, and the flow-through was discarded. The membrane was washed and centrifuged twice with 500 μl of Buffer RPE. To ensure appropriate washing, the column was placed in a new 2 ml collection tube and centrifuged at full speed for 1 minute. The flow-through was discarded and the spin column was placed in a new 1.5 ml microcentrifuge tube. Finally, RNA elution was carried out by addition of 30-50 μl RNase-free water to the membrane and centrifugation at 13,000 rpm for 1 minute.

2.4.4 Reverse-transcription PCR

Reverse transcription PCR (RT-PCR) was performed using a RETROscript® Reverse Transcription Kit (Ambion ™ - Cat. No. AM1710). Reactions mixture (20 μl) included 1 μg total RNA, 2 μl Oligo(dT) or Random Decamers, 2 μl 10X RT Buffer, 4 μl dNTP MIX, 1 μl placental RNase Inhibitor, 1 μl MMLV-RT and nuclease free water. The thermocycler parameters are specified in **Table 2-13**. The final cDNA was stored at -20°C.

Table 2-13. Thermocycler conditions for Reverse transcription PCR (RT-PCR)

Segment	Number of cycles	Temperature	Duration
1	X1	55°C	60 minutes
2	X1	92°C	10 minutes

2.4.5 Real time PCR (qPCR)

Total RNA was extracted from human laryngeal muscles samples as previously described (Section 2.4.2). Contaminating DNA was digested in solution using RNase-Free DNase Set Kit (Section 2.4.3) and converted into cDNA with RETROscript® Reverse Transcription Kit (Ambion ™ - Cat. No. AM1710) using Random Decamers to prime the reverse transcription reaction (Section 2.4.4). A sample containing no RNA was reverse transcribed as a negative control for genomic DNA contamination. Quantitative PCR (qPCR) was conducted using the Applied Biosystems® 7500 Real Time PCR System and Power SYBR® PCR Master Mix (Life Technologies – Cat. No.4367659).

Target-specific primers for cDNA amplification were designed using Primer3 web version 4.0.0 (http://primer3.ut.ee/). All primers were designed to amplify exon-exon boundaries if possible and had the following parameters: 18-25 bp length, 40-60% GC content,

amplicon size between 70 and 150 bp, and a primer melting temperature (*Tm*) of 55-65°C with pairs no differing by more than 2°C. The specificity of the primers designed was checked with Primer-BLAST (http://www.ncbi.nlm.nih.gov/tools/primer-blast/). A dilution series of gene-specific templates was used to establish a standard curve to determine the PCR efficiency for each primer pair (Efficiency= $10^{(-1/slope)} - 1$) **(Figure 2-4)**. Primer pairs with efficiencies below 90% were discarded. Finally, the specificity of each primer pair was ensured with the use of negative control templates and melting curve (dissociation curve) analysis. A list of the primer pairs used in the qPCR reactions provided in **Table 2-14**.

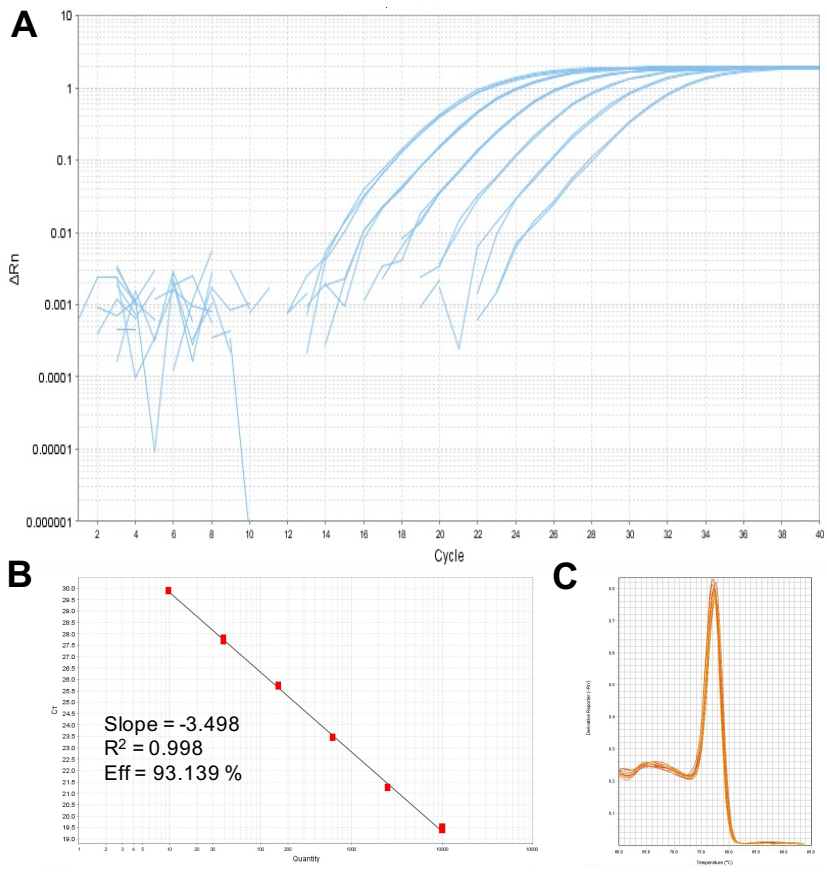


Figure 2-4. Assessment of qPCR primers efficiency and specificity

(A) Representative image of amplification plots using gene-specific template serial dilutions. **(B)** Standard curve analysis (primer efficiency). **(C)** Melting curve analysis (primer specificity).

Reactions were performed in technical triplicates in MicroAmp Fast Optical 96-well plates (Life Technologies – Cat. No. 4360954) with optical adhesive covers (Life Technologies – Cat. No. 4360954). For each reaction, a no reverse transcriptase control (NRT) was used to rule out genomic DNA contamination, and a no template control (NTC) was used to exclude reagents contamination or primer-dimer formation. The data was recorded using the Applied Biosystems 7500 Real-Time PCR Software v2.0.6.

Table 2-14 Sequences of oligonucleotides used in qPCR reactions

Primer pairs used in qPCR reactions						
Target	**Name**	**Tm (°C)**	**Amp. (bp)**	**Effic. (%)**	**Cross**	**Primer Sequence 5'-3'**
ADRB2	ADRB2_1_F	58	87	97.1	No	TGGACTCCGCAGATCTTCCA
	ADRB2_1_R	58				CAGAGGGTGAAAGTGCCCAT
AGRN *	New_Agrin_1_F	59	107	90.2	Yes	GAGATGCGCTGTGAGTTCGG
	New_Agrin_1_R	58				CCACAGACCTTGGTAGCGTT
CHAT	Hu_CHAT_F_QPCR	58	95	91.1	1.5 Kb intron	CAGCCCTGCCGTGATCTTT
	Hu_CHAT_R_QPCR	56				TGTAGCTGAGTACACCAGAGATG
CHRNA1	New_CHRNA1_1_F	60	116	99.4	Yes	ATCAACCCGGAAAGCGACCA
	New_CHRNA1_1_R	60				GTGTCGGGGCAGCAGGAATA
CHRND	Hu_CHRND_F_QPCR	58	85	97.0	Yes	GGAGAACAACAATGACGGCTC
	Hu_CHRND_R_QPCR	57				TGGCAGCCAGTACACGAAG
CHRNE	Hu_CHRNE_F_QPCR	57	80	92.5	Yes	CTCCTGGGCAGGTTCCTTAT
	Hu_CHRNE_R_QPCR	57				GACACGTTGAGCACGATGAC
CHRNG	Hu_CHRNG_F_QPCR	58	71	99.5	Yes	CTCATCTCCCTGAACGAGCG
	Hu_CHRNG_R_QPCR	58				TAGTCGCACCACTGCATCTC
COLQ	Hu_COLQ_F_QPCR_3	58	114	90.2	2 Kb intron	GATGTGGGTGACGACTGCAT
	Hu_COLQ_R_QPCR_3	58				GGTCTCGCATGTCAGGTAGC
DOK7	Hu_DOK7_F_QPCR	58	84	94.3	Yes	TCCTGTTCGACTGCATCGTC
	Hu_DOK7_R_QPCR	57				GGGGACTTGGGTCTGGTAG

GAPDH	New_GAPDH_2_F	57	83	94.1	Yes	CTGCACCACCAACTGCTTAG
	New_GAPDH_2_R	57				GGACTGTGGTCATGAGTCCTT
LRP4	New_LRP4_1_F	59	110	91.2	Yes	TACAGCAACCCCTCCTACCG
	New_LRP4_1_R	60				TGGTCAGGCCCTCCCTCTTT
MUSK	Hu_MUSK_F_QPCR	59	109	93.1	13 Kb intron	CTGGTTGCCTTCAGCGGAA
	Hu_MUSK_R_QPCR	56				CTGCACACATGAAAGTAGCCA
RAPSN	Hu_RAPSN_F_QPCR	57	92	91.4	Yes	ATGCCCACAACAATGATGACG
	Hu_RAPSN_R_QPCR	58				GGCTTTCTCGTAGTCCTTGACC

Tm, primer melting temperature; Amp, amplicon size; Effic, primer efficiency; Cross, amplification of exon-exon boundaries. * Primers used do not differentiate between muscle and neural forms of agrin.

Differences in gene expression between the PCA and IA laryngeal muscle samples were analysed using the comparative Ct (cycle threshold) method for relative quantification (Schmittgen and Livak, 2008). In brief, ΔCt was used to measure the values for a gene of interest (GOI) from both the PCA and IA muscles samples adjusted in relation to a normaliser gene (norm) from the same two samples. The fold difference in gene expression was calculated as 2 to the power of ΔC_t and represented as individual points in dot plots on log2-scaling. The statistical analysis was performed using Wilcoxon matched-pairs signed rank test after $2^{-\Delta Ct}$ transformation.

$\Delta\Delta C_t$ was used to compare the results from the affected muscle (PCA muscle) to both a calibrator sample (IA muscle) and a normaliser gene. The fold difference in gene expression was calculated as 2 to the power of $\Delta\Delta C_t$ and represented as the mean ± error propagation on a log2-scale. The normaliser genes (endogenous controls) used in the experiments were glyceraldehyde-3-phosphate dehydrogenase *(GAPDH)*, AChR α1 subunit (*CHRNA1*) and AChR ε subunit (*CHRNE*). *GADPH* was used as a house-keeping gene to normalised for the amount of starting material (Rapacz, 2013). *CHRNA1* and *CHRNE*

were used to normalised the gene expression results to the relative “endplate density” in the muscle tissue sample.

$\Delta C_{t\ PCA} = C_{t\ GOI}^{\ PCA} - C_{t\ norm}^{\ PCA}$

$\Delta C_{t\ IA} = C_{t\ GOI}^{\ IA} - C_{t\ norm}^{\ IA}$

Fold difference = $2^{-\Delta Ct}$

$\Delta\Delta C_t = \Delta C_{t\ PCA} - \Delta C_{t\ IA}$

Fold difference = $2^{-\Delta\Delta Ct}$

2.5 Protein methods

2.5.1 Protein extraction from cell cultures

The cells cultured in 6-well plates were washed with PBS and re-suspended in 500 µl protein lysis buffer (10 mM Tris, 100 mM NaCL, 1 mM EDTA, 1% Triton X-100, pH 7.4) supplemented with protease inhibitor cocktail (Sigma – Cat No. P8340) at 1:100 dilution. The cell lysates were incubated at 4°C for 1 hour with gentle rotation, and then centrifuged at 13000 rpm for 10 minutes. The supernatant was collected and used in subsequent experiments.

2.5.2 Protein extraction form muscle tissue

A total of 10-15 mg of human muscle tissue were added to 500 µl protein lysis buffer (10 mM Tris, 100 mM NaCL, 1 mM EDTA, 1% Triton X-100, pH 7.4) supplemented with protease inhibitor cocktail (Sigma – Cat No. P8340) at 1:100 dilution. The sample was transferred to a Precellys® Ceramic kit 2,8 mm (VWR – Cat no. 32-0141) and homogenised with the Precellys® 24 system from Bertin instruments (VWR – Cat no. 432-3750) at 6000

rpm – 2 x 30-5 seconds. Subsequently, the samples were further homogenised using disposable 1 ml syringes and 23G 1 in. – 0.6 mm x 25 mm (BD – Cat no. 305892), and then incubated at 4°C for 1 hour with gentle rotation, and centrifuged at 13000 rpm for 10 minutes. The supernatant was collected and used in subsequent experiments.

2.5.3 Determination of protein concentration

Protein concentration was determined using a colorimetric Pierce™ BCA Protein Assay Kit (Life Technologies – Cat no. 23225). Cellular and muscle lysates were adjusted to 20 and 50 µg total protein respectively using a standard curve analysis.

2.5.4 Sodium dodecyl sulphate polyacrylamide gel electrophoresis

Samples containing 20-50 µg total protein were denatured in (4X) NuPAGE® LDS Sample Buffer (Life Technologies – Cat no. NP0007) and (10X) NuPAGE® sample reducing agent (Life Technologies – Cat no. NP0004), and boiled at 90°C for 10 minutes. The samples were loaded into NuPAGE® 4-12% Bis-Tris protein gels, 1.0 mm, 10-12 wells (Life Technologies – Cat no. NP0321-2). SeeBlue® Plus 2 Pre-stained Standard (Life Technologies – Cat no. LC5925) was used as a protein marker. The samples were resolved by sodium dodecyl sulphate-polyacrylamide gel electrophoresis (SDS-PAGE) at 150 V using the XCell SureLock™ Mini-Cell Electrophoresis System (Life Technologies – Cat no. EI0001) and 1xNuPAGE® MOPS (3-Morpholinopropane-1-sulfonic acid) SDS Running Buffer (Life Technologies – Cat no NP0001). Resolved proteins were transferred for 2 hours at 30 V on to Amersham™ Protran™ Premium 0.45 µm Nitrocellulose Blotting Membranes (GE Healthcare – Cat no. 10600003) after filling the inner and outer chambers with transfer

buffer. This was prepared by mixing 50 ml of NuPAGE® Transfer Buffer (20X) (Life Technologies – Cat No. NP0006-1), 200 ml 100% methanol, and 700 ml deionised water.

The membrane was incubated in 5% Marvel (milk powder) in PBST (Phosphate buffer Saline – 0.1% Tween® 20) for 1 hour at room temperature to block non-specific binding of proteins. The membranes were incubated with primary antibodies diluted in 1% marvel in PBST at 4°C overnight, and then washed in PBST for 30 minutes with 3 changes of solution. Afterwards, the membranes were incubated with HRP-conjugated secondary antibodies in 1% Marvel in PBST at room temperature for 1 hour and then washed for 30 minutes with 3 changes of solution. A list of the primary and secondary antibodies used is provided in **Table 2-15**.

Table 2-15. Summary of antibodies used in western blotting

Primary antibodies			
Antigen	Host / Clone	Dilution	Provider / Cat no.
α-tubulin	Mouse monoclonal IgG	1:1000	Sigma T75168
AChRε	Goat polyclonal IgG	1:100	Santa Cruz (C20) sc-1454
AChRε	Goat polyclonal IgG	1:100	Santa Cruz (M20) sc-1455
c-myc	Mouse monoclonal IgG	1:500	Abcam 9E10
Col13a1	Rabbit polyclonal IgG	1:500	St Johns Lab STJ92376
DOK7	Rabbit polyclonal IgG	1:250	Santa Cruz (H-284) sc-50463
DOK7	Goat polyclonal IgG	1:100	Santa Cruz (S17) sc-55169
EGFP	Rabbit polyclonal IgG	1:2000	Abcam ab6556

GAPDH	Rabbit polyclonal IgG	1:500	Abcam ab36840
MuSK	Goat polyclonal IgG	1:300	R&D AF-562
MuSK	Goat polyclonal IgG	1:100	Santa Cruz (C-19) sc-6009
MuSK Serine-P	Rabbit polyclonal IgG	1:250	Homemade (gift from Ruth Herbst)
Anti-phosphotyrosine	Mouse monoclonal IgG	1:1000	Millipore 4G10
HRP-conjugated Secondary antibodies			
Antigen	Host / Clone	Dilution	Provider / Cat no.
Goat IgG	Rabbit polyclonal	1:1000	Dako P0449
Mouse IgG	Goat polyclonal	1:1000	Dako P0447
Rabbit IgG	Goat polyconal	1:1000	Dako P0448

Detection of HRP-conjugated antibodies was performed by incubating the membranes with ECL reagent (GE Healthcare, Cat No RPN2106) and exposing them to autoradiography films (Fujifilm – Cat. No. 47410 19284). Films were imaged using GelDoc-It®2 Imaging System and VisionWorks® Acquisition and Analysis software on an external computer. Quantification of protein bands was performed by densitometry using Image J Software version 2.0.0-rc-54/1.51g.

2.5.5 Blue native polyacrylamide gel electrophoresis

Native proteins were resolved using NativePAGE™ Bis-Tris Gel System (Life technologies, Cat. No. BN 1002). The cells cultured in a 6-well plates were washed in PBS and lysed with 500 µl native extraction buffer (NativePAGE™ 4X Sample Buffer, 1-10% specific detergent, and deionised water). The samples were homogenised by pipetting the solution up and down several times and by gentle rotation at 4°C for 1 hour. Subsequently, the lysates

were centrifuged at 20,000 x g for 30 minutes at 4°C. The supernatant was aliquoted into sterile microcentrifuge tubes and store at -80°C until use.

The inner-chamber of a XCell SureLock™ Mini-Cell Electrophoresis System (Life Technologies – Cat. No. EI0001) was filled with 200 ml of pre-chilled Dark Blue NativePAGE™ Cathode Buffer 1X. This was prepared by mixing 10 ml NativePAGE™ 20X Running Buffer (Life Technologies – Cat. No. BN2001), 10 ml NativePAGE™ 20X Cathode Buffer Additive (Life Technologies – Cat. No. BN2002), and 180 ml deionised water. The outer-chamber was filled with 600 ml of pre-chilled anode buffer. This was prepared by mixing 50 ml NativePAGE™ 20X Running Buffer and 950 ml deionised water. NativePAGE™ 5% G-250 Sample Additive (Life Technologies - Cat no. BN20041) was added to samples prior to loading so that the final G-250 concentration was 1/4th the detergent concentration. The samples were loaded into NativePAGE™ 4-16% Bis-Tris gels (Life Technologies – Cat. No. BN2111) together with a NativeMarkTM Unstained Protein Standard (Life Technologies- Cat. No. LC0725).

The electrophoresis was performed at 4°C at maximum voltage (150 mV) until the dye migration completed the first third of the gel. The electrophoresis was then paused, and the cathode buffer was replaced with 200 ml of pre-chilled Light Blue NativePAGE™ Cathode Buffer 1X. This was prepared by mixing 10 ml NativePAGE™ 20X Running Buffer (Life Technologies – Cat. No. BN2001), 1 ml NativePAGE™ 20X Cathode Buffer Additive (Life Technologies – Cat. No. BN2002), and 189 ml deionised water. The electrophoresis was restarted and then continued at the same voltage until the dark dye left the bottom of the gel.

The proteins were transferred to an Amersham Hybond™-P polyvinylidene difluoride (PDVF) membrane (GE Healthcare – Cat. No. RPN303F) prior incubation in 100% methanol for 30 seconds, washing in deionised water for 5 minutes and pre-equilibration for 10 minutes in NuPAGE® Transfer Buffer (20X) (Life Technologies – Cat. No. NP0006-1). This was prepared by mixing 50 ml Transfer Buffer (20X) and 950 ml deionised water. The gel and the PDVF membrane were placed in a XCell SureLock™ Mini-Cell together with sponges and filter paper pre-wet in transfer buffer. The inner and outer chambers were filled with transfer buffer. The transfer procedure was carried at 25 mV for 1 hour.

Afterwards, the PDVF membrane was fixed in 20 ml 8% acetic acid for 15 minutes, washed in deionised water 5 minutes, and air-dried overnight. The following day, the PDVF membrane was re-hydrated in 100% methanol for 30 seconds, washed in deionised water for 15 minutes, and incubated in 5% Marvel (milk powder) in PBST (Phosphate buffer Saline – 0.1% Tween® 20) for 1 hour at room temperature. Standard immunoblotting was continued as previously described. Detection was performed by using ECL (GE Healthcare – Cat. No. RPN2106).

2.5.6 Protein gel staining methods

2.5.6.1 Coomassie Blue staining of proteins in polyacrylamide gels

Coomassie G-250 staining was performed using SimplyBlue™ Safe Stain (Life Technologies – Cat. No. LC6060). After electrophoresis, the protein gel was washed 3 times for 5 minutes with 100 ml of deionised water to remove SDS and buffer salts. Then, the gel was incubated with 20 ml of SimplyBlue™ Safe Stain solution for 1 hour until the protein bands were developed. Afterwards, the gel was washed in 100 ml deionised water

for 1 hour. Pictures were taken using GelDoc-It®2 Imaging System and VisionWorks® Acquisition and Analysis software on an external computer.

2.5.6.2 Silver staining of proteins in polyacrylamide gels

Silver staining was performed using a Pierce® Silver Stain Kit for Mass Spectrometry (Life Technologies – Cat. No. 24600). After resolution of samples by SDS-PAGE electrophoresis, the protein gel was washed in Milli-Q water 2 times for 5 minutes each, and subsequently incubated in *fixing solution* (30% ethanol, 10% acetic acid, 60% Milli-Q water) at room temperature 2 times for 15 minutes. The gel was washed twice with 10% ethanol for 5 minutes, and then washed in Milli-Q water for 5 minutes. Next, the gel was incubated in *sensitizer working solution* (50 µL Silver Stain Sensitizer, 25 ml Milli-Q water) for 1 minute and then washed with two changes of Milli-Q water for one minute each.

The gel was incubated in *silver stain solution* (0.25 ml Silver Stain enhancer, 25 ml Silver Stain) for 5 minutes and then rinsed in Milli-Q water for 40 seconds with two changes of solution. Afterwards, the gel was immediately incubated with *developer working solution* (0.25 ml Silver Stain enhancer, 25 ml Silver Stain Developer) for 1-3 minutes until protein bands appeared. When the desired band intensity was reached, the developer solution was replaced by *stop solution* (5% acetic acid, 95% Milli-Q water). Finally, the gel was briefly washed in Milli-Q water, and incubated for 10 minutes in stop solution. Pictures were taken using GelDoc-It®2 Imaging System and VisionWorks® Acquisition and Analysis software on an external computer.

For mass spectrometry analysis, the gel bands were immediately excised after visualisation using a clean scalpel and placed in sterile 0.5 ml microcentrifuge tubes. Destaining solution was prepared by mixing 74 µL of Silver Destain Reagent A, 245 µL of Silver Destain Reagent B and 4 mL of Milli-Q water. Each gel piece was incubated with 0.2 ml of destaining solution at room temperature for 30 minutes with one change of solution. The destaining solution was removed and the gel pieces were washed three times for 10 minutes each in 0.2 ml of *wash solution.* This was prepared by mixing 25 mM ammonium bicarbonate (Sigma-Aldrich – Cat. No. 09830) and 50% acetonitrile (Sigma-Aldrich – Cat. No. 34967). Finally, the gel pieces were digested with trypsin in preparation for the mass spectrometry procedures (Section 2.6).

2.5.7 Immunoprecipitation and coimmunoprecipitation assays

HEK-293T cells were seeded at a density of $3x10^5$ cells per well in 6-well plates. The following day, cells were transfected with 3-6 µg of mammalian expression vectors encoding MuSK, DOK7, LRP4-EGFP or CASPR2-COLQ-myc. For immunoprecipitation from whole cell lysates, 48 hours after transfection cells were re-suspended in 500 µl cold lysis buffer supplemented with protease inhibitor cocktail (Sigma – Cat. No. P8340) at 1:100 dilution, and rotated for 1 hour at 4°C. Afterwards, the cell lysates were centrifuged for 15 min at 12000 g at 4°C. A 20 µl aliquot of the supernatant was reserved as whole cell lysate loading control. Dynabeads® (Life technologies – Cat. No. 10003D) were resuspended and 50 µl per reaction were transferred to a tube. After washing for 3 times in PBS, the beads were typically incubated with 5 µg of antibody at 4°C for 1 hour with gentle shaking **(Table 2-16)**. Then, the beads were added to the remaining supernatant and incubated at 4°C overnight with gentle rotation.

The beads were washed 3 times in 1 ml lysis buffer, resuspended in 25 µl of NuPAGE® LDS Sample Buffer 4X (Life Technologies, NP0007) with NuPAGE® Sample Reducing Agent 10X (Life Technologies, NP0009) and lysis buffer, and heated for 10 minutes at 90°C. For immunoprecipitation from the surface of HEK-293T cells, the cells were incubated 48 hours after transfection with 5 µg of the selected antibody diluted in 500 µ culture medium at 37°C for 3 hours, washed 3 times in growth medium, and resuspended in 500 µl cold lysis buffer supplemented with protease inhibitor cocktail (Sigma – Cat. No. P8340) at 1:100 dilution.

Finally, the protein samples were separated by SDS-PAGE electrophoresis, transferred onto nitrocellulose membrane, and analysed by western blotting (Section 2.5.4). For the detection of coimmunoprecipitated proteins, the nitrocellulose membrane was incubated with harsh stripping buffer (20 ml SDS 10%, 12.5 ml Tris HCl pH 6.8 0.5 M, 67.5 ml ultra-pure water and 0.8 ml of ß-mercaptoethanol) and then reproved with the corresponding primary and secondary HRP-conjugated antibodies. Densitometry of bands was quantified with Image J software.

Table 2-16. Antibodies used in pull-down assays

Target	Antibody	Amount per reaction	Provider
CASPR2-COLQ-myc	9E10	5 µg	Abcam
DOK7	H284	5 µg	Santa Cruz
LRP4-EGFP	6556	5 µg	Abcam
MuSK	AF562	5 µg	R&D

2.5.8 Phosphorylation assays

For the analysis of MuSK phosphorylation in HEK-293T cells, $3x10^5$ cells were plated in 6 well plates and transfected with the constructs encoding WT or mutant MuSK and DOK7-EGFP or LRP4-EGFP if necessary. Forty-eight hours after transfection, the cells were starved for 2 hours and resuspended in cold lysis buffer supplemented with protease inhibitor cocktail (Sigma – Cat. No. P8340) and phosphatase inhibitor cocktail (Sigma – Cat. No. P8340). Immunoprecipitation was performed as described in Section 2.5.7. Protein samples were separated by SDS-PAGE electrophoresis and transferred onto nitrocellulose membrane.

The membrane was blocked in 5% Bovine serum albumin (BSA) at 4°C overnight. For the detection of MuSK tyrosine-phosphorylation, the membrane was incubated with 1:1000 anti-phosphotyrosine antibody clone 4G10® (Millipore – Cat. No. 16-101) and secondary HRP-conjugated goat anti-mouse antibody (Dako, P0447). For the detection of MuSK, the membrane was incubated with harsh stripping buffer (20 ml SDS 10%, 12.5 ml Tris HCl pH 6.8 0.5 M, 67.5 ml ultra-pure water, and 0.8 ml of ß-mercaptoethanol) and then reproved with anti-MuSK antibody (R&D, cat no. AF562) at 1:300 dilution and secondary HRP-conjugated rabbit anti-goat antibody (Dako, P0449). Detection was performed by using ECL (GE Healthcare – Cat. No. RPN2106).

For the analysis of MuSK phosphorylation in muscle cells, C2C12 *Musk*-KO muscle cells overexpressing MuSK WT or mutant variants were differentiated at 37°C for 5-7 days until the formation of myotubes. The cells were starved for 3 hours and subsequently incubated with full-length human agrin at 1:100 dilution. Cells were harvested at 0 min,

10 min, 40 min, 60 min, 2 hours, 4 hours, 12 hours, and 24 hours after agrin incubation, and protein extracts were processed as previously described in this section. Special care was taken to assure that the beads-protein incubation time was similar across samples. MuSK Tyrosine-phosphorylation was detected as previously described in this section.

2.5.9 Cyclohexamide chase assay

To study the effect of MuSK variants on protein stability, HEK-293T cells were co-transfected with WT or mutant human MuSK expression vectors, and pEGFP_N1 to control for transfection efficiency. Thirty-six hours after transfection, the cells were exposed to the protein biosynthesis inhibitor cycloheximide at the concentration of 20 µg/ml, and the cells were incubated for 0, 1, 2, 4, 8, 12 or 24 hours. Subsequently, the cells were extracted and resolved by SDS-PAGE. Immunoblotting was performed with goat polyclonal anti-MuSK antibody (R&D – Cat. No. AF562), mouse monoclonal anti α-tubulin (Sigma-Aldrich, Cat. No. T75168), and HRP-conjugated secondary antibodies.

2.5.10 Fluorescence-activated cell sorting

Fluorescence-activated cell sorting (FACS) was used for identification and cloning of C2C12 cells successfully electroporated with the px335-MuSK-EGFP-GuideA and px335-MuSK-EGFP-GuideB plasmids (Section 2.3.2). Cells were collected and re-suspended in 5 ml growth medium. The fluorescence intensity of the enhanced green fluorescent protein (EGFP) was measured using a FACSAria ™ Fusion Cell Sorter (Becton Dickinson). The cells with the greater intensity were individually sorted into Corning ® 96-well flat-bottomed culture plates.

2.5.11 AChR-clustering assay

C2C12 and C2C12 *Musk*-KO cells were differentiated for 5-7 days at 37°C until the formation of myotubes (Section 2.8.2). The cells were incubated overnight (16-18 hours) with soluble full–length neuronal agrin for the induction of acetylcholine receptor (AchR) clusters **(Figure 2-5)**. The most common concentration of agrin used was 1:100, and this was determined by a previous agrin titration experiment. The myotubes were incubated with Alexa Fluor® 488 or 594-conjugated α-bungarotoxin (Life technologies – Cat. No. B13423) at 1 µg/ml for 1 hour at 37°C, washed 3 times in PBS, and fixed for 10 minutes in 3% PFA at room temperature. The fixative was removed by washing with PBS. The images were captured on an IX71 Olympus fluorescent microscope with Simple PCI software (Digital Pixel Imaging System, Brighton, UK).

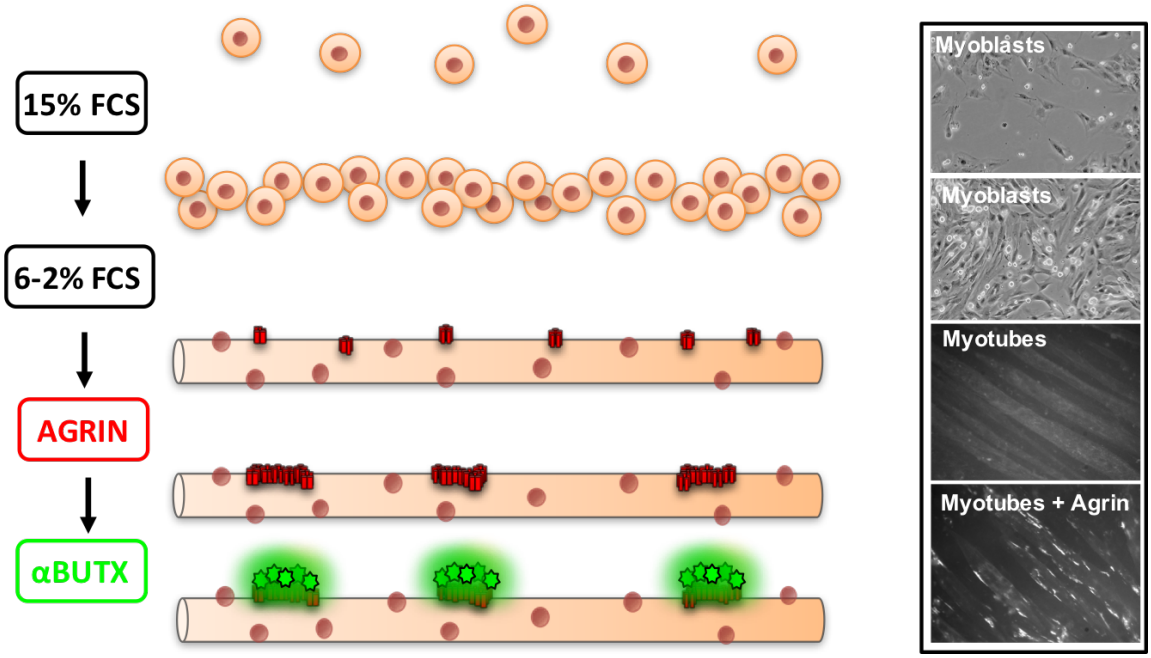


Figure 2-5. Schematic representation of the AChR clustering assay

The figures show the different stages involved in the AChR clustering assay from the seeding of C2C12 myoblasts to the incubation of C2C12 myotubes with full–length neuronal agrin for the induction of acetylcholine receptor clusters and the subsequent labelling with fluorescently conjugated α-bungarotoxin.

2.5.12 Immunofluorescence staining of muscle sections

Human and mouse muscles were dissected, snap-frozen in isopentane (VWR – Cat No. 24872.323) cooled in liquid nitrogen for one minute, and kept at -80°C until further use. The muscles were processed using a Thermo Fisher Scientific ™ Shandon ™ FSE cryostat at -18°C to obtain 8-10 µm longitudinal and transverse sections, and then mounted on SuperFrost® Plus slides coated with 3-aminopropyltrielthoxysilane (VWR – Cat. No. 631-0108). Sections were left to dry overnight at room temperature and store at -80°C.

After thawing, the sections were fixed for 10 minutes and rinsed in PBS 3 times for 5 minutes. Fixation was performed with 3% PFA at room temperature, pre-chilled acetone (Honeywell Riedel-de Haën ™ – Cat. No. 24201) at -20°C or pre-chilled methanol (VWR – Cat. No. 20847.307) with 5% acetic acid at -20°C depending on the primary antibody used. Incubation in 1% bovine serum albumin (Sigma-Aldrich – Cat. No. A7906-100G) in PBS for 60 minutes was used to block non-specific binding. Additional permeabilisation with 0.1% Triton X-100 diluted in 1% BSA for 30 minutes was performed if required.

Incubation with primary antibodies was typically performed at 4°C overnight using dilutions detailed in **Table 2-17**. Afterwards, the sections were washed 3 times in PBS for 5 minutes, and incubated with the appropriate fluorescently conjugated secondary antibodies diluted in 1% BSA for 1 hour at room temperature. If the labelling of acetylcholinesterase or AChRs was desired, fluorescent conjugated neurotoxins were used together with the secondary antibodies. Finally, the sections were washed 3 times in PBS for 5 minutes and mounted in confocal-UV-matrix® (Micro tech lab) and microscope slide coverglass 22x70mm #1 thickness (.13-.17 mm)

Table 2-17. Antibodies used for immunofluorescence staining of muscle sections

Primary antibodies				
Antigen	**Host / Clone**	**Dilution**	**Fixation Fluor**	**Provider / Cat. No.**
COL13A1 N-term (53-81 aa)	Rabbit polyclonal IgG	1:100	3% PFA	Aviva OAAB08101
COL13A1 C-term (442-463 aa)	Guinea pig polyclonal IgG	1:500	3% PFA/ Acetone	Eurogentec (custom)
DOK7	Rabbit polyclonal IgG	1:50	Acetone	Santa Cruz H284
Fast myosin	Mouse monoclonal IgG	1:250	Acetone	Novocastra NCL-MHCf
MuSK	Rabbit polyclonal IgG	1:100	Acetone	Abcam ab92950
Neurofilament	Mouse monoclonal IgG1	1:1000	3% PFA	Abcam ab7795
S100β	Mouse monoclonal IgG1	1:1000	3% PFA	Sigma Aldrich SAB1402349
Synaptophysin Ab-4	Rabbit Polyclonal IgG	1:100	3% PFA	Thermo-Fisher RB-1461-P0
Alexa Fluor® Conjugated Secondary antibodies				
Guinea pig IgG	Goat polyclonal	1:500	568	Life Technologies A11075
Rabbit IgG	Goat polyclonal	1:500	568	Life Technologies A11011
Mouse IgG	Donkey polyclonal	1:500	594	Life Technologies R37115
Goat IgG	Donkey polyclonal	1:500	594	Life Technologies A11058
Rabbit IgG	Goat polyclonal	1:100 1:500	647	Life Technologies A21246
Chicken IgG	Goat polyclonal	1:100 1:500	647	Life Technologies A21449
Fluorescent conjugated neurotoxins				
AChR	α-bungarotoxin	1:500	594	Life Technologies B13423
Acetylcholinesterase	Fasciculine 2	1:500	488	Life Technologies (special order)

2.5.13 Fibre typing of muscle sections

The proportion of type I and type II fibres in human laryngeal muscles was studied using immunohistochemistry. Muscles were snap frozen in isopentane cooled in liquid nitrogen and 8-10 µm transverse sections were prepared using a Thermo Fisher Scientific ™ Shandon ™ FSE cryostat at -18°C as previously described (Section 2.5.12). Prior to Immunolabelling, the sections were rehydrated in PBS and then fixed in 1% PFA for 20 minutes. Subsequently, the sections were blocked with 5% FCS/NRS in PBS for 20 minutes at room temperature.

Primary antibodies for fast or slow myosin were diluted 1:50 in 1% FCS/NRS in PBS, and incubated with the sections for 1 hour at room temperature. The sections were washed 3 times for 5 minutes in PBS, and incubated with peroxidase-conjugated anti-mouse IgG (Dako – Cat. No. P0477) at 1:100 dilution in 1% FCS/NRS for 30 minutes at room temperature.

Finally, the slides were rinsed in PBS 3 times for 1 minute, and the peroxidase activity was developed using 3-amino-9-ethylcarbazole (AEC) (Sigma – Cat. No. A5754). A solution was prepared by mixing 4.6 ml sodium acetate (NaAC) buffer (0.1 M, pH 5.2), 0.3 ml AEC in dymethylformamide (DMF) (5 mg/ml) and 3 µl H_2O_2. The solution was filtered and applied to the sections for 10 minutes at room temperature. Afterwards, the slides were rinsed in PBS and mounted in confocal-UV-matrix® (Micro tech lab) and microscope slide coverglass 22 x 70 mm #1 thickness (.13-.17 mm). Images were taking using a light microscope. The composition of type I and II fibres was determined by counting labelled

and unlabelled fibres from central and peripheral areas separate by ruled grids on 10 images taken at 10X magnification.

2.5.14 Immunofluorescence labelling of teased muscle fibres

Tibialis anterior mouse muscles were collected using standard procedures, pinned out by their tendons and fixed immediately with 1 % PFA for 30 minutes. Muscles were rinsed in PBS, teased into several bundles and labelled directly with Alexa Fluor® 594-conjugated α-bungarotoxin (Life technologies – Cat. No. B13423) for 1 hour at RT, and then washed in PBS at 4°C overnight.

The following day, the muscles were placed in 7 ml glass tubes and dehydrated with absolute ethanol followed by absolute methanol, each for 10 min at -20°C. The muscles were washed in PBS 3 x 5 min, and then permeabilised with 0.1% Triton X-100 diluted in 3% BSA for 30 minutes. After washing in PBS 3 x 5 min, the muscles were incubated with chicken polyclonal antibody to neurofilament heavy polypeptide (Abcam – Cat. No. ab4680) at 1:200, and rabbit polyclonal anti-synaptophysin antibody (Thermo Fisher Scientific – Cat. No. RB-1461-P0) at 1:1000, diluted in PBS containing 3% BSA at 4°C overnight.

The next day, the muscles were washed in PBS 6 x 10 minutes and incubated with the corresponding fluorescently conjugated secondary antibodies at 1:100, diluted in PBS containing 3% BSA at room temperature for 3 hours. The muscles were subsequently washed in PBS at 4°C overnight with 6 x 10 minutes' additional washes the following morning. Finally, the muscle bundles were teased apart on slides into multiple fibres. The

slides were mounted using Confocal-Matrix (Micro-Tech-Lab, Graz, Austria). Images were captured on an IX71 Olympus fluorescence microscope using Simple PCI software (Digital Pixel Imaging Systems, Brighton, UK). Untransfected regions were excluded and only endplates showing EGFP-positive nuclei were taken into consideration to ensure that the NMJ belong to an electroporated muscle fibre. A total of 25 muscle endplates were analysed per muscle.

The muscle endplates were classified according to the fluorescent labelling of AChRs as intact or dismantle: intact endplates stand for continuous, bright and pretzel-shaped endplates; dismantle stands for endplates broken up into fragments or pretzel morphology not present. The innervation pattern of the endplates was classified as normal or aberrant: normal innervation is when the axonal branches innervate a well-defined synaptic structure; aberrant innervation stands for absence of axons or presence of remodelation (partial innervation, nodal or terminal sprouts and ectopic formation).

2.5.15 Immunocytofluorescence

HEK-293T cells were plated on coverslips coated with poly-L-lysine (Sigma-Aldrich – Cat. No. P8920) and transfected with 3-6 μg of the desired constructs. 36 hours after transfection, the coverslips were transferred to a 24-well cell culture plates and incubated for one hour at room temperature with the primary antibody diluted in assay buffer (DMEM, 20 mM HEPES (4-(2-hydroxyethyl)-1-piperazineethanesulfonic acid), 1% BSA). After washing, the cells were fixed in 3% PFA diluted in DMEM, washed, and incubated with the appropriate fluorescently conjugated Alexa Fluor® secondary antibodies. After washing, the coverslips were mounted in and visualised under a fluorescence microscope.

Some of the primary antibodies used in immunocytofluorescence (e.g. anti-c-Myc and anti-agrin antibodies) did not bind to antigens expressed in the cell surface unless fixed. In this case, cells were fixed prior to antibody incubation.

2.6 Mass spectrometry methods

Mass spectrometry experiments were performed at the Target Discovery Institute (University of Oxford) by collaborators at the Mass Spectrometry facility. Technical details are included for information purposes.

2.6.1 LC-MS/MS analysis

Liquid chromatography (LC) with mass spectrometry (MS) was performed on in-gel digested protein material after silver staining of proteins in polyacrylamide gels (Section 2.5.6.2).

High performance liquid chromatography (HPLC) was performed using an Ultimate 3000 nano-HPLC system (Dionex, Sunnyvale, CA, USA) comprising a WPS-3000 micro auto sampler, a FLM-3000 flow manager and column compartment, a UVD-3000 UV detector, a LPG-3600 dual-gradient micro-pump, and a SRD-3600 solvent rack controlled by Hystar (Bruker Daltonics, Billerica, MA, USA) and DCMS link 2.0 software. Samples were concentrated on a trapping column Dionex (Sunnyvale, CA, USA), 300 µm i.d., 0.1 cm) at a flow rate of 20 µL/min. For the separation with a C18 Pepmap column (75 µm i.d., 15 cm, Dionex), a flow rate of 250 nL/min was used as generated by a cap-flow splitter cartridge (1/1000). Peptides were eluted by the application of a 30 minutes multi-step

gradient using solvents A (98% H_2O, 2% acetonitrile, 0.1% formic acid) and B (80% acetonitrile, 20% water, 0.1% formic acid).

The liquid chromatography was interfaced directly with a 3D high capacity ion trap mass spectrometer (Amazon; Bruker Daltonics) utilising 10 µm i.d. distal coated SilicaTips (New Objective, Woburn, MA, USA) and nano-ESI mode. SPS parameter settings on the ion trap were tuned for a target mass of 850 *m/z*, compound stability 100% and a smart ICC target of 250,000. MS/MS analysis was initiated on a contact closure signal triggered by HyStar software (version 3.2). Up to five precursor ions were selected per cycle with active exclusion (0.5 min) in collision-induced dissociation (CID) mode. CID fragmentation was achieved using helium gas and a 30%–200% collision energy sweep with amplitude 1.0.

2.6.2 Data processing and database analysis

Raw LC-MS/MS data were processed and Mascot compatible files were created using DataAnalysis 4.0 software (Bruker Daltonics). Database searches were performed using the Mascot algorithm (version 2.4) and the UniProt_SwissProt database with mammalian taxonomy restriction (v2015.11.26, number of entries 549,832).

2.7 Bacterial cell culture

2.7.1 Type of cells used

Competent cells were used for the amplification of DNA plasmids. The *Escherichia coli* strains used were NEB®10-beta (NEB – Cat. No. C3019I), JM109 (Promega – Cat. No. L2001), XL10-Gold® Ultracompetent Cells (Stratagene – Cat. No. 200314), and One Shot® TOP10 (Invitrogen – Cat. No. C404003).

2.7.2 Transformations

The bacterial cells were defrosted from -80°C on ice. Immediately after, 50 µl of bacterial glycerol solution were transferred to an Eppendorf tube and mixed with 100 ng of plasmid DNA by tapping the tube gently. The plasmid-bacteria mixture was incubated on ice and then briefly heated to 42°C (heat shock) to allow the DNA to enter the cell through the disruption of membranes. The mix was placed back on ice to retain the plasmid in the bacteria. Details of transformation conditions are shown in **Table 2-18**. Afterwards, 450 µl of LB medium were added to the mix and incubated at 37°C for 1 hour in a shaker. Finally, the mix was plated onto LB-agar plates supplemented with the appropriate antibiotics **(Table 2-19)**.

Table 2-18. Conditions for transformation of competent cells

	NEB®10-beta	JM109	One Shot® TOP10
Incubation on ice	30 minutes	10 minutes	30 minutes
Heat shock	42°C for 30 seconds	42°C for 30 seconds	42°C for 30 seconds
Incubation on ice	5 minutes	2 minutes	2 minutes

2.7.3 Growth conditions

All *Escherichia coli* strains were grown at 37°C in LB medium (10 g/L NaCL, 10 g/L tryptone, and 5 g/L yeast extract all purchased from BD Bionutrients™) in a shaker incubator or on LB agar plates (15 g of agar/1 L of LB). Typically, ampicillin or kanamycin were added to the LB medium for the selection of antibiotic-resistance bacteria. For the colour screening of colonies following cloning with PGEM®-T Easy, LB-agar plates were supplemented with ampicillin, isopropyl ß-D-1-thiogalactopyranoside (IPTG) and 5-bromo-4-choro-3-indolyl-ß-D-galactopyranoside (X-Gal).

Table 2-19. Antibiotics used for selection of bacterial cultures

Antibiotic	Concentration	Provider
Ampicillin	100 µg/ml	Sigma – A0166
Kanamycin	50 µg/ml	Sigma – K1377
IPTG	0.5 mM	Sigma – 367-93-1
X-GAL	80 µg/ml	Sigma – 7240-90-6

2.8 Mammalian cell culture

2.8.1 Growth conditions

The cells used in this work were cultured in sterile conditions using Corning® culture flasks and the specifications detailed in **Table 2-20**.

Table 2-20. Growth conditions for mammalian cells

Cell line	Culture medium	Incubator conditions
HEK-293T	DMEM + 10% FCS + 1% PSA	37°C, 8% CO_2 33°C, 5% CO_2
Phoenix™-ECO	DMEM + 10% FCS + 1% PSA	37°C, 8% CO_2
C2C12	DMEM + 15% FCS + 1% PSA	37°C, 8% CO_2
C2C12 *Musk*-KO	DMEM + 15% FCS + 1% PSA	37°C, 8% CO_2
TE671	DMEM + 10% FCS + 1% PSA	37°C, 8% CO_2
HT1080	DMEM + 10% FCS + 1% PSA	37°C, 8% CO_2

DMEM = Dulbecco`s Modified Eagle Medium (Life Technologies - Cat. No. 41965-062). FCS = Foetal Calf Serum (Gibco – Cat. No. 10270-106, Lot 42F2250K). PSA = penicillin, streptomycin and amphotericin B (Invitrogen – Cat. No. 15240-026)

2.8.2 Differentiation conditions

C2C12 cells were plated and cultured in growth medium for 24 hours at 37°C until 90% confluency. Subsequently, the medium was changed to differentiation medium (DMEM,

2% FCS, 1 %PSA), and cells were cultured for 5-7 days at 37°C until the formation of myotubes. For the differentiation of C2C12 *Musk*-KO cells, the cells were plated at a lower concentration and culture in growth medium for 48 hours at 37°C until 80% confluency. Subsequently, the FCS in the culture medium was reduced gradually: first by changing to a transitional differentiation medium for 12 hours (DMEM, 6% FCS, 1% PSA), and then to differentiation medium (DMEM, 2% FCS, 1% PSA) upon 100% confluency. Afterwards, the medium was changed every 24 hours to improve the quality of the myotubes.

2.8.3 Selection conditions

Selection of antibiotic-resistant cells was done by adding antibiotics to the medium as described below **(Table 2-21)**.

Table 2-21. Antibiotics used for selection of mammalian cultures

Antibiotic	Concentration	Provider
Geneticin	400-1000 µg/ml	Life Technologies Cat. No. 10131027
Puromycin	5 µg/ml	Sigma Cat. No. A1113802

2.8.4 Polyethylenamine transfection

Polyethylenamine (PEI) was generated by diluting 45 mg PEI in 8 ml distilled water and adjusting the pH to 7.2 with HCL. The mix was filter sterilised using a syringe filter (Appleton woods – Cat. No. fc121). The first day, $3x10^5$ HEK-293T cells were plated per well of a 6-well plate (Corning ®Costar® Flat Bottom Cell Culture Plates – Cat. No. CLS3516). The second day, the cells were incubated with a transfection mix for 12 hours. The usual transfection mixed contained 3-6 µg DNA, 1.25-2.5 µl 20% glucose in nuclease-free water, 1.5 µl PEI, 1-2 µl nuclease free water, and 1 ml growth medium. If required,

100 ng of pEGFP-N1 were added to the DNA mix as a marker of transfection efficiency. On the third day, the medium was replaced with 2 ml per well of fresh medium. The cells were further cultured for 24-72 hours depending on the procedure. Additional transfection mixes are detailed in **Table 2-22**.

Table 2-22. Conditions used for PEI transfection

Cell type	Amount of cells	Total DNA	20% glucose	Water	PEI	Medium
HEK-293T	$3x10^5$	3 µg	1.25 µl	1 µl	1.5 µl	1 ml
HEK-293T	$3x10^5$	6 µg	2.5 µl	2 µl	1.5 µl	1 ml
HEK-293T	$2x10^6$ (T75)	18 µg	7.5 µl	up to 45 µl	9 µl	6 ml
Phoenix™-ECO	$2x10^6$ (T25)	12.5 µg	5.25 µl	3.5 µl	3.75 µl	2.5 ml

2.8.5 Electroporation transfection

The Neon® Transfection System (Life Technologies) was used for electroporation of DNA into C2C12 muscle cells. Typically, $6.25x10^5$ cells per reaction were transferred to a sterile Eppendorf tube and centrifuged at 1200 rpm for 5 minutes. The pelleted cells were re-suspended in 125 µl Resuspension Buffer R. A Neon® Electroporation Pipette and Tip was used to collect 100 µl mix and transfer it to a Neon® Transfection Tube filled with 3 ml of Buffer E2. The cells were electroporated following the conditions detailed in **Table 2-23**, and then transferred to a Corning ® T25 culture flask containing 15% FCS growth medium without antibiotics. The following day, the cells were checked for green fluorescence under the microscope if applicable, and the growth medium was replaced with the regular one containing antibiotics.

Table 2-23. Conditions used for electroporation

Cell line	Number of cells	DNA amount	Voltage	Pulse width	Pulse number
C2C12	$6.25x10^5$	20 µg	1650 V	10 ms	3

2.8.6 Retroviral production and infection

The Phoenix™-ECO cells were used together with the pBabe retroviral expression vector system for the generation of retrovirus and subsequent infection of C2C12 *Musk* KO cells. Typically, $1x10^6$ Phoenix™-ECO cells per condition were plated in a Corning ® T75 culture flask and PEI-transfected the following day with 10 µg of pBabe-puro-MuSK-IRES-EGFP WT or mutant constructs, and pBabe-puro-IRES-EGFP (empty vector) as a control. The cells were grown for 72 hours in 7 ml of growth medium (DMEM, 10% FCS, 1% PSA). The medium was harvested and centrifuged to remove cell debris, and stored at -80°C until use. For the infection of C2C12 *Musk* KO cells, $5x10^4$ *Musk* KO cells were plated in a Corning ® T25 culture flask. The following day, the cells were incubated with 1 ml of medium containing the retrovirus supplemented with 1 µl of polybrene (Sigma-Aldrich – Cat. No. TR-1003-G) at 37°C overnight. Then, the medium was replaced with growth medium and the cells were moved to a Corning® T25 culture flask. Cell selection with 1% puromycin (5 µg/ml) was started 48 hours after retroviral infection and subsequently maintained in the growth medium.

2.8.7 Production of recombinant agrin and soluble COL13A1

$2x10^6$ HEK-293T cells were plated on T75 flasks and transfected with cDNA encoding the full-length human agrin or WT COL13A1 using conditions detailed in **Table 2-22**. Sixteen hours after transfection, the culture medium was replaced by 6 ml of growth medium.

The cells were cultured for a further 72 hours, and the medium containing soluble agrin or COL13A1 was harvested and centrifuged at 2000rpm for 10 minutes. The supernatant was kept and stored at -20°C until use.

2.9 Cell based assay for the detection of autoantibodies to COL13A1

2.9.1 Developing a cell-based assay

Cell based assays (CBA) involve the overexpression of antigens on the surface of HEK-293T cells after transfection with a plasmid encoding the desired protein. The cells can then be incubated with serum from patients, and the binding of human antibodies can be scored visually using indirect immunocytofluorescence (Leite *et al.*, 2008). Advantages of live CBAs include the possibility of achieving high-expression levels of antigens and their localisation in natural membrane environments, where they adopt native conformational states and glycosylation levels. In addition, the expression of antigens in live cells avoid the detection of antibodies to intracellular epitopes, which are unlikely to be pathogenic.

The pcDNA3.1-Hygro-COL13A1 construct was mutated at the cleavage site to prevent the secretion of the COL13A1 ectodomain and reach high-expression levels at the cell surface (Section 4.4). HEK-293T cells were plated on coverslips coated with poly-L-lysine (Sigma-Aldrich – Cat. No. P8920) and co-transfected with 6 µg of COL13A1 and 100 ng of EGFP as a marker of transfection efficiency.

36 hours after transfection, the coverslips were transferred to 24-well cell culture plates and incubated with the patients´ serum diluted 1:20 in assay buffer (DMEM, 20 mM HEPES (4-(2-hydroxyethyl)-1-piperazineethanesulfonic acid), 1% BSA) for one hour at room

temperature. After washing, the cells were fixed in 3% PFA, washed, and incubated with one of the following secondary antibodies as appropriate: Alexa Fluor® 568 goat anti-human IgG (Heavy +Light) or goat anti-human IgG Fc(γ) (Thermo Fisher Scientific – Cat. No. 12-4998-82). The anti-Fc antibody was not fluorescently labelled and, therefore, an Alexa Fluor® 568 mouse anti-goat tertiary antibody was added in this case. After washing, the coverslips were mounted in and visualised under a fluorescence microscope.

2.9.2 Cell-based assay scoring

The intensity of the red staining was measured by indirect immunofluorescence using a visual score ranging from 0 to 4 **(Figure 2-6)**. A positive control with a commercial antibody was always used to ensure adequate surface expression.

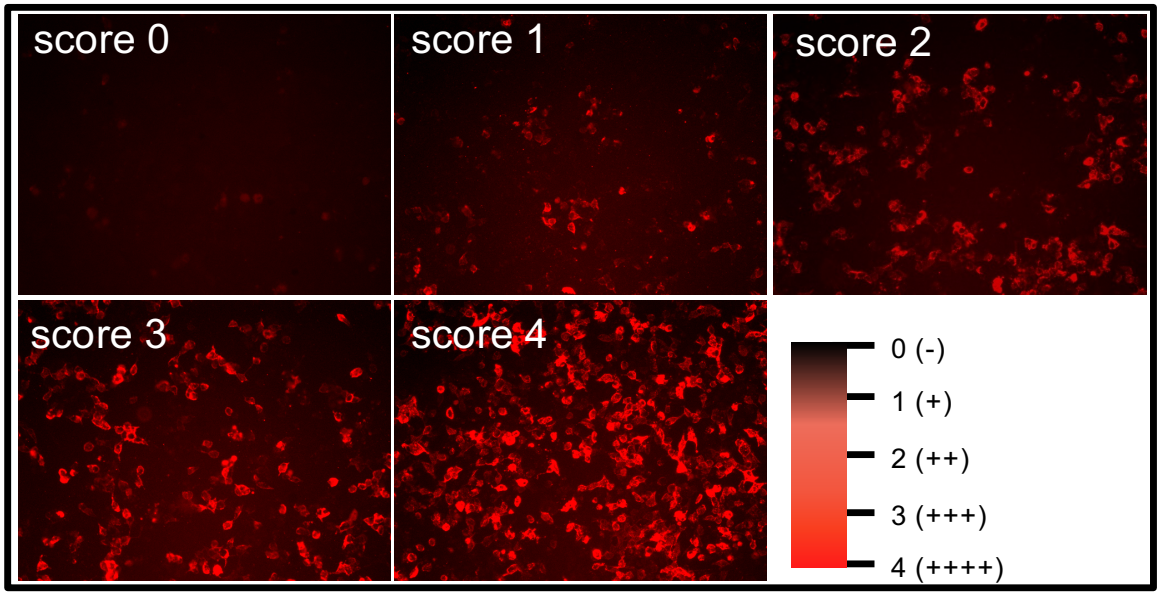


Figure 2-6. Visual score used to measure the intensity of the red fluorescent staining after indirect immunofluorescence. The samples were considered positive if the score given was greater than or equal to 1.

2.9.3 Methodology for the testing and interpretation of CBA results

If the initial CBA using Alexa Fluor® 568 goat anti-human IgG (Heavy +Light) was positive, a second experiment was conducted using three different conditions in parallel. First, the assay was repeated using the anti-human IgG (H+L) secondary antibody. Second, the assay was conducted using the antibody against the Fragment crystallisable (Fc) region of the human IgG and a tertiary fluorescent antibody to exclude false positive results due to IgM binding. Since both IgG and IgM molecules have Heavy and Light chains in their structure, the use of a secondary antibody to Heavy and Light IgG chains could prompt to the detection of IgM binding leading to false positive results. Third, the assay was conducted on mock transfected cells to rule out non-specific binding of the serum to the cell surface. The final interpretation of results was based on the results of the four different assays.

2.10 Standard Buffers

PBS

Phosphate Buffered Saline (PBS) (3.2 mM Na_2HPO_4, 0.5 mM KH_2PO_4, 1.3 mM KCL, 135 mM NaCL) was prepared by dissolving Oxoid™ phosphate buffer saline (Dulbecco A) tablets (Thermo Fisher Scientific – Cat. No. BR0014G) in distilled water.

PBST

Phosphate Buffered Saline – Tween® 20 (PBST) (3.2 mM Na_2HPO_4, 0.5 mM KH_2PO_4, 1.3 mM KCL, 135 mM NaCL, 0.05% Tween®20, pH 7.4) was prepared by dissolving Oxoid™ phosphate buffer saline (Dulbecco A) tablets (Thermo Fisher Scientific – Cat. No. BR0014G) in distilled water supplemented with Tween® (Sigma-Aldrich – Cat. No. P2287) to a final concentration of 0.05%.

TBST

Tris Buffered saline – Tween® 20 (TBST) (20 mM Tris, 150mM NaCl, 0.1% Tween®20) was prepared as a 10x concentrated stock by dissolving 24g Tris base, 88 g NaCl, and 1 ml Tween® 20 in 900 ml distilled water. The pH was adjusted to 7.6 and distilled water was added until a final volume of 1 litre.

TBE

Tris-Borate-EDTA buffer (TBE) (90 mM Trizma base, 90mM boric acid, 2mM EDTA) was prepared as 5X concentrated stock by dissolving 54g Trizma base, 27.5 g boric acid and 20 ml 0.5 M EDTA in 1 litre of deionised water.

Harsh stripping buffer

Harsh stripping buffer was prepared by mixing 20 ml SDS 10%, 12.5 ml Tris HCl pH 6.8 0.5 M, 67.5 ml ultra-pure water and 0.8 ml of ß-mercaptoethanol.

2.11 In vivo methods

2.11.1 Mouse In-vivo electroporation

Experiments were performed in adult wild-type C57BL/6 mice at the age of 8 weeks. Mice were anesthetised following standard procedures. The hair from the leg being treated was removed using hair removal cream to ensure optimal contact between the electroporation electrodes and the skin. A total of 10 µg of mammalian expression vectors for human WT or mutant MuSK constructs, and 5 µg of nls-EGFP construct (Addgene plasmid #67652) were diluted in 30 µl of 0.9% NaCl solution. The nls-EGFP construct express EGFP with a nuclear localisation signal, and was used as a reporter plasmid to

identify the areas of the muscle that successfully took up the nucleic acid. DNA was injected in the *tibialis anterior* muscle using a 1 ml syringe with a 27-gauge needle at the point where muscle endplates are concentrated. Special care was paid during the injection procedure since muscle gene transfer is dependent on the quality of the injection. After the application of electroconductive paste to the muscle, electrical pulses were administrated using a ECM^{TM} 830 electroporation system (BTX-Harvard Apparatus, Massachusetts) and the following conditions: 200 V/cm, 4 pulses, 20 ms duration, frequency of 1 Hz. Subsequently, polarity was reversed across the electrodes.

2.11.2 Quantitative Myasthenia Gravis (QMG) test

The QMG test was routinely performed in patients with CMS during clinic visits, and was used to monitor fatigable muscle weakness. The QMG test is a severity score design to quantify muscle weakness in myasthenia gravis (MG) and related disorders such as Lambert Eaton myasthenic syndrome (LEMS) and congenital myasthenic syndromes (CMS) (Jaretzki *et al.*, 2000). The QMG test has a good interrater reliability and correlates with the MG activities of daily living scores system (MG-ADL). This test is made up of 13 components **(Table 2-24)**, each scored from 0 (normal) to 3 (severe weakness). Components for ptosis, diplopia, swallowing, speech, and facial muscles are based on clinical interpretation. Components for arm raise time, leg raise time, grip strength, head lift time, and forced vital capacity (FVC) are based on objective, continuous values assigned to a range (e.g., for arm raise time 0 = >240 s, 1 = 91-240 s, 2 = 11-90 s, 3 = <11 s), and are amenable to sub-analysis.

Table 2-24. Quantitate myasthenia gravis score

Weakness	none	mild	moderate	severe	
Score	**0**	**1**	**2**	**3**	
Lateral diplopia (s)	>60	11-60	1-10	0	
Ptosis (s)	>60	11-60	1-10	0	
Swallowing	Normal	Occasional chocking	Consistent chocking	Unable to swallow	
Facial muscles (eyelid closure)	Normal	Some resistance to opening	Unable to resist opening	Incomplete eyelid closure	
Head lift 45° (s)	>120	30-120	0-30	Unable	
R arm 90° (s) Arms tested together	>240	91-240	11-90	0-10	
L arm 90° (s) Arms tested together	>240	91-240	11-90	0-10	
Counting 1-50 Dysarthria / nasal speech	None	At 30-49	At 10-29	Before 9	
R Leg 45° (s) Legs tested separately	>100	31-100	1-30	0	
L Leg 45° (s) Legs tested separately	>100	31-100	1-30	0	
Vital Capacity Best of 3 trials	M > 3.5 F > 2.5	M 2.6-3.5 F 1.9-2.5	M 1.5-2.5 F 1.2-1.8	M <1.5 F <1.2	
R Grip (Kg) Support dynamometer	M > 45 F > 31	M 16-45 F 11-31	M 5-15 F 5-10	M < 5 F < 5	
L Grip (Kg) Support dynamometer	M > 45 F > 31	M 16-45 F 11-31	M 5-15 F 5-10	M < 5 F < 5	
				Total score	**/39**

2.12 Microscopy methods

2.12.1 Fluorescence microscopy

Fluorescence images were acquired using an Olympus IX71 fluorescence microscope and Simple PCI software (Digital Pixel Imaging Systems, Brighton, UK).

2.12.2 Confocal microscopy

Confocal images were acquired using a Zeiss LSM 880 confocal microscope and ZEN 2.3 black edition software (Carl Zeiss AG, Oberkochen, Germany), or Zeiss LSM 510 inverted confocal microscope and ZEN 2011 blue edition software (Carl Zeiss AG, Oberkochen, Germany).

2.12.3 Quantification of mean fluorescence intensity

Image analysis was performed using ImageJ version 2.0.0-rc54/1.51g. Muscle endplates areas were selected after adjusting the threshold manually **(Figure 2-7)**, then mean fluorescence intensity was quantified. Special care was taken to avoid saturation of images.

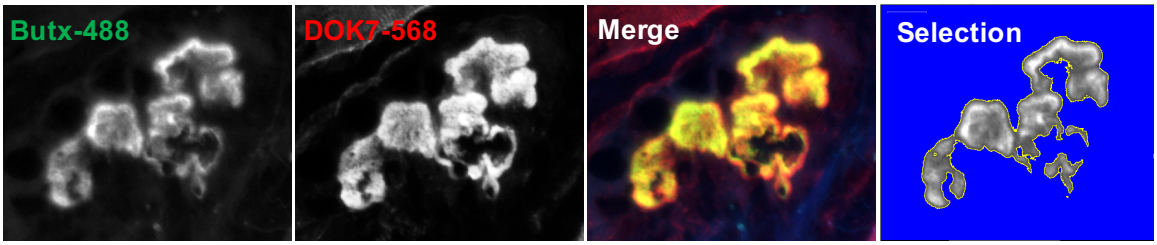


Figure 2-7. Representative images of muscle endplates for image analysis

2.12.4 Quantification of AChR clusters

Images from C2C12 myotubes cultures incubated with full-length agrin and Alexa Fluor® 594-conjugated α-bungarotoxin were taken using an Olympus IX71 fluorescence microscope and Simple PCI software (Digital Pixel Imaging Systems, Brighton, UK). Images were acquired using a 20x magnification objective. An automated ImageJ matrix previously developed by Dr Dominic Waithe (Image Analyst Specialist, Wolfson Imaging Centre, WIMM) and Dr Jonathan Cheung (former DPhil student) was slightly modified for the current experiments **(Figure 2-8).** The number, length, area and intensity of AChR clusters per microscope field were quantified by running this matrix in ImageJ version 2.0.0-rc54/1.51g. To ensure the specificity of the procedure, the parameters of the matrix (threshold, particles size, and sigma) were adjusted for each experiment using a "no agrin" control sample where AChR clusters were not present **(Figure 2-9).** Alternative controls included C2C12 *Musk* KO myotubes incubated with full-length agrin overnight.

```
title = getTitle();
run("Clear Results");
run("Colors...", "foreground=black background=white selection=yellow");
roiManager("reset");
run("Set Scale...", "distance=312 known=100 pixel=1 unit=um");
run("8-bit");
run("Duplicate...", "title=image-2");
run("Duplicate...", "title=image-1");
run("Gaussian Blur...", "sigma=x");
imageCalculator("Subtract create", "image-2","image-1");
run("Gaussian Blur...", "sigma=x");
setThreshold(x, 255);
run("Convert to Mask");
run("Analyze Particles...", "size=0.0-Infinity circularity=0.00-1.00 show=[Overlay Outlines] display summarize add");
selectWindow("image-2");
roiManager ("Show All");
roiManager ("Measure");
run("Flatten");
selectWindow("image-2");
close();
selectWindow("Result of image-2");
close();
selectWindow("image-1");
close();
for(c=0;c<nResults;c++){
ar = getResult("Area",c);
print(ar);
}
```

Figure 2-8. ImageJ macro commands for the analysis of AChR clusters in C2C12 myotubes

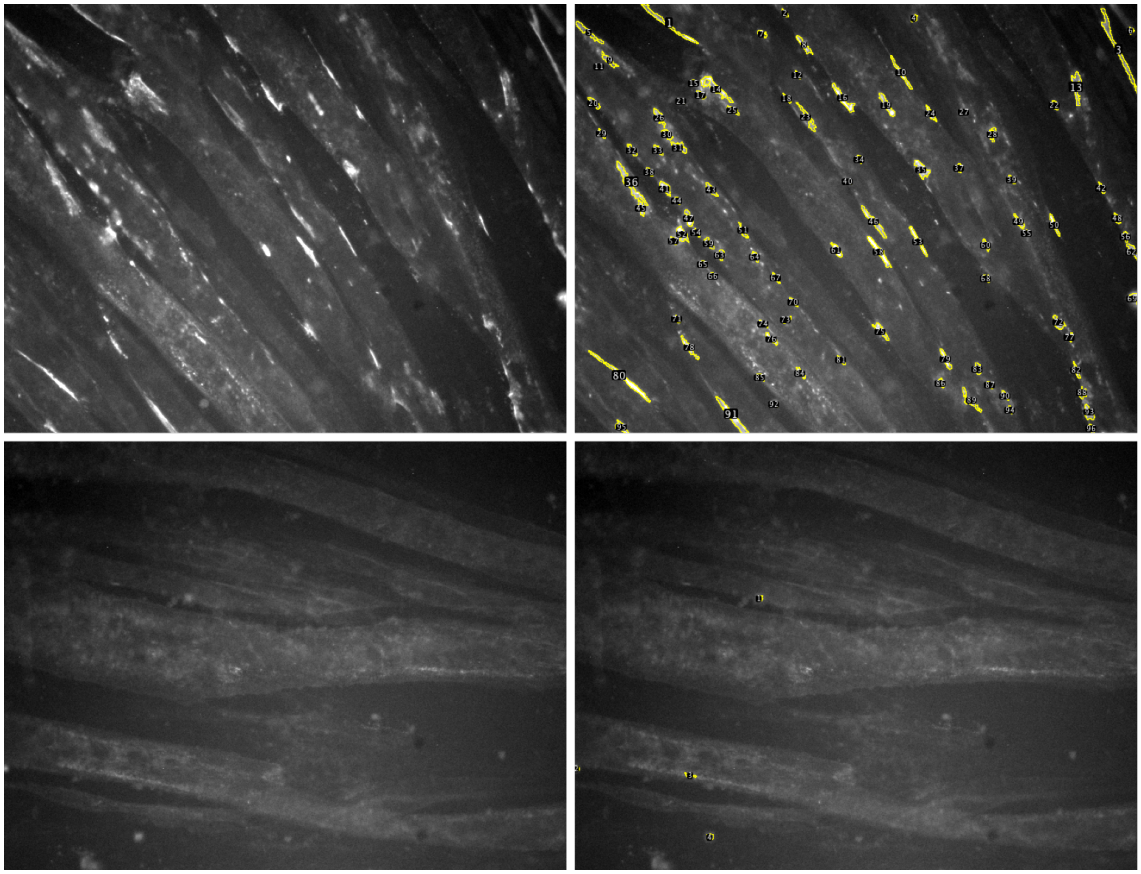


Figure 2-9. Representative images of ImageJ macro analysis of AChR clusters in C2C12 myotubes and C2C12 *Musk*-KO cells

2.13 Bioinformatics

The pathogenicity of amino acid substitutions on the structure and function of COL13A1 and MuSK proteins was analysed using PolyPhen-2 (http://genetics.bwh.harvard.edu/pph2/). PyMOL Molecular Graphics System Version 1.7.4.5 Edu (Schrödinger, LLC) was used to study the effect of missense variants on the macromolecular structure of MuSK, and to model the dimerisation of MuSK kinase domain based on the known dimerisation of the Insulin-like Growth Factor 1 Receptor (IGF1R) and the Epidermal Growth Factor Receptor (EGFR) kinase domains. The Genome Aggregation Database [(gnomAD, Cambridge, MA (URL:

http://gnomad.broadinsitute.org)] (Lek *et al.*, 2016) was used to investigate the presence and frequency of *MUSK* and *COL13A1* variants in the general population.

2.14 Statistical analysis

Prism software version 7.0b (GraphPad Software, La Jolla, California) was used for the statistical analyses. A p-value of 0.05 was used as the cut-off for statistical significance.

Chapter 3

The Differential Diagnosis of CMS and SNMG: Usefulness of the Clustered-AChR Cell-based Assay

3.1 Introduction

The clinical diagnosis of CMS is based on the presence of fatigable muscle weakness, usually from birth or early in life, and neuromuscular transmission abnormalities on electrophysiological testing (Palace and Beeson, 2008). The genetic diagnosis is complex with more that 30 CMS-causing genes identified to date (Beeson, 2016), each with their own, often distinct, phenotype, and approximately 10% of patients having no identified genetic abnormalities (Finlayson, 2013).

The differential diagnosis of CMS is wide, with a range of disorders going from autoimmune myasthenia gravis (MG) to congenital myopathies and muscular dystrophies. The lack of detectable antibodies in patients with myasthenic weakness, always raises the possibility of an underlying genetic disorder of the neuromuscular junction. The not uncommon presence of non-specific histological abnormalities on CMS muscle biopsies, such as variation in fibre size, type I fibre predominance, core-like areas (Klein *et al.*, 2013) or mild dystrophic features may lead to misdiagnosis of congenital myopathy or muscular dystrophy (Mahjneh *et al.*, 2013). This is also the case using muscle MRI where a study has shown there is a wide range of MRI appearance from normal to marked abnormalities depending upon the CMS subtype (Finlayson *et al.*, 2016). On the

other hand, the lack of specificity of single fibre electromyography (SFEMG) for NMT abnormalities may contribute to misdiagnosis of other neuromuscular disorders with CMS (Shields, 1984; Girlanda *et al.*, 1999; Hatanaka and Oh, 2007).

Among the conditions mimicking CMS, two groups deserve special attention: patients with MG lacking detectable antibodies, and patients with congenital myopathies and secondary neuromuscular transmission abnormalities. The overall importance of getting the right diagnosis lies on the possibility of providing early symptomatic treatment to improve muscle strength and functionality, avoiding unnecessary immunosuppression, and to give the appropriate advice and genetic counselling for the patients.

3.1.1 Seronegative myasthenia gravis

MG is the main differential diagnosis of CMS. Approximately 80% of patients with generalised MG and 50% with ocular MG have autoantibodies against the muscle nicotinic acetylcholine receptor (AChR) measured by radioimmunoprecipitation assay (RIA) (Lindstrom *et al.*, 1976; Vincent and Newsom-Davis, 1985). AChR antibodies are predominantly IgG1 and IgG3 subclasses and produce severe loss of AChRs by complement-mediated damage to the postsynaptic membrane, receptor endocytosis, and occasionally direct AChR block (Vincent, 2002). These patients are classically known as seropositive MG.

Autoantibodies to muscle specific tyrosine kinase (MuSK) measured by RIA have been reported in a variable proportion of patients with SNMG ranging from 0 to 70% (Hoch *et al.*, 2001; Scuderi *et al.*, 2002; Shiraishi *et al.*, 2005; Niks *et al.*, 2007; Kostera-Pruszczyk *et*

al., 2008; Chang *et al.*, 2009). Autoantibodies to MuSK are mainly of the IgG4 subclass, which does not activate complement. They prevent the interaction of MuSK with lipoprotein receptor-related protein-4 (LRP4) and, therefore, inhibit agrin-dependent AChR clustering (Koneczny *et al.*, 2013). MuSK autoantibodies identified MG patients with distinctive clinical features such as high female prevalence and prevalent involvement of cranial, bulbar and respiratory muscles (Evoli *et al.*, 2003; Sanders *et al.*, 2003).

MG patients lacking detectable AChR and MuSK antibodies by RIA are classically known as seronegative MG (SNMG), which is the most challenging group of patients in the differential diagnosis with CMS. For the improved detection of AChR antibodies in patients previously seronegative by RIA, a cell-based assay (CBA) was developed using AChRs clustered by the anchoring protein Rapsyn (Leite *et al.*, 2008) **(Figure 3-1).** The proportion of SNMG with autoantibodies to clustered AChRs ranges from 16-60% (Leite *et al.*, 2008; Jacob *et al.*, 2012; Devic *et al.*, 2014). These antibodies are mainly complement-fixing IgG1 subtype and have similar pathogenic mechanisms to those detected by RIA [16]. The clinical features of this subset of patients and the usefulness of this test in clinical practice are not well defined.

Lately, several groups reported autoantibodies against other components of the neuromuscular junction namely agrin, LRP4 and COLQ in a variable and generally low proportion of SNMG patients (Pevzner *et al.*, 2012; Zisimopoulou *et al.*, 2013; Gasperi *et al.*, 2014; Zhang *et al.*, 2014), although their biological relevance is not well understood. More recently, antibodies to cortactin have also been reported (Gallardo *et al.*, 2014). Cortactin is an intracellular protein involved in AChR clustering (Madhavan *et al.*, 2009).

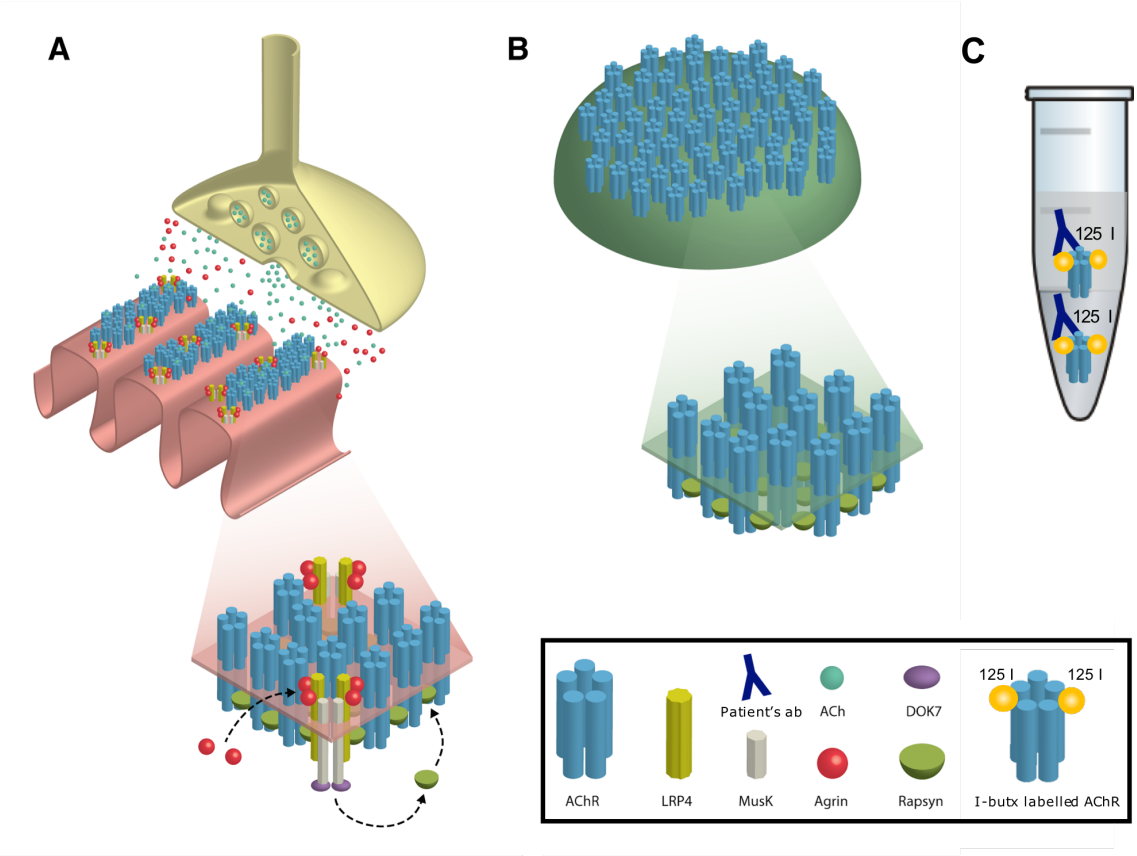


Figure 3-1. Schematic representation of the NMJ and the tests used for the detection of AChR antibodies

(A, B) The clustered-AChR CBA (green) involves expressing AChRs on the surface of a human embryonic kidney cells (HEK-293T) and clustering by co-expression with the intracellular anchoring protein Rapsyn. This is performed by transfecting the live HEK-293T cells with the appropriate cDNAs encoding these proteins using PEI. The binding of AChR antibodies can be scored (0-4) visually using indirect immunofluorescence (Section 2.9.2). This CBA, unlike most other diagnostic antibody tests, allows detection of antibodies binding to AChRs in a natural membrane environment, where they adopt native conformational states and appropriate glycosylation levels, and clustered as they are at the neuromuscular junction (red colour).

(C) On the other hand, the radioimmunoprecipitation assay (RIA) is based on the immunoprecipitation by the patient's IgG antibodies of solubilised AChRs labelled with radiolabelled [^{125}I] α-bungarotoxin (Vincent and Newsom-Davis, 1985). The assay is performed in solution phase and thus AChRs are not expressed on the membrane surface. The binding of patients' antibodies to solubilised AChRs is mainly monovalent.

3.1.2 Congenital myopathies with abnormalities in the neuromuscular transmission

Congenital myopathies are a clinically and genetically heterogeneous group of disorders characterized by early onset weakness, hypotonia and characteristic, but not pathognomonic, structural abnormalities in muscle fibres (Engel and Franzini-Armstrong C, 2004). The genetic diagnosis of congenital myopathies is complex since different genetic entities can share similar pathological findings (Maggi *et al.*, 2013). The clinical diagnosis is made in individuals with often static or minimally progressive weakness, usually of congenital or early childhood onset, and in whom other conditions such as muscular dystrophies, myofibrillar myopathies, CMS, and neurogenic conditions have been excluded by appropriate investigations (Maggi *et al.*, 2013). The presence of early onset myasthenic symptoms suggests CMS. However, some patients with congenital myopathies may present with myasthenic features suggesting CMS. In keeping with this, there are an increasing number of reports of patients with genetically and pathologically confirmed congenital myopathies, that originally were thought to have CMS due to the presence of fatigue, positive response to acetylcholinesterase inhibitors or neuromuscular transmission (NMT) defects on neurophysiology. The differential diagnosis with CMS in these cases is especially challenging.

In the appendix section, the reader can find the first report of a patient with cap myopathy and myasthenic features due to *TPM2* mutations and a review of the literature on congenital myopathies associated with features suggestive of secondary neuromuscular transmission defects (Rodríguez Cruz *et al.*, 2014). This review highlights the overlap of features in congenital myopathies and CMS with references to several cases seen in our service.

3.2 Aims

The aim of this chapter was to determine the diagnostic usefulness of the clustered-AChR CBA in the diagnosis of SNMG (and in the differential diagnosis of CMS), and to compare the clinical features of patients with antibodies only to clustered AChRs with those of patients with SNMG.

3.3 Clinical material

This study was approved by the Clinical Audit Team at the John Radcliffe Hospital in Oxford (Datix ID 2837). All Oxford patients tested for antibodies against clustered AChRs by CBA between November 2009 and November 2013 were assessed, all of whom had been negative by RIA for AChR and MuSK antibodies. The request of the clustered AChR assay came from clinicians during routine clinical practice and, therefore, this might not include all patients who were RIA negative for AChR and MuSK antibodies during the same period.

MG was diagnosed by clinical and electromyographic criteria. In those patients with normal neurophysiology and lacking detectable autoantibodies, MG was diagnosed based on the presence of fatigable weakness and a positive response to treatment with cholinesterase inhibitors or immunosuppression by experienced myasthenia physicians from the Oxford Nuffield Department of Clinical Neurosciences.

In the present study, patients with MG lacking detectable AChR antibodies by RIA and CBA, and lacking MuSK antibodies by RIA were referred to as having SNMG. All available samples from these patients were retrospectively tested for LRP4 antibodies using a cell-based assay. The cases where a final diagnosis was not achieved were termed "uncertain

diagnosis". If a final diagnosis other than MG was made, subjects were classified under "other diagnosis".

Data on the individual MG patients, including demographic data were collated, and the clinical features were graded on a 0-3 scale from 0: absent, 1: mild; 2: moderate; 3: severe. The distribution and severity of myasthenic weakness was classified according to the Myasthenia Gravis Foundation of America (MGFA) grading system (Jaretzki *et al.*, 2000). The clinical state of MG patients after institution of treatment was classified according to the MGFA Post-intervention Status (PIS) classification (Jaretzki *et al.*, 2000). The clinical features of SNMG patients were compared with those of MG with antibodies only to clustered AChRs. The CBA results were scored from 0 to 4 using a visual scale (Section 2.9.2).

3.4 Subjects included in the study

A total of 138 subjects were tested for clustered-AChR antibodies during this period **(Figure 3-2)**. 42 subjects (30.43%) had a final clinical diagnosis of MG, 51 (36.95%) had an uncertain diagnosis, and 45 (32.61%) had other conditions **(Table 3.1)**. The subjects with a clinical diagnosis of MG represented all the AChR and MuSK negative MG cases by RIA encountered during the period of study.

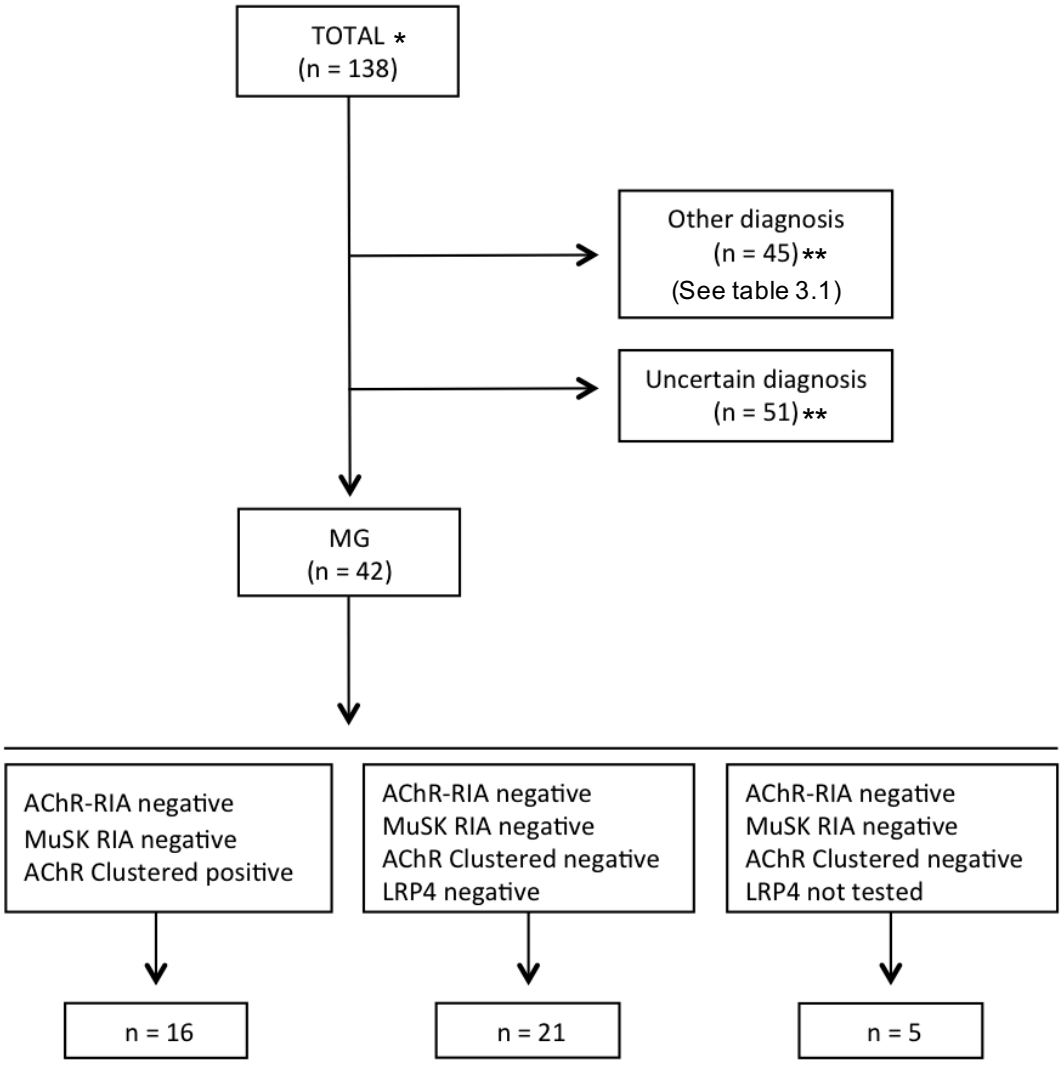


Figure 3-2. Flowchart showing patients included in the study

The clustered AChR cell-based assay detected antibodies in 16 out of 42 (38.1%) patients with (RIA)–negative MG. * All patients tested were negative for AChR and MuSK antibodies by RIA. ** All patients with uncertain and other diagnosis were also negative for antibodies to clustered AChRs.

Among the 45 patients with alternative diagnosis included in the present study, 13 (28.9%) had a final diagnosis of CMS confirmed by genetic analysis. This is the most representative disorder in this group and, therefore, highlights the usefulness of the CBA with respect to the differential diagnosis with CMS. The second most representative disorder was cranial nerve abnormalities, either acquired or congenital in the form of cranial dysinnervation syndromes, with 9 (20%) subjects.

Table 3-1. Patients with other diagnosis included in the study

Diagnosis	Number of patients (n=45)
Acquired cranial nerve palsy	4
Brainstem pathology	2
Chronic fatigue syndrome	4
Congenital cranial dysinnervation syndrome	5
Congenital myasthenic syndromes	13
Functional neurological disorder	3
Mitochondrial myopathy	2
Motor neuron disease	1
Oculopharyngodistal myopathy	1
Other	6
Primary ocular pathology	4

3.5 Antibody results on RIA and CBA in total cohort

All subjects with 'uncertain' and 'other diagnoses' were negative for clustered AChR antibodies. In the MG group, 16 out of 42 (38%) were positive for clustered AChR antibodies: median CBA score 2, range 1-3. One subject with an unclear CBA result was designated SNMG. Individual scores are provided in **Table 3.2**. All SNMG patients tested for LRP4 antibodies (21/26) were negative by CBA **(Figure 3-2)**.

3.6 Clinical characterisation of MG patients with positive CBA and negative results on RIA

The clinical characteristics of the 16 subjects with clustered AChR antibodies are detailed in **Table 3.2**. Ten of the 16 were female. The age range was wide (age range, 1-52 years) and 63% were children (age range, 1-10 years) with 8 of 10 children presenting before age 5 years. Seven patients (43.8%) were of Black British, Caribbean or African ethnicity (4 individuals) or mixed White-Asian (3 individuals). The rest were White-British or White-other. Neurophysiology at diagnosis was abnormal in 8 subjects (50.0%), normal in 6 (37.5%), and not performed in 2 (12.5%). Chest imaging was normal in the three patients scanned.

The presentations were predominantly ocular (62.5%) with ptosis and restricted eye movements, with no generalisation during the follow-up period. Bulbar symptoms were scarce and mild (25.0%) and none had respiratory weakness. The maximum MGFA grades related to age at onset, showed a greater proportion of patients with onset less than 10 years having the least severe grades (I and II) **(Figure 3-3A)**.

Most of the cases were successfully treated with pyridostigmine and prednisolone, or pyridostigmine alone, and only two patients (12.5%) needed further immunosuppression with azathioprine. Five were on immunosuppressive treatment at the time of antibody testing. Thymectomy was performed only in one case with the highest MGFA (IVA). Pathological examination showed an atrophic thymus with no evidence of thymoma or lymphocytic infiltrations.

The mean (SD) follow-up period was 54.5 (40.6) months. Among 14 patients with adequate follow-up, the outcome was good in all but 3 patients, with complete stable remission in 4 of whom all were children, pharmacological remission in 3, and minimal manifestations in 4. The mean (SD) time from onset of symptoms to complete resolution was 78.75 (55.33) months. However, 3children with ocular or mild generalised disease did not attain remission.

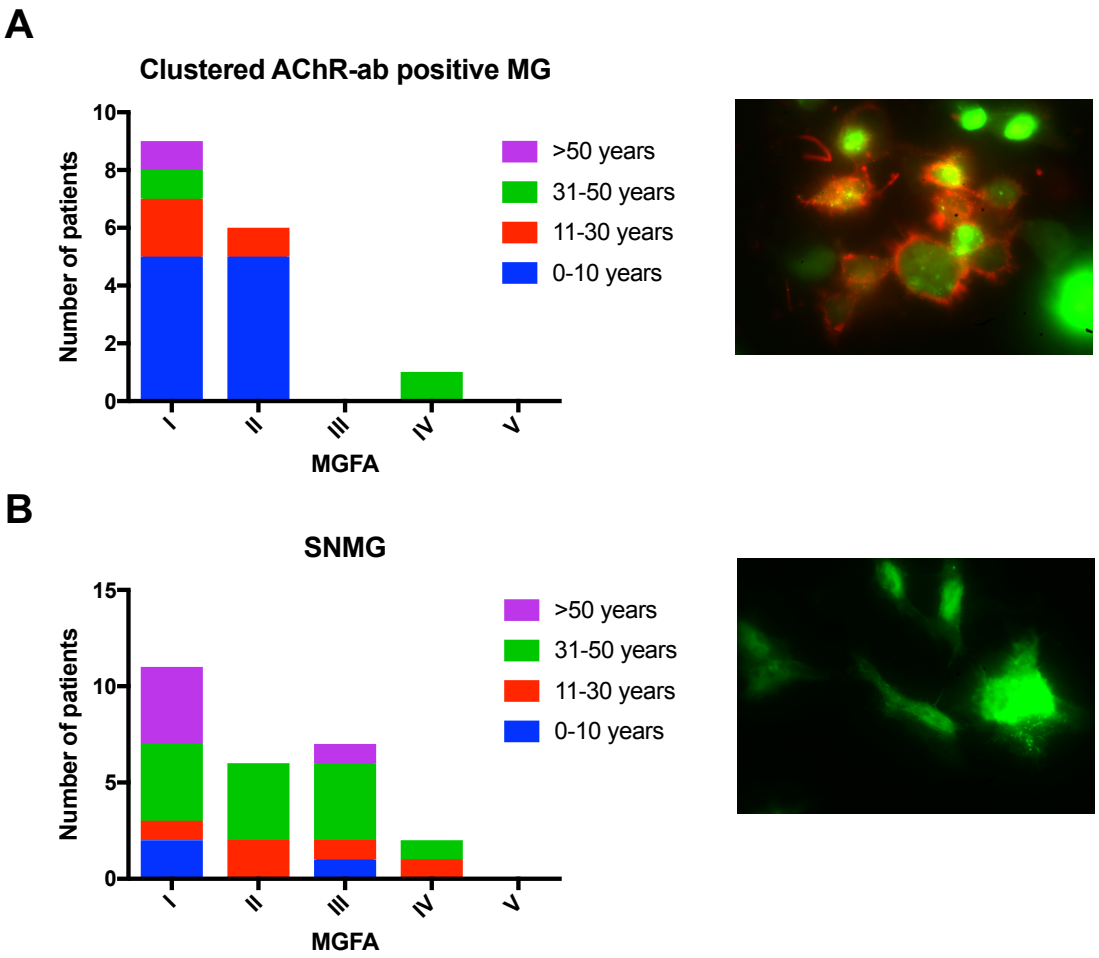


Figure 3-3. Maximum MGFA and age at onset in patients with antibodies to clustered-AChRs on CBA (negative on RIA) or no detectable AChR antibodies (SNMG)

Patients with antibodies only to clustered AChRs **(A)** had a younger age at onset and a milder MGFA grade than patients with SNMG **(B)**. Representative images of positive and negative CBA for clustered AChR antibodies are displayed on the right side of the figure: green, HEK-293T cells expressing AChRs + rapsyn-EGFP ; Red, serum + Alexa Fluor® 594-conjugated anti-human IgG

Table 3-2. Clinical features of patients with antibodies to clustered AChRs (negative on RIA)

n	G	E	Age	Onset	RNS	SFEMG	CBA	Features during follow-up								MGFA (max)	Treatment	Thy	PIS	FU
								P	O	D	F	B	N	L	R					
1	F	B	1	P,O,L	Normal	Not done	2.5*	2	3	0	1	1	1	1	0	IIA	Py, Pd, Aza	No	PR, I	116
2	F	W	1	P,L	Abnormal	Abnormal	1	1	0	1	1	1	0	1	0	IIA	Py, Pd, DAP	No	CSR, I	147
3	F	A	2	P,O	Abnormal	Not done	3*	2	2	0	0	0	0	0	0	I	Py, Pd	No	NR, I	22
4	F	W	2	P	Not done	Not done	2*	2	1	0	0	0	0	0	0	I	Py, Pd, Ivlg	No	MM-3, I	24
5	F	B	2	P	Not done	Not done	2*	2	0	0	0	0	0	0	0	I	Py, Pd	No	PR, I	69
6	M	W	3	P	Normal	Not tolerated	2	2	0	0	0	0	0	0	0	I	No	No	CSR, I	12
7	F	A	3	P,F	Normal	Not done	3	1	0	1	1	0	1	1	0	IIA	Py	No	CSR, I	84
8	M	W	4	P,F,B	Abnormal	Not done	3	2	0	0	1	1	1	0	0	IIA	Py, Pd	No	NR, I	47
9	M	B	7	P,O	Not done	Abnormal	1	2	2	2	0	0	0	0	0	I	Py	No	NR, I	24
10	F	W	10	P,O	Normal	Normal	2	2	2	1	0	0	0	0	0	I	Py	No	CSR, I	72
11	M	A	18	P,O	Normal	Abnormal	1.5	2	3	2	0	0	0	0	0	I	Py, Pd	No	**	6
12	F	B	23	O	Not done	Normal	3	2	2	1	0	0	0	0	0	I	Py, Pd	No	MM-1, I	84
13	M	W	25	L	Abnormal	Abnormal	1	2	1	0	1	0	0	1	0	IIA	Py	No	MM-2, U	74
14	F	W	42	P,O	Normal	Normal	1.5	2	2	1	1	0	0	0	0	I	Py, Pd	No	**	6
15	F	W	47	L,O	Abnormal	Abnormal	2*	3	0	1	1	2	0	3	0	IVA	Py, Pd, Aza, Ivlg	Yes	MM-3, I	37
16	M	W	52	P,O	Not done	Abnormal	1.5	3	1	1	0	0	0	0	0	I	Py, Pd	No	PR, I	48

Aza = Azathioprine; B= bulbar weakness; CBA = Cell Based Assay score (0: no signal, 0.5 unclear, 1: weak positive, 2: moderate positive, 3: strong positive, 4: very strong positive); D= diplopia; DAP= 3,4-Diaminopyridine; E = ethnicity (A: Asian; B: Black; W: White); F= facial weakness; Features during follow-up: 0 = absent; 1 = mild; 2 = moderate; 3 = severe; FU = follow-up (months); G = gender; Ivlg= Intravenous Immunoglobulin; L= limb weakness; MGFA = Myasthenia Gravis Functional Assessment scale (MGFA grade I, IIA, IIB, IIIA, IIIB, IVA, IVB, V); n = patient number; N = neck weakness; O = ophtalmoparesis; P = ptosis; PIS = Post-intervention Status (NR = no remission; MM = Minimal Manifestations; PR = Pharmacological Remission, U = Unchanged; I = Improved; E = Exacerbation; D = Died of myasthenia gravis); Py = Pyridostigmine; Pd = prednisolone; R = respiratory weakness; RNS = Repetitive Nerve Stimulation; SFEMG = Single Fibre Electromyography; TAS: Treatment at sample (immunosuppression); Thy = thymectomy. Five patients were on immunosuppressive treatment at the time of antibody testing (*). Post-intervention status was not applicable to two patients in whom the disease duration was less than 12 months (**).

3.7 Comparison with MG subjects without clustered–AChR antibodies

The clinical characteristics of the 26 SNMG subjects with negative CBA results are detailed below **(Figure 3-4; Table 3-3)**. Overall, the patients with clustered-AChR antibodies had younger age at onset (Mann Whitney U-test; p=0.02), a trend towards milder disease (Fisher's exact test; p=0.06), and a higher proportion attained clinical remission (Fisher's exact test; p=0.03) compared to the SNMG patients who did not have clustered-AChR antibodies.

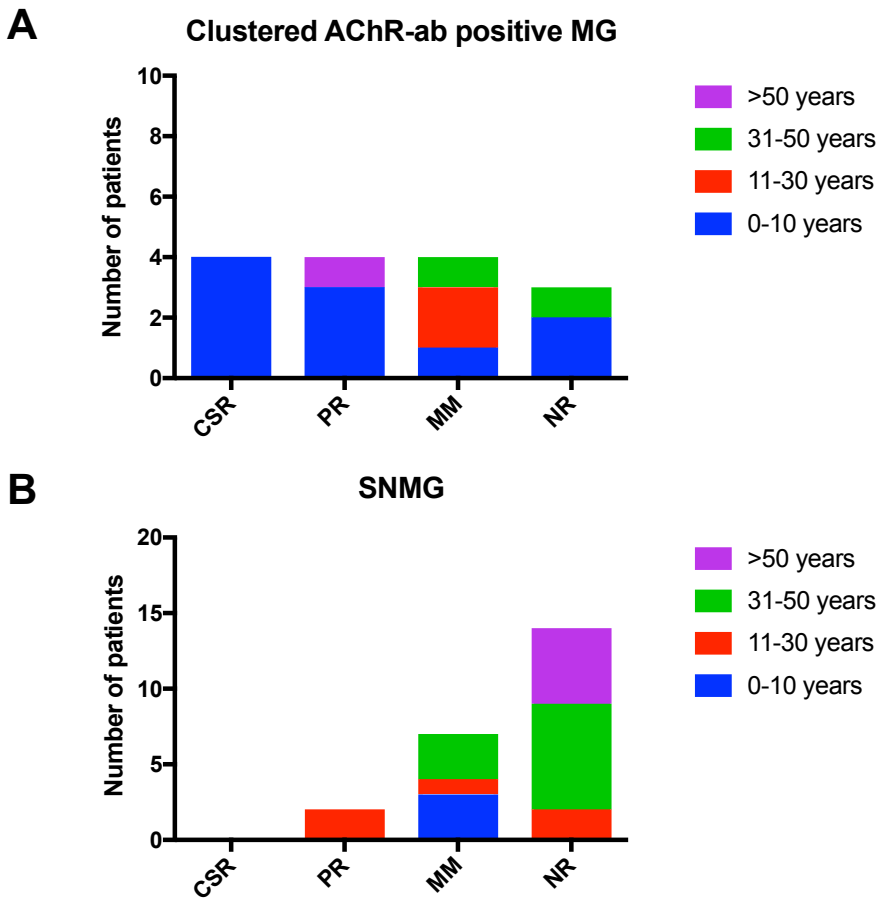


Figure 3-4. MGFA post-intervention status and age at onset in patients with antibodies to clustered-AChRs on CBA (negative on RIA) or no detectable AChR antibodies (SNMG) Patients with clustered AChR antibodies **(A)** had a younger age at onset and went into remission in a higher proportion compared to SNMG **(B)**. CSR: Complete Stable Remission; MM: Minimal Manifestations; NR: No Remission: PR, Pharmacological Remission.

Table 3-3. Clinical features of seronegative MG patients compared to patients with antibodies only to clustered AChRs.

Variable	SNMG (n=26)	Clustered AChR-ab positive MG (n= 16)
Male: female ratio	1: 5.5	1:1.7
Median age at onset (range)	38 years (2-72)	6 years (1-52) **
Prepubertal age	3 (12.0%)	10 (62.5%) **
Clinical presentation		
Ocular	15 (57.7%)	11 (68.7%)
Bulbar	5 (19.2%)	1 (6.3%)
Limb	0 (0.0%)	1 (6.3%)
Generalised	6 (23.1%)	3 (18.7%)
Clinical subtype		
Ocular	11 (42.3%)	10 (62.5%)
Generalised	15 (57.3%)	6 (37.5%)
Clinical features		
MGFA (max)	I (11); IIA (4); IIB (2); IIIA (3); IIIB (4); IVB (2)	I (10); IIA (5); IVA (1)
Bulbar symptoms	12 (46.2%)	4 (25.0%)
Respiratory symptoms	6 (23.1%)	0 (0.0%)
Abnormal neurophysiology	16 (61.5%)	8/14 (57.1%)
Treatment		
Prednisolone use	15 (57.7%)	11 (68.7%)
Other immunosuppression	11 (42.3)	2 (12.5%)
Thymectomy	5 (19.2%; 1 thymoma)	1 (6.2%)
*Post-intervention Status **		
Remission (CSR/PR)	2 (9.0%)	7 (50.0%) **
Follow-up (months)	61.27 ± 79.96	54.50 ± 40.60

Post-intervention status was not applicable to two SNMG and two clustered-AChR positive patients in whom the disease duration was less than 12 months (*). p≤0.05 (**). CSR= Complete Stable Remission; PR= Pharmacological Remission.

3.8 Discussion

This study confirmed that the clustered-AChR CBA improves diagnostic sensitivity for MG and showed for the first time that patients with these antibodies have a milder phenotype than those patients without any detectable AChR antibodies, with complete or pharmacological remissions in 7 of the 14 patients with adequate follow-up. In addition, patients with antibodies only to clustered AChRs had younger age at onset, and thus the usefulness of this test in the differential diagnosis with CMS, the major group with an alternative diagnosis at that age.

CBAs were recently established for the improved detection of AChR antibodies in patients who were previously seronegative (Leite *et al.*, 2008). CBAs also detect AChR antibodies positive using the RIA, although this is not performed routinely due to the relatively high cost and time-consuming nature when compared to the RIA. This study showed that the CBA is helpful in the diagnostic work-up of MG in routine clinical practice, detecting AChR antibodies in 36% (15/42) of negative MG patients with 100% specificity. On the other hand, none of the SNMG patients tested for LRP4 antibodies were positive. This is in keeping with the ongoing observations from our group that the incidence of this antibody is very low. It is possible that the relatively high proportion of positive results reported by other groups (Pevzner *et al.*, 2012; Zisimopoulou *et al.*, 2013) is due to the presence of non-specific interactions from using fixed cells in their assays or lacking the appropriate controls.

Autoantibodies detected by CBA have similar pathogenic mechanisms to those detected by RIA, and would include complement-mediated lysis (Leite *et al.*, 2008; Jacob *et al.*,

2012). Complement deposition was noted in a passive transfer model of clustered AChR antibody MG (Jacob *et al.*, 2012). Although not formally described, it is likely that the IgG1 antibodies detected by CBA cross-link the clustered AChRs on the cell surface by divalent binding, thus explaining the increased sensitivity of the CBA. Alternatively, a less likely explanation could be the loss of antigenic determinants in the solubilised AChRs used in the radioimmunoprecipitation assay. CBAs require the use of live cells, tissue culture facilities and expertise with performing and interpreting the assay, which are scored visually using indirect immunofluorescence. Due to these limitations, their current use is mainly confined to specialised research centres. However, if these difficulties were overcome, fluorescence-activated cell sorting (FACS) analysis (Leite *et al.*, 2008) could be a suitable option for an automated and objective analysis.

Patients with antibodies only to clustered AChRs had very early onset and overall milder disease with predominantly isolated ocular symptoms, low generalisation rate, better prognosis and no need for thymectomy. These results differ from those of patients with SNMG in the present study. Although there was no actual comparison with RIA positive patients, the results also differ from the classic AChR-MG phenotype seen in large series with respect to age at onset, MGFA grades at maximum severity and prognosis (Beghi *et al.*, 1991; Mantegazza *et al.*, 2003). However, due to the small numbers of patients included, their low MGFA scores were not significantly different compared to SNMG (p= 0.12). Our group previously found 50% of patients with RIA seronegative ocular MG had complement-fixing IgG1 clustered AChR antibodies (Jacob *et al.*, 2012). Results from two other studies have suggested that subjects with antibodies to clustered AChRs have a milder disease (Chang *et al.*, 2014; Devic *et al.*, 2014) but those studies did not include

paediatric populations. Overall, these observations are likely to have implications in planning treatment of MG patients with clustered-AChR antibodies, especially in children.

Juvenile MG, especially in prepubertal children, is reported to differ from adult MG with more ocular myasthenia, lower rates of generalisation, a better prognosis with a higher probability of achieving remission and a lower frequency of AChR antibodies by RIA (Andrews *et al.*, 1993; Ashraf *et al.*, 2006; Chiang *et al.*, 2009; Pineles *et al.*, 2010). However, the previous observation of similar female-male prevalence differs from the 2:1 ratio seen in those with clustered-AChR positivity. SNMG was more common in prepubertal (44%) compared to peripubertal (18%) and postpubertal onset MG (0%) (Andrews *et al.*, 1993). Although it is possible that some of those subjects had an undiagnosed CMS, we also found a high proportion of prepubertal onset MG (62.5%) in the group of patients with autoantibodies against clustered AChRs who were previously negative on RIA. Thus the usefulness of the CBA with respect to the differential diagnosis with CMS since this is the major group with an alternative diagnosis, and both are rare disorders in childhood (Parr *et al.*, 2014).

Thymectomy should be considered as a treatment option early in the course of generalised AChR antibody-positive JMG (Heng *et al.*, 2014). However, indications for thymectomy within the prepubertal and seronegative groups are less clear (Ionita and Acsadi, 2013). In the current cohort of paediatric patients with antibodies to clustered AChRs, thymectomy was not performed probably related to the mildness of disease, high rate of pharmacological remission and young age of some patients. In the study from the French group, thymectomy was performed in two subjects with antibodies to clustered

AChRs of 14 and 18 years, which revealed thymus hyperplasia and thymoma (Devic *et al.*, 2014). A further study in adult patients reported evidence of thymic involvement with typical lymphocytic infiltrates and germinal centres less striking but in a similar fashion to the classic AChR-MG (Leite *et al.*, 2008). The recently completed Thymectomy Trial in Non-thymomatous Myasthenia Gravis Patients Receiving Prednisone Therapy (MGTX) did not include paediatric patients (Wolfe *et al.*, 2017).

The reasons underlying the clinical differences between prepubertal JMG and adult MG are unknown. There was female predominance and a high proportion of non-Caucasian patients (40%) within the present cohort, especially Black-British individuals. This agrees with the observations that juvenile MG is rare in Caucasians (Parr *et al.*, 2014). In Asian populations, JMG and ocular MG have been reported to represent almost half of the cases (Chiu *et al.*, 1987). These ethnic groups have also been reported to have lower antibody titres on RIA that could be related to a higher frequency of ocular cases or milder disease (Zhang *et al.*, 2007).

In conclusion, this study shows that measuring antibodies to clustered AChRs by CBA is helpful for the diagnosis of SNMG and the differential diagnosis with CMS. This is particularly true in children, who tend to have early onset, milder disease, and increased chance of spontaneous remission. These observations are likely to have implications in planning treatment.

Chapter 4

Clinical and Molecular Characterisation of Congenital Myasthenic Syndrome due to Mutations in *COL13A1*

4.1 Introduction

The use of next generation sequencing (NGS) in clinical diagnosis together with the better characterisation of genetic variation within the general population has allowed the identification of novel disease genes in neuromuscular disorders. The identification of previously unknown variants has an important effect in diagnosis, genetic counselling and treatment (Taylor *et al.*, 2015). Approximately 10% of individuals with CMS in the UK have no identified mutations in the known CMS-associated genes (Finlayson, 2013). Whole exome sequencing was used to identify mutations in *COL13A1* (collagen type XIII alpha 1 chain) in three individuals with CMS from two different kinships.

The collagen family of proteins consist of 28 members numbered with Roman numerals in vertebrates (I-XXVIII) with characteristic tissue distribution and function (Ricard-Blum, 2011). The common structural feature is the presence of a triple helix motif composed of three collagen α-chains made of Gly-X-Y repeats that can be grouped into homotrimers or heterotrimers (Shoulders and Raines, 2009). Collagens are typically divided into fibrillar collagens, which contain one continuous triple-helical domain, and non-fibrillar collagens, which are multidomain molecules with several triple-helical domains of variable length interrupted by non-collagenous domains. The heterogeneous group of non-fibrillar

collagens can be further divided into fibril-associated collagens with interrupted triple-helices (FACIT), multiplexins, and membrane collagen subfamilies (Ricard-Blum, 2011).

COL13A1 [MIM 120350] in *Homo Sapiens (Human)* is located in the long (q) arm of chromosome 10 at position 22.1 and is 135 kb in size (www.genecards.org). *COL13A1* encodes the collagen type XIII alpha1 chain (COL13A1), which is a single-pass type II transmembrane protein made of a short intracellular domain, a single transmembrane domain, and a triple-helical collagenous ectodomain **(Figure 4-1)**. The extracellular domain contains three collagenous domains separated by short non-collagenous domains. Unlike most of the collagens, COL13A1 is anchored to the plasma membrane by an hydrophobic transmembrane segment (Hägg *et al.*, 1998). The presence of a predicted proprotease recognition site in the ectodomain suggests that the c-terminus can be proteolytically cleaved and expressed extracellularly. COL13A1 is an atypical non-fibrillar collagen believed to form homotrimers whose three collagenous domains are in triple helical conformation (Snellman *et al.*, 2000).

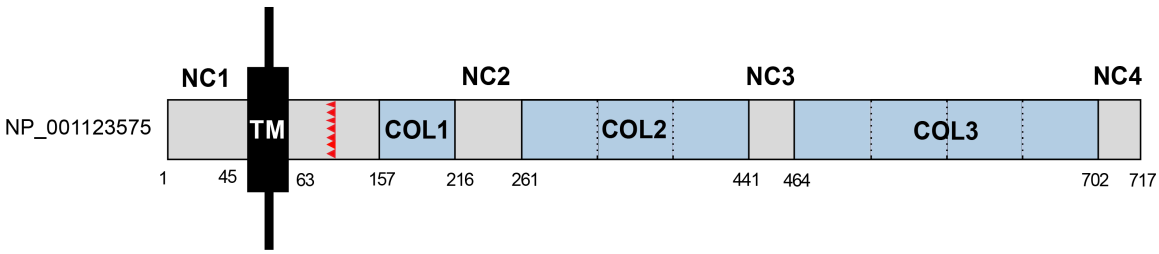


Figure 4-1. Schematic representation of the COL13A1 main transcript

COL13A1_001 (NP_001123575) consist of a short intracellular domain (NC1), a single transmembrane domain (TM), and the extracellular region with three collagenous domains (COL1-3) separated by short non-collagenous domains (NC2-3). The predicted proprotease recognition site is labelled in red colour. Numbers indicate the amino acid residues composing each domain. Because of complex alternative splicing, primary structures can vary.

COL13A1 transcripts undergo complex alternative splicing involving at least nine exons (Pihlajaniemi and Tamminen, 1990). This process is predicted to affect the structures of the COL1, NC2, COL3 and NC4 domains of Col13a1 transcripts. On the other hand, the COL2 domain remains invariant suggesting that the central portion of the molecule may have an important role in the stability of the protein (Snellman *et al.*, 2000).

The function of the *COL13A1* gene product is unknown, although mRNA expression has been detected at low levels in a wide range of tissues **(Figure 4-2)** suggesting a general role in the function of connective tissues such as cell-matrix and cell-cell interactions (Peltonen *et al.*, 1999). In keeping with this, COL13A1 has shown *in vitro* binding with α1ß1 integrin (Nykvist *et al.*, 2000) ,fibronectin, heparin, nidogen, and perlecan (Tu *et al.*, 2002), indicating that it is likely to mediate multiple interactions with the extracellular matrix. It should be noted that these studies of expression in muscle by RNA Seq or arrays do not take account the location and specific expression from sub-synaptic nuclei that will determine protein expression levels at the NMJ.

Temporal expression and localisation studies in developing mice have shown marked COL13A1 expression in central and peripheral nervous systems in mid-gestation (Sund *et al.*, 2001). During late development, COL13A1 was observed in many tissues including cartilage, skeletal muscle, and skin, with remarkable expression shifts in bone and lung, which suggests a potential role in endochondral ossification and lung morphogenesis. An additional report showed that COL13A1 is widely expressed in the human eye at the protein level, mainly in the optic nerve and the neural retina (Sandberg-Lall *et al.*, 2000).

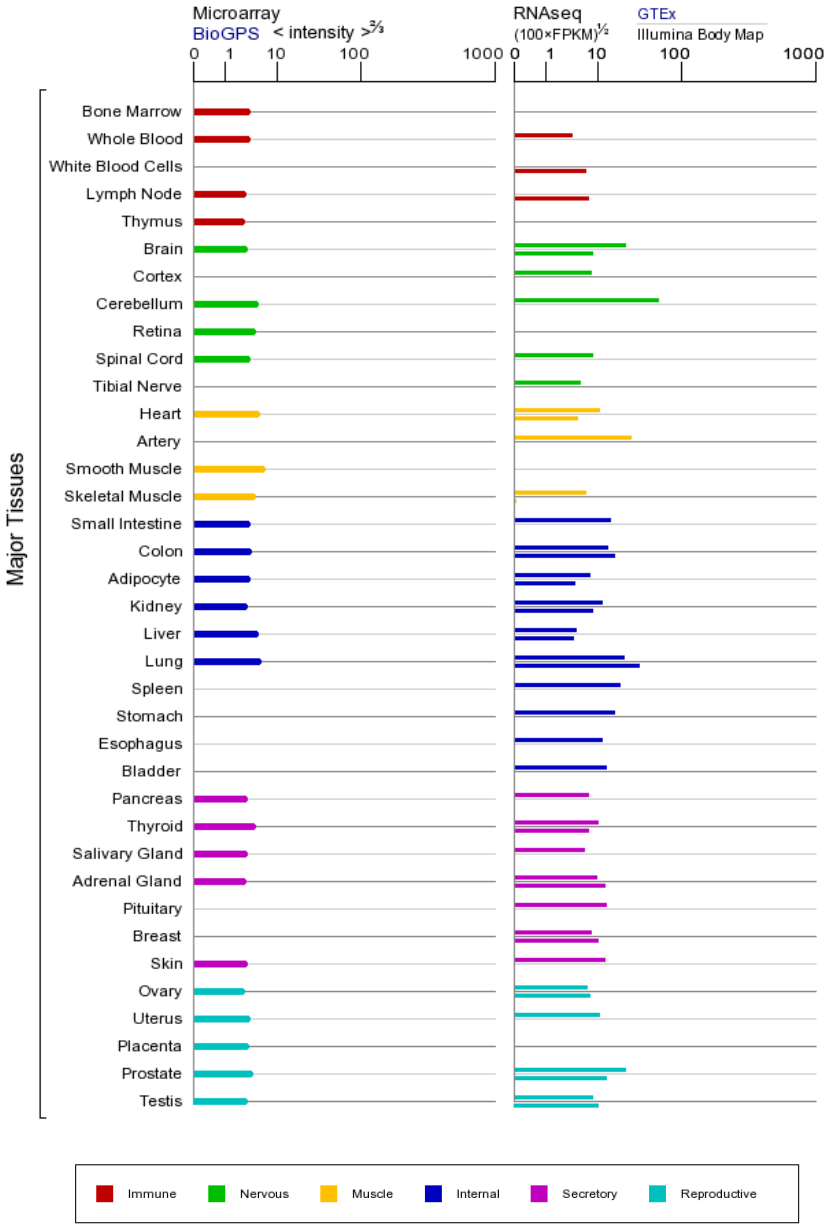


Figure 4-2. mRNA expression in normal tissues for *COL13A1* gene

Expression data displayed come from different sources including the BioGPS platform (http://biogps.gnf.org) (Wu *et al.*, 2009), RNASeq data from Illumina's Human BodyMap 2.0 project (https://www.ebi.ac.uk/gxa/home) and the Genotype-Tissue Expression (GTEx) project (https://gtexportal.org) (Wheeler *et al.*, 2016). Source (www.genecards.org).

Studies using *Col13a1* transgenic mice have been conducted to elucidate COL13A1 function. Firstly, animals lacking the cytosolic and transmembrane domains resulted in progressive myopathy, suggesting a role in the linkage between muscle fibres and the

basement membrane (a P. Kvist *et al.*, 2001). Secondly, *Col13a1*$^{-/-}$ animals have shown a potential role of COL13A1 in the regulation of the NMJ maturation both at pre and postsynaptic levels (Latvanlehto *et al.*, 2010). Thirdly, a *Col13a1*$^{tm/tm}$ mouse model in which the ectodomain shedding was annulled lacked most of the defects seen in the KO animal suggesting that the transmembrane form is the major actor of COL13A1 effects at the NMJ (Härönen *et al.*, 2017). Therefore, *COL13A1* has been postulated as a potential CMS-associated gene (Ricardo A. Maselli *et al.*, 2012), although its precise molecular function is still unknown and no patients carrying *COL13A1* mutations have been reported to date. Another proposed role is bone remodelling, since mice overexpressing COL13A1 developed an increase in bone mass (Ylönen *et al.*, 2005).

4.2 Aims

NGS was used to identify mutations in *COL13A1* in three patients with CMS from two different kinships. The main purpose of this study was to investigate whether the specific DNA changes identified were responsible for the patients' symptoms. The objectives were

1) Clinical characterisation of patients with *COL13A1* mutations
2) Study of COL13A1 expression in human muscle tissue
3) Study of COL13A1 interactions with other key NMJ proteins
4) Study the effect of *COL13A1* mutations on protein expression and AChR clustering
5) Develop a COL13A1-CBA for the screening of autoantibodies to COL13A1 in SNMG

4.3 Clinical features of individuals with mutations in *COL13A1*

Individual 1 (affected individual II:1 in family 1; **Table 4-1**) of white European origin was born after a normal pregnancy. She required intermittent ventilation for apnoeas after

birth. General hypotonia and poor suck were also noted and, therefore, she was fed via nasogastric tube. At 7 months, a Nissen fundoplication was performed to treat gastroesophageal reflux and a gastrostomy-feeding device fitted. During infancy she had recurrent episodes of sudden deterioration in respiratory function lasting days or weeks related to respiratory infections, needing non-invasive ventilation. Examination showed mild bilateral ptosis with normal eye movements, no facial weakness, but poor head control and marked neck weakness as well as limb hypotonia, with inability to sit. There were no joint contractures. By the age of two cognitive developmental delay was evident and dysmorphic features were noted in the face and chest, with low-set ears, micrognathia, retrognathia, high-arched palate, and *pectus carinatum* **(Figure 4-3A)**. A quadriceps muscle biopsy at 6 months of age revealed abnormal variation in fibre size, and increased staining for foetal myosin. Respiratory chain enzymes were normal with many mitochondria appearing swollen (**Figure 4-4 & 4-5**). Whole-muscle MRI was normal. Serum creatine kinase levels were within normal range. Stimulated single fibre electromyography (SFEMG) of the left *orbicularis oculi* muscle showed increased jitter values and blocks (mean MCD of 133.36 ±41.9 µs and 14% blocking), consistent with a diagnosis of CMS. Repetitive nerve stimulation in right *abductor digiti minimi* and left *flexor hallucis brevis* showed significant decrement >20% at rest at 3 Hz stimulation rates (**Figure 4-6**). Treatment with pyridostigmine (1 mg/kg/day) did not have a significant effect on muscle strength. Subsequent treatment with 3,4-diaminopyridine (0.3 mg/kg/day) and salbutamol (0.56 mg/kg/day) produced a remarkable improvement in her motor and respiratory function: head control improved, and she could achieve unassisted sitting. Non-invasive ventilation requirement went down to nocturnal only and episodes of respiratory deterioration abated. At the age of 3 years her condition was stable.

Table 4-1. Summary of clinical features of individuals with mutations in *COL13A1*

Kinship		family 1	family 2	family 2
Affected individual		II:1	II:1	II:2
Consanguinity		n	y	y
Mutation (Homozygous)		c.1171delG (frameshift)	c.523-1delG (splice-site/frameshift)	c.523-1delG (splice-site/frameshift)
Sex		F	M	F
Age	Current	24m	27y	died 8y
	Assessed	5m	24y	5y
	Onset	birth	birth-1y	birth
Presenting symptoms		BD, FD	pt, FD	BD, FD
Ptosis		+	+	+
Ophthalmoparesis		-	-	-/+
Facial weakness		+	+	+
Bulbar weakness		+	-	+
Proximal weakness	Upper limbs	+	-	+
	Lower limbs	+	-	+
Distal weakness	Upper limbs	+	+	+
	Lower limbs	+	-	+
Axial weakness		+	-/+	+
Distal joint laxity		+	-	+
Contractures		-	-	-
Spinal rigidity		-	+	+
Dysmorphic features		+	+	+
Mild learning difficulties		NK	+	NK
Decrement on RNS		+	+	NA
Abnormal Jitter		+	+	NA
Other		LRTI	LRTI	CLD, hh, LRTI
Response to treatment		DAP, sb, NIV, py-ve	none	NIV, py-ve

Ap, apnea; BD, breathing difficulties; CLD, chronic lung disease; DAP, 3,4-diaminopyridine; F, female; FD, feeding difficulties; hh, hiatus and diaphragmatic hernia; hyp, global hypotonia; LRTI, lower respiratory tract infection; m, months; M, male; n, no; NA, not assessed; NIV, non-invasive ventilation; NK, not known; pt, ptosis; py, pyridostigmine; RNS, repetitive nerve stimulation; sb, salbutamol; y, years; Y, yes.

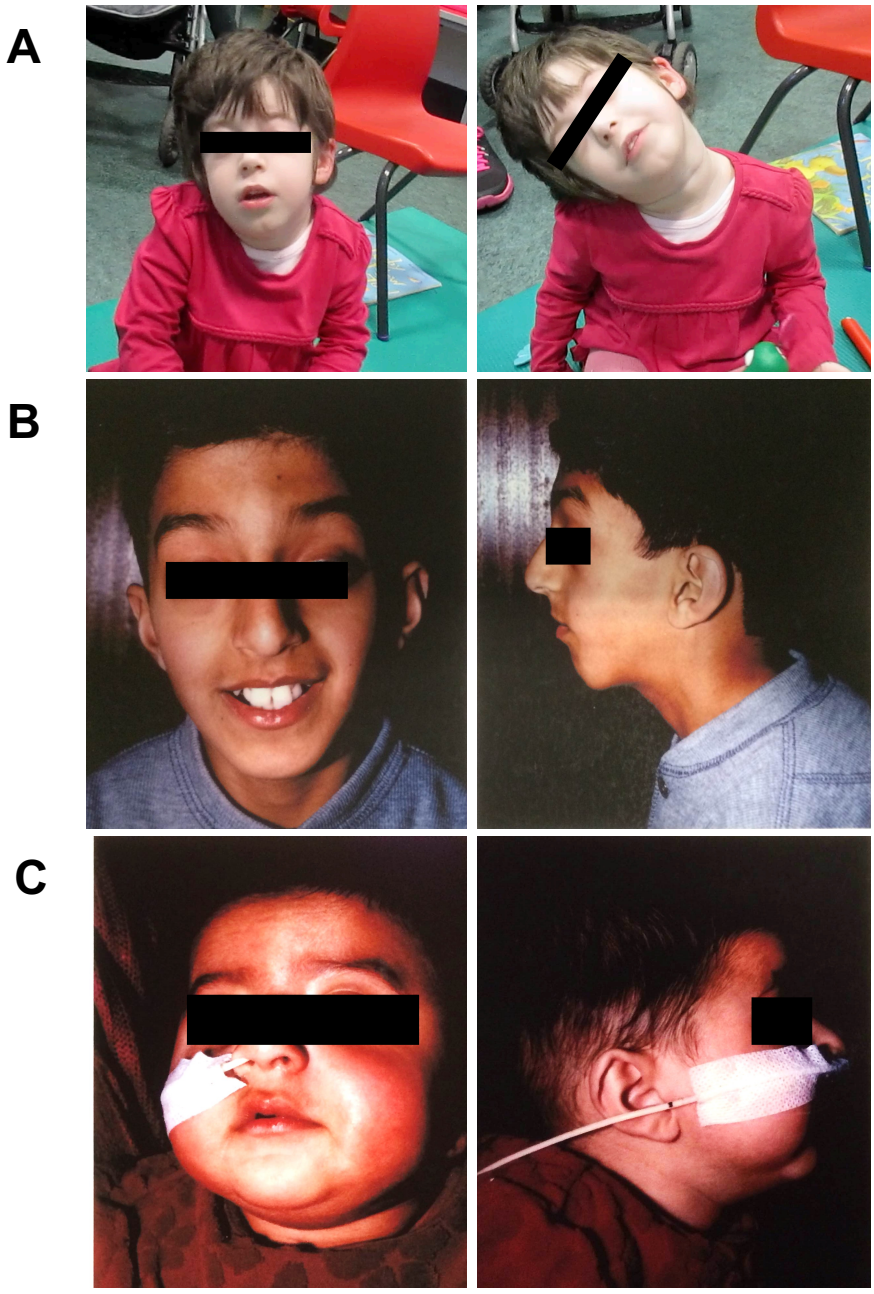


Figure 4-3. Clinical features of individuals with *COL13A1* mutations

(A) Individual I at 3 years of age show the presence of bilateral ptosis, facial weakness and marked neck weakness with impossibility to hold the head.

(B, C) Individuals 2 and 3 at the age of 12 and 2 years, respectively, show bilateral ptosis and facial dysmorphism with micrognatia and low-set ears.

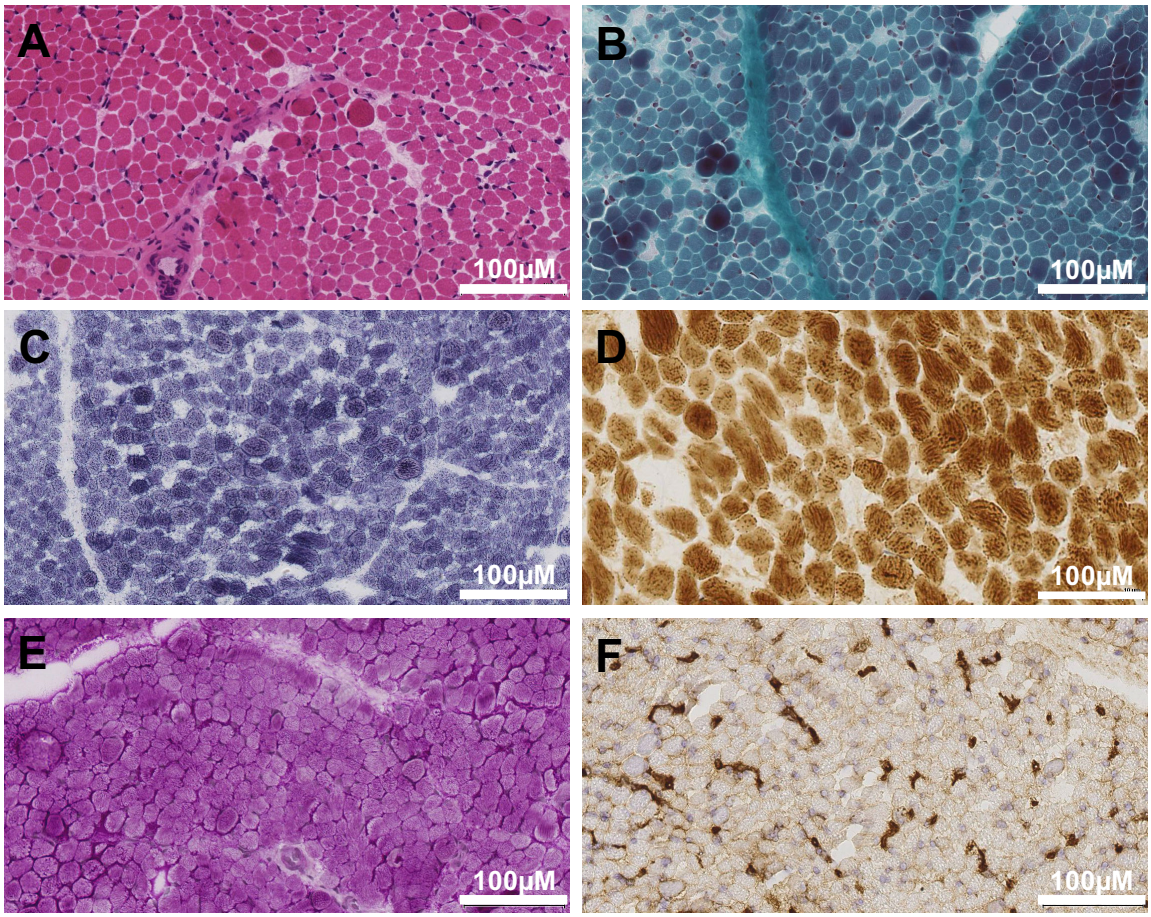


Figure 4-4. Muscle biopsy of Individual I at 6 months of age

(A) Haematoxylin & Eosin staining shows abnormal variation in fibre size, few central nuclei, and occasional vacant peripheral vacuole-like areas. Fibre size ranges from 4 to 18 µm. **(B)** Gomori trichrome staining shows several hypercontracted fibres and enlarged mitochondria. **(C)** Staining for nicotinamide adenine dinucleotide tetrazolium reductase (NADH-TR) shows occasional fibres with a halo-like appearance. **(D)** Cytochrome-c oxidase/succinate dehydrogenase (COX-SDH) staining does not show signs of COX negative fibres. **(E)** Periodic Acid-Schiff (PAS) staining does not show abnormal accumulation of glycogen or other polysaccharides. **(F)** Staining for the major histocompatibility complex type I (MHC-I) shows occasional weak to moderate positivity in the sarcolemma of muscle fibres. Scale bars represent 100 µm.

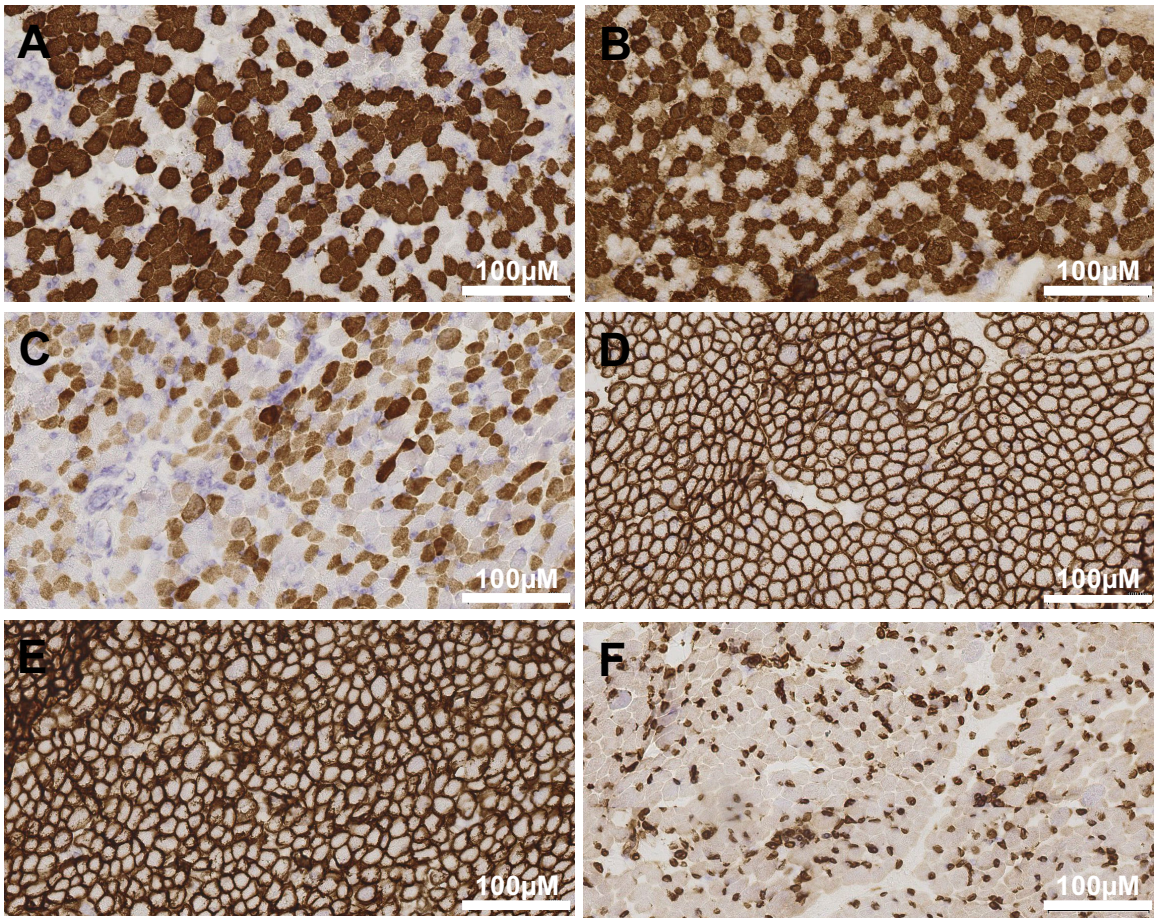


Figure 4-5. Muscle biopsy of Individual I at 6 months of age

Immunohistochemical characterisation of fast **(A)** and slow **(B)** myosins shows normal fibre type distribution. **(C)** Immunohistochemical staining shows several populations of fibres staining positive for foetal myosin. **(D)** Immunohistochemical staining for dystrophin shows a normal staining pattern of the sarcolemma. **(E)** Immunohistochemical staining for laminin-α2 (merosin) shows no abnormalities in the membrane staining pattern. **(F)** Immunohistochemical staining for emerin shows normal perinuclear staining of muscle nuclei. Scale bars represent 100 µm.

Individuals 2 and 3 (affected individuals II:1 and II:2 in family 2; **Table 4-1**) are siblings with parental consanguinity whose family came from the Indian subcontinent. Individual 2 (individual II:1) was born after a normal pregnancy. He required ventilation for the first few days after birth and subsequently had feeding difficulties in the first year of life. He was noted to have ptosis shortly after birth. Although his motor milestones were normal, during childhood he had dyspnoea on exertion, recurrent chest infections, and mild learning difficulties. The course of disease was stable, with lack of progression and even improvement over the years. At the age of 25, examination showed constant moderate bilateral ptosis (30%), mild weakness of eye closure and facial movements, and mild weakness of hip extensors. There was facial dysmorphism with micrognatia, low-set ears, and a high arched palate **(Figure 4-3B).** In addition, skeletal abnormalities such as *pectus carinatum* and marked bilateral *pes cavus* were also present. There was a degree of spinal rigidity with mild limitation of neck extension but no distal contractures. Neurophysiology was performed at age 18. Repetitive nerve stimulation at 3Hz in the right *anconeous* muscle showed significant decrement >20%. SFEMG in right *extensor digitorum communis* showed 50% increased jitter with 0% blocking and MCD of 69.8 ± 34.4 µs. Treatment with pyridostigmine up to 6 mg/kg/day had no effect.

Individual 3 (affected individual II:2 in family 2; **Table 4-1**) was more severely affected than her brother. She was born after a normal pregnancy, and had severe breathing and feeding difficulties after birth, partly due to a combined hiatus and diaphragmatic hernia. She was oxygen-dependent until age 2 and had recurrent chest infections, after which she developed chronic lung disease. She had delayed motor milestones and did not walk until age 2. She remained predominantly gastrostomy fed and had limited walking and exercise

tolerance with progressive fatigue. Examination at age 5 years showed bilateral ptosis, mild limitation of eye movements and mild facial weakness **(Figure 4-3C)**. Muscle bulk was reduced generally, although all muscles other than neck flexors had only mild weakness. However, she had difficulty jumping and was unable to hop. Facial dysmorphism was similar to her brother (Individual 2). In addition, *pectus carinatum* and a degree of spinal rigidity with kyphotic posture, predominantly at the cervical-thoracic region, were present but no distal contractures. She had a Tensilon test with no obvious improvement. Pyridostigmine was not initiated due to parents' choice. This individual died at age 8 due to severe respiratory problems related to muscle weakness and her long-standing chronic lung disease.

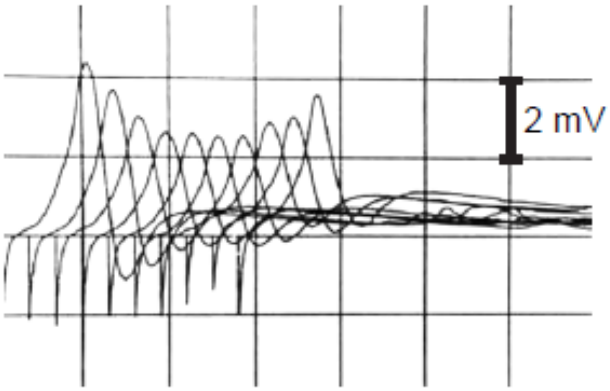


Figure 4-6. Neurophysiological studies of individual 1 at 6 months of age

Image of repetitive nerve stimulation from right *abductor digiti minimi* of individual 1 showing significant decrement >20% at rest to low stimulation rates, consistent with diagnosis of CMS.

4.3 Genetic results

4.3.1 Identification of mutations in COL13A1

For individual 1 (II:1 in family 1), a homozygous frameshift variant in *COL13A1* (NM_001130103.1, c.1171delG, (p.Leu392S*fs**71) was identified (**Figure 4-7A**). For individual 2, a homozygous splice-site mutation c.523-1delG in *COL13A1* was identified (**Figure 4-7B**). This variant was predicted to allow splicing but lead to premature termination due to a single base deletion in the coding sequence (p.Gly175V*fs**20). Neither individual carried putative "functional" pathogenic variants in other known CMS-related genes. Sanger sequencing confirmed that individual 3 was also homozygous for the c.523-1delG splice-site mutation. Both mutations segregated with the disease in their respective families (**Figure 4-8**) and are absent in the 61,486 individuals of the ExAC (Exome Aggregation Consortium) dataset and 3,100 ethnically-matched individuals in an in-house dataset. During this study, a further 12 individuals with genetically undiagnosed CMS were screened by Sanger sequencing for mutations in *COL13A1*, but no further putative pathogenic variants were identified. However, during the writing-up of this thesis three novel *COL13A1* variants were identified in two CMS individuals by groups in the United Kingdom and Canada that contacted the CMS advisory service in Oxford. The first individual was compound heterozygous for c.621delA (p.Gly208Dfs*5) and p.R91X. These variants are predicted to cause loss of normal protein function either through protein truncation or non-sense-mediated mRNA decay. The second individual was homozygous for the missense variant p.G643R. This variant is of interest since it is the first missense mutation in *COL13A1* that we have identified, and is currently undergoing functional studies.

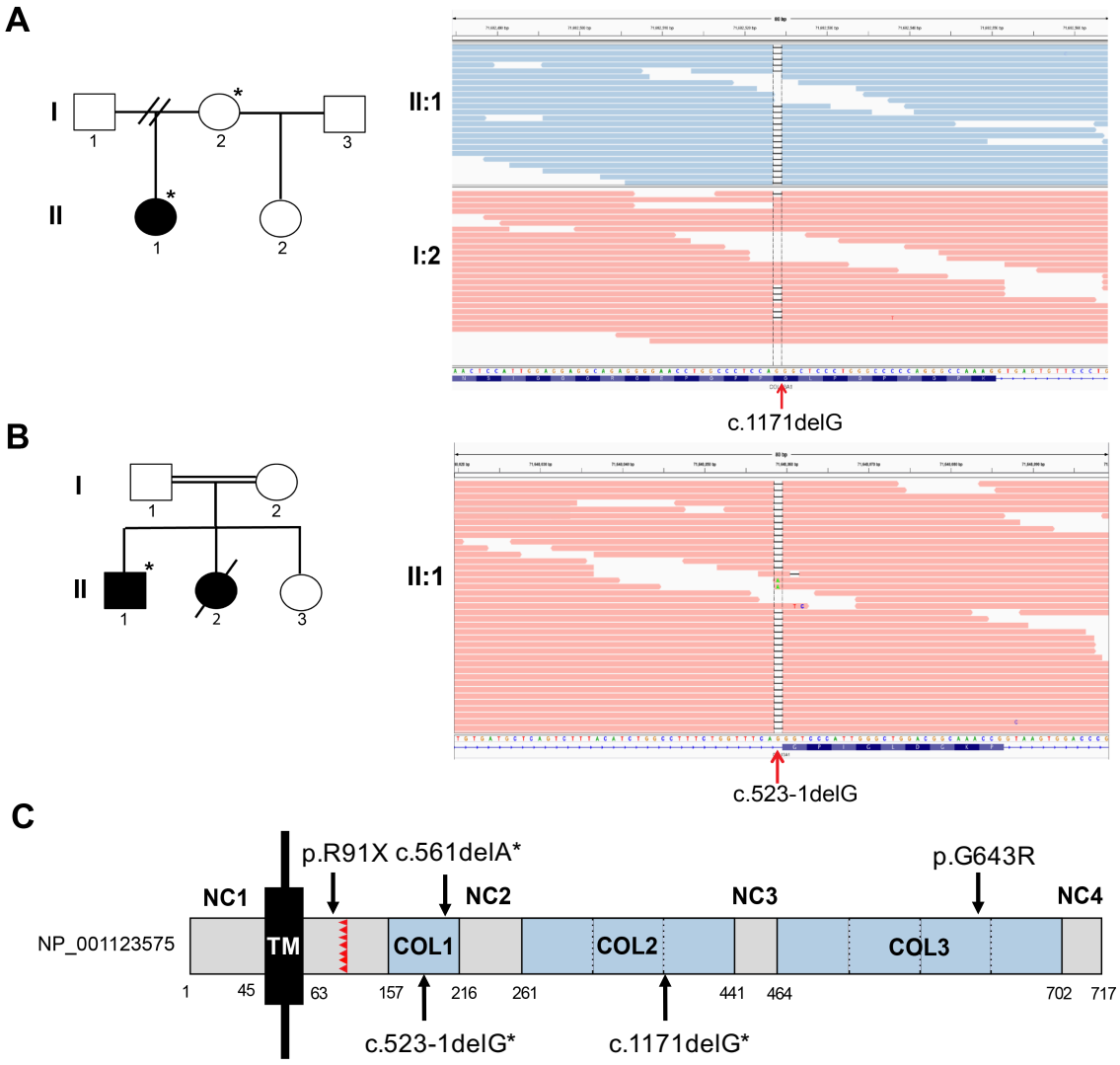


Figure 4-7. Sequence analysis of *COL13A1* mutations and schematic representations of the COL13A1 protein together with the localisation of COL13A1 variants

(A) Pedigree for affected individual II:1 in family 1, with IGV (Integrative Genomics Viewer) pileup of sequencing reads (blue), showing the homozygous frame-shifting mutation c.1171delG (red arrow). The unaffected mother (I:2; sequencing reads represented in pink) is heterozygous for this mutation. Numbers at the top show physical location (based on GRCh37), with nucleotides and amino acid residues represented below. Individuals analysed by whole exome sequencing are indicated by asterisks.

(B) Pedigree for affected individuals II:1 and II:2 in family 2, with pileup of sequencing reads for II:1 (pink), showing the homozygous splice-site mutation c.523-1delG (red arrow).

(C) Schematic representation of the full-length COL13A1 isoform 1 protein (NP_001123575) and the variants identified in the domains of COL13A1.

4.3.2 Segregation analysis of COL13A1 mutations

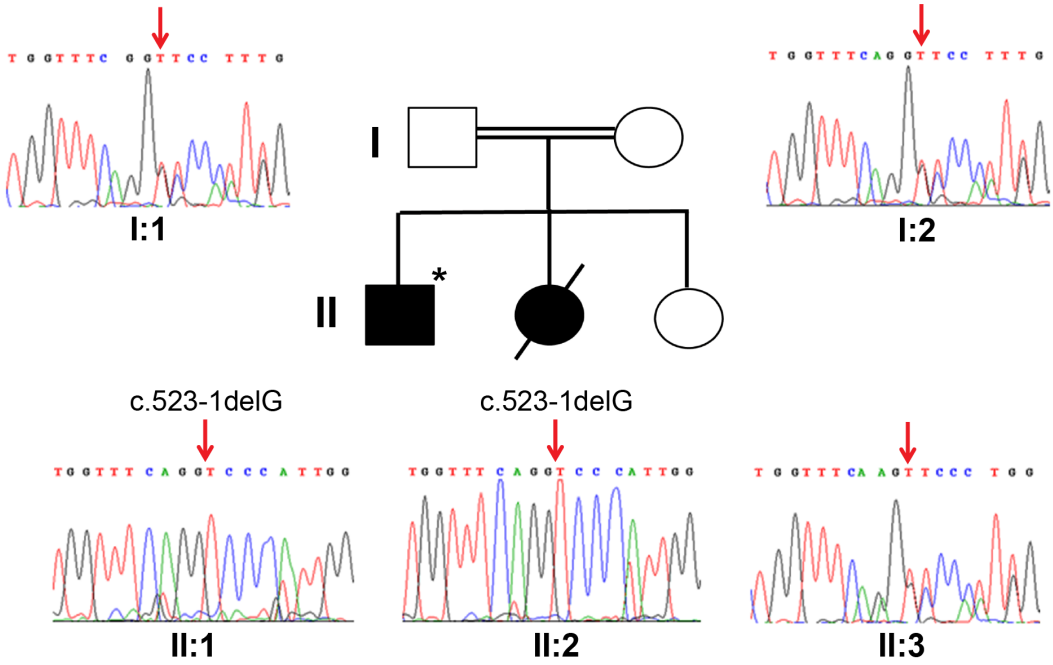


Figure 4-8. Segregation analysis of COL13A1 c.523-1del splice-site mutation in family 2

Electropherograms showing the segregation of *COL13A1* c.523-1del splice-site mutation with disease in the pedigree of family 2. Both affected siblings, II:1 and II:2, are homozygous whereas the unaffected sibling II:3 and the parents (I) are heterozygous carriers (arrows). Segregation analysis was performed by Susan Maxwell (University of Oxford).

4.4 Study of COL13A1 predicted cleavage site

Extrapolating from the mouse *Col13a1* study, the analysis of the coding sequence of the full-length COL13A1 protein using ProP 1.0 Server (http://www.cbs.dtu.dk/services/ProP/) showed a predicted furin-type cleavage site (score 0.649) at position 108 **(Figure 4-9A)**. To confirm this hypothesis, the four Arginine residues at the predicted cleavage site were mutated to Alanine using a QuickChange® Multi Site-Directed Mutagenesis Kit (Section 2.2.7). The effect of mutagenesis on protein expression was evaluated in HEK-293T cells transfected with the WT and mutant COL13A1

constructs by indirect immunocytofluorescence (Section 2.5.15) and western blotting (Section 2.5.4).

The results show how the mutagenesis of the cleavage site significantly increased the surface expression of COL13A1 in HEK-293T cells by indirect immunofluorescence **(Figure 4-9B)**. Western blotting showed the successful detection of the full-length COL13A1 protein in cell lysates and the secreted fraction in the culture medium **(Figure 4-10)**. The mutagenesis of the cleavage site significantly increased the proportion of COL13A1 at the plasma membrane ($p<0.001$) and decreased the fraction detected in the culture medium ($p<0.0001$). COL13A1 was not detected in cell lysates or medium from HEK-293T cells transfected with pcDNA3.1 Hygro (+). Overall, these experiments confirm that human COL13A1 is also a transmembrane protein with a proprotease cleavage site that allows the cleavage and secretion of the ectodomain.

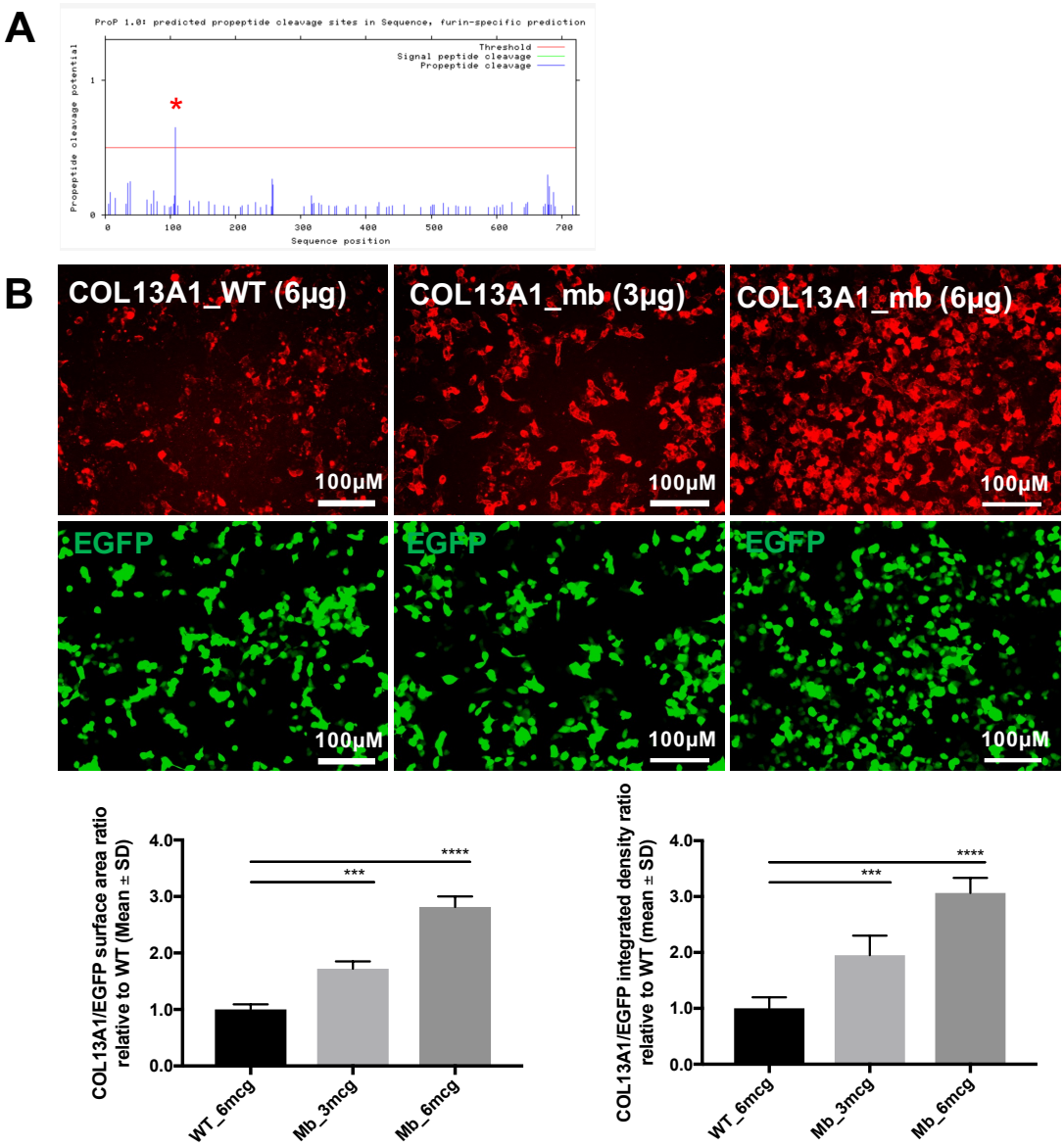


Figure 4-9. Analysis of the COL13A1 cleavage site by immunocytofluorescence

(A) ProP plot shows a potential cleavage site above threshold (red asterisk) at position 108.

(B) HEK-293T cells were transiently transfected with cDNA of WT- or Membrane-bound (Mb) COL13A1 and EGFP as a transfection efficiency control. 48 hours after transfection, the cells were incubated with a guinea pig anti-COL13A1 antibody against the C-terminal region and the corresponding fluorescently conjugated secondary antibody. The area and integrated density of the fluorescent staining were measured using ImageJ software. The results (ratio COL13A1/EGFP) are represented as mean ± SD relative to WT from 15 different images per condition. One-way ANOVA and Dunnett´s multiple comparison test (***p<0.001; ****p<0.0001).

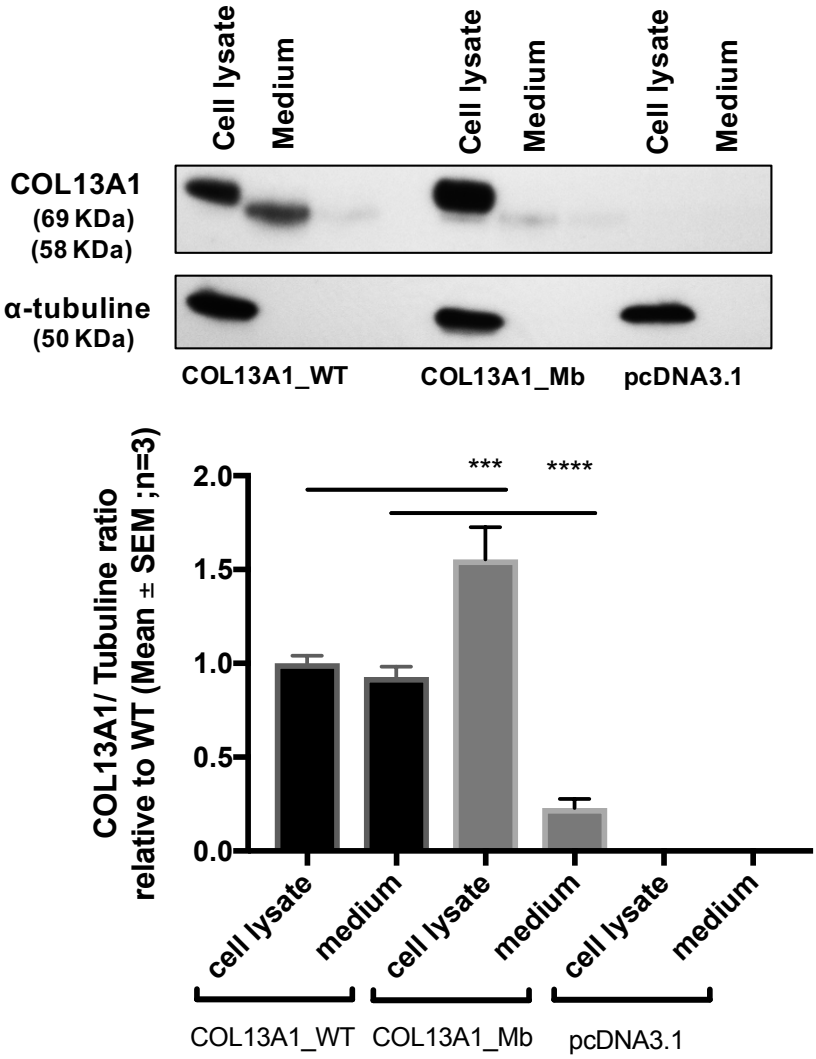


Figure 4-10. Analysis of the COL13A1 cleavage site by western blotting

HEK-293T cells were transiently transfected with cDNA of WT- or membrane-bound (Mb)-COL13A1, or pcDNA3.1 as a negative control. 48 hours after transfection, the cells lysates and the cultured medium were resolved by SDS-PAGE and the membrane was incubated with antibodies against the C-terminal domain of COL13A1 and α-tubuline for loading control. The ratios of COL13A1:α-tubuline were obtained by densitometry analysis, and the results were normalised to the expression levels of COL13A1 WT. The results are represented as mean ± SEM relative to WT from n= 3 experiments. One-way ANOVA and Sidak´s multiple comparison test (***p<0.001; ****p<0.0001).

4.5 COL13A1 expression in human muscle tissue

4.5.1 Validation of antibodies against the N- and C-terminus domains of COL13A1

These experiments were performed to confirm the specific recognition of over-expressed COL13A1 at the cell surface of HEK-293T cells by antibodies against COL13A1 **(Figure 4-11)**.

```
  1 MVAERTHKAA ATGARGPGEL GAPGTVALVA ARAERGARLP SPGSCGLLTL
 51 ALCSLALSLL AHFRTAELQA RVLRLEAERG EQQMETAILG RVNQLLDEKW
101 KLHSRRRREA PKTSPGCNCP PGPPGPTGRP GLPGDKGAIG MPGRVGSPGD
151 AGLSIIGPRG PPGQPGTRGF PGFPGPIGLD GKPGHPGPKG DMGLTGPPGQ
201 PGPQGQKGEK GQCGEYPHRE CLSSMPAALR SSQIIALKLL PLLNSVRLAP
251 PPVIKRRTFQ GEQSQASIQG PPGPPGPPGP SGPLGHPGLP GPMGPPGLPG
301 PPGPKGDPGI QGYHGRKGER GMPGMPGKHG AKGAPGIAVA GMKGEPGIPG
351 TKGEKGAEGS PGLPGLLGQK GEKGDAGNSI GGGRGEPGPP GLPGPPGPKG
401 EAGVDGQVGP PGQPGDKGER GAAGEQGPDG PKGSKGEPGK GEMVDYNGNI
451 NEALQEIRTL ALMGPPGLPG QIGPPGAPGI PGQKGEIGLP GPPGHDGEKG
501 PRGKPGDMGP PGPQGPPGKD GPPGVKGENG HPGSPGEKGE KGETGQAGSP
551 GEKGEAGEKG NPGAEVPGLP GPEGPPGPPG LQGVPGPKGE AGLDGAKGEK
601 GFQGEKGDRG PLGLPGASGL DGRPGPPGTP GPIGVPGPAG PKGERGSKGD
651 PGMTGPTGAA GLPGLHGPPG DKGNRGERGK KGSRGPKGDK GDQGAPGLDA
701 PCPLGEDGLP VQGCWNK
```

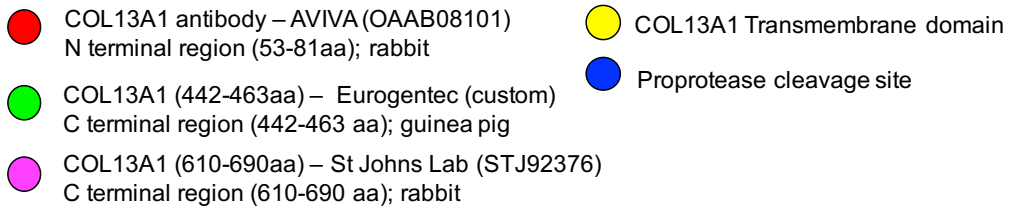


Figure 4-11. COL13A1 peptide sequence and immunogenic targets from the different COL13A1 antibodies used in this chapter

The peptide sequence for the full COL13A1 isoform 1 protein (NP_001123575) is shown with its respective numbering. The transmembrane domain is highlighted in yellow and the proprotease recognition site is coloured blue. The COL13A1 antibody (AVIVA – OAAB08101) is raised against the 53-81 aminoacids of the N-terminal region (red colour), which include part of the transmembrane domain. For the detection of the C-terminal region, an affinity-purified guinea pig anti-COL13A1 antibody (Eurogentec SA, Liege Science Park, Belgium) and a rabbit anti-COL13A1 antibody (St John's Laboratory – STJ92376) raised against aminoacids 442-463 (green colour) and 610-690 (pink colour), respectively, were used.

HEK-293T cells were transiently transfected with cDNA of COL13A1 or pcDNA3.1/Hygro(+) as a negative control. For the validation of the affinity-purified guinea pig antibody against the C-terminal region of COL13A1, 48 hours after transfection, live cells were incubated at room temperature for 1 hour with the antibody diluted in DMEM, 1% bovine serum albumin (BSA) and 20 mM HEPES (pH 7.4) and the corresponding Alexa Fluor® 568 goat anti-guinea pig IgG (H+L) secondary antibody. For the validation of the COL13A1 antibody against the N-terminal region, the cells were fixed with pre-chilled methanol at -20°C for 10 minutes, rinsed in PBS, and incubated for 1 hour with 1% BSA and 0.5% Tween®20 for blocking and gentle permeabilisation of the plasma membrane. Subsequently, the cells were incubated for one hour at room temperature with the COL13A1 antibody against the N-terminal region diluted in 1% BSA and 0.5% Tween®20 and the corresponding Alexa Fluor® 568 goat anti-rabbit IgG (H+L) secondary antibody.

The results showed how the guinea pig antibody against the C-terminal region of COL13A1 binds specifically to HEK-293T cells transfected with COL13A1 but not to mock transfected cells **(Figure 4-12)**. The rabbit antibody against the N-terminal region of COL13A1 also bound specifically to HEK-293T cells transfected with COL13A1, but only when these were fixed with pre-chilled methanol at -20°C and permeabilised gently with Tween®20 **(Figure 4-13)**. Staining of live cells and other fixation and permeabilisation methods such as 3% PFA, pre-chilled acetone, and Triton X-100 were unsuccessful for the binding of the antibody in probable relation with this being raised against part of the transmembrane domain and, therefore, being of difficult access for the antibody.

To confirm the specificity of this antibody, a further experiment was conducted using HEK-293T cells transfected with MuSK, COLQ or pcDNA3.1/Hygro(+) as additional negative controls **(Figure 4-14)**.

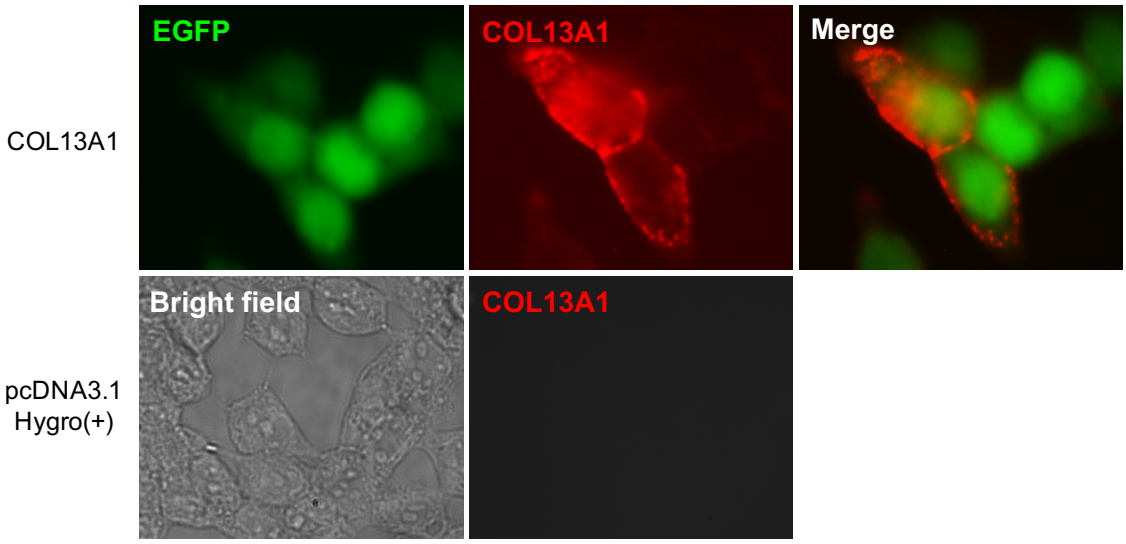


Figure 4-12. Validation of the guinea pig antibody against the COL13A1 C-terminal region

HEK-293T cells were transiently co-transfected with cDNA of COL13A1 and EGFP or pcDNA3.1/Hygro(+) as a control. 48 hours after transfection, the cells were incubated with a guinea pig anti-COL13A1 antibody against the C-terminal region of COL13A1 and the corresponding Alexa Fluor® 568 fluorescently conjugated secondary antibody.

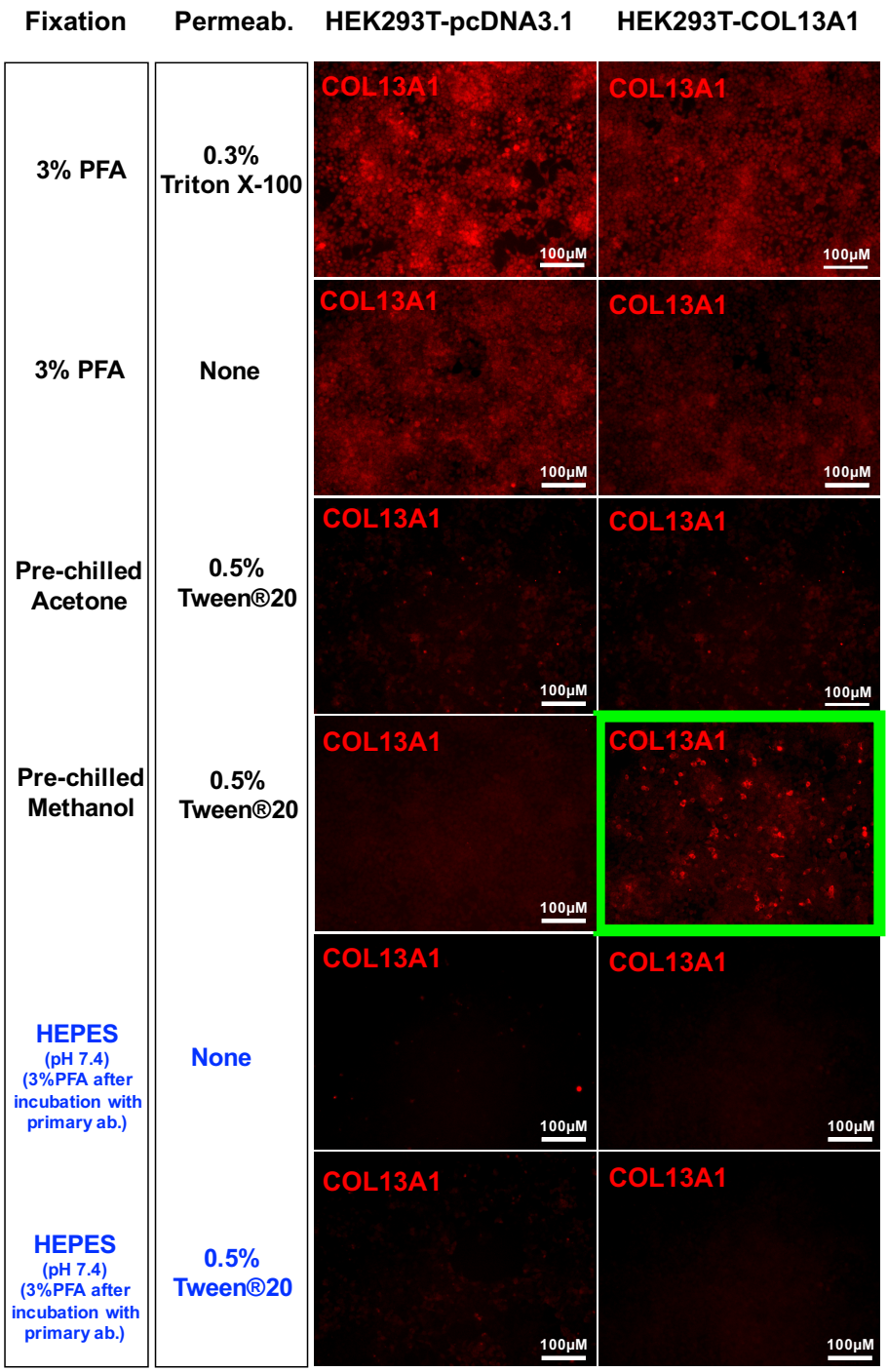


Figure 4-13. Validation of the antibody against the N-terminal region of COL13A1

HEK-293T cells were transiently co-transfected with cDNA of COL13A1 or pcDNA3.1. 48 hours after transfection, the cells were fixated and/or permeabilised with different methods prior to the incubation with the rabbit anti-COL13A1 antibody against the N-terminal domain and the corresponding Alexa Fluor® 568 fluorescently conjugated secondary antibody. The figure shows the specific binding of the antibody to HEK-293T cells expressing COL13A1 (green box).

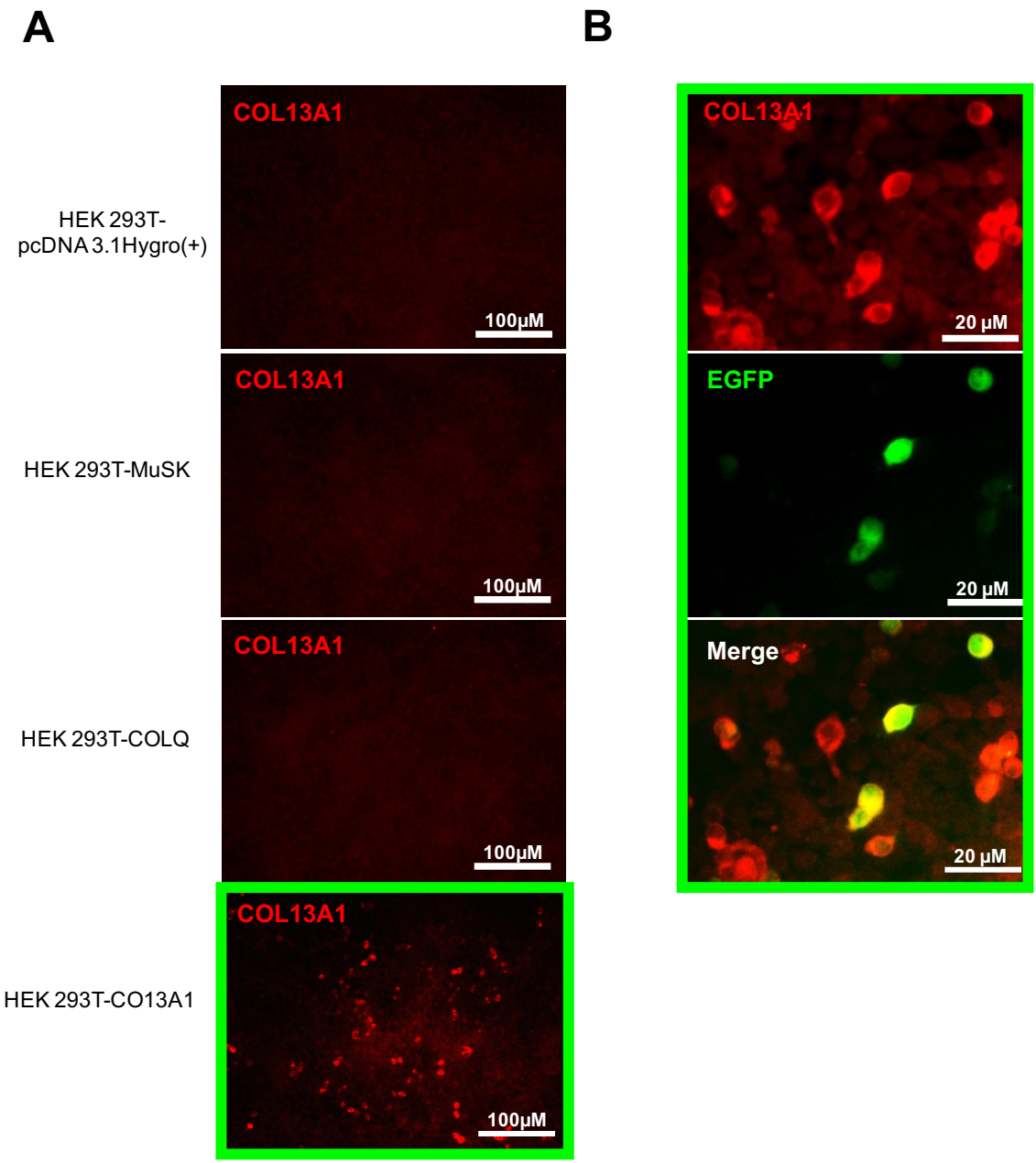


Figure 4-14. Specificity of the antibody against the N-terminal region of COL13A1

(A) HEK-293T cells were transiently transfected with cDNA from COL13A1 or cDNA from MuSK, COLQ or pcDNA3.1/Hygro(+) as negative controls. 48 hours after transfection, the cells were fixed with pre-chilled methanol, permeabilised with 0.5% Tween®20, and incubated with an antibody against the N-terminal region of COL13A1 and the corresponding fluorescently conjugated secondary antibody. The figure shows how the antibody binds specifically to HEK-293T cells expressing COL13A1 (green box).

(B) Representative image at higher magnification showing COL13A1 binding and colocalisation with EGFP.

4.5.2 Immunofluorescence of human muscle sections in control and affected individuals

To investigate the localisation and potential role of COL13A1 at the NMJ, I used the quadriceps muscle biopsy from individual 1 and human laryngeal muscles from unaffected individuals undergoing therapeutic laryngectomy as controls. Laryngeal muscles have a relatively small size and high endplate density, which facilitates the visualization of muscle endplates. Transverse 8-10 µm sections from fresh frozen tissues were obtained using a cryostat and processed for immunofluorescence microscopy as previously described (Section 2.5.12). Antibodies against synaptophysin and neurofilament were used to label the presynaptic terminal in NMJs, or against S100 calcium-binding protein ß (S100ß) to stain Schwann cells. Alexa Fluor® 488-fasciculin or Alexa Fluor® 488-α-bungarotoxin and antibodies against DOK7 and MuSK were used to label the intersynaptic space and key postsynaptic proteins, respectively.

4.5.2.1 Immunofluorescence of motor endplates using a COL13A1 C-terminal antibody

An affinity-purified guinea pig antibody against the C-terminal region of COL13A1 was used to demonstrate the presence or absence of COL13A1 in muscle. The epitope of this antibody is located at aminoacids 442-463 and, therefore, is not expected to bind COL13A1 in the patient´s muscle biopsy as a consequence of the c.1171delG [p.Leu392Sfs*71] mutation **(Figure 4-11)**. The staining of human muscle sections showed that COL13A1 was enriched at the motor endplates in control human muscles **(Figure 4-15A)** but was absent in endplates from individual 1 **(Figure 4-15B)** carrying the homozygous frameshift *COL13A1* mutation, which causes loss of COL13A1 accumulation. The COL13A1 staining along the muscle fibres from the control muscle was rather

indistinct with scarce and punctuate staining in the sarcolemma, whereas this was not the case for the distinct staining at the NMJ **(Figure 4-15C)**.

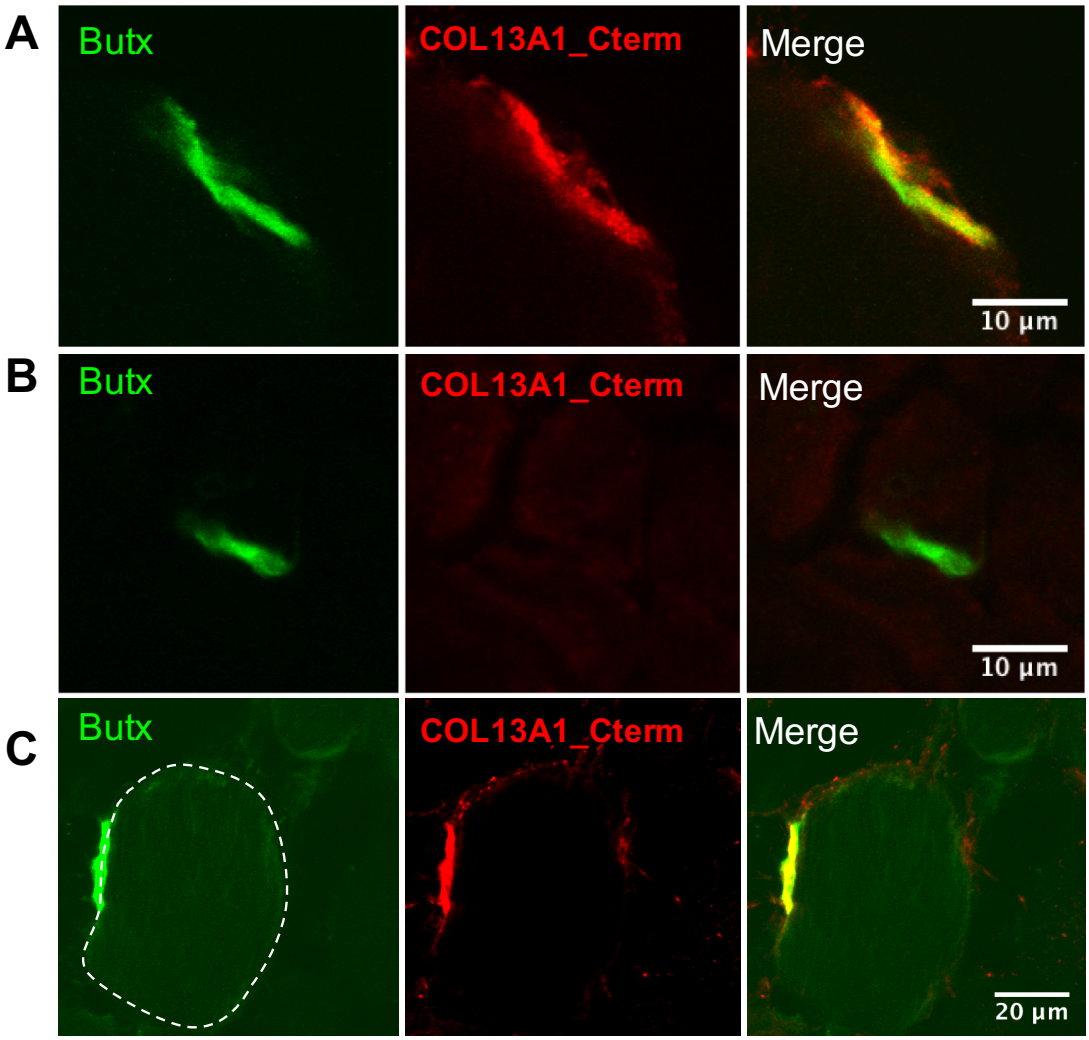


Figure 4-15. Representative images of human muscle endplates stained with an antibody against the C-terminal region of COL13A1

Control and disease human muscle sections were incubated with Alexa Fluor® 488-conjugated α-bungarotoxin, COL13A1 C-terminal antibody and the corresponding fluorescently conjugated secondary antibody. Images were taken using a Zeiss LSM 510 inverted confocal microscope. **(A)** COL13A1 is enriched at NMJs (marked by α-Butx-green) of control muscle. **(B)** COL13A1 is not present at NMJs from the individual carrying the homozygous frameshift mutation. **(C)** COL13A1 staining along the muscle fibre (white dashed line) was rather indistinct. Scale bar = 10-20 µm.

4.5.2.2 Immunofluorescence of motor endplates using a COL13A1 N-terminal antibody

A rabbit antibody against the N-terminal region of COL13A1 was used to study the localisation of COL13A1 at the plasma membrane. The staining of control muscle showed that COL13A1 was concentrated at the NMJ **(Figure 4-16A)**. Co-staining with other endplate markers showed that N-terminal COL13A1 was localised presynaptically **(Figure 4-16B, C)**. A further experiment using an antibody against S100ß (Schwann cell marker) confirmed that COL13A1 was localised presynaptically **(Figure 4-16D).**

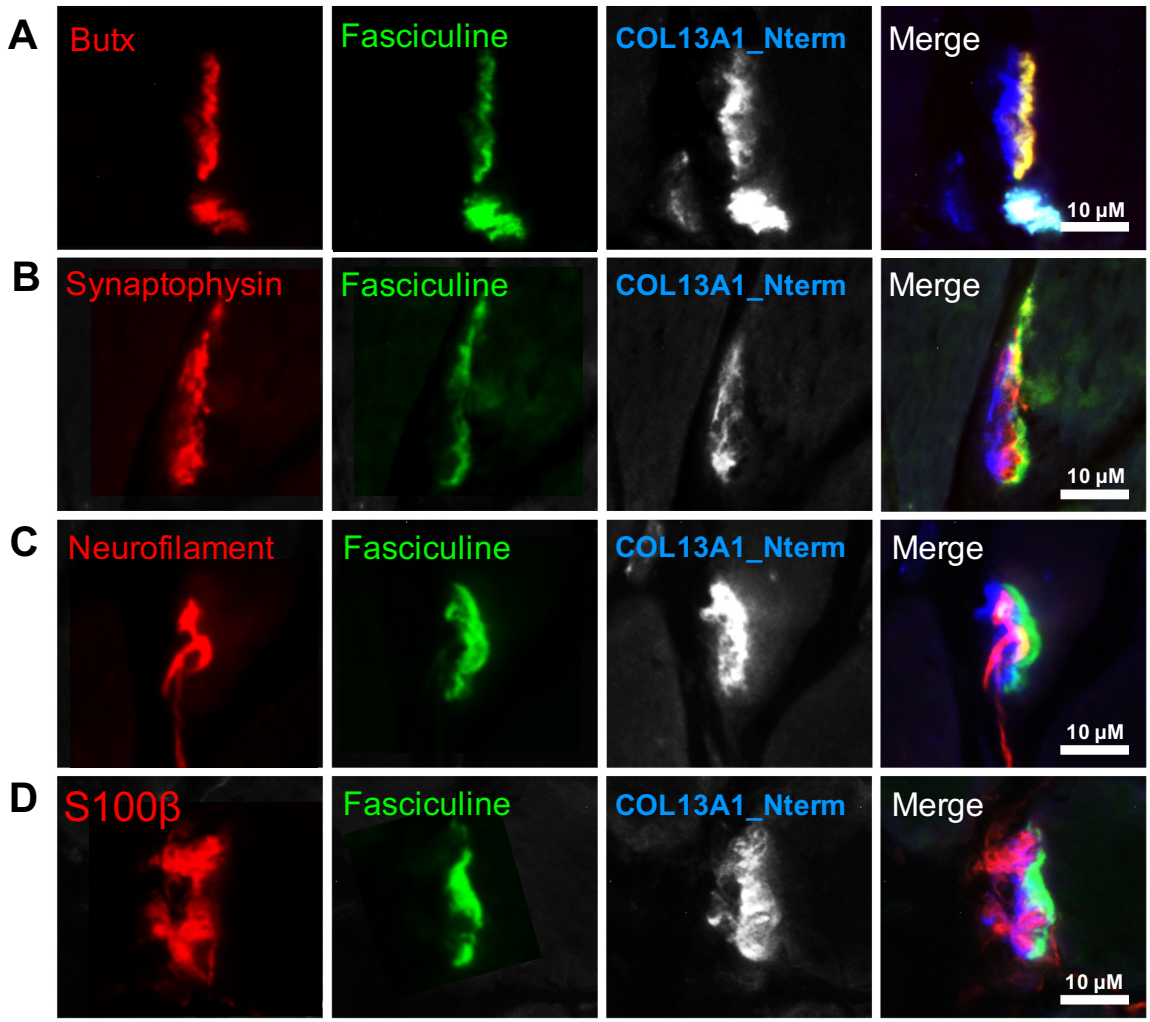


Figure 4-16. Representative images of control muscle endplates stained with an antibody against the N-terminal region of COL13A1

Control human muscle sections were incubated with Alexa Fluor® 488-conjugated fasciculine, antibodies against COL13A1 N-terminal region and other markers of the NMJ, and the corresponding fluorescently conjugated secondary antibodies. Images were taken using an Olympus IX71 fluorescent microscope. **(A)** COL13A1 staining is located presynaptically opposite fasciculine (intersynaptic space) and bungarotoxin (postsynaptic membrane). **(B)** COL13A1 staining is present opposite fasciculine (intersynaptic space) and synaptophysin (presynaptic terminal). **(C)** COL13A1 staining does not colocalise with fasciculine (intersynaptic space) and neurofilament (presynaptic terminal)**. (D)**. COL13A1 staining has a similar distribution to S100β (presynaptic terminal) at the NMJ. Scale bar = 10 µm.

The staining of muscle sections from individual 1 showed positive staining at motor endplates and similar presynaptic distribution to the Schwann cell marker S100ß (yellow arrows) **(Figure 4-17)**. Some of the terminal Schwann cells covered the endplates appropriately (white arrows) while others seemed not to fully reach the NMJs (asterisks). There was also occasional extra-junctional staining for S100ß that could represent Schwann cells processes approaching nearby endplates beyond the current sections. The use of transverse 8-10 µm muscle sections coupled with the lack of an age-matched control muscle biopsy makes it difficult to determine whether the terminal Schwann cells are correctly wrapping the nerve terminals or, as reported in the *Col13a1*$^{-/-}$ mouse model, this represents retraction and/or invagination of the Schwann cells processes into the synaptic cleft. Overall, the positive staining using the COL13A1 N-terminal antibody suggests that the c.1171delG mutation preserved the truncated version of the protein located at the plasma membrane.

4.5.2.3 Immunofluorescence of other key NMJ proteins in disease muscle

In order to study whether loss of COL13A1 at the motor endplates could affect the expression of other key NMJ proteins, further staining was conducted using antibodies against DOK7, MuSK and synaptophysin. The results showed normal expression and localisation of markers for the NMJ suggesting that the *COL13A1* loss-of-function mutation did not have a dramatic effect on the expression of the key presynaptic and postsynaptic NMJ proteins studied **(Figure 4-18)**.

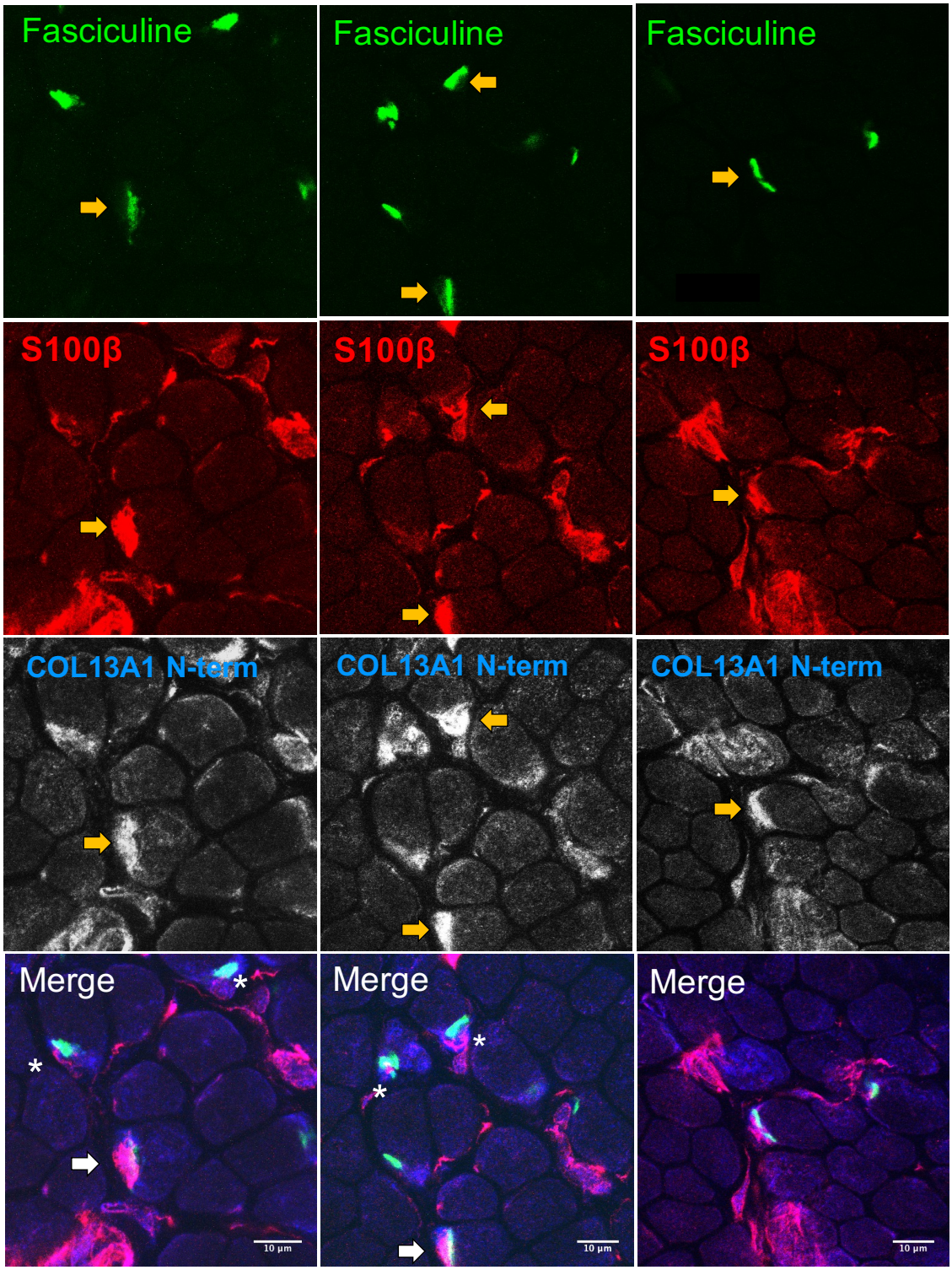


Figure 4-17. Representative images of muscle endplates from individual 1 using antibodies against the N-terminal region of COL13A1 and S100β

Muscle sections from individual 1 were incubated with Alexa Fluor® 488-conjugated fasciculine, antibodies against COL13A1 N-terminal region and S100β, and the corresponding fluorescently conjugated secondary antibodies. Images were taken using a Zeiss LSM 510 inverted confocal microscopy. Scale bar represents 10 µm.

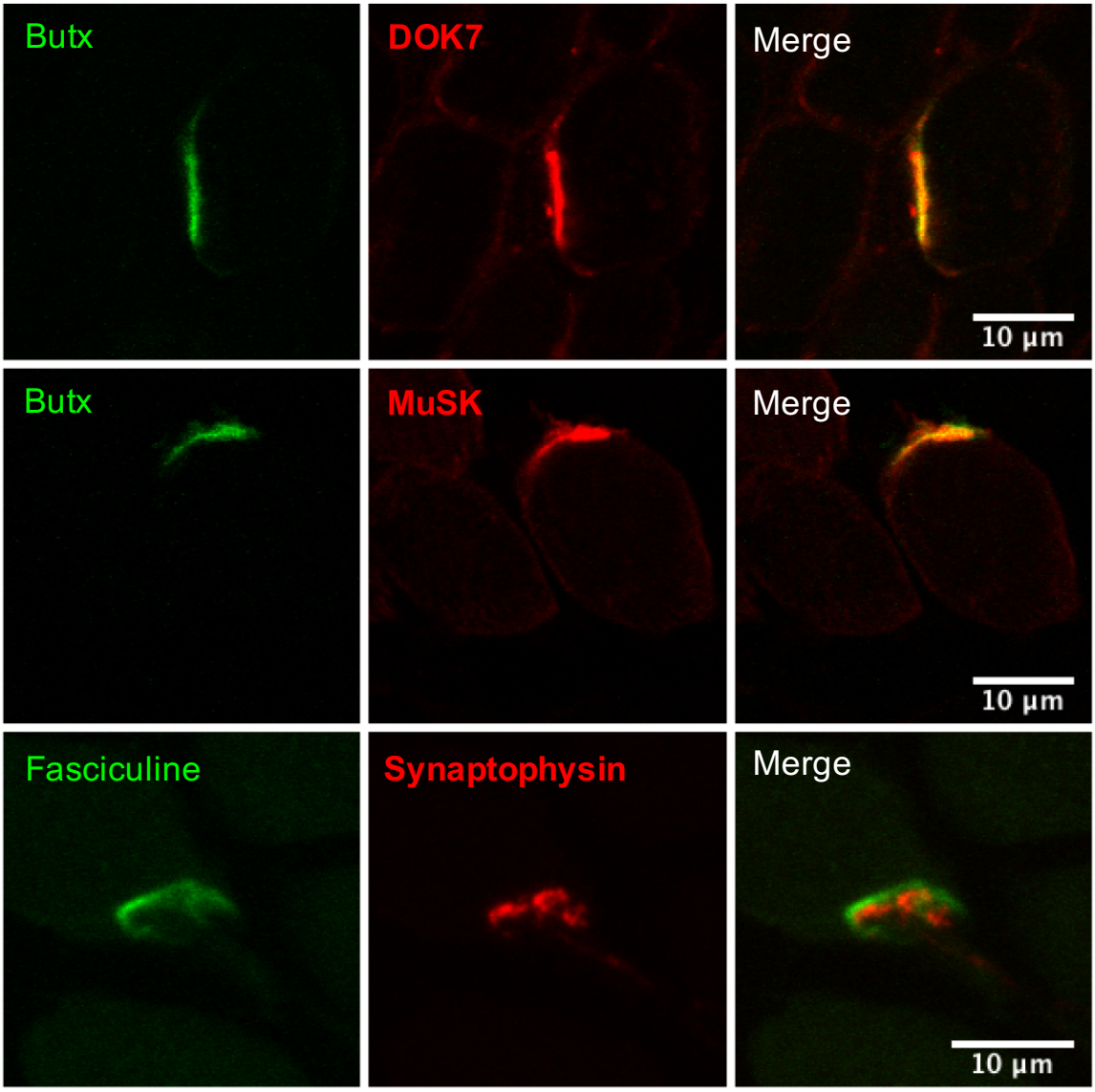


Figure 4-18. Representative images of muscle endplates from individual 1 using different NMJ markers

Muscle sections from individual 1 were incubated with Alexa Fluor® 488-conjugated fasciculine and α-bungarotoxin, antibodies against MuSK, DOK7 and S100 β and the corresponding fluorescently conjugated secondary antibodies. Images were taken using a Zeiss LSM 510 inverted confocal microscopy. The figures show normal expression and localisation of markers of the NMJ. Scale bar represents 10 µm.

4.5.3 COL13A1 expression studies in human muscle by western blot

Lysates from human muscle tissue and HEK-293T cells transfected with pcDNA3.1/Hygro(+) and COL13A1 WT as controls were prepared using standard methods

(Sections 2.5.1 and 2.5.2). A total of 25 µg soluble protein was resolved by SDS-PAGE. The over-expressed full-length COL13A1 or the endogenous COL13A1 isoforms were immunodetected with a rabbit antibody against the C-terminal region of COL13A1 (St. John's Laboratory Ltd., London UK) and the corresponding HRP-conjugated secondary antibody.

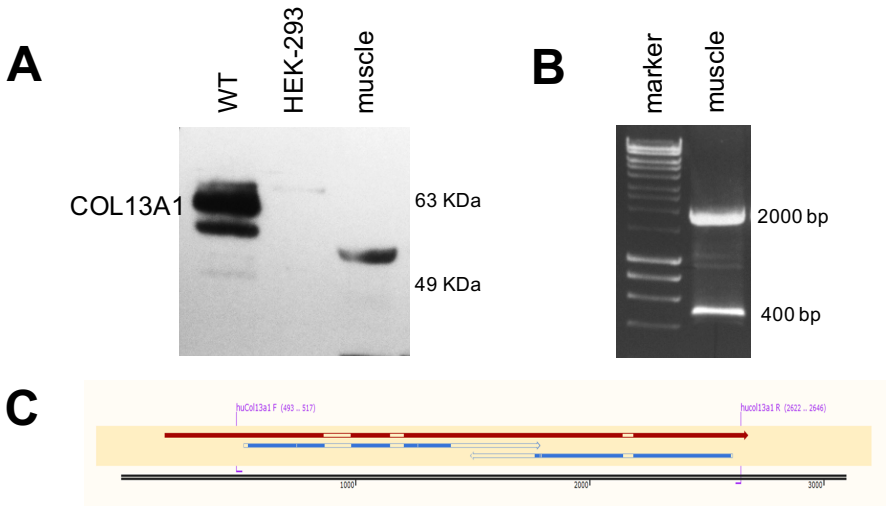
The results demonstrated that endogenous COL13A1 was present in human muscle and had an approximate molecular weight of 55 KDa by western blot analysis **(Figure 4-19A)**. The over-expressed full-length COL13A1 isoform 1 produced two different bands of approximately 70 and 60 KDa corresponding to the full-length protein and the cleaved fraction, as previously shown in Section 4.4.

4.5.4 Study of COL13A1 transcripts in human muscle

The over-expressed full-length COL13A1 isoform 1 (RefSeq NP_001123575) has length 717 aa and predicted mass 70 kDa. In order to study why the endogenous COL13A1 protein had a lower apparent mass by western blot than the full-length COL13A1 isoform 1, RNA was extracted from human muscle and reverse transcribed using RETROscript® Reverse Transcription Kit (Ambion ™) and Oligo(dT) primers (Section 2.4.4). The obtained cDNA was processed using primers designed to amplify the full-length COL13A1 isoform 1 **(Table 2.6)** and resolved by gel electrophoresis **(Figure 4-19B)**. The 2000 bp product was gel extracted and analysed by Sanger sequencing using COL13A1 primers **(Table 2.1)**.

The results confirmed that the endogenous muscle protein was produced from RefSeq NM_080798, encoding COL13A1 isoform 11 (RefSeq NP_542988). This transcript has

length 645 aa and predicted mass 63 KDa. Alignment analysis showed that exons 3, 5, 6, and 30 spliced out compared to the major transcript **(Figure 4-19C, D)**.



D

Name	Transcript ID	bp	Protein	Biotype	CCDS	RefSeq
COL13A1-001	ENST00000398978	3093	717 aa	Protein coding	CCDS44419	NM_001130103 NP_001123575
COL13A1-002	ENST00000354547	3027	695 aa	Protein coding	CCDS44424	NM_080801 NP_542991
COL13A1-011	ENST00000520267	2276	645 aa	Protein coding	CCDS44427	NM_080798 NP_542988
COL13A1-014	ENST00000522165	2061	686 aa	Protein coding	CCDS44425	NM_080800 NP_542990
COL13A1-013	ENST00000517713	2007	668 aa	Protein coding	CCDS44423	NM_080802 NP_542992
COL13A1-015	ENST00000520133	1833	610 aa	Protein coding	CCDS44428	NM_080805 NP_542995
COL13A1-004	ENST00000357811	2991	683 aa	Protein coding	-	-
COL13A1-201	ENST00000398969	2267	642 aa	Protein coding	-	-
COL13A1-006	ENST00000398975	1057	247 aa	Protein coding	-	-
COL13A1-008	ENST00000456019	749	174 aa	Protein coding	-	-
COL13A1-003	ENST00000479733	2934	582 aa	Nonsense mediated decay	-	-
COL13A1-007	ENST00000484990	360	No protein	Processed transcript	-	-
COL13A1-012	ENST00000518052	290	No protein	Processed transcript	-	-
COL13A1-009	ENST00000478219	2586	No protein	Retained intron	-	-

Figure 4-19. Study of COL13A1 transcripts in human muscle. (A) Cell lysates from HEK-293T cells overexpressing COL13A1 isoform 1 or pcDNA3.1/Hygro(+) and human muscle were analysed by western blot. **(B)** cDNA from human muscle tissue was amplified with COL13A1 primers and resolved by gel electrophoresis. **(C)** PCR products were analysed by Sanger sequencing and align with COL13A1 isoform 1 (RefSeq NP_001123575) using SnapGene®. **(D)** COL13A1 transcripts in *homo sapiens* as provided by Ensemble Genome Browser (http://www.ensembl.org). COL13A1 muscle transcript highlighted in red.

4.6 COL13A1 interacting partners

In order to have a better understanding of the role of COL13A1 at the neuromuscular junction, pull-down (Section 2.5.7) and immunocytofluorescence (Section 2.5.15) experiments were performed to investigate the potential interaction of COL13A1 with other key NMJ proteins having extracellular domains. In brief, HEK-293T cells were transiently co-transfected with cDNA from WT or membrane-bound (mb) COL13A1 and the protein of interest, co-immunoprecipitated using antibodies conjugated with Dynabeads® and resolved by western blotting. For immunocytofluorescence, colocalisation and fluorescence intensity was measured using Simple PCI software.

4.6.1 Study of COL13A1 – Collagen Q interaction

Co-transfection of CASPR2-COLQ-Myc with both the WT or membrane-bound forms of COL13A1 caused an approximate 90.2 ± 2.5% reduction in the intensity of the red fluorescence staining **(Figure 4-20)**. This suggests that CASPR2-COLQ-Myc is blocking the binding site of the guinea-pig anti-COL13A1 antibody. A total amount of 6 µg of cDNA per reaction were used to ensure the immunocytofluorescence results were not related to the use of uneven concentrations of cDNA. The results from the co-immunoprecipitation experiment showed that the anti-c-Myc antibody was able to pull-down CASPR2-COLQ-Myc successfully, and both the WT and membrane-bound forms of COL13A1 were co-immunoprecipitated **(Figure 4-21)**. The specificity of the pull-down assay was confirmed by the negative immunoprecipitation of HEK-293T cells uniquely transfected with COL13A1 or pcDNA3.1/Hygro(+). Overall, these results suggest that COL13A1 interacts with COLQ.

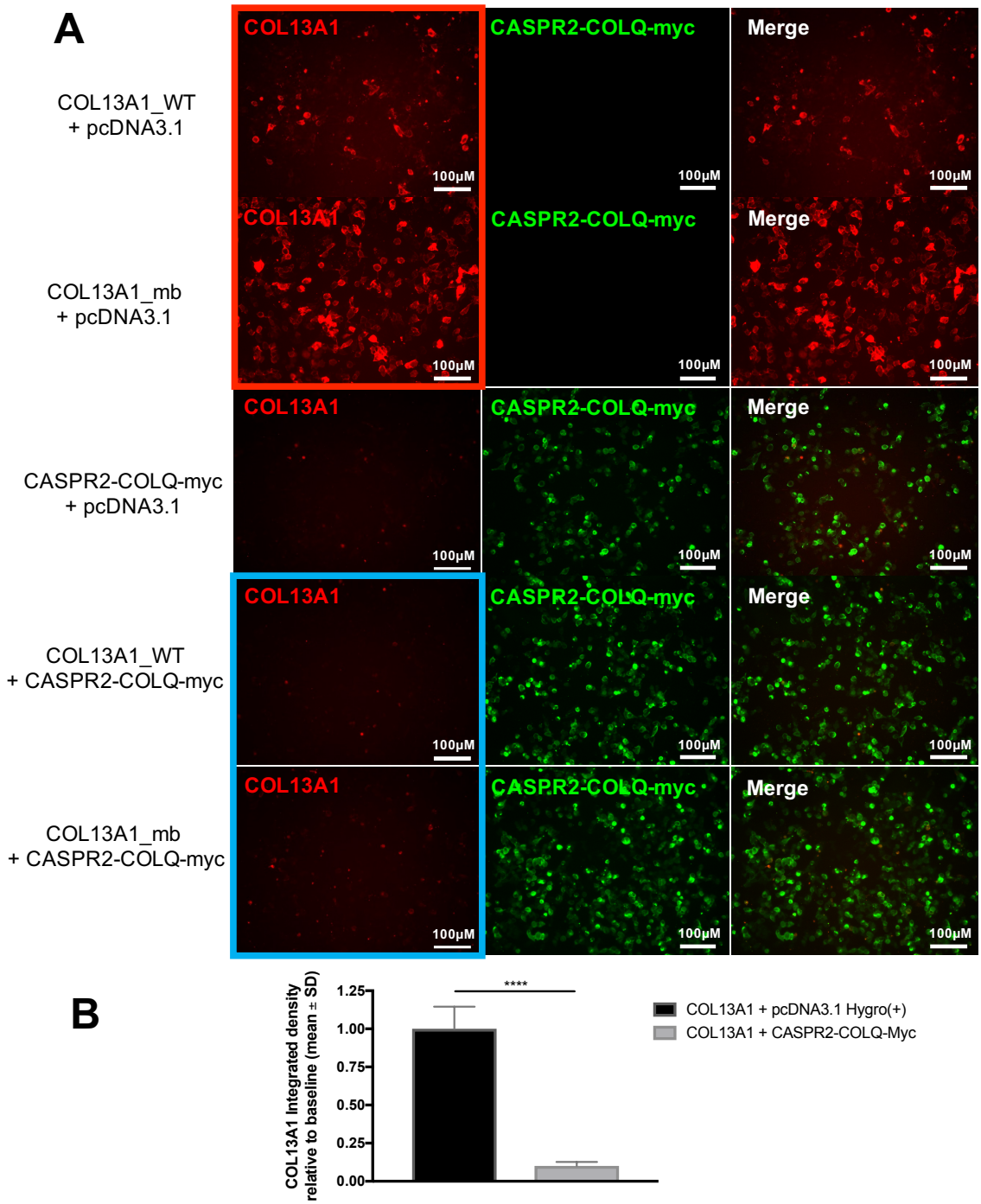


Figure 4-20. Study of COL13A1-COLQ interaction by immunocytofluorescence

(A) HEK-293T cells were transiently co-transfected with 6 µg of total cDNA. 48 hours after transfection, the cells were incubated with a guinea pig anti-COL13A antibody and a mouse anti-c-Myc antibody, and the respective fluorescently conjugated secondary antibodies. **(B)** The figure shows a significant decrease in the red fluorescence staining (blue box) when COL13A1 is coexpressed with CASPR2-COLQ-Myc compared to COL13A1 alone (red box). Two tailed unpaired t-test (****p<0.0001; n=20).

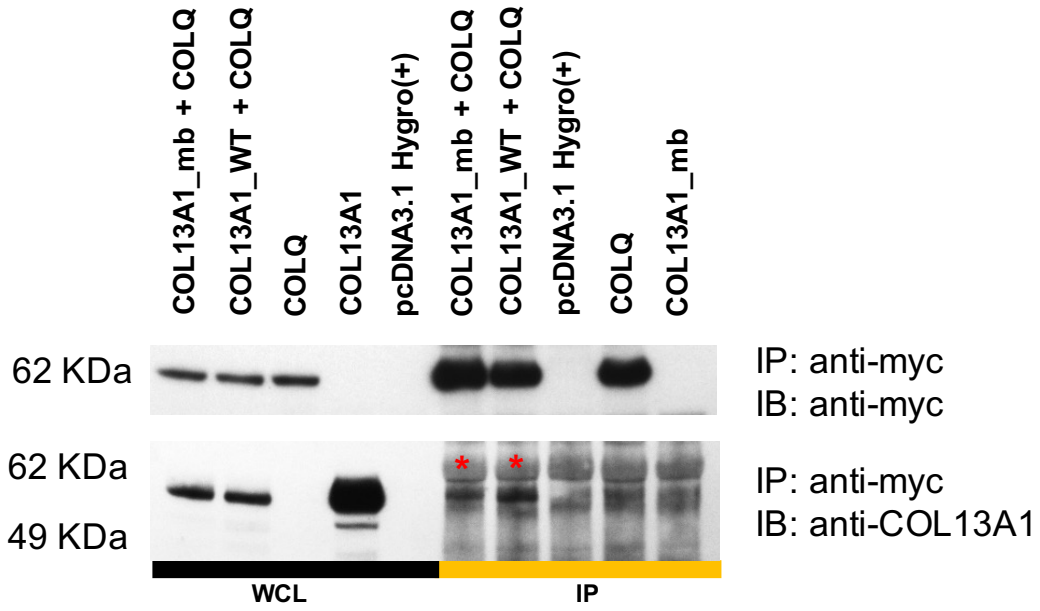


Figure 4-21. Study of COL13A1-COLQ interaction by coimmunoprecipitation

Cell lysates from HEK-293T cells overexpressing the above proteins were immunoprecipitated using an anti-c-Myc antibody and analysed by western blot. The figure shows that the anti-c-Myc antibody pulled-down CASPR2-COLQ-Myc, and that both COL13A1 WT and membrane-bound COL13A1 (COL13A1_mb) were successfully co-immunoprecipitated (red asterisks).

4.6.2 Study of COL13A1 – MUSK / LRP4 /Agrin interaction

Co-transfection of COL13A1 with CASPR2-Agrin, MUSK-EGFP or LRP4-EGFP did not cause major differences in the intensity of the red fluorescence staining compared to COL13A1 and pcDNA3.1/Hygro(+) after incubation with the guinea-pig anti-COL13A1 antibody and the respective fluorescently conjugated secondary antibody **(Figure 4-22)**. Pull-down assays using goat anti-MuSK or rabbit anti-EGFP antibodies were able to pull-down MuSK and LRP4-EGFP, respectively, but COL13A1 was not co-immunoprecipitated suggesting a lack of interaction between proteins **(Figure 4-23)**. The specificity of the pull-down assays was confirmed by the negative immunoprecipitation of HEK-293T cells transfected only with pcDNA3.1/Hygro(+).

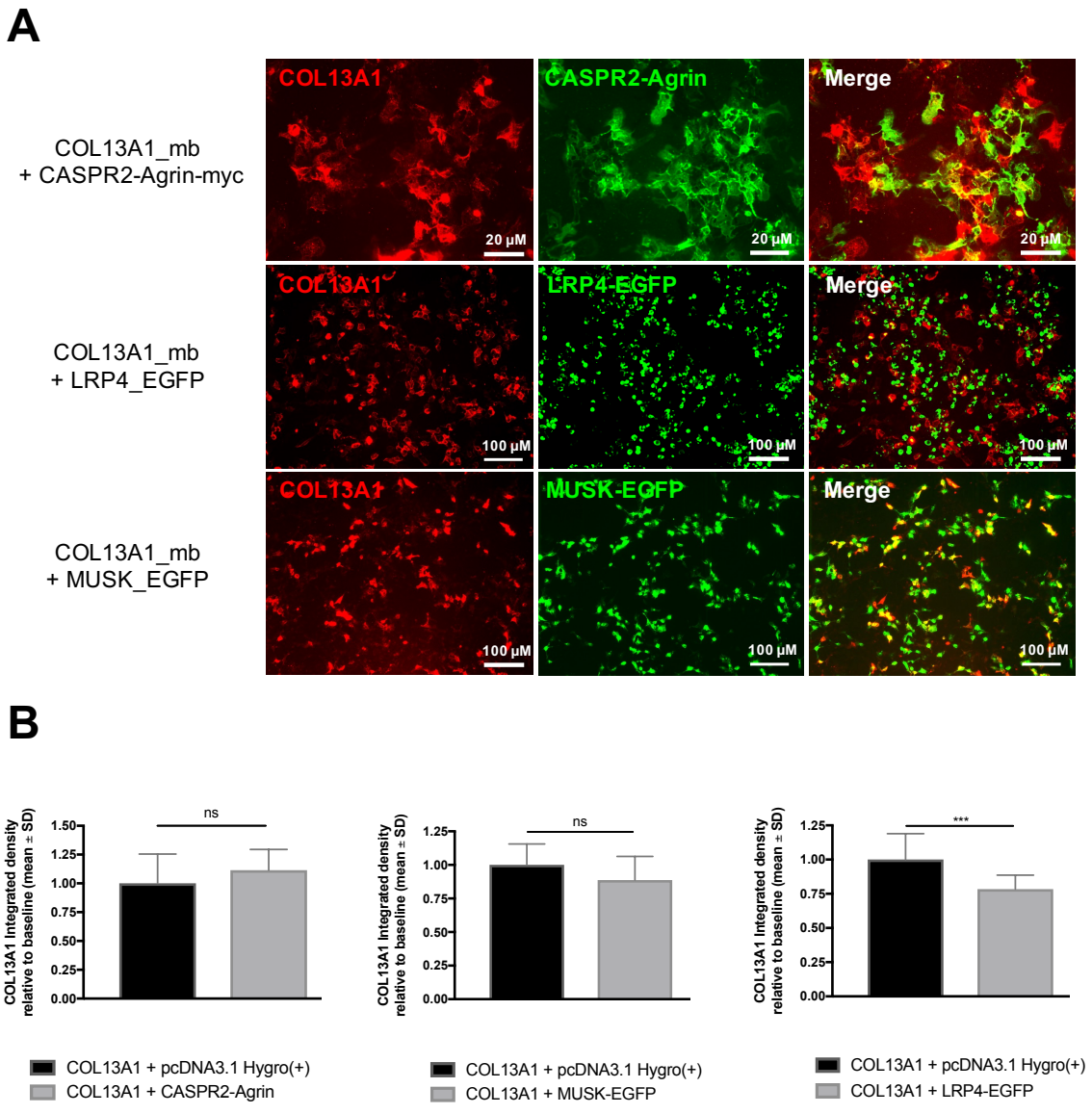


Figure 4-22. Study of COL13A1-Agrin / MuSK/ LRP4 interaction by immunofluorescence

(A) HEK-293T cells were transiently co-transfected with 6 µg of total cDNA. 48 hours after transfection, the cells were incubated with a guinea pig anti-COL13A antibody (and a H-300 rabbit polyclonal antibody for agrin detection – Santa Cruz Cat. No. 25528) and the respective fluorescently conjugated secondary antibodies. **(B)** The figures show robust COL13A1 expression when this is cotransfected with CASPR2-Agrin, MuSK-EGFP or LRP4-EGFP. Quantitative analysis showed a 21.6 ± 8.7% reduction in the intensity of the red fluorescence staining when COL13A1 was co-transfected with LRP4-EGFP compared to COL13A1 co-transfected with pcDNA3.1/Hygro(+). There were no significant differences for CASPR2-Agrin and LRP4-EGFP. Two tailed unpaired t-test (***, $p<0.001$; ns = non-significant).

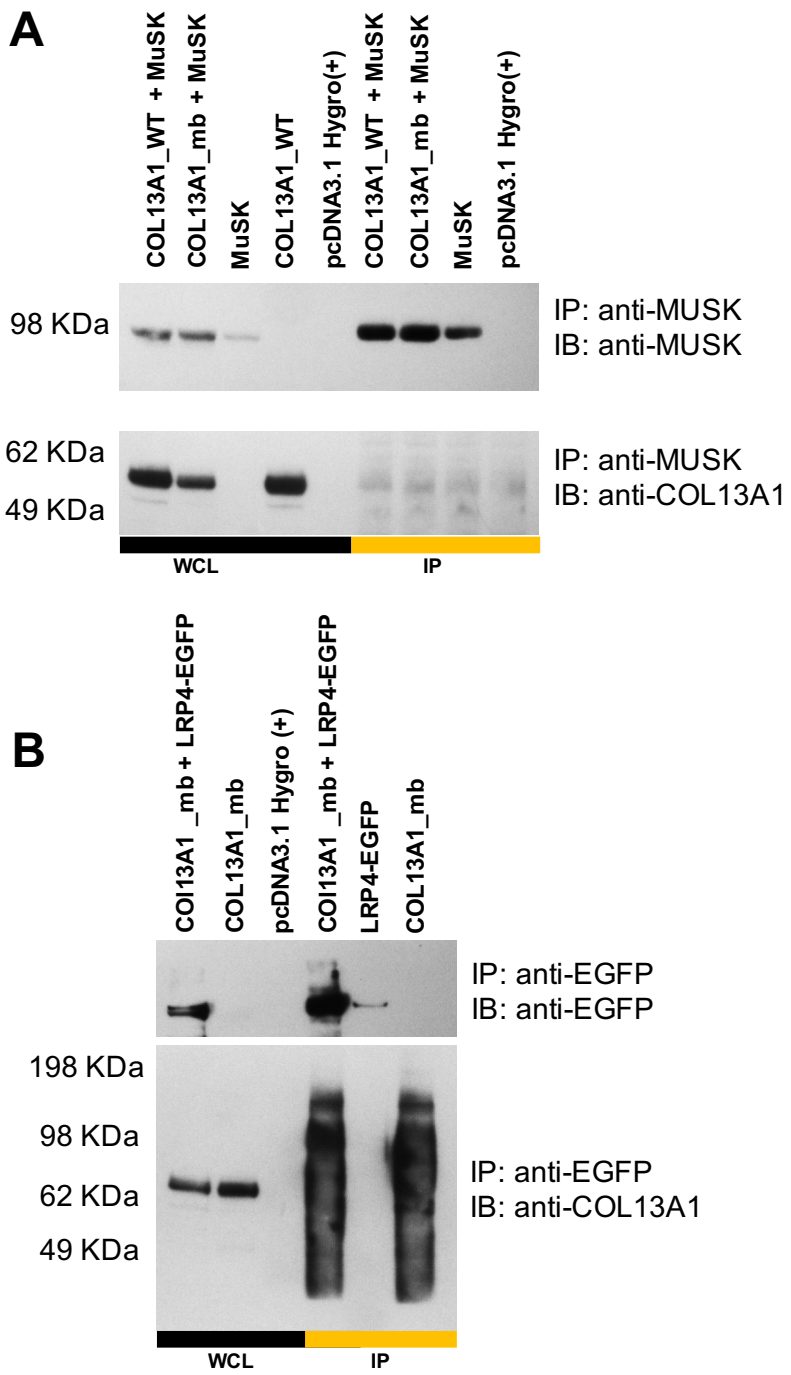


Figure 4-23. Study of COL13A1-MuSK and COL13A1-LRP4 interaction by Co-IP

Cell lysates from HEK-293T cells overexpressing the above proteins were immunoprecipitated using a goat anti-MUSK or a rabbit anti-EGFP antibodies and analysed by western blot. **(A)** The figure shows that the anti-MUSK antibody was able to pull-down MUSK but failed to co-immunoprecipitate COL13A1, suggesting lack of protein interaction. **(B)** The figure shows that the anti-EGFP antibody was able to pull-down LRP4-EGFP but failed to co-immunoprecipitate COL13A1, suggesting lack of protein interaction.

4.7 Effect of *COL13A1* c.1171delG mutation on acetylcholinesterase expression

Since co-immunoprecipitation and immunocytofluorescence studies pointed to the interaction between COL13A1 and COLQ (a collagen-like molecule associated with acetylcholinesterase), a further experiment was conducted to evaluate the effect of the c.1171delG mutation on acetylcholinesterase expression using the muscle biopsy from individual 1. Fresh frozen muscle sections were incubated with Alexa Fluor® 488-fasciculin and Alexa Fluor® 594-α-bungarotoxin and analysed using confocal microscopy and ImageJ software. Special care was taken to avoid saturation by adjusting laser power and detector gain of the confocal microscope.

The result showed that both Alexa Fluor® 488-fasciculin and Alexa Fluor® 594-α-bungarotoxin labelled the NMJs of the individual carrying the c.1171delG mutation. However, there was not, as expected, a complete overlap between the two fluorescent dyes **(Figure 4-24A).** As shown in the images, the contour of the acetylcholinesterase staining (green) exceeded the limits of the α-bungarotoxin staining (red). In keeping with this, the quantification of the endplate area labelled by Alexa Fluor® 594-α-bungarotoxin was 22.03 ± 6.73% smaller in size compared to Alexa Fluor® 488-fasciculin **(Figure 4-24B)**. This could mean that the c.1171delG mutation is affecting the localisation of acetylcholinesterase by exceeding the boundaries of the synaptic region, or alternatively, this could represent a deleterious effect of the c.1171delG mutation on the expression of AChRs at the postsynaptic membrane. However, the lack of a healthy age-matched control muscle biopsy to compare with makes the interpretation of these results non-conclusive. A representative image from a control human muscle endplate displaying the complete overlap of fasciculin and α-bungarotoxin is also shown **(Figure 4-24C)**.

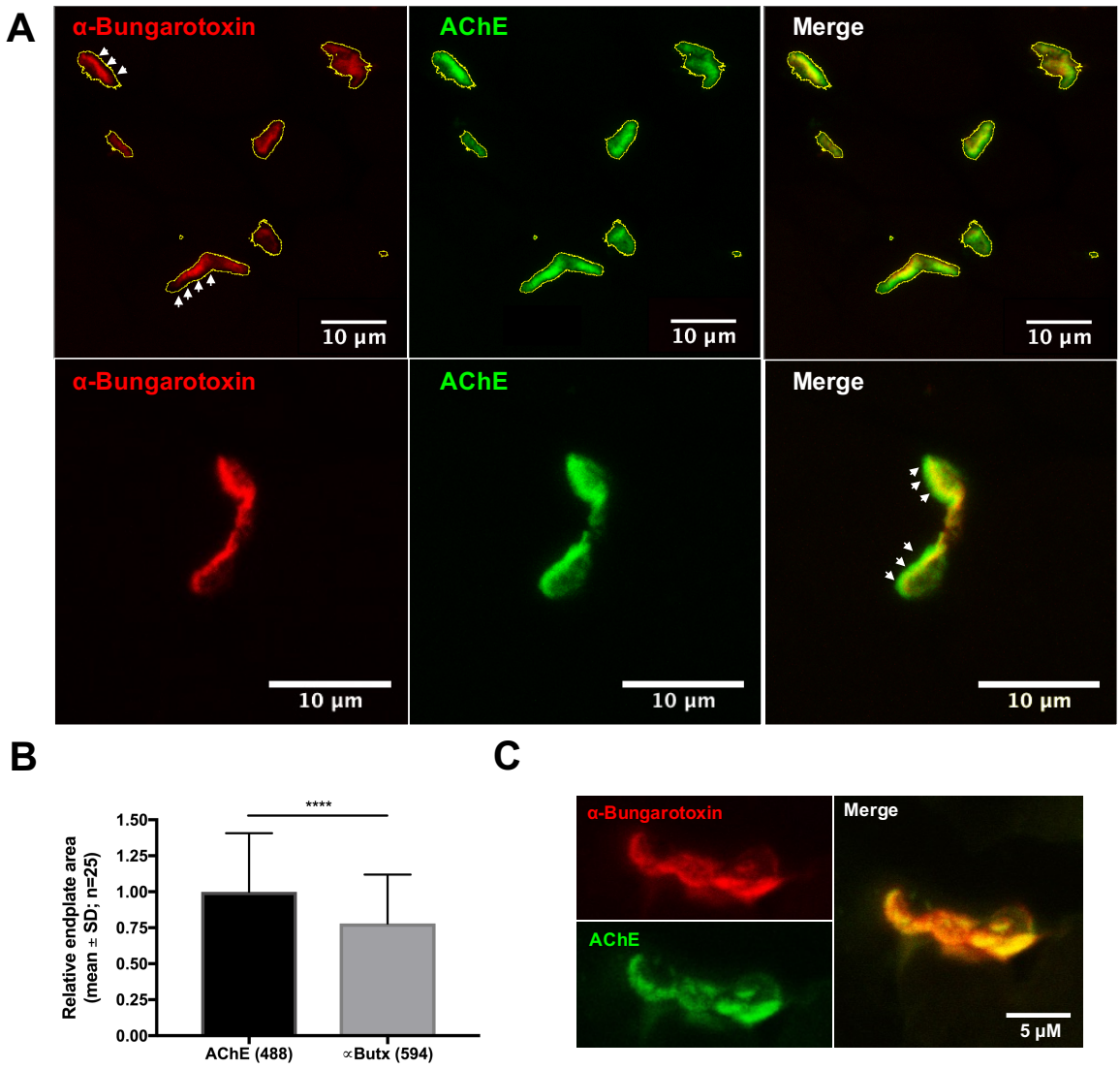


Figure 4-24. Representative images of acetylcholinesterase expression in muscle biopsy from individual 1 carrying the c.1171delG mutation

(A) Fresh frozen muscle sections were labelled with Alexa Fluor® 488-fasciculin and Alexa Fluor® 594-α-bungarotoxin and analysed using confocal microscopy and ImageJ software. The contour of the motor endplates corresponding to the fasciculine staining (green) was selected (yellow line) and then applied to the red channel. As shown by the white arrows, the α-bungarotoxin staining (red) did not fulfil completely the selection area.

(B) Quantification of endplate area labelled by Alexa Fluor® 594-α-butx and Alexa Fluor® 488-fasciculin in the patient's muscle biopsy. Two tailed paired t-test (****p<0.0001).

(C) Representative image of control human muscle endplate.

4.8 Effect of *COL13A1* mutations on protein expression

Site-directed mutagenesis (section 2.2.7) was used to introduce the c.1171delG and c.523-1delG variants found in the patients into the pcDNA3.1/Hygro(+)COL13A1 construct. Since the c.523-1delG variant is predicted to allow splicing but lead to premature termination due to a single-base deletion in the coding sequence (p.Gly175Vfs*20), this was engineered as c.523delG in the cDNA construct. Western blotting using an antibody against the C-terminal region of COL13A1 confirmed the truncation of both mutant proteins **(Figure 4-25)**.

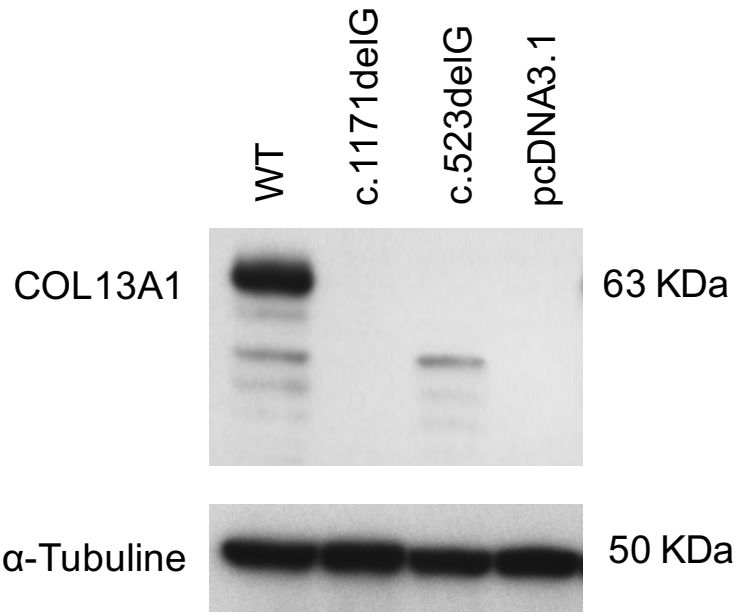


Figure 4-25. Western blotting analysis of COL13A1 WT and variants

HEK-293T cells were transiently transfected with cDNA encoding WT or mutant COL13A1, resolved by SDS-PAGE, and analysed by western blotting using a rabbit anti-COL13A1 antibody (St John's Laboratory –STJ92376) raised against aminoacids 610-690 and α-tubulin antibody. HEK-293T cells transfected with pcDNA3.1/Hygro(+) were used as a negative control.

4.9 Study of functional effects of COL13A1 on AChR clustering

4.9.1 Incubation of C2C12 myotubes with the soluble fraction of COL13A1

It has been suggested that the addition of the COL13A1 ectodomain to C2C12 laminin-coated cultures has no effect on the number of AChR clusters but accelerates their development from plaque-like to pretzel-like structures and accelerates their final dispersion into fragments (Latvanlehto *et al.*, 2010). In order to study the effect of COL13A1 in AChR clustering, C2C12 myoblasts were differentiated into myotubes and incubated overnight with full-length agrin at 1:100 dilution together with the soluble fraction of COL13A1 at different dilutions ranging 1:1 to 1:10000. A control experiment using the culture medium from HEK-293T cells transfected with pcDNA3.1/Hygro(+) was set up in parallel to rule out the effect of any other substance within the culture medium. The generation of recombinant soluble COL13A1 is detailed in Section 2.8.7.

Fluorescence microscopy analysis showed a significant reduction in the number and size of AChR clusters after incubation with COL13A1 medium at 1:1 and 1:5 dilutions, and pcDNA3.1/Hygro(+) medium at 1:20 and 1:1 dilutions **(Figure 4-26)**. There was also a significant reduction in AChR cluster size at 1:1 dilutions for both COL13A1 and pcDNA3.1/Hygro(+). The comparison between myotubes incubated with medium from HEK-293T cells transfected with COL13A1 or mock transfected cells showed overall no significant differences in AChR clusters number ($p=0.3003$) or size ($p=0.8558$). This shows that the effect seen on AChR clustering is non-specific and derived from any other components in the culture medium other than the soluble fraction of COL13A1.

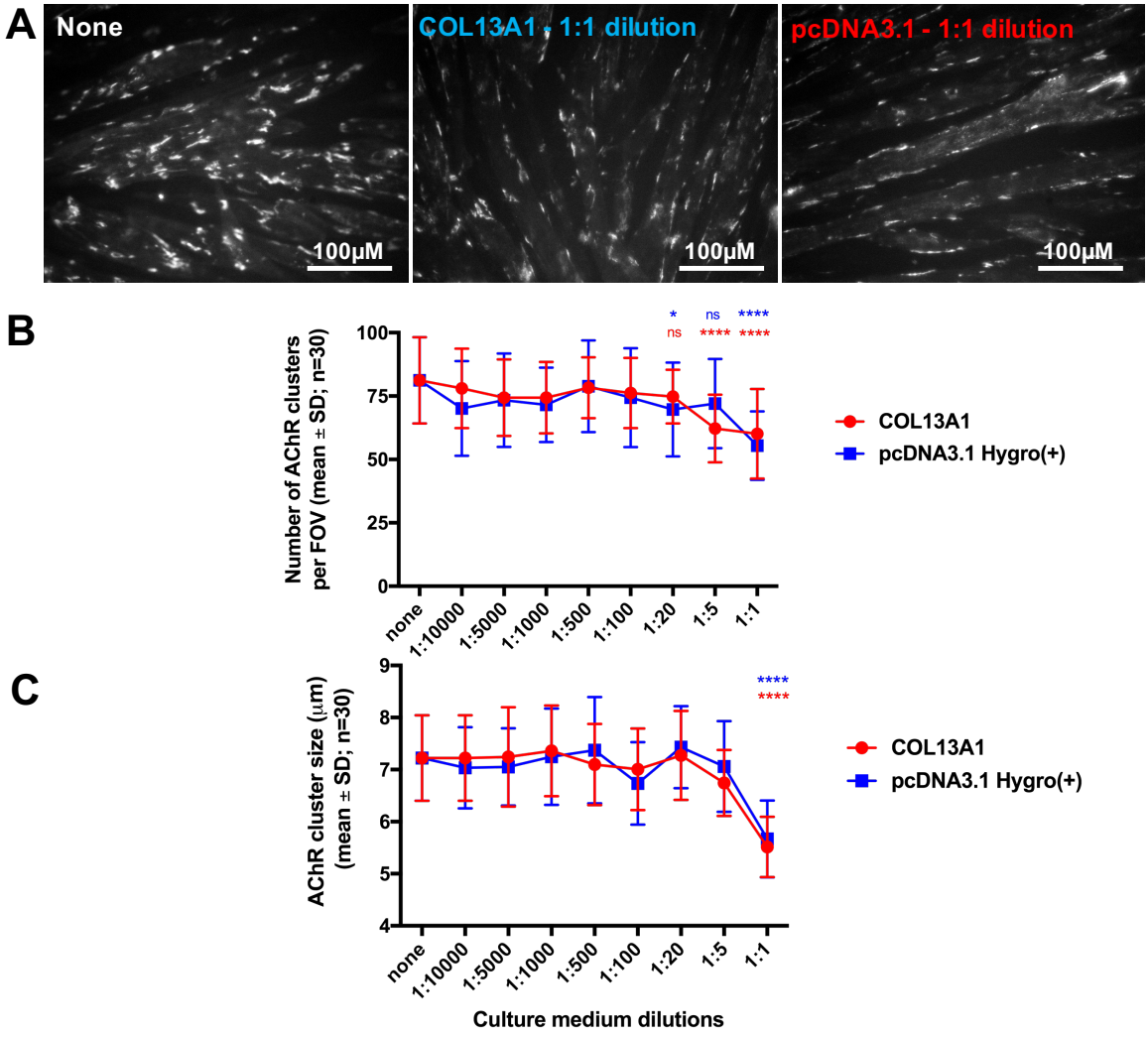


Figure 4-26. Quantification of AChR clusters in C2C12 myotubes incubated with the soluble fraction of COL13A1

C2C12 myoblast were differentiated into myotubes and incubated for 16 hours with full-length agrin and increasing dilutions of culture medium from HEK-293T cells transfected with COL13A1 or pcDNA3.1/Hygro(+) diluted in DMEM + 2% FCS. None stands for cells incubated only with DMEM + 2% FCS. **(A)** Representative microscopic fields of AChR clusters labelled with Alexa Fluor® 594-α-bungarotoxin after overnight incubation with the different dilutions of experimental and control medium. (**B, C)** Quantification of AChR clusters number and size. Data points represent the mean ± SD from 30 images for each condition. Two-way RM ANOVA with Sidak´s multiple comparisons test. (*p<0.05; ****p<0.0001).

A final experiment was carried out to determine whether COL13A1 could promote AChR clustering in the absence of agrin. C2C12 myoblasts were differentiated into myotubes and incubated overnight (in the absence of agrin) with the soluble fraction of COL13A1 at increasing dilutions ranging 1:1 to 1:10000. C2C12 myotubes incubated with agrin were used as a positive control. Fluorescent microscopy analysis showed that soluble COL13A1 was unable to promote AChR clustering in the absence of agrin in C2C12 myotubes **(Figure 4-27)**.

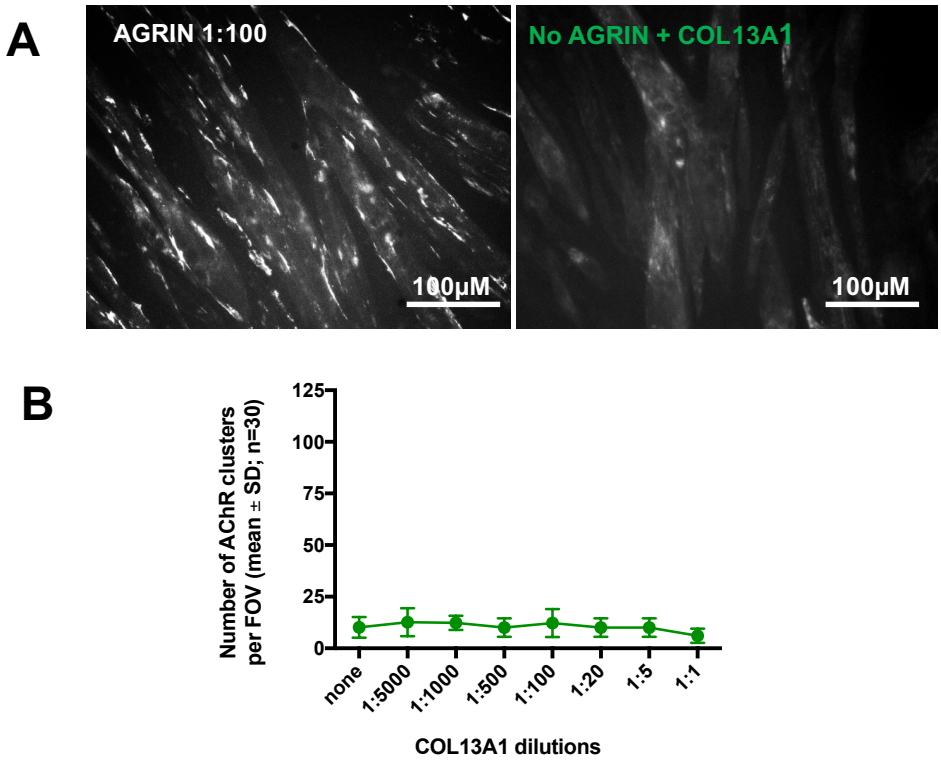


Figure 4-27. Quantification of AChR clusters in C2C12 myotubes incubated with the soluble fraction of COL13A1

(A) Representative microscopic fields of AChR clusters labelled with Alexa Fluor® 594-α-bungarotoxin after overnight incubation with agrin (control) or with the soluble fraction of COL13A1 at 1:10 dilution in the absence of agrin. **(B)** Quantification of AChR clusters per microscope field of vision. Data points represent the mean ± SD from 30 images for each condition.

4.9.2 Effect of the COL13A1 c.1171delG mutation on AChR clustering

To determine the effect of COL13A1 loss on endplate development and NMJ maturation, the homologous *COL13A1* c.1171delG mutation was engineered into the mouse myoblast C2C12 cell-line using CRISPR-Cas9 nickase genome-editing technology (Fa Ann Ran *et al.*, 2013). This experiment was conducted by Dr Judy Cossins (University of Oxford) and details are provided in the appendix section. The c.1171delG mutation caused an approximate 50% decrease in the number of AChR clusters longer than 3µm in differentiated myotubes, compared with mock transfected (wildtype) or non-transfected C2C12 myotubes **(Figure 4-28)**. The average size of the AChR clusters was not affected.

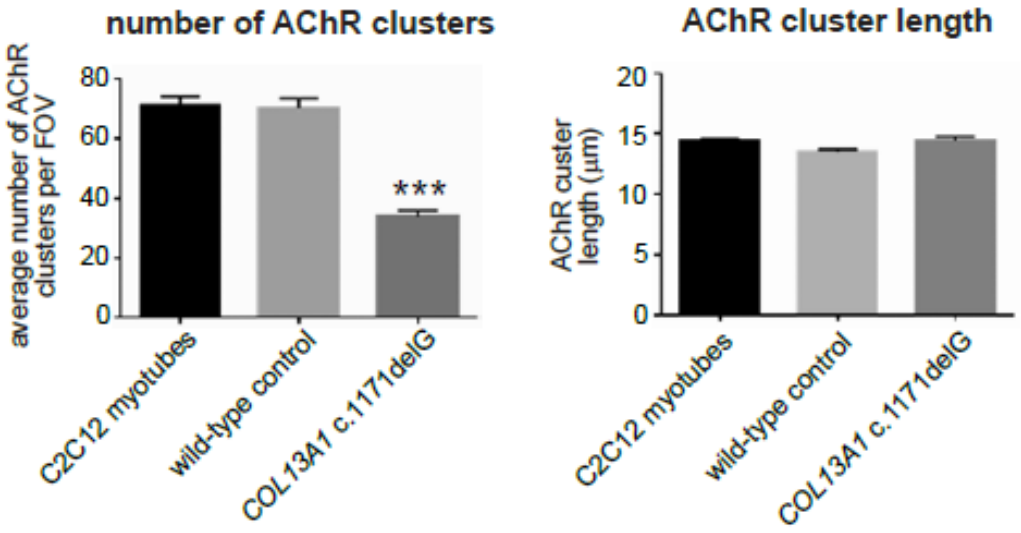


Figure 4-28. Quantification of AChR clusters in *COL13A1* c.1171delG C2C12 myotubes

C2C12 myoblasts engineered with the *COL13A1* c.1171delG variant were differentiated into myotubes and incubated for 16 hours with full-length agrin. AChR clusters were labelled with Alexa Fluor® 594-α-bungarotoxin. Bar graphs represent the mean ± SEM from three different experiments and 60 images per condition. One-way ANOVA with Tukey's multiple comparison test (*** $p < 0.001$).

4.10 Screening of autoantibodies to COL13A1 in patients with MG

COL13A1 is an extracellular protein concentrated at the NMJ, which has been shown to affect neuromuscular transmission. It is speculated that COL13A1 could be accessible to antibodies present in serum. However, the potential presence of such antibodies has never been studied in patients with autoimmune myasthenia gravis (MG). Therefore, a cell-based assay (CBA) was developed for the screening of COL13A1 antibodies in a cohort of patients with MG. A cohort of patients with demyelinating disorders was used as a disease control.

4.10.1 Cohort of patients with MG

The cohort of patients with MG was selected by Professor Angela Vincent (Oxford, UK) and Dr Angelina Maniaol (Oslo, Norway). The cohort comprised a total of 212 serum samples from MG patients from different countries including Cyprus, Italy, Norway, Holland, Japan, and USA **(Figure 4-29A; Table 4-2)**. As part of previous studies (Vincent *et al.*, 2012; Zoltowska Katarzyna *et al.*, 2014), all samples included had been previously tested for other autoantibodies **(Figure 4-29B)** including AChR and MUSK antibodies by Radio Immunoprecipitation Assay (RIA), antibodies to clustered AChR by CBA, and antibodies to Agrin, COLQ and LRP4 by CBA.

4.10.2 Disease control cohort

The disease control cohort was kindly provided by Dr Jacqueline Palace (Oxford, UK) from the Oxford Neuromyelitis Optica Tissue Bank (OXREC 10/H0606/56). The cohort comprised a total 100 serum samples from a wide range of patients suffering mainly from demyelinating disorders **(Figure 4-30)**.

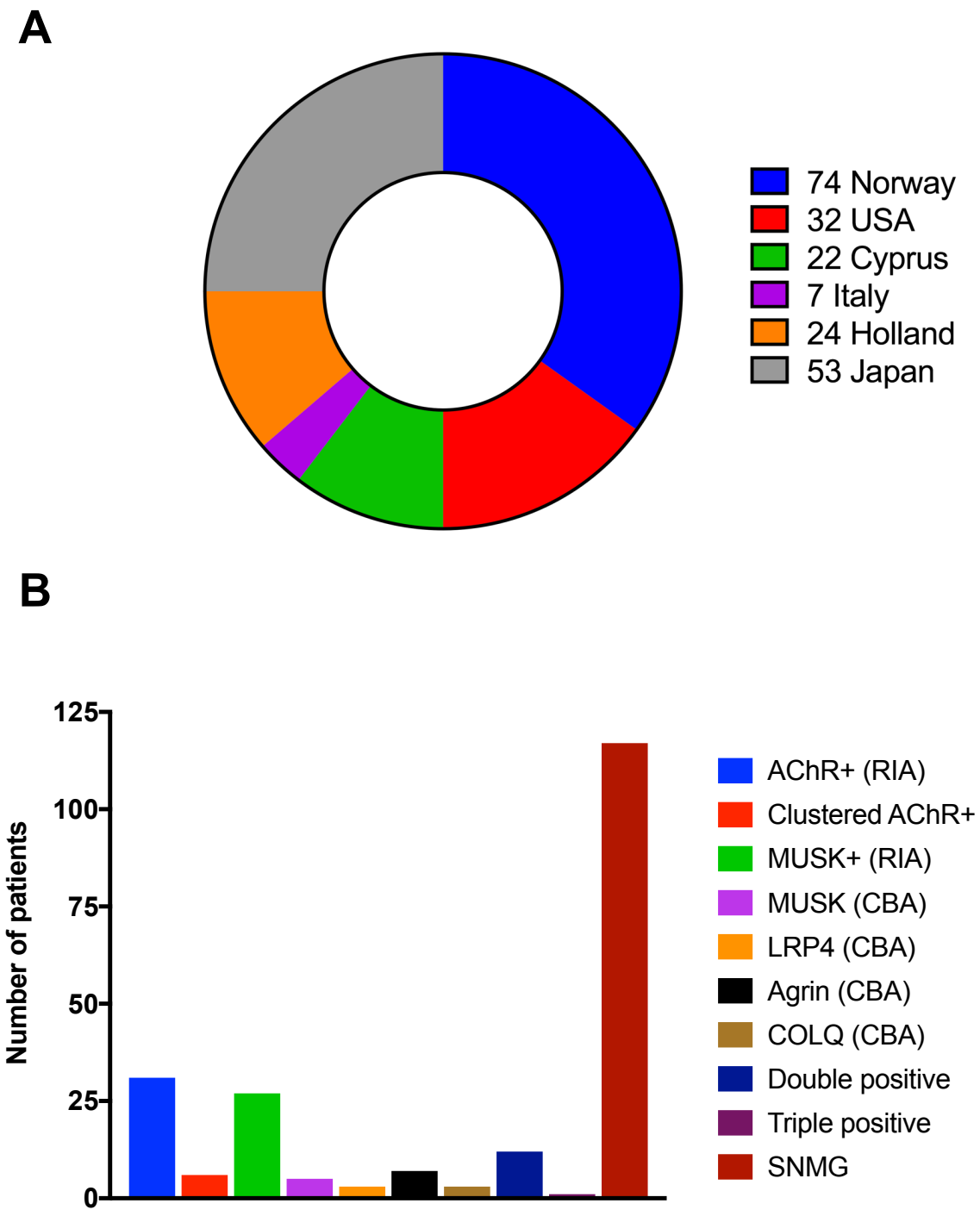


Figure 4-29. Cohort of patients with MG included in the study

(A) Number of MG patients included in the study from each country.

(B) Number of MG patients with previous positive results included in the study and those with seronegative MG (SNMG).

Table 4-2. Details of patients with MG included in the study

Country	Centre	Referring Clinicians	AChR+ RIA	AChR+ CBA	MuSK+ RIA	MuSK CBA	LRP4- CBA	Agrin- CBA	COLQ- CBA	Double +	Triple +	SNMG	Total
Norway	Oslo University Hospital	Dr A. Manialol	1	4	4	5	0	5	1	2	1	51	**53**
USA	John Hopkins Hospital	Dr D.B. Drachman	3	1	7	0	2	0	1	3	0	15	**22**
Cyprus	Cyprus Institute of Neurology and Genetics	Dr Kyriacis	2	0	5	0	1	0	1	0	0	13	**24**
Italy	Policlinico Universitario A. Gemeli	Dr A Evoli	0	0	2	0	0	0	0	2	0	3	**07**
Holland	Leiden University Medical Centre	Dr JJ Verschuuren	5	0	5	0	0	0	0	0	0	14	**74**
Japan	Chiba University & Nagasaki-Kawatana Medical centre	Dr Sasaki, Dr Kuwabara, Dr Masa	20	1	4	0	0	2	0	5	0	21	**32**
Total			31	6	27	5	3	7	3	12	1	117	212

Footnote: information on country and centre of origin, referring clinicians and antibody testing results from previous studies performed in Oxford were provided by Professor Angela Vincent (University of Oxford).

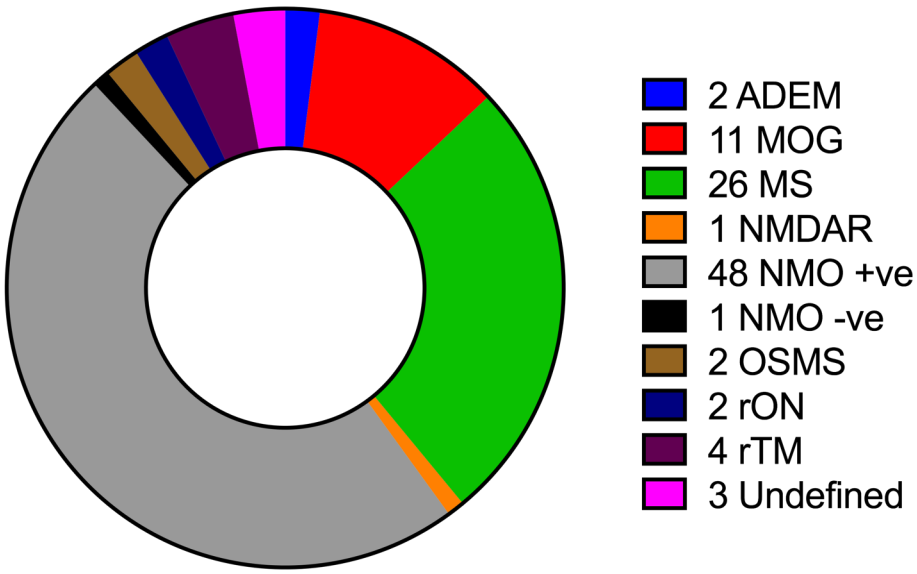


Figure 4-30. Disease control cohort of patients included in the study

Pie chart representing the number and type of patients included in the disease control cohort. Disorders included acute demyelinating encephalomyelitis (ADEM), myelin oligodendrocyte glycoprotein (MOG) antibody-associate disease, multiple sclerosis (MS), N-Methyl-D-aspartate receptor antibody encephalitis (NMDAR), neuromyelitis optica with Aquaporin-4 antibodies (NMO +ve), seronegative neuromyelitis optica (NMO –ve), opticospinal multiple sclerosis (OSMS), recurrent optic neuritis (rON), recurrent transverse myelitis (rTM), and undefined demyelinating disorders (Undefined).

4.10.3 Developing a CBA for the detection of antibodies to COL13A1

CBAs involve the overexpression of antigens on the surface of HEK-293T cells after transfection with a plasmid encoding the desired protein. The cells can then be incubated with serum from patients, and the binding of human antibodies can be scored visually using indirect immunocytofluorescence (Rodriguez Cruz *et al.*, 2015). Optimal COL13A1 cell-surface expression was achieved by transfection of cells with 6 µg of cDNA encoding membrane-bound COL13A1 **(Figure 4-31).** The CBA for the detection of COL13A1 antibodies was developed as previously detailed (Section 2.9). Briefly, this included a routine CBA using anti-human IgG (H+L) as secondary antibody and, if positive, a second

experiment using a secondary antibody against the Fc region of the human IgG (to exclude false positive results due to IgM binding) and mock transfected cells (to rule out non-specific binding of the serum to the cell surface) **(Figure 4-32)**.

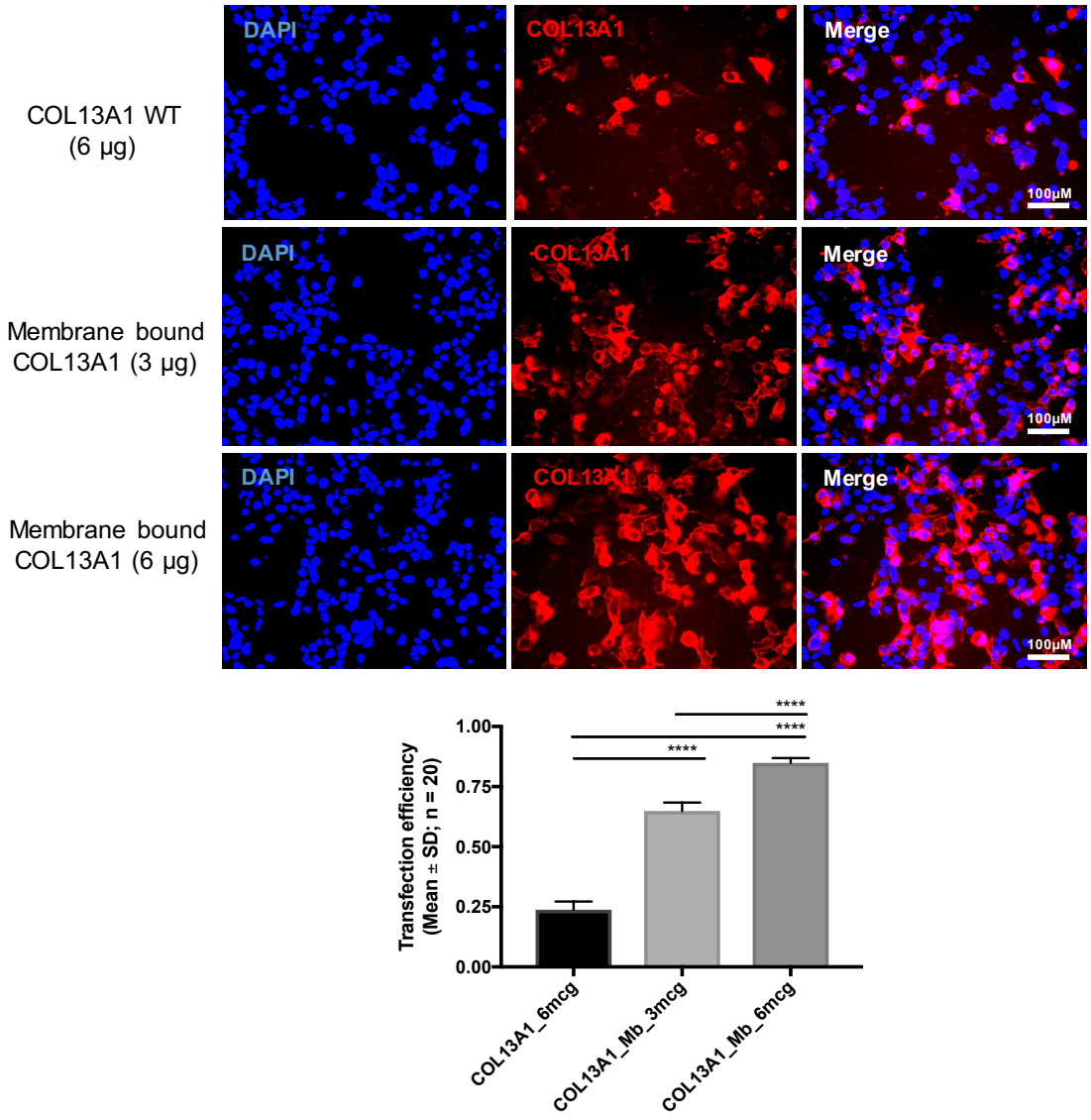
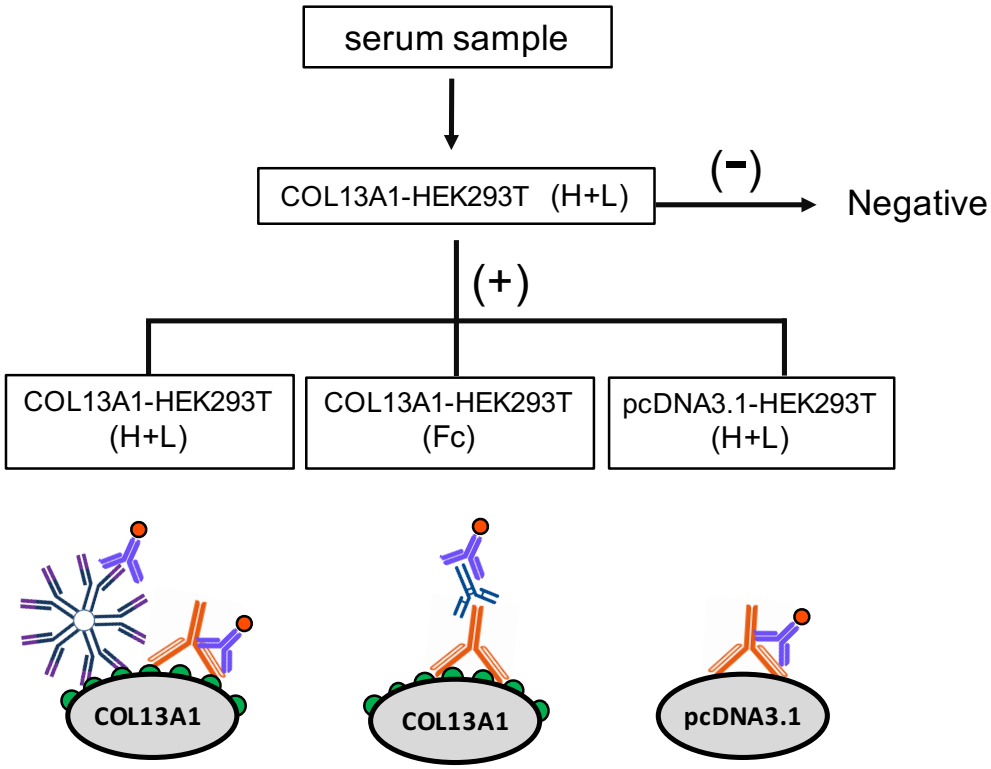


Figure 4-31. Quantification of transfection efficiency in HEK-293T cells expressing WT and membrane-bound COL13A1 constructs

HEK-293T cells were transfected with cDNA encoding WT or membrane-bound (Mb) COL13A1 and incubated with a guinea pig anti-COL13A1 antibody and the respective fluorescent secondary antibody. DAPI (4',6-diamidino-2-phenylindole) was used to stain cell nuclei. Transfection efficiency was measured using ImageJ software. Bar graphs represent de mean ± SD from 20 images per condition. One-way ANOVA and Dunnett´s multiple comparison test (****p<0.0001).



+	+	-	True positive
+	+	+	False positive (Non-specific binding)
+	-	-	False positive (IgM binding)
-	-	-	Negative

Figure 4-32. Procedure for the screening of serum samples and interpretation of results for the COL13A1 CBA. HEK-293T cells transfected with COL13A1 were incubated with serum samples diluted 1:20, and patient's antibodies were detected with an anti-human IgG (H+L) secondary antibody. If positive, a second experiment was conducted using three different conditions in parallel to exclude false positive results due to IgM binding or non-specific binding to the cell membrane. Interpretation of the results is summarised in this table: samples yielding a positive result on mock transfected cells were considered to represent false positives due to non-specific binding to the cell membrane. Samples yielding a positive result using the secondary anti-human IgG (H+L) antibody but negative with the anti-Fc antibody were considered false positives due to IgM binding. If a sample previously positive (especially low positives) tested negative on the second occasion, it was considered negative or equivocal. Samples binding to the cells but not to the cell surface where the antigen is expressed were considered negative.

4.10.4 Results of the COL13A1 cell-based assay in the MG cohort

Among 212 samples from MG patients, 18 samples (8.5%) tested positive (CBA score ≥ 1) in the first experiment using Alexa® Fluor 568 anti-human IgG (H+L) as a secondary antibody **(Figure 4-33A)**. In the second experiment, the number of positives results was reduced to eight patients (3.8%) due to the presence of IgM binding or non-specific binding of the serum to the surface of HEK-239T cells **(Figure 4-33B)**. Representative images of the results are provided in **Figure 4-34**. The clinical details of patients positive for COL13A1 antibodies are summarised in **Table 4.3**.

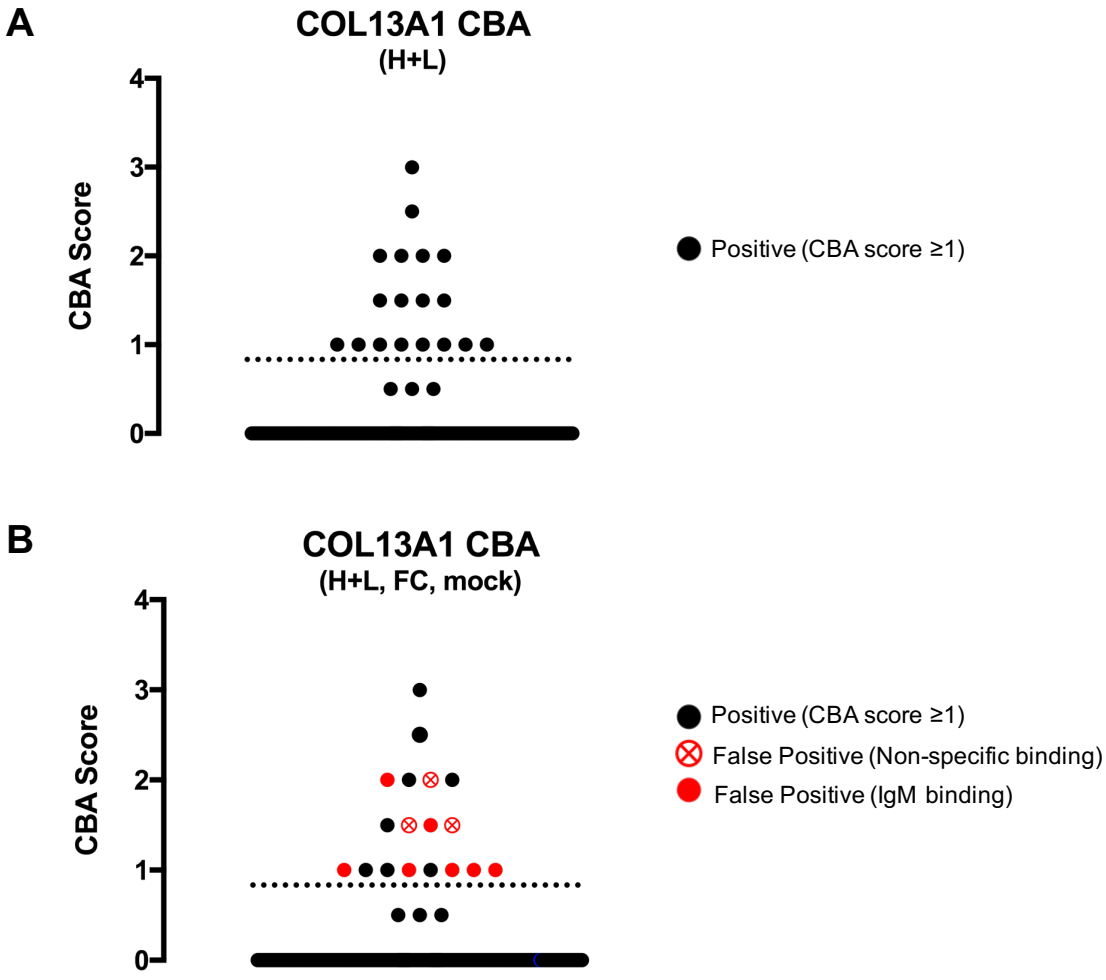


Figure 4-33. Summary of the screening for COL13A1 antibodies in the MG cohort

A total of 8 patients out of 212 (3.8%) tested positive (CBA score ≥ 1). False positive results due to IgM-binding or non-specific binding are marked in red colour.

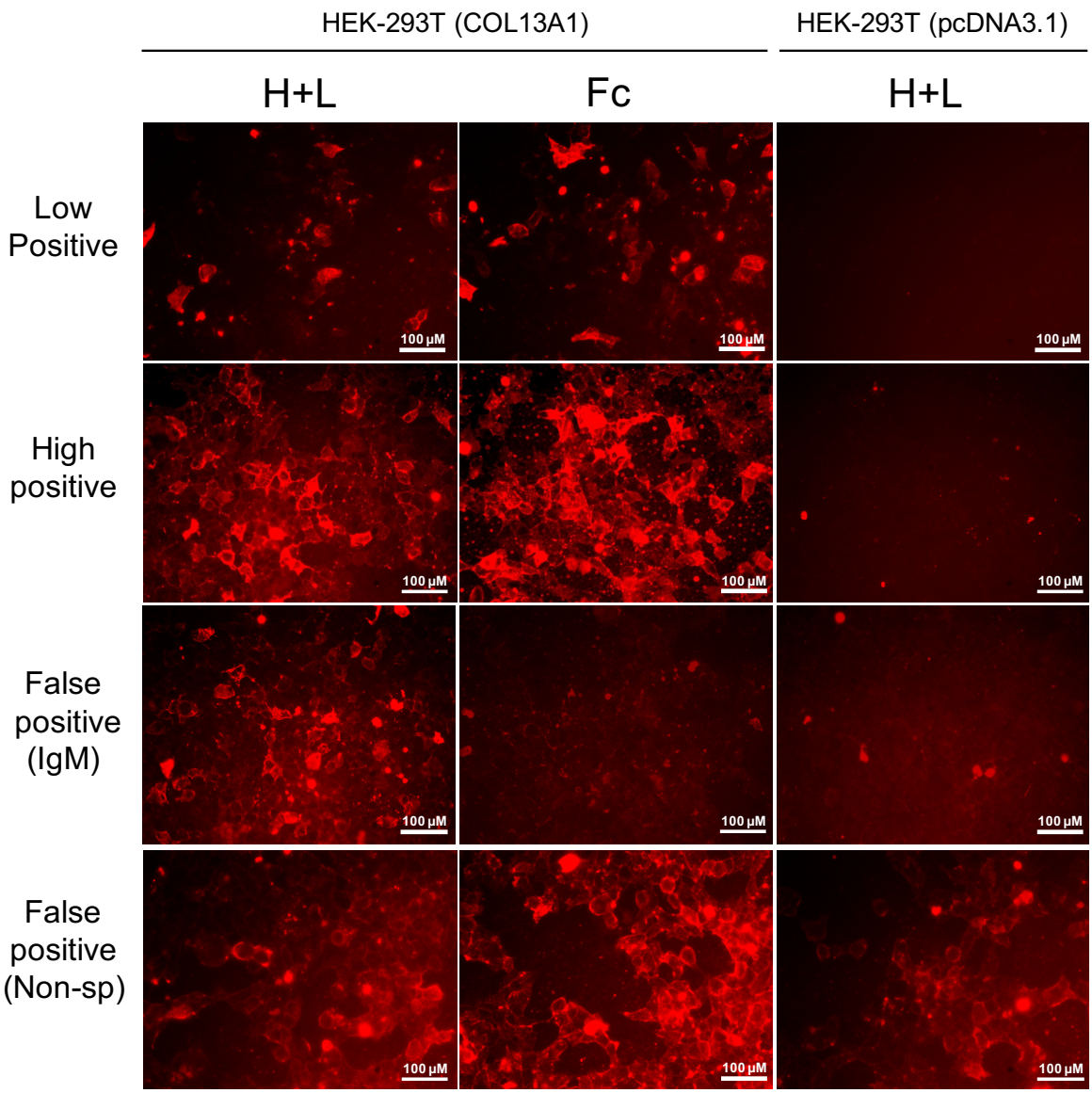


Figure 4-34. Representative images of the screening for COL13A1 antibodies in the MG cohort. Instructions for the interpretation of results are provided in the legend of figure 4-32. It was noted that the use of the anti-Fc antibody and the corresponding fluorescent tertiary antibody often produced higher red fluorescence intensity than the anti-IgG (H+L) alone. This is probably related to the amplification effect from using a third antibody.

Table 4-3. Clinical data of MG patients with positive results on the COL13A1-CBA.

Sample Identifier	Clinician / Centre / Country	COL13A1-CBA SCORE			Other antibodies (score)	Sex	Ethnicity	Age onset	MGFA onset	MGFA max	MGFA final	Therapy	Tx	Histology
		H+L	FC	Mock										
D1G21	Dr D.B. Drachman (USA) John Hopkins	1	2	0	MUSK-RIA (4668)	F	Afro-Caribbean	30	3a	3a	0	?	?	?
C1F02	Dr Sasaki (Japan) Chiba School of Medicine	1.5	1	0	None	n/a	n/a	n/a	n/a	n/a	n/a	n/a	n/a	n/a
C1F04	Dr Sasaki (Japan) Chiba School of Medicine	2.5	1.5	0	None	n/a	n/a	n/a	n/a	n/a	n/a	n/a	n/a	n/a
E1B08	Dr Masa (Japan) Nagasaki Medical Centre	3	4	0	AChR-RIA (2494)	F	Asian	13	n/a	4a	n/a	Steroids	Yes	Hyperplasia
B1F14	Dr Evoli (Italy) Policlinico Univ. A. Gemeli	2	2	0	None	M	Caucasian	31	2a	3a	0	Steroids AZA, py*	Yes	Normal
E1A03	Dr Kuwabara (Japan) Chiba School of Medicine	1.5	2	0	None	F	Asian	59	3a	3a	2a	Steroids Tacrolimus	No	-
5001	Dr Maniaol (Norway) Oslo University Hospital	1	1.5	0	None	M	Caucasian	42	1	2a	2a	Steroids AZA, py*	No	-
1124	Dr Maniaol (Norway) Oslo University Hospital	1.5	2	0.5	MUSK-CBA (1.5/4)	F	Caucasian	21	1	1	1	py*	No	-

Footnote: AZA, azathioprine; F/M, female/male; n/a, not available; py, pyridostigmine, py*, no response to pyridostigmine; Tx, Thymectomy.

4.10.5 Colocalisation of human IgG and guinea pig anti-COL13A1 antibody

In order to determine whether the antibodies detected by the cell-based assay were indeed binding to COL13A1 expressed at the surface of HEK-293T cells, a colocalisation experiment was conducted using MG sample B1F14 and a commercial antibody to COL13A1. Results were assessed by confocal microscopy. Positive colocalisation at the cell surface level was observed between the commercial antibody to COL13A1 (red channel) and the human IgG (green channel) suggesting that the IgG detected in the serum samples was specifically binding to COL13A1 **(Figure 4-35)**.

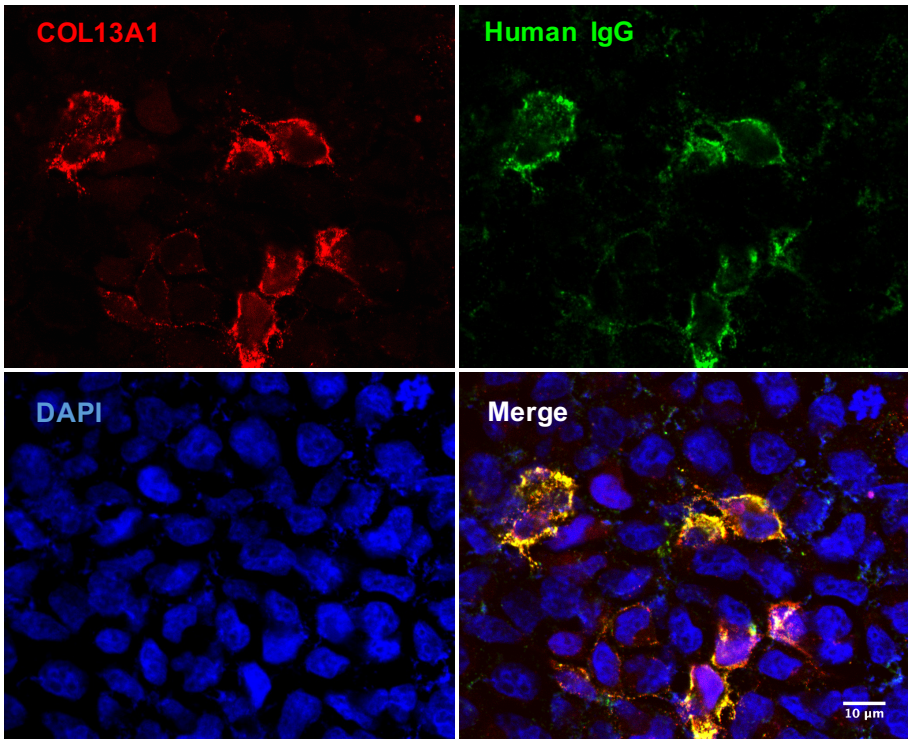


Figure 4-35. Representative images of colocalisation experiment

HEK-293T cells were transfected with cDNA encoding COL13A1. 48 hours after transfection, cells were incubated with a guinea pig anti-COL13A1 antibody, serum 1:20 dilution, and the respective fluorescent secondary antibodies. Finally, the cells were incubated with DAPI (4',6-diamidino-2-phenylindole) to stain cell nuclei, and analysed using a Zeiss LSM 880 confocal microscope and ZEN 2.3 black edition software.

4.10.6 Results of COL13A1 cell-based assay in the disease control cohort

Among a total of 100 samples from patients with demyelinating disorders, 27 samples (27.0%) tested initially positive (CBA score ≥ 1) **(Figure 4-36A)**. After the second experiment, the number of positives results was reduced to 13 (13.0%) due to the presence of IgM binding or non-specific binding of the serum to the cell-surface **(Figure 4-36B)**. Patients with positive results included those with a diagnosis of Neuromyelitis optica (8), MOG-ab disease (3), Multiple sclerosis (2) and Opticospinal MS (1). Representative images of the results are provided in **Figure 4-37**.

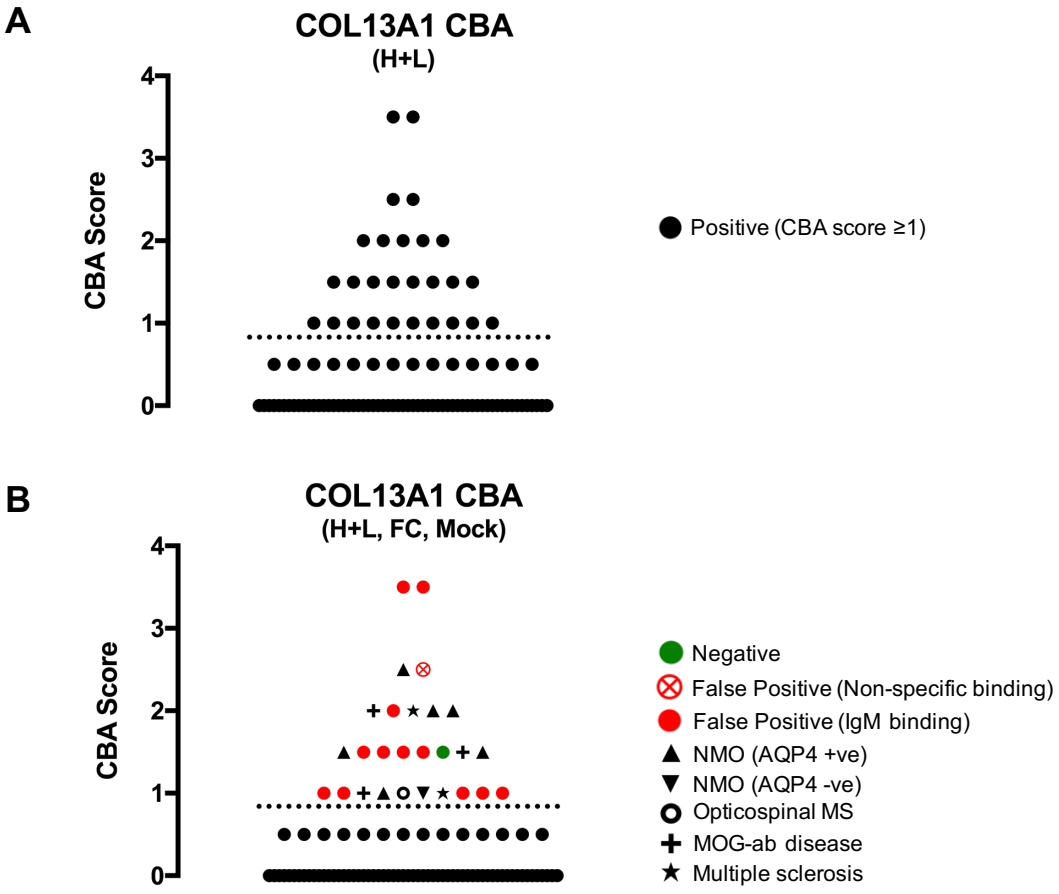


Figure 4-36. Summary of the screening for COL13A1 antibodies in the disease control cohort. A total of 13 patients out of 100 (13%) tested positive (CBA score ≥ 1). False positive results due to IgM-binding or non-specific binding are marked in red colour. A low-positive sample that tested negative in the second experiment is labelled in green colour.

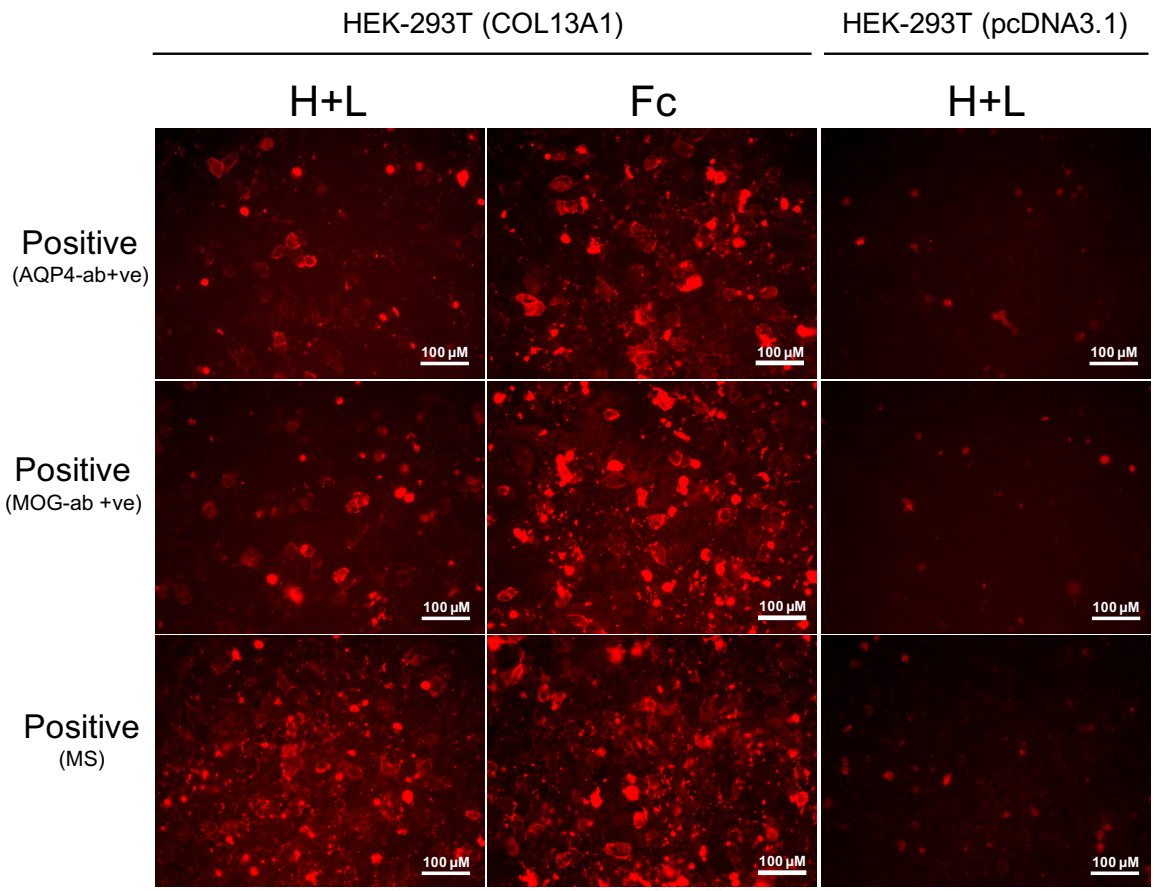


Figure 4-37. Representative images of the screening for COL13A1 antibodies in the disease control cohort. Instructions for the interpretation of results are provided in figure 4-32 legend. AQP4 +ve, aquaporin-4 antibody positive; MOG-ab +ve= myelin oligodendrocyte glycoprotein antibody positive; MS, Multiple sclerosis.

The high number of positive results within the disease control cohort of patients with demyelinating disorders was unexpected. In fact, there was a significantly higher number of patients (13.0% vs 3.8%) with positive results than in the MG cohort (Fisher's exact test; p = 0.0017). An explanation for these observations is unclear. However, it suggests that the COL13A1 CBA developed is *a priori* unreliable for the screening of antibodies to COL13A1 in serum samples from MG patients.

4.11 Discussion

The findings of these investigations have shown that COL13A1 is a membrane protein expressed at the human NMJ and cleaved via ectodomain shedding into a soluble form that is part of the synaptic basal lamina (the membrane-bound form will also project into the basal lamina). Immunofluorescence on muscle sections showed that full-length COL13A1 was absent from the muscle biopsy of the affected individual carrying the c.1171delG loss-of-function mutation, and functional analysis showed a deleterious effect on AChR clustering *in vitro*. Overall, segregation, biochemical and functional studies suggest that the *COL13A1* variants identified are responsible for the myasthenic syndromes observed in the three patients presented from two different kinships. In addition, this work has led to a detailed clinical characterisation of individuals with this condition, which has already facilitated the identification of three new cases by other clinicians.

COL13A1 is a cleaved protein localised at the NMJ and this raises the question of where in the neuromuscular synapse it is generated: terminal Schwann cell, motor neuron or muscle. In a study using a receptor mouse line, in which β-galactoside was inserted into the *Col13a1* locus to replace the extracellular sequences and eliminate the cleavage site, COL13A1 was detected at the postsynaptic membrane suggesting that muscle was the main source of COL13A1 at the mouse NMJ (Latvanlehto *et al.*, 2010). The fact that current immunofluorescence experiments in human muscle sections showed that membrane-bound COL13A1 may be located presynaptically is puzzling. In the first place, this could be related to species differences between mouse and human, as is the case for AChR subunits gene expression (Cossins *et al.*, 2004). Another possibility is the lack of specificity

of the COL13A1 N-terminal antibody nevertheless it was successfully validated in HEK-293T cells. Since COL13A1 was detected in the muscle biopsy from individual 1 using a COL13A1 N-terminal antibody, but not a C-terminal, this suggests that the c.1171delG mutation preserved the truncated version of the protein located at the plasma membrane.

Col13a1$^{-/-}$ mice have shown abnormal maturation of postsynaptic structures where endplates remained small, immature, and fragmented compared to WT animals (Latvanlehto *et al.*, 2010). This is consistent with the current *in vitro* results showing abnormal AChR clustering with COL13A1 loss of function. In the present study, no abnormalities were seen in the expression of key postsynaptic molecules such as MuSK and DOK7. This suggests that the deleterious effects seen in AChR clustering and, therefore, in NMJ formation and maintenance, are independent of the Agrin-LRP4-MUSK-DOK7 clustering pathway. Since the *Col13a1* $^{tm/tm}$ mouse model, in which the ectodomain shedding is annulled, also exhibited defective NMJs with enlarged and fragmented endplates (Härönen *et al.*, 2017), the effect on postsynaptic maturation *in vivo* could either come from the membrane-bound COL13A1 or the cleaved ectodomain.

Col13a1$^{-/-}$ animals showed considerable presynaptic defects such as abnormal clustering of synaptic vesicles at the nerve terminal and reduced terminal complexity with defective nerve endings unable to cover the muscle endplates (Latvanlehto *et al.*, 2010). Moreover, the mice showed retraction of terminal Schwann cells and abnormal invagination of the Schwann cell processes into the synaptic cleft impairing the contact between the nerve terminals and the muscle. On the other hand, *Col13a1*$^{tm/tm}$ animals showed NMJs

comparable to WT mice (Härönen *et al.*, 2017). This may indicate that membrane-bound COL13A1 is the main form promoting presynaptic differentiation and supporting the integrity of the presynaptic terminal. In this regard, it is possible that COL13A1 takes part in trans-synaptic adhesion by binding directly to nerve terminal and Schwann cells and/or functioning in a retrograde manner (Latvanlehto *et al.*, 2010; Härönen *et al.*, 2017).

In the present study, confocal microscopy of presynaptic markers (synaptophysin and protein S100ß) showed preserved expression and normal localisation in the muscle biopsy from the individual with *COL13A1* loss-of-function mutations. Although some of the terminal Schwann cells appeared retracted or did not fully reach the NMJ, a definitive assessment of their morphology was not possible due to the use of transverse 8-10 µm muscle sections and the lack of an age-matched control muscle biopsy. Overall, putting together the findings from the animal models with that of the patients, it is likely that COL13A1 is important for both the presynaptic and postsynaptic integrity of the NMJ.

An additional report of a mouse model with N-terminally altered COL13A1 molecules lacking the short cytosolic and transmembrane domains, but retaining the large collagenous ectodomain, showed the presence of abnormal myofibres with vacuolisation, disorganised sarcolemma and basement membrane (A. Kvist *et al.*, 2001). The findings were of progressive deterioration in strength and the mice suffered from exercise-induced muscle damage. The patients described in this chapter did not show clear evidence of a concomitant myopathy since all individuals had normal CK levels, normal fibre type distribution and few central nuclei were displayed in the muscle biopsy. However, the presence of occasional vacant peripheral vacuole-like areas in the H&E

staining from individual 1 could be consistent with the findings observed in the mice, although artefact cannot be excluded. In addition, immunofluorescence studies did not show distinct COL13A1 expression in muscle fibres.

The COL13A1 ectodomain is thought to interact with fibronectin, heparin, and basement membrane proteins nidogen-2 and perlecan (Tu *et al.*, 2002), although determining interaction of collagen molecules can be difficult due to non-specific binding. The α1 subunit of the α1ß1 integrin was reported to be a receptor for COL13A1 in cultured cells (Nykvist *et al.*, 2000) and to be present at motor nerve terminals from mice (Martin *et al.*, 1996) thus α1ß1 integrin may be a potential interacting partner on the presynaptic side. Recently, and of more relevance from the clinical point of view, it has been reported that COL13A1 binds to ColQ extracted from *Torpedo californica* or *Electrophorus electricus in vitro* and that AChE staining in *Col13a1* $^{-/-}$ mice diffuses beyond the postsynaptic receptor area compared to WT mice (Härönen *et al.*, 2017). This suggests that COL13A1 could be involved in the correct distribution of AChE at the motor endplate. These findings are consistent with the results of the pull-down assays presented in this chapter and with the observation that cotransfection of HEK-293T cells with COL13A1 and ColQ dramatically reduced COL13A1 immunostaining by probable blockage of the antibody binding site. The specificity of these findings is supported by the negative results of COL13A1 interaction with MuSK, LRP4, and Agrin using both pull down assays and immunocytofluorescence. In the muscle biopsy from individual 1, it was also noted that fasciculin staining spread beyond α-bungarotoxin staining, although there was not an age-matched control biopsy available to compare with.

The mechanism by which the abnormal interaction of COL13A1 and ColQ could alter AChR clustering is unknown. However, it is plausible that if *COL13A1* mutations affect the correct functioning of AChE, this could lead to reduced AChR clustering via increased dispersion mediated by acetylcholine (Lin *et al.*, 2005). In addition, it has been proposed that ColQ and MuSK interact (Cartaud *et al.*, 2004). If COL13A1 affects ColQ localisation at the muscle endplate, this could have an implication for MuSK, although no COL13A1-MuSK interaction was seen in the current study.

From the clinical point of view, the phenotype of the three individuals reported most closely resemble CMS due to *RAPSN* mutations (Cossins *et al.*, 2006) in particular the clinical history of onset at birth, breathing and feeding difficulties, slight dysmorphic facial features, and ptosis with preservation of eye movements. However, these differ from Rapsyn-CMS because of the presence of *pectus carinatum*, limited fatigability of the ptosis, and absence of a beneficial response to anticholinesterase medication.

The characterisation of the myasthenic syndrome in individual 1 prompted treatment with 3,4-DAP and salbutamol, which had good clinical effect. The ß2-adrenergic receptor agonists salbutamol and ephedrine have been found to be beneficial for CMS due to *DOK7* mutations (Lashley *et al.*, 2010) that affect the maturation and maintenance of NMJ structure, whereas 3,4-DAP enhances acetylcholine release from the presynaptic nerve terminal. The beneficial effect of salbutamol would be consistent with *COL13A1* mutations affecting AChR clustering and maturation of postsynaptic structures. The positive effect of 3,4-DAP is supported by the presynaptic abnormalities seen in the *Col13a1*$^{-/-}$ mouse model such as abnormal clustering of synaptic vesicles. In a similar way

to CMS patients with mutations within the AChR clustering pathway, pyridostigmine was not beneficial in the patients reported.

The results of the screening for antibodies to COL13A1 in MG patients are difficult to interpret due to the unexpected high number of positive results within the disease control cohort of patients with demyelinating disorders. The COL13A1 CBA developed used the specific anti-Fc secondary antibody and mock transfected cells to rule out IgM and non-specific binding to the cell surface, respectively. Therefore, it is possible that COL13A1 behaves as a "sticky" antigen resulting in non-specific binding of patient´s serum irrespective of the antibody content. However, it is worth mentioning that COL13A1 is highly expressed in the human optic nerve (Sandberg-Lall *et al.*, 2000) and since this is often targeted in patients with demyelinating disorders such MS and NMO, this might warrant further investigation. Additional studies using serum samples from healthy controls and HEK-293T cells transfected with additional antigens as a control would be useful.

In summary, this study reports the clinical details of individuals with mutations in *COL13A1* for the first time and emphasises the role of extracellular-matrix proteins, other than the Agrin-LRP4MuSK-DOK7 pathway, in the formation and maintenance of the NMJ. In addition, it supports the use of genetic testing as an essential tool for the differential diagnosis of CMS subtypes and other neuromuscular conditions to help refine treatment and prognosis for individuals affected by these conditions. Finally, the clinical and molecular characterisation of this condition facilitated the implementation of appropriate treatment strategies for these patients and the recognition by other clinicians.

Chapter 5

Clinical Characterisation of the Myasthenic Syndrome Arising from Mutations in *GMPPB*

5.1 Introduction

Most of the genes involved in congenial myasthenic syndromes (CMS) encode proteins with a direct role in neuromuscular transmission such as the AChR subunits, or in the development or maintenance of the NMJ integrity such as DOK7 or Rapsyn (Ohno *et al.*, 2002; Beeson *et al.*, 2006). More recently, an unexpected relationship between defects in the glycosylation of proteins and CMS was found by using NGS technology (K Belaya *et al.*, 2012; Cossins *et al.*, 2013; Zoltowska *et al.*, 2013). Mutations in *ALG2, ALG14* (Cossins *et al.*, 2013)*, DPAGT1* (K Belaya *et al.*, 2012) *and GFPT1* (Zoltowska *et al.*, 2013) were shown to produce a myasthenic disorder with a predominantly limb girdle pattern of muscle weakness and minimal facial and ocular involvement.

Glycosylation is a ubiquitous pathway defined by the sequential attachment of sugar moieties to the polypeptide backbone. Post-translational modifications of proteins are crucial for protein folding, transport and functionality (Moremen *et al.*, 2012). In CMS, one suggested mechanism is through glycosylation of AChR subunits, which is required for the correct assembly and efficient export to the cell surface of the AChR pentamers (Gehle *et al.*, 1997). Therefore, abnormal glycosylation results in a reduction of AChRs at the muscle endplates and a reduced synaptic response to acetylcholine (Zoltowska *et al.*,

2013). Other key NMJ proteins such as MuSK, agrin, integrins and neural cell adhesion molecules (NCAM) are also glycosylated (Martin, 2003). Their abnormal glycosylation could also contribute to the pathogenic effect. In fact, almost all secreted and membrane-associated proteins of eukaryotic cells are glycosylated. Therefore, it is puzzling why defects in a ubiquitous process result in a dysfunction mainly restricted to the NMJ.

GMPPB is a recently reported CMS-associated glycosylation gene (Belaya, 2015). *GMPPB* encodes GDP-mannose pyrophosphorylase B that catalyses the conversion of mannose-1-phosphate and GTP to GDP-mannose. *GMPPB* contributes to both the N-glycosylation and the *O*-mannosylation pathways **(Figure 5-1)**. Mutations within the O-mannosylation pathway were originally identified in patients with a form of muscular dystrophy within the spectrum of dystroglycanopathies (Muntoni *et al.*, 2011). These disorders are characterised by reduction in α-dystroglycan glycosylation, which is the most well characterised and functionally relevant O-mannosylated protein.

Patients with autosomal recessive mutations in *GMPPB* had reduced glycosylation of α-dystroglycan in skeletal muscle and variable degree of clinical severity ranging from congenital muscular dystrophies and additional associated structural brain involvement, to milder limb-girdle muscular dystrophy variants of late childhood onset (Carss *et al.*, 2013). Recently, our group showed that autosomal recessive mutations in *GMPPB* can also cause CMS and bridge myasthenic disorders with dystroglycanopathies (Belaya, 2015). This increased the spectrum of disorders caused by *GMPPB* mutations and confirmed the importance of glycosylation for the integrity of neuromuscular transmission.

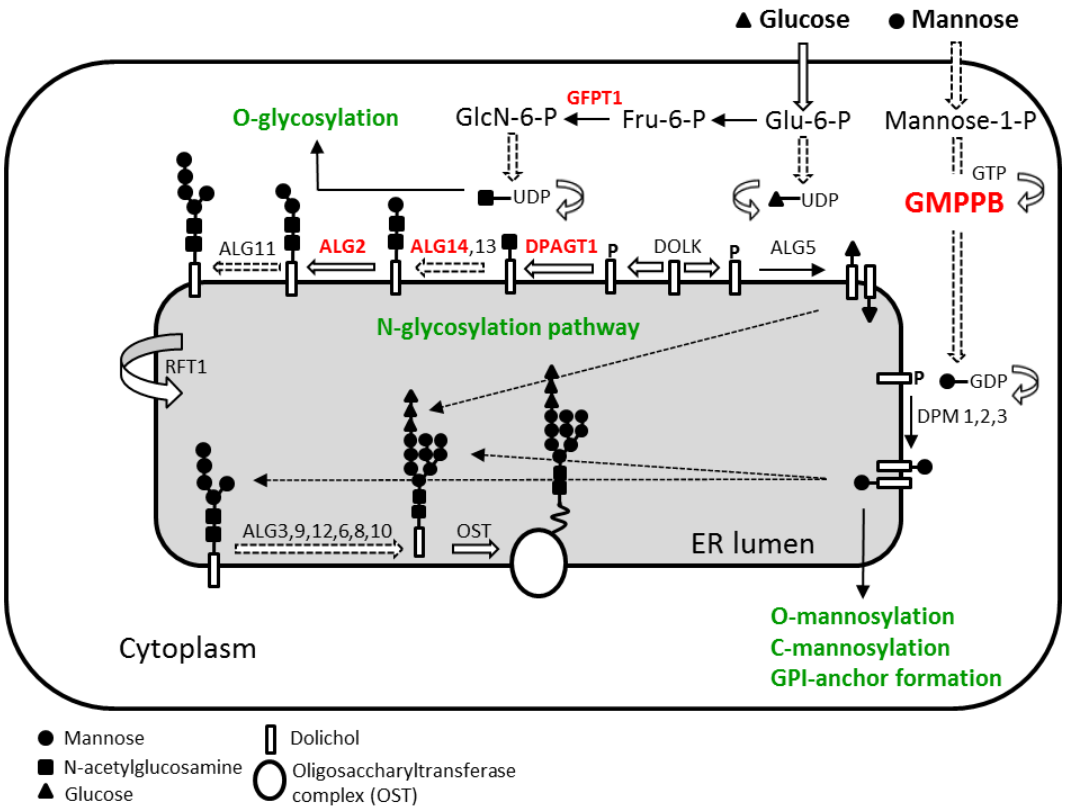


Figure 5-1. Schematic representation of the N-glycosylation pathway

CMS-causing genes are displayed in red colour. Initial steps of N-linked protein glycosylation take place in the Endoplasmic reticulum (ER). It starts with the assembly of the core glycan on the lipid dolichol, and follows the incorporation of sugar moieties by a series of glycosyltransferases, first on the cytoplasmic face of the ER and then in the ER lumen, once the product is flipped. The core glycan is then released from dolichol and transferred to asparagine residues of nascent proteins by the multimeric oligosaccharyl transferase complex (OST). GMPPB catalyses the formation of GDP-mannose from GTP and mannose-1-phospate; GFPT1 synthesizes UDP-GlcNAc (Uridine diphosphate N-acetylglucosamine). While ALG2, ALG13/14 and DPAGT1 are glycosyltransferases implicated specifically in the N-linked glycosylation of proteins, GFPT1 and GMPPB are also involved in other glycosylation pathways (green colour). Of note, GMPPB is involved in the O-mannosylation pathway, which is required for the glycosylation of α-dystroglycan (α-DG), and thus is of special relevance to the dystroglycanopathies. DOLK, dolichol kinase; DPM, dolichol-phosphate mannose synthase; Fru-6-P, fructose-6-phosphate; GlcN-6-P, glucosamine-6-phosphate; Glu-6-P, glucose-6-phosphate.

5.2 Aims

I reviewed in detail the clinical notes and investigation results of eight patients with CMS due to mutations in *GMPPB* and investigated CMS syndrome-specific CK values within the Oxford CMS cohort. The aims were to describe the clinical phenotype allowing improved recognition of this recently described condition often misdiagnosed as an isolated muscle disorder, and to confirm that measuring serum CK can be useful in differentiating GMPPB-CMS from other CMS subtypes (using the local upper limit of normal range 200 IU/L).

5.3 Patients included in the study

NGS and Sanger screening identified the underlying genetic mutations in *GMPPB* in 8 individuals from 6 different kinships **(Table 5-1)** with similar clinical features and a decremental response of compound muscle action potentials (CMAP) to repetitive nerve stimulation as described previously by our group (Belaya, 2015). Patients 1-5 are White European originating from the UK. Patients 6-8 belong to the same kinship and originate from Iran. Cases 9-11 (Belaya, 2015), who have a muscular dystrophy dystroglycanopathy due to mutations in *GMPPB* but no clear defect in neuromuscular transmission were not included but will be addressed in the discussion. Consent for DNA analysis of DNA and tissue samples and publication of data was obtained from all patients (Section 2.1.1)

5.4 Mutations identified in GMPPB

All cases were autosomal recessively transmitted. A total of 9 different mutations were identified in 8 patients **(Figure 5-2, Table 5-1).** There were 7 missense mutations, one non-sense mutation resulting in a premature stop codon (p.Gln187*), and one splice-site mutation (c.130-3C>G) leading to the production of a truncated protein.

Table 5-1 Clinical features of patients with GMPPB-CMS

		Case 1	Case 2	Case 3	Case 4	Case 5	Case 6	Case 7	Case 8
Mutation, protein		p.Asp27His p.Arg287Trp	p.Arg261Cys Splicing	p.Asp27His p.Val254Met	p.Asp27His p.Leu303Phe	p.Gln187* p.Ile193Thr	p.Pro103Leu	p.Pro103Leu	p.Pro103Leu
Gender		F	F	F	F	F	F	F	M
Age (y)	**presentation**	24	15	20	25	1.5	16	22	31
	current	48	68	28	44	18	43	45	35
Presenting symptoms		Limited march tolerance (influenza)	Unable to run	Unable to get up from the floor and lift weights	Unable to climb up ramps	Acute episode of weakness	Difficulty in climbing stairs, cramps	Difficulty in climbing stairs, cramps	Difficulty in climbing stairs, cramps
Ptosis		No	No	No	Mild, not fatigable**	No	Mild	No	No
Ophthalmoplegia		No	No	No	No	No	Mild	No	No
Facial weakness		No	No	No	No	No	No	No	No
Bulbar weakness		No	No	No	No	No	Mild	No	No
Neck weakness		Mild	No	Mild	Mild	Moderate	No	No	No
Proximal weakness	**UL**	Moderate	Moderate	Moderate	Moderate	Moderate	Mild	Mild	No
	LL	Severe	Severe	Moderate	Moderate	Severe	Moderate	Moderate	Mild
Distal weakness	**UL**	No	No	No	No	Mild	No	No	No
	LL	No	No	No	No	Mild	No	No	No
Axial weakness		Moderate	Moderate	No	Mild	Severe	Severe	Severe	No
Respiratory weakness		No	No	No	No	No	No	No	No
Cognitive impairment		No	No	Mild	No	No	No	No	No
Other features				Cramps	Calves hypertrophy	Cataracts Cramps	Cramps	Cramps	Cramps
Treatment		P, D, S	P, S	P	P, S	P	P	P	P

D, 3,4-DAP; LL, lower limbs; P, pyridostigmine; S, salbutamol; UL, upper limbs. ** Ptosis appeared at age 26 after developing thyrotoxicosis and receiving treatment for it.

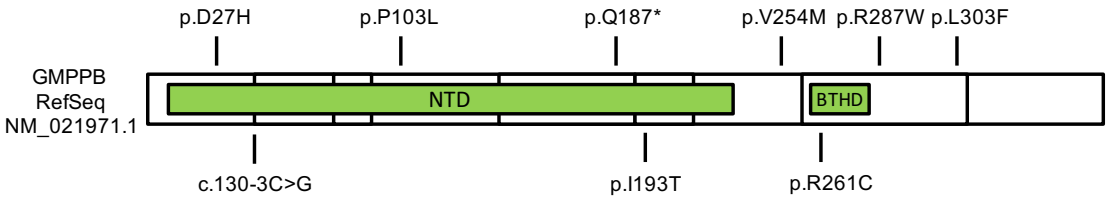


Figure 5-2. Schematic representation of GMPPB and location of mutations

GMPPB (RefSeq NM_021971.1) is a 360-aa polypeptide with 9 coding exons and two predicted Pfam (http://pfam.xfam.org/) functional domains coloured in green. The nucleotidyl transferase domain (NTD) is present in a wide range of enzymes that transfer nucleotides onto phosphosugars. The bacterial transferase hexapeptide domain (BTHD) contains a repeat structure composed of tandem repeats of [LIV]-G-X(4) hexapeptide, which is present in a number of different transferase protein families. Five of the nine mutations described were located within the NTD domain while the rest of mutations were located towards the C-terminal region. GMPPB has another isoform (RefSeq NM_013334.2), which has limited expression in muscle tissue (Carss *et al.*, 2013) and will not be used for the annotation of variants in this study .

5.5 Clinical features

5.5.1 Clinical presentation

Pregnancy and early-life features were uneventful in all patients except in case 4 with congenital hip dislocation and resulting delayed motor milestones. None of the patients were ventilated as infants or had feeding difficulties. The median age of onset was 22 years (range 1.5 - 50 years). Case 1 presented at age 24 years with limited walking tolerance following an influenza illness. Previously her gait was unrestricted. Case 2 was unable to run during her teens and had lumbar hyperlordosis noted from her 20s. Case 3 was unable to get up off the floor and had difficulty lifting heavy objects at age 20 years. She also had decreased walking tolerance and had to rest after 5 minutes of walking. Case 4 had difficulty climbing-up ramps and walking long distances noted from her mid-20s.

Case 5 presented at 18 months with an acute episode of generalised weakness and raised CK. Subsequently, she remained clumsier and slow at school compared to peers. Cases 6-8 presented with gait disturbance (waddling), difficulty climbing stairs, and muscle cramps at the ages of 16, 22 and 31 years, respectively. Of note, even though most patients had onset in adult life, they recall being slower than peers at school and not good at sports.

5.5.2 Pattern of weakness at assessment

All patients had a predominantly limb-girdle pattern of muscle weakness, which was more severe in the lower than in the upper limbs, with moderate to severe impairment and marked waddling gait in some cases. Mild distal weakness was present only in cases 5 and 8. Facial and eye movements were normal in all patients, and only case 6 had mild fatigable ptosis. Two patients complained of occasional double vision (cases 2 and 6), although no ophthalmoparesis was elicited during examination. Neck muscles were mild to moderately weak in 4 patients without manifest flexor/extensor preponderance. Axial weakness was present in 6 patients with moderate to severe lumbar hyperlordosis in 5. Mild swallowing difficulties, in the absence of speech abnormalities, were reported by case 7. Only case 2 suffered from shortness of breath on exertion, although there was a background history of asthma. None of the patients have required respiratory support. Unlike other myasthenic syndromes, most of the patients did not have easily demonstrable short-term fatigability of muscle strength on bed side testing.

5.5.3 Additional clinical features

Episodes of muscle aches and cramps were reported (case 3, 5 and 6-8), mainly in the calves, and activity-induced, such as with walking. Cramps were occasional but variable in

frequency depending on the period, and usually subsided by stretching the affected muscle. Case 4 had hypertrophic calves and thighs on physical examination. Case 5 was diagnosed with cataracts aged 9. Contractures were found only in case 5 with tightness of Achilles tendons bilaterally. Case 3 had mild learning difficulties in school. None of the patients had known cardiac involvement.

5.5.4 Course of disease

The long-term course of disease was generally progressive with gradual deterioration in muscle strength and mobility over time. In addition, there were significant deteriorations during intercurrent illnesses. Case 1 currently walks only for short distances with assistance and requires physical assistance in terms of activities of daily living and self-care. Case 2, with onset in her teens, has been unable to climb stairs for the last decade, and has difficulties in standing from a seated position. Although she could lift loads during her adult life, she developed significant proximal arm weakness in her fifth decade. Case 3 is currently stable on treatment, and mainly finds it difficult to hold heavy objects and walk long distances. Case 4 had a slowly progressive deterioration of her waddling gait, with more recent requirement of a walking stick. Case 5 gradually deteriorated during childhood and adolescence with proximal weakness and mobility problems. Prior to treatment, she had limited walk tolerance, and on a bad day she could only walk around the house and used a wheelchair for distance. Cases 6-8 still walk independently although have had progressive deterioration in their gait over the years. Fluctuations of muscle strength over the course of days and weeks were reported in cases 1-5. They were commonly related to intercurrent viral infections, although they also occurred following no particular precipitant (case 1 and 5). Cases 3, 4 and 6 reported significant worsening of

symptoms with menstruation. Case 6 also reported worsening of symptoms during pregnancy.

5.5.5 Response to treatment

All patients treated with pyridostigmine had a positive response to treatment. The effect was notable in cases 1,3,5,6,7 and 8 but mild in cases 2 and 4. Case 3 increased her endurance so that she can walk up to 10 minutes without fatigue and is able to manage stairs at home independently. She recalls omitting her medication by accident on a few occasions and being much weaker afterwards. For Case 4, walking improved such that she stopped using her walking stick. Her proximal strength in the upper and lower limbs is now graded MRC 5 from a previous MRC score of 4. Case 5 reported improvement in her muscle strength and walking speed, with less fatigability and reduced wheelchair use. After pyridostigmine, Case 6 improved her long distance walking and improvements of ptosis and dysphagia were noted. Cases 1 reported additional benefit from 3,4-DAP (30 mg/day) and salbutamol (0.1 mg/Kg/day), and cases 2 and 4 reported benefit from additional salbutamol (0.05-0.2 mg/Kg/day).

5.6 Investigations

A summary of all investigations is provided in **Table 5-2**.

5.6.1 Neurophysiological studies

All patients had findings consistent with abnormal neuromuscular transmission on electrophysiological testing. Of note, repetitive nerve stimulation (RNS) and single fibre EMG (SFEMG) abnormalities were present only in proximal muscles, while testing of distal

and facial muscles was normal in 4/4 cases tested, in keeping with the clinical absence of facial and distal involvement **(Figure 5-3)**. Repetitive discharges were not observed in any case. Concentric needle EMG examination of affected muscles showed mild to moderate myopathic changes in 7/7 subjects tested. Of note, case 1 had 70% increment in CMAP amplitude following voluntary contraction and high frequency stimulation. Mild post-exercise facilitation was also seen in cases 2, 3 and 6.

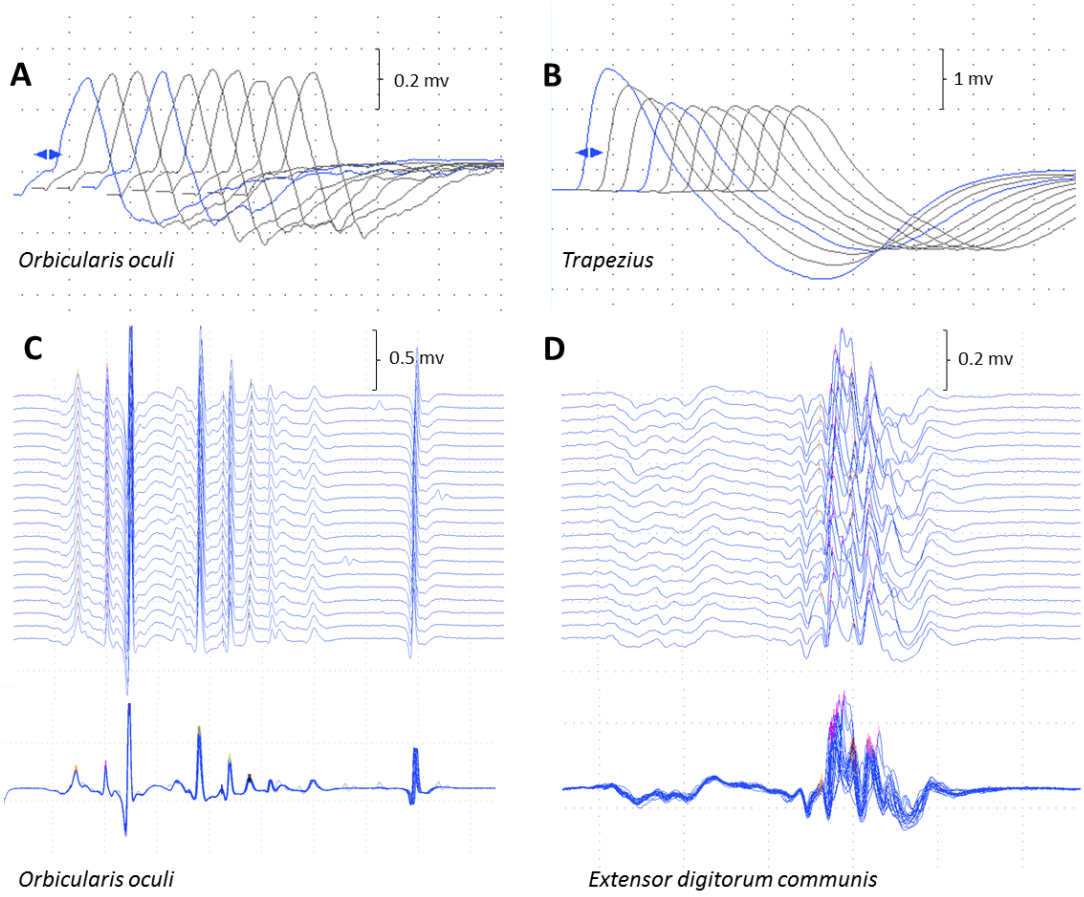


Figure 5-3. Neurophysiological studies in patients with GMPPB-CMS

(A) Repetitive nerve stimulation (RNS) in case 5 was normal in *orbicularis oculi*. **(B)** RNS in *trapezius* showed 25% decrement. **(C)** The stimulated SFEMG study of *orbicularis oculi* was normal (MCD 16.2 µs; 62% of the upper limit of normal). **(D)** SFEMG examination of *extensor digitorum communis* showed instability of the neuromuscular junction (MCD 54.7 µs; 210% of the upper limit of normal), as seen in the superimposed traces.

Table 5-2. Clinical investigations of patients with GMPPB-CMS

		Case 1	Case 2	Case 3	Case 4	Case 5	Case 6	Case 7	Case 8
RNS * Muscle Decrement (%)		Anconeus (42%)	Anconeus (14%)	ADM (<10%) Anconeus (50%)	ADM (<10%) Trapezius (30%)	EDC (37%) FCU (17%) Nasalis (4%) OO (5%) Trapezius (25%)	APB (<10%) Nasalis (<10%) Trapezius (20%)	-	-
SFEMG		EDC Abnormal	EDC Abnormal	OO Normal EDC Abnormal	EDC Abnormal	OO Normal EDC Abnormal	-	-	-
Myopathic EMG		Yes	Yes	Yes	Yes	Yes	Yes	-	-
Cardiac studies		-	Normal ECG	-	Normal ECG	Normal echo	-	-	-
CK (Normal ≤ 200)**		2800	418	1600	2668	4807	701	-	-
Biopsy	**Muscle**	Quadriceps	-	Quadriceps	Quadriceps	Quadriceps	-	-	-
	Age	27	-	25	35	10	-	-	-
	Features	Dystrophic	-	Dystrophic	Dystrophic	Dystrophic	-	-	-
	Alpha-DG	-	-	Reduced	Reduced	Reduced	-	-	-
Muscle MRI	**Age (y)**	-	66	-	42	8	-	-	-
	Result	-	Abnormal	-	Abnormal	Normal	-	-	-

ADM, *abductor digiti minimi*; APB, *abductor pollicis brevis*; CK, creatine kinase; EDC, *extensor digitorum communis*; FCU, *flexor carpi ulnaris*; OO, *orbicularis oculi*. * A decrement of more than 10% in CMAP amplitude indicates a defect in neuromuscular transmission; **The specific reference range for CK in serum depends on individual laboratories but values greater than 200 are in general considered abnormal.

5.6.2 Cardiac studies

No abnormalities were found in two patients undergoing electrocardiogram and one patient undergoing echocardiogram.

5.6.3 Muscle biopsy

Cases 1, 3, 4, and 5 underwent muscle biopsy. All cases showed dystrophic features and reduced labelling for α-dystroglycan when immunohistochemical staining was performed. Secondary reduction of laminin-α2 chain on immunoblotting was noted in case 3 and 4. Cases 3 and 5 showed sparse inflammation and focal upregulation of MHC-I complex, mostly within regenerating fibres. Tubular aggregates, which have previously been described in some forms of CMS due to glycosylation pathway defects, were not found in any of the samples. The muscle biopsy from case 3 is described in detail **(Figure 5-4A-I)**.

5.6.4 Muscle MRI

Muscle MRI from cases 2 and 4, at age 66 and 42 years respectively, showed extensive changes in T1-weighted sequences in pelvis and thighs, with predominant involvement of the posterior compartment of the thighs and relative sparing of certain muscle groups. Case 2 had MRI of the calves that showed additional involvement of the anterior compartment and the superficial posterior compartment. Case 5 had a normal muscle MRI at age 10 years. The muscle MRI studies from case 2 and 4 are described in detail **(Figure 5-5 & 5-6)**.

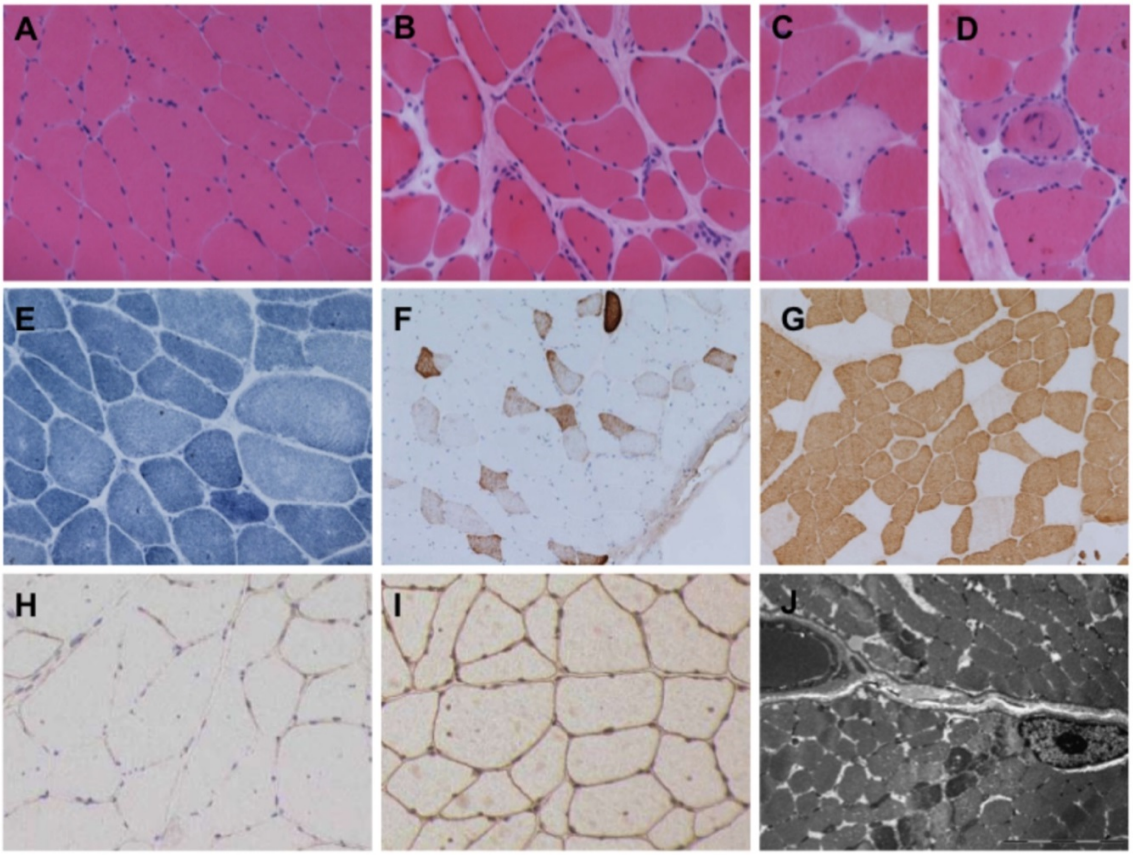


Figure 5-4. Representative images of muscle biopsy

Muscle biopsy from *quadriceps femoris* in case 3 at age 25 years, showing variation in fibre size with occasional atrophic fibres and increase in internal nucleation with haematoxylin and eosin staining **(A)**. There is a focal increase in endomysial collagen **(B)**, occasional necrotic fibres **(C)** and regenerating fibres **(D)**. NADH (*nicotinamide adenine dinucleotide diaphorase)* staining shows mild disturbance of the internal architecture in a number of fibres **(E)**. Numerous fibres express neonatal myosin **(F)**. There is a pattern of slow fibre predominance with these being of generally small size **(G)**. Immunohistochemical staining shows reduced labelling for α-dystroglycan **(H)** compared to β-dystroglycan **(I)**. Ultrastructural examination shows lack of accumulation of granular material, rimmed vacuoles or tubular aggregates **(J)**. Range of fibre size A-I = 30-120 µm; bar in J =5 µm

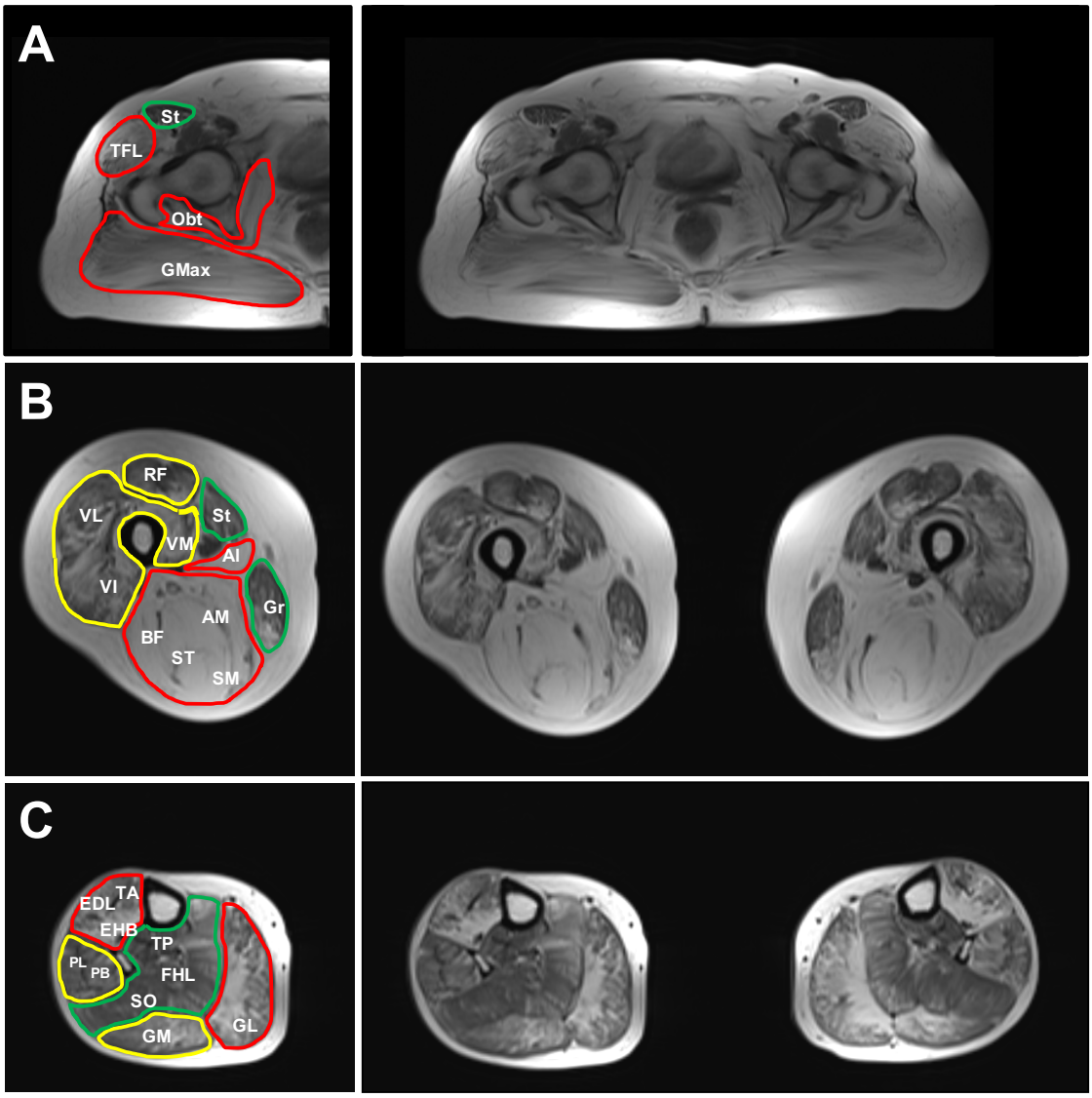


Figure 5-5. Representative images of muscle MRI study from case 2

Individual muscles are labelled on the left side of the figure and coloured according to severity into spared/mild (green), moderate (yellow) and severe (red); complete T1 weighted sequences are shown on the right side. **(A)** In the pelvis, there was prominent involvement of the gluteal muscles, *TFL* and *obturator internus* muscles with relative sparing of *sartorius* muscle. **(B)** In the thighs, there was prominent end-stage appearance of the posterior (BF, ST, SM, AM) and medial (Al) compartments, and moderate increased signal in the anterior compartment (VL, VI, VM, RF), with relative sparing of *sartorius* and *gracillis* muscles. **(C)** In the calves there were confluent areas of increased signal especially in GL, TA, EDL and EHB. Al, *adductor longus*; AM, *adductor magnus*; BF, *biceps femoris*; EDL, *extensor digitorum longus*; EHB, *extensor hallucis brevis*; FHL, Flexor hallucis longus; GM, gastrocnemius medialis; GL, gastrocnemius lateralis; GMax, *gluteus maximus*; Gr

Gracillis; Obt, *obturator internus*; PB, *peroneus brevis*; PL, *peroneus longus*; RF, *rectus femoris*; SM, *semimembranosus*; SO, Soleus; ST, *semitendinosus;* St, *sartorius*; TA, *tibialis anterior*; TP, *tibialis posterior*; TFL *tensor fascia latae*; VI, *vastus intermedius*; VL, *vastus lateralis*: VM, *vastus medialis*.

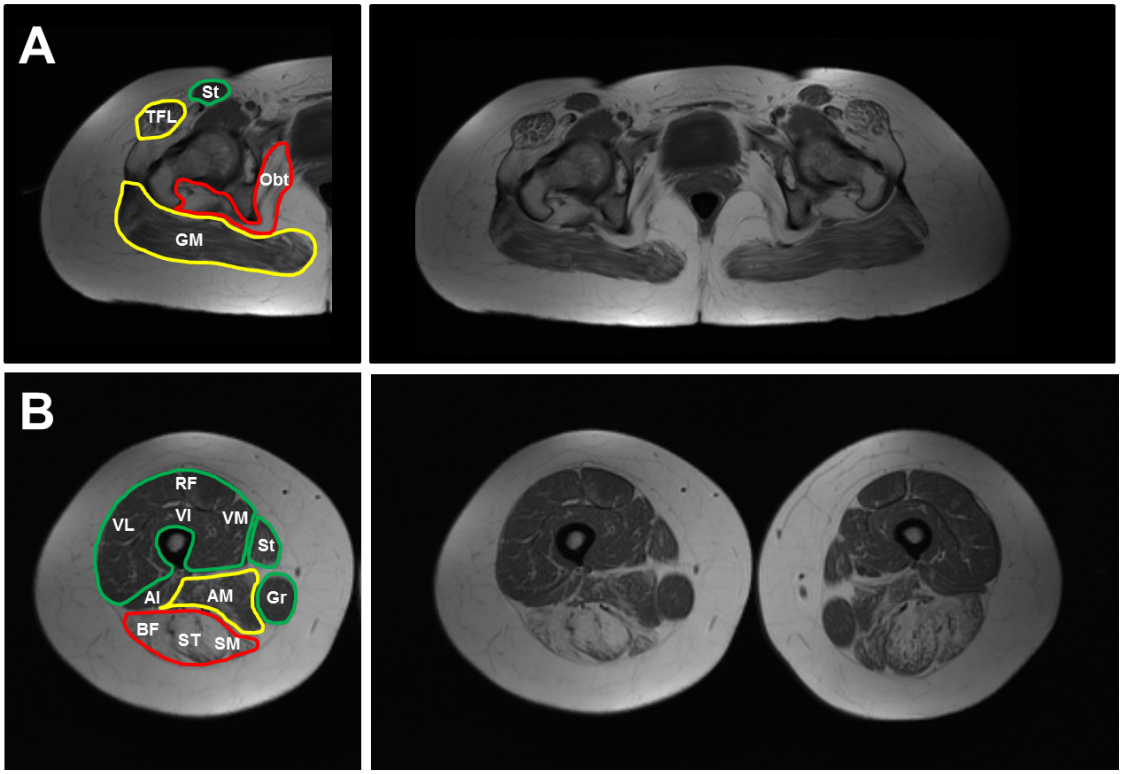


Figure 5-6. Representative images of muscle MRI study from case 4

Individual muscles are labelled on the left side of the figure and coloured according to severity into spared/mild (green), moderate (yellow) and severe (red); complete T1 weighted sequences are shown on the right side. **(A)** In the pelvis, there was prominent involvement of the gluteal muscles, *tensor fasciae latae* and *obturator internus* muscles. **(B)** In the thighs, there is prominent involvement of the hamstrings and adductors and, relative sparing of the anterior thigh musculature, *sartorius* and *gracilis* muscles. AI, *adductor longus*; AM, *adductor magnus*; BF, *biceps femoris*; GM, *gluteus maximus*; Gr *Gracillis*; Obt, *obturator internus*; RF, *rectus femoris*; SM, *semimembranosus*; ST, *semitendinosus;* St, *sartorious*; TFL *tensor fascia latae*; VI, *vastus intermedius*; VL, *vastus lateralis*: VM, *vastus medialis*.

5.6.5 Serum creatine kinase values

The serum CK values of 133 available patients with CMS were reviewed **(Figure 5-7)**. All GMPPB-CMS patients tested had raised creatine kinase levels in serum (2350 ± 660 UI/L; range 418-4807 UI/L). The mean serum CK value of GMPPB-CMS patients was 10.74 times above the upper limit of normal and was significantly higher than in any other CMS subtype ($p<0.001$). Occasionally, patients with DOK7-CMS, slow channel syndrome and GFPT1-CMS had modestly raised CK values. Mean ± SD values are provided in **Table 5-3**.

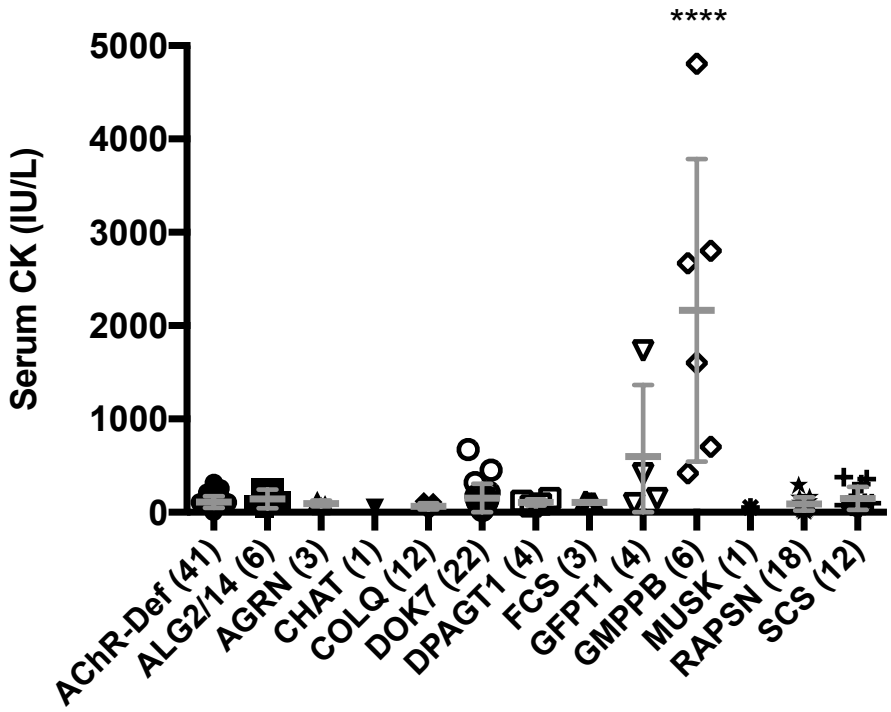


Figure 5-7. CMS subtype-specific serum creatine kinase levels

The figure shows Individual serum CK values for each CMS subtype together with mean ± SD for each CMS subtype. Numbers of patients included from each CMS category are displayed in brackets. The local upper limit of normal range 200 was IU/L. Patients with GMPPB-CMS had greater CK values in serum than any other CMS subtype. One-way ANOVA with Dunnett's multiple comparison test (****$p<0.001$).

Table 5-3. CMS subtype-specific serum creatine kinase levels within the Oxford CMS Cohort

CMS subtype	CMS gene	n	CK range (IU/L) <200 = normal	Mean ± SD
Glycosylation				
ALG-2/14	*ALG-2, ALG14*	6	38-269	145.0 ± 99.4
DPAGT1	*DPAGT1*	4	69-146	106.2 ± 33.7
GFPT1	*GFPT1*	4	95-1731	596.7 ± 769.0
GMPPB	*GMPPB*	6	418-4807	2149 ± 1452.1
Presynaptic				
Choline acetyltransferase	*CHAT*	1	49	-
Synaptic				
Agrin	*AGRN*	3	normal *	-
Endplate AChE deficiency	*COLQ*	12	14-64	43.0 ± 21.2
Postsynaptic				
DOK7	*DOK7*	22	19-672	148.3 ± 152.9
Fast channel syndrome	*CHRNA, CHRNB, CHRND, CHRNE*	3	119, normal *	-
MuSK	*MUSK*	1	54	-
Primary AChR-deficiency	*CHRNA, CHRNB, CHRND, CHRNE*	41	6-258	109.3 ± 60.7
Rapsyn	*RAPSN*	18	18-295	93.7 ± 65.0
Slow channel syndrome	*CHRNA, CHRNB, CHRND, CHRNE*	12	51-376	154.4 ± 126.7

* Specific CK values were not available, but contemplated as normal in the patients' notes.

5.7 Discussion

We describe the clinical and complementary features of a new CMS subtype due to mutations in *GMPPB*, and show that high serum CK values are a key marker for differential diagnosis from other CMS. GMPPB-CMS shares the features of fatigable muscle weakness, significant decrement on RNS and a positive response to cholinesterase inhibitors typical of the majority of patients with CMS. However, there are features that may help differentiate it from the more common CMS subtypes. First, a later clinical onset; second,

presentation is with proximal muscle weakness and, unlike many CMS, with sparing of ocular, bulbar and respiratory muscles; and third, the presence of additional clinical features such as raised CK, dystrophic changes on muscle biopsy, activity-induced muscle cramps, and variable association with cognitive impairment and cataracts.

Most, though not all of the more common forms of CMS, present earlier in life and have characteristic features such as severe ophthalmoplegia (AChR-mutations), respiratory crisis (Rapsyn-CMS, ChAT-CMS and fast channel syndrome) and worsening with pyridostigmine (slow channel syndrome and COLQ-CMS). DOK7-CMS can have a late presentation with proximal weakness (Palace *et al.*, 2007), but lacks the positive response to pyridostigmine and the dystrophic changes on muscle biopsy. Slow channel syndrome (Chaouch *et al.*, 2012) and DOK7-CMS (Klein *et al.*, 2013) can have a myopathic component with non-specific changes on muscle biopsy (such as increased variation in fibre size and core-like areas) and mildly raised CK levels, but these are rarely above 5 times the upper limit of normality. Cramps can also be seen in patients with DOK7-CMS, and may worsen on treatment with ß2-adrenergic agonists.

CMS due to other glycosylation pathway defects (GFPT1 (Senderek *et al.*, 2011; Zoltowska *et al.*, 2013), DPAGT1 (S Finlayson *et al.*, 2013) and ALG2/14 (Cossins *et al.*, 2013)) have clinical similarities to GMPPB-CMS, including clinical presentation, pattern of weakness, and response to treatment. However, GMPPB-CMS has a greater degree of myopathic involvement as shown by the higher CK levels and dystrophic changes on muscle biopsy. This is likely due to the additional role of GMPPB in the O-mannosylation pathway and glycosylation of α-dystroglycan. GFPT1, DPAGT1 and ALG2-CMS can have tubular

aggregates on muscle biopsy (Schiaffino, 2012). These have not been detected in GMPPB-CMS although electron microscopy, which is a more sensitive method to detect tubular aggregates, was only performed in one case at the age of 25 years. However, it is possible that tubular aggregates may appear at later stages of the disease. GFPT1-CMS can display modestly raised CK values (Guergueltcheva *et al.*, 2012) but in our experience these are not as high as seen in GMPPB-CMS. Extensive abnormalities in muscle MRI have also been seen in GFPT1, DPAGT1 and ALG2/14-CMS, but not consistently in the more common CMS subtypes, although some patients with slow channel syndrome and *DOK7* and *RAPSN* mutations can show a wide range of fatty infiltration (Finlayson *et al.*, 2016). It is, therefore, understandable that most of these disorders were classified previously as non-specific myopathies. Cases 3 and 5 were initially misdiagnosed as autoimmune myopathies and treated with immunosuppression without improvement. Serum CK levels are significantly higher in patients with GMPPB-CMS, and so will be helpful in the differential diagnosis. Biochemical studies of transferrin glycosylation on serum samples have been found to be abnormal in only a few of our patients with *DPAGT1* mutations (S Finlayson *et al.*, 2013), but could be abnormal in GMPPB-CMS. However, we believe that a combination of decrement of CMAP with repetitive nerve stimulation on EMG with measurement of serum CK will give simpler and better diagnostic pointer.

There were no heart abnormalities in 3 patients with GMPPB-CMS undergoing routine cardiac studies. However, a small study showed mild cardiac abnormalities in CMS patients with mutations in *GFPT1* and *DPAGT1*, including abnormal electrocardiography (repolarization and deep S waves or marked ventricular hypertrophy by voltage criteria), myocardial fibrosis, diastolic dysfunction and impaired energetics by cardiovascular

magnetic resonance, despite normal systolic function (Lewis *et al.*, 2014). In depth cardiac assessments were not performed on our patients.

Dystroglycanopathies are genetically heterogeneous (Muntoni *et al.*, 2011) and classified into three different groups according to the phenotype (https://www.omim.org/): muscular-dystrophy-dystroglycanopathy with brain and eye anomalies – Type A (MDDGA1 to MDDGA14), muscular dystrophy-dystroglycanopathy with mental retardation – Type B (MDDGB1-B6, and 14) and limb-girdle muscular dystrophy-dystroglycanopathy – Type C (MDDGC1-7,9,12 and 14). In keeping with this, mutations in *GMPPB* underlie a wide clinical spectrum. At the severe end of the spectrum, mutations in *GMPPB* lead to CMD with eye and brain anomalies (MDDGA14). At the middle part, mutations in the GMPPB gene can also cause a less severe congenital muscular dystrophy-dystroglycanopathy with mental retardation (MDDGB14) and a limb-girdle muscular dystrophy-dystroglycanopathy (MDDGC14) (Carss *et al.*, 2013). Patients within this group present during childhood with variable degrees of weakness and cognitive involvement. At the mild end of the spectrum*, GMPPB* mutations cause adult onset LGMD (Cabrera-Serrano *et al.*, 2015) and CMS (Belaya, 2015), with mild or absent intellectual disability. Cases of isolated rhabdomyolysis have also been reported (Cabrera-Serrano *et al.*, 2015). There is no clear genotype/phenotype correlation in disorders due to *GMPPB* mutations, and thus what drives the striking differences in the phenotype remains to be determined. Remarkable intrafamilial variability has also been reported (Diana X *et al.*, 2015).

All subjects harbouring *GMPPB* mutations present with consistent muscle abnormalities. In skeletal muscle, the dystroglycan complex works as a link between the extracellular

matrix and the cytoskeleton, providing structural integrity in muscle tissue (Ibraghimov-Beskrovnaya *et al.*, 1992). Post-translational glycosylation of α-dystroglycan is essential for its function and binding to extracellular ligands (Michele, Barresi, Kanagawa, Saito, Kelley, *et al.*, 2002). A reduction in the glycosylation levels disrupts molecular interactions and contributes to sarcolemma instability and eventual muscle damage. In many cases *GMPPB* mutations do not lead to abnormal neuromuscular transmission (Belaya, 2015). However, it is worth performing neurophysiological studies in all patients to rule out a myasthenic component, which can be treated symptomatically. In keeping with this, it is possible that such patients may have myasthenic weakness assumed to be all myopathic. Finally, several GMPPB-CMS patients had mild facilitation in RNS that could indicate additional presynaptic dysfunction.

The clinical deterioration seen in GMPPB-CMS during intercurrent illnesses is also of interest. This is a classic feature of CMS, but clearly not unique to CMS, as it is also seen in dystroglycanopathies due to *FKTN* mutations (Murakami and Ishigaki K, Shirakawa S, Ikenaka H, Sakauchi M, 2012) and other gene defects (F. Muntoni, personal observation). Interestingly, *FKTN* mutations have shown to compromise AChR clustering due to decreased α-dystroglycan aggregation, with NMJs and neural terminals showing aberrant morphology by electron microscopy and neurophysiological abnormalities (Taniguchi *et al.*, 2006). The progressive nature of GMPPB-CMS, which is not typical of CMS, is slow and probably due to the non-myasthenic muscle component.

In conclusion, this chapter describes the clinical and complementary features of a new CMS subtype due to mutations in the glycosylation-pathway gene *GMPPB*. Patients with

GMPPB-CMS have a comparable phenotype to other CMS subtypes with mutations affecting the early stages of the glycosylation pathway. They harbour additional features, shared with the dystroglycanopathies, including dystrophic changes on muscle biopsy and raised CK levels. This CMS occurs in the absence of classic myasthenic manifestations such as ptosis, ophthalmoplegia or facial weakness and, therefore, is likely to be under-diagnosed. The current investigation suggests performing RNS on weak muscles in patients with the phenotype described (or in patients in whom *GMPPB* mutations have been detected) to determine if there is involvement of neuromuscular transmission. This study adds to the expanding clinical spectrum of *GMPPB* mutations and should facilitate the recognition of a subset of this genetic disorder, which can be treated symptomatically. Finally, this research encourages the investigation of NMJ abnormalities in patients with dystroglycanopathies.

Chapter 6

Unravelling Impaired Mechanisms of Neuromuscular Transmission in CMS due to *MUSK* mutations

6.1 Introduction

The NMJ is a complex and highly specialised synapse between the motor neuron and the muscle fibre. The Agrin-LRP4-MuSK-DOK7 pathway is a signalling pathway essential for the formation and maintenance of the NMJ **(Figure 6-1)**. In this pathway, MuSK phosphorylation signaling plays a central role by orchestrating the events that lead to cytoskeletal reorganisation (Dai *et al.*, 2000) and clustering of AChRs following neural agrin-mediated activation (Wu *et al.*, 2010). MuSK is composed of three IgG-like domains, a frizzled domain (FZD), a short transmembrane domain (TM), a juxtamembrane region (JMR), a kinase domain (KD), and a short C-terminal tail **(Figure 6-2)**.

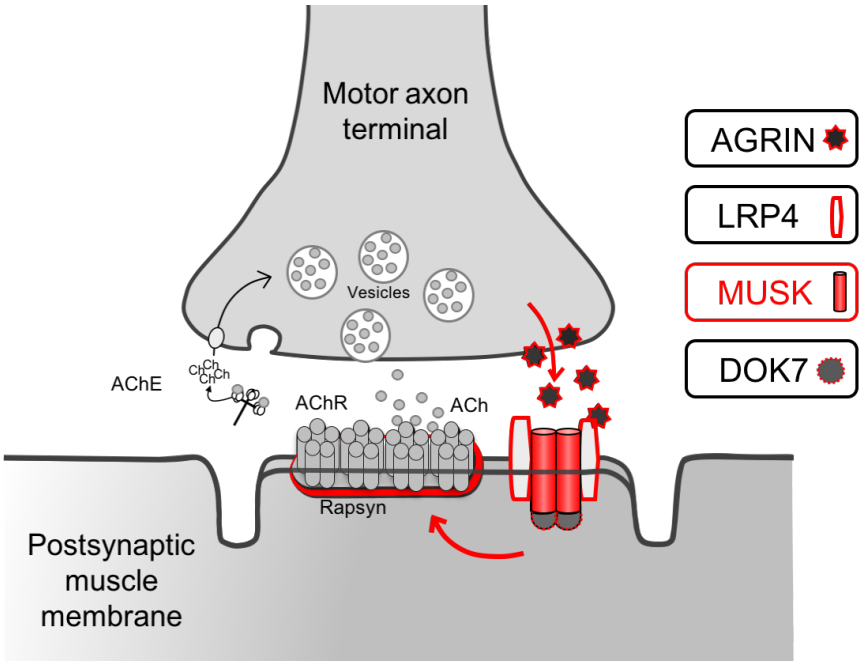


Figure 6-1. Schematic of the NMJ and the Agrin-LRP4-MuSK-DOK7 pathway

6.1.1 MuSK kinase activity and the Agrin-LRP4-MuSK-DOK7 pathway

When the nerve terminal releases agrin **(Figure 6-1)**, an heparan sulphate proteoglycan, this binds to the low-density lipoprotein receptor-related protein 4 (LRP4) on the postsynaptic membrane forming a tetrameric complex (Zong *et al.*, 2012). This enhances the binding of LRP4 to the first IgG-like domain of the muscle-specific receptor tyrosine kinase (MuSK) (Zhang *et al.*, 2012), resulting in MuSK activation via MuSK dimerisation and trans-autophosphorylation of specific tyrosine residues within the cytoplasmic region (Schlessinger, 2000) **(Figure 6-2)**. The increase in the catalytic activity of MuSK creates active binding sites for DOK7, a muscle-specific cytoplasmic adaptor of MuSK with a phosphotyrosine binding domain (PTB). Dimerisation of MuSK-associated DOK7 further stimulates MuSK kinase activity, which propagates the signal downstream through still unknown mechanisms eventually leading to the clustering of AChRs.

MuSK can be also partially activated in the absence of agrin due to its interaction with LRP4. This seems to be important for the for pre-patterning of AChRs prior to innervation (Yang *et al.*, 2001; Yumoto *et al.*, 2012).

6.1.2 Regulation of MuSK kinase activity

MuSK kinase activity is strictly regulated to limit ligand-independent activation through the juxtamembrane region and the activation loop (Till *et al.*, 2002). In addition, a serine phosphorylation site within this loop (Ser751) was recently reported as a modulator of MuSK activity (Camurdanoglu *et al.*, 2016). The juxtamembrane region of MuSK interacts with the kinase core to inhibit kinase activity. The activation loop occupies the active site cleft of MuSK kinase domain by adopting a pseudo-substrate conformation that impedes

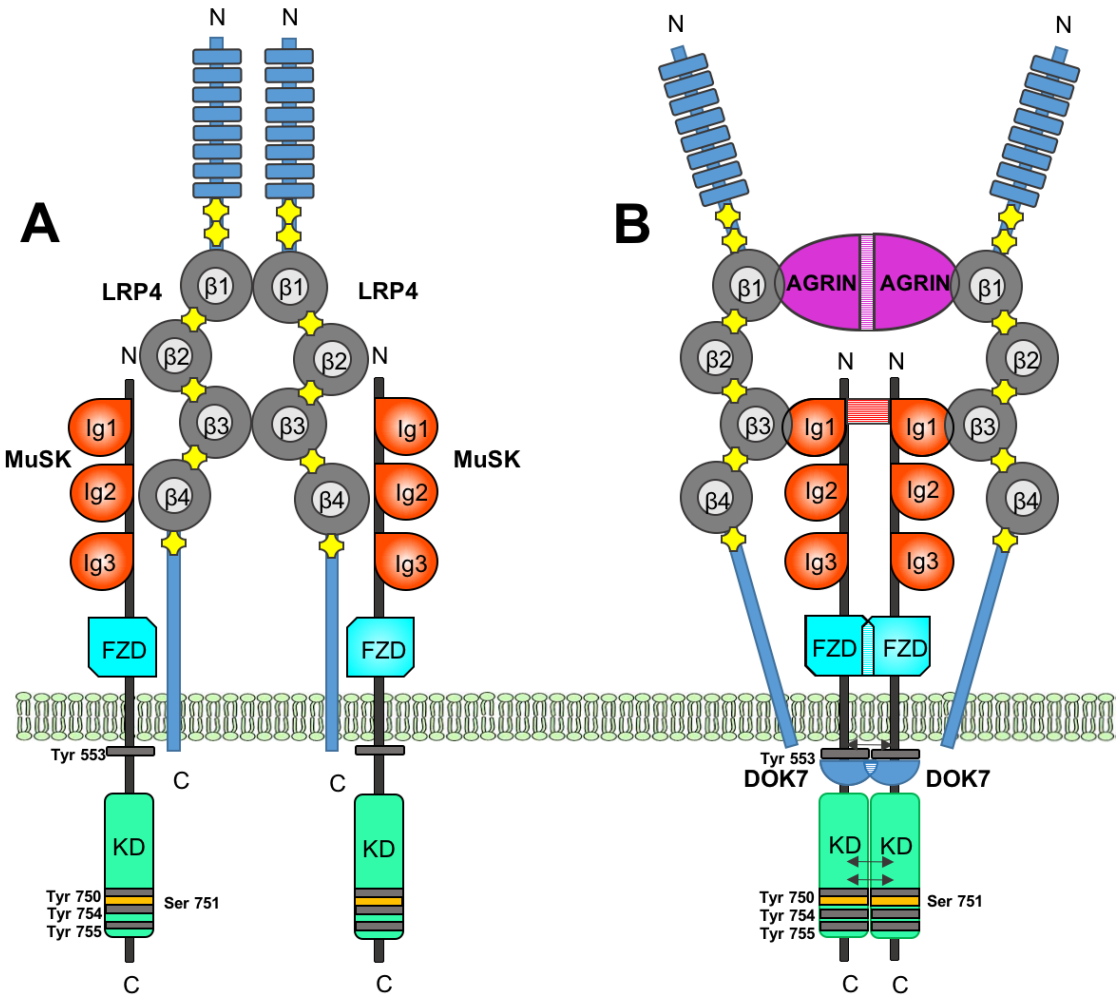


Figure 6-2. Inactive and active states of the LRP4-MuSK complex

(A) LRP4 self-associates and interacts with MuSK in the absence of agrin (inactive state), but is not capable of activating MuSK (Kim *et al.*, 2008). This could be important for AChRs pre-patterning prior to innervation (Yang *et al.*, 2001; Yumoto *et al.*, 2012).

(B) The binding of agrin to the N-terminal region of LRP4 induces a conformational change (active state) promoting the binding between LRP4 and MuSK first IgG-like domain (Zhang *et al.*, 2011). This results in MuSK activation via dimerisation and trans-autophosphorylation of tyrosine residues within the cytoplasmic region (Schlessinger, 2000) through a not fully known mechanism. The increase in the catalytic activity creates active binding sites for other proteins such as DOK7, which amplifies the signal downstream. LRP4 is composed of 8 low density lipoprotein Class A (LDLa) domains (blue) at the N terminus, followed by 4 YWTD ß-propeller domains (grey) bounded by epidermal growth factor-like modules (yellow) and a short C-terminal domain (Springer, 1998)

ATP and other substrates binding thus blocking kinase activation (Till *et al.*, 2002). These regulatory mechanisms seem important to control postsynaptic differentiation of the NMJ (Madhavan and Peng, 2005). Upon agrin release by the nerve terminal, agrin-mediated MuSK activation causes MuSK dimerisation and trans-autophosphorylation of Tyr-553, destabilising the juxtamembrane conformation that prevents phosphorylation of the activation loop **(Figure 6-3)**. The subsequent transphosphorylation of the activation loop (Tyr 750, Tyr 754, Tyr 755) leads to full kinase activation. However, how exactly the kinase domain gets activated after dimerisation is not known.

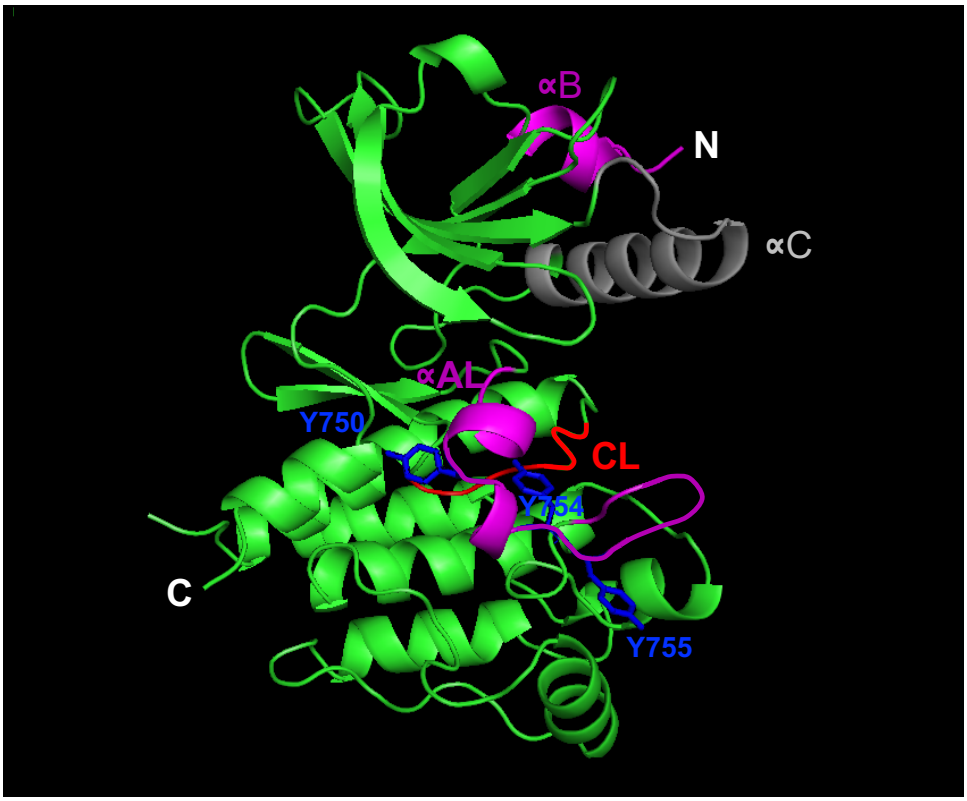


Figure 6-3. Ribbon diagram of MuSK kinase domain and its regulatory elements
MuSK KD structure is made of ß-strands and α-helices (green). MuSK activity is regulated by the juxtamembrane domain at the N-terminus (αB) and the activation loop (αAL) (pink). The tyrosine residues within the activation loop (Tyr-750/754/755) are shown in stick representation (blue). The catalytic loop (CL) is represented in red colour. Structural elements are labelled according to (Till *et al.*, 2002)

6.1.3 Mutations in MUSK

Mutations in *MUSK* are known to cause CMS, but a very limited number of cases have been reported to date (Chevessier *et al.*, 2004; Mihaylova *et al.*, 2009; Maselli *et al.*, 2010; Ammar *et al.*, 2013). This could be related to the fact that severe *MUSK* mutations may be incompatible with life, and mild *MUSK* variants cause no significant manifestations. Half of *MUSK* mutations reported to date are located in the kinase domain, although they have also been described in the IgG and frizzle domains **(Figure 6-4A)**. As for the pathogenic mechanisms, *MUSK* mutations have been shown to diminish expression and stability of MuSK (Chevessier *et al.*, 2004), impair MuSK-DOK7 interaction (Maselli *et al.*, 2010), and reduce sensitivity to Agrin (Ammar *et al.*, 2013).

6.2 Aims

The aims of this study are to elucidate the underlying molecular mechanisms of impaired synaptic transmission in a patient with CMS harboring two novel missense mutations in *MUSK* (p.Cys317Arg and p.Ala617Val) using *in vitro* studies and to direct the appropriate treatment strategy for the patient based on the molecular findings. Previous expression studies and clustering assays in our laboratory failed to show any detrimental effect of variant p.Ala617Val. Therefore, novel approaches with CRISPR-Cas9 cutting-edge technology were used to generate a *Musk* KO muscle cell line lacking endogenous Musk expression for a more precise study of the effects of both mutations.

6.3 Clinical features of the patient with congenital myasthenic syndrome

This female patient had onset of symptoms at birth with hypotonia, severe muscle weakness, respiratory problems and failure to thrive. She underwent tracheostomy after birth due to congenital upper airways obstruction secondary to bilateral vocal cord palsy. She was PEG-fed from an early age. Electromyography showed abnormal RNS of anconeus and deltoid muscles (>20% decrement) and abnormal SFEMG of *extensor digitorum communis* (Mean consecutive difference (MCD) 65.8 µs; normal ≈ 30 µs) suggesting a disorder of neuromuscular transmission. Of note, RNS of distal muscle *abductor digiti minimi* was normal. AChR and MuSK antibodies were not present. At the age of 2 years, she was started on pyridostigmine at 4 mg/kg/day. The initial improvement over the first 48 hours eventually led to a dramatic deterioration in muscle strength with need for ventilation and intensive care support during the following 4 weeks. After discharge, the patient was off-treatment and confined to a wheelchair until the age of 18 years when she was seen at the Oxford Referral Centre for CMS (John Radcliffe Hospital, Oxford, UK). Examination showed fatigable ptosis, mild facial weakness and normal eye movements. She was PEG-fed and carried a permanent tracheostomy. Muscle strength was profoundly decreased proximally in upper and lower limbs with inability to produce movements against gravity (MRC scale 2/5). Muscle strength in distal muscles was only mildly affected (MRC scale 4/5). The patient was unable to walk, and only able to stand for few seconds with bilateral aid. She required continuous use of a wheelchair and was dependent for most activities of daily living. Her QMG score (severity) (Section 2.11.2) was 29 out of 39.

6.4 Identification of *MUSK* mutations

CMS causative genes were screened by bi-directional sequencing of PCR amplicons

(Weatherall Institute of Molecular Medicine DNA sequencing facility). Variants were assessed for conservation across species using ClustalW2 (http://www.ebi.ac.uk/Tools/msa/clustalw2) and pathogenicity using PolyPhen2 (http://genetics.bwh.harvard.edu/pph2). Initial screening for mutations in *CHRNE*, *RASPN*, and *COLQ* was negative.

The sequencing of the coding exons and flanking regions of *MUSK* was performed in the year 2001 following the discovery of MuSK (DeChiara *et al.*, 1996). This revealed that the patient was compound heterozygous for two missense variants in *MUSK* **(Figure 6-4A)**. The first variant was a transition in exon 9, leading to the substitution of Cysteine to a positively charged Arginine in the Frizzled-like cysteine-rich domain (c.949T>C; p.Cys317Arg). The second variant was a transition in exon 14, leading to the substitution of Alanine to Valine in the Kinase domain (c.1850C>T;p.A617V) **(Figure 6-4A)**. Both the Cys317 and Ala617 residues are conserved across species **(Figure 6-4B)**. Sanger sequencing showed segregation of the two *MUSK* variants within the family **(Figure 6-4C)**. The p.Cys317Arg is predicted to disrupt one of the key cysteine residues essential for the formation of the MuSK frizzle domain. The p.Ala617Val variant is predicted to be possibly pathogenic (PolyPhen-2 score 0.685).

None of the variants were listed in the Genome Aggregation Database [(gnomAD, Cambridge, MA (URL: http://gnomad.broadinsitute.org) (Mar 2017)] (Lek *et al.*, 2016), which spans 123,136 exome sequences and 15,496 whole-genome sequences from unrelated individuals sequenced as part of various disease-specific and population genetic studies **(Figure 6-4D)**. Finally, full-length screening of *DOK7* by Sanger sequencing ruled

out mutations in the *DOK7* gene. This was performed due to the clinical similarities of the current patient with DOK7-CMS.

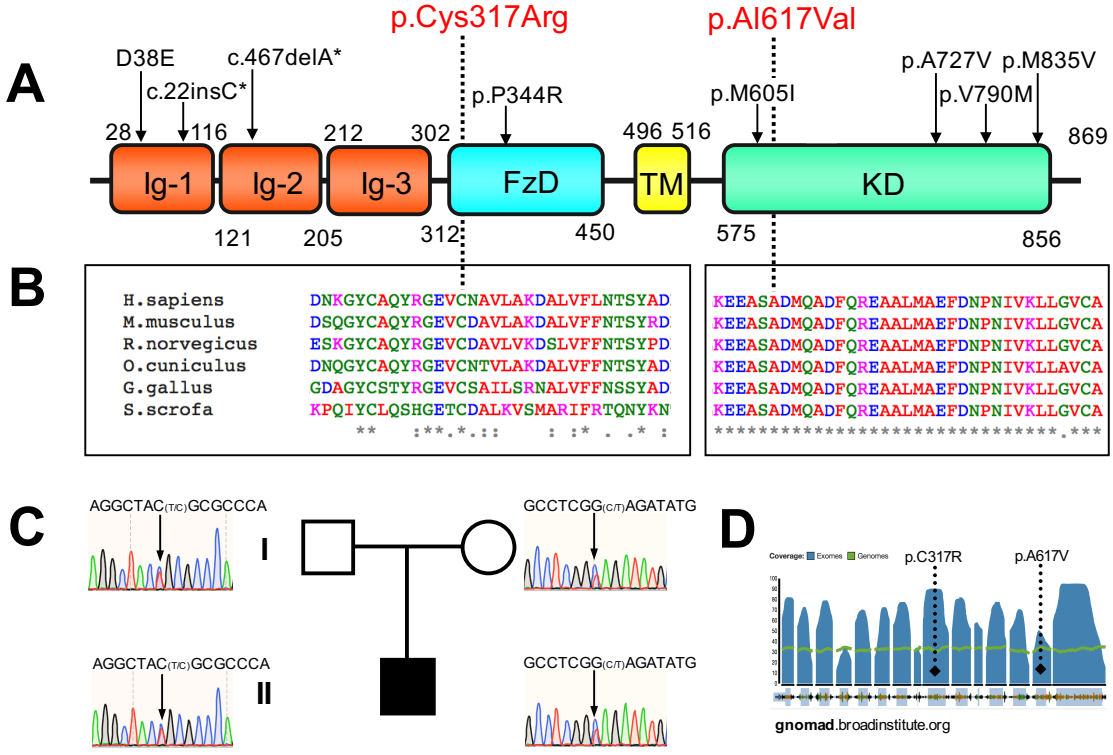


Figure 6-4. MUSK domains structure and conservation

(A) Schematic representation of MuSK drawn to linear scale and location of variants found in the patient (red) and mutations previously reported in the literature (black). MuSK (NP_005583.1) is composed of three IgG-like domains, a frizzled domain (FZD), a short transmembrane domain (TM), a juxtamembrane region (JMR), a kinase domain (KD), and a short C-terminal tail. **(B)** Protein alignments were performed using the ClustalW2 multiple sequence alignment program (http://www.ebi.ac.uk/Tools/msa/clustalw2/). **(C)** Segregation analysis of *MUSK* variants in the family. Pedigree symbols are shaded according to the presence of clinical symptoms. **(D)** Coverage plot from gnomAD exome sequences (blue) and whole-genome sequences (green) corresponding to the individual MUSK exons and location on MuSK variants.

6.5 Molecular modelling of *MUSK* mutations

Modelling of MuSK WT and MuSK variants was performed using PyMOL v1.7.4.5 Edu

software. The Cys317 residue contributes to the formation of an essential disulphide bond for MuSK FzD architecture **(Figure 6-5A)**, which is disrupted by the p.Cys317Arg mutation **(Figure 6-5C)**. The Ala617 residue contributes to the formation of the αC-helix in the N-terminal lobe of the MuSK KD **(Figure 6-5B)**, which may be necessary for the optimal positioning of the critical lysine residues with respect to ATP binding (Till *et al.*, 2002). The p.Ala617Val substitution did not cause changes in distance or clashes with other residues using the crystal structures available **(Figure 6-5D)**.

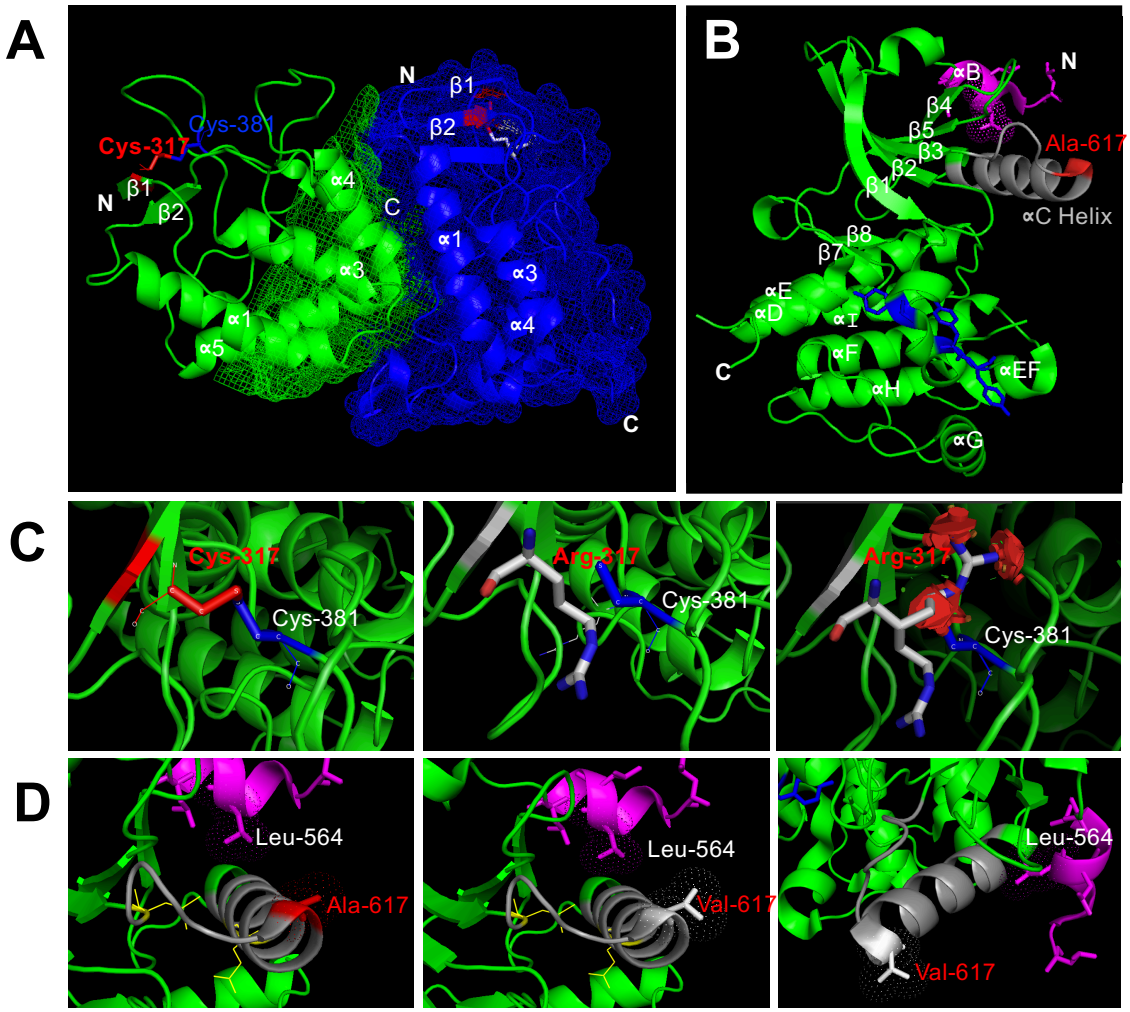


Figure 6-5. Molecular modelling of MuSK variants

(A) Cartoon representation of the MuSK Frizzled-like domain structure (MMDB ID: 76272) with two copies of the asymmetric dimmer coloured in green and blue. Structural elements are labelled in white text according to (Amy L. Stiegler, Steven J. Burden, 2009) and the p.Cys317 residue in red text. **(B)** Cartoon representation of the MuSK KD structure

(MMDB ID: 20673). Structural elements are labelled in white text according to (Till *et al.*, 2002). The αC helix is coloured grey and the p.Ala617 residue red. The tyrosines within the activation loop (Tyr-750/754/755) are shown in blue. The crystal structure of the MuSK KD after dimerisation is not known. **(C)** The residue p.Cys317 forms a disulphide bond with p.Cys381. Modelling of p.Cys317Arg variant shows how the substitution of Cysteine to an Arginine result in the disruption of an essential disulphide bond leading to multiple clashes with the neighboring residues. **(D)** The p.Ala617 residue (red colour) is located in the αC-helix at the N-terminal lobe of the MuSK KD. Using the crystal structure by (Till *et al.*, 2002), the substitution of Alanine to Valine does not result in changes in distance and/or a clashes with other residues.

6.6 Generation of *Musk* KO C2C12 muscle cells using the CRISPR-Cas9n system

C2C12 myoblasts were electroporated with 10µg of each pX335_Cas9n plasmid containing the single strand oligonucleotides MUSK guides A or B (Section 2.3.1) in order to produce spontaneous indels via non-homologous end-joining leading to protein truncation. This was confirmed functionally using the AChR clustering assay, in addition to Sanger sequencing and western blot analysis of MuSK protein. Full details are provided in the appendix section.

6.7 Functional effects of MuSK variants on agrin-induced AChR clustering

6.7.1 Retroviral infection of MuSK KO cell line

The pBabe retroviral expression vector system was used for the generation of retrovirus and subsequent infection of C2C12 *Musk* KO cells with cDNA encoding human MuSK (RefSeq NM_005592) WT or mutant variants, or an empty vector as a control (Section 2.8.6). Visualisation of EGFP was used to confirm successful retroviral infection.

6.7.2 Effect of MuSK variants on AChR clusters formation

In order to assess the functional effect of MuSK variants on the formation of AChR clusters (Section 2.5.11), *Musk* KO myoblasts expressing human WT or mutant MuSK variants were differentiated into myotubes and incubated overnight with full-length human agrin at 1:100 dilution. Retroviral infection of C2C12 *Musk* KO cells recovered protein expression and AChR clustering function **(Figure 6-6A)**. Acquisition of images and automated quantification of AChR clusters (Section 2.13.4) was performed blindly. The p.C317R variant abrogated AChR clustering by reducing the number of AChR clusters greater than 2.5 µm by 95% compared to WT ($p<0.0001$), while the p.A617V variant caused an approximate 10% increase ($p=0.849$).

There were no differences in the total AChR cluster area between MuSK WT and A617V myotubes ($p=0.229$), but the analysis of the average AChR cluster size and RawIntDent (sum of pixels 'values from each AChR cluster) showed that the A617V clusters were approximately 21% smaller in size and 24% less bright compared to WT ($p<0.01$) **(Figure 6-6B, C).** These results suggest that MuSK A617V myotubes present abnormalities in the clustering process that make AChR clusters more fragmented **(Figures 6-7, 6-8 & 6-9)**.

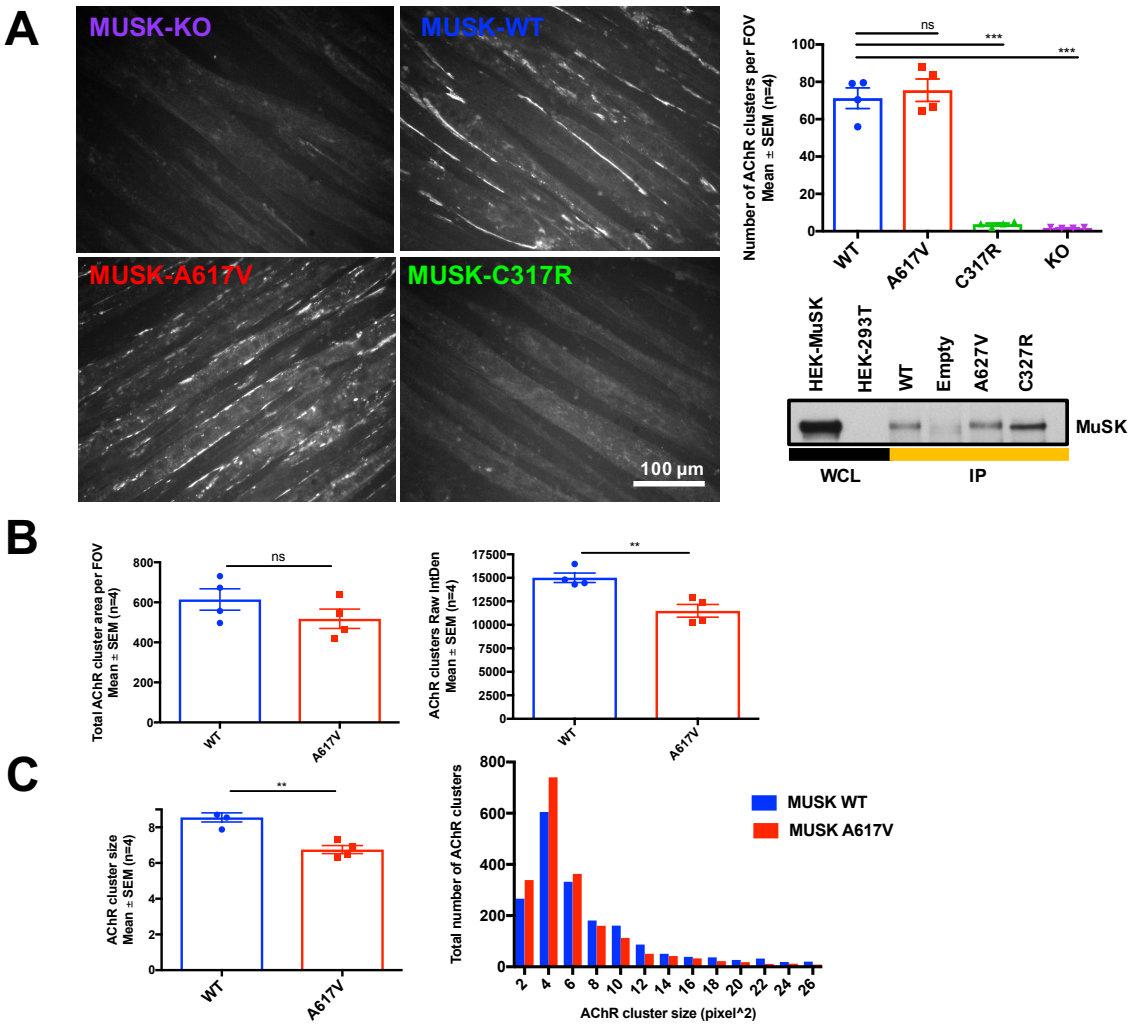


Figure 6-6. Effect of MuSK variants on AChR clustering

(A) The retroviral infection of C2C12 *MusK* KO recovered successfully MuSK protein expression and AChR clustering function. Bar graphs show the quantification of AChR clusters from MuSK WT and variants. Data points represent the mean data from 40 images for each condition per experiment (n=4). One-way ANOVA and Tukey`s multiple comparisons test (***p<0.001).

(B) Quantification of total AChR cluster area per field of vision (FOV) and raw integrated density in MuSK WT and A617V myotubes. Data points represent the mean data from 40 images for each condition per experiment (n=4). Two-tailed unpaired t-test (**p<0.01).

(C) Quantification of the average AChR cluster size in MuSK WT and A617V myotubes (left). Data points represent the mean data from 40 images for each condition per experiment (n=4). Two-tailed unpaired t-test (**p<0.01). The histogram (right) shows the effect of MuSK A617V in the distribution of total AChR clusters size from one experiment.

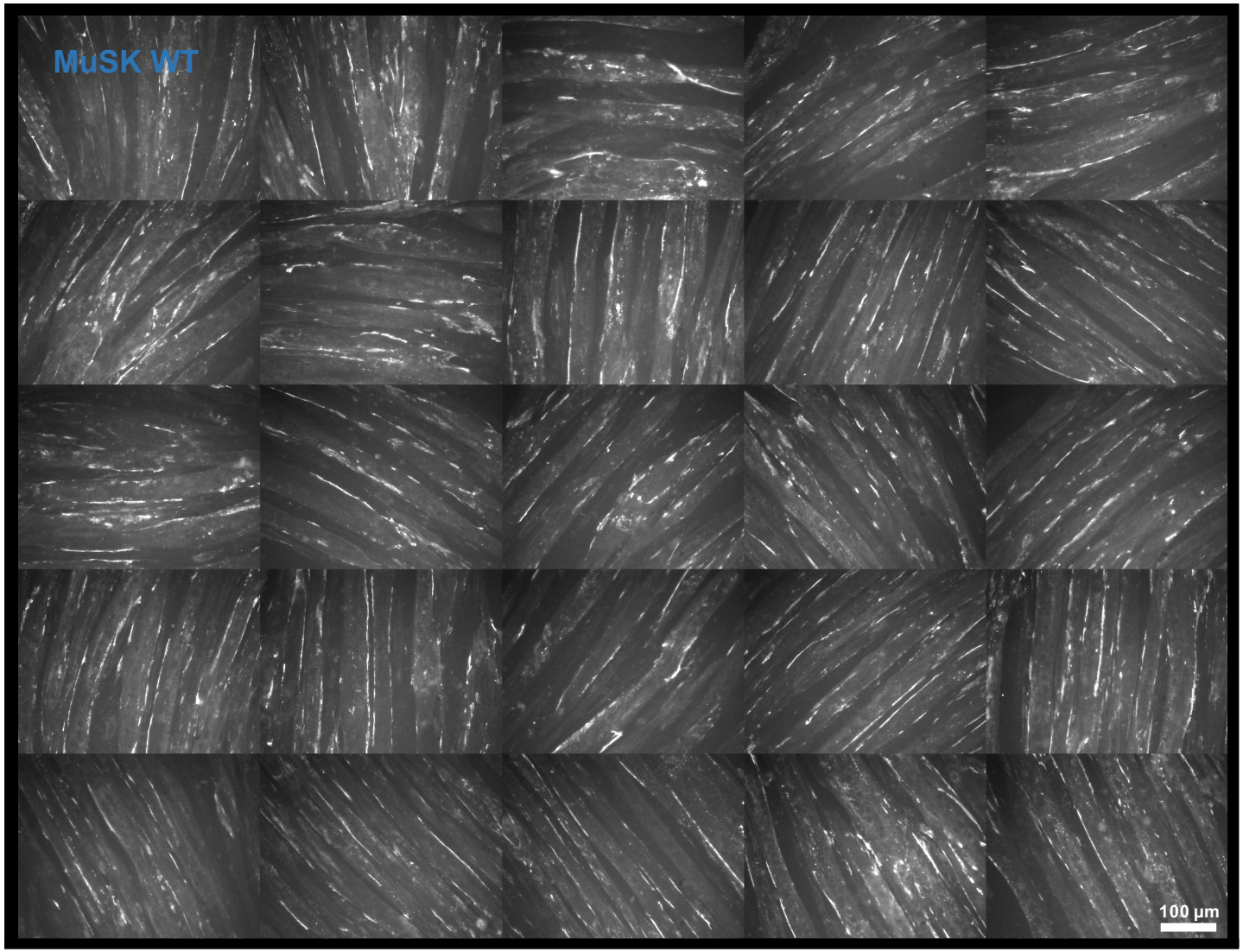


Figure 6-7. Representative images of AChR clusters in C2C12 *Musk* KO cells overexpressing human MuSK WT

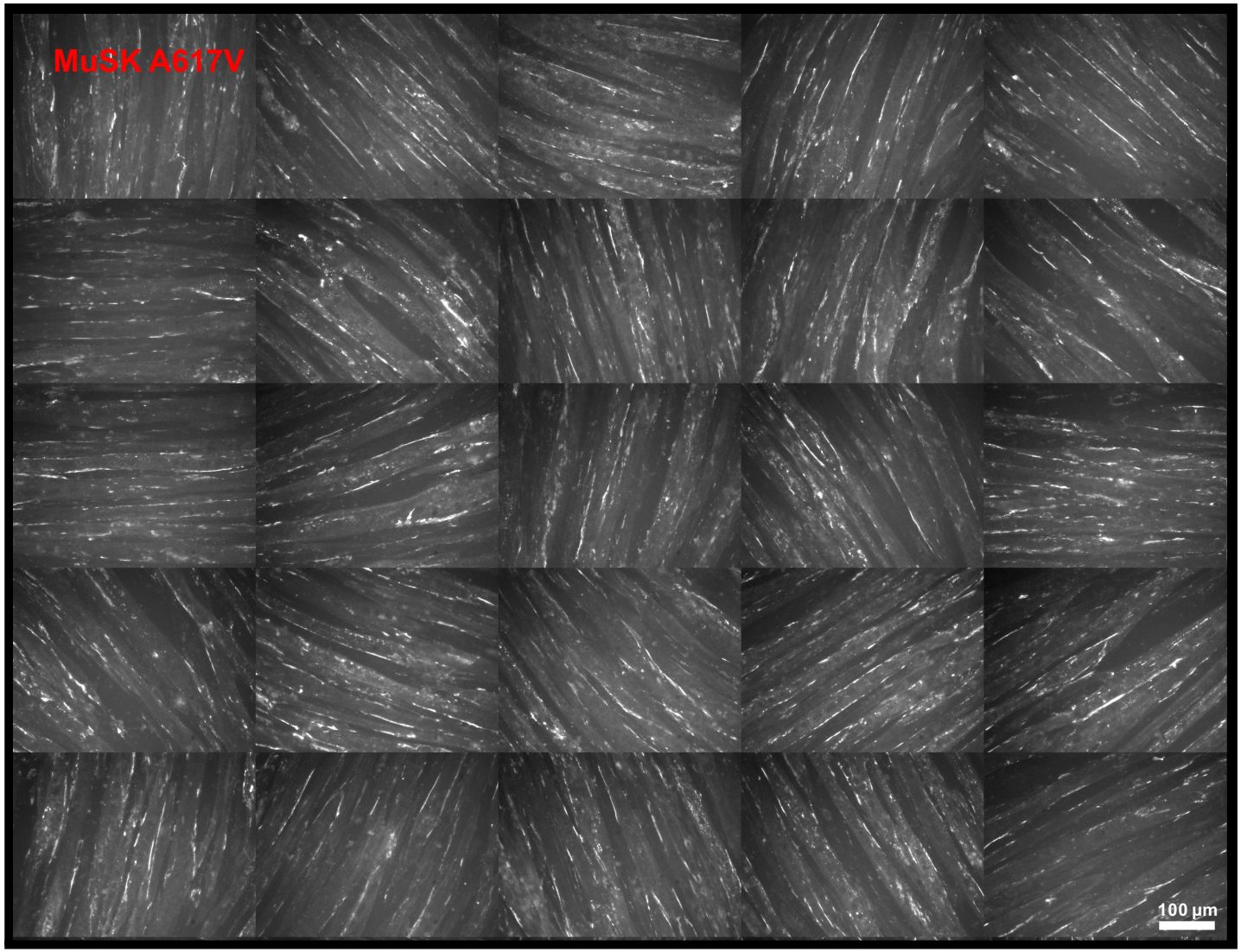


Figure 6-8. Representative images of AChR clusters in C2C12 *Musk* KO cells overexpressing human MuSK A617V

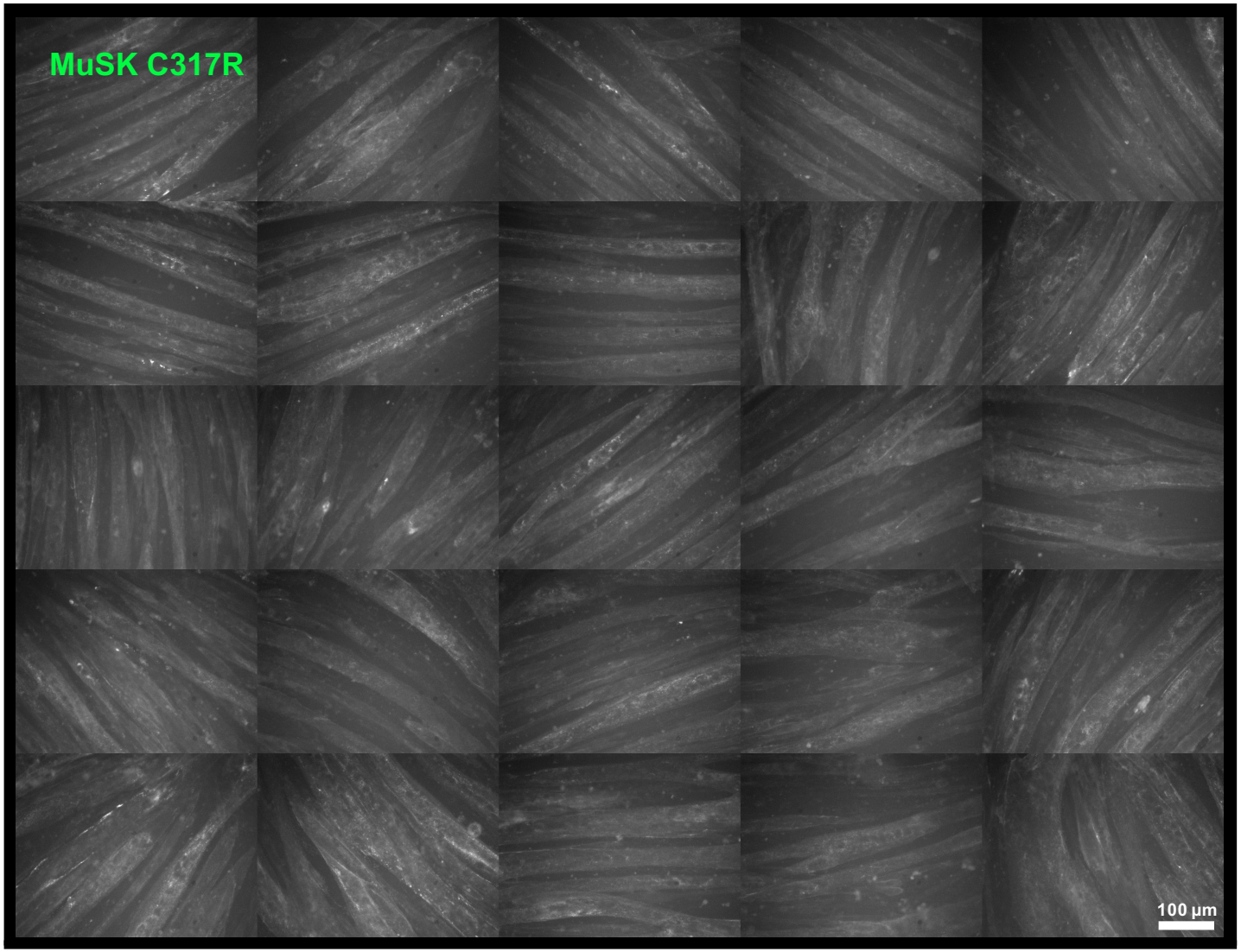


Figure 6-9. Representative images of AChR clusters in C2C12 *Musk* KO cells overexpressing human MuSK C317R

6.7.3 Effect of MuSK variants on AChR clusters formation in the presence of non-saturating concentrations of agrin

The MuSK A617V variant produced AChR clusters significantly smaller than the WT isoform, but there were no differences in the number of AChR clusters after incubation with full-length agrin at 1:100 dilution for 16 hours. To investigate whether the lack of differences was related to the use of saturating concentrations of agrin, a further experiment was conducted using a wide range of agrin dilutions in culture medium.

The analysis of AChR clusters number did not show significant differences between MuSK WT and A617V in any of the agrin dilutions tested **(Figure 6-10)**. However, there was an overall modest increase in the number of AChR clusters in the mutant form in most of the dilutions. *MuSK* KO cells infected with an empty vector were used as a negative control.

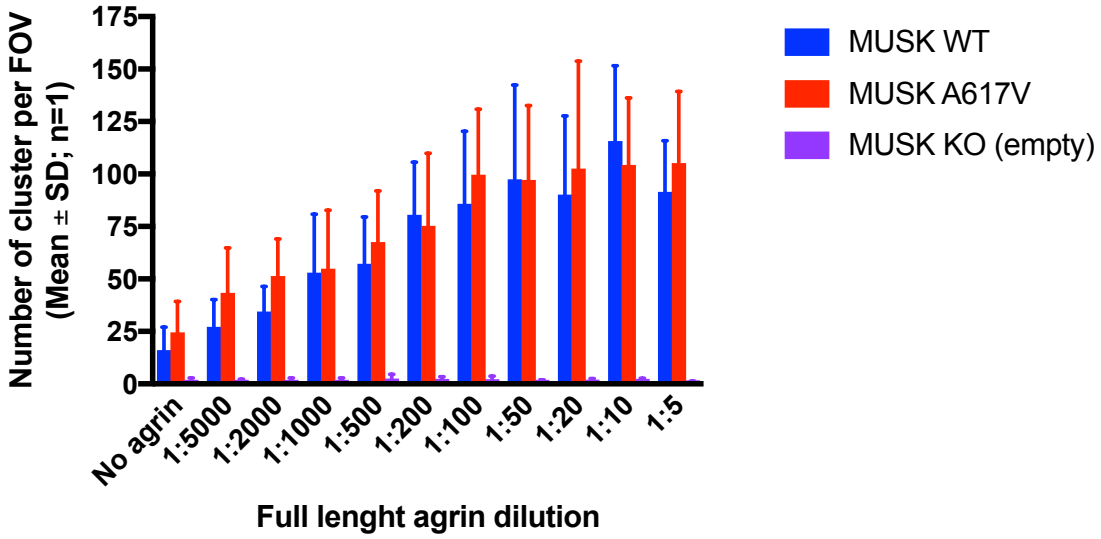


Figure 6-10. Quantification of AChR clusters following agrin titration

C2C12 *MuSK* KO cells overexpressing human MuSK WT or A617V were differentiated into myotubes, incubated overnight with human full-length agrin at different dilutions, and labelled with Alexa Fluor® 594 α-butx. Bar graphs represent the mean data from 20 images for each condition. Two-way ANOVA with Sidak´s multiple comparison test.

6.7.4 Effect of MuSK variants on the stability of AChR clusters

Pyridostigmine (Mestinon®) works by blocking the action of acetylcholinesterase, which increases the level of acetylcholine at the NMJ (Krsti *et al.*, 2013). The current CMS case under study in this chapter had a life-threating deterioration on treatment with pyridostigmine at an early age. Similar observations have been reported in patients with autoimmune MuSK-MG (Evoli *et al.*, 2003). The reasons underlying this phenomenon are unknown but it is possible that pyridostigmine, as seen in patients on chronic treatment, causes disorganisation of the postsynaptic muscle membrane (Chang *et al.*, 1973; Engel *et al.*, 1973; Gillies and Allen, 1977). If an individual with an already abnormal AChR clustering system is started on pyridostigmine, which can disrupt the postsynaptic membrane, this is likely to cause a further reduction on the safety margin of neuromuscular transmission leading to increased muscle weakness, or in this particular case, to a life-threatening deterioration.

Carbachol is an AChR agonist that destabilises and disrupts AChR clusters on cultured myotubes without causing myotube loss (Bloch, 1986). As such, studying the carbachol induced AChR cluster loss on cultured myotubes could be used as a model to study the effect of MuSK A617V substitution on the stability of agrin-induced AChR clusters, and potentially mimic the life-threating situation *in vitro*.

MuSK WT and A617V myotubes were incubated with full-length human agrin at 1:100 dilution for 16 hours to induce AChR clustering. Afterwards, the excess of agrin was washed off and replaced by culture medium containing carbachol (Sigma – Cat. No. C4382) at 0.4 mM concentration. The cells were labelled with Alexa Fluor® 594-α-bungarotoxin and fixed before (0h) or 2, 4, 12 and 24 hours after the introduction of

carbachol.

Carbachol treatment caused an important reduction in the number and total area of AChR clusters compared to baseline for both WT and A617V MuSK myotubes from 4 hours' incubation onwards **(Figure 6-11A)**, with the exception of A617V MuSK myotubes total area at 12 hours (p=0.140). Differences in the average size of AChR clusters compared to baseline were only present at 24 hours after carbachol incubation in A617V myotubes, which could be related to the disruption of smaller clusters and permanence of more stable clusters.

The comparison of AChR clusters between WT and A617V MuSK myotubes relative to 0 hour did not show major differences in the patterns of AChR clusters loss **(Figure 6-11B)**. However, there were minor differences at individual time points in the number of AChR clusters at 2 hours and average size of AChR clusters at 24 hours.

Further experiments in cultured myotubes were conducted using higher concentrations of carbachol up to 2mM for shorter incubation periods in order to have a more incisive effect on AChR clusters loss. After 2 hours of carbachol incubation, there was a significant reduction in the number, total area, and average size of AChR clusters **(Figure 6-12A).** However, the quantification of AChR clusters relative to 0 hour did not show significant differences between WT and A617V myotubes **(Figure 6-12B)**. Overall, these results suggest that the MuSK A617V variant does not affect the stability of AChR clusters after full-length agrin incubation in cultured myotubes. Representative images from carbachol-induced AChR clusters loss experiments are provided for illustration purpose **(Figure 6-13).**

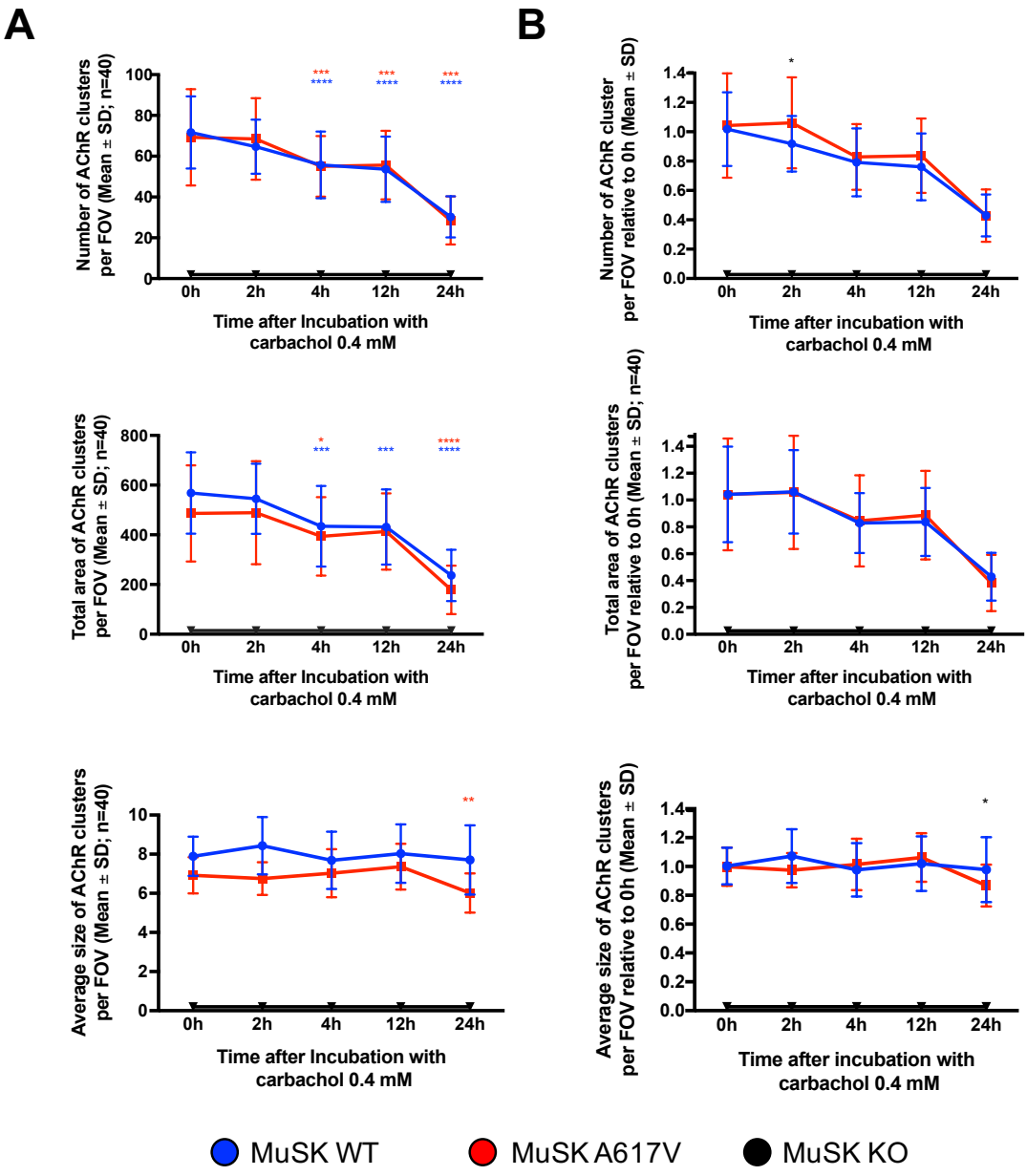


Figure 6-11. Quantification of carbachol-induced AChR-cluster loss (0.4mM) in C2C12 *Musk* KO myotubes expressing human WT and A617V MuSK

Myotubes expressing WT or A617V MuSK were treated with full length agrin for 16 hours, washed-off, and incubated with 0.4mM carbachol. Myotubes were labelled with α-BuTx-594 and fixed before or at 2, 4, 12 and 24 hours after the initiation of treatment. Data points represent 40 images/ condition. Two-way ANOVA with Sidak´s multiple comparisons (****p<0.0001, ***p<0.001, **p<0.01, *p<0.05).

(A) The data are represented as mean ± SD from n=1 experiment.

(B) The data are represented as mean ± SD relative to 0h from n=1 experiment.

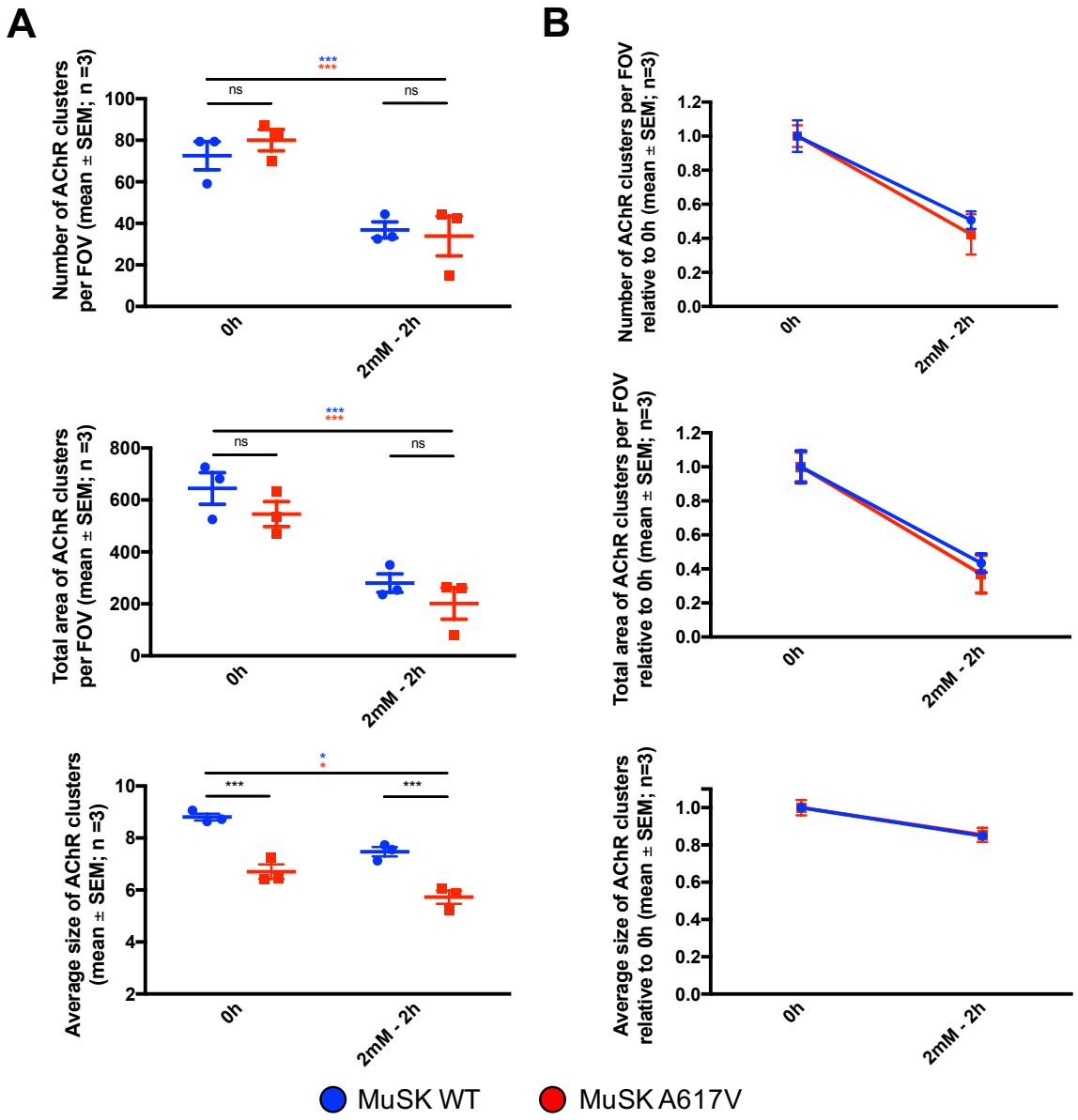


Figure 6-12. Quantification of carbachol-induced AChR-clusters loss (2mM) in C2C12 *Musk* KO myotubes expressing human WT and A617V MuSK

Myotubes expressing WT or A617V MuSK were treated with full length agrin for 16 hours, washed-off, and incubated with 2mM carbachol. Myotubes were labelled with α-BuTx-594 and fixed before or 2 hours after incubation with carbachol. Data points represent 30 images per condition. Two-way ANOVA with Sidak´s multiple comparisons tests (***p<0.001, *p<0.05, ns =not significant).

(A) The data are represented as mean ± SEM from n= 3 experiments.

(B) The data are represented as mean ± SEM relative to 0h from n= 3 experiments.

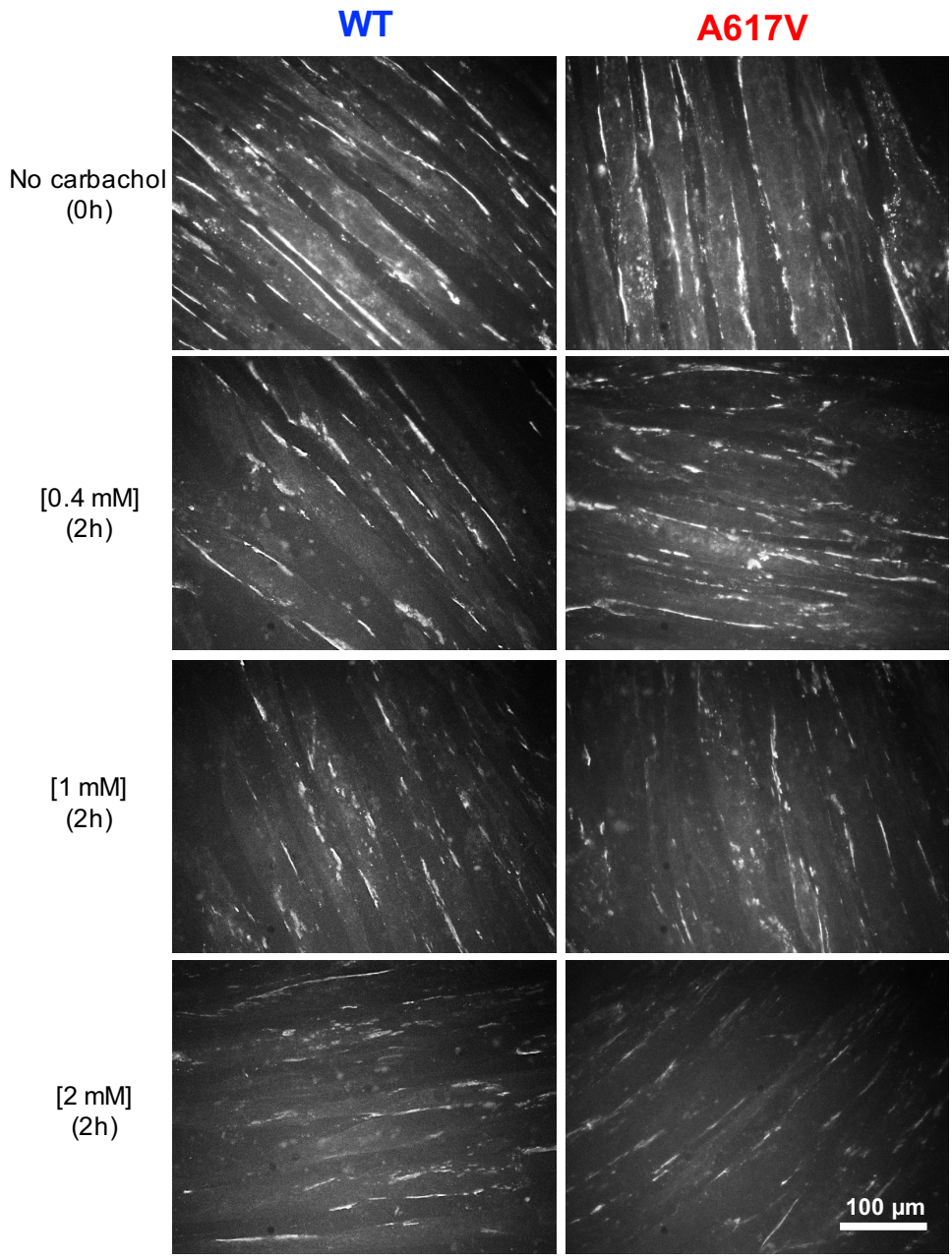


Figure 6-13. Representative images of AChR-clusters loss in C2C12 *Musk* KO myotubes expressing human WT and A617V MuSK

Myotubes expressing WT or A617V MuSK were treated with full length agrin for 16 hours, washed-off, and incubated with 0.4, 1 or 2mM carbachol. Myotubes were labelled with α-BuTx-594 and fixed before or 2 hours after incubation with carbachol at 0.4 mM, 1mM and 2 mM concentrations. The figure shows the disruption of AChR clusters with increasing concentrations of carbachol.

6.8 Effect of MuSK variants on protein expression, localisation and stability

6.8.1 Study of MuSK protein expression and localisation

To investigate whether the functional effects of MuSK variants were related to abnormalities in protein expression, human MuSK WT and mutant variants were expressed in HEK-293T cells and resolved by western blotting **(Figure 6-14A).** MuSK p.A617V showed no significant differences in protein expression compared to WT. On the other hand, MuSK p.C317R expression was significantly reduced by approximately 40% compared to WT in whole cell lysates ($p<0.01$). An additional immunofluorescence experiment using human WT and mutant mCherry-tagged MuSK expression constructs in HEK-293T cells showed that MuSK p.C317R failed to express correctly at the cell surface remaining mostly intracytoplasmic **(Figure 6-14B; green arrows).** This was confirmed by pull-down assays from the cell surface (Section 2.5.7) showing a dramatic reduction in the amount of MuSK being immunoprecipitated **(Figure 6-14C).** No abnormalities were seen for the A617V variant. Overall, this suggests that severe reduced cell surface expression is the primary pathogenic mechanism responsible for the functional abnormalities seen on the AChR clustering assay. This confirms, as seen in the molecular model, the importance of the p.Cys317 residue for the structural integrity of MusK.

6.8.2 Study of MuSK protein stability

A cycloheximide chase assay (Section 2.5.9) over a 24-hour incubation course was conducted to evaluate the stability of MuSK A617V compared to WT in HEK-293T cells. This showed lack of significant differences in protein expression at 12 and 24 hours compared to baseline between the WT and mutant proteins **(Figure 6-14D)**.

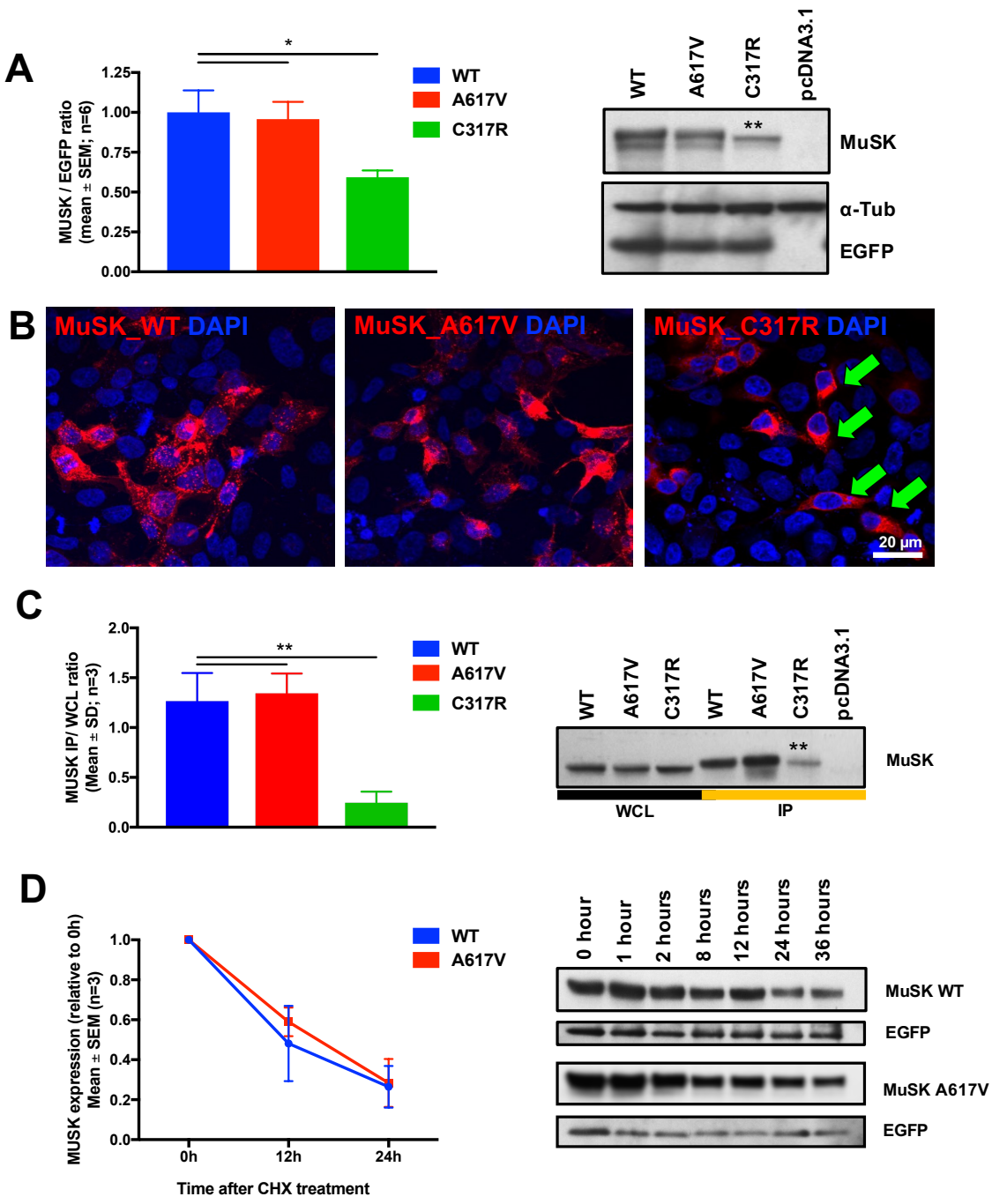


Figure 6-14. Effect of MuSK variants on protein expression, stability and localisation

(A) Human MuSK (RefSeq NM_005592) WT and mutant constructs were transfected in HEK-293T cells and resolved by western blot with antibodies to MuSK, EGFP, and α-tubuline. There was no difference in protein expression levels between MuSK WT and A617V. MuSK C317R expression was significantly reduced to 59.28 ± 4.27% compared to WT. Mean transfection efficiency was normalised through co-expression with EGFP. The results (ratio MuSK/EGFP) are given as mean ± SEM relative to WT from n=6 (**p<0.01).

(B) MuSK-WT and A617V expressed correctly at the cell surface of HEK-293T cells after PEI transfection of WT and mutant pMUSK-mCherryN1 constructs, while MuSK C317R remained mostly cytoplasmic (green arrows). Cell nuclei were stained with DAPI.
(C) Pull-down of MuSK C317R from the cell surface of HEK-293T was reduced to 19.43 ± 8.78% compared to WT. The results (Ratio IP: WCL) are represented as mean ± SEM from n=3 experiments. One-way ANOVA and Dunnett´s multiple comparisons test (**p<0.01).
(D) MuSK protein expression relative to baseline did not show significant differences between MuSK WT and A617V after incubation for 12 and 24 hours with cycloheximide at 20 µg/ml. The results are shown as mean ± SEM relative to WT from n=3 experiments.

6.9 Effect of MuSK A617V on MuSK interaction with LRP4 and DOK7

It is possible that the MuSK p.A617V variant is causing abnormalities in AChR clustering by impairing protein interaction with other key partners of the Agrin-LRP4-MuSK-DOK7 pathway. This was investigated by co-immunoprecipitation assays (Section 2.5.7) from the surface of HEK-239T cells transiently transfected with plasmids encoding human MuSK and LRP4, or human MuSK and DOK7 constructs.

The results showed that MuSK p.A617V had no major effects on the amount of LRP4 or DOK7 being pulled-down compared to MuSK WT **(Figure 6-15**). A weak signal was observed in the LRP4-EGFP and DOK7-EGFP only lanes in probable relation with non-specific binding of EGFP to the magnetic beads. This is unlikely to affect the interpretation of the results.

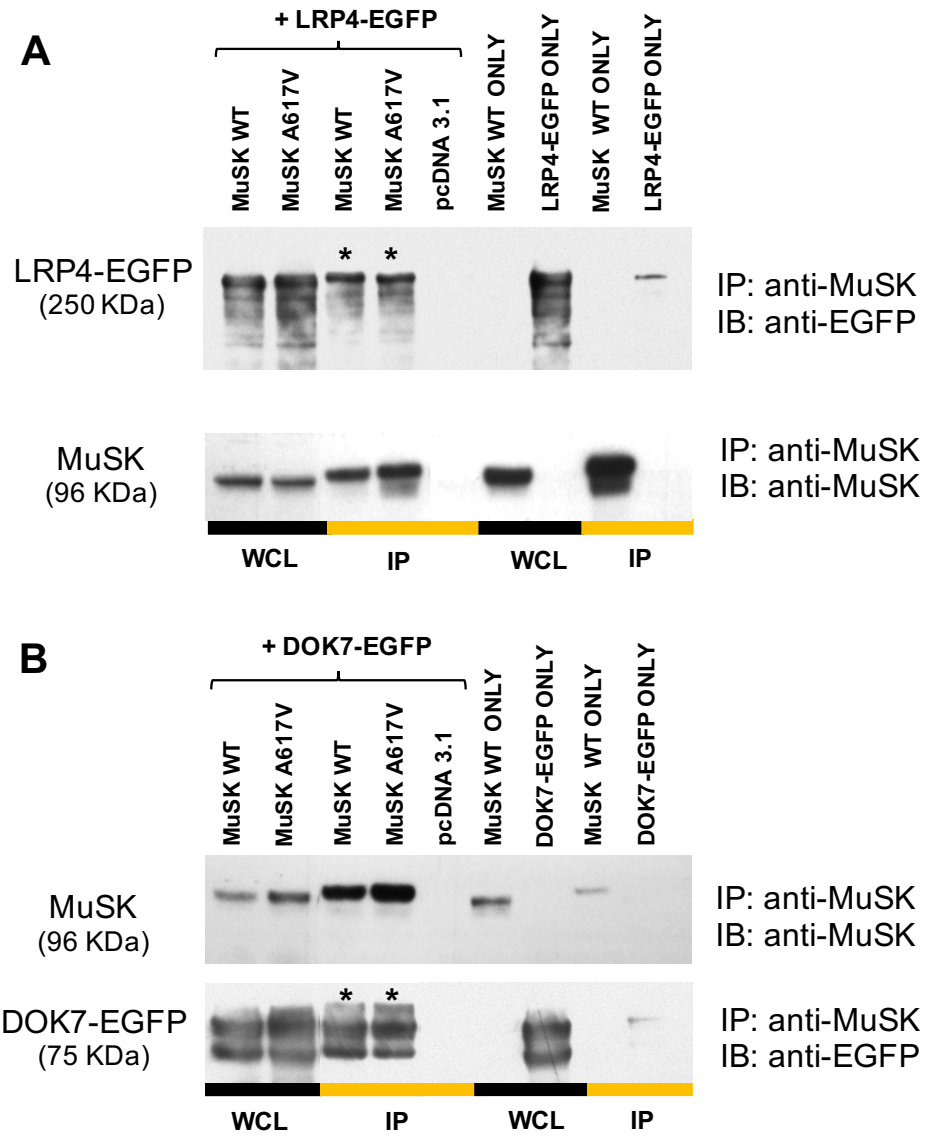


Figure 6-15. Coimmunoprecipitation assays of MuSK WT and variants with LRP4 and DOK7

(A) LRP4-EGFP was successfully co-immunoprecipitated from the surface of HEK-293T cells expressing both MuSK and LRP4-EGFP using an anti-MuSK antibody and detected with anti-EGFP antibody. MuSK p.A617V had no effect on the amount of LRP4-EGFP being pulled-down (*) suggesting no impairment of protein interaction. WCL were used as loading controls.

(B) DOK7-EGFP was successfully co-immunoprecipitated from the surface of HEK-293T cells expressing both MuSK and DOK7-EGFP with an anti-MuSK antibody and detected with an anti-EGFP antibody. MuSK p.A617V had no effect on the amount of DOK7-EGFP being pulled-down (*) suggesting no abnormalities on protein interaction.

6.10 Effect of MuSK A617V on MuSK phosphorylation

MuSK tyrosine phosphorylation was investigated to elucidate whether abnormalities in kinase signalling could explain the functional effect of MuSK variants on AChR clustering.

6.10.1 Study of MuSK phosphorylation in HEK-293T cells

Co-immunoprecipitation experiments in HEK-293T cells (Section 2.5.8) overexpressing MuSK and LRP4, following incubation with full length agrin at 1:100 dilution for 1 hour, showed that MuSK tyrosine phosphorylation was significantly increased by approximately 2.14 fold ($p<0.01$) in the p.A617V variant compared to WT **(Figure 6-16A)**. Interestingly, this effect was seen independently of agrin incubation **(Figure 6-16B)**, which suggests that MuSK A617V is constitutively activated.

A further pull-down experiment was conducted where MuSK was co-expressed with DOK7 or expressed alone. This showed no differences in tyrosine phosphorylation between MuSK WT or A617V when co-expressed with DOK7 **(Figure 6-17A)** or expressed alone **(Figure 6-17B)**. Overall, these results suggest that MuSK A617V affects MuSK tyrosine phosphorylation when interacting with LRP4.

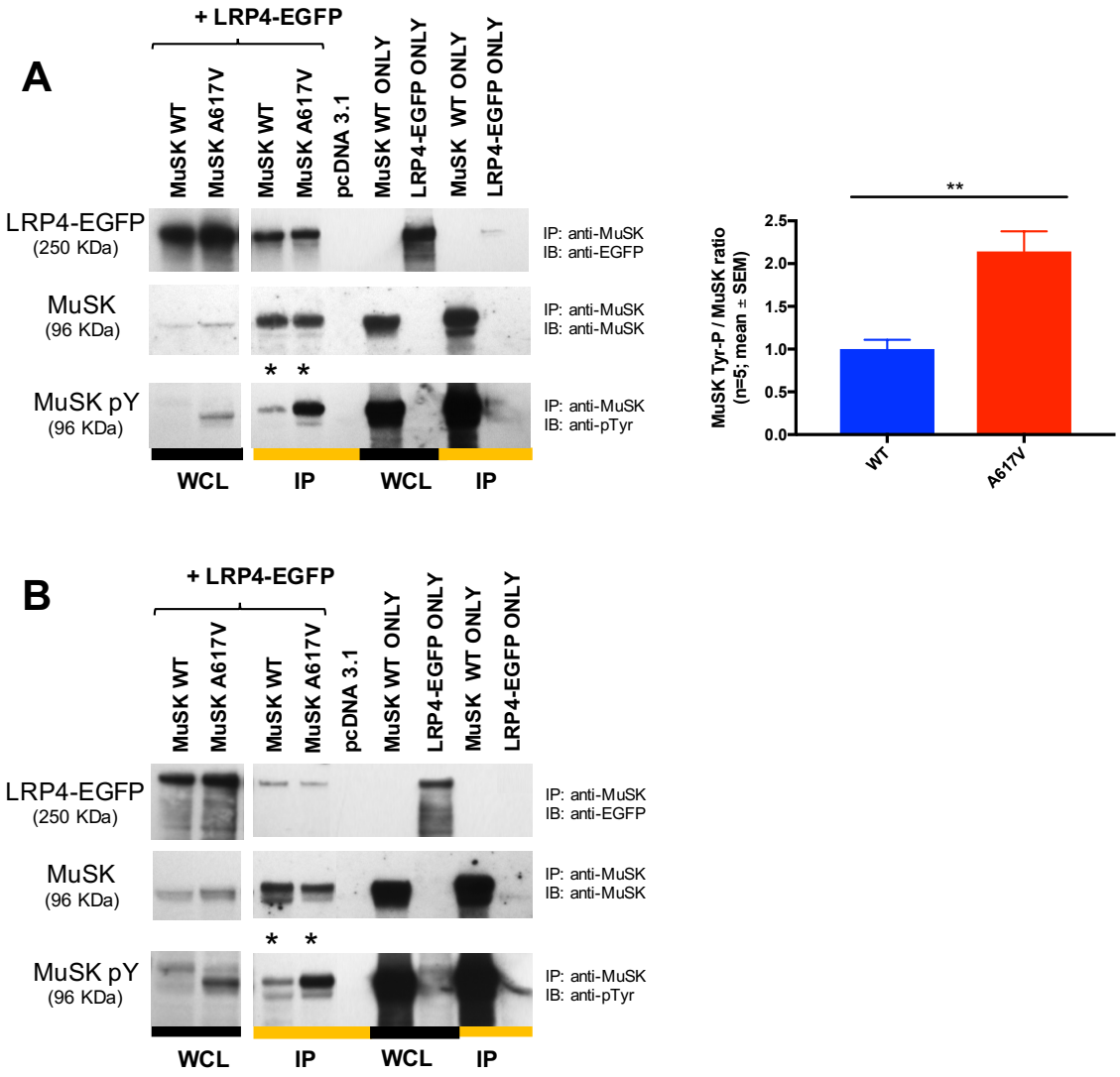


Figure 6-16. Effect of MuSK A617V variant on MuSK tyrosine phosphorylation in HEK-293T cells co-expressing LRP4-EGFP

HEK-293T cells were cotransfected with the above constructs and incubated with full-length human agrin for 1 hour. Subsequently, cell lysates were coimmunoprecipitated with an anti-MuSK antibody, and analysed by western blotting with antibodies to P-Tyr, MuSK and EGFP.

(A) Densitometry analysis showed that MuSK tyrosine phosphorylation was significantly increased in the A617V variant compared to WT (*). Results are shown as mean ± SEM relative to WT from n=5 experiments. One-way ANOVA and Dunnett´s multiple comparisons test (**p<0.01).

(B) Tyrosine phosphorylation was also increased in the MuSK A617V variant in the absence of agrin incubation (*).

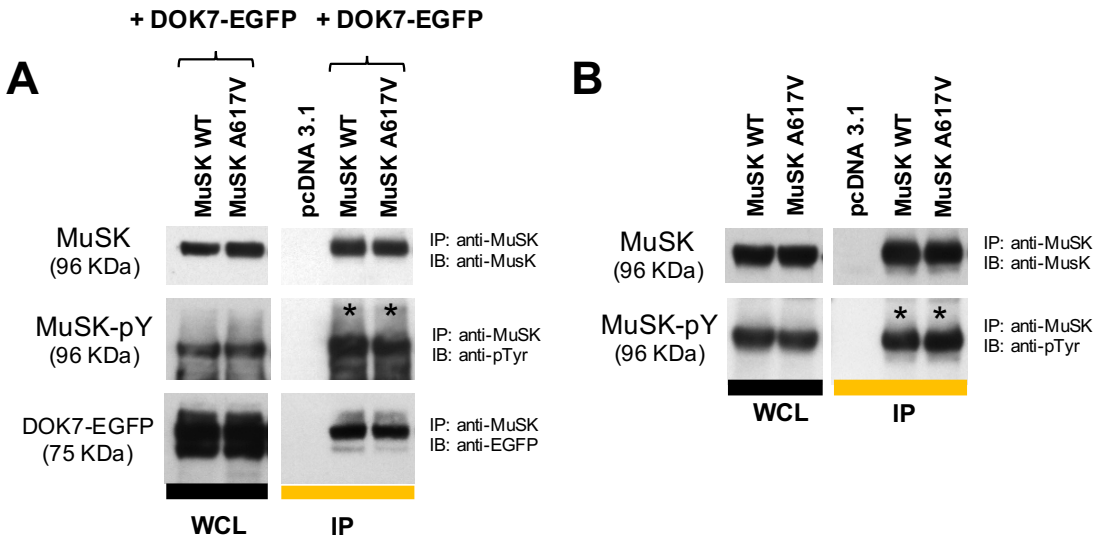


Figure 6-17. Effect of MuSK A617V variant on MuSK tyrosine phosphorylation in HEK-293T cells co-expressing DOK7-EGFP or alone.

HEK-293T cells were cotransfected with the above constructs and incubated with full-length human agrin for 1 hour. Subsequently, cell lysates were coimmunoprecipitated with an anti-MuSK antibody, and analysed by western blotting with antibodies to P-Tyr, MuSK and EGFP.

(A) Densitometry analysis showed no differences in tyrosine phosphorylation (*) between MuSK WT and MuSK A617V when MusK was co-expressed with DOK7-EGFP.

(B) Densitometry analysis showed no differences in tyrosine phosphorylation (*) between MuSK WT and MuSK A617V when other proteins were not co-expressed.

6.10.2 Study of MuSK phosphorylation in C2C12 muscle cells

MuSK A617V was previously shown to be constitutively activated in HEK-293T cells. In order to assess the effect of MuSK variants in a more physiological environment, MuSK tyrosine phosphorylation was studied in C2C12 *Musk* KO myotubes infected with retrovirus expressing human MuSK (RefSeq NM_005592) WT or mutant constructs in the absence and presence of full-length agrin incubation.

6.10.2.1 Constitutive activation of MuSK in C2C12 muscle cells

MuSK tyrosine phosphorylation was studied in WT and A617V myotubes in the absence of agrin incubation using pull-down assays (Section 2.5.8). The results showed increased signal for tyrosine phosphorylation in the A617V variant **(Figure 6-18)**. This suggests that MuSK A617V is constitutively activated in muscle cells in keeping with previous observations in HEK-293T cells.

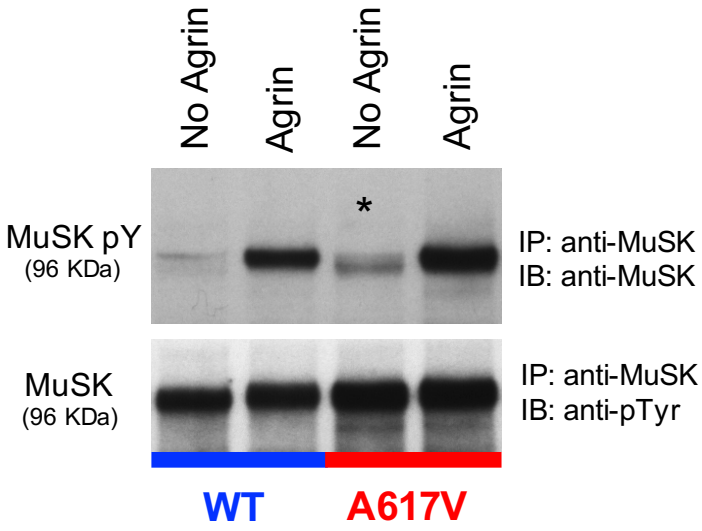


Figure 6-18. Effect of MuSK A617V on baseline MuSK kinase activity in muscle cells

C2C12 *MuSK* KO myoblasts infected with retrovirus expressing WT and A617V human MuSK constructs were differentiated into myotubes. Protein lysates were prepared, immunoprecipitated with anti-MuSK antibodies and analysed by western blot with antibodies to phosphotyrosine and MuSK. Representative image from n=3 experiments showing increased tyrosine phosphorylation in the A617V variant (*).

6.10.2.2 Temporal activation profile of MusK in C2C12 muscle cells

The aim of this experiment was to study the repercussions of MuSK constitutive activation on MuSK tyrosine phosphorylation following incubation with full-length human agrin. Since the abnormalities in AChR clustering were observed 18 hours after agrin incubation

(Section 6.7.2), this was evaluated during a 24-hour period using pull-down assays at different time points (full details in Section 2.5.8).

The analysis of the temporal activation profile of MuSK over a 24-hour period following incubation with full-length human agrin showed significantly different patterns of MuSK tyrosine phosphorylation between WT and A617V myotubes (two-way ANOVA repeated measures; p=0.0031) **(Figure 6-19A)**. An initial faster increase in MuSK kinase activity after incubation with agrin was observed in A617V myotubes compared to WT. This was followed by a faster and deeper decrease from 2 hours onwards.

The A617V substitution was previously shown to cause a constitutive activation of MuSK kinase activity in both HEK-293T and muscle cells. The current findings of decreased MuSK tyrosine phosphorylation in muscle cells from 2 hours onwards after agrin incubation suggest that the constitutive activation of MuSK A617V is impairing agrin-induced MuSK phosphorylation levels in muscle cells. In conclusion, this demonstrates that the levels of MuSK phosphorylation are essential for the integrity of AChR clusters.

MuSK-tyrosine phosphorylation was nullified in MuSK C317R myotubes after incubation with agrin **(Figure 6-19B)** in agreement with the lack of agrin-induced AChR clusters previously reported **(Figure 6-6)**.

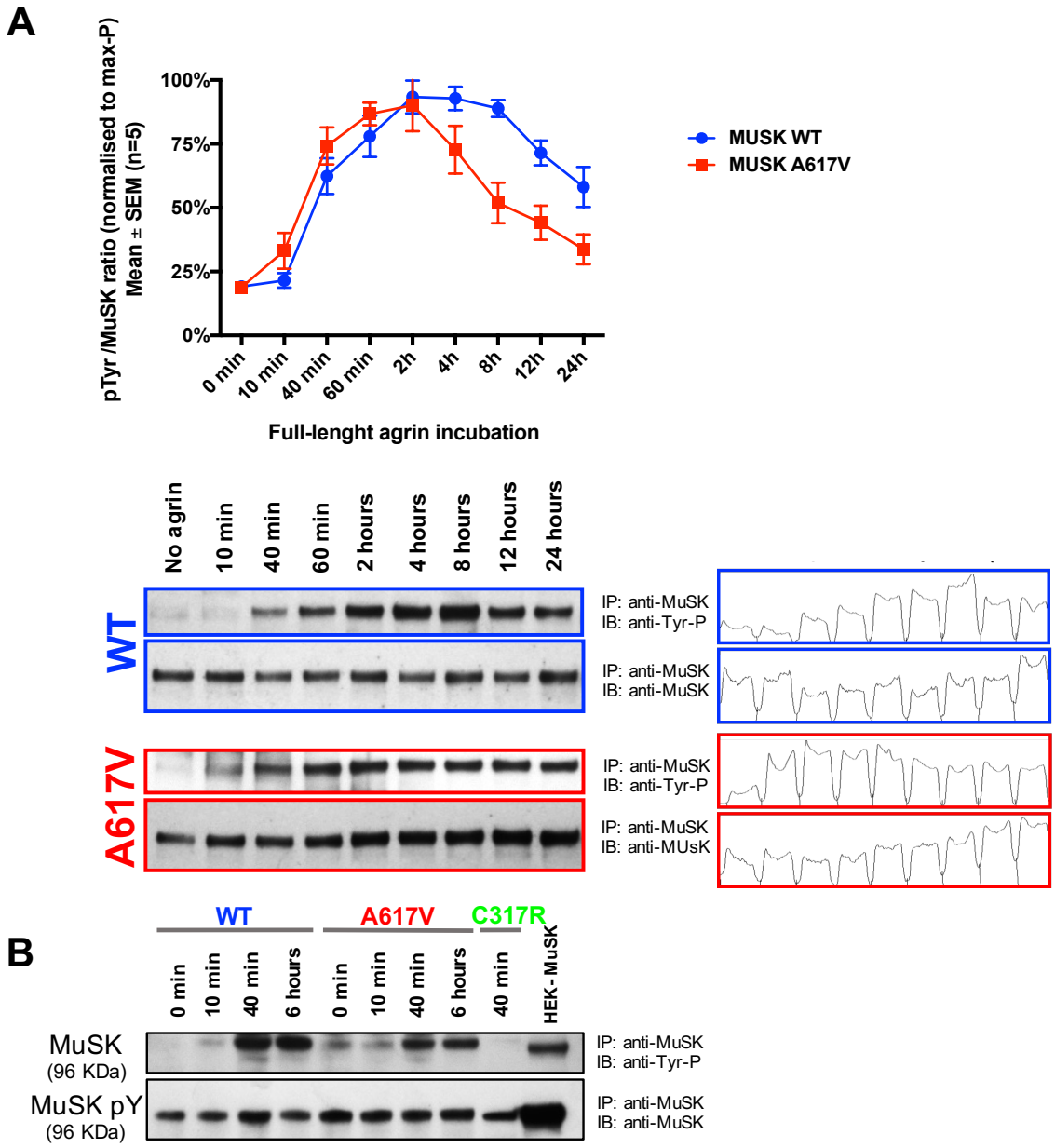


Figure 6-19. Effect of MuSK A617V variant on the temporal activation profile of MuSK in muscle cells

C2C12 *MuSK* KO myotubes infected with retrovirus expressing WT and mutant MuSK constructs were incubated with full-length agrin for 0-24 hours. Cell lysates were prepared, immunoprecipitated with anti-MuSK antibodies and analysed by western blotting with antibodies to phosphotyrosine and MuSK. **(A)** The results are shown as mean ± SEM from n=5 experiments relative to the maximum phosphorylation from each individual experiment. Repeated measures two-way ANOVA (p=0.0031). Representative images of western blots and densitometry analysis are provided below. **(B)** MuSK phosphorylation was nullified in C317R myotubes.

6.11 Study of potential molecular mechanisms leading to abnormal MuSK phosphorylation

Phosphorylation assays in HEK-293T showed a constitutive activation of MuSK A617V when MuSK was coexpressed with LRP4 (Section 6.12.1). Several potential molecular mechanisms leading to increased MuSK phosphorylation are proposed in this section.

6.11.1 Dysregulation of MuSK kinase activity

A Serine phosphorylation site within the MuSK kinase loop (S751) has been recently reported to behave as a modulator of MuSK kinase activity by relieving the autoinhibition of the MuSK activation loop upon its phosphorylation (Camurdanoglu *et al.*, 2016). In addition, a phosphomimetic mutant of S751 has been shown to increase basal and agrin-induced MuSK kinase activity. Therefore, we asked whether the abnormalities seen in MuSK A617V tyrosine phosphorylation could be related to differences in the phosphorylation of MuSK Ser751.

C2C12 *Musk* KO myoblasts expressing human WT or A617V MuSK (RefSeq NM_005592) were differentiated into myotubes and incubated with human full-length agrin for 8 hours (time point where biggest differences in MuSK tyrosine phosphorylation were previously observed in muscle cells (Section 6.11.2). Then MuSK was immunoprecipitated from cell lysates and phosphorylation was evaluated by western blotting with antibodies to MuSK, phospho-tyrosine, and phospho-serine-751. This antibody (Camurdanoglu *et al.*, 2016) was kindly provided by Dr Ruth Herbst (Centre for Brain Research, Medical University of Vienna, Austria). An additional experiment was conducted to evaluate MuSK S751 phosphorylation in HEK-293T cells using methods previously described (Section 6.10.1)

Immunoblotting with the antibody to detect MuSK Ser751 phosphorylation levels did not show significant differences between WT and A617V myotubes after incubation with human full-length agrin for 8 hours **(Figure 6-20A)**. In addition, Ser751 phosphorylation levels showed no differences between MuSK WT and A617V in HEK-239T cells **(Figure 6-20B)**. These results suggest that the abnormalities seen in tyrosine phosphorylation derived from the A617V substitution are not caused by differences in the Ser751-related modulation of MuSK activity.

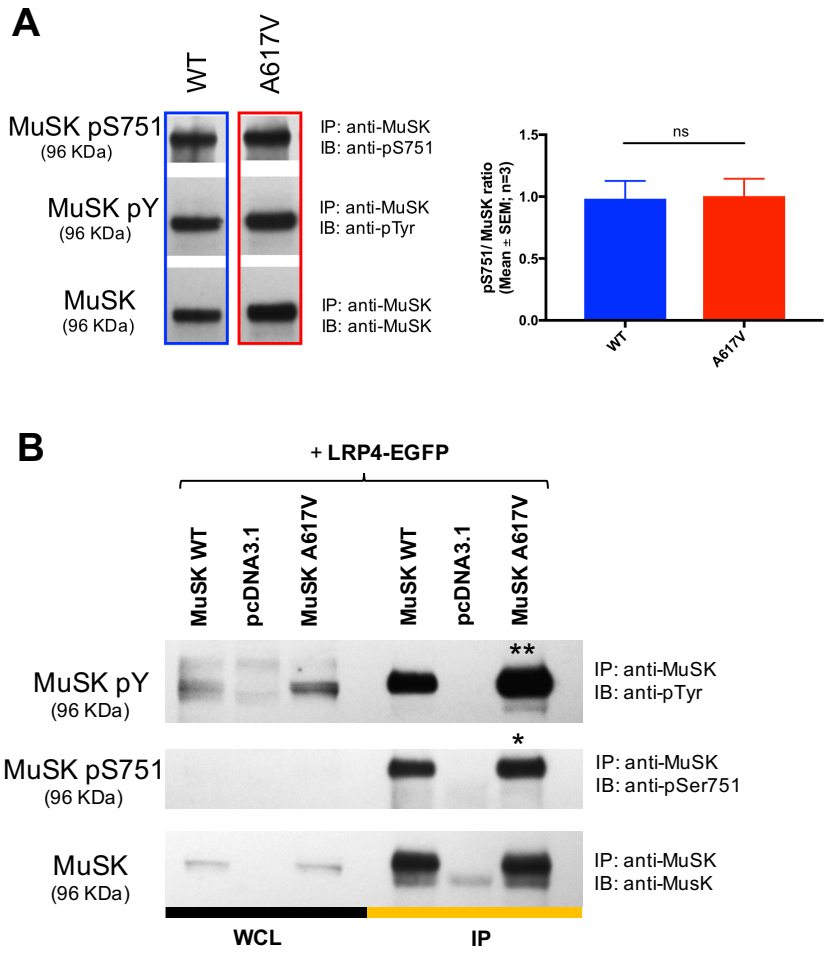


Figure 6-20. Effect of MuSK variants on MuSK S751 phosphorylation in muscle cells

(A) C2C12 *MuSK* KO cells infected with retrovirus expressing human WT and A617V MuSK (RefSeq NM_005592) constructs were incubated with full-length agrin for 8 hours. MuSK was immunoprecipitated from cell lysates with anti-MuSK antibodies and analysed by western blot with antibodies to pSer751, pTyr, and MuSK. Bar graphs represent

pS751/MuSK ratio in WT and A617V myotubes. Results are given as mean ± SEM relative to WT from n=3 experiments. Two-tailed unpaired t-test (ns = non-significant).
(B) HEK-293T cells were cotransfected with the above constructs. Cell lysates were prepared, coimmunoprecipitated with an anti-MUSK antibody and analysed by western blot with antibodies to pSer751, pTyr, and MuSK. The results showed no differences in pS751 (*) despite the increase in tyrosine phosphorylation (**) of MuSK A617V.

6.11.2 Abnormal dimerisation of MuSK

Since dimerisation of MuSK is crucial for MuSK activation (Hopf *et al.*, 1998), it is possible that abnormal dimerisation could affect MuSK phosphorylation. This could occur by altering MuSK dimerisation itself or the stability of the MuSK dimer. Typically, ligands binding to the extracellular domains of receptor tyrosine kinases (RTKs) cause receptor dimerisation and subsequent activation. However, it is important to make clear that the dimerisation of the extracellular domain of RTKs that follows the binding of extracellular ligands is different from the subsequent dimerisation of the intracellular KD domain and transphosphorylation of tyrosine residues (Lemmon and Schlessinger, 2010).

The structure of the MuSK kinase domain dimer has not yet been resolved (Till *et al.*, 2002). Understanding the pathogenic mechanisms of the MuSK A617V substitution at the structural level based on the monomer structure is challenging because the αC-helix from the kinase domain (where the p.A617 residue is located) is exposed to a large void in the crystal (Till *et al.*, 2002) **(Figure 6-5B)**. Insights from other RTKs have shown that the dimerisation of kinase domains can occur in a symmetric or asymmetric way (Zhang *et al.*, 2006; Lemmon and Schlessinger, 2010).

6.11.2.1 Modelling of MuSK kinase domain dimerisation

There are many conserved features among kinases regarding their structures and catalytic mechanisms (Hanks *et al.*, 1987). Based on this premise, a model of MuSK-KD dimerisation was generated by homology modelling based on the KD dimer structures of two well-known RTKs: Insulin-like Growth Factor 1 Receptor (IGF1R) and Epidermal Growth Factor Receptor (EGFR). On the one hand, the IGF1R-KDs form a symmetric dimer **(Figure 6-21A)** where the juxtamembrane region of one monomer interacts with the αC-helix of the contralateral monomer (Cabail *et al.*, 2015). In the three dimensional sequence alignment of MuSK-KD with IGF1R-KD, MuSK p.Ala617 residues are exposed to a void in the crystal **(Figure 6-21B)** and there are no obvious structural effects derived from the p.Ala617Val substitution **(Figure 6-21C)**. On the other hand, the EGFR-KDs form an asymmetric dimer **(Figure 6-22A)** essential for EGFR activation where the αH-helix of one monomer interacts with the αC-helix and ß4 sheet of the contralateral monomer and the kinase core is dominated by hydrophobic interactions (Zhang *et al.*, 2006). The 3D sequence alignment of MuSK-KD with EGFR-KD locates the p.Ala617 residue at the αC helix, which is part of the dimerisation interface responsible for the interaction of monomers **(Figure 6-22B)**.

The p.Ala617Val substitution at the αC helix could increase the hydrophobic interface for the docking of the contralateral monomer **(Figure 6-22C)**. Mutations affecting the asymmetric dimer interface of EGFR have been shown to affect the catalytic activity of the EGFR kinase domain (Zhang *et al.*, 2006). Therefore, this is a potential mechanism implicated in the impairment of MuSK phosphorylation. The generation of MuSK KD dimer models was done with the advice of Alexandr Kornev (Department of Pharmacology, University of California at San Diego, La Jolla).

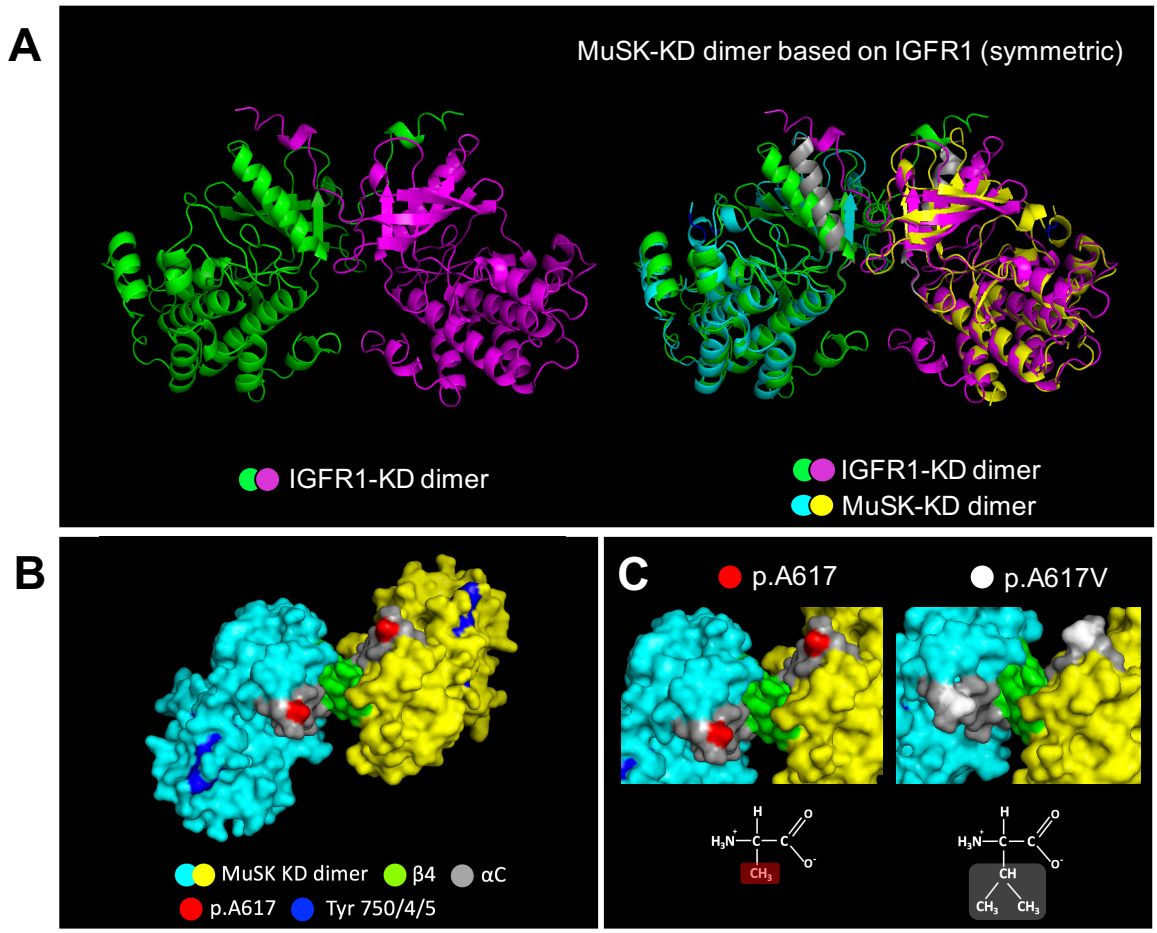


Figure 6-21. Molecular modelling of MuSK KD dimerisation based on the IGF1R KD dimer structure

(A) MuSK KD symmetric dimer built by homology modelling based on the crystal structure of the Insulin-like growth factor 1 receptor (IGFR1) KD dimer (MMDB ID: 128136).

(B) Surface representation of MuSK KD dimer (cyan and yellow) based on the IGFR1 dimer. In the proposed structure, MuSK-KDs, coloured cyan and yellow, form a symmetric dimer where the αC helix (grey) from one monomer binds to the juxtamembrane region (αB) of the contralateral monomer at the N-terminus (green). In this model, the p.Ala617 residues (red) are exposed to a void in the crystal. The tyrosines within the activation loop (Tyr-750/754/755) are shown in blue.

(C) The figure shows how the substitution of Alanine to Valine (p.Ala617Val) does not generate any obvious structural effects on the molecule.

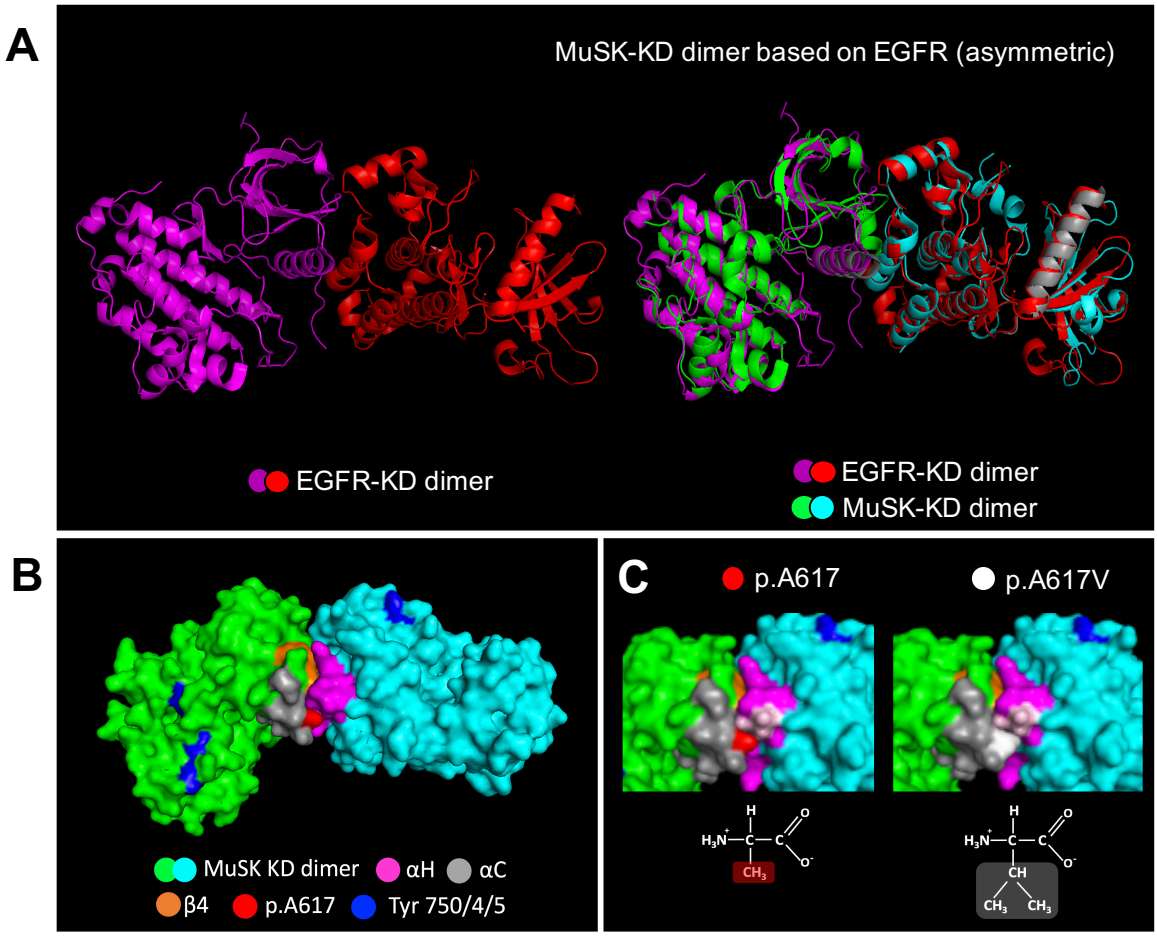


Figure 6-22. Molecular modelling of MuSK KD dimerisation based on the EGFR KD dimer structure

(A) MuSK KD asymmetric dimer built by homology modelling based on the crystal structure of the Epidermal Growth Factor Receptor (EGFR) KD activated dimer (MMDB ID: 40024).

(B) Surface representation of MuSK KD dimer (green and cyan) based on the EGFR dimer. In the proposed structure, MuSK-KDs, coloured green and cyan, form an asymmetric dimer with the H-helix (pink) of one monomer binding to αC helix (grey) and ß4 sheet (orange) from the contralateral monomer. The p.Ala617 residue (red) is located within the αC helix at the dimerisation interface. The tyrosines within the activation loop (Tyr-750/754/755) are in blue.

(C) The figure shows how the p.Ala617Val substitution modifies the dimerisation interface increasing the hydrophobic interface for the docking of the contralateral MuSK KD. In this model, the p.Ala617 residue (red) interacts with the p.Ala842 and p.Asp843 residues (light purple) from the H-helix (purple) at the dimerisation interface.

6.11.2.2 Increased stability of MuSK KD dimer

The 3D model of MuSK KD asymmetric dimer built by homology modelling from the EGFR structure showed that the p.Ala617 MuSK residue was located at the dimerisation interface, and thus the A617V substitution could increase the hydrophobic interface for the docking of the contralateral monomer **(Figure 6-22C)**. Since Valine is the second most hydrophobic amino acid (Kyte and Doolittle, 1982), the p.Ala617Val substitution could result in a more stable dimer with increased catalytic activity. In order to test this hypothesis, site-directed mutagenesis was used to mutate the p.Ala617 residue into other aminoacids that could affect dimer formation and hence kinase activity.

An A617G substitution was made to decrease the hydrophobic binding of the contralateral monomer by introducing Glycine (G), an amino acid with a single hydrogen atom as its side chain. A617D and A617N substitutions were constructed to reduce the hydrophobic interactions at the dimerisation interface by introducing aminoacids with hydrophilic properties such as Aspartic acid (D) and Asparagine (N). 3D Modelling of MuSK A617G, A617D, and A617N KD dimers did not show any apparent structural abnormalities derived from the amino acid substitutions (data not shown). Therefore, any effects seen in MusK tyrosine phosphorylation would be likely to derive from changes in hydrophobic interactions.

The results showed an unexpected increased in MuSK tyrosine phosphorylation in the A617G and A617N variants compared to WT, in a similar fashion to the A617V variant **(Figure 6-23)**. The A617D variant had no effect on MuSK tyrosine phosphorylation.

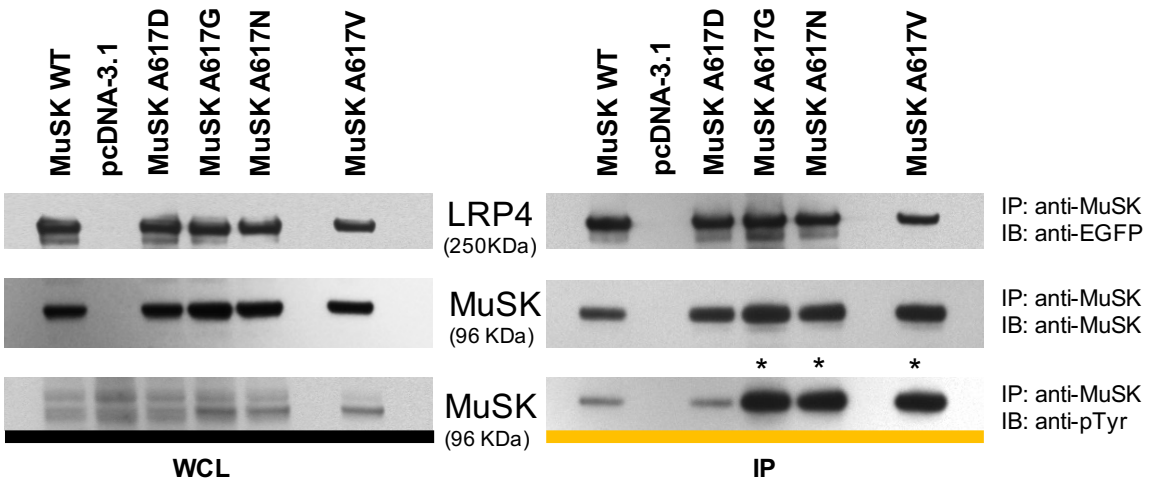


Figure 6-23. Effect of MuSK A617 mutagenesis on MuSK Tyr-P in HEK-293T cells

HEK-293T cells were transiently transfected with mammalian expression constructs encoding MuSK WT or variants and LRP4-EGFP. 48 hours later, cell lysates were prepared, coimmunoprecipitated with an anti-MuSK antibody and subsequently analysed by western blotting with antibodies to phosphotyrosine, MuSK, and EGFP. Densitometry analysis was performed using ImageJ software.

6.12 Effect of MuSK variants in vivo

To study the effect of MuSK variants in vivo via gene transfer into muscle (Section 2.11.1), the *tibialis anterior* (TA) muscles of adult wild-type C57BL/6 mice were electroporated at the age of 8 weeks with 10 µg of mammalian expression vectors encoding for human WT or mutant MuSK constructs, and 5 µg of nls-EGFP construct to identify areas of the muscle that successfully took up the nucleic acid. Two types of negative controls were used: a mouse electroporated with saline only (no DNA control), and a non-injected/non-electroporated mouse (no electroporation control). The muscles were extracted 4 weeks after electroporation following standard procedures. Immunofluorescence labelling of teased muscle fibres was performed as described in methods (Section 2.5.13).

The visualisation of the "no electroporation control" muscle fibres showed normal pretzel-shaped endplates and nerve terminals **(Figure 6-24A)**. Muscle fibres expressing EGFP at cell nuclei **(Figure 6-24B)** were less than 5% in keeping with a low transfection efficiency. Visualisation of muscle fibres electroporated with saline only (no DNA control) showed the presence of both pretzel-shaped and aberrant endplates broken up into multiple fragments **(Figure 6-24C).** This was also the case for muscles electroporated with WT and mutant MuSK constructs **(Figure 6-24 D-F)**. The presence of abnormal endplates in the saline only (no DNA control) group suggests that electroporation itself was responsible for disrupting the muscle endplates and, therefore, this might not be a reliable technique to look at the morphology of endplates in vivo.

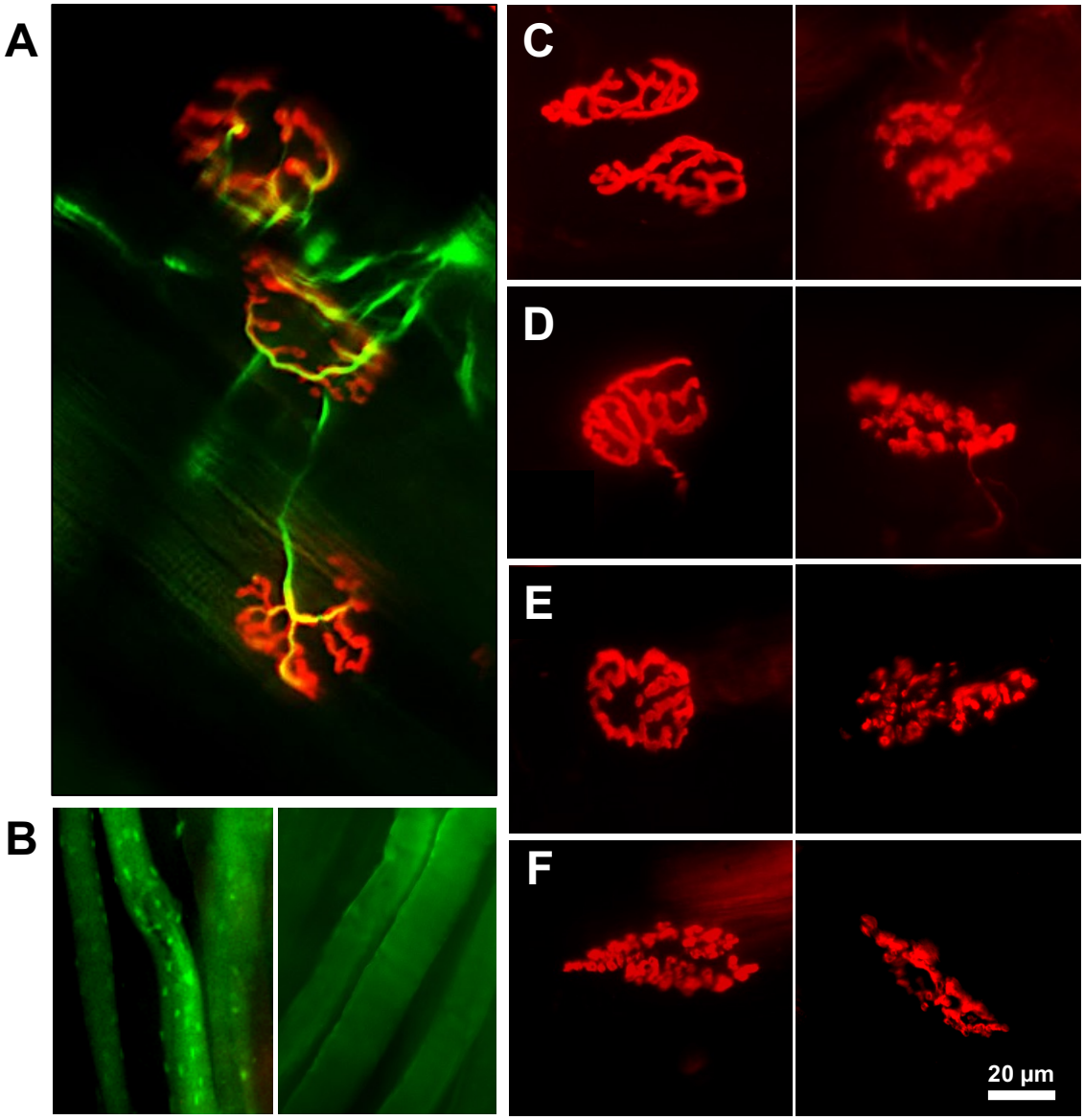


Figure 6-24. Representative images of mouse muscles electroporated with MuSK constructs and controls. TA muscles were dissected from WT C57BL/6 mice and labelled with Alexa Fluor® 594-α-bungarotoxin and antibodies against neurofilament and synaptophysin. Teased muscle fibres were assessed by fluorescence microscopy.

(A) Representative images of endplates from mice non-electroporated/non-injected

(B) Representative images of electroporated muscle fibres expressing EGFP at the cell nuclei (left) or non-electroporated (right).

(C) Representative images of endplates from mice electroporated with saline only

(D) Representative images of endplates from mice electroporated with MuSK WT

(E) Representative images of endplates from mice electroporated with MuSK A617V

(F) Representative images of endplates from mice electroporated with MuSK C317R

6.14 Response to treatment with ß2-adrenergic agonists

Based on the previous experience from our group with ß2-adrenergic agonists in patients with *DOK7* mutations, treatment with oral salbutamol 4 mg twice a day (0.2 mg/kg/day) was initiated. The drug had a remarkable effect in muscle strength and functionality from the first month onwards. From being unable to walk, after six months the patient was able to walk short distances and performed the 10 metre timed walk test unaided in 25 seconds **(Figure 6-25A)**. This had a definitive impact in quality of life and activities of daily living, as measured by the Barthel Activities of Daily live index (Mahoney and Barthel, 1965) **(Figure 6-25B)**. The beneficial effect has persisted over the 24-month follow-up period since the initiation of treatment.

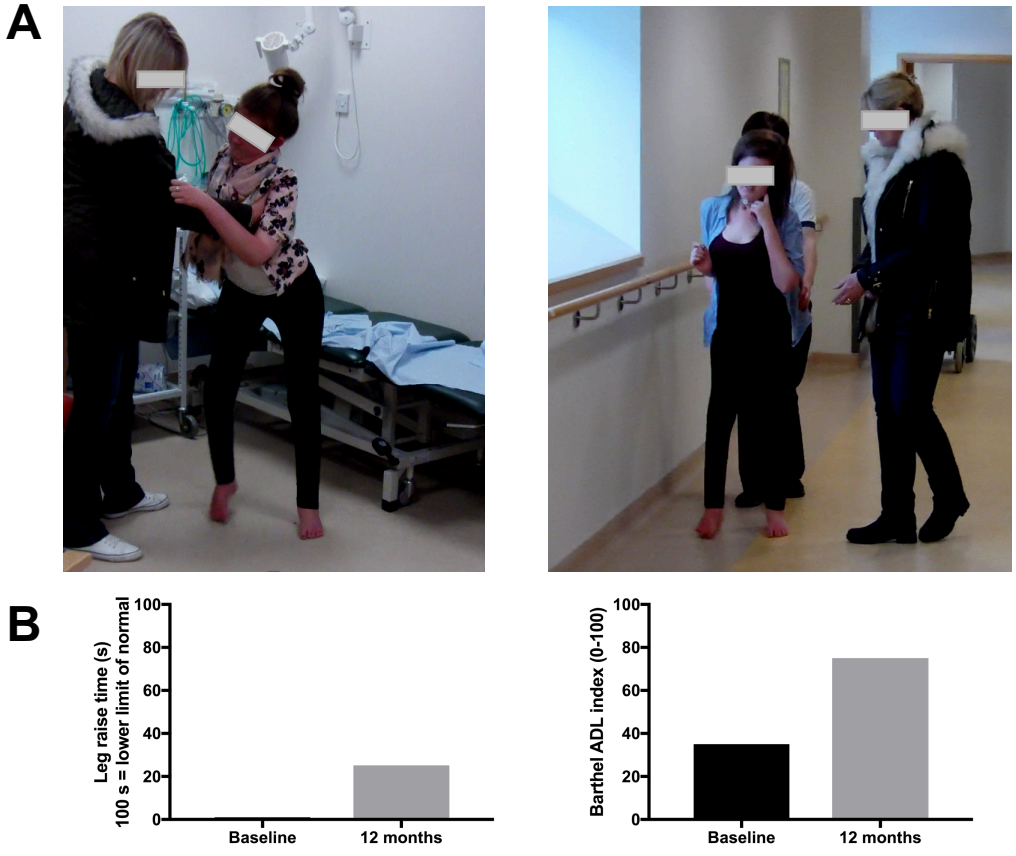


Figure 6-25. Clinical response to treatment with ß2-adrenergic agonists

(A) Representative images of the patient before (left) and after (right) treatment.

(B) Measurement of leg rise time and Barthel ADL index before and after treatment.

6.15 Discussion

MuSK is a key element of the Agrin-LRP4-MuSK-DOK7 kinase signalling pathway, which is essential for the formation and maintenance of the NMJ (DeChiara *et al.*, 1996; Burden *et al.*, 2013). This study shows the pathogenic mechanisms underlying two novel missense variants in *MUSK* causing CMS. These findings point to a novel pathogenic mechanism and show how MuSK phosphorylation levels are important in maintaining synaptic structure. Finally, this study was useful in guiding appropriate therapy to the patient with ß2-adrenergic agonist. Based on the clinical experience of our group with CMS patients harboring mutations within the Agrin-LRP4-MuSK-DOK7 pathway, the clear response to treatment with salbutamol supports that the p.A617V mutation is pathogenic.

MUSK mutations are extremely rare with only a few cases reported to date (Engel *et al.*, 2015). This differs greatly from the much wider spectrum of *DOK7* mutations (Cossins *et al.*, 2012), which stands for approximately a third of the CMS population in the United Kingdom (Finlayson, 2013). The underlying reasons explaining this phenomenon are unknown, but could be related to the fact that severe *MUSK* mutations are incompatible with life and mild *MUSK* variants are mostly asymptomatic. In keeping with this, it has been reported that mice homozygous for the pathogenic V790M Musk mutation found in a CMS patient (Chevessier *et al.*, 2004) had no abnormal phenotype regarding weight, muscle function and viability (Chevessier *et al.*, 2008). By contrast, mice heterozygous for the V790M mutation and a null allele were severely impaired.

The clinical phenotype of the current case has similarities to patients with *DOK7* mutations with regard to the presence of neonatal stridor, limb girdle weakness, ptosis,

normal eye movements and worsening with cholinesterase inhibitors (Palace *et al.*, 2007). Some patients with *MUSK* mutations had onset of symptoms with limb-girdle weakness after normal motor milestones (Mihaylova *et al.*, 2009; Ammar *et al.*, 2013; Gallenmüller *et al.*, 2014). On the other hand, others had severe neonatal onset with hypotonia, stridor, respiratory failure, and need for mechanical ventilation (Chevessier *et al.*, 2004; Maselli *et al.*, 2010).

The first CMS case described with *MUSK* mutations showed positive response to treatment with pyridostigmine 120-240 mg per day and 3,4-DAP given at 30-50 mg per day (Chevessier *et al.*, 2004). However, cholinesterase inhibitors were not beneficial in other cases reported. Treatment with ß2-adrenergic agonists resulted in dramatic improvement in two siblings heterozygous for *MUSK* D38E and a genomic deletion affecting exons 2–3 of *MUSK*, and in moderate improvement in a patient heterozygous for *MUSK* M605I and A727V. The molecular mechanism of ß2-adrenergic agonists at the NMJ is not known, but it is likely that they stabilise motor endplates´ structure through activation of 2nd messenger signalling that compensates for the impairment in the Agrin-LRP4-MuSK-DOK7 signalling pathway. A recent study has proposed that NMJs are innervated by sympathetic neurons, which are crucial for the integrity of the endplates (Khan *et al.*, 2016), thus speculating that this could be the target of ß2-adrenergic agonists at the NMJ.

The p.C317R mutation nullified AChR clustering and MuSK phosphorylation after agrin incubation, thus behaving as a null mutation. The p.Cys317 residue contributes to the formation of an essential disulphide bond for MuSK FzD architecture, which is disrupted

by the cysteine to arginine substitution. The impairment of the FzD architecture results in a dramatic reduction of MuSK cell surface expression which cannot then be activated by its extracellular ligand agrin. Only one additional mutation (P344R) has been reported in this domain although functional studies were not conducted (Mihaylova *et al.*, 2009).

The p.A617V mutation showed impaired AChR clustering and altered MuSK kinase activity. The AChR clustering abnormalities seen in A617V myotubes were based on the presence of significantly smaller and less bright AChR clusters. The constitutive activation of MuSK lead to a time-dependent reduction in agrin-induced MuSK tyrosine phosphorylation levels in muscle cells. This suggests that MuSK phosphorylation levels are crucial to maintain synaptic integrity and thus disrupting the control of MuSK phosphorylation levels may be a novel pathogenic mechanism for CMS.

MuSK activation is closely related to its dimerisation (Hopf *et al.*, 1998). To understand how MuSK A617V is constitutively activated, and how this leads to the reduction of agrin-induced MuSK phosphorylation levels is challenging, especially in the absence of a crystal structure for the MuSK kinase domain dimer. A previous study has shown similar findings for the p.M835V mutation (Ammar *et al.*, 2013), which could point to a common pathogenic mechanism. Novel findings from other RTKs have shown that the dimerisation of KDs can occur in symmetric or asymmetric ways (Zhang *et al.*, 2006). Furthermore, recent insights from the study of other protein kinases have shown that both asymmetric and symmetric conformations can be adopted in different catalytic states, and that symmetry-asymmetry transitions could be important for kinases function (Bhate *et al.*, 2015).

The 3D model of MuSK KD asymmetric dimer based on EGFR showed that the p.A617 residue is located at the dimerisation interface, and that the A617V substitution could increase the hydrophobic interface for the docking of the contralateral monomer resulting in a more stable dimer. Unexpectedly, MuSK variants A617G and A617N, but not A617D, also showed increased MuSK tyrosine phosphorylation in HEK-293T cells. These findings are difficult to interpret in the absence of the MuSK KD dimer structure.

It is possible that changes in the allosteric conformational equilibrium derived from the amino acid substitutions (Weinkam *et al.*, 2013) could lead to the loss of kinase autoinhibition by the juxtamembrane domain or the activation loop. Further studies using *in vitro* techniques such as the use of lipid vesicles (Zhang *et al.*, 2006) would be useful to elucidate the mechanisms of MuSK KD dimerisation and have a better understanding on the effects of MuSK variants.

Another possibility would be that the A617V substitution is affecting the dynamics of the αC-helix. In keeping with this, it is known that differences related to αC-helix positioning characterise autoinhibitory mechanism throughout the EGFR family (Dixit and Verkhivker, 2011), and that allosteric targeting via displacement of the αC-helix enables a direct and specific modulation of protein kinases activity (Palmieri and Rastelli, 2013), which is of important relevance in cancer biology (Wood *et al.*, 2004).

The constitutive activation of MuSK caused a reduction of agrin-induced MuSK tyrosine phosphorylation levels in A617V myotubes, which suggests the existence of a regulatory

mechanism not present in HEK-293T cells. It is believed that MuSK activation levels are set, at least in part, by tyrosine phosphatases, and that MuSK signalling normally activates tyrosine phosphatases to limit its own spread (Madhavan and Peng, 2005). This fine balance of MuSK stimulation with that of tyrosine phosphatases could modulate the level, duration or range of the MuSK signalling, which would help cluster AChRs at sites where MuSK is maximally activated. It is also known that this fine balance is important for the maintenance and stabilisation of AChR clusters (Camilleri *et al.*, 2007) in keeping with tyrosine kinase inhibitors dispersing agrin-induced preformed AChR clusters (Ferns *et al.*, 1996). We could speculate that the constitutive activation of MuSK A617V is impairing agrin-induced MuSK tyrosine phosphorylation levels by affecting the tight coupling between kinase and phosphatase activities that is essential for the formation and maintenance of AChR clusters.

In conclusion, this study shows that MuSK C317R and A617V are pathogenic mutations responsible for the patient´s myasthenic syndrome and uncovers previously unrecognised mechanisms of how levels of MuSK phosphorylation are critical to maintain synaptic structure. This study also highlights the importance of understanding disease mechanisms to guide appropriate pharmacological treatment.

Chapter 7

Clinical and Molecular Basis of Stridor in Patients with CMS and *DOK7* mutations

7.1 Introduction

The discovery of *DOK7* mutations resulted in the identification of a group of patients with a previously undefined limb-girdle myasthenic syndrome (Beeson *et al.*, 2006). Further clinical characterisation showed that most patients harbouring *DOK7* mutations presented with difficulty in walking after normal motor milestones, proximal muscle weakness greater than distal, and spared eye movements (Palace *et al.*, 2007). In addition, the patients did not benefit from cholinesterase inhibitors but responded dramatically to ß2-adrenergic agonists (Lashley *et al.*, 2010).

Despite the increased awareness and detailed clinical characterisation of this condition, patients with *DOK7* mutations are still mistaken for congenial myopathies and other non-CMS muscle disorders due to clinical similarities, presence of abnormalities in muscle biopsy, and lack of response to cholinesterase inhibitors. Therefore, the diagnostic delay from first symptoms to diagnosis and treatment can be many years. The importance of genetic diagnosis relies on the possibility of treating with ß2-adrenergic agonists, which can have dramatic effects in muscle strength and quality of life. Although not proven, it is possible that early introduction of treatment with ß2-adrenergic agonists can slow down disease progression and improve functionality by reducing the development of

concomitant myopathy, scoliosis and muscle contractures. Obviously, some patients are also mistaken for seronegative MG, due to the presence of fatigable muscle weakness and negative results for AChR and MuSK antibodies, and thus it is not rare to find patients with *DOK7* mutations on immunosuppression.

7.1.1 Stridor in DOK7-CMS

A more recent feature identified in patients with *DOK7* mutations is the presence of stridor due bilateral vocal cord palsy (Jephson *et al.*, 2010). Stridor is defined as a high-pitched noise resulting from turbulent airflow through a partially obstructed upper airway that warrants immediate attention to secure airway permeability (Majumdar *et al.*, 2006). Stridor can be caused by a large list of conditions: laryngotracheobronchitis (croup), epiglottitis, retropharyngeal abscess, foreign bodies, laryngomalacia, vocal cord paralysis, subglottic stenosis, and tracheomalacia. Bilateral vocal cord paralysis is a rare cause of congenital stridor accounting for less than 10% of cases (Zoumalan *et al.*, 2007).

In DOK7-CMS, stridor can appear at birth (congenital), either in isolation or associated with feeding difficulties, or manifest with exacerbations of myasthenic weakness related to infections during childhood and adulthood (Klein *et al.*, 2013). Mild continuous stridor with breathing is also common. The clinical recognition of stridor may serve as an early diagnostic clue that warrants neurophysiological and genetic testing for *DOK7* mutations (Klein *et al.*, 2013). This is particularly relevant in infants with congenital bilateral vocal cord palsy which appears to be idiopathic (Jephson *et al.*, 2010), or in children and adults with limb-girdle weakness and continuous stridor or stridor related to exacerbations of myasthenic weakness.

7.1.2 Stridor in other myasthenic disorders

Stridor is very rare in MG due to AChR antibodies (Hanson *et al.*, 1996), but seems more frequent in patients with MuSK antibodies, where several cases of dyspnoea due to vocal cord abduction paresis have been described (Hara *et al.*, 2007; Eker *et al.*, 2008; Jiménez Caballero *et al.*, 2012). There are also reports of stridor due to maternal transfer of MuSK antibodies (Béhin *et al.*, 2008) and most interestingly, in patients with AGRN-CMS (Nicole *et al.*, 2014). Overall, it appears that patients with defects in the Agrin-MuSK-DOK7 clustering pathway are predisposed to suffer from stridor. Nevertheless, stridor may also occur very rarely in CMS patients with *RAPSN* mutations (Khan *et al.*, 2011) and Fast Channel Syndrome (Palace *et al.*, 2012), although this is usually in the context of severe generalised muscle weakness and respiratory distress . There are no published reports to date of stridor in Lambert Eaton myasthenic syndrome.

7.1.3 The mechanisms underlying stridor in DOK7-CMS

Laryngoscopy studies in patients with *DOK7* mutations and stridor have shown the presence of bilateral vocal cord palsy (Jephson *et al.*, 2010; Klein *et al.*, 2013). In these patients, laryngeal examination has shown a selective impairment of vocal cord abductors with normal functioning of vocal cord adductors and tensors (unpublished observations). This causes failure to dilate the glottis thereby increasing the airway resistance and the load on the respiratory pump muscles. As the muscles are easily fatigable due to the abnormalities in neuromuscular transmission, this leads to respiratory distress requiring ventilation and often tracheostomy.

The posterior cricoarytenoid muscles (PCA) is the only laryngeal muscle in charge of vocal cord abduction **(Figure 7-1)**. The reason why this particular muscles is affected in patients with *DOK7* mutations while adductors (interarytenoid muscle – IA; thyroarytenoid muscle – TA; lateral cricoarytenoid muscle – LCA) and tensors muscles of the larynx (cricothyroid muscle – CT) are spared is not known. It is possible that differences in the structural, functional or molecular properties of the PCA muscle make it more susceptible to defects in the Agrin-MuSK-DOK7 pathway.

7.2 Aims

In this chapter, the presence of stridor within the CMS patients currently followed up in the Oxford CMS service was studied by retrospective review of clinical notes. The aim was to provide a better understanding on the frequency, genetic associations, clinical course, and outcome of this particular manifestation. In addition, the molecular properties of muscle fibres and neuromuscular junctions were investigated, using control human laryngeal muscles, in order to understand the reasons underlying the susceptibility of the PCA muscle to be affected in DOK7-CMS. Special attention was paid to the expression levels of DOK7 and MuSK, which are key elements of the AChR clustering pathway. As previously detailed in the methods chapter **(Section 2.1.3)**, the experiments were conducted in human PCA (laryngeal abductor - affected) and IA muscles (laryngeal adductor - non-affected) from donors undergoing therapeutic laryngectomy. The dissection of the IA muscle can be performed with relative ease without damaging the diagnostic specimen and, therefore, it was chosen as a control muscle.

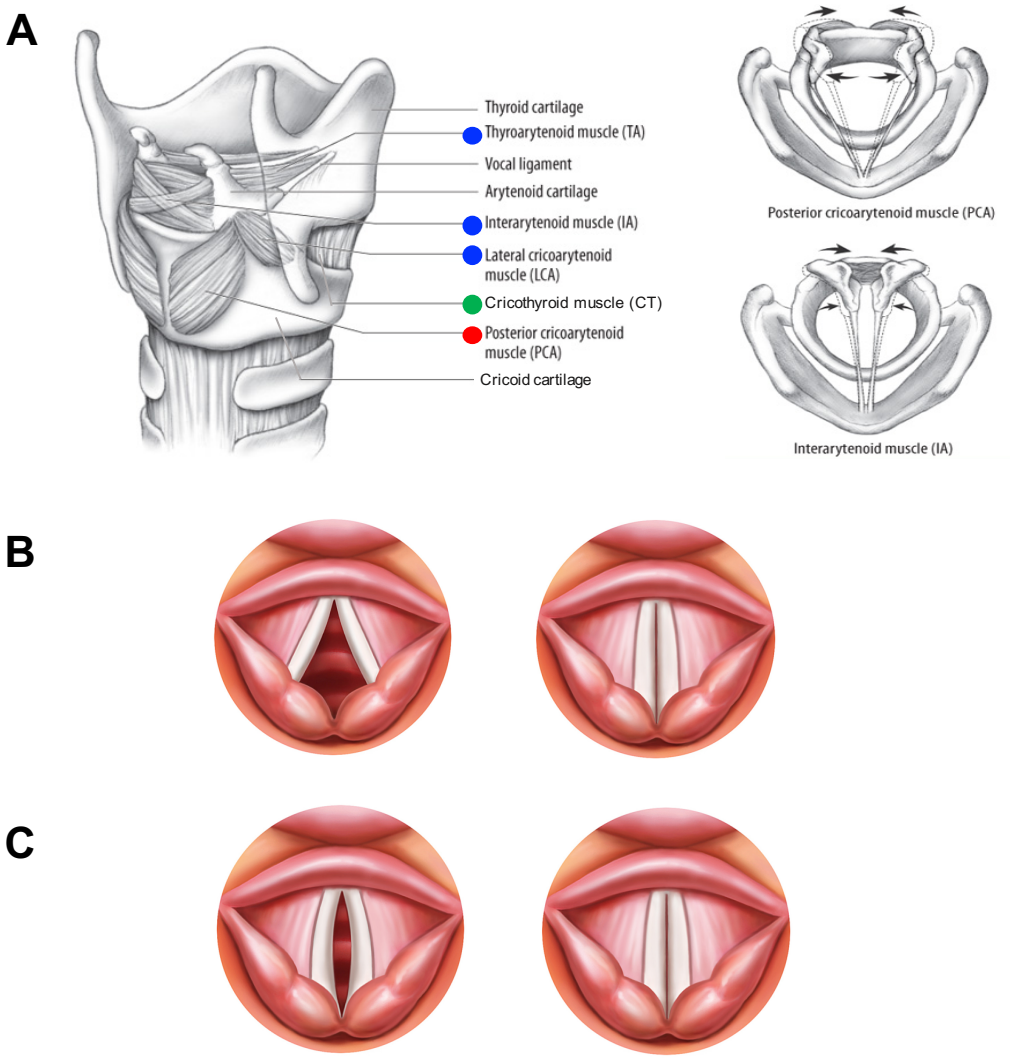


Figure 7-1. Schematic representation of human laryngeal muscles

(A) The intrinsic muscles of the human larynx are responsible for modifying the length, tension and spatial position of the vocal cords. These are classified into vocal cord abductors that open the glottis (red), vocal cord adductors that close the glottis (blue), and vocal cord tensors that regulate vocal cord length and tension (green). The extrinsic muscles of the larynx (suprahyoid, infrahyoid, and stylopharyngeus muscles) provide laryngeal stabilisation and indirectly may affect vocal cord position. Modified with permission from the National Spasmodic Dysphonia Association (NDSA).

(B) Schematic representation of normal vocal cords during inspiration (abducted-opened) and phonation (adducted-closed).

(C) In individuals with bilateral paralysis of vocal cord abductors, the cords are adducted and the glottis fails to dilate during inspiration thus enhancing airflow resistance and leading to stridor. Vocal cord adduction and phonation is preserved.

7.3 Presence of stridor in the different CMS-subtypes

The clinical notes of CMS patients actively seen within the Oxford Congenital Myasthenia Service were reviewed and the following items were collated: demographic data; genetic diagnosis and mutation analysis; onset, course and current presence of stridor; severity of stridor; factors precipitating and/or worsening stridor; laryngoscopy findings; laryngeal surgery; tracheostomy and decannulation; abnormalities in voice volume and pitch control. The severity of stridor was classified as mild, moderate or severe depending on symptomatology and the need for external ventilation.

Stridor was found in 24 out of 49 patients (48.9%) with *DOK7* mutations currently followed-up in our service **(Figure 7-2)**, which represents a significantly higher proportion than any other CMS subtype ($p < 0.001$). A total of 6 patients with other CMS subtypes also manifested clinically with stridor: AChR-deficiency syndrome (1/51; 1.9%), Agrin-CMS (1/1; 100%), fast-channel syndrome (1/15; 6.6%), MuSK-CMS (1/1; 100%), and Rapsyn-CMS (2/41; 4.1%). No CMS patients with slow-channel syndrome, *COLQ* mutations or mutations within the glycosylation pathway suffered from stridor.

Most patients with DOK7-CMS included in this study were on treatment with ß2-adrenergic agonists salbutamol or ephedrine.

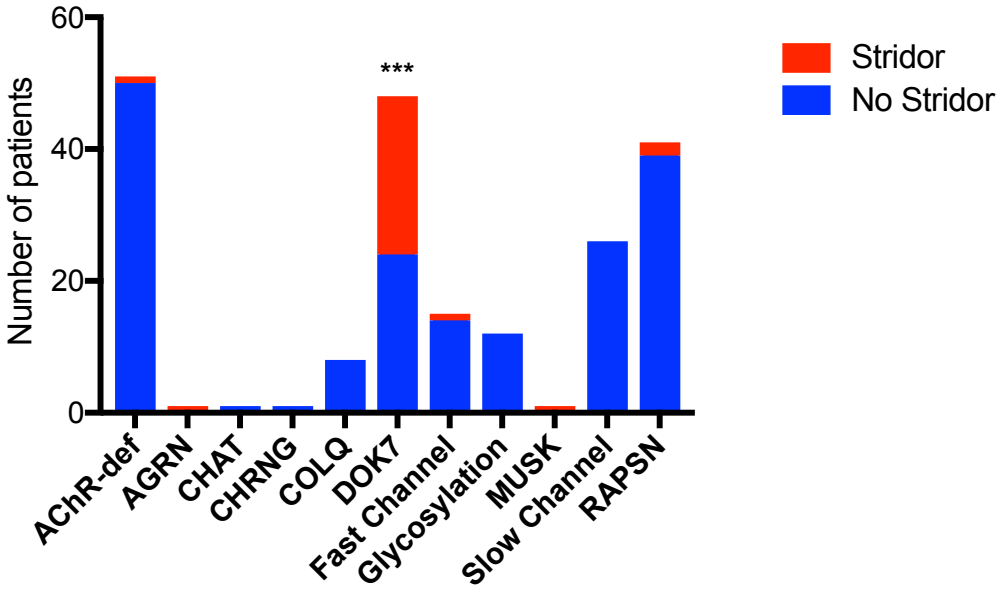


Figure 7-2. Presence of stridor in the different CMS subtypes

The clinical notes of 205 patients with CMS currently attending the Oxford CMS service were retrospectively reviewed and the patients were classified according to the presence of stridor and the genetic subtype. Chi-square (***p<0.001).

7.4 Clinical features of stridor in patients with DOK7-CMS and other CMS-subtypes

7.4.1 Clinical presentation

The clinical presentation of stridor in patients with *DOK7* mutations was variable. A total of 12 patients (50.00%) had congenital onset of stridor at birth or within the first days of life. From these, 7 out of 12 had isolated stridor and 5 had other concomitant manifestations such as feeding difficulties or hypotonia. The remaining 12 patients (50.00%) with *DOK7* mutations had an insidious onset of stridor during childhood or adulthood, typically manifesting during an exacerbation of symptoms related to concomitant infections or other precipitating factors. One patient had severe onset of stridor at the age of 40 years.

The presentation of stridor in the patient with fast channel syndrome and the patients with mutations in *MUSK* and *AGRN* occurred at birth, in the context of marked hypotonia and muscle weakness. The onset of stridor in the two patients with *RAPSN* mutations occurred at 8 weeks and 16 years, respectively.

7.4.2 Outcome and course of stridor

Of the 12 patients with congenital onset stridor, 8 needed invasive ventilation, and 7 underwent tracheostomy due to severe respiratory distress. Of the 7 patients that underwent tracheostomy, 3 were eventually decannulated at the age of 1, 3, and 7 years old respectively, while the other four have had permanent tracheostomies to date. In addition, 3 patients underwent surgical interventions (aryepiglottoplasty, division of epiglottic folds or laser cordotomy) to their vocal cords early in life to increase the glottic gap and reduce the airflow resistance.

In patients with non-congenital onset, stridor was mostly mild and continuously present with breathing in the form of a wheeze, but was worsened by precipitating factors such as infections. For example, one patient had two admissions in intensive care at the age of 19 and 24 years due to worsening respiratory problems. Another patient suffered a severe deterioration at the age of 40 needing respiratory support and permanent tracheostomy.

Overall, stridor improved over time for most of the patients with congenital stridor and remained mild for those with adult onset, with the exceptions of the few patients described above. In addition, it did not seem that the presence of congenital stridor influenced the development of motor milestones.

7.4.3 Additional clinical features related to abnormalities in the vocal cords

The PCA muscle is implicated in vocal cord abduction but also participates in the phonation process as demonstrated by electromyographic activity (Martin and Thumfart, 1990). Therefore, it is not surprising that 6 out of 24 patients (25%) with *DOK7* mutations and stridor had additional speech difficulties related to voice volume and pitch control.

7.5 Complementary findings in patients with stridor

The human laryngeal glottis widens on inspiration and narrows on expiration. The study of the pattern of movements of the vocal cords in relation to breathing has shown that the larynx participates in respiratory regulation by modulating airflow resistance (T. Brancatisano *et al.*, 1984). The respiratory movements of the vocal cords are driven mainly by the balance of the phasic and tonic activity of the PCA laryngeal muscle, which is affected in patients with *DOK7* mutations. During inspiration, the phasic activation of the PCA muscle stabilises the airway and minimises resistance to airflow by increasing the glottic width by 2-3 folds prior to inspiration (T. P. Brancatisano *et al.*, 1984). During expiration, the PCA maintains tonic activity, which is approximately 30% of the phasic, so that the vocal cords move closer to the midline reducing the glottic gap.

A total of 9 patients with stridor underwent laryngo-bronchoscopy, which revealed bilateral vocal cord palsy in all cases. The examination commonly revealed vocal cords in an adducted position, with a reduced glottic gap. Interestingly, there was a lack of vocal cord movement with breathing, which translates into an increased resistance to air flow, especially during inspiration **(Figure 7-3)**. Vocal cord adduction was conserved in all cases as expected by with preserved phonation.

Several patients with *DOK7* mutations underwent routine respiratory studies that showed abnormal flow-volume loop curves related to airway obstruction. While expiratory loops shapes were fairly normal but reduced in size, the inspiratory loop curves were rather flat, consistent with airway obstruction at the laryngeal level.

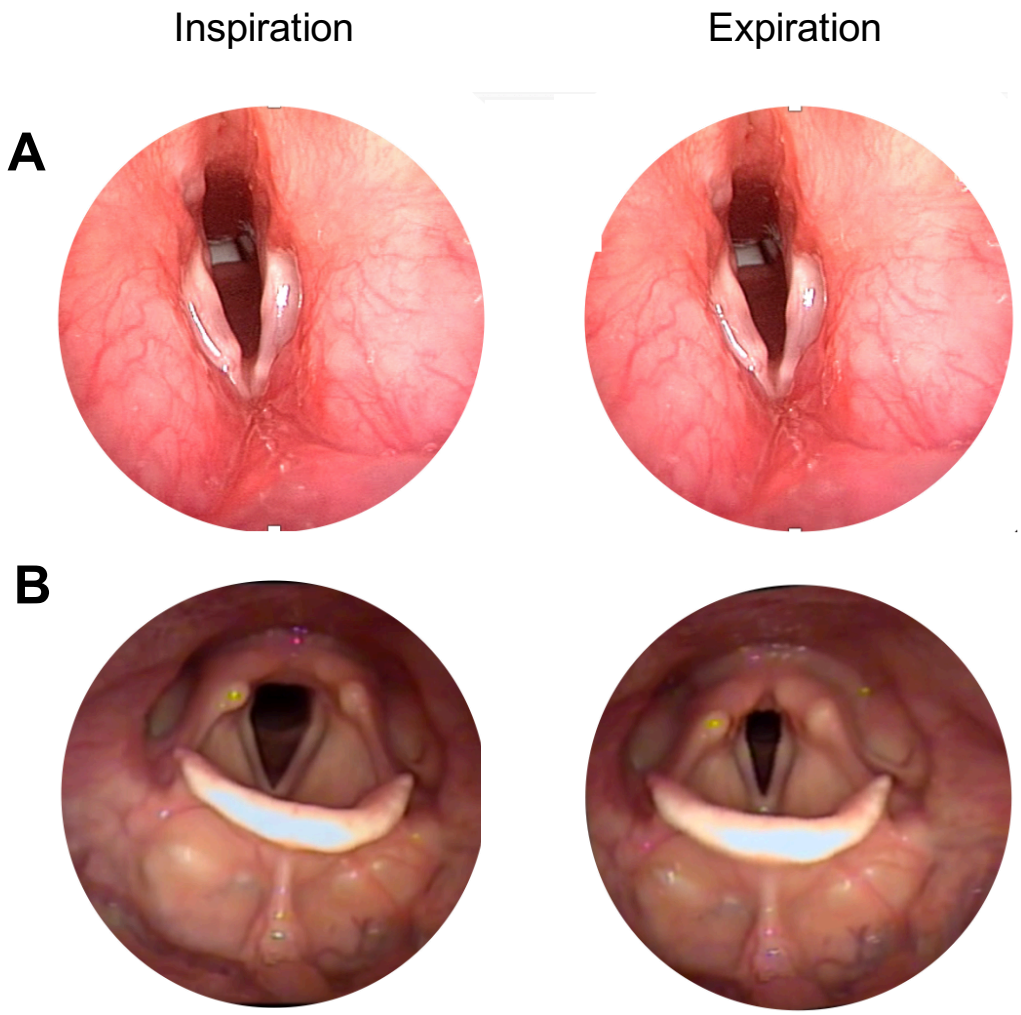


Figure 7-3. Laryngoscopy findings in patients with *DOK7* mutations

(A) Representative image from a laryngoscopy examination in a patient homozygous for *DOK7* c.415G>C, showing bilateral cord palsy and lack of vocal cord movements with breathing.

(B) Representative image from a control laryngoscopy examination showing vocal cord abduction and increased glottic gap during inspiration, and vocal cords in closer proximity during expiration.

7.6 Phenotype-genotype correlation of patients with *DOK7* mutations and stridor

DOK7 is an adaptor molecule composed of an N-terminal pleckstrin homology (PH) domain, a phosphotyrosine-binding (PTB) domain, and a C-terminal domain (Okada *et al.*, 2006) **(Figure 1-12)**. A total of 30 different *DOK7* mutations were identified in a cohort of 48 patients included in the present study. Most patients (93.75%) had at least one mutation within the C-terminal domain, with only 3 patients (6.25%) having mutations in both alleles 5' of this domain. The most common mutation in this cohort was, as previously reported (Cossins *et al.*, 2012), the frameshift duplication c.1124_1127dupTGCC in exon 7 and was present in at least one of the alleles in 27 patients (56.25%); this is followed by the frameshift duplication c.1339_1342dupCTGG, also in exon 7 and present in 8 patients (16.6%). Full details of genetic analysis are provided in the appendix section.

In order to study phenotype-genotype correlation in an autosomal recessive disorder such as DOK7-CMS, a visual analysis was performed using CIRCOS plots (Krzywinski *et al.*, 2009). These plots allow the circular visualisation of multiple data represented as segments. Connections within the same or different segments are represented as ribbons. Within the same segment, outgoing connections have the same colour while incoming connections take the colour from the segment of origin. Relative proportions of connections are shown as percentages.

Overall, the CIRCOS plots did not show overall major differences between patients with and without stridor when grouping the mutations into the different *DOK7* domains they belong to **(Figure 7-4)**.

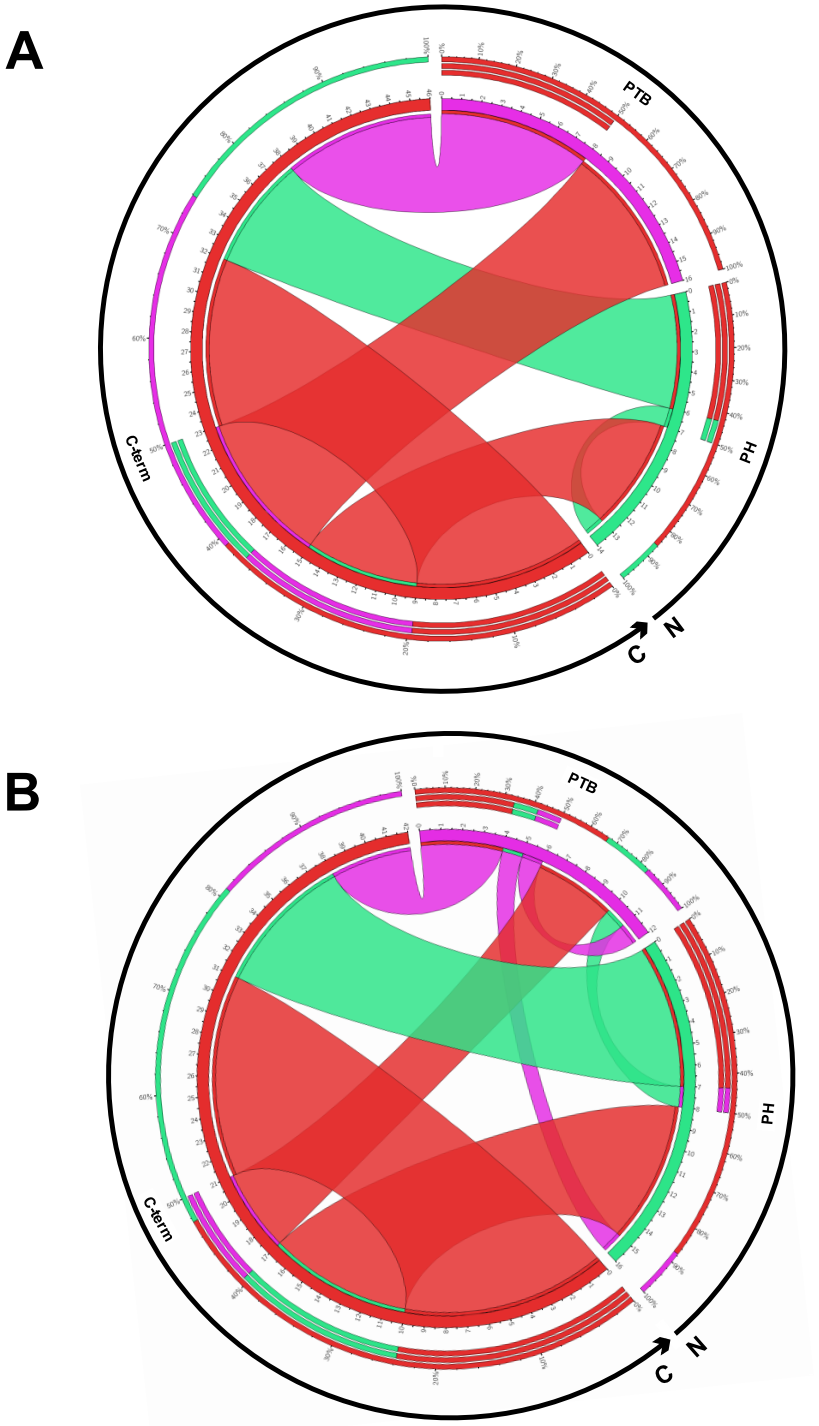


Figure 7-4. Circular representation of DOK7 mutations grouped by domains

The different DOK7 domains (PH, PTB, C-term) are represented in segments from N to C-terminus. The ribbons represent the different combinations of *DOK7* mutations grouped by domains from both alleles. Relative proportions of connections are shown as percentages.

(A) Spectrum of mutations in DOK7-CMS patients without stridor

(B) Spectrum of mutations in DOK7-CMS patients with stridor

In both groups, mutations localised at the C-terminus were overrepresented, in homozygosis or heterozygosis with pathogenic variants within the PH and PTB domains. In the non-stridor group, there was a single case homozygous for mutations localised within the PH domain. In the stridor group, one patient was homozygous for mutations within the PTB domain, and another was compound heterozygous for mutations within the PH and PTB domains.

A more detailed visual analysis using specific *DOK7* mutations (not grouped by domains) showed several differences between patients with and without stridor **(Figures 7-5 & 7-6).** Firstly, the common c.1124_1127dupTGCC mutation was present in at least one allele in 17/24 (75.00%) patients without stridor compared to 10/24 (41.6%) in the stridor-group. In addition, there were no patients homozygous for this mutation in the stridor group compared to 5 (20.83%) cases within the non-stridor group. Secondly, the c.1339_1342dupCTGG frameshift mutation was more common in the stridor group (29.16% vs 8.33%) than in the non-stridor group. Thirdly, in the non-stridor group, mutations close to the 3' end of the C-terminal domain tended to cosegregate more with mutations within the PTB domain. This contrasts with the stridor group where patients had mutations close to the 3' end of the C-terminal domain in both alleles. In addition, several mutations were unique to both groups.

The genetic data was also represented using a heat map containing the information on mutation frequency and distribution from both the stridor and non-stridor groups **(Figure 7-7).**

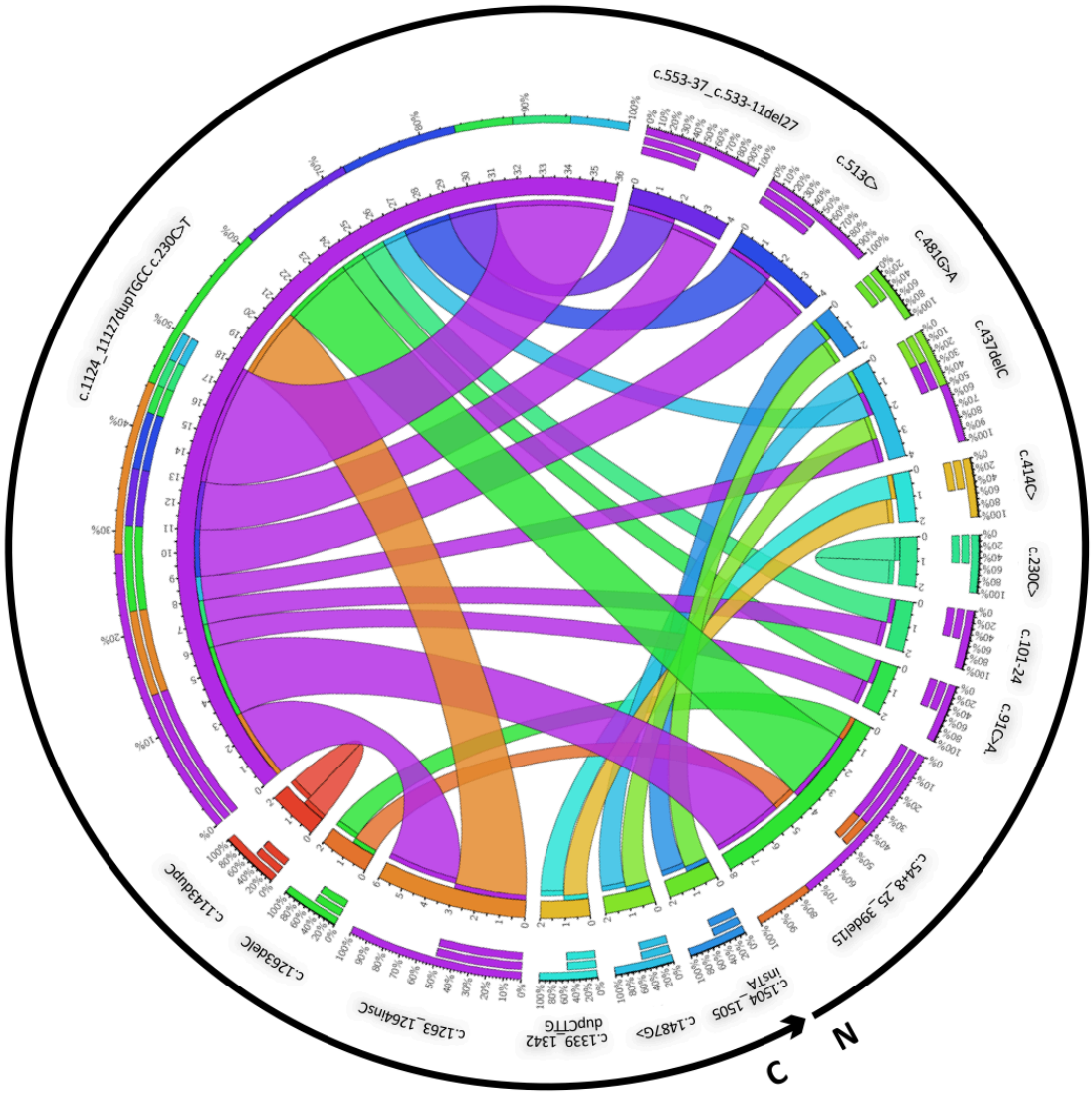


Figure 7-5. Circular presentation of *DOK7* mutations in the non-stridor group

The different *DOK7* mutations found within the group of patients without stridor are represented in segments around the circle from the N to the C-terminus. The size of the segments depends on the frequency of the mutation. Connections within the same or different segments are represented as ribbons. Within the same segment, outgoing connections have the same colour while incoming connexions take the colour from the segment of origin. Relative proportions of connections are shown as percentages.

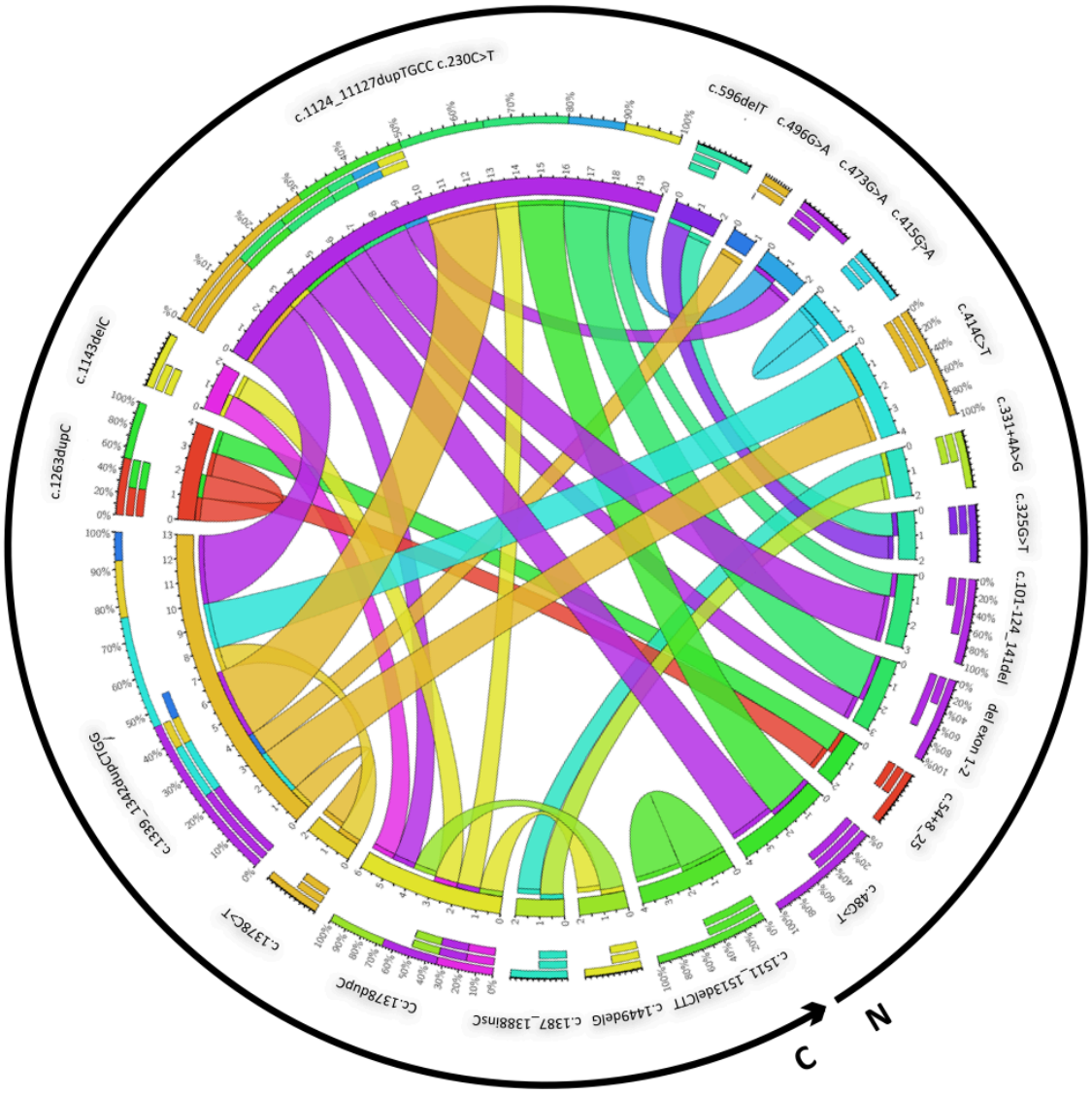


Figure 7-6. Circular presentation of *DOK7* mutations in the stridor group

The different *DOK7* mutations found within the group of patients with stridor are represented in segments around the circle from N to C-terminus. The size of the segments depends on the frequency of the mutation. Connexions within the same or different domains are represented as ribbons. Within the same segment, outgoing connexions have the same colour while incoming connexions take the colour from the segment of origin. Relative proportions of connexions are shown as percentages.

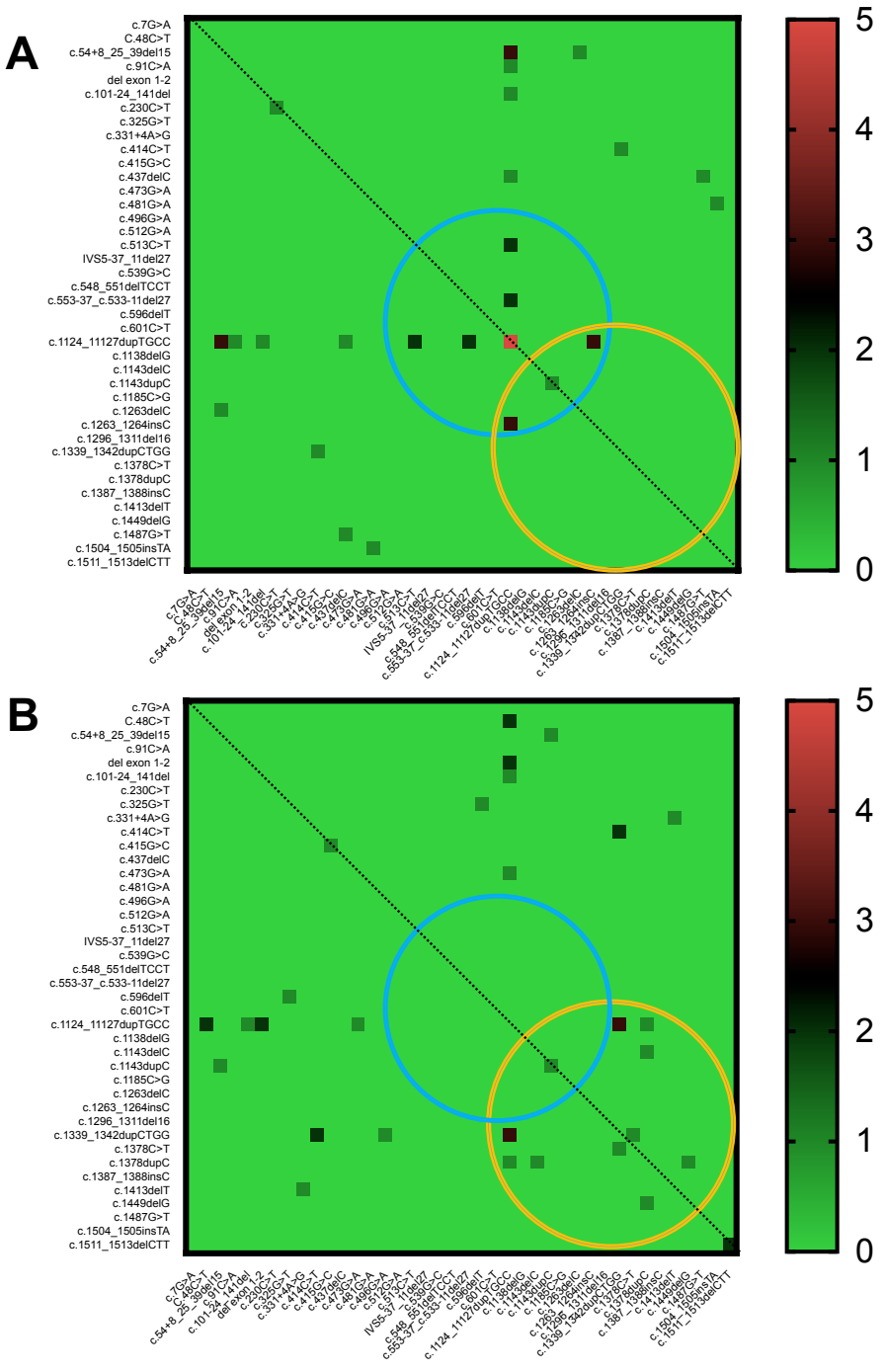


Figure 7-7. Frequency and distribution of *DOK7* mutations

The spectrum of *DOK7* mutations was represented from N to C-terminus and colour coded according to frequency in the non-stridor **(A)** and stridor **(B)** groups. Patients homozygous or compound heterozygous for the common c.1124_1127dupTGCC mutation were more frequent in the non-stridor group (blue cluster). Patients harbouring mutations close to the 3' end of the C-terminal domain in both alleles were more frequent in the stridor group (orange cluster). Several mutations were unique to both groups. Homozygous mutations are located on the punctuate midline.

7.7 Study of MuSK and DOK7 expression by indirect immunofluorescence

It has been reported that adult mouse muscles harbour different endogenous levels of MuSK and that these findings might explain the selective muscle involvement in neuromuscular disorders in which MuSK is diminished (Punga *et al.*, 2011). The hypothesis that differences in MuSK or DOK7 protein expression could be responsible for the selective impairment of the PCA muscle in DOK7-CMS was studied by indirect immunofluorescence of PCA and IA laryngeal muscles.

7.7.1 Optimisation of MuSK and DOK7 fluorescence staining in muscle sections

An initial optimisation step using different fixation methods (3% PFA at room temperature, pre-chilled acetone at -20°C or pre-chilled methanol with 5% acetic acid at -20°C – Details in section 2.5.12) and antibody concentrations was performed to determine the optimal working conditions for the quantification of fluorescence intensity in 8-10 µm transverse muscle sections. The results showed how fixation with cool acetone considerably improved antibody performance **(Table 7-1 & Figure 7-8)**.

Table 7-1. Optimisation of MuSK and DOK7 antibodies in muscle tissue

Antibody	Antigen	Dilution	Outcome		
			3% PFA	Acetone	Methanol
R&D AF562	MuSK	1:100	Suboptimal	Optimal	Poor
Abcam 92950	MuSK	1:1000	Suboptimal	Optimal	Poor
SC-N19	MuSK	1:50	Poor	Poor	Poor
SC-C19	MuSK	1:50	Poor	Suboptimal	Poor
SC-H300	MuSK	1:100	Poor	Poor	Poor
SC-H284	DOK7	1:500	Poor	Optimal	Poor
SC-S17	DOK7	1:500	Poor	Suboptimal	Poor

Acetone fixation provided the best staining results. MuSK antibodies AF562 & ab92950, and DOK7 antibody H284 were used for subsequent experiments.

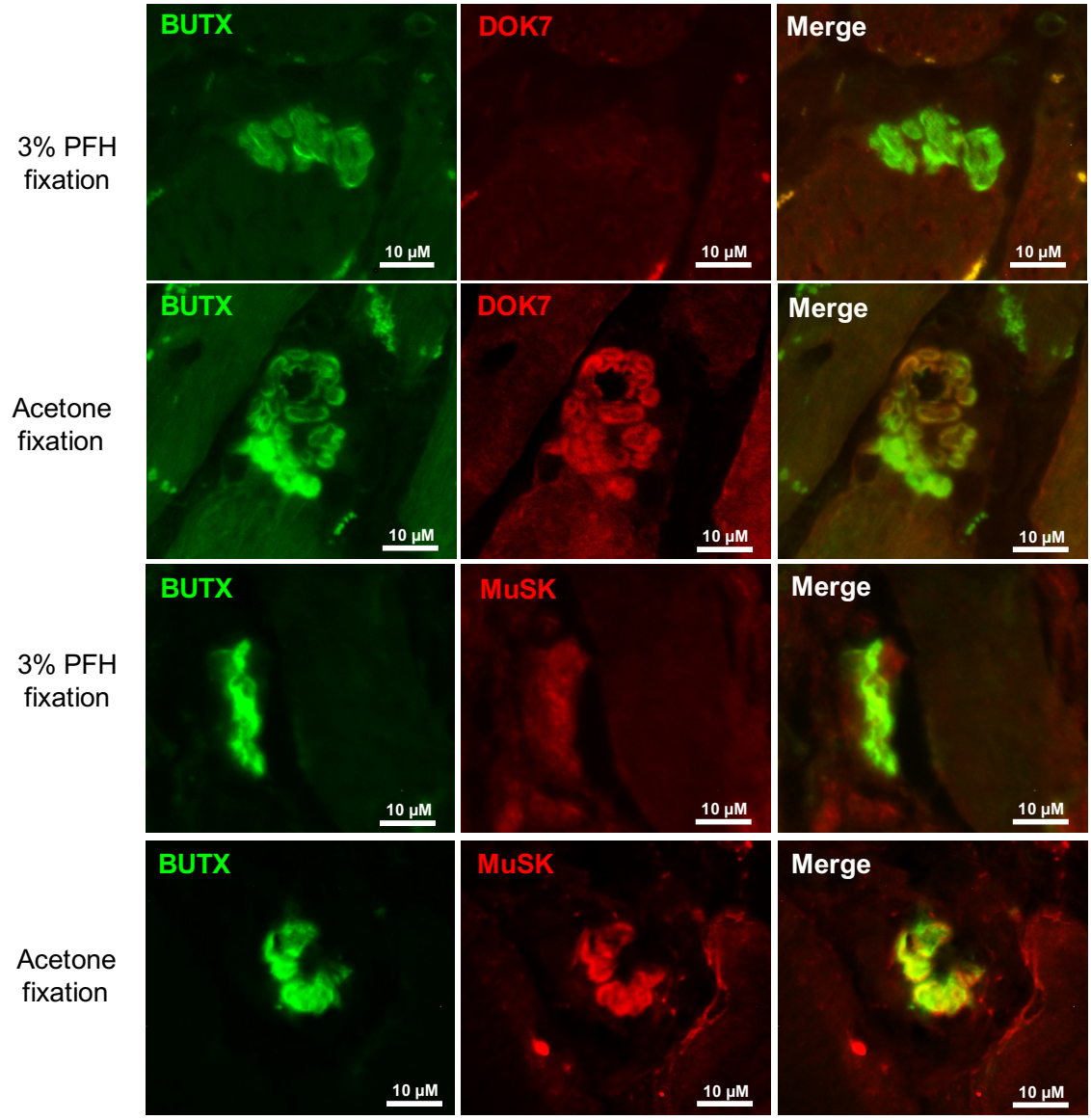


Figure 7-8. Representative images of human laryngeal muscle endplates stained with antibodies to DOK7 and MuSK

Muscle sections were fixed on 3% PFA at room temperature or pre-chilled acetone or methanol at -20°C. Subsequently, the sections were incubated with Alexa Fluor® 488-conjugated α-bungarotoxin, antibodies to DOK7 and MuSK, and the corresponding Alexa Fluor® fluorescently conjugated secondary antibodies. Finally, the sections were washed 3 times in PBS for 5 minutes and mounted in confocal-UV-matrix® and microscope slides cover-glass 22x70mm. Images were taken using an Olympus IX71 fluorescent microscope. Scale bar = 10 µm.

7.7.2 Quantification of MuSK and DOK7 fluorescence intensity at endplates from human laryngeal muscles

Quantification of mean fluorescence intensity at muscle endplates was performed using ImageJ software (Section 2.12.3). The results showed that DOK7 and MuSK were enriched at neuromuscular junctions of both PCA and IA muscles, and colocalised with Alexa Fluor® 488-conjugated α-bungarotoxin **(Figure 7-9)**. There were no signs of extra-junctional staining (DOK7 or MuSK expression outside motor endplates) in any of the samples. Quantification of DOK7 fluorescence intensity showed a 28.49 ± 4.56% increment in PCA muscle compared to IA muscle ($p<0.001$), with no differences in the fluorescence intensity of Alexa Fluor® 488-conjugated α-bungarotoxin ($p=0.954$). The quantification of MuSK fluorescence intensity showed no significant differences ($p=0.110$) between both muscles. In addition, the fluorescence intensity of Alexa Fluor® 488-conjugated α-bungarotoxin was similar ($p=0.6071$).

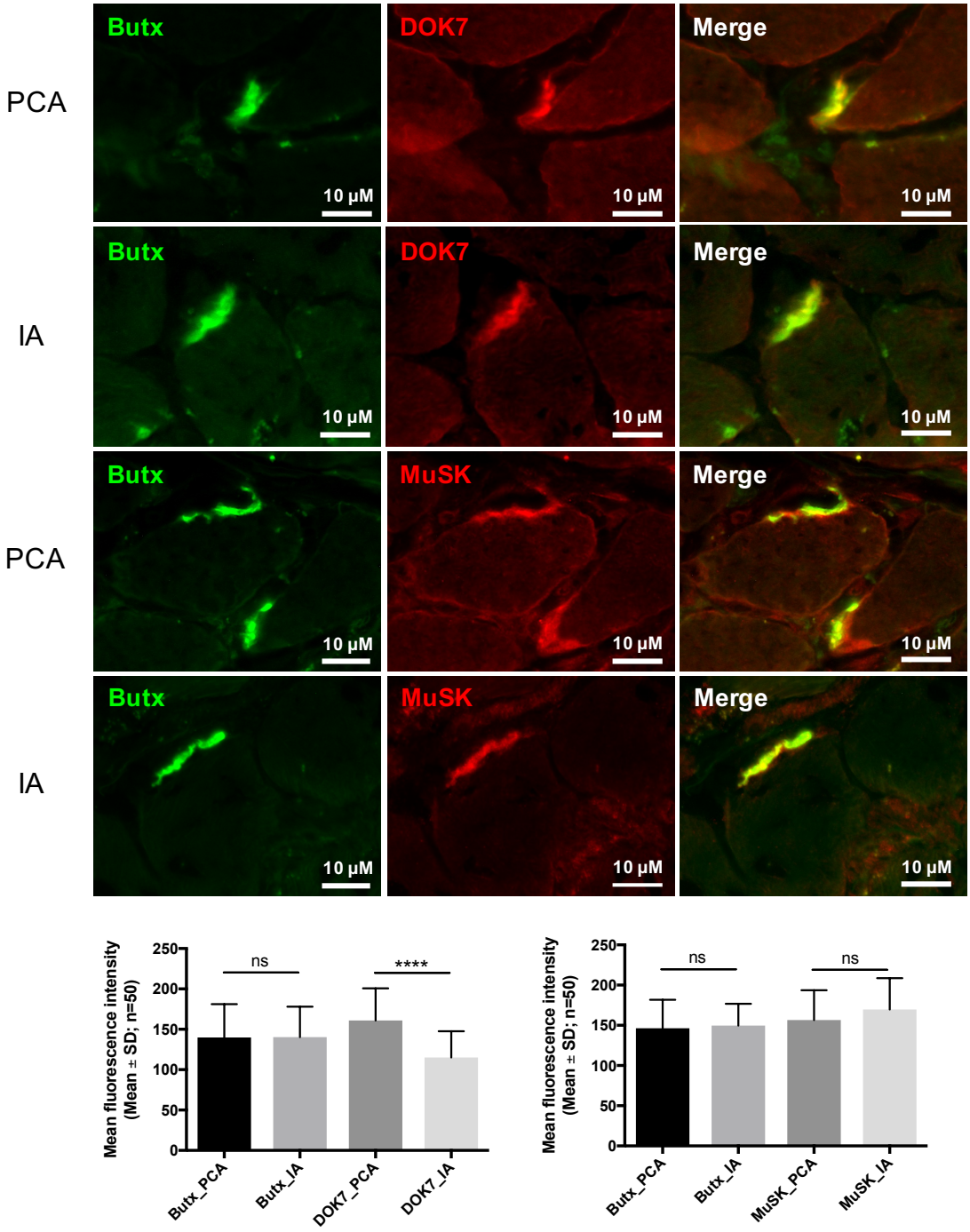


Figure 7-9. Representative images of human laryngeal muscle endplates stained with antibodies to DOK7 and MuSK

Muscle sections were fixed with acetone, and incubated with Alexa Fluor® 488-conjugated α-bungarotoxin, antibodies to DOK7 and MuSK, and the corresponding Alexa Fluor® fluorescently conjugated secondary antibody. Images were taken using an Olympus IX71 fluorescent microscope. Bar graphs represent the mean ± SD from 50 endplates for each condition. Two-tailed unpaired t-test (**** $p<0.001$). PCA = posterior cricoarytenoid muscle; IA = interarytenoid muscle; Scale bar = 10 µm.

7.8 Study of MuSK and DOK7 expression in fast and slow muscle fibres by indirect immunofluorescence

Skeletal muscle fibre types are classified into slow twitch or type-I muscle fibres and fast-twitch or type-II muscle fibres, which are then further classified as types IIA (oxidative) and IIX (glycolytic) based on their Myosin ATPase activity following preincubation in acid and alkaline media (Schiaffino and Reggiani, 1994). Different fibre types present different myosin heavy chain (MHC) isoforms, which is the principal regulator of muscle contraction and the most representative marker for fibre typing (Pette and Staron, 2000). The human PCA muscle of the larynx has a predominant type I fibre signature (60-80%) compared to other human laryngeal muscles, which are predominantly made of type II fibres (Claassen and Jochen, 1992). In keeping with this, the human IA muscle fibre type composition is made of 35% type I fibres, 45% type IIA fibres, 15% type IIX fibres, and 5% or fewer fibres, which co-express MHC isoforms (Tellis *et al.*, 2004). The fast twitch fibre density of TA, IA and LCA muscles allow rapid muscle contraction to close the glottis and protect the airway. In contrast, the slow twitch fibres of the PCA muscle make it fatigue-resistant for continuous opening of the airway during breathing (Malmgren and Gacek, 1981). To evaluate whether differences in muscle function and structure could be translated into molecular differences at the NMJ, DOK7 and MuSK expression levels were studied by indirect immunofluorescence in endplates from fast and slow laryngeal muscle fibres.

7.8.1 Fibre typing of human PCA muscle

The fibre type composition (Section 2.5.13) of the PCA muscle obtained from therapeutic laryngectomy was investigated to validate the findings in the literature. This showed, as expected, a higher proportion of slow twitch (type I) muscle fibres **(Figure 7-10)**.

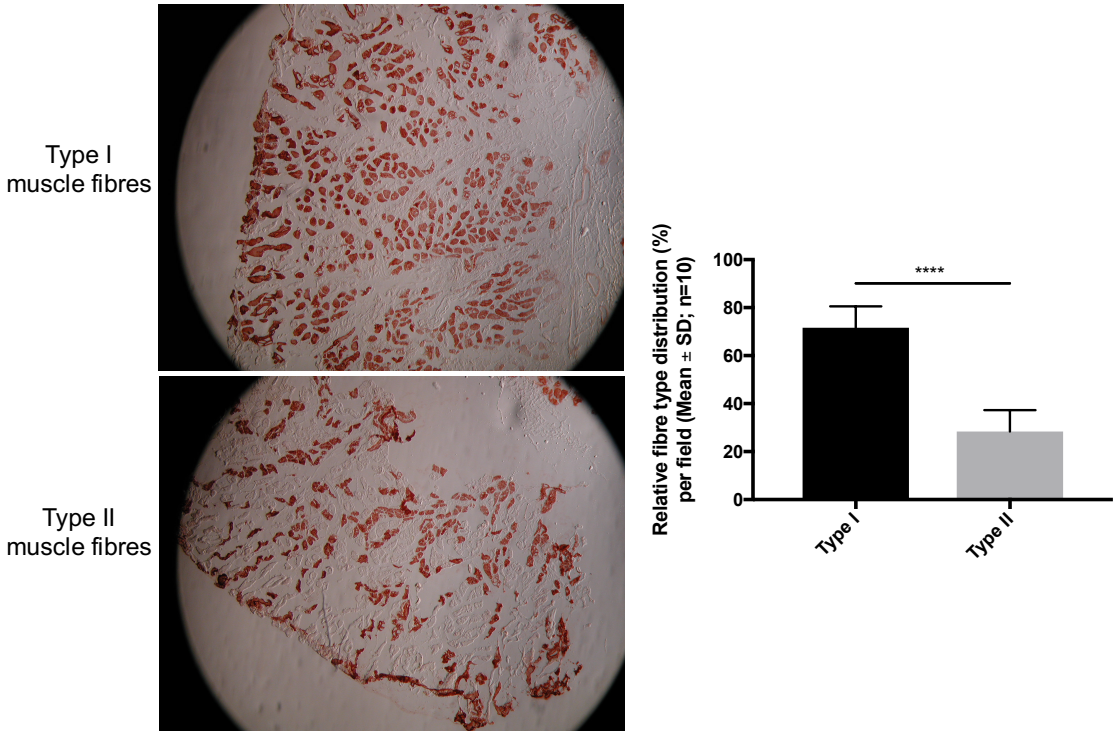


Figure 7-10. Photomicrographs of immunohistochemical staining for slow and fast myosin in PCA muscle sections

PCA muscle sections were incubated with monoclonal antibodies to fast or low MHC and HRP-conjugated antibodies, and developed using AEC (Section 2.5.13). Images were taken using a light microscopy. The frequency distribution of slow and fast fibres was quantified manually on 10 images at 10X magnification. Bar graphs represent the mean ± SD from 10 different fields. Two-tailed unpaired t-test (**** $p<0.001$).

7.8.2 Quantification of MuSK and DOK7 expression in PCA fast and slow muscle fibres

The quantification of DOK7 mean fluorescence intensity **(Figure 7-11)** at the muscle endplates from slow fibres showed a significantly (11.33%) higher intensity compared to fast muscle fibres ($p=0.026$). There were no differences in the quantification of Alexa Fluor® 488-conjugated α-bungarotoxin staining ($p=0.945$), which was used as a control. The quantification of MuSK mean fluorescence intensity **(Figure 7-12)** at the muscle endplates showed no significant differences between slow and fast fibres ($p=0.175$).

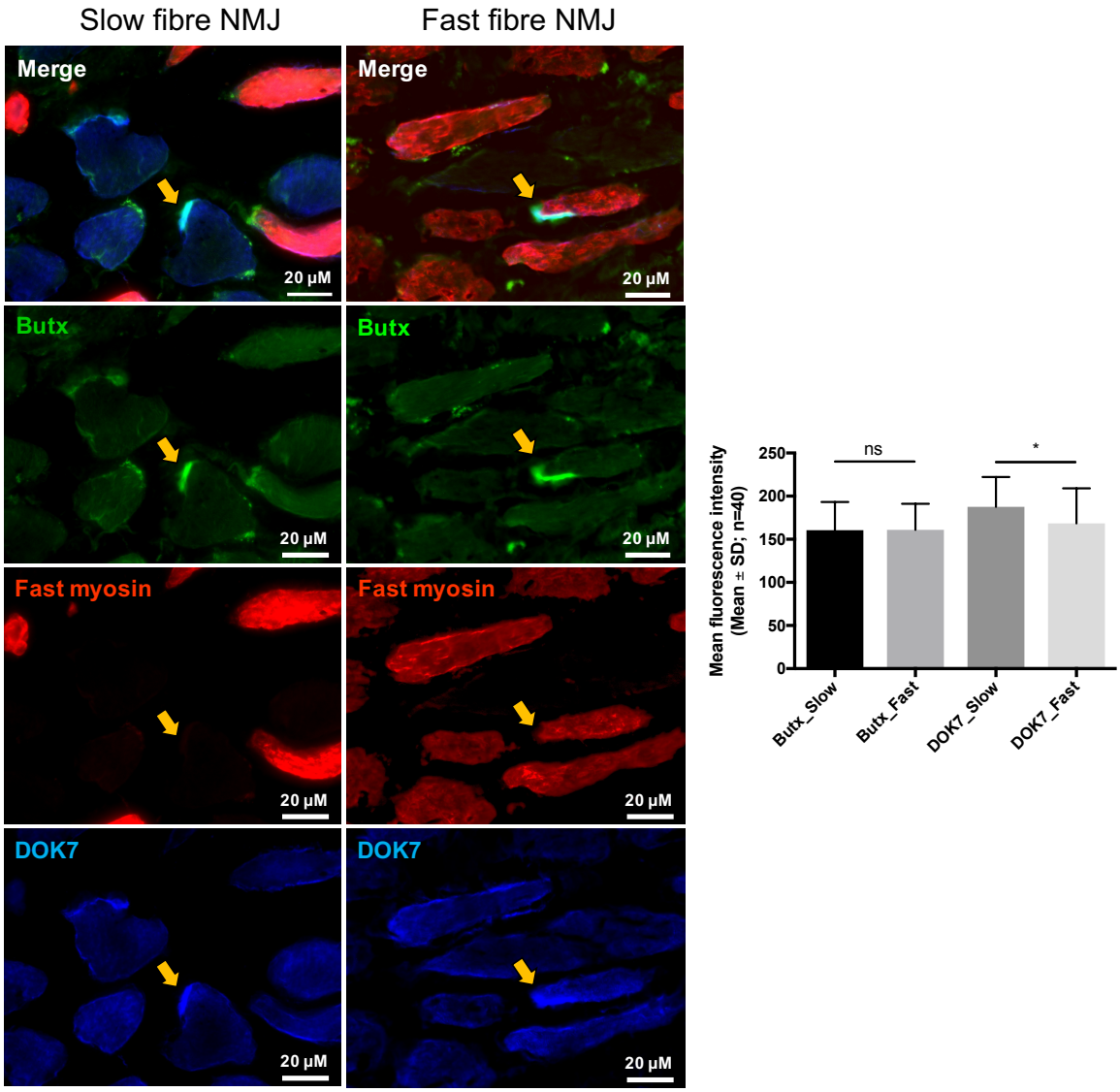


Figure 7-11. Representative images and quantification of DOK7 expression in endplates from fast and slow muscle fibres

PCA muscle sections were incubated with Alexa Fluor® 488-conjugated α-bungarotoxin, antibodies to fast MHC and DOK7, and the corresponding Alexa Fluor® fluorescently conjugated secondary antibodies. Images were taken using an Olympus IX71 fluorescent microscope. The yellow arrows point to the localisation of the NMJ. Mean fluorescence intensity was quantified using Image J software. Bar graphs represent the mean ± SD from 40 endplates for each condition. Two-tailed unpaired t-test (* $p<0.05$; ns= non-significant). Scale bar = 10 µm.

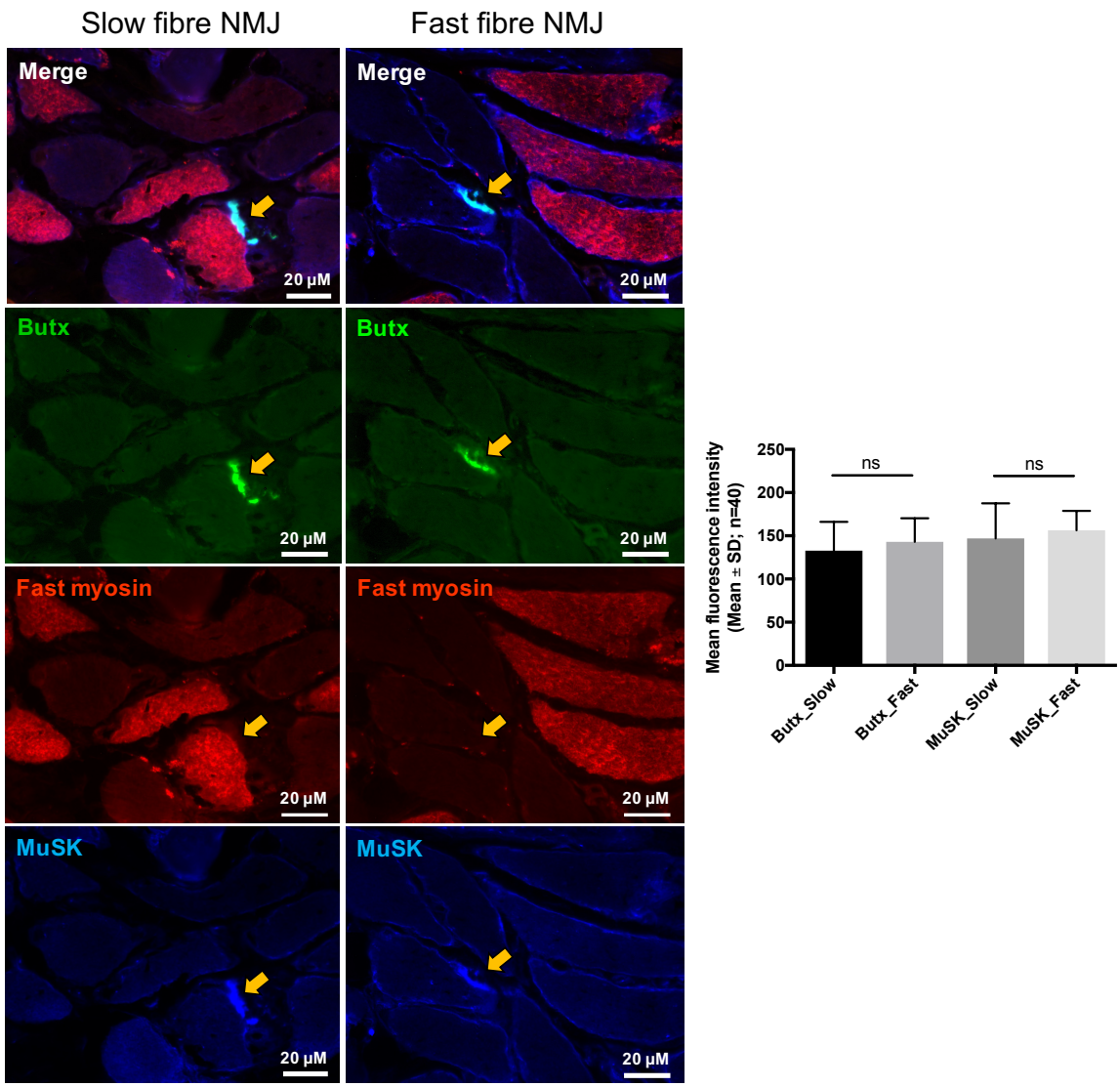


Figure 7-12. Representative images and quantification of MuSK expression in endplates from fast and slow muscle fibres

PCA muscle sections were incubated with Alexa Fluor® 488-conjugated α-bungarotoxin, antibodies to fast myosin and MuSK, and the corresponding Alexa Fluor® fluorescently conjugated secondary antibodies. Images were taken using an Olympus IX71 fluorescent microscope. The yellow arrows point to the localisation of the NMJ. Mean fluorescence intensity was quantified using image J software. Bar graphs represent the mean ± SD from 40 endplates for each condition. Two-tailed unpaired t-test (ns= non-significant). Scale bar = 10 µm.

7.9 Study of MuSK and DOK7 expression in human laryngeal muscles by western blotting

DOK7 and MuSK expression was studied in protein extracts from 3 sets of muscles from 3 different donors by western blotting (Section 2.5). Results were normalised to GAPDH for protein loading control or to the epsilon subunit of the AChR to control for the amount of motor endplates in each sample (Section 7.11.2).

7.9.1 DOK7 protein expression

The results in muscle lysates showed the unexpected appearance of a double protein band at the correct apparent molecular weight (53 KDa) for DOK7 **(Figure 7-13A)**. There were no significant differences in DOK7 expression levels relative to AChR-ε (p=0.771) or GAPDH (p=0.636) between the PCA and IA muscles **(Figure 7-13B, C)**. However, densitometry analysis showed that in the PCA muscle the expression of the lower protein band was significantly higher than the upper band (p=0.017). There were no significant differences between the upper and lower bands for the IA samples (p=0.982).

7.9.2 MuSK protein expression

Western blotting revealed a single band at the predicted molecular weight (97 KDa) for MuSK. Densitometry analysis did not show significant differences in MuSK protein expression relative to AChR-ε (p=0.727) or GAPDH (p=0.497) between the PCA and IA muscles **(Figure 7-14)**.

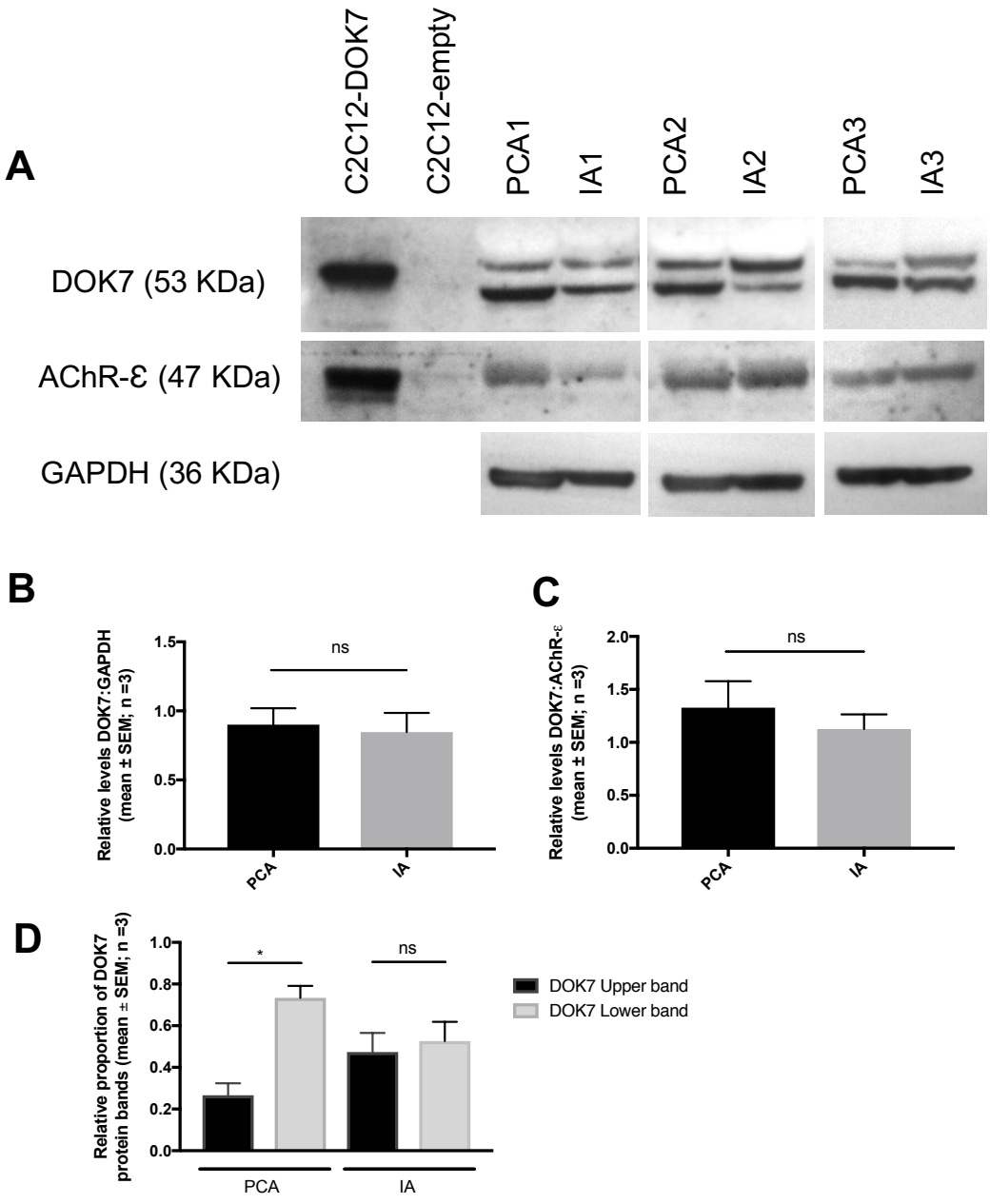


Figure 7-13. Western blot analysis of DOK7 expression in human PCA and IA muscles

(A) Protein extracts from human laryngeal muscles and cells overexpressing DOK7, AChR-ε or an empty vector, as controls, were prepared, resolved by SDS-PAGE, and analysed by western blot with antibodies to DOK7, AChR-ε, and GAPDH. **(B, C)** The ratios of DOK7:AChR-ε and DOK7:GAPDH were obtained by densitometry analysis. Two tailed paired t-test (ns= $p>0.05$). The results represent the mean ± SEM from n=3 experiments. **(D)** The relative proportion of DOK7 protein bands was obtained by densitometry. The results are represented as mean ± SEM from n=3 experiments. One-way ANOVA and Sidak´s multiple comparisons test (*$p<0.05$).

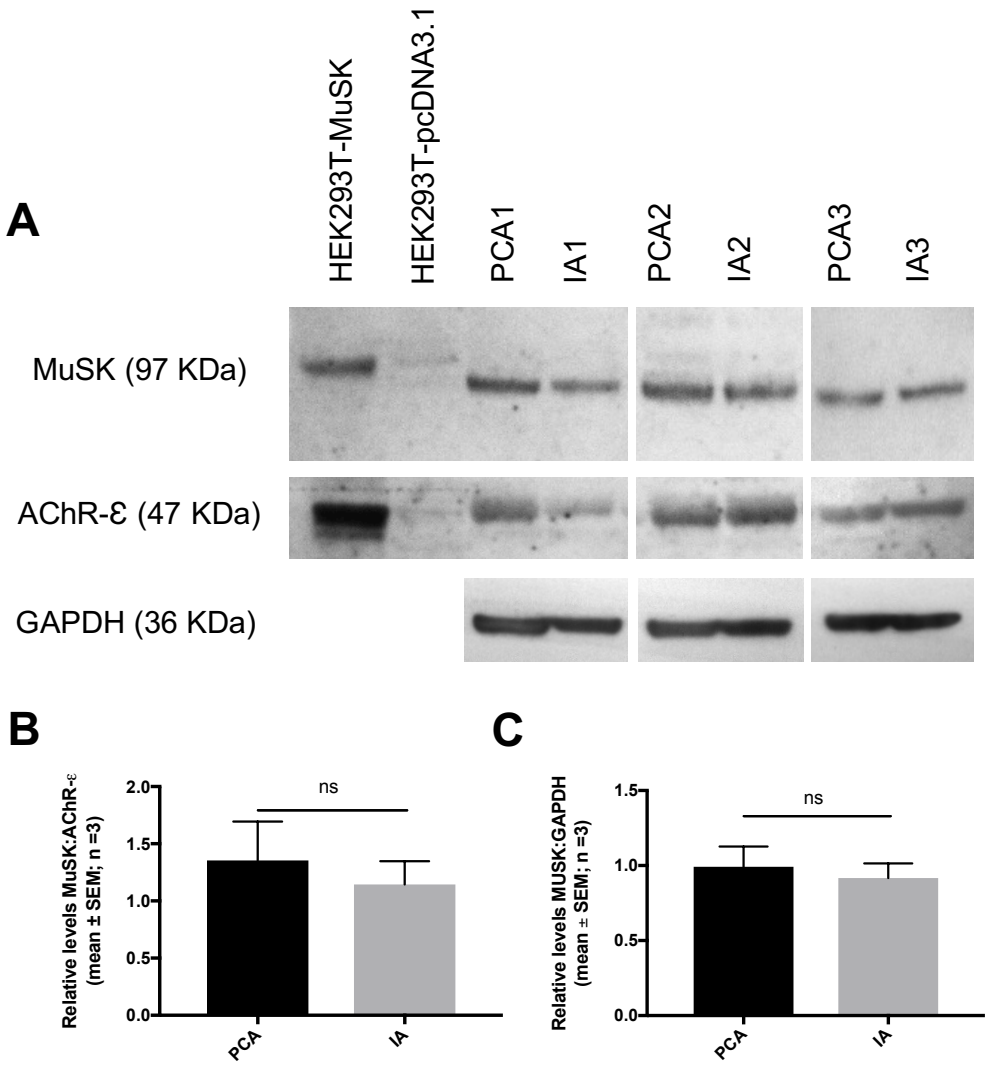


Figure 7-14. Western blot analysis of MuSK expression in human PCA and IA muscles

(A) Protein extracts from human laryngeal muscles and HEK-293T cells overexpressing MuSK, AChR-ε or an empty vector as controls were prepared, resolved by gel SDS-PAGE, and analysed by western blot with antibodies to MuSK, AChR-ε, and GAPDH. **(B, C).** The ratios of MuSK:AChR-ε and MuSK:GAPDH were obtained by densitometry analysis. The results are represented as mean ± SEM from n=3 experiments using samples from different donors. Two tailed paired t-test (ns= p>0.05).

7.10 Study of DOK7 muscle isoforms in human laryngeal muscles

The unexpected results from the western blot experiments showing a double band of approximately 53 and 49 KDa respectively, raised the question of whether several DOK7 isoforms were present in human laryngeal muscles. Interestingly, a similar double protein band can also be seen in protein lysates from HEK-293T and mouse muscle C2C12 cells transfected with cDNA encoding human DOK7 but not in mouse muscle lysates (data not shown).

On the one hand, it is possible that different DOK7 transcripts are generated via alternative splicing, alternative initiation or termination of mRNA precursors. On the other hand, post-translational modifications of proteins such as covalent addition of functional groups, proteolytic cleavage or protein degradation could also increase DOK7 protein diversity. NCBI Reference Sequence data (https://www.ncbi.nlm.nih.gov/refseq/) shows the existence of 4 mRNA DOK7 transcript variants and 4 DOK7 protein isoforms in *Homo sapiens* **(Table 7-2)**. The role of protein variety and functional diversity in human DOK7 is unknown.

Table 7-2. DOK7 transcript variants and DOK7 protein isoforms in *Homo sapiens*

Transcript variant, mRNA			Protein		
Number	**RefSeq**	**bp**	**Isoform**	**RefSeq**	**aa**
1	NM_173660.4	2583	1	NP_775931.3	504
2	NM_001164673.1	2572	2	NP_001158145.1	255
3	NM_001256896.1	2281	3	NP_001243825.1	194
4	NM_001301071.1	2545	4	NP_001288000.1	608

7.10.1 Study of DOK7 isoforms by RT_PCR

The cDNA from two sets of human laryngeal muscles was amplified using primers designed to cover the full-length DOK7 cDNA (RefSeq NM_173660.4) **(Table 2-4)**. The resolution of PCR products showed a single band of approximately 1500 bp in all muscle samples. Sanger sequencing confirmed that the band corresponded to DOK7 transcript variant 1. This suggests that the different DOK7 proteins bands observed by western blotting are unlikely to be generated from different DOK7 mRNA transcripts.

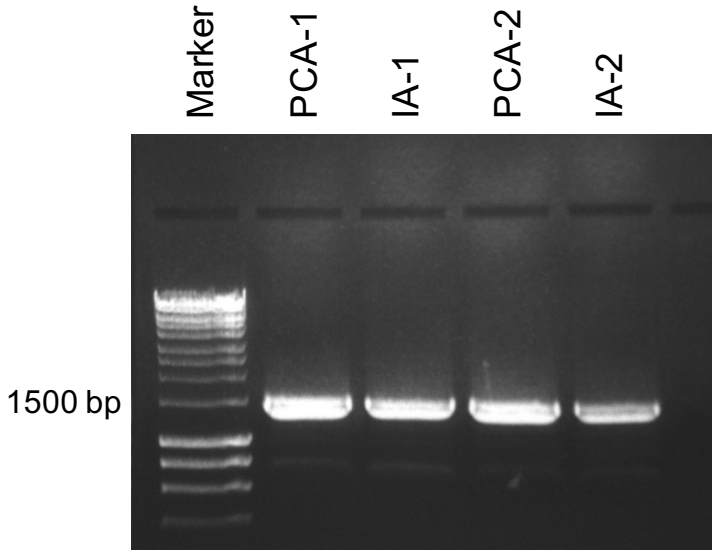


Figure 7-15. Resolution of PCR products encompassing DOK7 amplification in human laryngeal muscles

cDNA was prepared from two sets of PCA and IA human laryngeal muscles (Section 2.4.2-4) and amplified using primers designed to cover the full-length DOK7 cDNA. The products were resolved by gel electrophoresis, gel-extracted and analysed by Sanger sequencing. IA, interarytenoid; PCA, posterior cricoarytenoid.

7.10.2 Study of DOK7 isoforms by Mass Spectrometry

7.10.2.1 DOK7 immunoprecipitation from HEK-293T cells

An initial experiment was set up to test DOK7 immunoprecipitation from protein lysates of HEK-293T overexpressing human DOK7 (Section 2.5.7). Western blot analysis showed the appearance of two bands in both WCL and IP samples **(Figure 7-16)** in a similar fashion as to the human laryngeal muscle lysates previously shown. A double band was also present in lysates from mouse muscle C2C12 cells transfected with cDNA encoding human DOK7. Increasing the boiling temperature of samples from 90°C to 100°C prior to SDS-PAGE resolution did not have any effect on protein migration suggesting that the presence of the double protein band was not related to protein aggregation.

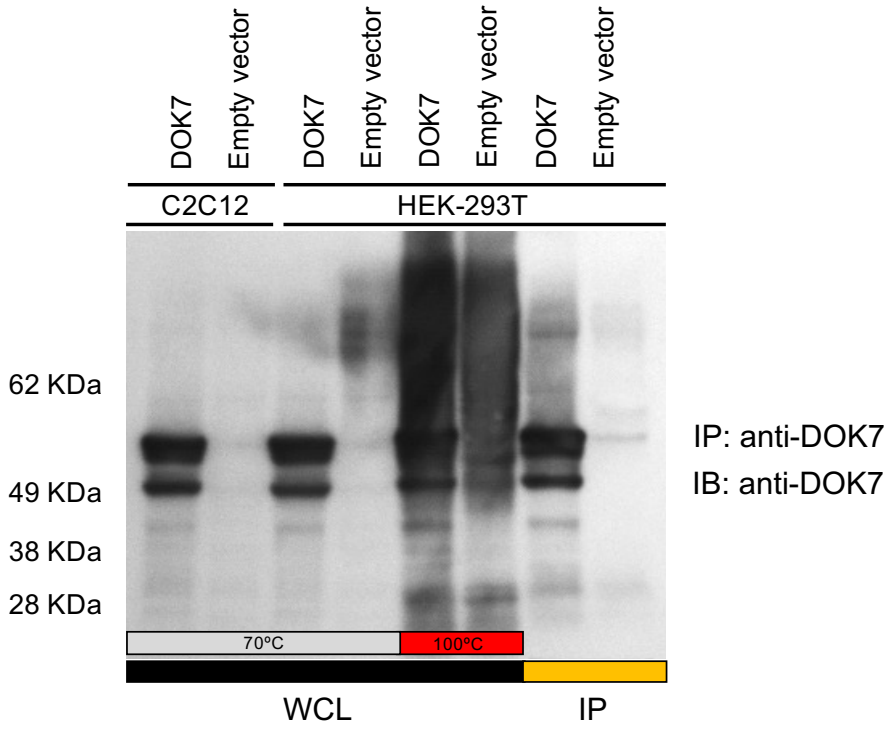


Figure 7-16. DOK7 immunoprecipitation from HEK-293T cells

Cell lysates from HEK-293T cells overexpressing DOK7 or pcDNA3.1/Hygro(+) were immunoprecipitated and analysed by western blot. The figure shows that the anti-DOK7 antibody was able to pull-down DOK7 successfully. Whole cell lysates (WCL) are shown in the left side of the image.

7.10.2.2 Silver staining of DOK7 immunoprecipitated products

Protein lysates from HEK-293T cells overexpressing DOK7-EGFP, DOK7 and pcDNA3.1/Hygro(+) were immunoprecipitated and resolved by SDS-PAGE. The protein bands corresponding to DOK7 were visualised by silver staining (Section 2.5.6.2) **(Figure 7-17)**, excised, and independently analysed by tandem mass spectrometry (Section 2.6).

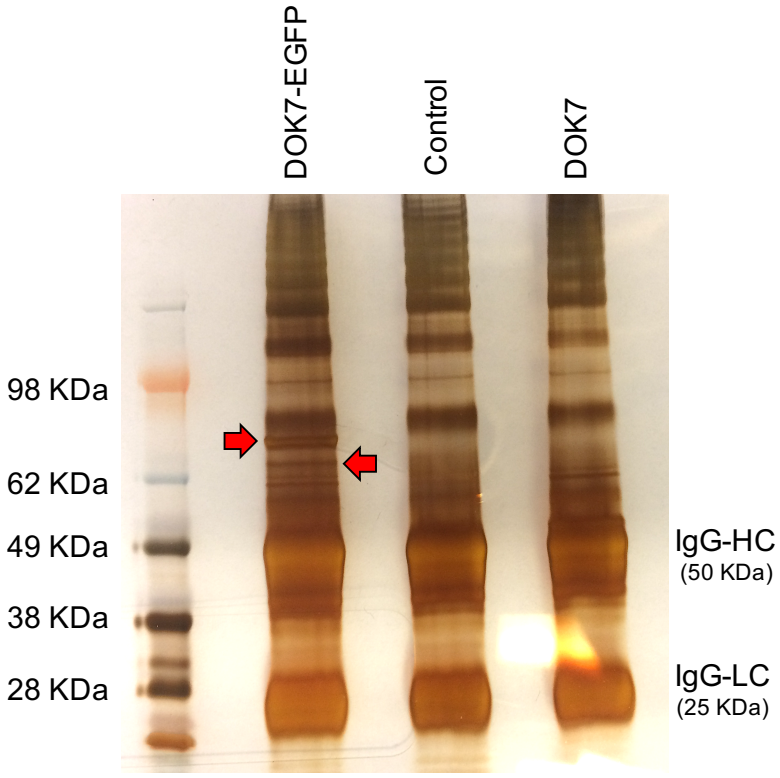


Figure 7-17. Silver stain in-gel protein detection following DOK7-IP

HEK-293T cells were transfected with constructs encoding DOK7, DOK7-EGFP and pcDNA3.1/Hygro(+). The DOK7-EGFP tagged construct was used to increase the molecular weight of the protein and avoid the interference with the IgG-Heavy chain (50 KDa) from the antibody used for immunoprecipitation. The cell lysates were immunoprecipitated using a rabbit anti-DOK7 antibody, resolved by SDS-PAGE and visualised by silver staining. Two bands (red arrows) present in the first lane but not in the control lane were excised for in-gel tryptic digestion of proteins and subsequent analysis by tandem mass spectrometry. An extra band from a non-relevant region was used as a control.

7.10.2.3 Tandem mass spectrometry analysis

Peptide sequencing by tandem mass spectrometry was performed as previously described (Section 2.6). The analysis of the upper band products identified a total of 401 peptides with 91% coverage of protein DOK7 isoform 1 [Homo sapiens] (RefSeq NP_775931.3) **(Figure 7-18)**. The analysis of the lower band identified a total of 102 peptides with a 60% and 49% coverage of protein DOK7 isoform 1 [Homo sapiens] (RefSeq NP_775931.3) and 4 [Homo sapiens] (RefSeq NP_001288000.1), respectively **(Figure 7-19)**. The analysis of the control band did not show any traces of DOK7 protein.

Protein alignment analysis using COBALT (Constrained-based Multiple Alignment Tool - https://www.ncbi.nlm.nih.gov/tools/cobalt/re_cobalt.cgil) of peptides obtained by mass spectrometry from the band with the lower molecular weight and DOK7 isoforms 1/2/3/4 did not allow for the differentiation between DOK7 isoforms 1 and 4 **(Figure 7-20)**. However, the fact that DOK7 protein isoform 4 is greater in size (608 aa) than isoform 1 (504 aa) makes the first less likely due to the smaller molecular weight of the protein band found by western blot.

The results from the tandem mass spectroscopy analysis of the lower protein band showed DOK7 coverage from the third methionine codon (position 88), and thus missing most of the pleckstrin-homology (PH) domain (position 4-109). This suggests that there is a non-canonical isoform of DOK7 that could either be a cleaved product or be produced by an alternative start codon using a different methionine codon to start translation. The latter possibility was subsequently investigated by side-directed mutagenesis of the third DOK7 methionine codon at position 88.


1 MTEAALVEGQ VKLRDGKKWK SRWLVLRKPS PVADCLLMLV YKDKSERIKG LRERSSLTLE DICGLEPGLP YEGLVHTLAI
81 VCLSQAIMLG FDSHEAMCAW DARIRYALGE VHRFHVTVAP GTKLESGPAT LHLCNDVLVL ARDIPPAVTG QWKLSDLRRY
161 GAVPSGFIFE GGTRCGYWAG VFFLSSAEGE QISFLFDCIV RGISPTKGPF GLRPVLPDPS PPGPSTVEER VAQEALETLQ
241 LEKRLSLLSH AGRPGSGGDD RSLSSSSSEA SHLDVSASSR LTAWPEQSSS SASTSQEGPR PAAAQAAGEA MVGASRPPPK



Figure 7-18. Analysis of DOK7 peptides sequence data (higher protein band)

The figure shows the individual peptide sequences obtained by tandem mass spectrometry together with the different post-translational modifications as detailed in the figure legend. The peptide sequences were aligned with protein DOK7 isoform 1 [Homo sapiens] (RefSeq NP_775931.3) and had 91% protein coverage.

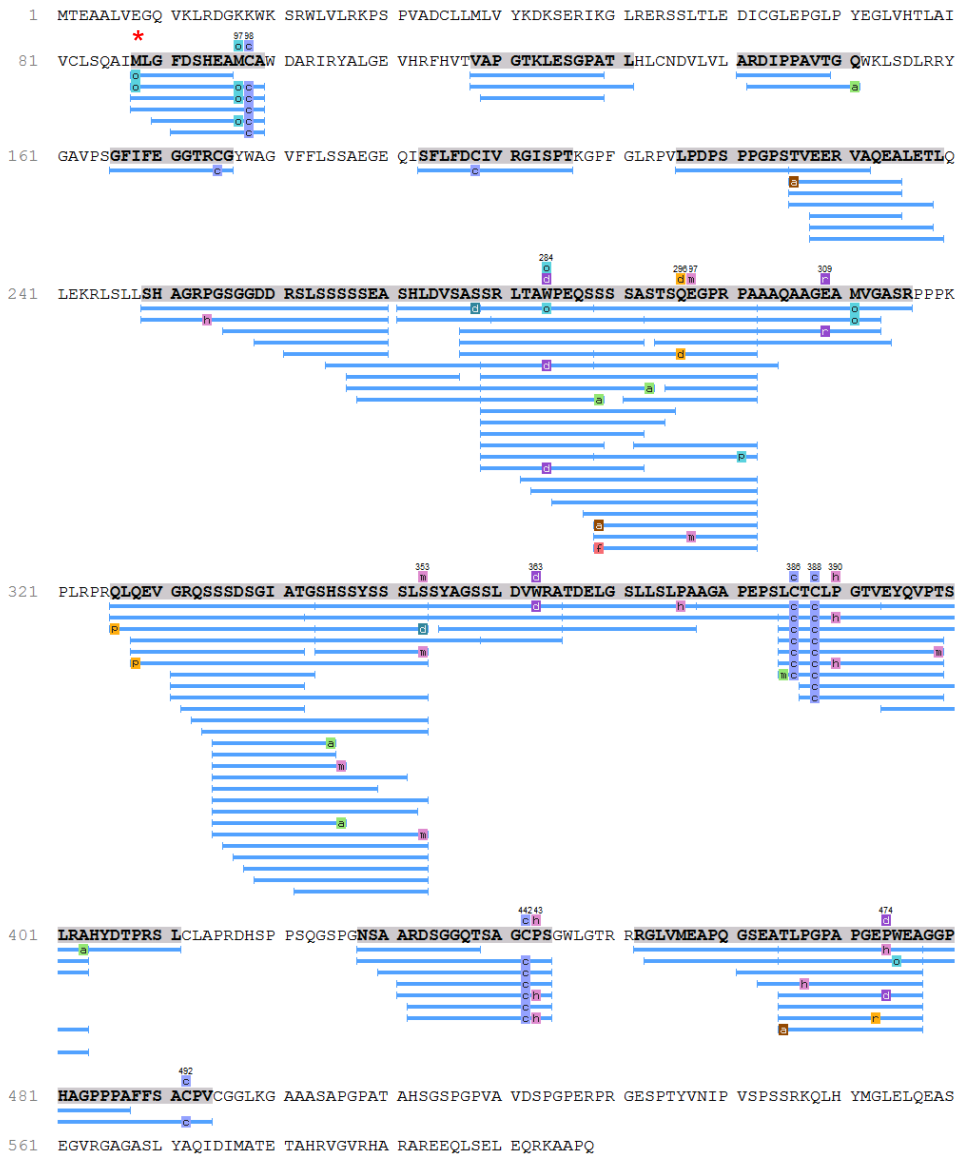


Figure 7-19. Analysis of peptides sequence data (lower protein band)

The figure shows the alignment of individual peptide sequences obtained by tandem mass spectrometry with protein DOK7 isoform 4 [Homo sapiens] (RefSeq NP_775931.3). The protein coverage for the peptides obtained was 49%. The third methionine codon at position 88 is marked with a red asterisk. Post-translational modifications are detailed in figure legend 7-18.

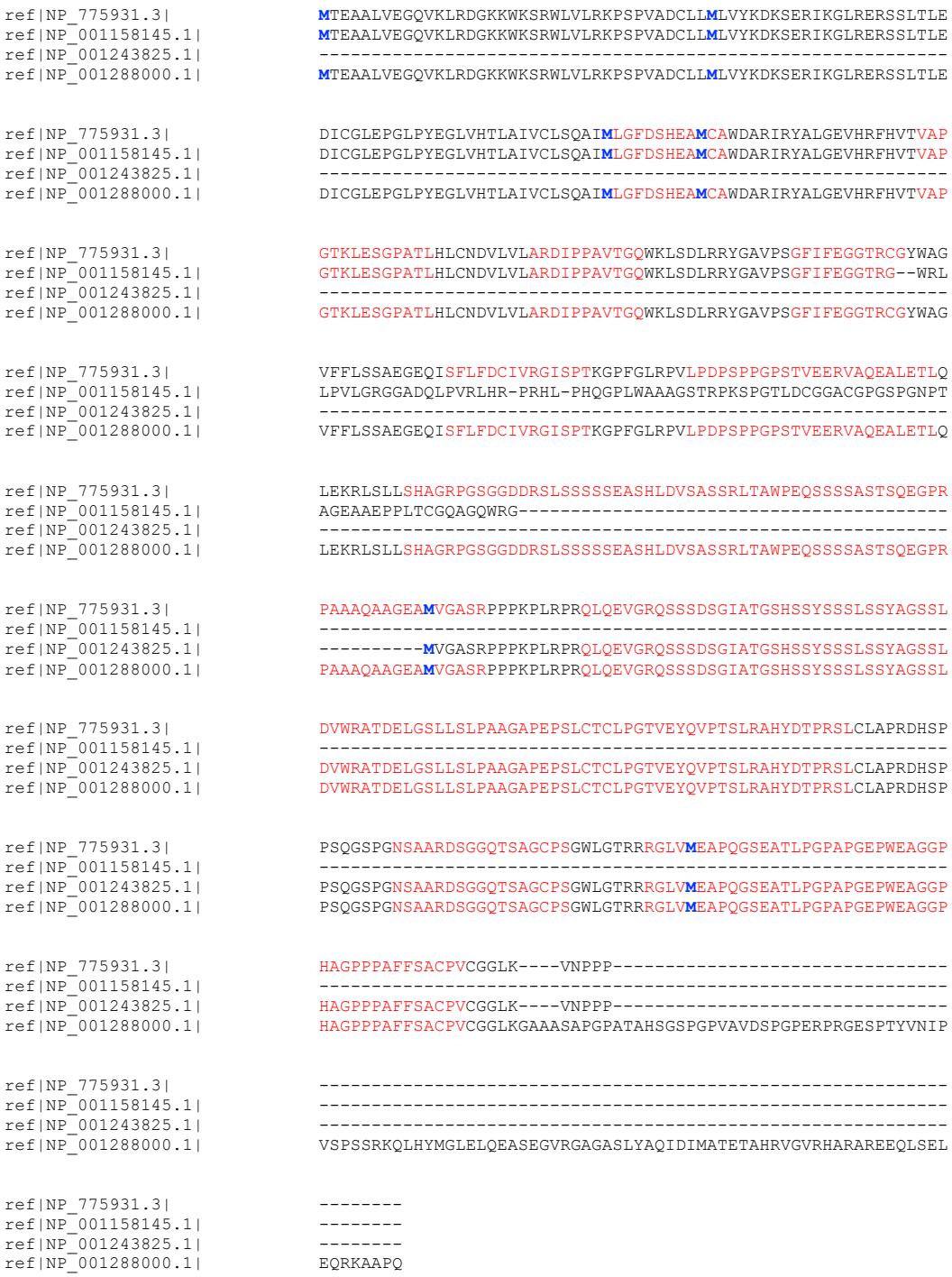


Figure 7-20. Alignment of DOK7 protein isoforms 1/2/3/4 and peptides sequences obtained by tandem mass spectrometry analysis of the lower protein band

The figure shows 60% and 49% coverage (red colour) of protein DOK7 isoform 1 [Homo sapiens] (RefSeq NP_775931.3) and 4 [Homo sapiens] (RefSeq NP_001288000.1) respectively. Peptides sequences expand beyond the boundaries of isoform 2 [Homo sapiens] (RefSeq NP_001158145.1) and 3 [Homo sapiens] (RefSeq NP_001243825.1). Methionine residues are represented in blue.

7.10.3 Study of DOK7 isoforms by site-directed mutagenesis of DOK7 Met residues

Site directed mutagenesis of the first five methionine residues did not cause apparent changes in protein expression assessed by immunofluorescence **(Figure 7-21A)**. Western blot analysis showed that p.M1A mutation caused a shift in protein size due to alternative initiation from p.Met 38. However, DOK7 short isoform expression was not affected by the mutagenesis of the different methionine residues **(Figure 7-21B)**. It is possible that combined mutagenesis of contiguous Met residues is needed to stop the translation of the smaller protein band.

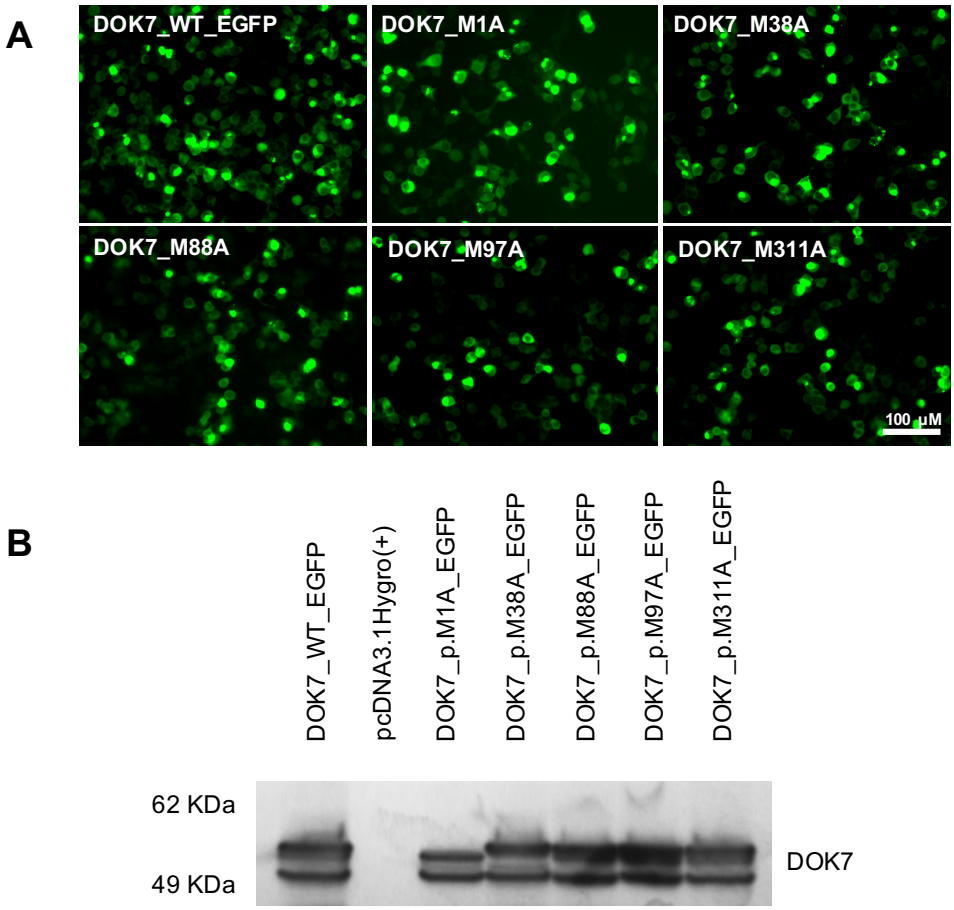


Figure 7-21. DOK7 expression following site-directed mutagenesis of met residues

(A) HEK-293T cells were transfected with 3 µg of the above constructs and visualised using an Olympus IX71 fluorescent microscope. **(B)** Subsequently, cell lysates were prepared, resolved by SDS-PAGE, and immunoblotted using a rabbit anti-EGFP antibody and the corresponding HRP-conjugated secondary antibody. Scale bar = 100 µm.

7.11 Study of NMJ gene expression levels in human laryngeal muscles by QPCR

A 96-well plate gene expression panel was developed as previously described in methods (Section 2.4.5). Differences in gene expression between the PCA (affected) and IA (non-affected) laryngeal muscles were tested in 8 biological replicates from 8 different donors.

7.11.1 mRNA expression levels normalised to GAPDH

Gene expression data were normalised to *GAPDH* mRNA expression to account for differences in the amount of starting material between muscle samples. Data analysis showed that *DOK7* expression was 1.55-fold higher ($p = 0.0391$) in the PCA muscle samples compared to the IA muscle samples. **(Figure 7-22A)**. There were no significant differences for other genes tested. Relative abundances of mRNA levels are provided separately (**Figure 7-22B)**. It is noteworthy the relatively high levels of *CHRND* mRNA expression, which are closer to the levels of *CHRNA1* than to *CHRNE* as it would be expected. The $2^{-\Delta\Delta Ct}$ analysis showed an overall high variability in fold change mRNA levels among the different biological replicates **(Figure 7-22C)**.

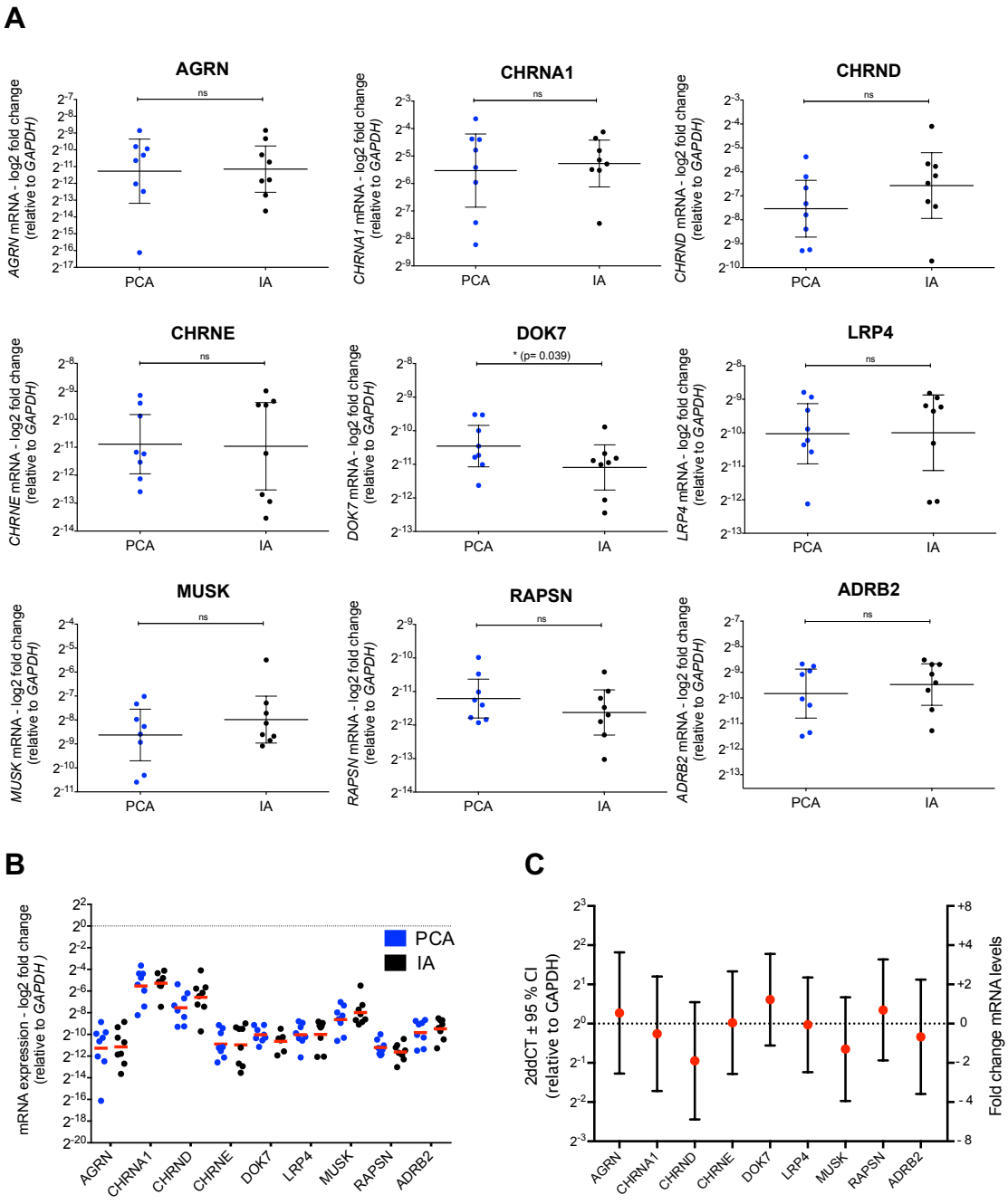


Figure 7-22. mRNA expression levels in PCA and IA muscles normalised to *GAPDH*

(A) Dot plots representation of mRNA levels as fold change (*log2*) in expression relative to *GAPDH* using $2^{-\Delta Ct}$. The data points correspond to individual values for each muscle, and the results are summarised by geometric mean and 95% CI. Two-tailed Wilcoxon matched-pairs signed rank test (*p <0.05; ns= non-significant). **(B)** Relative abundances of mRNA levels. **(C)** $2^{-\Delta\Delta Ct}$ fold change in PCA muscle mRNA levels compared to IA. Mean and 95% CI are displayed on a *log2* scale. *Dashed lines (2^0) represents baseline mRNA levels for GAPDH.*

7.11.2 mRNA expression levels normalised to CHRNE & GAPDH

The pentameric composition of the AChRs and its distribution along the muscle fibres are regulated during development. In foetal muscles, foetal AChRs (α2ßγδ) are distributed along the muscle fibres, while in adult muscle, AChRs (α2ßγε) are concentrated predominantly at the NMJ (Hartzell and Fambrough, 1972). The synaptic localisation of the AChR subunits is believed to arise from selective down regulation at extra-synaptic regions, except for the AChR-ε subunit, which is thought to be induced locally through a signal that is restricted to the NMJ (Brenner *et al.*, 1990). Even after denervation at birth, and prior to the gamma-epsilon switch occurs (Missias *et al.*, 1996), the AChR-ε subunit expression arises at former synaptic locations (Gundersen *et al.*, 1993). Therefore, *CHRNE* mRNA expression could be used as an "endplate control" for the normalisation of gene expression data to the relative amount of muscle endplates within the sample.

A more accurate method for gen data normalisation by geometric averaging of multiple internal control genes (Vandesompele *et al.*, 2002) was used to control for differences in the amount of starting material (*GAPDH*) and motor endplates (*CHRNE*) between muscle samples. Data analysis showed a 1.50-fold increase in *DOK7* expression ($p = 0.023$) for the PCA muscle samples compared to the IA muscle **(Figure 7-23A)**. This is in keeping with a 28.49 ± 4.56% increase in DOK7 fluorescence intensity previously described in the PCA muscle (Section 7.7.2). Relative abundances of mRNA levels are provided in a separate graph (**Figure 7-23B)**. The $2^{-\Delta\Delta Ct}$ method showed an overall high variability in fold change mRNA levels among the different biological replicates **(Figure 7-23C)**. The dashed line represents baseline mRNA levels for *GAPDH* and *CHRNE*.

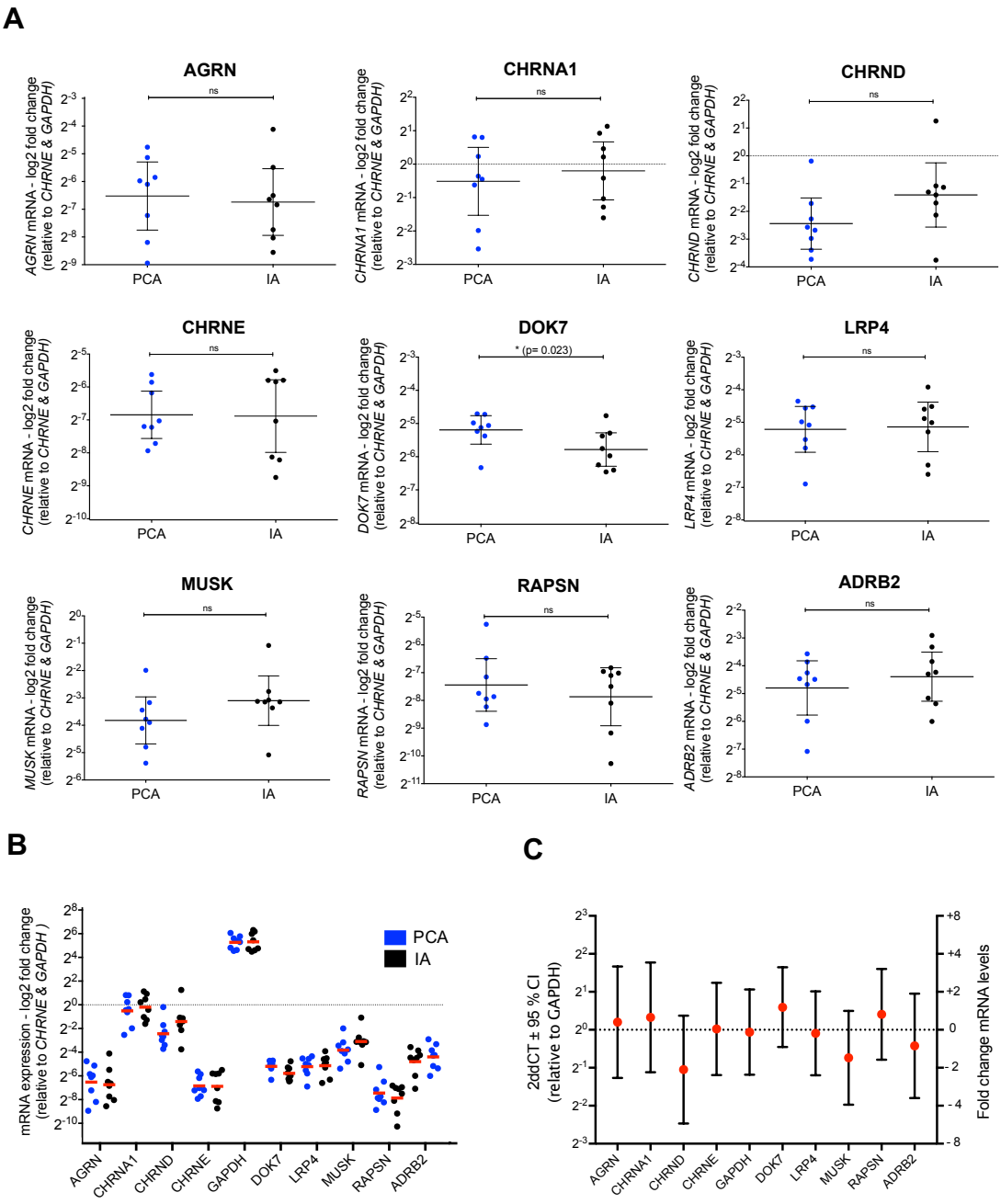


Figure 7-23. mRNA expression levels in PCA and IA muscle normalised to *CHRNE* & *GAPDH*

(A) Dot plots representation of mRNA levels as fold change (*log2*) expression relative to *CHRNE* & *GAPDH* using $2^{-\Delta Ct}$. Data points correspond to individual values for each muscle, and the results are summarised by geometric mean and 95% CI. Two-tailed Wilcoxon matched-pairs signed rank test (*p <0.05; ns= non-significant). **(B)** Relative abundances of mRNA levels. **(C)** $2^{-\Delta\Delta Ct}$ fold change in PCA mRNA levels compared to IA. The mean and 95% CI are displayed on a *log2* scale. Dashed lines (2^0) represent baseline mRNA levels for *CHRNE & GAPDH.*

7.12 Discussion

The findings of this investigation have shown that laryngeal stridor is present in approximately 50% of patients with *DOK7* mutations and, therefore, it should be incorporated as a core clinical feature of this condition. Genotype-phenotype correlation revealed differences in the frequency and compound heterozygosity of *DOK7* mutations between groups, although it is clear that stridor was not related to mutations causing truncation of DOK7. Expression studies in laryngeal muscles showed no differences in MuSK levels between PCA and IA muscles. However, there were small differences in DOK7 levels and above all, the identification of a smaller DOK7 isoform (enriched in the PCA muscle) warrants further investigation to elucidate its functional role in AChR clustering. This might assist in a better understanding of the molecular basis of stridor in DOK7-CMS.

In the current cohort of patients with *DOK7* mutations, stridor was present in approximately 50% of the cases. The presence of stridor in the very few cases with *AGRN* and *MUSK* mutations included in this cohort suggests that individuals with genetic abnormalities within the AChR clustering pathway are susceptible to develop stridor. In keeping with this, patients with other common myasthenic syndromes such as AChR-Deficiency, Rapsyn-CMS and CMS due to glycosylation abnormalities very rarely developed stridor and this usually occurred in the context of severe hypotonia and generalised weakness.

The clinical presentation of stridor in this cohort of patients with *DOK7* mutations was very heterogeneous. Approximately 50% of patients presented with stridor at birth either in isolation or in conjunction with other symptoms such as feeding difficulties or

hypotonia. The remainder of patients had stridor during childhood and adulthood, mainly in the context of exacerbations of myasthenic weakness related to infections or other causes. Quite often, adult patients with *DOK7* mutations only suffered from mild stridor, which was noticeable with breathing in form of a wheeze.

From the observations of this study, it is clear that patients with congenital onset stridor suffered from severe manifestations, which usually warranted external ventilation and long-term, sometimes life-long, tracheostomy. Moreover, two patients underwent laryngeal surgical procedures to increase the glottic gap and reduce airway resistance such as vocal cord cordotomy or division of aryepiglottic folds. On the other hand, patients with childhood and adulthood onset stridor seem to have had milder manifestations, which were usually less problematic than the limb muscle weakness. Obviously, there were exceptions as demonstrated by a case of DOK7-CMS with severe onset of stridor at the age of 40 years who now carries a long-term tracheostomy.

The clinical course of stridor in patients with DOK7-CMS seemed to improve with time in the congenital-onset cases and remained relatively mild and stable in the adults on treatment, although there were three exceptions where decannulation was not achieved. There are important anatomical differences between the adult and paediatric airways (Hudgins *et al.*, 1997) that might support the improvement of stridor over time with growth. Firstly, the paediatric larynx is positioned higher in the neck at the C2-C3 level. Secondly, the airway is smaller than the adult airway, and is narrowest at the infraglottic portion. Thirdly, the laryngeal cartilaginous structures are not ossified, with the exception of the hyoid bone, giving it a softer consistency.

Using the Hagen-Poiseuille's law, which states that the change in air flow resulting from a reduction in airway diameter is directly proportional to the airway radius elevated to the fourth power, $Q = (\Delta P \pi r^4)/(8 \eta L)$, we can infer that the paediatric airway is especially susceptible to reduction of airflow with obstruction of the airway (Wheeler *et al.*, 2007) as is the case in DOK7-CMS. These anatomical differences are most important in the infant`s airway and become less important as the child grows and finally assumes the features of the adult airway by the age of 8 years (Brown, 2000). In addition, the treatment with ß2-adrenergic agonists might help to improve stridor over time, as well as improving limb and respiratory muscle weakness. Overall, the outcome of stridor in DOK7-CMS is relatively favourable with only 3 patients being unable to be decannulated in adulthood in the context of poor respiratory function.

The reason why some patients with *DOK7* mutations develop stridor and others do not is unknown. The presence of stridor in this cohort was clearly not related to mutations causing truncation of DOK7 since they were also present in the non-stridor group. The differences identified in the genotype of DOK7-CMS between the stridor and non-stridor groups using CIRCOS plots are difficult to interpret. It is therefore unclear whether variability in the frequency and compound heterozygosity of *DOK7* mutations could somehow be related to the clinical presence of stridor.

Laryngoscopy examinations in all nine patients with stridor demonstrated bilateral vocal cord palsy due to selective impairment of vocal cord abductors. It is not known why this condition targets the PCA muscle so specifically while other neighbouring laryngeal muscles, implicated in vocal cord adduction or tension, are not affected. The same enigma

applies to the involvement of the proximal limb muscles, while distal limb muscles and eye muscles are usually spared. Although most of the mammalian skeletal muscles have one motor endplate per muscle fibre, laryngeal muscles (Rossi and Cortesina, 1964) and eye muscles (Spencer and Porter, 2006) have a variable proportion of multiply innervated muscle fibres (more than one NMJ on a single muscle fibre). The biological and functional significance of multiple innervation of individual muscle fibres is not well understood and neither is its role in disorders of the neuromuscular junction such as MG or CMS. The PCA muscle has the lowest proportion of multiple innervated fibres within the laryngeal muscles (Yoshihara *et al.*, 1984).

The results from the present study showed a 28% higher DOK7 protein expression by immunofluorescence of muscle sections, and a 1.55 folds' increase in DOK7 mRNA expression by real-time PCR in the PCA muscle compared to the IA muscle. Although statistical tests were significant, it is unclear whether relatively mild differences in DOK7 expression can firmly justify the dramatic clinical differences. In addition, western blot analysis did not show significant differences in MuSK and DOK7 expression. In conclusion, it seems there are no striking differences in the expression levels of key NMJ proteins between the PCA and IA muscles. This contrasts with a study reporting that adult mouse skeletal muscles differ in their endogenous levels of MuSK, and that prominent MuSK immunostaining is present in extrasynaptic regions of the soleus muscle but not in the EDL (*extensor digitorum longus*) muscle (Punga *et al.*, 2011). In relation to this, the present study did not find signs of extrasynaptic staining for MuSK and DOK7 in any of the human laryngeal muscle samples studied.

Another study showed differential expression patterns of the AChR α-subunit gene in mouse adult soleus (slow twitch fibres) and sternomastoid (slow and fast twitch fibres) muscles, which were assessed in relation to the fibre type properties of the muscles (Kues *et al.*, 1995). This idea was investigated by looking at DOK7 and MuSK expression in slow and fast muscle fibres of the PCA muscle by immunofluorescence, although major differences were not observed. It has also been proposed using zebrafish models that DOK7 has an additional role in maintaining intact slow muscle fibre morphology (Müller *et al.*, 2010). Since the human PCA muscle of the larynx has a predominant type I fibre signature (60-80%), it is possible that this could be of relevance for stridor. Studies looking at the properties of slow twitch muscle fibres in mouse models of DOK7-CMS could be of interest.

The presence of a double protein band in the western blot analysis of DOK7 expression in human muscle suggested the presence of several DOK7 isoforms. Further studies are being conducted in our lab to elucidate the functional role of the smaller DOK7 isoform in AChR clustering. If this isoform is not implicated in clustering, we could speculate that muscles enriched with the short isoform might be more susceptible to inhibition of Agrin-MuSK signalling resulting in fatigable muscle weakness. This hypothesis could be applied to the PCA muscle causing stridor.

Another interesting idea to take on board in future studies regarding the selective affect on specific muscles in DOK7-CMS is the developmental origin of muscles. Limb and trunk muscles are derived from somites while craniofacial muscles, including laryngeal and extraocular muscles have a more complex origin (Buckingham *et al.*, 2003). However, it

seems that all laryngeal muscles derive from the same specific muscular cranial mesoderm (Tabler *et al.*, 2017), which in principle would not be useful in answering why the PCA laryngeal muscle is specifically affected in DOK7-CMS.

The main limitation of the current study was the scarce availability of human laryngeal tissue. The IA muscle was used as a control because it was more easily dissectible than other intrinsic muscles of the larynx. It is possible that other human laryngeal muscles would be more appropriate as controls. However, the use of diagnostic laryngeal specimens often limits the possibilities of dissecting additional muscles in order not to avoid compromising the pathological diagnosis. In an ideal scenario, it would be interesting to compare the PCA muscle to all other laryngeal muscles, and also to distal and proximal muscles from the limbs.

In conclusion, stridor is present in a great proportion of DOK7-CMS patients. In patients with congenital onset stridor and idiopathic bilateral vocal cord palsy, mutations in *DOK7* should be investigated. In adult patients with limb-girdle weakness, the recognition of stridor can also help in guiding genetic screening. Non-invasive ventilation can be helpful in cases of documented bilateral cord palsy to carry out investigations, start treatment and delay the need for tracheostomy.

Chapter 8

Optimisation of Pharmacological Therapy in Severe Cases of AChR-deficiency due to *CHRNE* Mutations

8.1 Introduction

The most common subtype of CMS is acetylcholine receptor (AChR) deficiency syndrome, which represents approximately 30% of the UK CMS cohort (Finlayson, 2013). The majority of these cases are due to either missense or frameshift mutations within the gene encoding the adult-specific ε-subunit of the AChR (*CHRNE*) (Beeson and Newson-Davis, 2000). The mutations decrease the response to acetylcholine by reducing the number of receptors at the muscle endplate and simplifying the post-junctional folds (Vincent *et al.*).

The clinical features of patients with AChR deficiency vary from mild to severe (Engel, 2012b). The most severely affected have ocular, bulbar, limb and respiratory weakness from birth, while the mildly affected tend to have a marked limitation of ocular movements, but only mild limb weakness and fatigable ptosis. Subjects with AChR deficiency respond favourably to acetylcholinesterase (AChE) inhibitors (Engel, 2007) and 3,4-diaminopyridine (Palace *et al.*, 1991; Harper and Engel, 2000). However, in the severe cases, the response is generally incomplete and the prolonged use may result in a relatively modest improvement (unpublished observations).

Salbutamol and ephedrine are β2-adrenergic receptor agonists used with benefit in CMS due to *DOK7* mutations (Lashley *et al.*, 2010; Burke *et al.*, 2013; Lorenzoni *et al.*, 2013) and congenital endplate AChE deficiency (Bestue-Cardiel *et al.*, 2005; Mihaylova *et al.*, 2008; Chan *et al.*, 2012). Moreover, anecdotal reports suggest that patients with *CHRNE* mutations may improve with salbutamol (Sadeh M, Xin-Ming S, 2012).

8.2 Aims

The study presented in this chapter was designed to answer one primary question: can the addition of salbutamol or ephedrine lead to improvement in the muscle strength and function of patients with severe AChR deficiency due to *CHRNE* mutations on pyridostigmine. The rationale was that β2-adrenergic receptor agonists could help to stabilise the muscle endplate architecture by preventing the dispersal of AChRs resulting from chronic administration of AChE inhibitors (Engel *et al.*, 1973).

8.3 Study design

8.3.1 Inclusion criteria

Patients with severe AChR deficiency caused by *CHRNE* mutations despite optimal therapy sustained for several years were included. The condition was defined as severe by a baseline QMG (severity) score worse than 15 out 39 (Jaretzki *et al.*, 2000). All patients were attending the UK National Diagnostic and Advisory CMS Service in Oxford and were followed up over the past 3 years. Written informed consent for analysis and publication of genetic and clinical data was obtained for all patients (Oxfordshire REC B, 04.OXB.017 and C, 09/H0606/740).

8.3.2 Medication dosages

Medication was started on an outpatient basis with incremental dosage dependent on body weight and tolerability, final dose ranged between 0.5-1 mg/kg/day for ephedrine and 0.05-0.2 mg/Kg/day for salbutamol. In all patients, baseline therapy with pyridostigmine and 3,4-DAP or pyridostigmine alone remained unchanged for at least a year prior to adding salbutamol or ephedrine and during the follow-up period. Blood pressure, heart rate, and electrocardiogram (ECG) were performed prior to treatment and at each dosage increment to screen for cardiac side effects.

8.3.3 Clinical outcomes

Clinical details, objective strength measures and functional scores were recorded routinely at each clinical visit. These included the QMG score (Section 2.11.2) and mobility score using the 10 metre timed walk test (Jaretzki *et al.*, 2000). In the latter, the patient was asked to have a usual or comfortable walking pace, and there was no verbal encouragement during the test. Measures were recorded prior to the initiation of treatment and 6-8 months later. Lifestyle improvements were also recorded.

8.4 Patients included in the study

A total of six patients with severe AChR deficiency were included in the study **(Table 8-1)**. Five received salbutamol and one ephedrine, in addition to their previous therapy, which remained unchanged prior to and during the follow-up period. Median age was 25 years (range 14-53 years) and the male: female ratio was 4:2. All patients tolerated the additional medication without side effects. To illustrate the response to therapy, two cases are briefly described below.

Table 8-1. Patients with severe AChR deficiency included in the study

Patient	Patient 1	Patient 2*	Patient 3	Patient 4*	Patient 5	Patient 6
Kinship	1	1	2	2	3	4
Gender	Male	Male	Male	Female	Male	Female
Mutations (*CHRNE*)	c.554-560del c.IV58-1G>A	c.554-560del c.IV58-1G>A	c.554-560del c.554-560del	c.554-560del c.554-560del	c.972+1G>T c.972+1G>T	c.1267-32_1319del c.1267-32_1319del
Gender	F	F	F	F	M	F
Treatment	Salbutamol	Salbutamol	Salbutamol	Salbutamol	Salbutamol	Ephedrine
Age treatment started (years)	14	18	36	32	53	15
Treatment dosage at last follow-up	4 mg twice a day (0.18 mg/kg/day)	4 mg twice a day (0.15 mg/kg/day)	4 mg twice a day (0.13 mg/kg/day)	4 mg twice a day (0.15 mg/kg/day)	4 mg once a day (0.05 mg/kg/day)	15 mg twice a day (0.42 mg/kg/day)
Other treatments	Pyridostigmine 3,4-DAP	Pyridostigmine 3,4-DAP	Pyridostigmine 3,4-DAP	Pyridostigmine 3,4-DAP	Pyridostigmine 3,4-DAP	Pyridostigmine
10-m timed walk test baseline (s)	Unable to walk	Unable to walk	Unable to walk	Unable to walk	ND**	ND**
10-m timed walk test end (s)	10.1	7.9	8.8	29.1^	ND	8.4
QMG baseline/39	28	27	17	18	19	21
QMG end/39	20	19	15	13	11	16

3,4-DAP, 3,4-Diaminopyridine; (*) Patient 2 and 4 are briefly described in Section 8.4 as Case 1 and Case 2, respectively; (**) Patient 5 and 6 were ambulant prior to starting treatment with salbutamol and ephedrine but mobility was mainly indoor or reduced to closed environments; (^) Unilateral aid; ND, not done

8.4.1 Case 1 (Patient 2)

An 18-year-old man was unable to walk or dress himself and required a wheelchair full time despite optimal treatment with pyridostigmine and 3,4-diaminopyridine. Initial examination revealed severe limb weakness with inability to produce movements against gravity. Treatment with salbutamol 4 mg twice a day produced a marked effect in muscle strength within weeks, especially in the limbs. Whereas he was previously non-ambulant, six months later he was able to walk short distances and performed the 10 metre timed walk test unaided in 7.9 seconds **(Figure 8-1)**. At six months, the time for keeping his limbs outstretched had increased from 0 to 33 seconds in the arms and from 0 to 9 seconds in the legs. Distally, his handgrip had increased from 3 to 14 kg and the FVC had increased from 2.60 to 3.47 L. Of note, from being initially unable to rise up from the floor, at six months he was able to rise to stand within 6.3 seconds.

From the functional point of view, the changes in muscle strength were translated into a dramatic improvement in functionality and autonomy becoming more independent. From being previously dependent in most activities of daily living, he went to live independently in a different city from his family to study at the university. “I expected I’d get stronger, but had no idea I’d be able to walk again”, “I still use my wheelchair out and about, but at home I walk around – just getting dressed, washing and cooking, it’s amazing to be able to normal things.” Fragments taken from the patient’s interview published in the Daily Mail Journal (http://www.dailymail.co.uk/health/article-2698312/The-asthma-drug-used-beat-paralysis.html).

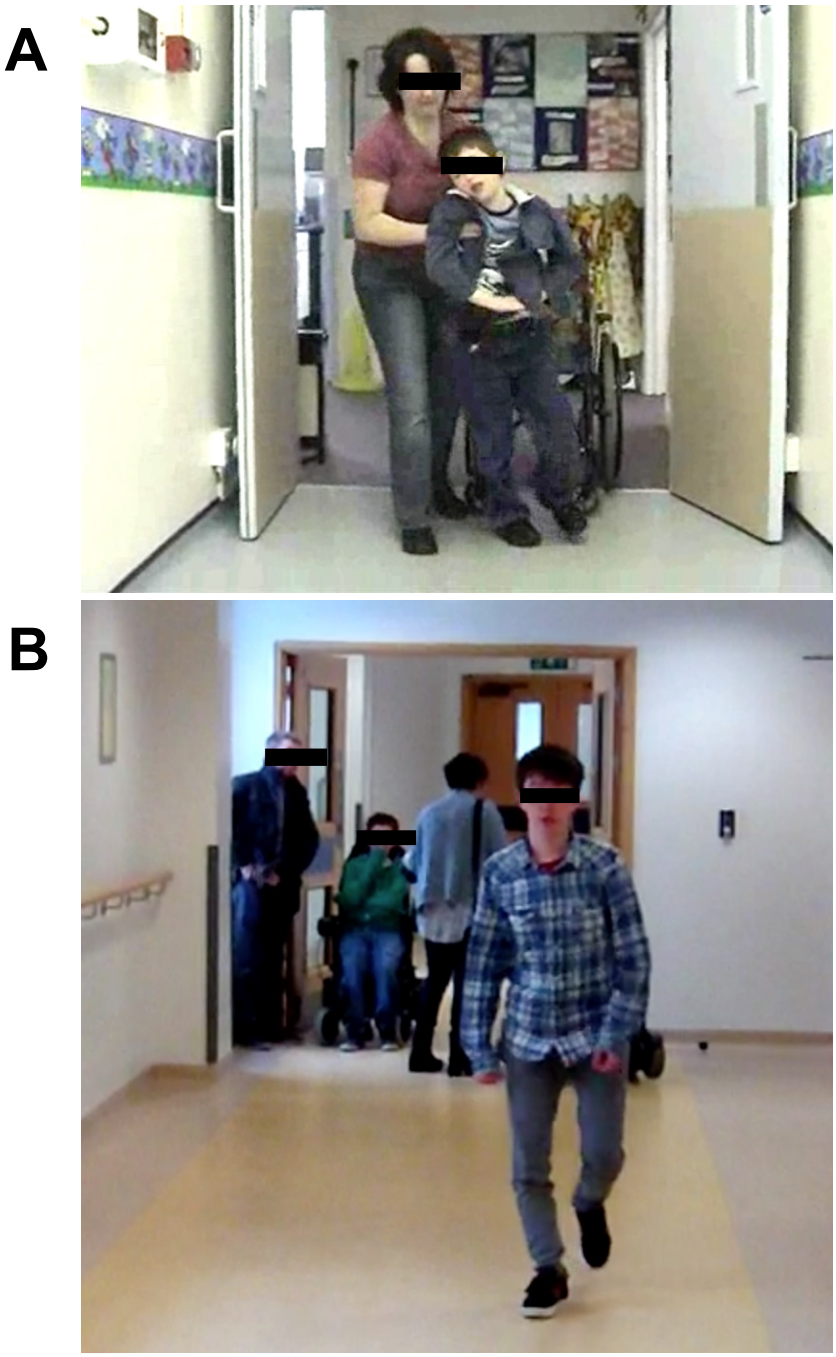


Figure 8-1. Representative images showing the clinical response to salbutamol in Patient 2

(A) At the age of 9 years, the patient was unable to walk independently despite optimal therapy with 3,4-DAP and pyridostigmine. This disability continued unaltered over the subsequent years. **(B)** At the age of 18 years, and after six months on treatment with salbutamol, the patient was able to complete a 10 meter walk test unaided in 7.9 seconds.

8.4.2 Case 2 (Patient 4)

A 32-year-old woman with generalised muscle weakness was unable to walk and only able to stand for a few seconds despite optimal treatment. Examination revealed severe muscle weakness, especially in the neck muscles and lower limbs. She was prescribed 4 mg of salbutamol twice a day and felt a significant improvement from the second week of treatment. She is now able to walk around the house and to drive a car, which is something she could not do before. By six months, the time for keeping her right leg outstretched increased from 3 to 15 seconds and from 21 to 33 seconds in the right arm. Timed head lift improved from 0 to 31 seconds and distally, right handgrip increased from 5 to 16 kg.

8.5 Medication dosage and adverse effects

Patients 1-to 4 were started on 2 mg of salbutamol twice a day, approximately 0.05 mg/Kg/day. During the course of 6-8 months from the initial visit, medication was increased progressively up to 4 mg of salbutamol twice a day, which correspond approximately to 0.1 mg/kg/day. This was done in two-steps by adding 2 mg of salbutamol in the morning (0.075 mg/kg/day), and subsequently 2mg in the afternoon (0.1 mg/kg/day). Patient 5 was reluctant to increase his medication further from 4 mg of salbutamol once a day (0.05 mg/kg/day) as he felt already an improvement in muscle function. Patient 6 was started on ephedrine 15 mg twice a day, approximately 0.5 mg/kg/day, and chose not to increase it further. During the follow-up period, none of these patients reported adverse effects derived from the medication. In addition, there was no change in blood pressure or ECG findings before and after the initiation of treatment.

8.6 Quantitative myasthenia gravis (severity) score

All patients reported a progressive improvement in muscle strength from the second week of treatment. The mean QMG scores (a higher score indicates greater disability) significantly improved from baseline to the 6-to 8-month follow-up from 21.67± 4.72 to 15.67± 3.45 (p = 0.027) as shown in **Figure 8-2.**

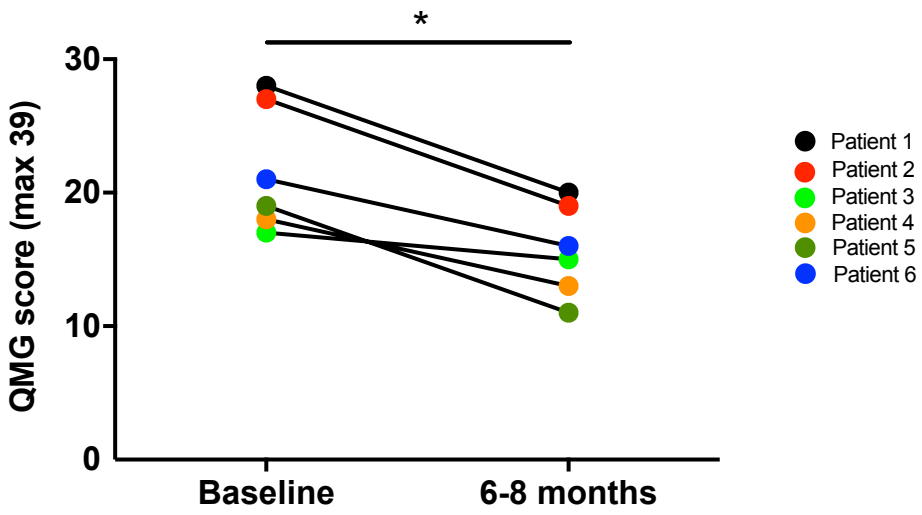


Figure 8-2. Change in performance for the QMG score

Data points represent individual QMG scores for each patient. Wilcoxon matched-pairs signed rank test (* p <0.05; n=6)

8.7 Quantitative myasthenia gravis score components

Scores for diplopia, swallowing, and counting were mainly normal at baseline, and thus had no scope for improvement. Treatment did not have an effect on ptosis, ophthalmoplegia or facial weakness, which was present in all subjects. Improvements over the follow-up period occurred in QMG components for head lift, arm raise time, leg raise time, and less markedly for handgrip and FVC **(Figure 8-3A)**. Times for arm and leg raise had an overall significant improvement (p =0.0312) compared to baseline **(Figure 8-3B, C)**. Full details of QMG components results are provided in **Table 8.2**.

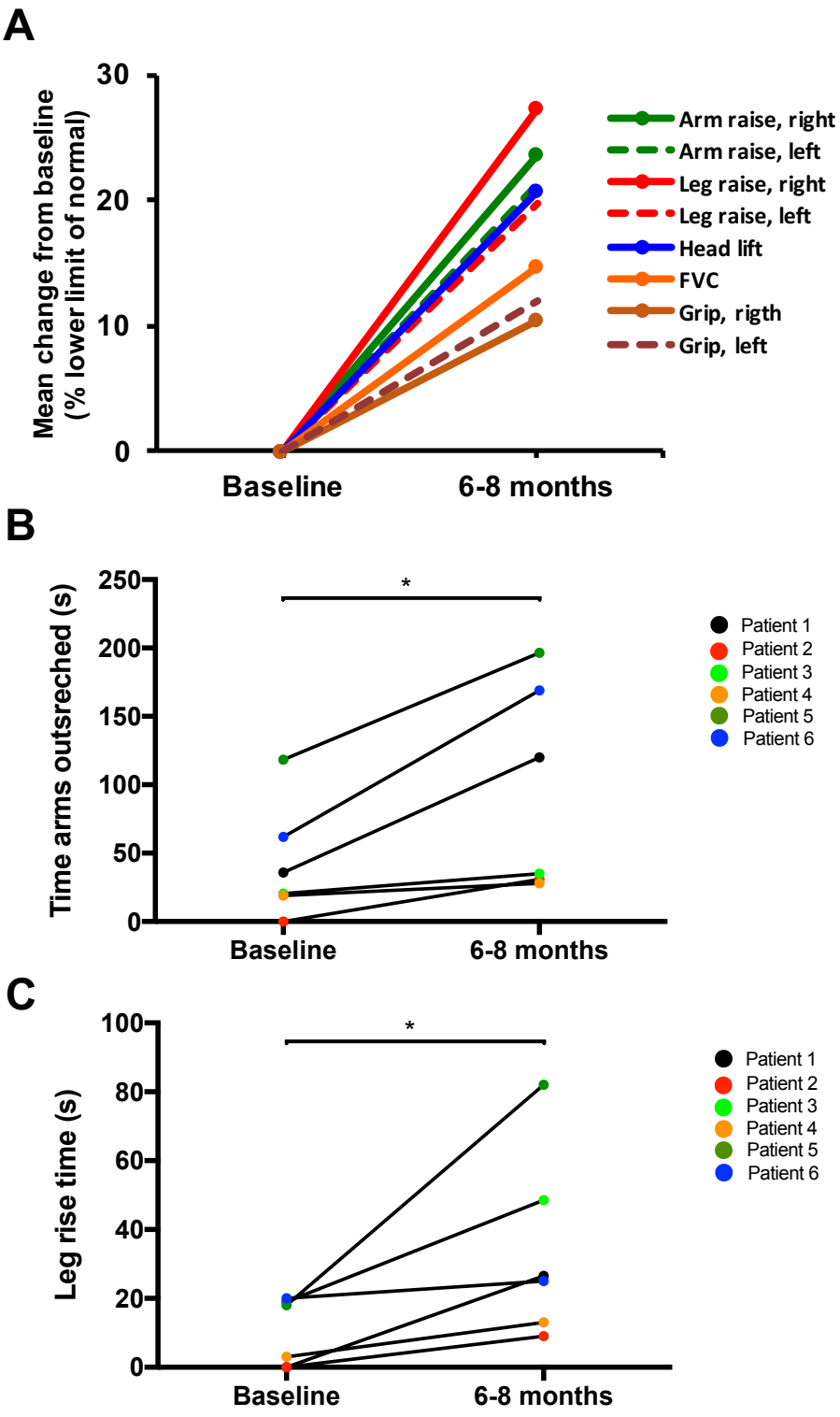


Figure 8-3. Change in performance for subcomponents of the QMG score

(A) Mean change in percentage of the lower limit of normal (minimum required to achieve 0 on the QMG scale). **(B)** Times for individual patients for arm raise at 90°. **(C)** Times for individual patients for leg raise at 45°. Data points represent the mean of right and left side scores. Wilcoxon signed matched pairs rank test (*p<0.05).

Table 8-2. Mean values at baseline and at 6- to 8-month follow-up and percentage increment in relation to baseline measures

Components	Lower limit of normal	Baseline	6-8 months	Improvement (%)
Right arm raise (s)	240	48	104	+ 119%
Left arm raise (s)	240	38	89	+ 136%
Right leg raise (s)	100	11	39	+ 245%
Left leg raise (s)	100	10	30	+ 200%
Head lift (s)	120	38	63	+ 66%
FVC (L)	2.5 (F) 3.5 (M)	2.4	2.8	+ 18%
Right grip (Kg)	31 (F) 45 (M)	8	13	+ 58%
Left grip (Kg)	31 (F) 45 (M)	9	13	+ 44%

8.8 Mobility scores

At baseline, four patients were unable to walk due to extreme weakness (patient 1-4). In the follow-up assessment, all four were able to complete the test, with three of them scoring 10 or less seconds **(Table 8.1)**. Patient 4 had developed severe fixed joint contractures of knees and hips, which made walking difficult even though she showed considerable improvement in strength. Pre-assessment 10-m walk time was not done for patients 5 and 6.

8.9 Long term follow-up analysis

Strength measures are routinely performed during clinic visits and, therefore, QMG scores were performed beyond the end of the study at 6-to 8-month after initiation of treatment with salbutamol or ephedrine. These showed that the benefit derived from adding

salbutamol or ephedrine to the baseline therapy persisted over time in the cases reported **(Figure 8-4).**

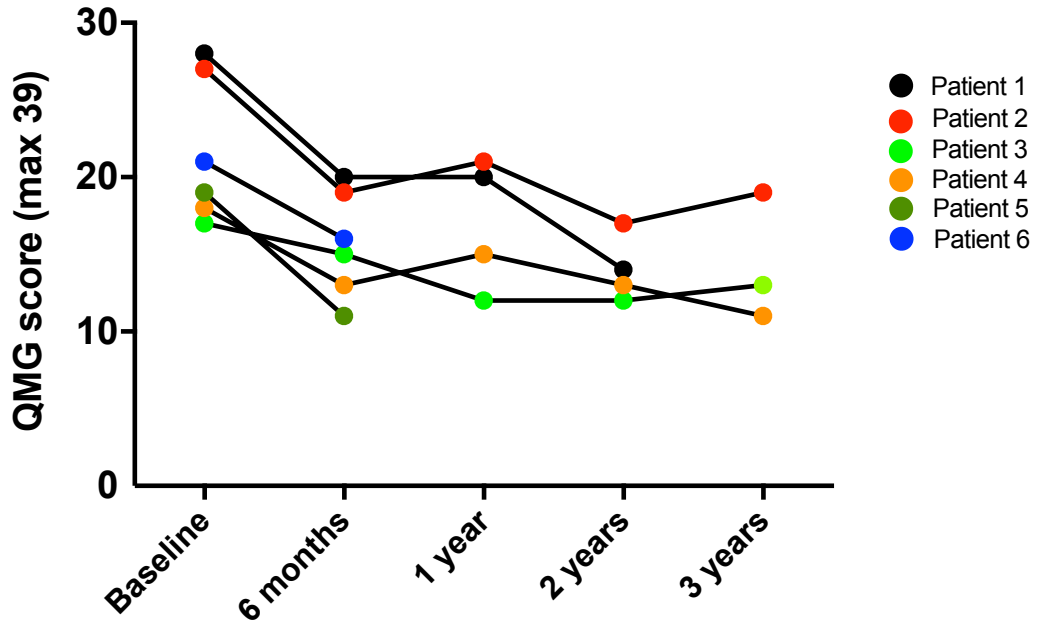


Figure 8-4. Long-term follow-up in performance for the QMG score. Data points represent individual QMG scores for each patient.

8.10 Discussion

This study demonstrates that for CMS patients with severe AChR-deficiency due to *CHRNE* mutations taking pyridostigmine, the addition of either salbutamol or ephedrine medication can substantially improve muscle strength, as confirmed by the QMG severity score and 10 metre timed walk test, without notable adverse effects. These cases showed an unequivocal improvement in functional ability. Four patients who had been non-ambulant for many years acquired the ability to walk independently. This beneficial effect

seems to be stable over time as shown by the QMG scores during the long-term follow-up.

A beneficial response to albuterol in two adult female patients with CMS due to epsilon mutations has been reported previously (Sadeh M, Xin-Ming S, 2012), although quantitative assessment of improvement using pre and post-treatment measures was not performed.

In our experience, AChR deficiency patients with milder phenotypes also report an increase in stamina and function with the addition of salbutamol or ephedrine to their treatment regime. However, the improvement is more marked in the severe patients, probably due to the fact that profound weakness provides a greater margin to record improved muscle function. We found that patients' perception of the positive treatment response and their reported improvement of activities of daily living was greater than the objective measurement scores revealed, especially handgrip. QMG seems a rather insensitive score, with a 3-point difference equating to a large clinical improvement. In addition, it is likely that fatiguabilty of weakness in everyday tasks is not easily measured in a single outpatient assessment. As reported in previous studies of ephedrine (Lashley *et al.*, 2010) and salbutamol (Burke *et al.*, 2013; Lorenzoni *et al.*, 2013) in patients with DOK7-CMS, it would be very useful to develop a more sensitive scale able to capture the physical and functional benefits derived from treatment in CMS patients.

The commonly used maintenance dose for salbutamol was 4 mg twice a day though most of the patients reported a clear benefit within the first two weeks of starting at 2 mg twice a day. One of the subjects (patient 5) improved significantly despite only taking

salbutamol 4 mg once a day. This differs from the slower response we observe in DOK7-CMS, where patients benefit slowly but progressively over a period of months before stabilizing at between 6-24 months (Lashley *et al.*, 2010). In general, we would recommend increasing salbutamol progressively up to 4 mg twice a day in the course of 6 months when side effects are not apparent. Medication can be increased further up to 8 mg twice a day in older children/adults if required. Patient 6 improved on ephedrine 15 mg twice a day although higher doses can be used. Three additional patients with severe AChR deficiency due to *CHRNE* mutations have been reviewed in clinic on long-term treatment with pyridostigmine, who have started ephedrine, where baseline formal strength measures were incomplete. All reported a clear benefit after the initiation of ephedrine with dosages between 15 mg od and 30 mg bd with no side effects. In DOK7-CMS, ephedrine doses of 30-45 mg bd-tds are often needed. Thus, from our limited experience, the effects of salbutamol and ephedrine in CMS due to AChR deficiency may occur at lower doses. Ephedrine and salbutamol can be used interchangeably, although salbutamol is more frequently used because there is more safety data for its use in children (Burke *et al.*, 2013) and it is more familiar to general doctors and easier to obtain. However, ephedrine is a good alternative if salbutamol is not well tolerated.

In this study, none of the patients reported adverse effects derived from treatment with ß2-adrenergic agonists, which usually include fine tremor, headache, muscle cramps, increased blood pressure and palpitations. High doses of medication can be associated with hypokalaemia, and thus it is advisable to check potassium levels in blood, especially in children. These drugs should be used with caution in hyperthyroidism, cardiovascular disease, arrhythmias, susceptibility to QT-interval prolongation and hypertension.

In this quantitative study, there was a positive response to treatment in subjects of different ages (range 14-53 years). Although patients with AChR deficiency usually do not deteriorate markedly with time (Burke *et al.*, 2004), it is possible that early introduction of salbutamol or ephedrine may improve mobility over the long-term.

A limitation of this study is the lack of a control group not treated with with β2-adrenergic receptor agonist. This is due to the rare occurrence of severe AChR deficiency and thus the low patient numbers. However, the prolonged response over time along with their poor response to the other treatment changes, and the improvements in the timed tests done months apart would be hard to reproduce voluntarily. The present report applies to patients with severe AChR deficiency due to mutations in *CHRNE*. We have not assessed this treatment option on severe AChR-deficiency due mutations in other subunits of the acetylcholine receptor that are extremely rare.

The molecular mechanisms for ephedrine and salbutamol at the neuromuscular junction are not known. Patients with mutations in the AGRN-LRP4-MUSK-DOK7 pathway (proteins which promote clustering of AChRs at the NMJ) improve with these treatments, and one of the plausible explanations is that β2-adrenergic agonists provide a compensatory mechanism to stabilise motor endplate structures and thus partially mitigate disruption of the MuSK signaling pathway (Glass *et al.*, 1996). In the experience of this clinical service, patients with AChR deficiency report that the early beneficial response to cholinesterase inhibitors is less effective with their longer-term use. The cause may be an additional reduction in the number of endplate AChR sites as a result of

disorganization of the postsynaptic muscle membrane resulting from the pyridostigmine (Chang *et al.*, 1973; Engel *et al.*, 1973; Gillies and Allen, 1977). This would further decrease the safety margin of neuromuscular transmission and thus lead to additional muscle weakness. It is tempting to think that β2-adrenergic agonists can optimize the beneficial response to pyridostigmine by increasing stability of the muscle endplate structures and prevent the additional loss of endplate AChRs that results from chronic anticholinesterase medication. Further information on the AChR clustering and dispersal pathways is provided in the introduction chapter (Section 1.8.3)

It is also unclear why patients with AChR deficiency respond faster to β2-adrenergic receptor agonists and need smaller doses of medication than in DOK7-CMS. Since patients with AChR deficiency have intact their innate AChR clustering mechanisms, it is possible that the drugs only need to overcome the dispersal effect of pyridostigmine in contrast to patients with mutations within the AGRN-LRP4-MUSK-DOK7 pathway where the AChR clustering mechanism itself is impaired.

In conclusion, this study reports a robust improvement in all six patients assessed with severe AChR deficiency following the addition of oral salbutamol or ephedrine to their long-term treatment regime that included pyridostigmine. Due to the fact that ε-subunit AChR mutations causing AChR deficiency represent the commonest CMS subtype in the UK, these results represent an important beneficial therapeutic step in treatment. This study was rated Class IV evidence (Gross and Johnston, 2009) because of the absence of a control group not treated with β2-adrenergic receptor agonists.

Chapter 9

Conclusions and Future Perspectives

9.1 Conclusions

The current research showed that the clustered AChR cell-based assay was able to detect antibodies in 38.1% of RIPA-negative patients with MG with 100% specificity. This was particularly useful for the differential diagnosis of CMS and SNMG in routine clinical practice. In addition, this study showed that patients with antibodies only to clustered AChRs had a younger age at onset and a milder phenotype than patients with SNMG. These observations may have implications in planning treatment, especially with regards to the use of long-term immunosuppression and thymectomy. Additional studies using different cohorts would be important to investigate whether these findings can be generalised. Difficulties might arise from the fact that CBAs are costly and time consuming, and require personnel with expertise in tissue culture techniques (Rodriguez Cruz *et al.*, 2015). In addition, there is currently no commercial assay available for the testing of antibodies to clustered AChRs.

The discovery of *COL13A1* and *GMPPB* as novel CMS causative genes was of great interest to increase our understanding on the physiology of the NMJ. COL13A1 was enriched at human muscle endplates but was absent from the muscle biopsy of the affected individual carrying the c.1171delG mutation. Functional analysis showed a deleterious effect of this mutation on AChR clustering *in vitro.* This emphasises the role of extracellular-matrix

proteins, other than the Agrin-LRP4-MuSK-DOK7 pathway, in NMJ formation and maintenance. The finding that fasciculin staining spread beyond α-bungarotoxin staining in the patient's muscle biopsy suggests that the impairment in AChR clustering might be related to the acetylcholinesterase mislocation. The latter is supported by results of the pull-down assays showing interaction of COLQ and COL13A1. Patients with *COL13A1* mutations had no beneficial response to anticholinesterase medication but did improve on β2-adrenergic agonists consistent with the fact that *COL13A1* mutations affect the maturation and maintenance of the synaptic structure. Treatment with 3,4-DAP was also beneficial in keeping with the importance of COL13A1 for the integrity of the presynaptic terminal reported in the animal models. The description of novel cases with *COL13A1* mutations will help to draw more precisely the clinical phenotype of these patients.

The report of patients with CMS and mutations in *GMPPB* confirmed the relevance of protein glycosylation for adequate neuromuscular transmission. The evaluation of the clinical features showed presentation with proximal muscle weakness and, unlike many CMS, with sparing of ocular, bulbar and respiratory muscles. This phenotype was similar to patients with mutations within the early stages of the N-glycosylation pathway. However, GMPPB-CMS patients had a greater degree of myopathic involvement as shown by the higher CK levels and dystrophic changes on muscle biopsy. This is most likely related to the additional role of GMPPB in the O-mannosylation pathway and the glycosylation of α-dystroglycan, a major component of the dystrophin–glycoprotein complex. Long-term follow-up studies are necessary to evaluate disease progression, which is likely to be driven by the muscle component of the disease.

Alpha-dystroglycan is necessary for the stabilisation of AChRs at the NMJ and formation of the synaptic basement membrane (Jacobson *et al.*, 2001). Reports of aberrant NMJs in other subtypes of dystroglycanopathies such as Fukuyama-type congenital muscular dystrophy (Taniguchi *et al.*, 2006) suggest that clinical studies looking at the presence of neuromuscular transmission abnormalities in patients with dystroglycanopathies would be of interest. If present, these patients could benefit from symptomatic treatment of the myasthenic component with cholinesterase inhibitors and 3,4-DAP..

The study on the molecular mechanisms underlying two novel missense variants in *MUSK, p.C317R and p.A617V,* uncovered previously unrecognised mechanisms of how the levels of MuSK phosphorylation are critical to maintain synaptic structure. These findings helped to direct the appropriate treatment strategy with salbutamol for the patient but also raised new questions, such as those concerning the dimerisation of MuSK kinase domain. Structural biology approaches would be useful to resolve the crystal structure of MuSK kinase domain upon dimerisation and elucidate the precise molecular mechanisms involved in MuSK activation.

The study on the clinical and molecular basis of stridor in CMS has shown that stridor is present in approximately 50% of patients with *DOK7* mutations. Although the onset and severity of stridor is variable, these findings suggest that stridor is a core clinical feature of DOK7-CMS. Current molecular studies using human donor samples ruled out the hypothesis that the selective impairment of the PCA muscle was driven by major differences in the expression levels of key NMJ proteins. However, the fact that the PCA muscles were enriched with a shorter DOK7 isoform warrants further investigation. The

novel isoform identified lacks part of the PH domain and, therefore, is likely not to promote MuSK phosphorylation and AChR clustering. In fact, a potential role of this isoform could be to disperse aneural clusters of AChRs by impairing MuSK signaling in extrasynaptic regions. Further studies will help to elucidate its function and hopefully gain further insight on why certain muscles are predominantly affected in DOK7-CMS.

Finally, this work helped to optimise the CMS treatment strategy due to the observation that patients with AChR-deficiency benefit substantially from the addition of ß2-adrenergic agonists to their baseline treatment with pyridostigmine. Salbutamol is believed to cause cAMP/PKA activation (Musa Zamah *et al.*, 2002) but the precise molecular mechanism of action at the NMJ is not known. Increasing evidence suggests that salbutamol improves neuromuscular transmission by stabilising and slowly remodelling the muscle endplates (Mcmacken *et al.*, 2018). Future research will help us to understand the role of the ß2-adrenergic receptor in NMJ development and maintenance. The generation of more specific ß2-adrenergic receptor agonists would be of interest to maximize the benefits of pharmacological treatment while avoiding side effects.

9.2 Future perspectives

Future aspects in the field of myasthenia research will include the identification of novel CMS genes using NGS technology. Functional and basic studies employing cell and animal models will help to elucidate the role of novel proteins in neuromuscular transmission, and provide a better understanding on the NMJ physiology in health and disease. In addition, carefully designed studies looking at the prevalence and pathogenic relevance

of recently described autoantibodies in SNMG (Agrin, COLQ, LRP4, and Cortactin) are necessary since the overall contribution of these autoantibodies to the disease is unclear (Vincent *et al.*, 2018). This might include the development of more reliable diagnostic assays and the study of specific phenotypes associated with the presence of autoantibodies. If they are proved to be relevant in the future, the development of a reliable, cheap, and portable MG antibody panel could be useful for point-of-care testing, perhaps by using paper-based lateral flow immunoassays technology (Koczula and Gallotta, 2016).

The current treatment strategy of patients with CMS has greatly improved with the incorporation of ß2-adrenergic agonists to the therapeutic repertoire (Lashley *et al.*, 2010). Efforts to develop more specific ß2-adrenergic agonist are ongoing in order to maximise the therapeutic effect of the drug and reduce side effects. However, there is also scope for the development of novel treatments strategies, and modulation of the Agrin-LRP4-MuSK AChR-clustering pathway seems a very attractive one. It is known that C2C12 myotubes transfected with cDNA encoding human DOK7 develop AChR clusters in the absence of neuronal agrin (Okada *et al.*, 2006). More recent studies have shown that the overexpression of human DOK7 using adeno-associated virus (AAV) in a mouse model of DOK7-CMS resulted in enlargement of NMJs ("super synapses") and increment in muscle strength and life span (Arimura *et al.*, 2014).

Interestingly, this approach has also been shown effective in animal models of other neuromuscular conditions such as amyotrophic lateral sclerosis (ALS) and autosomal dominant Emery-Dreifuss muscular dystrophy. AAV-mediated overexpression of DOK7 in

a SOD1-G93A mouse model of ALS suppressed motor nerve terminal degeneration and muscle atrophy, increasing motor activity and life span (Miyoshi *et al.*, 2017). Based on the same concept, an anti-MuSK antibody that triggers MuSK phosphorylation has shown to preserve neuromuscular synapses in a SOD1-G93A mouse model of ALS (Cantor *et al.*, 2018). Small agrin peptides were used successfully in the treatment of a mouse model of muscular dystrophy (Moll *et al.*, 2001). Additional approaches such as the modulation of the AChR clustering signal downstream of DOK7 could be of interest, especially for patients with *DOK7* mutations.

it is believed that patients with null mutations in the AchR epsilon (adult) subunit are able to survive due to residual expression levels of the AChR gamma (foetal) subunit (Cossins *et al.*, 2004). In this connection, a novel treatment strategy for patients with AChR deficiency due to *CHRNE* mutations could result from the up-regulation of the AChR gamma subunit. Patients with kinetic abnormalities of the AChR, especially fast channel syndrome (Palace *et al.*, 2012), do not respond fully to current treatments available and, therefore, efforts should be addressed for the development of novel therapies. In this regard, recent technological developments such as CRISPR/Cas9 technology (Sander and Joung, 2014; Konermann *et al.*, 2015) and antisense oligonucleotides-based strategies (Rinaldi and Wood, 2017) could be of relevance in the near future.

The initiation of clinical trials (some of them with very promising results) in disorders that erstwhile were untreatable such as spinal muscular atrophy (Finkel *et al.*, 2017; Mendell *et al.*, 2017) and Duchenne muscular dystrophy is very encouraging for the field of neuromuscular disorders (Mercuri, 2018). Difficulties for the development of novel

therapies in CMS include the rareness of the disease, the highly heterogeneous mutational background, and the high number of patients harbouring private mutations. Difficulties might also arise from meeting the challenges related to the design of clinical trials for orphan diseases.

Finally, our understanding of the AChR clustering pathway has greatly improved in the last decade thanks to the description of the main elements of the Agrin-LRP4-MuSK-DOk7 complex (Glass *et al.*, 1996; Kim *et al.*, 2008). However, little is still known on key biological processes necessary for the formation and maintenance of the NMJ such as the release mechanism of Agrin by the nerve terminal, the dimerisation of MuSK, or the molecules involved in the clustering of AChRs downstream of DOK7. There is also scope for increasing our knowledge on the molecular organisation of the NMJ. Ultrastructural studies in the past have shown the architecture of active zones at the presynaptic terminals, and the complexity of the postsynaptic membrane with AChRs concentrated at the crests of postsynaptic folds. However, the molecular assembly of the main components of the NMJ is not well known, including the structure of Rapsyn-AChR networks and their linkage to the actin cytoskeleton. The recent development of novel techniques such as high-throughput immunohistochemistry (Rimm, 2014) and cryo-electron microscopy (Bai *et al.*, 2015) could be useful to make further progress in this field.

Bibliography

Abicht A, Dusl M, Gallenmüller C, Guergueltcheva V, Schara U, Della Marina A, et al. Congenital myasthenic syndromes: achievements and limitations of phenotype-guided gene-after-gene sequencing in diagnostic practice: a study of 680 patients. Hum. Mutat. 2012; 33: 1474–84.

Abicht A, Müller JS, Lochmüller H. Congenital myasthenic syndromes. Gene Reviews. Seattle (WA): University of Washington; 2016.

Ammar A Ben, Soltanzadeh P, Bauché S, Richard P, Goillot E, Herbst R, et al. A Mutation Causes MuSK Reduced Sensitivity to Agrin and Congenital Myasthenia. PLoS One 2013; 8(1): e53826. doi:10.1371/journal.pone.0053826

Amy L. Stiegler, Steven J. Burden and SRH. Crystal Structure of the Frizzled-like Cysteine-rich Domain of the Receptor Tyrosine Kinase MuSK. J Mol Biol. 2009; 16: 1–14.

Andrews PI, Massey JM, Sanders DB. Acetylcholine receptor antibodies in juvenile myasthenia gravis. Neurology 1993; 43: 977–82.

Apel ED, Roberds SL, Campbell KP, Merlie JP. Rapsyn May Function as a Link between the Acetylcholine Receptor and the Agrin-Binding Glycoprotein Complex. Neuron 1995; 15: 115–126.

Aran A, Renbaum P, Oliphant S, Weinberg- A, Zeligson S, Lee MK, et al. Vesicular acetylcholine transporter defect underlies devastating congenital myasthenia syndrome. Neurology 2017; 88: 1021–1028.

Arikawa-hirasawa E, Rossi SG, Rotundo RL, Yamada Y. Absence of acetylcholinesterase at the neuromuscular junctions of perlecan-null mice. Nat Neurosci 2002 Feb;5(2)119-23

Arimura S, Okada T, Tezuka T, Chiyo T, Kasahara Y, Yoshimura T, et al. *DOK7* gene therapy benefitsmouse models of diseases characterized by defects in the neuromuscular junction. Science 2014; 345: 1505–1508.

Arredondo J, Lara M, Jr SMG, Mazia CG, Garcia-erro M, Bowe C, et al. Choline acetyltransferase mutations causing congenital myasthenic syndrome: molecular findings and genotype- phenotype correlations. Hum. Mutat. 2016; 36: 881–893.

Arvidsson ULF, Riedl M, Elde R. Vesicular acetylcholine transporter (VAChT) protein : A Novel and Unique Marker for Cholinergic Neurons in the central and perypheral nervous systems. Nature 1997; 467: 454–467.

Ashraf VV, Taly AB, Veerendrakumar M, Rao S. Myasthenia gravis in children: a

longitudinal study. Acta Neurol. Scand. 2006; 114: 119–23.

Bai X chen, McMullan G, Scheres SHW. How cryo-EM is revolutionizing structural biology. Trends Biochem. Sci. 2015; 40: 49–57.

Basiri K, Belaya K, Liu WW, Maxwell S, Sedghi M, Beeson D. Clinical features in a large Iranian family with a limb-girdle congenital myasthenic syndrome due to a mutation in DPAGT1. Neuromuscul. Disord. 2013; 23: 469–72.

Bauché S, O'Regan S, Azuma Y, Laffargue F, McMacken G, Sternberg D, et al. Impaired Presynaptic High-Affinity Choline Transporter Causes a Congenital Myasthenic Syndrome with Episodic Apnea. Am. J. Hum. Genet. 2016; 99: 753–761.

Bauché S, Vellieux G, Sternberg D, Fontenille MJ, Bruyckere E De, Sophie C, et al. Mutations in GFPT1 - related congenital myasthenic syndromes are associated with synaptic morphological defects and underlie a tubular aggregate myopathy with synaptopathy. J. Neurol. 2017; 264: 1791–1803.

Beeson D. Congenital myasthenic syndromes. Curr Opin Neurol 2016 Oct;29(5):565-71

Beeson D, Higuchi O, Palace J, Cossins J, Spearman H, Maxwell S, et al. Dok-7 mutations underlie a neuromuscular junction synaptopathy. Science 2006; 313: 1975–8.

Beeson D, Newson-Davis J. Mutations affecting muscle nicotinic acetylcholine receptors and their role in congenital myasthenic syndromes. In: Lehmann-Horn F, Jurkat-Rott K, editor(s). Channelopathies—common mechanisms in aura, arrhythmia and alkalosis. Amsterdam: Elsevier; 2000. p. 85–114.

Beghi E, Antozzi C, Batocchi a P, Cornelio F, Cosi V, Evoli a, et al. Prognosis of myasthenia gravis: a multicenter follow-up study of 844 patients. J. Neurol. Sci. 1991; 106: 213–20.

Béhin A, Mayer M, Kassis-Makhoul B, Jugie M, Espil-Taris C, Ferrer X, et al. Severe neonatal myasthenia due to maternal anti-MuSK antibodies. Neuromuscul. Disord. 2008; 18: 443–6.

Belaya K, Rodriguez Cruz PM, Liu WW, Maxwell S, McGowan S, Farrugia ME, et al. Mutations in GMPPB cause congenital myasthenic syndrome and bridge myasthenic disorders with dystroglycanopathies. Brain 2015 Sep;138(Pt 9):2493-504.

Belaya K, Finlayson S, Cossins J, Liu WW, Maxwell S, Palace J, et al. Identification of DPAGT1 as a new gene in which mutations cause a congenital myasthenic syndrome. Ann. N. Y. Acad. Sci. 2012; 1275: 29–35.

Belaya K, Finlayson S, Slater CR, Cossins J, Liu WW, Maxwell S, et al. Mutations in DPAGT1 cause a limb-girdle congenital myasthenic syndrome with tubular aggregates. Am. J. Hum. Genet. 2012; 91: 193–201.

Bestue-Cardiel M, Sáenz de Cabezón-Alvarez a, Capablo-Liesa JL, López-Pisón J, Peña-Segura JL, Martin-Martinez J, et al. Congenital endplate acetylcholinesterase deficiency responsive to ephedrine. Neurology 2005; 65: 144–6.

Bhate MP, Molnar KS, Goulian M, Degrado WF, Francisco S. Signal Transduction in Histidine Kinases: Insights from New Structures. Structure 2015; 23: 981–994.

Bloch RJ. Loss of acetylcholine receptor clusters induced by treatment of cultured rat myotubes with carbachol . J Neurosci 1986; 6: 691–700.

Brancatisano T, Collett PW, Engel LA. Respiratory movements of the vocal cords. J. Appl. Physiol. 1984; 57: 1269–1276.

Brancatisano TP, Dood DS, Engel LA. Respiratory activity of posterior cricoarytenoid muscle and vocal cords in humans. J. Appl. Physiol. 1984; 57: 1143–1149.

Brenner H, Witzemann V, Sakmann B. Imprinting of acetylcholine receptor messenger RNA accumulation in mammalian neuromuscular synapses. Nature 1990 Apr 5;344(6226)544–7.

Bretthauer RK. Structure, expression, and regulation of UDP-GlcNAc: dolichol phosphate GlcNAc-1-phosphate transferase (DPAGT1). Curr. Drug Targets 2009; 10: 477–82.

Bridgman PC. Myosin Motor Proteins in the Cell Biology of Axons and Other Neuronal Compartments. In: Koenig E, editor(s). Cell Biology of the Axon. Springer Berlin Heidelberg; 2009. p. 91–105.

Brose N, Hofmann K, Hata Y, Su TC. Mammalian Homologues of Caenorhabditis elegans unc-13 Gene Define Novel Family of C2-domain Proteins. J Biol Chem 1995; 270: 25273–25280.

Brown O. Structure and function of the upper airway. In: Westmore R, Muntz H, McGill T, editor(s). Pediatric Otolaryngology. Principles and Practice Pathways. New York: Thieme Medical Publishers; 2000. p. 679–688.

Buckingham M, Bajard L, Chang T, Daubas P, Hadchouel J, Meilhac S, et al. The formation of skeletal muscle : from somite to limb. J Anat. 2003 Jan;202(1)59–68.

Burattini S, Ferri P, Battistelli M, Curci R, Luchetti F, Falcieri E. C2C12 murine myoblasts as a model of skeletal muscle development: morpho-functional characterization. Eur. J. Histochem. 2004; 48: 223–233.

Burden SJ, Yumoto N, Zhang W. The role of MuSK in synapse formation and neuromuscular disease. Cold Spring Harb. Perspect. Biol. 2013; 5: 1–11.

Burke G, Cossins J, Maxwell S, Owens G, Vincent A, Robb S, et al. Rapsyn mutations in hereditary myasthenia Distinct early- and late-onset phenotypes. Neurology 2003 Sep 23;61(6):826-8.

Burke G, Cossins J, Maxwell S, Robb S, Nicolle M, Vincent A, et al. Distinct phenotypes of congenital acetylcholine receptor deficiency. Neuromuscul Disord 2004; 14: 356–64.

Burke G, Hiscock A, Klein A, Niks EH, Main M, Manzur AY, et al. Salbutamol benefits children with congenital myasthenic syndrome due to DOK7 mutations. . Neuromuscul. Disord. 2013; 23: 170–5.

Cabail MZ, Li S, Lemmon E, Bowen ME, Hubbard SR, Miller WT. The insulin and IGF1 receptor kinase domains are functional dimers in the activated state. Nat. Commun. 2015 Mar 11; 6: 6406.

Cabrera-Serrano M, Ghaoui R, Ravenscroft G, Johnsen RD, Davis MR, Corbett A, et al. Expanding the phenotype of GMPPB mutations. Brain 2015 Apr;138(Pt 4):836-44.

Camilleri AA, Willmann R, Sadasivam G, Lin S, Rüegg MA, Gesemann M, et al. Tyrosine phosphatases such as SHP-2 act in a balance with Src-family kinases in stabilization of postsynaptic clusters of acetylcholine receptors. BMC Neurosci. 2007 Jul 2;8:46.

Camurdanoglu BZ, Hrovat C, Dürnberger G, Madalinski M, Mechtler K, Herbst R. Musk Kinase Activity is Modulated By A Serine Phosphorylation Site in The Kinase Loop . Sci. Rep. 2016; 6: 33583.

Cantor S, Zhang W, Delestrée N, Remédio L, Mentis GZ, Burden SJ. Preserving neuromuscular synapses in ALS by stimulating MuSK with a therapeutic agonist antibody. Elife 2018; 7: 1–19.

Carss KJ, Stevens E, Foley a R, Cirak S, Riemersma M, Torelli S, et al. Mutations in GDP-mannose pyrophosphorylase B cause congenital and limb-girdle muscular dystrophies associated with hypoglycosylation of α-dystroglycan. Am. J. Hum. Genet. 2013; 93: 29–41.

Cartaud A, Strochlic L, Guerra M, Blanchard B, Lambergeon M, Krejci E, et al. MuSK is required for anchoring acetylcholinesterase at the neuromuscular junction. J. Cell Biol. 2004; 165: 505–15.

Chan SHS, Wong VCN, Engel AG. Neuromuscular junction acetylcholinesterase deficiency responsive to albuterol. Pediatr. Neurol. 2012; 47: 137–40.

Chang CC, Chen TF, Chuang ST. Influence of chronic neostigmine treatment on the number of acetylcholine receptors and the release of acetylcholine from the rat diaphragm. J. Physiol. 1973; 230: 613–8.

Chang T, Gunaratne P, Gamage R, Riffsy MTM, Vincent A. MuSK-antibody-positive

myasthenia gravis in a South Asian population. J. Neurol. Sci. 2009; 284: 33–5.

Chang T, Leite MI, Senanayake S, Gunaratne PS, Gamage R, Riffsy MTM, et al. Clinical and serological study of myasthenia gravis using both radioimmunoprecipitation and cell-based assays in a South Asian population. J. Neurol. Sci. 2014; 343: 82–7.

Chaouch A, Müller JS, Guergueltcheva V, Dusl M, Schara U, Rakocević-Stojanović V, et al. A retrospective clinical study of the treatment of slow-channel congenital myasthenic syndrome. J. Neurol. 2012; 259: 474–81.

Chapman ER, An S, Barton N, Jahn R. SNAP-25, a t-SNARE Which Binds to Both Syntaxin and Synaptobrevin via Domains That May Form Coiled Coils. J. Biol. Chem. 1994; 269: 27427–27432.

Chen F, Qian L, Yang Z, Huang Y, Ngo ST, Ruan N, et al. Rapsyn Interaction with Calpain Stabilizes AChR Clusters at the Neuromuscular Junction. Neuron 2007; 55: 247–260.

Chen YA, Scheller RH, Medical HH. Snare-mediated membrane fusion. Nature 2001; 2: 98–106.

Chevessier F, Faraut B, Ravel-Chapuis A, Richard P, Gaudon K, Bauché S, et al. MUSK, a new target for mutations causing congenital myasthenic syndrome. Hum. Mol. Genet. 2004; 13: 3229–3240.

Chevessier F, Girard E, Molgó J, Bartling S, Koenig J, Hantai D, et al. A mouse model for congenital myasthenic syndrome due to MuSK mutations reveals defects in structure and function of neuromuscular junctions. Hum. Mol. Genet. 2008; 17: 3577–3595.

Chiang LM, Darras BT, Kang PB. Juvenile myasthenia gravis. . Muscle Nerve 2009; 39: 423–31.

Chiu HC, Vincent A, Newsom-Davis J, Hsieh KH, Hung T. Myasthenia gravis: population differences in disease expression and acetylcholine receptor antibody titers between Chinese and Caucasians. Neurology 1987; 37: 1854–7.

Claassen H, Jochen AW. Anatomy and Embryology Fiber differentiation of the human laryngeal muscles using the inhibition reactivation myofibrillar ATPase technique. Anat Embryol 1992; 186: 341–346.

Claeys KG, Maisonobe T, Böhm J, Laporte J, Hezode M, Romero NB, et al. Phenotype of a patient with recessive centronuclear myopathy and a novel BIN1 mutation. Neurology 2010; 74: 519–21.

Cong L, Ran FA, Cox D, Lin S, Barretto R, Habib N, et al. Multiplex Genome Engineering Using CRISPR/Cas Systems. Science 2013; 339: 819–823.

Cossins J, Belaya K, Hicks D, Salih M a, Finlayson S, Carboni N, et al. Congenital myasthenic

syndromes due to mutations in ALG2 and ALG14. Brain 2013; 136: 944–56.

Cossins J, Burke G, Maxwell S, Spearman H, Man S, Kuks J, et al. Diverse molecular mechanisms involved in AChR deficiency due to rapsyn mutations. Brain 2006; 129: 2773–83.

Cossins J, Liu WW, Belaya K, Maxwell S, Oldridge M, Lester T, et al. The spectrum of mutations that underlie the neuromuscular junction synaptopathy in DOK7 congenital myasthenic syndrome. Hum. Mol. Genet. 2012; 21: 3765–75.

Cossins J, Webster R, Maxwell S, Burke G, Vincent A, Beeson D. A mouse model of AChR deficiency syndrome with a phenotype reflecting the human condition. Hum. Mol. Genet. 2004; 13: 2947–2957.

Dai Z, Luo X, Xie H, Peng HB, Hill C, Carolina N. The Actin-Driven Movement and Formation of Acetylcholine Receptor Clusters. J Cell Biol. 2000; 150: 1321–1334.

DeChiara TM, Bowen DC, Valenzuela DM, Simmons M V, Poueymirou WT, Thomas S, et al. The receptor tyrosine kinase MuSK is required for neuromuscular junction formation in vivo. Cell 1996; 85: 501–12.

Denzer AJ, Brandenberger R, Gesemann M, Chiquet M, Ruegg MA. Agrin Binds to the Nerve–Muscle Basal Lamina via Laminin. 1997; 137: 671–683.

Devic P, Petiot P, Simonet T, Stojkovic T, Delmont E, Franques J, et al. Antibodies to clustered acetylcholine receptor: expanding the phenotype. Eur. J. Neurol. 2014; 21: 130–4.

Diana X B-G, Neil E, Wiggs E, Winder TL, Moore SA. Intrafamilial variability in GMPPB-associated dystroglycanopathy: broadening the phenotype. Neurology 2015: 1495–1497.

Dixit A, Verkhivker GM. Computational Modeling of Allosteric Communication Reveals Organizing Principles of Mutation-Induced Signaling in ABL and EGFR Kinases. PLoS Comput Biol. 2011 Oct;7(10):e1002179.

Donger C, Krejci E, Serradell a P, Eymard B, Bon S, Nicole S, et al. Mutation in the human acetylcholinesterase-associated collagen gene, COLQ, is responsible for congenital myasthenic syndrome with end-plate acetylcholinesterase deficiency (Type Ic). Am. J. Hum. Genet. 1998; 63: 967–75.

Ealing J, Webster R, Brownlow S, Abdelgany A, Oosterhuis H, Muntoni F, et al. Mutations in congenital myasthenic syndromes reveal an e subunit C-terminal cysteine, C470 , crucial for maturation and surface expression of adult AChR. Hum Mol Genet. 2002; 11: 3087–3096.

Eaton LM, Lambert EH. Electromyography and electric stimulation of nerves in diseases

of motor unit; observations on myasthenic syndrome associated with malignant tumors. J. Am. Med. Assoc. 1957; 163: 1117–24.

Eker A, Saka E, Dalmau J, Kurne A, Bilen C, Ozen H, et al. Dyspnoea due to vocal fold abduction paresis in anti-MuSK myasthenia gravis. J. Neurol. Neurosurg. Psychiatry 2008; 79: 1082–3.

Elferink LA, Trimbles WS. Two Vesicle-associated Membrane Protein Genes Are Differentially Expressed in the Rat Central Nervous System. J. Biol. Chem. 1989; 264: 11061–11064.

Engel A, Franzini-Armstrong C. Myology. 3rd ed. New York: McGraw Hill; 2004.

Engel AG. The Therapy of Congenital Myasthenic Syndromes. Neurotherapeutics 2007; 4: 252–257.

Engel AG. Current status of the congenital myasthenic syndromes. Neuromuscul. Disord. 2012a; 22: 99–111.

Engel AG. Congenital myasthenic syndromes in 2012. Curr. Neurol. Neurosci. Rep. 2012b; 12: 92–101.

Engel AG, Lambert EH, Santa T. Study of long-term anticholinesterase therapy. Effects on neuromuscular transmission and on motor end-plate fine structure. Neurology 1973; 23: 1273–81.

Engel AG, Selcen D, Shen X-M, Milone M, Harper CM. Loss of MUNC13-1 function causes microcephaly , cortical hyperexcitability , and fatal myasthenia. Neurol Genet 2016; 5: e105.

Engel AG, Shen X, Selcen D, Sine SM. Congenital myasthenic syndromes : pathogenesis , diagnosis , and treatment . Lancet Neurol. 2015; 14: 420–434.

Evoli A, Tonali P a, Padua L, Monaco M Lo, Scuderi F, Batocchi AP, et al. Clinical correlates with anti-MuSK antibodies in generalized seronegative myasthenia gravis. Brain 2003; 126: 2304–11.

Ferns M, Deiner M, Hall Z. Agrin-induced Acetylcholine Receptor Clustering in Mammalian Muscle Rexluires Tyrosine Phosphorylation. 1996; 132: 937–944.

Ferns MJ, Campanelli JT, Scheller RH, Hall Z. The Ability of Agrin to Cluster AChRs Depends on Alternative Splicing and on Cell Surface Proteoglycans. Neuron 1993; 11: 491–502.

Finkel RS, Mercuri E, Darras BT, Connolly AM, Kuntz NL, Kirschner J, et al. Nusinersen versus Sham Control in Infantile-Onset Spinal Muscular Atrophy . N. Engl. J. Med. 2017; 377: 1723–1732.

Finlayson S. Congenital myasthenic syndromes : an update. Pract. Neurol. 2013; 13: 80–91.

Finlayson S, Morrow JM, Rodriguez Cruz PM, Sinclair CDJ, Fischmann A, Thornton JS, et al. Muscle MRI in congenital myasthenic syndromes. Muscle Nerve 2016: 1–9.

Finlayson S, Palace J, Belaya K, Walls T, Norwood F, Burke G, et al. Clinical features of congenital myasthenic syndrome due to mutations in DPAGT1. J. Neurol. Neurosurg. Psychiatry 2013; 84: 1119–25.

Finlayson S, Spillane J, Kullmann DM, Howard R, Webster R, Palace J, et al. Slow channel congenital myasthenic syndrome responsive to a combination of fluoxetine and salbutamol. Muscle and Nerve 2013; 47: 279–282.

Fox MA, Ho MSP, Smyth N, Sanes JR. A synaptic nidogen : Developmental regulation and role of nidogen-2 at the neuromuscular junction. Neural Dev. 2008 Sep 25; 3: 24.
.

Gallardo E, Martínez-Hernández E, Titulaer MJ, Huijbers MG, Martínez MA, Ramos A, et al. Cortactin autoantibodies in myasthenia gravis. . Autoimmun. Rev. 2014; 13: 1003–7.

Gallenmüller C, Felber WM, Dusl M, Stucka R, Guergueltcheva V, Blaschek A, et al. Salbutamol-responsive limb-girdle congenital myasthenic syndrome due to a novel missense mutation and heteroallelic deletion in MUSK. Neuromuscul. Disord. 2014; 24: 31–5.

Gasperi C, Melms A, Schoser B, Zhang Y, Meltoranta J, Risson V, et al. Anti-agrin autoantibodies in myasthenia gravis. . Neurology 2014; 82: 1976–83.

Gautam M, Noakes PG, Mudd J, Nichol M, Chu GC, Sanes JR, et al. Failure of postsynaptic specialization to develop at neuromuscular junctions of rapsyn-deficient mice. Nature 1995; 377: 232–236.

Gehle VM, Walcott EC, Nishizaki T, Sumikawa K. N-glycosylation at the conserved sites ensures the expression of properly folded functional ACh receptors. Brain Res. Mol. Brain Res. 1997; 45: 219–29.

Gibbs EM, Clarke NF, Rose K, Oates EC, Webster R, Feldman EL, et al. Neuromuscular junction abnormalities in DNM2-related centronuclear myopathy. J. Mol. Med. (Berl). 2013; 91: 727–37.

Gillies JD, Allen J. Effects of neostigmine and pyridostigmine at the neuromuscular junction. . Clin. Exp. Neurol. 1977; 14: 271–9.

Girlanda P, Toscano A, Nicolosi C, Sinicropi S, Picciolo G, Macaione V, et al. Electrophysiological study of neuromuscular system involvement in mitochondrial cytopathy. Clin Neurophysiol. 1999 Jul;110(7):1284-9.

Glass DJ, Bowen DC, Stitt TN, Radziejewski C, Bruno J, Ryan TE, et al. Agrin acts via a MuSK receptor complex. Cell 1996; 85: 513–23.

Gross RA, Johnston KC. Levels of evidence Taking Neurology ® to the next level. 2009 Jan 6;72(1):8-10

Guergueltcheva V, Müller JS, Dusl M, Senderek J, Oldfors A, Lindbergh C, et al. Congenital myasthenic syndrome with tubular aggregates caused by GFPT1 mutations. J. Neurol. 2012; 259: 838–50.

Gundersen K, Sanes JR, Merlie JP. Neural Regulation of Muscle Acetylcholine Receptor E- and a-Subunit Gene Promoters in Transgenic Mice. J. Cell Biol. 1993; 123: 1535–1544.

Hägg P, Rehn M, Huhtala P, Väisänen T, Tamminen M, Pihlajaniemi T. Type XIII collagen is identified as a plasma membrane protein. J. Biol. Chem. 1998; 273: 15590–15597.

Hallock PT, Xu C, Park T, Neubert TA, Curran T, Burden SJ. Dok-7 regulates neuromuscular synapse formation by recruiting Crk and Crk-L. Genes Dev. 2010; 24: 2451–2461.

Haltiwanger RS, Lowe JB. Role of glycosylation in development. . Annu. Rev. Biochem. 2004; 73: 491–537.

Hanks SK, Quinn AM, Hunter T. The Protein Kinase Family : Conserved Features and Deduced Phylogeny of the Catalytic Domains. Science 1988 Jul 1;241(4861):42-52.

Hanson J a, Lueck CJ, Thomas DJ. Myasthenia gravis presenting with stridor. Thorax 1996; 51: 108–9.

Hara K, Mashima T, Matsuda A, Tanaka K, Tomita M, Shiraishi H, et al. Vocal cord paralysis in myasthenia gravis with anti-MuSK antibodies. Neurology 2007; 68: 621–2.

Härönen H, Zainul Z, Tu H, Naumenko N, Sormunen R, Miinalainen I, et al. Collagen XIII secures pre- and postsynaptic integrity of the neuromuscular synapse. Hum. Mol. Genet. 2017 Jun 1;26(11):2076-2090.

Harper C, Engel A. Treatment of 31 congenital myasthenic syndrome patients with 3,4-diaminopyridine. Neurology 2000; 54(suppl 3):A39. Neurology 2000; 54(suppl3): A39.

Harper CM, Fukodome T, Engel AG. Treatment of slow-channel congenital myasthenic syndrome with fluoxetine. Neurology 2003; 60: 1710–1713.

Hartman MA, Finan D, Sivaramakrishnan S, Spudich JA. Principles of Unconventional Myosin Function and Targeting. Annu Rev Cell Dev Biol 2011; 27: 133–155.

Hatanaka Y, Oh SJ. Single-fiber electromyography in sporadic inclusion body myopathy. . Clin. Neurophysiol. 2007; 118: 1563–8.

Heng HS, Lim M, Absoud M, Austin C, Clarke D, Wraige E, et al. Outcome of children with acetylcholine receptor (AChR) antibody positive juvenile myasthenia gravis following thymectomy. Neuromuscul. Disord. 2014; 24: 25–30.

Henriquez JP, Webb A, Bence M, Bildsoe H, Sahores M, Hughes SM, et al. Wnt signaling promotes AChR aggregation at the neuromuscular synapse in collaboration with agrin. 2008: 2–7.

Herrmann DN, Horvath R, Sowden JE, Gonzalez M, Gonzales M, Sanchez-Mejias A, et al. Synaptotagmin 2 mutations cause an autosomal-dominant form of lambert-eaton myasthenic syndrome and nonprogressive motor neuropathy. Am. J. Hum. Genet. 2014; 95: 332–9.

Hoch W, McConville J, Helms S, Newsom-Davis J, Melms A, Vincent A. Auto-antibodies to the receptor tyrosine kinase MuSK in patients with myasthenia gravis without acetylcholine receptor antibodies. Nat. Med. 2001; 7: 365–8.

Hoffmann K, Müller JS, Stricker S, Megarbane A, Rajab A, Lindner TH, et al. Escobar Syndrome Is a Prenatal Myasthenia Caused by Disruption of the Acetylcholine Receptor Fetal γ Subunit. Am. J. Hum. Genet. 2006; 79: 303–312.

Hopf C, Hoch W, Tu D-. Dimerization of the Muscle-specific Kinase Induces Tyrosine Phosphorylation of Acetylcholine Receptors and Their Aggregation on the Surface of Myotubes *. 1998; 273: 6467–6473.

Hudgins PA, Siegel J, Jacobs I, Abramowsky CR. The Normal Pediatric Larynx on CT and MR. Am J Neuroradiol 1997; 18: 239–245.

Huh S-Y, Kim H-S, Jang H-J, Park Y-E, Kim D-S. Limb-girdle myasthenia with tubular aggregates associated with novel GFPT1 mutations. Muscle Nerve 2012; 46: 600–4.

Hutchinson DO, Walls TJ, Nakano S, Camp S, Taylor P, Harper CM, et al. Congenital endplate acetylcholinesterase deficiency. Brain 1993; 116: 633–653.

Ibraghimov-Beskrovnaya O, Ervasti JM, Leveille CJ, Slaughter CA, Sernett SW, Campbell KP. Primary structure of dystrophin-associated glycoproteins linking dystrophin to the extracellular matrix. . Nature 1992; 355: 696–702.

Illingworth M a, Main M, Pitt M, Feng L, Sewry C a, Gunny R, et al. RYR1-related congenital myopathy with fatigable weakness, responding to pyridostigimine. Neuromuscul. Disord. 2014; 24: 707–12.

Ionita CM, Acsadi G. Pediatric Neurology Management of Juvenile Myasthenia Gravis . Pediatr. Neurol. 2013; 48: 95–104.

Jackson BJ, Kukuruzinska MA, Robbins P. Biosynthesis of asparagine-linked oligosaccharides in Saccharomyces cerevisiae: the alg2 mutation. Glycobiology 1993; 3:

357–64.

Jacob S, Viegas S, Leite MI, Webster R, Cossins J, Kennett R, et al. Presence and pathogenic relevance of antibodies to clustered acetylcholine receptor in ocular and generalized myasthenia gravis. . Arch. Neurol. 2012; 69: 994–1001.

Jacobson C, Côté PD, Rossi SG, Rotundo RL, Carbonetto S. The Dystroglycan Complex Is Necessary for Stabilization of Acetylcholine Receptor Clusters at Neuromuscular Junctions and Formation of the Synaptic Basement Membrane. Journa Cell Biol. 2001; 152: 435–450.

Jaeken J, Martens K, Francois I, Eyskens F, Lecointre C, Derua R, et al. Deletion of PREPL, a gene encoding a putative serine oligopeptidase, in patients with hypotonia-cystinuria syndrome. . Am. J. Hum. Genet. 2006; 78: 38–51.

Jaeken J, Matthijs G. Congenital disorders of glycosylation. Annu. Rev. Genomics Hum. Genet. 2001; 2: 129–51.

Jaretzki A, Barohn RJ, Ernstoff RM, Kaminski HJ, Keesey JC, Penn AS, et al. Myasthenia gravis: recommendations for clinical research standards. Task Force of the Medical Scientific Advisory Board of the Myasthenia Gravis Foundation of America. Neurology 2000; 55: 16–23.

Jephson CG, Mills NA, Pitt MC, Beeson D, Aloysius A, Muntoni F, et al. Congenital stridor with feeding difficulty as a presenting symptom of Dok7 congenital myasthenic syndrome. Int. J. Pediatr. Otorhinolaryngol. 2010; 74: 991–994.

Jiménez Caballero PE, Fermin Marrero J a, Trigo Bragado I, Casado Naranjo I. Vocal cord paralysis as a manifestation of myasthenia gravis with anti-MuSK antibodies. Neurologia 2014 May;29(4):253-4.

Jinek M, Chylinski K, Fonfara I, Hauer M, Doudna JA, Charpentier E. A Programmable Dual-RNA – Guided DNA Endonuclease in Adaptive Bacterial Immunity. Science 2012 Aug 17; 337: 816–821.

Karakaya M, Ceyhan-Birsoy O, Beggs AH, Topaloglu H. A novel missense variant in the AGRN gene; congenital myasthenic syndrome presenting with head drop. J Clin Neuromuscul Dis 2017; 18: 147–151.

Khan A, Hussain N, Gosalakkal J. Bulbar dysfunction: An early presentation of congenital myasthenic syndrome in three infants. J. Paediatr. Neurosci. 2011; 6: 124–126.

Khan MM, Lustrino D, Silveira WA, Wild F, Straka T, Issop Y, et al. Sympathetic innervation controls homeostasis of neuromuscular junctions in health and disease. Proc Natl Acad Sci U S A. 2016 Jan 19;113(3):746-50.

Kim M-H, Hersh LB. The vesicular acetylcholine transporter interacts with clathrin-associated adaptor complexes AP-1 and AP-2. J. Biol. Chem. 2004; 279: 12580–7.

Kim N, Stiegler AL, Cameron TO, Hallock PT, Gomez AM, Huang JH, et al. Lrp4 Is a Receptor for Agrin and Forms a Complex with MuSK. Cell 2008; 135: 334–342.

Klein A, Pitt MC, McHugh JC, Niks EH, Sewry C a, Phadke R, et al. DOK7 congenital myasthenic syndrome in childhood: Early diagnostic clues in 23 children. Neuromuscul. Disord. 2013 Nov;23(11):883-91.

Koczula KM, Gallotta A. Lateral flow assays . Essays Biochem. 2016; 60: 111–120.

Koneczny I, Cossins J, Waters P, Beeson D, Vincent A. MuSK myasthenia gravis IgG4 disrupts the interaction of LRP4 with MuSK but both IgG4 and IgG1-3 can disperse preformed agrin-independent AChR clusters. PLoS One 2013; 8: e80695.

Konermann S, Brigham MD, Trevino AE, Joung J, Abudayyeh OO, Barcena C, et al. Genome-scale transcriptional activation by an engineered CRISPR-Cas9 complex. Nature 2015; 517: 583–588.

Kostera-Pruszczyk A, Kamińska A, Dutkiewicz M, Emeryk-Szajewska B, Strugalska-Cynowska MH, Vincent a, et al. MuSK-positive myasthenia gravis is rare in the Polish population. Eur. J. Neurol. 2008; 15: 720–4.

Krsti DZ, Lazarevi TD, Bond AM, Vasi VM. Acetylcholinesterase Inhibitors : Pharmacology and Toxicology. 2013: 315–335.

Krzywinski M, Schein J, Birol I, Connors J, Gascoyne R, Jones SJ, et al. Circos : an Information Aesthetic for Comparative Genomics. Genome Res 2009; 19: 1639–45.

Kues WA, Sakmann B, Witzemann V. Differential Expression Patterns of Five Acetylcholine Receptor Subunit Genes in Rat Muscle During Development. Eur. J. Neurosci. 1995; 7: 1376–1385.

Kvist a P, Latvanlehto a, Sund M, Eklund L, Väisänen T, Hägg P, et al. Lack of cytosolic and transmembrane domains of type XIII collagen results in progressive myopathy. Am. J. Pathol. 2001; 159: 1581–92.

Kvist A, Latvanlehto A, Sund M, Eklund L, Va T. Lack of Cytosolic and Transmembrane Domains of Type XIII Collagen Results in Progressive Myopathy. Am. J. Pathol. 2001; 159: 1581–1592.

Kyte J, Doolittle R. A simple method for displaying the hydropathic character of a protein. J Mol Biol. 1982; 157: 105–32.

Lai Y, Choi UB, Leitz J, Brose N, Rhee J, Brunger AT, et al. Molecular Mechanisms of Synaptic Vesicle Priming Article Molecular Mechanisms of Synaptic Vesicle Priming by

Munc13 and Munc18. Neuron 2017; 95: 591–607.

Lashley D, Palace J, Jayawant S, Robb S, Beeson D. Ephedrine treatment in congenital myasthenic syndrome due to mutations in DOK7. Neurology 2010; 74: 1517–23.

Latvanlehto A, Fox M a, Sormunen R, Tu H, Oikarainen T, Koski A, et al. Muscle-derived collagen XIII regulates maturation of the skeletal neuromuscular junction. J. Neurosci. 2010; 30: 12230–41.

Lee Y, Rudell J, Yechikhov S, Taylor R, Swope S, Ferns M. Rapsyn carboxyl terminal domains mediate muscle specific kinase-induced phosphorylation of the muscle acetylcholine receptor. Neuroscience 2008; 153: 997–1007.

Leite MI, Jacob S, Viegas S, Cossins J, Clover L, Morgan BP, et al. IgG1 antibodies to acetylcholine receptors in ' seronegative ' myasthenia gravis y. Brain 2008 Jul;131(Pt 7):1940-52.

Lek M, Karczewski KJ, Minikel E V, Samocha KE, Banks E, Fennell T, et al. Analysis of protein-coding genetic variation in 60,706 humans . Nature 2016; 536: 285–291.

Lemmon MA, Schlessinger J. Cell signaling by receptor-tyrosine kinases. Cell 2010; 141: 1117–1134.

Lewis AJM, Finlayson S, Mahmod M, Karamitsos TD, Dass S, Ashrafian H, et al. A novel cardiac phenotype in patients with GFPT1 or DPAGT1 mutations . Exp. Clin. Cardiol. 2014; 20: 3139–3145.

Liewluck T, Selcen D, Engel AG. Beneficial effects of Albuterol in congenital endplate acetylcholinesterase deficiency and DOK-7 myasthenia. Muscle Nerve 2011; 44: 789–794.

Lin W, Dominguez B, Yang J, Aryal P, Brandon EP, Gage FH, et al. Neurotransmitter acetylcholine negatively regulates neuromuscular synapse formation by a Cdk5-dependent mechanism. Neuron 2005; 46: 569–579.

Lindstrom JM, Seybold ME, Lennon VA, Whittingham S, Duane DD. Antibody to acetylcholine receptor in myasthenia gravis. Prevalence, clinical correlates, and diagnostic value. Neurology 1976; 26: 1054–9.

Linnoila J, Wang Y, Yao Y, Wang ZZ. A Mammalian Homolog of Drosophila Tumorous Imaginal Discs, Tid1, Mediates Agrin Signaling at the Neuromuscular Junction. Neuron 2008; 60: 625–641.

Liu Y, Sugiura Y, Lin W. The role of Synaptobrevin1 / VAMP1 in Ca 2 + -triggered neurotransmitter release at the mouse neuromuscular junction. J Physiol 2011; 7: 1603–1618.

Logan C V., Cossins J, Rodríguez Cruz PM, Parry DA, Maxwell S, Martínez-Martínez P, et al.

Congenital Myasthenic Syndrome Type 19 Is Caused by Mutations in COL13A1, Encoding the Atypical Non-fibrillar Collagen Type XIII α1 Chain . Am. J. Hum. Genet. 2015; 97: 878–885.

Lone AM, Nolte WM, Tinoco AD, Saghatelian A. Peptidomics of the prolyl peptidases. AAPS J. 2010; 12: 483–91.

Lorenzoni PJ, Scola RH, Kay CSK, Filla L, Miranda APP, Pinheiro JMR, et al. Salbutamol therapy in congenital myasthenic syndrome due to DOK7 mutation. J. Neurol. Sci. 2013; 331: 155–7.

Lu J, Takahashi T, Ohoka A, Nakajima K, Hashimoto R, Miura N, et al. Alg14 organizes the formation of a multiglycosyltransferase complex involved in initiation of lipid-linked oligosaccharide biosynthesis. Glycobiology 2012; 22: 504–16.

Luk WKW, Chan WKB, Leung KW, Guo AJY, Chan GKL, Xu SL, et al. Molecular assembly and biosynthesis of acetylcholinesterase in brain and muscle : the roles of t-peptide , FHB domain , and N-linked glycosylation. Front Mol Neurosci. 2011 Oct 25;4:36.

Luo ZG, Wang Q, Zhou JZ, Wang J, Luo Z, Liu M, et al. Regulation of AChR Clustering by Dishevelled Interacting with MuSK and PAK1. Neuron 2002; 35: 489–505.

Ma C, Su L, Seven AB, Xu Y, Rizo J. Reconstitution of the Vital Functions of Munc18 and Munc13 in Neurotransmitter Release. Science 2013; 339: 421–426.

Madhavan R, Gong ZL, Ma JJ, Chan AWS, Peng HB. The function of cortactin in the clustering of acetylcholine receptors at the vertebrate neuromuscular junction. PLoS One 2009 Dec 29;4(12): e8478.

Madhavan R, Peng HB. Molecular Regulation of Postsynaptic Differentiation at the Neuromuscular Junction. IUBMB Life 2005; 57: 719–730.

Maggi L, Scoto M, Cirak S, Robb S a, Klein a, Lillis S, et al. Congenital myopathies - Clinical features and frequency of individual subtypes diagnosed over a 5-year period in the United Kingdom. Neuromuscul. Disord. 2013; 23: 195–205.

Mahjneh I, Lochmüller H, Muntoni F, Abicht A. DOK7 limb-girdle myasthenic syndrome mimicking congenital muscular dystrophy. Neuromuscul. Disord. 2013; 23: 36–42.

Mahoney F, Barthel D. Functional evaluation: The Barthel Index. Md State Med J 1965; 14: 61–5.

Majumdar S, Bateman NJ, Bull PD. Paediatric stridor. Arch. Dis. Child. - Educ. Pract. 2006; 91: ep101-ep105.

Mali P, Aach J, Stranges PB, Esvelt KM, Moosburner M, Kosuri S, et al. CAS9 transcriptional activators for target specificity screening and paired nickases for cooperative genome

engineering. Nat. Biotechnol. 2013; 31: 833–838.

Malmgren LT, Gacek RR. Histochemical Characteristics of Muscle Fiber Types in the Posterior Cricoarytenoid Muscle. Ann. Otol. Rhinol. Laryngol. 1981; 90: 423–429.

Mantegazza R, Baggi F, Antozzi C, Confalonieri P, L M, Bernasconi P, et al. Myasthenia Gravis (MG): Epidemiological Data and Prognostic Factors . Ann. N. Y. Acad. Sci. 2003; 998: 413–23.

Martens K, Derua R, Meulemans S, Waelkens E, Jaeken J, Matthijs G, et al. PREPL: a putative novel oligopeptidase propelled into the limelight. Biol. Chem. 2006; 387: 879–83.

Martin F, Thumfart WF. The Electromyographic Activity of the Posterior Cricoarytenoid Muscle During Singing. Journal of voice 1990; 4: 25–29.

Martin PT. Glycobiology of the neuromuscular junction. J. Neurocytol. 2003; 32: 915–29.

Martin PT, Kaufman SJ, Kramer RH, Sanes JR. Synaptic Integrins in Developing, Adult, and Mutant Muscle: Selective Association of α1, α7A, and α7B Integrins with the Neuromuscular Junction. Dev. Biol. 1996; 174: 125–139.

Maselli R a, Arredondo J, Cagney O, Ng JJ, Anderson J a, Williams C, et al. Mutations in MUSK causing congenital myasthenic syndrome impair MuSK-Dok-7 interaction. Hum. Mol. Genet. 2010; 19: 2370–9.

Maselli R a, Ng JJ, Anderson J a, Cagney O, Arredondo J, Williams C, et al. Mutations in LAMB2 causing a severe form of synaptic congenital myasthenic syndrome. J. Med. Genet. 2009; 46: 203–8.

Maselli RA, Arredondo J, Ferns MJ, Wollmann RL. Synaptic basal lamina-associated congenital myasthenic syndromes. Ann. N. Y. Acad. Sci. 2012; 1275: 36–48.

Maselli RA, Chen D, Delores M, Bowe C, Fenton G, Wollmann RL. Choline acetyltransferase mutations in myasthenic syndrome due to deficient acetylcholine resynthesis. Muscle Nerve 2003; 27: 180–187.

Maselli RA, Chong JX, Arredondo J, Vázquez J, Bamshad MJ, Nickerson DA, et al. Presynaptic congenital myasthenic syndrome with a homozygous sequence variant in LAMA5 combines myopia , facial tics , and failure of neuromuscular transmission. Am. J. Med. Genet. Part A 2017: 2240–2245.

Maselli RA, Fernandez JM, Arredondo J, Navarro C, Ngo M, Beeson D, et al. LG2 agrin mutation causing severe congenital myasthenic syndrome mimics functional characteristics of non-neural (z-) agrin. Hum Genet. 2012 Jul;131(7):1123-35.

Mcmacken G, Cox D, Roos A, Müller J, Whittaker R, Lochmüller H. The Beta-Adrenergic Agonist Salbutamol Modulates Neuromuscular Junction Formation in Zebrafish Models of Human Myasthenic Syndromes. Hum Mol Genet. 2018 May 1;27(9):1556-1564.

Mendell JR, Al-Zaidy S, Shell R, Arnold WD, Rodino-Klapac LR, Prior TW, et al. Single-Dose Gene-Replacement Therapy for Spinal Muscular Atrophy . N. Engl. J. Med. 2017; 377: 1713–1722.

Mercuri E. Neuromuscular disorders: 2017, a year to remember. Lancet Neurol. 2018; 17: 12–13.

Merlie JP, Sebbane R, Tzartos S, Lindstrom J. Inhibition of glycosylation with tunicamycin blocks assembly of newly synthesized acetylcholine receptor subunits in muscle cells. J. Biol. Chem. 1982; 257: 2694–701.

Michele DE, Barresi R, Kanagawa M, Saito F, Cohn RD, Satz JS, et al. Post-translational disruption of dystroglycan–ligand interactions in congenital muscular dystrophies . Nature 2002; 418: 417.

Michele DE, Barresi R, Kanagawa M, Saito F, Kelley RI, Somer H, et al. Post-translational disruption of dystroglycan – ligand interactions in congenital muscular dystrophies. 2002; 418: 417–422.

Mihaylova V, Müller JS, Vilchez JJ, Salih M a, Kabiraj MM, D'Amico A, et al. Clinical and molecular genetic findings in COLQ-mutant congenital myasthenic syndromes. Brain 2008; 131: 747–59.

Mihaylova V, Salih M a M, Mukhtar MM, Abuzeid H a, El-Sadig SM, von der Hagen M, et al. Refinement of the clinical phenotype in musk-related congenital myasthenic syndromes. Neurology 2009; 73: 1926–8.

Milone M, Shen XM, Selcen D, Ohno K, Brengman J, Iannaccone ST, et al. Myasthenic syndrome due to defects in rapsyn: Clinical and molecular findings in 39 patients. . Neurology 2009; 73: 228–35.

Missias AC, Chu GC, Klocke BJ, Sanes JR, Merlie JP. Maturation of the Acetylcholine Receptor in Skeletal Muscle : Regulation of the AChR g -to- e Switch. Dev Biol. 1996 Oct 10;179(1):223-38.

Miyoshi S, Tezuka T, Arimura S, Tomono T, Okada T, Yamanashi Y. *DOK7* gene therapy enhances motor activity and life span in ALS model mice. EMBO Mol. Med. 2017; 9: 880–889.

Mojica F, Díez-Villaseñor C, Soria E, Juez G. Biological significance of a family of regulatory spaced repeats in the genomes of Archaea, Bacteria and mitochondria. Mol. Microbiol. 2000; 36: 244–246.

Mokkapati S, Nischt R, Smyth N, Ho MSP, Bo K. Nidogens — Extracellular Matrix Linker Molecules. Microsc Res Tech. 2008; 395: 387–395.

Moll J, Barzaghi P, Lin S, Bezakova G, Lochmüller H, Engvall E, et al. An agrin minigene rescues dystrophic symptoms in a mouse model for congenital muscular dystrophy. Nature 2001; 413: 302–307.

Monies DM, Al-Hindi HN, Al-Muhaizea M a, Jaroudi DJ, Al-Younes B, Naim E a, et al. Clinical and pathological heterogeneity of a congenital disorder of glycosylation manifesting as a myasthenic/myopathic syndrome. Neuromuscul. Disord. 2014 Apr;24(4):353-9.

Moransard M, Borges LS, Willmann R, Marangi PA, Brenner HR, Ferns MJ, et al. Agrin Regulates Rapsyn Interaction with Surface Acetylcholine Receptors , and This Underlies Cytoskeletal Anchoring and Clustering. J. Biol. Chem. 2003; 278: 7350–7359.

Moremen KW, Tiemeyer M, Nairn A V. Vertebrate protein glycosylation: diversity, synthesis and function. Nat. Rev. Mol. Cell Biol. 2012; 13: 448–62.

Mouw JK, Ou G, Weaver VM, Regeneration T, Francisco S, Francisco S, et al. Extracellular matrix assembly: a multiscale deconstruction. Nat Rev Mol Cell Biol 2014; 15: 771–785.

Muller JS, Baumeister SK, Rasic VM, Krause S, Todorovic S, Abicht A, et al. Impaired receptor clustering in congenital myasthenic syndrome with novel RAPSN mutations. Neurology 2006; 67: 1159–1164.

Müller JS, Jepson CD, Laval SH, Bushby K, Straub V, Lochmüller H. Dok-7 promotes slow muscle integrity as well as neuromuscular junction formation in a zebrafish model of congenital myasthenic syndromes. Hum. Mol. Genet. 2010; 19: 1726–40.

Munot P, Lashley D, Jungbluth H, Feng L, Pitt M, Robb S a, et al. Congenital fibre type disproportion associated with mutations in the tropomyosin 3 (TPM3) gene mimicking congenital myasthenia. . Neuromuscul. Disord. 2010; 20: 796–800.

Muntoni F, Torelli S, Wells DJ, Brown SC. Muscular dystrophies due to glycosylation defects: diagnosis and therapeutic strategies. Curr. Opin. Neurol. 2011; 24: 437–42.

Murakami T, Ishigaki K, Shirakawa S, Ikenaka H, Sakauchi M OM. Severe muscle damage following viral infection in patients with Fukuyama congenital muscular dystrophy. Brain Dev 2012; Apr;34: 293–7.

Musa Zamah A, Delahunty M, Luttrell LM, Lefkowitz RJ. Protein kinase A-mediated phosphorylation of the β2-adrenergic receptor regulates its coupling to Gsand Gi: Demonstration in a reconstituted system. J. Biol. Chem. 2002; 277: 31249–31256.

Nakata T, Ito M, Azuma Y, Otsuka K, Noguchi Y, Komaki H, et al. Mutations in the C-terminal domain of ColQ in endplate acetylcholinesterase deficiency compromise ColQ-MuSK interaction. Hum. Mutat. 2013; 34: 997–1004.

Natera-de Benito D, Bestué M, Vilchez JJ, Evangelista T, Töpf A, García-ribes A. Long-term follow-up in patients with congenital myasthenic syndrome due to RAPSN mutations. Neuromuscul. Disord. 2016; 26: 153–159.

Nicole S, Chaouch A, Torbergsen T, Bauché S, de Bruyckere E, Fontenille M-J, et al. Agrin mutations lead to a congenital myasthenic syndrome with distal muscle weakness and atrophy. Brain 2014; 137: 2429–2443.

Niks EH, Kuks JBM, Verschuuren JJGM. Epidemiology of myasthenia gravis with anti-muscle specific kinase antibodies in The Netherlands. J. Neurol. Neurosurg. Psychiatry 2007; 78: 417–8.

Nykvist P, Tu H, Ivaska J, Ka J, Pihlajaniemi T. Distinct Recognition of Collagen Subtypes by alpha1beta1 and alpha2beta1 Integrins. J. Biol. Chem. 2000; 275: 8255–8261.

O'Connor E, Töpf A, Müller JS, Cox D, Evangelista T, Colomer J, et al. Identification of mutations in the MYO9A gene in patients with congenital myasthenic syndrome. Brain 2016 Aug;139(Pt 8):2143-53.

O'Grady GL, Verschuuren C, Yuen M, Webster R, Menezes M, Fock JM, et al. Variants in SLC18A3, vesicular acetylcholine transporter, cause congenital myasthenic syndrome. Neurology 2016; 87: 1442–1448.

Ohkawara B, Cabrera-Serrano M, Nakata T, Milone M, Asai N, Ito K, et al. LRP4 third β-propeller domain mutations cause novel congenital myasthenia by compromising agrin-mediated musk signaling in a position-specific manner. Hum. Mol. Genet. 2014 Apr 1;23(7):1856-68.

Ohno K, Brengman J, Tsujino a, Engel a G. Human endplate acetylcholinesterase deficiency caused by mutations in the collagen-like tail subunit (ColQ) of the asymmetric enzyme. . Proc. Natl. Acad. Sci. U. S. A. 1998; 95: 9654–9.

Ohno K, Engel AG, Brengman JM, Shen X, Heidenreich F, Vincent A, et al. The Spectrum of Mutations Causing End-Plate Acetylcholinesterase Deficiency. Ann Neurol 2000; 47: 162–170.

Ohno K, Engel AG, Shen X-M, Selcen D, Brengman J, Harper CM, et al. Rapsyn mutations in humans cause endplate acetylcholine-receptor deficiency and myasthenic syndrome. Am. J. Hum. Genet. 2002; 70: 875–85.

Ohno K, Hutchinson D, Milone M, Brengman JM, Bouzatt C, Sinet SM, et al. Congenital myasthenic syndrome caused by prolonged acetylcholine receptor channel openings due to a mutation in the M2 domain of the E subunit. Proc. Natl. Acad. Sci. 1995; 92: 758–762.

Ohno K, Tsujino A, Brengman JM, Harper CM, Bajzer Z, Udd B, et al. Choline

acetyltransferase mutations cause myasthenic syndrome associated with episodic apnea in humans. Proc. Natl. Acad. Sci. U. S. A. 2001; 98: 2017–22.

Ohno K, Wang H, Milone M, Bren N, Brengman JM, Nakano S, et al. Congenital Myasthenic Syndrome Caused by Decreased Agonist Binding Affinity Due to a Mutation in the Acetylcholine Receptor ♪ Subunit. Neuron 1996; 17: 157–170.

Okada K, Inoue A, Okada M, Murata Y, Kakuta S, Jigami T, et al. The muscle protein Dok-7 is essential for neuromuscular synaptogenesis. . Science 2006; 312: 1802–5.

Okuda T, Haga T, Kanai Y, Endou H, Ishihara T. Identification and characterization of the high-affinity choline. Nat Neurosci 2000 Feb;3(2):120-5.

Oyler GA, Higgins GA, Hart RA, Battenberg E, Billingsley M, Bloom FE, et al. The Identification of a Novel Synaptosomal-associated Protein, SNAP-25, Differentially Expressed by Neuronal Subpopulations. J. Cell Biol. 1989; 109: 3039–3052.

Palace J, Beeson D. The congenital myasthenic syndromes. J. Neuroimmunol. 2008; 201–202: 2–5.

Palace J, Lashley D, Bailey S, Jayawant S, Carr A, McConville J, et al. Clinical features in a series of fast channel congenital myasthenia syndrome. Neuromuscul. Disord. 2012; 22: 112–7.

Palace J, Lashley D, Newsom-davis J, Cossins J, Maxwell S, Kennett R, et al. Clinical features of the DOK7 neuromuscular junction synaptopathy. Brain 2007; 130: 1507–1515.

Palace J, Wiles CM, Newsom-Davis J. 3,4-Diaminopyridine in the treatment of congenital (hereditary) myasthenia. J. Neurol. Neurosurg. Psychiatry 1991; 54: 1069–1072.

Palmieri L, Rastelli G. Alpha-C Helix Displacement As a General Approach for Allosteric Modulation of Protein Kinases . Drug Discov. Today 2013; 18: 407–414.

Pang ZP, Melicoff E, Padgett D, Liu Y, Teich AF, Dickey BF, et al. Synaptotagmin-2 Is Essential for Survival and Contributes to Ca 2 ƨ Triggering of Neurotransmitter Release in Central and Neuromuscular Synapses. 2006; 26: 13493–13504.

Parr JR, Andrew MJ, Finnis M, Beeson D, Vincent A, Jayawant S. How common is childhood myasthenia? The UK incidence and prevalence of autoimmune and congenital myasthenia. Arch. Dis. Child. 2014: 5–9.

Patrick GN, Zukerberg L, Nikolic M, de la Monte S, Dikkes P, Tsai L-H. Conversion of p35 to p25 deregulates Cdk5 activity and promotes neurodegeneration. Nature 1999; 402: 615–622.

Peltonen S, Hentula M, Hägg P, Ylä-Outinen H, Tuukkanen J, Lakkakorpi J, et al. A novel component of epidermal cell-matrix and cell-cell contacts: Transmembrane protein type

XIII collagen. J. Invest. Dermatol. 1999; 113: 635–642.

Peng HB, Ali A, Dagget D, Rauvala H, Hassell J, Smalheiser N. The relationship between perlecan and dystroglycan and its implication in the formation of the neuromuscular junction. Cell Adhes Commun 1998; 5: 475–89.

Pette D, Staron R. Myosin isoforms, muscle fiber types, and transitions. Microsc Res Tech 2000; 50: 500–599.

Pevzner A, Schoser B, Peters K, Cosma N-C, Karakatsani A, Schalke B, et al. Anti-LRP4 autoantibodies in AChR- and MuSK-antibody-negative myasthenia gravis. J. Neurol. 2012; 259: 427–35.

Pihlajaniemi T, Tamminen M. The alpha1 chain of type XIII collagen consists of three collagenous and four noncollagenous domains, and its primary transcript undergoes complex alternative splicing. J. Biol. Chem. 1990; 265: 16922–16928.

Pineles SL, Avery RA, Moss HE, Finkel R, Blinman T, Kaiser L, et al. Visual and systemic outcomes in pediatric ocular myasthenia gravis. Am. J. Ophthalmol. 2010; 150: 453–459.

Punga AR, Maj M, Lin S, Meinen S, Rüegg MA, Ru MA. MuSK levels differ between adult skeletal muscles and influence postsynaptic plasticity. Eur. J. Neurosci. 2011; 33: 890–898

Ramarao MK, Bianchetta MJ, Lanken J, Cohen JB. Role of Rapsyn Tetratricopeptide Repeat and Coiled-coil Domains in Self-association and Nicotinic Acetylcholine Receptor Clustering. J. Biol Chem 2001; 276: 7475–83.

Ran FA, Hsu PD, Lin CY, Gootenberg JS, Konermann S, Trevino AE, et al. Double nicking by RNA-guided CRISPR cas9 for enhanced genome editing specificity . Cell 2013; 154: 1380–1389.

Ran FA, Hsu PPD, Wright J, Agarwala V, Scott D a, Zhang F. Genome engineering using the CRISPR-Cas9 system. Nat. Protoc. 2013; 8: 2281–308.

Kozera B, Rapacz M. Reference genes in real-time PCR. J Appl Genet. 2013 Nov;54(4):391-406

Régal L, Shen X-M, Selcen D, Verhille C, Meulemans S, Creemers JWM, et al. PREPL deficiency with or without cystinuria causes a novel myasthenic syndrome. Neurology 2014 Apr 8;82(14):1254-60.

Ricard-Blum S. The Collagen Family. Cold Spring Harb. Perspect. Biol. 2011: 1–9.

Richard P, Goillot E, Huze C, Gaudon K, Ammar A Ben, Chaboud A, et al. Identification of an Agrin Mutation that Causes Congenital Myasthenia and Affects Synapse Function. Am J Hum Genet. 2009 Aug;85(2):155-67.

Rimm D. Next-gen immunohistochemistry. Nat. Med. 2014; 20: 436–442.

Rinaldi C, Wood MJA. Antisense oligonucleotides: the next frontier for treatment of neurological disorders. Nat. Rev. Neurol. 2018 Jan;14(1):9-21.

Robb SA, Sewry CA, Dowling JJ, Feng L, Cullup T, Lillis S, et al. Impaired neuromuscular transmission and response to acetylcholinesterase inhibitors in centronuclear myopathies. Neuromuscul. Disord. 2011; 21: 379–86.

Rodriguez Cruz PM, Huda S, López-Ruiz P, Vincent A. Use of cell-based assays in myasthenia gravis and other antibody-mediated diseases. Exp. Neurol. 2015; 270: 66–71.

Rodríguez Cruz PM, Sewry C, Beeson D, Jayawant S, Squier W, McWilliam R, et al. Congenital myopathies with secondary neuromuscular transmission defects; A case report and review of the literature. Neuromuscul. Disord. 2014; 24: 1103–1110.

Rossi G, Cortesina G. Morphological study of the laryngeal muscles in man. Acta Otolaryngol. 1964; 59: 574–592.

Sadeh M, Xin-Ming S EA. Beneficial effect of albuterol in CMS with epsilon subunit mutations. Muscle Nerve 2012; 44: 289–291.

Salpietro V, Lin W, Vedove AD, Storbeck M, Liu Y, Efthymiou S, et al. Homozygous Mutations in VAMP1 cause a presynaptic congenital myasthenic syndrome. Ann Neurol 2017; 81: 597–603.

Samuel MA, Valdez G, Tapia JC, Lichtman JW, Sanes JR. Agrin and Synaptic Laminin Are Required to Maintain Adult Neuromuscular Junctions. PLoS One. 2012;7(10):e46663.

Sandberg-Lall M, Hägg PO, Wahlström I, Pihlajaniemi T. Type XIII collagen is widely expressed in the adult and developing human eye and accentuated in the ciliary muscle, the optic nerve and the neural retina. Exp. Eye Res. 2000; 70: 401–410.

Sander JD, Joung JK. CRISPR-Cas systems for genome editing, regulation and targeting. Nat. Biotechnol. 2014; 32: 347–355.

Sanders DB, El-Salem K, Massey JM, McConville J, Vincent a. Clinical aspects of MuSK antibody positive seronegative MG . Neurology 2003; 60: 1978–1980.

Sanes JR. The Basement Membrane / Basal Lamina of Skeletal Muscle. J. Biol. Chem. 2003; 287: 12601–4.

Sboner A, Mu XJ, Greenbaum D, Auerbach RK, Gerstein MB. The real cost of sequencing : higher than you think! Genom Biol. 2011 Aug 25;12(8):125.

Schara U, Christen H-J, Durmus H, Hietala M, Krabetz K, Rodolico C, et al. Long-term

follow-up in patients with congenital myasthenic syndrome due to CHAT mutations. . Eur. J. Paediatr. Neurol. 2010; 14: 326–33.

Schiaffino S. Tubular aggregates in skeletal muscle : Just a special type of protein aggregates ?. Neuromuscul. Disord. 2012; 22: 199–207.

Schiaffino S, Reggiani C. Myosin isoforms in mammalian skeletal muscle. J. Appl. Physiol 1994: 493–501.

Schlessinger J. Cell Signaling by Receptor Tyrosine Kinases. Cell October 2000; 103: 211–25.

Schmittgen TD, Livak KJ. Analyzing real-time PCR data by the comparative CT method . Nat. Protoc. 2008; 3: 1101–1108.

Schwab RS, Timberlake WH. Pyridostigmin (Mestinon) in the treatment of myasthenia gravis. N. Engl. J. Med. 1954; 251: 271–272.

Scuderi F, Marino M, Colonna L, Mannella F, Evoli A, Provenzano C, et al. Anti-p110 autoantibodies identify a subtype of 'seronegative' myasthenia gravis with prominent oculobulbar involvement. Lab. Invest. 2002; 82: 1139–46.

Selcen D, Ohkawara B, Shen X-M, McEvoy K, Ohno K, Engel AG. Impaired Synaptic Development, Maintenance, and Neuromuscular Transmission in LRP4-Related Myasthenia. JAMA Neurol. 2015; 72: 889–96.

Selcen D, Shen X-M, Milone M, Brengman J, Ohno K, Deymeer F, et al. GFPT1-myasthenia: clinical, structural, and electrophysiologic heterogeneity. Neurology 2013; 81: 370–8.

Selcen D, Shen X, Brengman J, Li Y, Stans AA, Wieben E, et al. DPAGT1 myasthenia and myopathy: Genetic, phenotypic, and expression studies. Neurology 2014; 82: 1822–1830.

Senderek J, Müller JS, Dusl M, Strom TM, Guergueltcheva V, Diepolder I, et al. Hexosamine biosynthetic pathway mutations cause neuromuscular transmission defect. Am. J. Hum. Genet. 2011; 88: 162–72.

Sframeli M, Sarkozy A, Bertoli M, Astrea G, Hudson J, Scoto M, et al. Congenital muscular dystrophies in the UK population: Clinical and molecular spectrum of a large cohort diagnosed over a 12-year period . Neuromuscul. Disord. 2017; 27: 793–803.

Shapira YA, Sadeh ME, Bergtraum MP, Tsujino A, Ohno K. Three novel COLQ mutations and variation of phenotypic expressivity due to G240X. Neurology 2002 Feb 26;58(4):603-9

Shen X-M, Crawford TO, Brengman J, Acsadi G, Iannaconne S, Karaca E, et al. Functional consequences and structural interpretation of mutations of human choline acetyltransferase. . Hum. Mutat. 2011; 32: 1259–67.

Shen X, Brengman J, Engel AG. Mutant SNAP25B causes myasthenia , cortical hyperexcitability , ataxia , and intellectual disability. Neurology 2014; 83: 2247–55.

Shi L, Fu AKY, Ip NY. Molecular mechanisms underlying maturation and maintenance of the vertebrate neuromuscular junction. Trends Neurosci. 2012; 35: 441–453.

Shields RW. Single fiber electromyography in the differential diagnosis of myopathic limb girdle syndromes and chronic spinal muscular atrophy. Muscle Nerve 1984; 7: 265–72.

Shiraishi H, Motomura M, Yoshimura T, Fukudome T, Fukuda T, Nakao Y, et al. Acetylcholine receptors loss and postsynaptic damage in MuSK antibody-positive myasthenia gravis. . Ann. Neurol. 2005; 57: 289–93.

Shoulders MD, Raines RT. Colagen structure and stability. Annu Rev Biochem 2009: 929–958.

Sine SM, Wang H, Shen X-M, Lee WY, Engel AG. Mechanistic diversity underlying fast channel congenital myasthenic syndrome. Ann. N. Y. Acad. Sci. 2003; 998: 128–137.

Snellman A, Keränen MR, Hägg PO, Lamberg A, Hiltunen JK, Kivirikko KI, et al. Type XIII collagen forms homotrimers with three triple helical collagenous domains and its association into disulfide-bonded trimers is enhanced by prolyl 4-hydroxylase. J. Biol. Chem. 2000; 275: 8936–8944.

Sobel A, Weber M, JP C. Large-Scale Purification of the Acetylcholine-Receptor Protein in Its Membrane-Bound and Detergent -Extracted Forms from Torpedo marmarota electric organ. Eur J Biochem 1977; 80: 215–224.

Spencer RF, Porter JD. Biological organization of the extraocular muscles. Prog. Brain Res. 2006; 151: 43–80.

Springer TA. An Extracellular B-Propeller Module Predicted in Lipoprotein and Scavenger Receptors, Tyrosine Kinases, Epidermal Growth Factor Precursor, and Extracellular Matrix Components. J Mol Biol 1998 Nov 6;283(4):837-62.

Sugiyama J, Bowen DC, Hall ZW. Dystroglycan Binds Nerve and Muscle Agrin. Neuron 1994; 13: 103–115.

Sund M, Väisänen T, Kaukinen S, Ilves M, Tu H, Autio-Harmainen H, et al. Distinct expression of type XIII collagen in neuronal structures and other tissues during mouse development. Matrix Biol. 2001; 20: 215–231.

Tabler JM, Rigney MM, Berman GJ, Gopalakrishnan S, Heude E, Al-lami HA, et al. PCilia-mediated Hedgehog signaling controls form and function in the mammalian larynx. Elife 2017; 6: 1–26.

Taniguchi M, Kurahashi H, Noguchi S, Fukudome T, Nonaka I, Toda T. Aberrant

neuromuscular junctions and delayed terminal muscle fiber maturation in alpha-dystroglycanopathies. Hum Mol Genet 2006; 15: 1279–1289.

Taylor C, Martin C, Lise S, Broxholme J, Cazier J-B, Rimmer A, et al. Factors influencing success of clinical genome sequencing across a broad spectrum of disorders. Nat. Genet. 2015; 47: 717.

Tellis CM, Rosen C, Thekdi A, Sciote JJ. Anatomy and fiber type composition of human interarytenoid muscle. Ann Otol Rhinol Laryngol 2004; 113: 97–107.

The 1000 Genomes Project. A global reference for human genetic variation. Nature 2015; 526: 68–74.

Thiel C, Schwarz M, Peng J, Grzmil M, Hasilik M, Braulke T, et al. A new type of congenital disorders of glycosylation (CDG-Ii) provides new insights into the early steps of dolichol-linked oligosaccharide biosynthesis. J. Biol. Chem. 2003; 278: 22498–505.

Till JH, Becerra M, Watty A, Lu Y, Ma Y, Neubert TA, et al. Crystal structure of the MuSK tyrosine kinase: Insights into receptor autoregulation. Structure 2002; 10: 1187–1196.

Tu H, Sasaki T, Snellman A, Göhring W, Pirilä PI, Timpl R, et al. The type XIII collagen ectodomain is a 150-nm rod and capable of binding to fibronectin, nidogen-2, perlecan, and heparin. J. Biol. Chem. 2002; 277: 23092–99.

Vandesompele J, De Preter K, Poppe B, Roy N Van, De Paepe A. Accurate normalization of real-time quantitative RT -PCR data by geometric averaging of multiple internal control genes. Genome Biol. 2002 Jun 18;3(7):RESEARCH0034.

Vincent A. Unravelling the pathogenesis of myasthenia gravis. Nat. Rev. Immunol. 2002; 2: 797–804.

Vincent A, Cull-Candy SG, Newsom-Davis J, Trautmann A, Molenaar PC, Polak RL. Congenital myasthenia: end-plate acetylcholine receptors and electrophysiology in five cases. Muscle Nerve 1981 Jul-Aug;4(4): 306–18.

Vincent A, Huda S, Cao M, Cetin H, Koneczny I, Rodriguez-Cruz P, et al. Serological and experimental studies in different forms of myasthenia gravis. Ann. N. Y. Acad. Sci. 2018 Feb;1413(1):143-153.

Vincent A, Newsom-Davis J. Acetylcholine receptor antibody as a diagnostic test for myasthenia gravis: results in 153 validated cases and 2967 diagnostic assays. J. Neurol. Neurosurg. Psychiatry 1985; 48: 1246–52.

Vincent A, Newson-Davis J, Wray D, Shillito P, Harrison J, Betty B, et al. Clinical and Experimental Observations in Patients with Congenital Myasthenic Syndromes. Ann. N. Y. Acad. Sci. 1993; 681: 451–460.

Vincent A, Waters P, Leite MI, Jacobson L, Koneczny I, Cossins J, et al. Antibodies identified by cell-based assays in myasthenia gravis and associated diseases. Ann. N. Y. Acad. Sci. 2012; 1274: 92–8.

Vogt J, Harrison BJ, Spearman H, Cossins J, Vermeer S, Naudin L, et al. Mutation Analysis of CHRNA1 , CHRNB1 , CHRND , and RAPSN Genes in Multiple Pterygium Syndrome / Fetal Akinesia Patients. Am. J. Hum. Genet. 2008; 88: 222–227.

Webster R, Maxwell S, Spearman H, Tai K, Beckstein O, Sansom M, et al. A novel congenital myasthenic syndrome due to decreased acetylcholine receptor ion-channel conductance. . Brain 2012; 135: 1070–80.

Weinkam P, Chen YC, Pons J, Sali A. Impact of mutations on the allosteric conformational equilibrium. J Mol Biol. 2013; 425: 647–661.

Wheeler DS, Spaeth JP, Mehta R, Hariprakash SP, Cox PN. Assessment and Management of the Pediatric Airway. In: Paediatric Critical Care Medicine Basic Science and Clinical Evidence. 2007. p. 223–253.

Wheeler HE, Shah KP, Brenner J, Garcia T, Aquino-Michaels K, Cox NJ, et al. Survey of the Heritability and Sparse Architecture of Gene Expression Traits across Human Tissues. PLoS Genet. 2016; 12: 1–23.

Wolfe GI, Kaminski HJ, Aban G, Minisman H, Kuo AM, Ströbel P, et al. Randomized Trial of Thymectomy in Myasthenia Gravis G.I. N. Engl. J. Med. 2017; 375: 511–522.

Wood ER, Truesdale AT, Mcdonald OB, Yuan D, Hassell A, Dickerson SH, et al. A Unique Structure for Epidermal Growth Factor Receptor Bound to GW572016 (Lapatinib): Relationships among Protein Conformation, Inhibitor Off-Rate, and Receptor Activity in Tumor Cells. Cancer Res. 2004 Sep 15;64(18):6652-9.

Wood SJ, Slater CR. Safety factor at the neuromuscular junction. Prog. Neurobiol. 2001; 64: 393–429.

Wu C, Orozco C, Boyer J, Leglise M, Goodale J, Batalov S, et al. BioGPS: an extensible and customizable portal for querying and organizing gene annotation resources. Genome Biol. 2009; 10(11): R130.

Wu H, Xiong WC, Mei L. To build a synapse : signaling pathways in neuromuscular junction assembly. Development 2010; 1033: 1017–1033.

Wu X, Rush JS, Karaoglu D, Krasnewich D, Lubinsky MS, Waechter CJ, et al. Deficiency of UDP-GlcNAc:Dolichol Phosphate N-Acetylglucosamine-1 Phosphate Transferase (DPAGT1) causes a novel congenital disorder of Glycosylation Type Ij. Hum. Mutat. 2003; 22: 144–50.

Yang X, Arber S, William C, Li L, Tanabe Y, Jessell TM, et al. Patterning of muscle

acetylcholine receptor gene expression in the absence of motor innervation. Neuron 2001; 30: 399–410.

Ylönen R, Kyrönlahti T, Sund M, Ilves M, Lehenkari P, Tuukkanen J, et al. Type XIII collagen strongly affects bone formation in transgenic mice. J. Bone Miner. Res. 2005; 20: 1381–1393.

Yoshihara T, Kanda T, Yaku Y, Kaneko T. Neuromuscular Junctions of the Posterior Cricoarytenoid Muscle in the Human Adult , Human Fetus and Cat. Acta Oto-laryngologica 1984; 97: 161–168.

Yumoto N, Kim N, Burden SJ. Lrp4 is a retrograde signal for presynaptic differentiation at neuromuscular synapses. Nature 2012; 489: 438–42.

Zenker M, Aigner T, Wendler O, Tralau T, Mu H, Royer-pokora B, et al. Human laminin beta2 deficiency causes congenital nephrosis with mesangial sclerosis and distinct eye abnormalities. Hum Mol Genet 2004 Nov 1;13(21):2625-32

Zhang B, Shen C, Bealmear B, Ragheb S, Xiong W-C, Lewis R a, et al. Autoantibodies to agrin in myasthenia gravis patients. . PLoS One 2014; 9: e91816.

Zhang B, Tzartos JS, Belimezi M, Ragheb S, Bealmear B, Lewis R a, et al. Autoantibodies to lipoprotein-related protein 4 in patients with double-seronegative myasthenia gravis. Arch. Neurol. 2012; 69: 445–51.

Zhang W, Coldefy A-S, Hubbard SR, Burden SJ. Agrin binds to the N-terminal region of Lrp4 protein and stimulates association between Lrp4 and the first immunoglobulin-like domain in muscle-specific kinase (MuSK). J. Biol. Chem. 2011; 286: 40624–30.

Zhang X, Gureasko J, Shen K, Cole PA, Kuriyan J. An Allosteric Mechanism for Activation of the Kinase Domain of Epidermal Growth Factor Receptor. Cell 2006; 125: 1137–1149.

Zhang X, Yang M, Xu J, Zhang M, Lang B, Wang W, et al. Clinical and serological study of myasthenia gravis in HuBei Province, China. J. Neurol. Neurosurg. Psychiatry 2007; 78: 386–90.

Zhu H, Pytel P, Gomez CM. Selective inhibition of caspases in skeletal muscle reverses the apoptotic synaptic degeneration in slow-channel myasthenic syndrome. Hum. Mol. Genet. 2014; 23: 69–77.

Zisimopoulou P, Evangelakou P, Tzartos J, Lazaridis K, Zouvelou V, Mantegazza R, et al. A comprehensive analysis of the epidemiology and clinical characteristics of anti-LRP4 in myasthenia gravis. J. Autoimmun. 2014 Aug; 52: 139-45.

Zoltowska K, Webster R, Finlayson S, Maxwell S, Cossins J, Müller J, et al. Mutations in GFPT1 that underlie limb-girdle congenital myasthenic syndrome result in reduced cell-surface expression of muscle AChR. . Hum. Mol. Genet. 2013; 22: 2905–13.

Zoltowska Katarzyna M, Belaya K, Leite M, Patrick W, Vincent A, Beeson D. Collagen Q - A potential target for autoantibodies in myasthenia gravis. J. Neurol. Sci. 2014; 348: 241–244.

Zong Y, Zhang B, Gu S, Lee K, Zhou J, Yao G, et al. Structural basis of agrin – LRP4 – MuSK signaling. 2012; 4: 247–258.

Zoumalan R, Maddalozzo J, Holinger LD. Etiology of stridor in infants. Ann. Otol. Rhinol. Laryngol. 2007; 116: 329–334.

Zuber B, Unwin N. Structure and superorganization of acetylcholine receptor – rapsyn complexes. PNAS 2013; 110: 10622–10627.

Appendix

10.1 Generation of C2C12 *Col13a1* 1171delG cell line

CRISPR-Cas9 genome-editing technology was used to engineered the homologous COL13A1 c.1171delG mutation into the mouse myoblast C2C12 cell line using standard methods (Fa Ann Ran *et al.*, 2013). As already stated in the main text, this experiment was performed by Dr Judy Cossins (University of Oxford) and details are provided for information purposes. In brief, guide oligonucleotides and a repair-template oligonucleotide (Integrated DNA Technologies) were cloned into an adapted plasmid based on pX335-U6-Chimeric_BB-CBh-hSpCas9n(D10A), a kind gift from Feng Zhang (Addgene plasmid no. 42335). Guide A oligonucleotide sequences were 5'-CACCGAGAGATATGGAGCCCCAAAG-3' (forward) and 5'-AAACCTTTGGGGCTCCATATCT CTC-3' (reverse). Guide B oligonucleotides were 5'-CACCGTGGCAGCAAAAACTCACCTT-3' (forward) and 5'-AAACAAGGTGAGTTTTTGCTGCCAC-3' (reverse). The repair template was 5'-CAGGGAGAAAAAGGTGATGCTGGCAATGCCATCGGAGGAGGCAGGGGGGAGCCTGGCCCC CCGGGGTCCCTGGGCCCCCTGGGCCAAAGGTGAGTTTTTGCTGCCATCTGCATTGAGAGAGATA TGGAGCCCCAAAGAGTCACAG-3'.

C2C12 cells were electroporated with 20 µg of plasmid and 10 µl repair-template oligonucleotide (10 µM) with a Neon electroporator (Life Technologies), selected with 1 mg/ml G418 (Life Technologies), and cloned by serial dilution in 96-well flat-bottomed culture plates. The clones were assessed by PCR of genomic DNA by using the primer pair 5'-GGTTGACCCAGAAACCCCAA-3' and 5'-ACTTATGACTCCATGCCCAGG-3'. Successful mutagenesis was confirmed by the creation of a new *KpnI* restriction site and the

presence of the deletion after Sanger sequencing. More details are available in (Logan *et al.*, 2015).

10.2 Generation of C2C12 *MuSK* KO cell lines

10.2.1 Use of CRISPR-Cas9 genome engineering system

C2C12 myoblasts were electroporated with 10µg of each pX335_Cas9n plasmid containing the single strand oligonucleotides MUSK guides A or B (Section 2.3.1) in order to produce spontaneous indels via non-homologous end-joining leading to protein truncation.

Myoblasts from different clones were differentiated into myotubes by serum starvation (Section 2.8.2) and incubated with full-length agrin overnight for the induction of AChR clusters (Section 2.5.10). From the 40 starting clones, 10 (25%) managed to differentiate into myotubes and 4 (10%) had complete absence of AChR clusters after incubation with full-length human agrin overnight. A number of clones producing abnormal clusters were considered non-optimal **(Figure 10-1).** Clonal line KO-1 was found to readily differentiate into myotubes and thus was selected for further experiments. Clonal line KO-7 was selected as a back-up clone. The DNA from each of these clones was extracted, amplified by PCR of genomic DNA (Section 2.3.2) and resolved by gel electrophoresis.

Sanger sequencing of clone KO-1 PCR products was difficult to interpret due to the presence of multiple overlapping sequences. Therefore, the PCR products were subcloned into pGEM-T-Easy for segregation. Subsequent sequencing showed the presence of four different variants **(Figure 10-2)**. Sanger sequencing of clone KO-7 showed a homozygous

216 bp deletion of exon 3 and intronic boundaries **(Figure 10-3A,B).** Amplification of cDNA after RNA extraction showed that the intronic deletion caused aberrant splicing of *Musk* exon 3 **(Figure 10-3C)**.

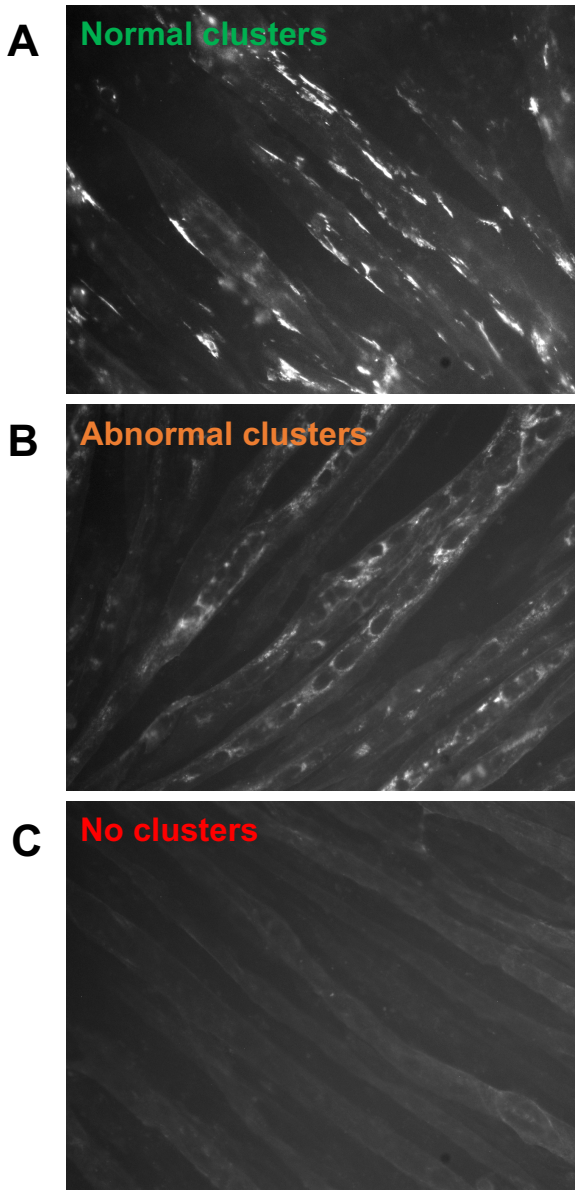


Figure 10-1. Representative images of AChR clusters in C2C12 myotubes engineered with CRISPR-Cas9n after incubation with agrin

C2C12 myoblasts were gene-edited with CRISPR-Cas9n via non-homologous end joining (NHEJ) followed by clonal isolation and expansion. Myoblast were differentiated into myotubes and incubated with full-length agrin overnight for 16 hours. Representative

microscopic fields of AChR clusters labelled with Alexa Fluor® 594-conjugated α-bungarotoxin showing the variety of AChR clusters resulting from the gene-editing process. Clonal lines producing normal **(A)** or abnormal **(B)** clusters were discarded as not indicative of definitive *Musk* KO. Only clonal lines completely lacking AChR clusters after agrin incubation were selected **(C)**.

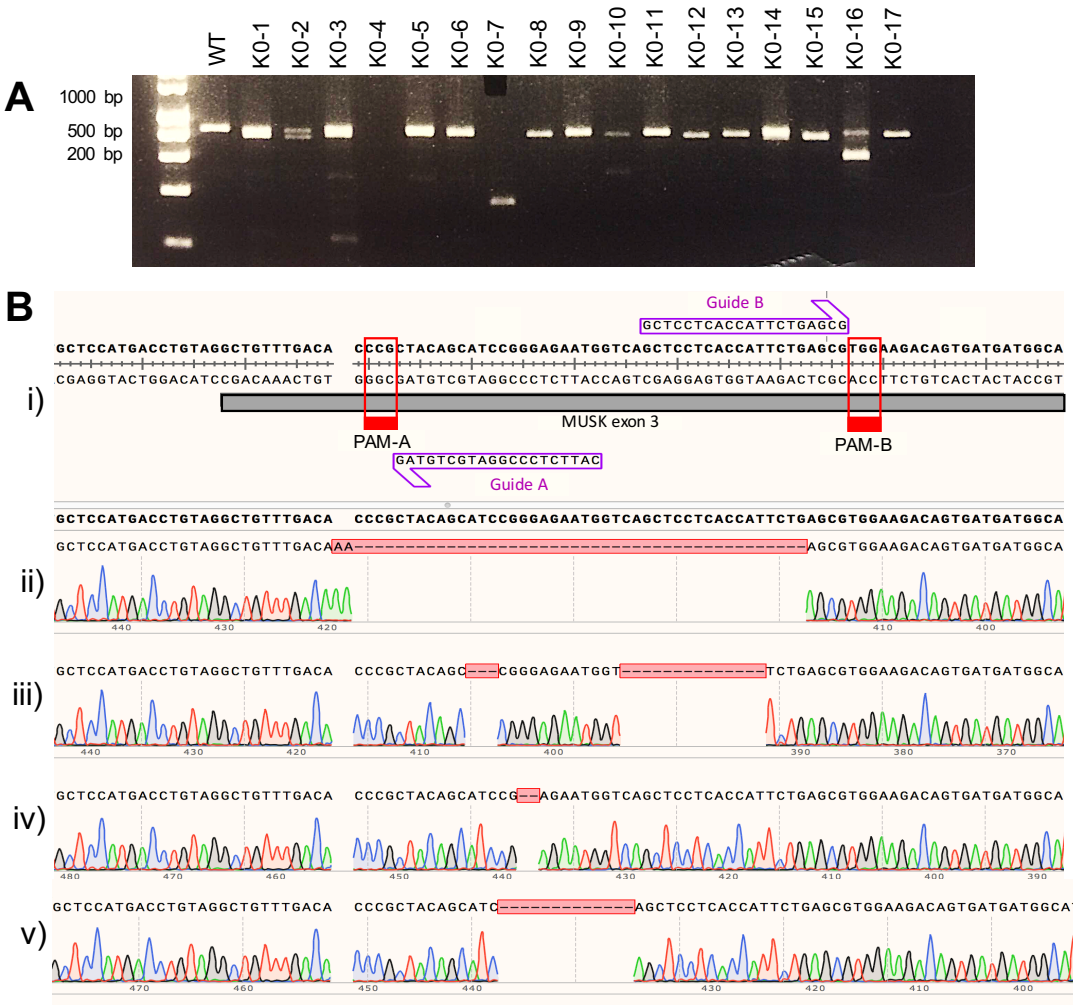


Figure 10-2. Genotype analysis of CRISPR-generated *Musk* KO clonal line KO-1

(A) Genomic PCR analysis of the *Musk* region comprising the CRISPR target sites for WT and *Musk* KO clonal cell lines. Expected product size was 810 bp in size.

(B) The PCR products from genomic DNA of KO-1 were subcloned into pGEM-T-Easy and segregated. Ten of the purified plasmids were analysed by DNA sequencing and 4 different variants of *Musk* compared to Ref Seq NM_001037127.2 were identified:

i) Representation of *Musk* exon 3 and genomic boundaries (Ref Seq NM_001037127.2) including the protospacer adjacent motifs (PAM) and genomic targets of CRISPR Cas9 gRNAs.

i) 2 bp insertion + 44 bp deletion: c.217_219insAA + c.211_255delCCCGCTACAGCATCCGGGA GAATGGTCAGCTCCTCACCATTCTG

ii) 3 bp deletion + 14 bp deletion: c.229_231delATC + c.243_255delCAGCTCCTCACCAT

iii) 2 bp deletion: c.233_235delGG

iv) 10 bp deletion: c.231_240delCGGGAGAATGGTC

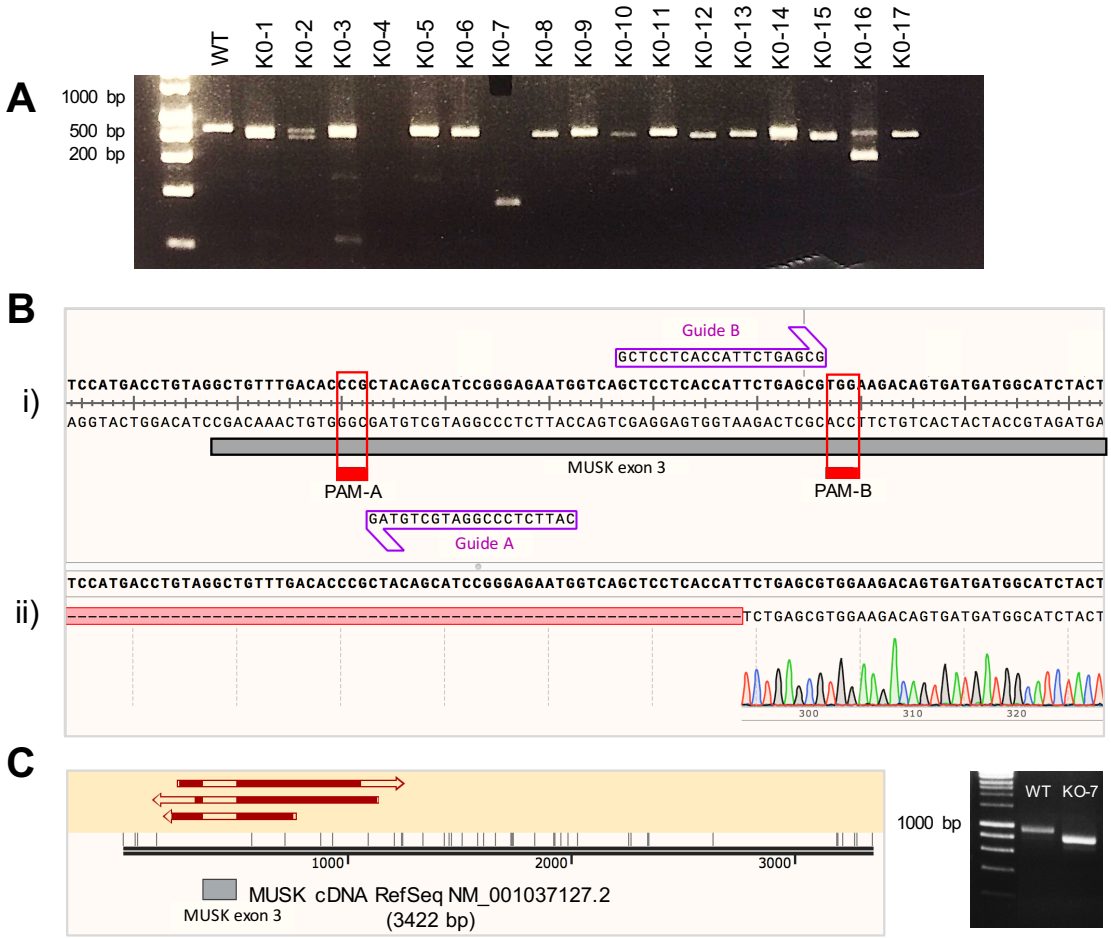


Figure 10-3. Genotype analysis of CRISPR-generated *Musk* KO clonal line KO-7

(A) Genomic PCR analysis of the *Musk* region comprising the CRISPR target sites for WT and *Musk* KO clonal cell lines. Expected product size was 810 bp in size.

(B) The PCR products from clone KO-7 were analysed by Sanger sequencing.

i) Representation of *Musk* exon 3 and genomic boundaries (RefSeq NM_001037127.2) including the protospacer adjacent motifs (PAM) and genomic targets of CRISPR Cas9 gRNAs.

ii) Alignment analysis showed a 216 bp deletion, comprising 51bp of exon 3 and 165bp of the intronic region: c.2017-165del + c.207_257del. Unlike clone KO1, there were no multiple sequences.

(C) RNA was extracted and reverse transcribed (Section 2.4.4). The obtained cDNA was amplified using primers in Table 2-4. The products were resolved by gel electrophoresis, gel-extracted and analysed by Sanger sequencing. The results show how the intronic deletion caused aberrant splicing of *Musk* exon 3.

Sanger sequencing analysis of KO-1 cell line PCR products after segregation showed the presence of 4 different DNA sequences. Similar observations have been made by members of our laboratory in other C2C12 clonal cell lines. This suggests that C2C12 is very likely to be a polyploid cell line, which contains more than 2 copies of *Musk* in a single cell. One study looking at the morpho-functional characterisation of C2C12 has also proposed this idea (Burattini *et al.*, 2004). An alternative, but less likely possibility, would be the generation of new indels by the Cas9n after clonal isolation. From the 4 variants detected in the KO-1 cell line, three originated a frameshift mutation leading to a premature stop codon and one caused a missense mutation (p.T73K) followed by a deletion of 14 aminoacids (p.R74_L87del) **(Figure 10-4)**. Since the KO-1 cell line did not generate AChR clusters after agrin incubation, it is likely that the allele containing the in frame deletion is non-functional and, therefore, all the variants identified in the KO-1 cell line lead to a non-functional MuSK protein.

RNA analysis of KO-7 cell line showed how *MusK* exon 3 was spliced from the cDNA sequence. Due to p.Ile70 being encoded by nucleotides from different exons at the exon-intron boundaries, the aberrant splicing changed the reading frame leading to a premature stop codon **(Figure 10-4).**

In summary, since the objective of this work was to generate a C2C12 cell line not expressing functional MuSK, both cell lines are appropriate. The decision to choose the KO-1 cell line for subsequent experiments was based on the better properties for differentiation into myotubes.

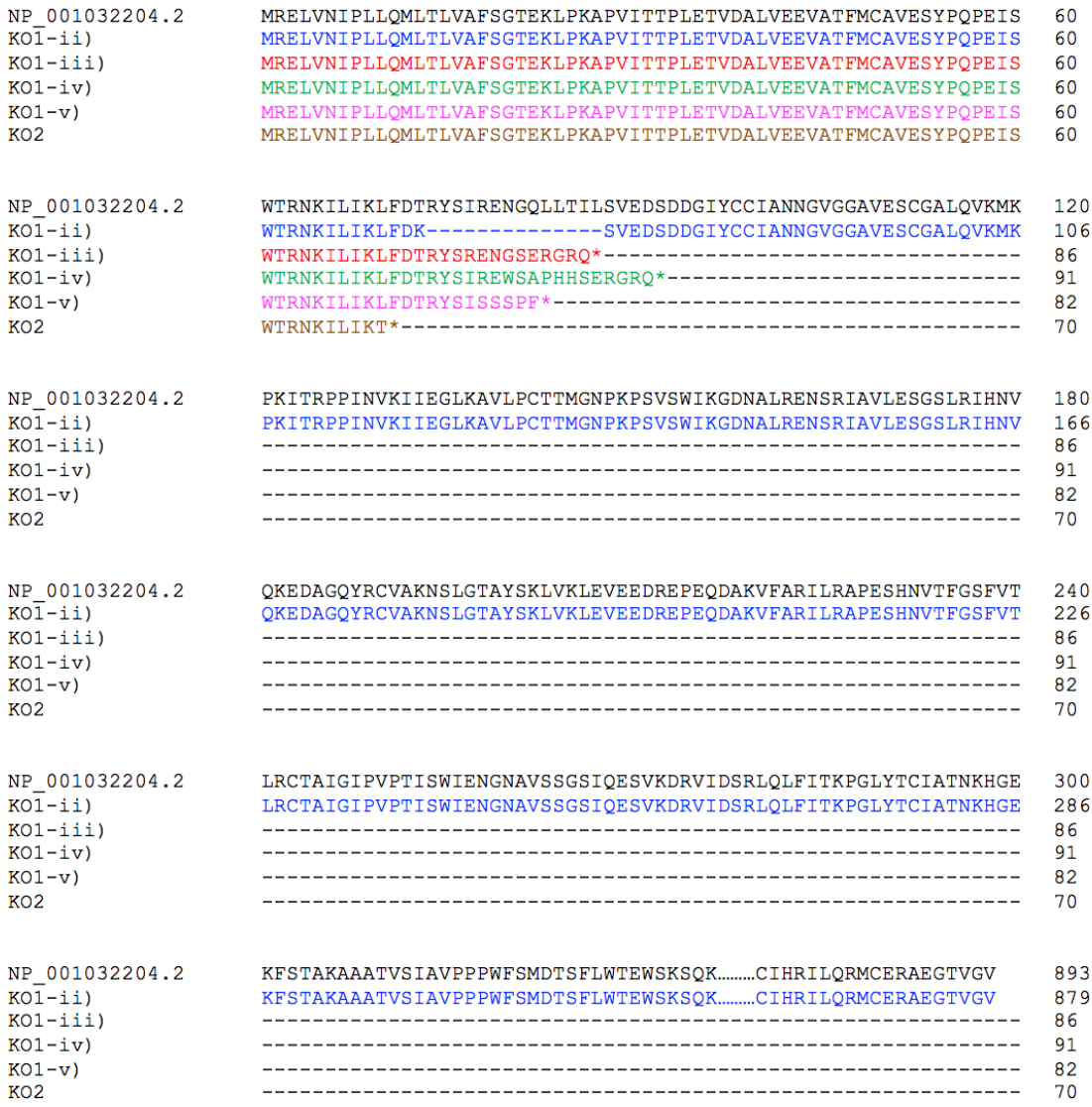


Figure 10-4. Alignment of amino acid sequences from mutant MuSK alleles in KO-1 and KO-2 clonal cell lines to WT sequence (NP_001032204.2)

The mutations identified in the alleles iii), iv) and v) from KO-1 cell line and the homozygous mutation in the KO-2 cell line shifted the coding sequences of MuSK resulting in the truncation of the protein. The mutation identified in the KO-1 ii) allele resulted in a missense mutation (p.T73K) followed by a deletion of 14 aminoacids (p.R74_L87del).

10.2.2 MuSK protein expression in C2C12 Musk KO clonal cell lines

To confirm that the mutations described above caused a truncation of MuSK protein, cell lysates from control C2C12, KO-1, and KO-7 myotubes were analysed by western blotting

with antibodies against MuSK and α-tubulin. According to the manufacturer, the R&D AF-562 anti-MuSK antibody was developed using mouse myeloma cell line NS0-derived recombinant rat MuSK. The results showed the lack of MuSK protein expression in the KO cell lines, thus confirming the truncation of the protein **(Figure 10-5)**.

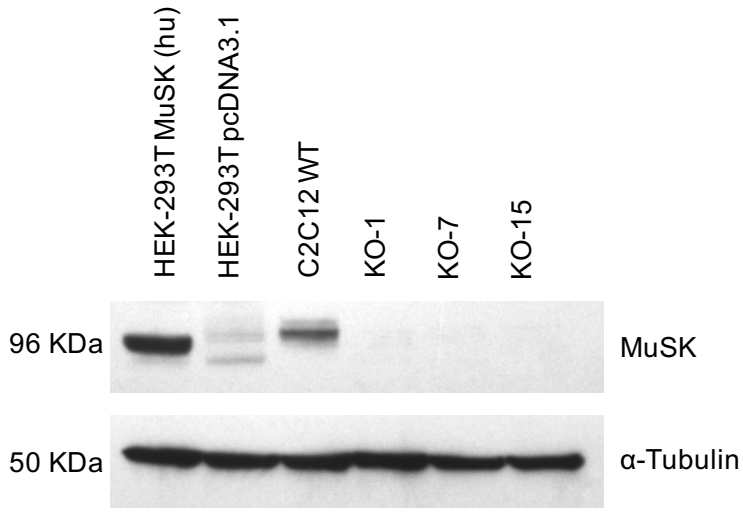


Figure 10-5. MuSK expression in C2C12 WT and *Musk* KO cell lines

Lysates from mouse C2C12 WT and *MusK* KO cell lines were prepared, resolved by SDS-PAGE, and analysed by western blotting using antibodies against MuSK and α-tubulin. HEK-293T cells transiently transfected with expression vectors encoding human MuSK transcript variant 1 (Refseq NM_005592) and pcDNA3.1/Hygro(+) were used as controls.

10.3 Details of patients with *DOK7* mutations included in this thesis

Details of patients with *DOK7* mutations with and without stridor included in Chapter 7 are provided in **Table 10-1** and **Table 10-2**.

Table 10-1. Details of DOK7-CMS patients with stridor

Age (y)	DOK7 mutations		Onset	Grade (*)	Tracheo	Decan.	Vent support	BVCP	Qx	Other
51	c.1124_1127dupTGCC	c.1339_1342dupCTGG	Birth	Mild	No	-	No	-	No	No
43	c.1143dupC	c.1143dupC	Birth	Mild	No	-	No	-	No	No
14	c.325G>T	c.596delT	Birth	Mild	No	-	No	-	No	Fd
19	c.415G>C	c.415G>C	Birth	Mild	No	-	No	Yes	No	Fd, Lw
14	c.1124_1127dupTGCC	c.10124_141del:176_206delinsAG	Birth	Severe	No	-	?	?	Yes	No
7	c.1511_1513delCTT	c.1511_1513delCTT	Birth	Severe	No	-	Yes	Yes	Yes	No
16	c.1124_1127dupTGCC	c.1378dupC	Birth	Severe	Yes	Yes (3y)	Yes	Yes	Yes	Fd
8	c.1143delC	c.1378dupC	Birth	Severe	Yes	No	Yes	Yes	No	No
19	c.1143dupC	c.54+8_25_39del15	Birth	Severe	Yes	Yes (1y)	Yes	-	No	Fd, Lw
20	c.1378C>T	c.1339_1342dupCTGG	Birth	Severe	Yes	No	Yes	Yes	No	No
41	c.414C>T	c.1339_1342dupCTGG	Birth	Severe	Yes	No	Yes	Yes	No	No
14	c.496G>A	c.1339_1342dupCTGG	Birth	Severe	Yes	Yes (7y)	Yes	Yes	No	No
35	c.1124_1127dupTGCC	c.1339_1342dupCTGG	Childhood	Mild	No	-	No	-	No	-
38	c.1124_1127dupTGCC	c.473G>A	Childhood	Mild	No	-	No	-	No	-
43	c.1124_1127dupTGCC	c.48C>T	Childhood	Mild	No	-	No	Yes	No	-
39	c.1124_1127dupTGCC	Deletion exon 1-2	Childhood	Mild	No	-	No	-	No	-

29	c.414C>T	c.1339_1342dupCTGG	Childhood	Mild	No	-	No	-	No	-
56	c.1124_1127dupTGCC	Deletion exon 1-2	Childhood	Moderate	No	-	Yes	-	No	-
45	c.1124_1127dupTGCC	c.1339_1342dupCTGG	Adulthood	Mild	No	-	No	-	No	-
68	c.1124_1127dupTGCC	c.48C>T	Adulthood	Mild	No	-	No	Yes	No	-
38	c.1378dupC	c.1449delG	Adulthood	Mild	No	-	No	-	No	-
37	c.1511_1513delCTT	c.1511_1513delCTT	Adulthood	Mild	No	-	No	-	No	-
66	c.331+4A>G (intronic)	c.1413delT	Adulthood	Mild	No	-	No	-	No	-
67	c.1124_1127dupTGCC	c.1124_1127dupTGCC	Adulthood	Severe	Yes	No	Yes	-	No	-

(*) The severity of stridor was classified as severe (need for tracheostomy or laryngeal surgery), moderate (need for ventilator support) or mild (rest). BVCP, Bilateral vocal cord palsy; Decan, decannulation; Fd, Feeding difficulties; Lw, limb weakness; y, years; Qx, laryngeal surgery.

Table 10-2. Details of DOK7-CMS patients without stridor

n	Age	DOK7 mutations		n	Age	DOK7 mutations	
1	-	c.1124_1127dupTGCC	c.101-24_141del:176_206delinsAG	16	-	c.1124_1127dupTGCC	c.54+8_54+17del10
2	-	c.1124_1127dupTGCC	c.1124_1127dupTGCC	17	-	c.1124_1127dupTGCC	c.553-37_c.533-11del27
3	-	c.1124_1127dupTGCC	c.1124_1127dupTGCC	18	-	c.1124_1127dupTGCC	c.553-37_c.533-11del27
4	-	c.1124_1127dupTGCC	c.1124_1127dupTGCC	19	-	c.1124_1127dupTGCC	c.91C>A
5	-	c.1124_1127dupTGCC	c.1124_1127dupTGCC	20	-	c.1143dupC	c.1143dupC
6	-	c.1124_1127dupTGCC	c.1124_1127dupTGCC	21	-	c.1263delC	c.54+8_54+17del10
7	-	c.1124_1127dupTGCC	c.1124_1127dupTGCC	22	-	c.230C>T	c.230C>T
8	-	c.1124_1127dupTGCC	c.1263dupC	23	-	c.414C>T	c.1339_1342dupCTGG
9	-	c.1124_1127dupTGCC	c.1263dupC	24	-	c.437delC	c.1487G>T
10	-	c.1124_1127dupTGCC	c.1263dupC	25	-	c.481G>A	C.1504_1505insTA
11	-	c.1124_1127dupTGCC	c.437delC				
12	-	c.1124_1127dupTGCC	c.513C>T				
13	-	c.1124_1127dupTGCC	c.513C>T				
14	-	c.1124_1127dupTGCC	c.54+8_25_39del15				
15	-	c.1124_1127dupTGCC	c.54+8_25_39del15				

10.4 Review on congenial myopathies with secondary neuromuscular transmission abnormalities

A review on this group of disorders is provided at the end of the appendix section.